SPATIAL AND TEMPORAL ANALYSIS OF SNOWPACK STRENGTH AND STABILITY AND ENVIRONMENTAL DETERMINANTS ON AN INCLINED, FOREST OPENING

by

Eric Robert Lutz

A dissertation submitted in partial fulfillment
of the requirements for the degree

of

Doctor of Philosophy

in

Earth Sciences

MONTANA STATE UNIVERSITY
Bozeman, Montana, U.S.A.

April 2009

APPROVAL

of a dissertation submitted by

Eric Robert Lutz

This dissertation has been read by each member of the dissertation committee and has been found to be satisfactory regarding content, English usage, format, citation, bibliographic style, and consistency, and is ready for submission to the Division of Graduate Education.

Dr. Katherine Hansen Crawford

Approved for the Department of Earth Science

Dr. Stephan Custer

Approved for the Division of Graduate Education

Dr. Carl A. Fox

STATEMENT OF PERMISSION TO USE

In presenting this dissertation in partial fulfillment of the requirements for a doctoral degree at Montana State University, I agree that the Library shall make it available to borrowers under rules of the Library. I further agree that copying of this dissertation is allowable only for scholarly purposes, consistent with "fair use" as prescribed in the U.S. Copyright Law. Requests for extensive copying or reproduction of this dissertation should be referred to ProQuest Information and Learning, 300 North Zeeb Road, Ann Arbor, Michigan 48106, to whom I have granted "the exclusive right to reproduce and distribute my dissertation in and from microform along with the non-exclusive right to reproduce and distribute my abstract in any format in whole or in part."

Eric Robert Lutz

April, 2009

ACKNOWLEDGEMENTS

To my wife, Rachel, and children, Elsa, Freya, and Theodore, I am grateful for your love and support. I am indebted to the field crew that brought invaluable enthusiasm and curiosity with them: Phillip 'Pip' Bell, Hayes Buxton, Kasper Engelhardt, Patricia 'Trish' Jenkins, Matt Klick, Kalle Kronholm, Signe Leirfallom, Spencer Logan, Shannon Moore, Kent Scheler, and my wife, Rachel. I am grateful to my project supervisors and scientific mentors, Karl Birkeland and Kathy Hansen Crawford, for your trust and guidance. I thank committee member Hans-Peter Marshall for advice on micro-mechanical models and statistical testing, and committee members Harry Benham, John Borkowski, and Stephan Custer for valuable feedback. I thank Martin Schneebeli for feedback that improved the quality of this study. SnowMicroPen technical support was also provided by Martin, and by Reto Wetter. I thank Richard Aspinall for inspiring conversations on spatial analysis, Ed Adams and Ladean McKittrick for discussions on radiation modeling, and Daryl Myers for enthusiastically helping me apply the Bird Radiation Model and for suggestions on atmospheric data sources. I thank Doug Chabot, Ron Johnson and Scott Schmidt of the Gallatin National Forest Avalanche Center for monitoring weak layer development and for providing snowmobiles when needed. I am grateful to Aiden Downey and Yanna Yannakakis, Karen and Stewart Mitchell, Erich Peitzsch, Simon Trautman, Ryan Bergstrom, Mark Skidmore, my parents, Margarethe and Mark Lutz, and siblings, Andrea, Christine, and Oliver, for continued guidance and moral support. Partial funding was provided by the U.S. National Science Foundation's Geography and Regional Science (Grant No. BCS-024310) and GK-12 Programs.

TABLE OF CONTENTS

TABLE OF CONTENTS - CONTINUED

TABLE OF CONTENTS - CONTINUED

TABLE OF CONTENTS - CONTINUED

TABLE OF CONTENTS - CONTINUED

TABLE OF CONTENTS - CONTINUED

TABLE OF CONTENTS - CONTINUED

LIST OF TABLES

Table Page

LIST OF TABLES - CONTINUED

Table Page

LIST OF TABLES - CONTINUED

Table Page

LIST OF TABLES - CONTINUED

Table Page

LIST OF TABLES - CONTINUED

Table Page

LIST OF FIGURES

LIST OF FIGURES - CONTINUED

LIST OF FIGURES - CONTINUED

LIST OF FIGURES - CONTINUED

Figure Page

LIST OF FIGURES - CONTINUED

Figure Page

LIST OF FIGURES - CONTINUED

Figure Page

LIST OF FIGURES - CONTINUED

Figure Page

LIST OF FIGURES - CONTINUED

Figure Page

LIST OF FIGURES - CONTINUED

Figure Page

LIST OF FIGURES - CONTINUED

Figure Page

GLOSSARY

List of symbols for terminology frequently referenced in this manuscript:

Radiation variables:

$v_{\%}$	Hemispheric sky visibility (%)
$L_{\downarrow}$	Incoming longwave radiation flux ($W \cdot m^{-2}$)
I_{max}	Maximum global (diffuse and direct) shortwave radiation on modeled surface ($W \cdot m^{-2}$)
$\sum I$	Cumulative global (diffuse and direct) shortwave radiation on modeled surface ($MJ \cdot m^{-2}$)
$\sum t_I$	Cumulative exposure time to direct shortwave radiation (Hrs)
t_{Imax}	Time of day at which I_{max} occurred

Stratigraphic variables:

HS	Vertical snow depth (cm)
$h_{snowpack}$	Slope-normal snowpack thickness (cm)
h_{base}	Slope-normal snow base thickness (below weak layer) (cm)
h_{wl}	Slope-normal weak layer thickness (mm)
h_{slab}	Slope-normal slab thickness (above weak layer) (mm)

Microstructural variables:

F	Penetration resistance (N)
F_m	Mean penetration resistance (N)
F_{max}	Maximum penetration resistance (N)
F_{cv}	Coefficient of variation of penetration resistance (%)
f	Rupture force (N)
f_m	Mean rupture force (N)

GLOSSARY – CONTINUED

f_{max}	Maximum rupture force (N)
f_{cv}	Coefficient of variation of rupture force (%)
L	Structural element length (mm)
L_{max}	Maximum structural element length (mm)
N_f	Number of ruptures in a SMP profile segment
N_F	Number of resistance recordings in a SMP profile segment
σ_{micro}	Micro-strength ($N \cdot mm^{-2}$)
$\Delta\ldots$	Microstructural step-change of …

Slab load-related variables

HSW_{slab}	Water equivalent of slab (mm)
V_{slab}	Slab vertical stress (Pa)
N_{slab}	Slab normal stress (Pa)
τ_{slab}	Slab shear stress (Pa)

Shear frame variables

τ_{250}	Observed shear strength (Pa)
$\tau_{expt.}$	Shear stress of experimental set-up (Pa)
τ_{total}	Total shear strength (Pa), $\tau_{250} + \tau_{expt.}$
τ_{∞}	Size-corrected τ_{total} (Pa), 0.65 * τ_{total}
τ_{resid}	Residual shear strength (Pa), τ_{∞} - τ_{total}
S	Stability index (Ratio), $\tau_{\infty} / \tau_{slab}$

Statistical values

P_{Wilco}	The pit-to-plot ratios for central tendency

GLOSSARY – CONTINUED

P_{KS}	The pit-to-plot ratios for distribution
p (-value)	Statistic that indicates whether or not a sample supports a null hypothesis. It is the probability of obtaining by chance a finding that indicates the null hypothesis can be rejected, despite the null hypothesis holding true.
r^2	Coefficient of determination of a linear fit
m	Coefficient describing the slope of a linear fit
b	y-intercept of a linear fit

ABSTRACT

Avalanche hazard evaluation relies on snowpack stability observations. Because snowpack properties can vary extensively over time and space, estimating slope-scale stability is difficult. This study addressed these challenges by implementing a methodology that 1. quantified spatial and temporal patterns of snowpack stability, 2. identified spatial associations between the strength and stability of a weak layer and slab load, and radiation properties, 3. identified internal associations between weak layer thickness, shear strength, microstructural properties, and slab load.

An instability associated with a buried surface hoar weak layer was examined on an inclined forest opening at Lionhead, southwest Montana, during February and March, 2005. During five sampling days, 824 snow depth and SnowMicroPen resistance profiles and 352 shear frame tests were performed. An objective texture-based stratigraphic sampling approach was developed to obtain microstructural estimates of a stratigraphic weakness and instability from SnowMicroPen profiles, utilizing the coefficient of variation of rupture force. Spatial models of hemispheric sky visibility, and incoming long- and shortwave radiation were generated for the surface hoar formation period using a Geographic Information System and independent optical observations.

Despite relative topographic uniformity, in a distance of 30 m, the buried surface hoar weak layer thicknesses varied between 3 – 21 mm. Before burial, the surface hoar persisted despite moderate winds and above freezing air temperatures. Spatial patterns of modeled incoming longwave and shortwave radiation explained the large variation in weak layer thickness and strength properties. Areas exposed to large amounts of radiation contained a strong, thin buried surface hoar layer, while in areas with limited incoming longwave (due to high sky visibility) and shortwave radiation (due to shading), the layer was thicker and possessed low shear and microstructural strengths.

Over time, the shear frame stability index and SnowMicroPen-derived micro-strength of the surface hoar layer increased and values became spatially more variable (divergence): it became harder to predict stability as the snowpack became more stable. A loading event then decreased stability and micro-strength and caused spatial uniformity (convergence), thereby increasing predictive strength of observations. The findings illustrate the usefulness of the SnowMicroPen for evaluating spatial patterns and load-related changes in snowpack stability.

INTRODUCTION

Snow avalanches pose a significant hazard to human populations and infrastructures in mountainous regions worldwide. Avalanche forecasting and hazard reduction methods rely heavily on the evaluation of snowpack stability information collected in the field. The reliability of these observations is compromised by uncertainty regarding the spatial and temporal variability of snowpack properties affecting stability. Despite large gains in our understanding of the causes of snowpack instabilities and the development of field methods for monitoring instabilities over time, it remains a predicament for the field observer or back country enthusiast to assess the stability of an individual slope based on their observations at 'representative', but safe, locations.

Previous studies demonstrate that spatial variability exists in strength and stability properties of the mountain snowpack (Conway and Abrahamson, 1988; Föhn, 1989; Birkeland, 1990; Birkeland et al., 1995; Jamieson, 1995; Landry, 2002; Kronholm and Schweizer, 2003; Logan et al., 2007). At the mountain range- and basin-scales of observation, spatial patterns in stratigraphic instabilities result directly from variations in environmental factors affecting weak layer and slab properties such as wind, topography, solar radiation, and re-radiation from topographic and vegetation features (Bader et al., 1939; Gubler and Rychetnik, 1991; Birkeland, 2001; Cooperstein et al., 2004; Höller, 2004). However, at the slope scale, determining local variations in snow properties is challenging. To estimate stability on potentially hazardous slopes there are two clear sampling options: 1) test a small, isolated portion of the slope in question, or 2) test a similar but less hazardous 'representative' slope (Greene et al., 2004). In both situations,

the observer draws on observations to estimate the conditions on the slope in question, thereby making the assumption that the observations are (at least in part) 'representative' of the slope.

However, recent work has shown that large amounts of spatial variability exist in snow stability even on a relatively uniform slope that is protected from ridge-top winds (Landry et al., 2004). Examining a large database collected by many practitioners using SnowPilot (Chabot et al., 2004), Birkeland and Chabot (2006) showed that approximately 1 out of every 10 stability observations indicated stable conditions, although the slope was deemed unstable based on empirical evidence such as widespread cracking, collapsing, or local avalanche activity. Further challenging our ability to estimate slope stability is the uncertainty associated with changes in spatial characteristics over time (Birkeland and Landry, 2002; Landry, 2002; Landry et al., 2004, Logan, 2007). As the snowpack evolves over time, our ability to predict snowpack stability across a slope might change as a result of internal or external processes such as metamorphism or a loading event, respectively.

This study addressed these challenges by developing and implementing a methodology that quantifies spatial and temporal patterns of snowpack stability. This was accomplished by acquiring and analyzing large spatial arrays of snow micro-penetrometry information and strength and stability observations of a stratigraphic weakness at multiple points in time. To limit the influences of obvious environmental factors such as topography and wind, a relatively wind-sheltered and topographically uniform mountain slope was selected in southwest Montana. Environmental factors

influencing weak layer development were also identified and quantified, allowing for slope-scale patterns of stability to be largely described by external conditions.

Purpose of Study

The purpose of this study was to increase our understanding of slope-scale snowpack stability and its variability across space and time. This purpose had three primary foci:

1. Slope-scale snowpack stability and it's variability across space and time.
2. The role that spatial variations in terrain, vegetation, and radiation play in snowpack properties related to strength and stability.
3. How spatial and temporal variations in slab load affect snowpack strength and stability.
4. Correlations between shear strength and microstructural properties of weak layers or interfaces.

A sound methodology for analysis of snowpack and environmental properties was needed. I identified three methodological objectives at the outset of this study:

1. To objectively analyze stratigraphic profiles of microstructural characteristics.
2. To effectively measure and model terrain, vegetation and radiation variables.
3. To objectively analyze spatial datasets.

Dissertation Organization

To provide the reader with a broad understanding of the framework and concepts presented in this dissertation, I briefly outline the basic concepts presented in each section of the dissertation.

Chapter 2 (Literature Review) provides an overview of key concepts and research related to spatial analysis of snowpack stability. Factors influencing spatial patterns and temporal evolution of snowpack stability are reviewed. Snow penetrometery is discussed as a viable technique for assessing spatial patterns of strength and stability. Lastly, the main research hypotheses are stated.

Chapter 3 (Methods) presents the methods of site selection and preparation, field observations (snowpack, weather station, and terrain and vegetation surveys) and analysis techniques (geostatistical, temporal, and pit-to-plot tests of uniformity). A detailed description of SnowMicroPen signal processing is given, including field measurement procedures, signal noise quantification, microstructural estimations, and stratigraphic sampling techniques. The three-dimensional transformation of snowpack observations to the terrain and vegetation model are presented, followed by the spatial modeling of long – and shortwave radiation, which utilized two independent estimation techniques: a Geographic Information System-based model and optical field measurements. Chapter 3 concludes with the statistical methodology utilized for the geostatistical quantifications, temporal anlaysis, bi-variate correlations, and pit-to-plot uniformity testing.

Chapter 4 (Results) presents the results of this study. It begins with a presentation of weather data collected at the study site during the surface hoar formation and

persistence periods. This is followed by the geostatistical results of environmental variables and snowpack properties. The temporal results illustrate changes in snowpack properties over the sampling period. Associations between radiation models and surface hoar weak layer properties (indicating external proceses) are followed by associations between snowpack properties (indicating internal processes). The results from the pit-to-plot uniformity tests focus on important snowpack variables related to snowpack stability and microstructure. A limited amount of discussion is incorporated in the results, primarily to help the reader make connections between different results.

Chapter 5 (Discussion) discusses the main results. The discussion is organized into the following practical concepts: meteorological conditions during surface hoar formation and persistence, spatial associations between surface hoar thickness (h_{wl}) and spatially modeled long- and short radiation estimates, implications of these associations on snowpack stablity, pit-to-plot uniformity, temporal processes influencing strength and stability, and, lastly, spatial variability over time.

Chapter 6 (Conclusions) begins with a summary of the main findings, framed in light of the tested hypotheses. This if followed by concluding remarks on the snowpack stability's dependence on environmental conditions during surface hoar exposure to the atmosphere, weak layer development, correlations between microstructure and shear strength (τ_∞), and lastly implications of the findings on slope-scale spatial variabltiy of snowpack stabitlity. Lastly, suggestions for future studies are provided.

The References section contains all cited literature, following citation criteria as applied in *Cold Regions Science and Technology*. The Appendicies include additional

information concerning the SMP signal processing, additional discussion on sky visibility estimations, atmospheric data sources, and manual snow profiles, and additional potential sources of error in field and analysis techniques.

LITERATURE REVIEW

Spatial Variability Research

Field studies explicitly focused on spatial dimensions and spatial variability[1] of snow properties influencing avalanche formation began in the 1980's, when fracture initiation research sparked debate on how large weak zones would need to be in order for zone failure to occur (Sommerfeld and Gubler, 1983). Conway and Abrahamson (1988) conducted the first field-based study quantifying weak zone dimensions and rationalized that spatial variations in strength along crown lines were evidence of such weak zones. Föhn (1989) also saw evidence of such weak zones but at a smaller scale. These results were limited in their interpretability due to fairly crude methodologies in use at the time.[2]

Birkeland (1990) conducted the first intensive slope-scale study that had the central goals of quantifying spatial patterns in snow strength on an intact slope and relating them to geographic phenomena. By applying the Digital Resistograph (Dowd and Brown, 1986; Birkeland, 1990; Brown and Birkeland, 1990) to a carefully planned spatial sampling scheme, Birkeland (1990) was able to observe snow hardness at a spatial and mechanical resolution that previously was unattainable (e.g., Bradley, 1966). The SnowMicroPen (SMP) (Johnson and Schneebeli, 1997, Schneebeli and Johnson, 1998), a mechanically and stratigraphically improved digital Resistograph, has been used in studies that conceptually build on Birkeland (1990) (Kronholm et al., 2003; Pielmeier,

[1] Although nearly all snow and avalanche studies implicitly involve spatial analysis, I am limiting this discussion to studies that use explicit spatial analysis. Generally defined, spatial analysis comprises the *manipulation*, *analysis* and *modeling* of spatial data (O'Sullivan and Unwin, 2002). More narrowly defined, spatial analysis utilizes descriptive, exploratory and statistical analytical techniques to obtain information that is spatial in nature.

[2] Conway and Abrahamson (1988) utilized an effective but non-standardized shear test technique and Föhn (1989) relied on 100 field assistants to conduct tests. Both techniques may have increased variability in results.

2003). Because of the efficient sampling technology, enough samples can be obtained across a slope to analyze both trend surfaces and auto-correlation characteristics of data.

Campbell and Johnson (2007) analyzed 705 Rutschblock tests in 29 spatial arrays and 930 fracture propagation tests in 23 spatial arrays in the Columbia Mountain Range (B.C., Canada). Most of these datasets observed surface hoar-related instabilities. The authors examined spatial variability of stability on slopes possessing pronounced variations in terrain (e.g. slope angle) or slab properties (e.g. slab thickness). The Rutschblock analysis indicated that spatial variability was largely related to slab thickness (h_{slab}), slope angle and aspect, and surface hoar thickness (h_{wl}). The authors also identified thinner slabs tended to be less stable, and in referencing Schweizer and Camponovo (2001) imply that this results from the applied stress concentration decreasing with increasing depth.

Campbell and Jamieson (2006) presented a spatial cluster analysis technique that allowed them to quantify clusters in stability observations derived from drop-hammer tests in spatial data arrays with relatively few observations (e.g., approximately 40 observations at a site). The authors speculated that the absence of clear spatial structure within the observed variability may have been the result of the limited observations or the sampling scales.

Other recent studies have attempted to evaluate how spatial patterns of stability change over time (Birkeland and Landry, 2002; Logan, 2005; Lutz et al., 2007; Hendrikx et al., 2008). By selecting uniform, wind-sheltered slopes, patterns caused by terrain and wind processes could be eliminated, thereby allowing the researchers to analyze more

subtle spatial patterns (otherwise obscured or masked by obvious wind or terrain related patterns) over space and time. Because their plots were not contiguous, Birkeland and Landry (2002) could not definitively differentiate spatial from temporal phenomenon. This study improves the field methodology by utilizing a sample scheme with four square plots embedded around a large central cross-plot. The central cross-plot quantified initial slope-scale conditions, while the smaller square plots quantified spatial patterns at four additional points in time. This technique was first described by Logan (2005). A complete review of spatial variability of snow research is provided by Schweizer et al. (2008).

Environmental Determinants of Spatial Stability Patterns

From the mountain range- to slope-scale of observation, spatial patterns in snowpack instabilities result directly from spatial variations of snowpack properties affecting the stratigraphic weakness. Setting aside changes occurring internally within the snowpack over time, a potentially large degree of spatial variation can exist in snowpack stability due solely to environmental conditions governing the weak layer formation and the amount of force exerted on the weak layer by the slab. Let us consider these two concepts separately.

Environmental Determinants of Weak Layer Formation

This study examined a buried surface hoar-related stratigraphic weakness. Surface hoar develops when the snow surface is cooled to well below the air temperature by a net longwave radiation loss, and excess water vapor from the near-surface air layer

deposits onto the snow surface. Studies have examined micro-meteorological conditions that facilitate surface hoar growth (Lang et al., 1984; Colbeck, 1987; Hachikubo, 2001). Surface hoar formation and growth are highly dependent on snow surface temperature (Oke, 1987; Gubler, 1998) and the degree of supersaturation at the boundary layer (Kobayashi (1961), in Jamieson and Schweizer, 2000). Light winds, which are spatially influenced by topography and vegetation, can foster vapor supply (Hachikubo and Akitaya, 1997).

Because local topography and vegetation affect the energy balance at the snow surface (by modifying long- and shortwave radiation across space), these environmental factors influence the formation and persistence of surface hoar and near surface facets (Gubler and Rychetnik, 1991; Birkeland, 2001; Höller, 2001; Cooperstein et al., 2004). Surface hoar development is hindered in thick forest cover due to re-radiation and surface hoar can quickly degrade on large open slopes that face the sun, due to incoming solar radiation (Gubler and Rychetnik, 1991). Höller (2001) showed that canopy cover greatly influenced snow surface temperature, which in turn hindered surface hoar formation. Cooperstein et al. (2004) and Cooperstein (2008) showed that differences in radiation fluxes related to slope aspect can cause surface hoar formation to be greatest on north slopes and less on south slopes, in the northern hemisphere.

In addition to the presence or absence of surface hoar, the amount of growth is highly dependent on the same environmental factors. Gubler and Rychetnik (1991) notably recognized that surface hoar formation is most productive in places where both shading from direct sunlight and unobstructed sky (high sky visibility) spatially coincide,

typically in openings at the edge of forests where partial shading reduces solar radiation and a relatively unobstructed sky view allows for nighttime surface cooling.

Feick et al. (2007) identified local winds and cumulative solar radiation as causes of spatial variations in surface hoar growth at the basin to range scales. However, they did not quantitatively consider spatial variations in sky visibility, which is a primary spatial determinant of net longwave flux. Sky visibility largely determines the snow surface's cooling potential and the potential to develop temperature gradients at the snow surface, which are prerequisites for surface hoar growth.

Under the pretense that surface hoar layers fail most easily where they are thickest, a buried surface hoar layer that is stressed uniformly by a slab load on a planar slope will be weakest where environmental factors foster its growth and persistence. Hence, assuming all other factors constant, we could predict surface hoar related instabilities to be most pronounced where sky visibility (or net longwave loss) is greatest and solar radiation is minimal.

Environmental Determinants of Slab Stresses

Initial spatial variations of the vertical load of the slab (V_{slab}) result from depositional processes. At the slope-scale, wind can interact with topography and vegetation to create uneven snowfall accumulation; once deposited, snow can be re-transported by wind (Lehning and Fierz, 2008). Preferential sublimation or evaporation may also cause variations in slab load. In addition to the variation caused by atmospheric processes, local variations in topography cause the slab's normal and shear stresses (N_{slab} and T_{slab}) to vary across a slope as a function of slope angle. Hence, relatively light slabs

on steep slopes may produce greater shear stress than heavier slabs on shallower slopes. Assuming a uniform weak layer structure exists across a slope, unstable zones can be identified by identifying what environmental properties have influenced, or are influencing, the slab load. This is very commonly applied using topographical factors, such as slope angle, to estimate where the weak layer is most stressed.

Evolution of Snowpack Stability

Snowpack stability describes the ability of stratigraphic features to support an applied overburden; it describes the relationship between the strength of potential weak layers (or interfaces) and the stress applied by the slab. Obvious signs of instability include recent avalanche activity, shooting cracks and 'whumpfing' (McClung and Schaerer, 1993). Less obvious, but as important, is the behavior of weaknesses when isolated and tested using column-oriented stability or shear frame tests (Greene et al., 2004). All these observations tell us whether, under a given load, a stratigraphic weakness is capable of withstanding additional stress.

While we are accustomed to thinking about snowpack stability at spatial scales equal to or greater than 250 cm^2 (shear frame), 900 cm^2 (compression test) or 30,000 cm^2 (Rutschblock) the physical relationships at the microstructural scale are similar. To understand how penetrometry can be applied to derive similar estimates at the microstructural scale, we need to consider how the snowpack reacts to stresses at the microstructural scale. First I consider a 'uniform' snowpack, containing no discrete stratigraphic weakness.

Immediately following a snowstorm, individual structures, bonds, and contact points throughout the snowpack will, on average, experience additional stress, which immediately causes elastic deformation; permanent deformation begins and continues as long as the stress, even if very small, continues to be applied (Paterson, 1994). Across one square-meter, at any depth within the old snowpack, thousands to millions of bonds or structures will deform elastically under the weight of the new snow and will, over time, deform plastically. Some bonds will fracture as deformation results in local stress concentrations, while new bonds will continually be forming. This process of plastic deformation and microstructural rearrangement will eventually result in the strengthening of the snowpack, through an increase in bond density and size (Bader et al., 1962). Salm (1977) demonstrated how 1 % deformation in uniaxial compression resulted in 20 % change in the viscosity of the sampled snow. Because snow microstructures tend to maintain equilibrium between forces, they will continue to deform until the internal forces are equalized. Equilibrium temperature metamorphism also strengthens the snowpack through increasing bond frequency and size, while temperature-gradient metamorphism results in decreased bond frequency and size (Schneebeli et al., 1999).

The mechanical outcome can be quite different if stratigraphic weaknesses are present as layers, or as transitions between layers. Potential stratigraphic weaknesses are those stratigraphic features that are least capable of resisting additional applied stresses (vertical, normal, or shear). After a loading event, significantly less force is required to rupture individual bonds within a stratigraphic weakness than was required prior to the loading event.

The above description illustrates how a loading event would influence microstructural temporal processes. Spatial variability of a load across a slope results in discrepancies of residual bond strength across space. Within a given stratigraphic weakness across a slope, deficit zones (Conway and Abrahamson, 1984) or regions of local weak layer failure (McClung, 1981) may exist.[3] In such deficit zones, the weak layer is no longer capable of supporting the overburden. This can cause progressive failure of the surrounding weak layer, which may lead to a broader fracture initiation and slope-scale fracture propagation. Following a loading event, potential deficit zones within a stratigraphic weakness will likely containing far fewer and significantly weaker microstructures than zones of localized pinning.

Whether instability is being quantified using stability tests over time (in a time series) or across space (in a spatial array), the weak layer residual strength is equal to the residual force needed to fracture it (i.e., the force applied by the slab plus external force added by operator) and the snowpack stability is equal to the ratio of the weak layer's residual strength (i.e., collapse force) to the slab's resting force. Theoretically, at the microstructural scale, the microstructural residual strength is equal to the residual force needed to rupture microstructures and the micro-scale stability is equal to the ratio of the microstructural residual strength (rupture force) to the force applied to the microstructures by the overlying slab.

---

3 Schweizer et al. (2003) clarify that "deficit zones" have been referred to in literature as "shear perturbations" (Perla and LaChapelle, 1970), "imperfections" (Lang and Brown, 1975), "zonal weakening of the snowpack" (Bradley et al., 1977), "shear bands or slip surfaces" (McClung, 1979, 1981, 1987), and "superweak zones" (Bader and Salm, 1990). This concept is not to be confused with the term "weak zone" which is a more general description of a weak area in the snowpack, including any overlying slab (e.g., Birkeland, 1995).

With time, if the added stress does not cause catastrophic fracture, it will cause permanent microstructural deformation, such as grains and bonds deforming (bending, shearing, compressing), grains penetrating into adjacent layers or crystals rotating (Jamieson and Schweizer, 2000). The end effect is an increase of bond density (Davis et al., 1998) and bond size (Davis et al., 1996), and weak layer thinning (Davis et al., 1996; Jamieson and Johnston, 1999; Jamieson and Schweizer, 2000). This permanent deformation allows for greater contact area between grains or a greater number of contacts between grains, which is a prerequisite for bond formation and weak layer strengthening (Shapiro et al., 1997). In summary, slab loads can momentarily increase instabilities but over time can foster strengthening of stratigraphic weaknesses (Jamieson and Johnston, 1999).

Since areas with heavy slabs experience greater stress than areas with lighter slabs, deformation of a weak layer is greatest where the slab is heaviest. In turn, the weak layer in these areas eventually should strengthen (Jamieson and Johnston, 1999). Logically, the weak layer would remain relatively weak where the slab is thinnest, due to the lack of stress that would otherwise foster deformation (that eventually causes strengthening). These areas would strengthen more slowly over time than areas with greater loads. In addition, slab thickness (h_{slab}) could influence existing temperature gradients which drive internal metamorphic processes.

Based on mechanical principles described by Shapiro et al. (1997), the microstructural strength of snow is more properly described as a function of bond density and size, than of density or porosity. Traditionally, snow density has been treated as a

main proxy for snow strength, partly because it is easily measured (e.g., Bader et al., 1939; Schweizer, 1999). However, this relationship is not deterministic but rather the coincidental side-effect of microstructural properties (Shapiro et al., 1997). Lacking more exact proxies that are based on microstructural phenomenon, this indirect relationship has proven useful, as evident by the numerous studies and overviews that document the correlations between density or porosity and strength (e.g., Bader et al., 1951; Mellor, 1975). It is more likely that snow strength is determined by bond and contact characteristics between snow grains. Shapiro et al. (1997) succinctly state that as deformation occurs, the apparent association between strength and density is more coincidental than deterministic and is thereby a poor surrogate for strength:

> "As the deformation process continues, an apparent relationship between density and mechanical properties may be established. The reason this relationship seems to exist is that both the mechanical properties and the density depend on the nature of the bonding/grain contact. Thus it is the bonding, and not the density, that is the critical variable, suggesting that some parameter that represents the influence of the bonding should replace the density in plots of snow strength or other properties."
>
> (Shapiro et al., 1997:6)

With the introduction of the modern penetrometer technologies, described in the following section, it is now possible to measure microstructural and micromechanical properties of snow *in-situ*. The SnowMicroPen (SMP) signal can be analyzed to derive: 1. how much force is needed to break bonds under a given load or under different loads, 2. how many bonds or contact points exist in a given volume of snow. Both estimates affect microstructural strength and hence are closely related to the strength and stability of a snowpack at traditional scales of observation. The following section addresses general advances in snow penetrometry and the SMP in greater detail.

Penetrometry-Derived Strength and Stability Estimates

Snow hardness has long been recognized as an important proxy in determining the structure and strength of mountain snowpacks (e.g., Welzenbach, 1930; Paulcke, 1938; in Pielmeier, 2003:12-17). Since the 1930's, researchers have developed a variety of penetrometers - ranging from manual to mechanical to digital - with the long-term goal of efficiently and objectively deriving stability information from resistance profiles (Bader et al., 1939; Bradley, 1968; Dowd and Brown, 1986; DeQuervain and Meister, 1987; Schneebeli and Johnson, 1998; Schweizer and Wiesinger, 2001; Mackenzie and Payten, 2002). Haefeli's Ramsonde was the first of such probes (Bader et al., 1939). Relationships between avalanche activity and generalized snowpack types derived from Ram profiles have been identified (DeQuervain and Meister, 1987) and used by avalanche forecasters (Schweizer and Wiesinger, 2001). However, the 40 mm wide cone fails to differentiate thin weak layers and subtle transitions (Haefeli, in Bader et al., 1939; Pielmeier and Schneebeli, 2003).

DeQuervain (1950) developed and tested the Kegelsonde (German for "cone probe"), a hand-held probe with a cone diameter of 10 mm. Bradley (1966) developed the Resistograph, the first automated snow penetrometer (Figure 1). This instrument allowed for objective hardness profiles to be recorded onto a paper slip that could then be ripped off the spool, resulting in instant resistance profile recording. Although by today's standards this instrument is dwarfed by the sensory and computational capabilities of

technologies such as the SMP, its conception marked a new era in snow science, where snow stratigraphy observations would become (semi)-automated.

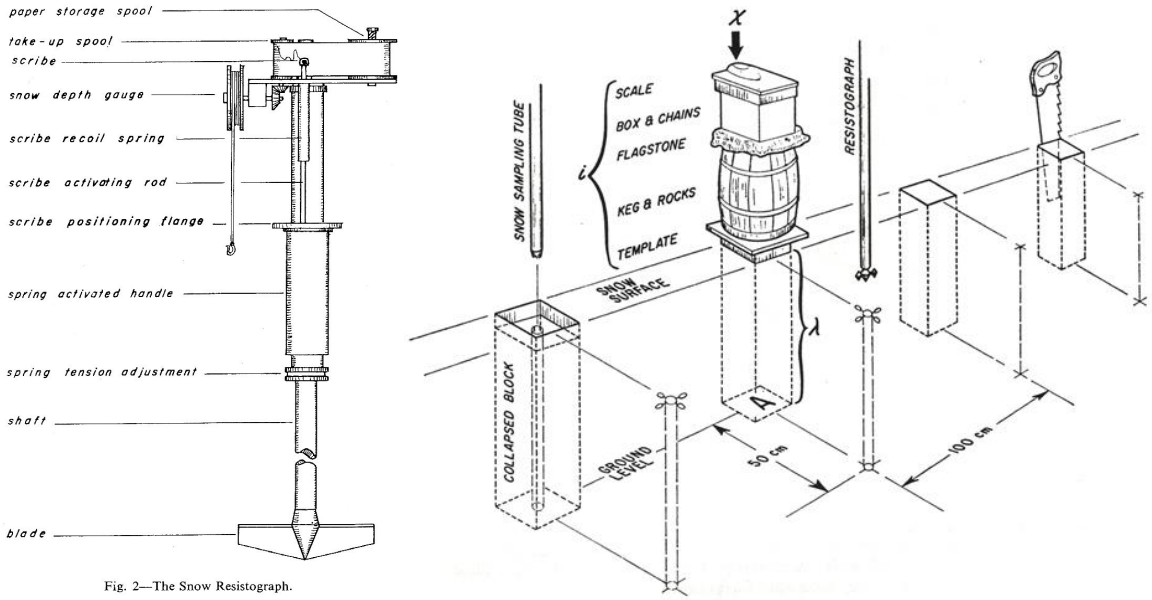

Figure 1. Illustrations by Bradley elegantly depict the Resistograph (left, Bradley, 1966:254) and his innovative experimental set-up for identifying potential associations between penetrometer-derived depth hoar hardness and compressive strength (right, Bradley, 1968:504).

Bradley (1968) also conceived of and implemented a practical field test to correlate depth hoar hardness and compressive strength using the Resistograph and a loaded column test (Figure 1). As stated by R. Haefeli, "The resistograph developed by the Earth Science Department [at Montana State University] and Prof. Bradley seems to be an excellent solution for a long desired instrument" (Bradley, 1966:260).

In the mid 1980's, Dowd (1984) and Dowd and Brown (1986) introduced the Digital Resistograph, which recorded resistance at 5 mm intervals with digital memory. An improved version of the Digital Resistograph was later utilized by Brown and Birkeland (1990). Navarre et al. (1994) described how, using an impact penetrometer,

penetration resistance can be calculated. Hardness information acquired from these penetrometers was limited in its interpretation for several reasons:

1. Penetrometer tips were too large to differentiate thin weak layers, such as surface hoar, from adjacent layers.
2. Relatively large penetrometer tips interact with many structures simultaneously, resulting in a quantification of the average (or aggregate) resistance of many structures, at best. However, large penetrometer tips (and non-conical tips) cause a compression zone in granular material, which results in a complex deformation field (Fritton, 1990; Huang et al., 1993). Since the compressive zone dimensions are unknown and change with snow type, the snow sample volume (and number of microstructures) is unknown, for a resistance value recorded by such instruments.
3. The averaging effect and compression zone effect of large penetrometer tips obscure interactions between the penetrometer tip and individual structures, making rupture strength and frequency analysis impossible.
4. Penetrometers that utilize drop weights and heights (such as the Rammsonde) offer fairly coarse resistance values. In addition, the recorded values are dependent on tip acceleration and deceleration with every load event, which likely varies for different snow types.
5. Penetrometers that utilize muscle strength to drive the penetrometer down or up through the snowpack (such the Resistograph) are dependent on the operators'

consistent force application. Muscle-derived force (which is not consistent) can cause changes in rate of loading that are not accounted for.

To overcome such limitations, in the late 1990's Jerry Johnson and Martin Schneebeli invented the SnowMicroPen (SMP) (Johnson and Schnebeli, 1997; Schneebeli and Johnson, 1998). Unlike previous snow penetrometers, the SMP possesses a small (5 mm diameter) cone mounted to a high-resolution piezo-electric force transducer that is driven at a constant velocity by a stepping motor. As the stepping motor drives the probe at a velocity of 20 mm sec^{-1}, the resistance is recorded at a frequency of 4.88 kHz, resulting in a force reading every 0.4 μm, or 244 measurements mm^{-1}.

Given that snow grains are typically smaller than 5 mm, the 5 mm diameter cone size interacts with a limited number of microstructures at any point in time, thereby reducing the possible effects of a compression zone. The high-resolution piezoelectric force sensor is capable of registering individual interactions between structures and the penetrometer tip. As a result of the small penetrometer tip being driven at a constant velocity, the recorded resistance values can be interpreted using micromechanical modeling.

The SMP offers two clear advantages over other penetrometers: 1. The SMP enables grain and bond-scale strength properties to be examined (Schneebeli and Johnson, 1998; Schneebeli et al., 1999), 2. Hardness properties of thin (e.g., 5 mm) weak layers can now be effectively quantified (Pielmeier and Schneebeli, 2003). The SMP

quantitatively records microstructural characteristics of snow stratigraphy (Johnson and Schneebeli, 1999; Pielmeier and Schneebeli, 2003; Pielmeier, 2003).

Several studies conducted with the SMP have found that the resistance profiles can be used to delineate snowpack stratigraphy and to characterize spatial variations in stratigraphy (Kronholm et al., 2003; Pielmeier, 2003; Pielmeier and Schneebeli, 2003; Birkeland et al., 2004; Kronholm, 2004; Sturm et al., 2004; Lutz et al., 2007). Pielmeier and Schneebeli (2003) have compared hardness profiles of the three most prominent methods at the time: the hand hardness test, the Ramsonde and the SMP. They found that the SMP was most capable of measuring microstructural characteristics such as thin weak layers.

More recent studies have linked SMP information with stability and shear strength. Lutz et al. (2007) and Trautman et al. (2006) identified associations between penetration resistance and stability and shear frame tests, respectively. Pielmeier and Schweizer (2007) identified basic microstructural estimates produced from SMP profiles that are related to snowpack stability. Most recently Lutz et al. (2008a) and Pielmeier and Marshall (2008) have definitively shown associations between microstructural estimates and changes in slab load and stability, respectively. I incorporate the microstructural estimates applied by Lutz et al. (2008a).

Other penetrometers that directly measure penetration resistance using electronic and digital technologies include the SABRE probe (Mackenzie and Payten, 2002) and the New Generation Ramsonde (Abe et al., 1999). Floyer and Jamieson (2008) conducted a compelling study that paired compression test fracture character with hardness and weak

layer thickness estimates derived from profiles measured using a modified SABRE probe. They found that weak layer thickness and the gradient in average hardness from the super-stratum to weak layer were the most effective variables at differentiating sudden fractures from other fractures. Floyer and Jamieson's (2008) study is unique in that it combines a simple field-based sampling scheme (conceptually very similar to Bradley's (1966) layout) with digital and mechanical instrumentation. Floyer (2008) also developed a weak layer detection algorithm that is based on curvelet and wavelet analysis that may be very useful for snow penetrometry, including the analysis of SMP derived estimates.

Floyer (2008) and Floyer and Jamieson (2008) have shown that average layer hardness and hardness gradients between layers, as derived from SABRE profiles, can provide valuable stability-related information. While their work shows clearly that the SABRE quantifies some natural phenomena related to stability, this study was conceived around employing the SMP to measure not only stratigraphic but also microstructural properties of the snowpack.

Individual interactions between microstructures and the sensor tip can be recorded using the SMP, because the sampling rate is sufficient and the instrument measures at high stratigraphic and force resolutions. Hence, in addition to average hardness information, the SMP signal can be used to derive average microstructural properties, such as the average rupture force (f_m) and structural element length (L) within a given sample.

Given the limitations associated with analyzing a one-dimensional force signal recorded in a complex anisotropic three-dimensional medium by a conical sensor tip that, depending on grain size, is larger or smaller than the contacted structure(s), it can be assumed that the actual processes of loading and rupturing of individual structures are obscured. That said, by applying the micro-mechanical models proposed by Johnson and Schneebeli (1999), Sturm et al. (2004), and Marshall and Johnson (in review), average microstructural properties can be estimated.

An additional concern of interpreting microstructural properties from penetrometer profiles involves a compressive zone between the penetrometer tip and a granular material (Fritton, 1990; Huang et al., 1993; Floyer, 2006). With the understanding that a compaction zone may have a real effect on estimates of microstructural dimensions, the existing micro-mechanical models have been shown to differentiate different snow types (e.g., Johnson and Schneebeli, 1999; Marshall and Johnson, in review). While the current models can certainly be used to estimate relative values, if future models account for changes in the size and influence of a compaction zone, they could be applied to the findings of this and previous studies to make them comparable.

Research Hypotheses

In this section, is a brief overview of the main research topics, mainly framed as hypotheses, that were central in this work.

Developments in Snow Texture-Based Stratigraphic Delineation

1. SnowMicroPen-derived snow texture estimates can be used to locate stratigraphic transitions.
2. The coefficient of variation of the rupture force (f_{cv}) is more effective than texture estimates that depend on the mean resistance, including the coefficient of variation of resistance (F_{cv}) and the Texture Index (TI).

Environmental Determinants of Weak Layer Formation and Persistence

Spatial patterns of surface hoar weak layer properties can be described by environmental variables, including:

3. Proximity to small vegetation.
4. Sky visibility ($v_{\%}$).
5. Night time cooling potential, approximated by modeling the incoming longwave radiation ($\downarrow L$).
6. Exposure to sunlight, approximated by modeling the daily cumulative shortwave radiation ($\sum I$), the duration of direct shortwave radiation ($\sum t_I$), and the maximum shortwave radiation (I_{max}).

Temporal Changes in Strength and Stability

1. The surface hoar weak layer will strengthen over time. Shear strength (τ_∞), microstructural rupture force (f_m), micro-strength (σ_{micro}) will increase. The microstructural element length (L) will decrease.

2. Without loading events, the snowpack will stabilize. The stability index (S), residual shear strength (τ_{resid}), microstructural rupture force (f_m), and micro-strength (σ_{micro}) will increase.
3. Loading events will cause a decrease in stability, microstructural rupture force (f_m), and micro-strength (σ_{micro}).

Internal Spatial Associations

1. A surface hoar weak layer will be strongest where it is thinnest.
2. Stability will be greatest where a weak layer is thinnest.
3. Over time, a surface hoar weak layer will strengthen most where the load is greatest.

Temporal Changes in Spatial Variability

1. Spatial variability of microstructure, strength, and stability will increase over time in the absence of new loading events (divergence).
2. Loading events will cause a decrease in spatial variability (convergence).

METHODS

Study Site

Study Site Selection

At the outset of this study, Karl Birkeland, Spencer Logan and I identified six study sites in three mountain ranges across southwest Montana (Figure 2). From south to north, we identified two sites on the Lionhead ridge in the Henry's Lake Mountains (Figure 2: field sites #1 and #2), one site at Middle Basin in the Madison Range (Figure 2: field sites #3), and three sites in the Bridger Range (Figure 2: field sites #4, #5 and #6).

All six field sites met specific climatic, topographic and operational factors, as listed here. The rationale for locating field sites in multiple mountain ranges was to

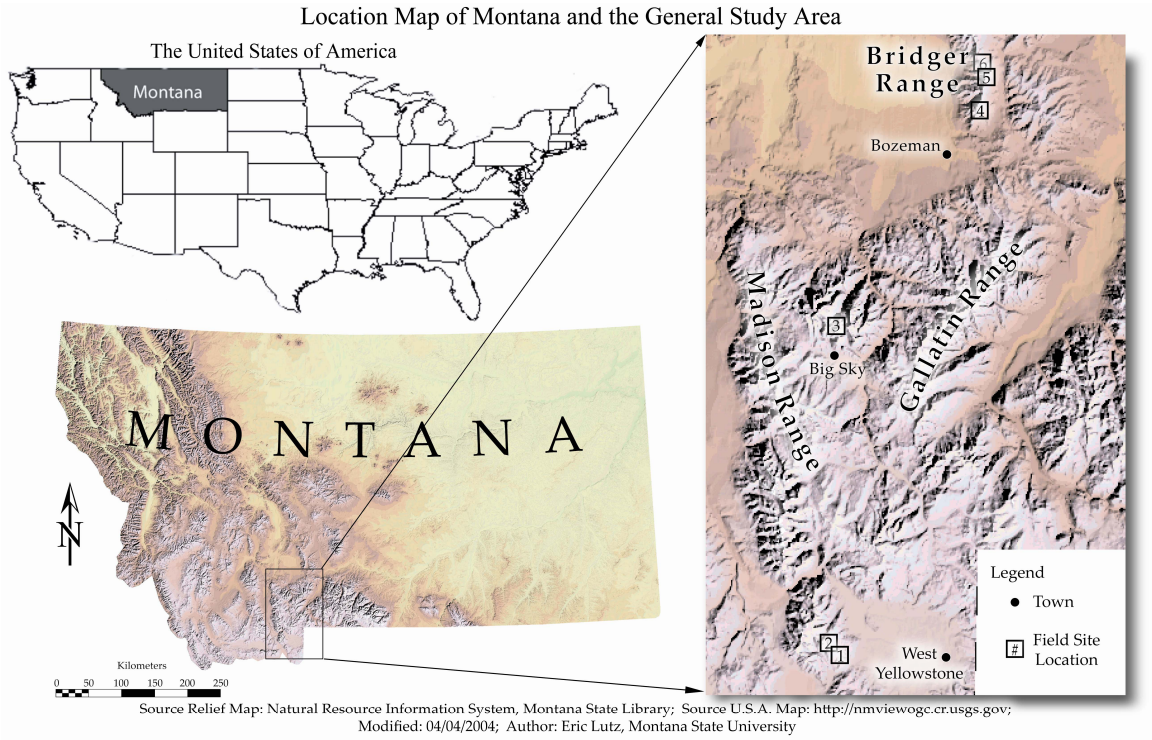

Figure 2. Location map of Montana, U.S.A., and the general study area (inset) including approximate locations of the six prepared field sites. I examined data collected at site #1.

increase the likelihood of at least one field site developing a testable, unstable snowpack that could be monitored throughout a winter season. The field work and later analysis would focus on that field site.

Over the course of two winters (2003-2004 and 2004-2005), many weak layers formed and were tested at the various sites. However, only one undisturbed surface hoar layer, which was observed at Lionhead in the winter of 2005, was strong enough to resist collapsing under my team's weight and still weak enough to yield pertinent stability information. Although this layer was present at two sites at Lionhead (Figure 2: field sites #1 and #2), the northern site ('Lionhead North') was compromised when half of the site was entrained by an avalanche. Hence, I focused my analysis on data collected at the southern Lionhead study site ('Lionhead South') during the winter of 2005 (Figure 2: field site #1).

Climatic Factors: North and northeastern aspects were sought out because these slopes gain only minimal direct heat from the sun and hence are conducive to preserving kinetic growth crystals such as surface hoar. Wind-sheltered slopes were also preferred because the depositional processes are more spatially uniform without wind-loading and because surface hoar is more easily formed (Hachikubo and Akitaya, 1997) and preserved (Feick et al., 2007) in the absence of strong winds. Four of the six sites were located at least 100 meters below ridge tops on the leeward slopes. Wind loading and scouring were greatly reduced at these sites.

Terrain Factors: Slopes needed to be at least 25° to approximate the topographic conditions under which avalanches occur. Although flat, protected slopes would pose no avalanche risk and would therefore be easier to manage, they do not experience shear stress or related effects such as creep, which may play an important role in snowpack evolution and avalanche formation (Louchet, 2001). For practical and safety reasons, slopes steeper than 40° were not considered. To limit the influences of variable terrain, fairly uniform, grassy slopes in forest openings were selected. Uniform, grassy slopes were chosen over talus, till, and bedrock outcrops because these irregular substrates would increase the complexity of stratigraphic features in a thin snowpack (Birkeland, 1990; Birkeland, 1995).

Operational Factors: Relatively small slopes were sought out to minimize avalanche hazards while conducting field work. The slopes were large enough to allow a 31 m x 31 m field site. Permission to access, establish and use field sites was obtained from the appropriate authorities.

Study Site Description

As an introduction to the study site environment, this section provides an overview of the landscape - its geology, geomorphology, climate, vegetation, fauna, and landscape overview.

Landscape Overview: The study site is in southwestern Montana (U.S.A.) in the Henry's Lake Mountains, a relatively small mountain range located south of the Madison Range and northeast of Centennial Range (Figure 3). The Henry's Lake Mountains

Regional Map of Study Site Location

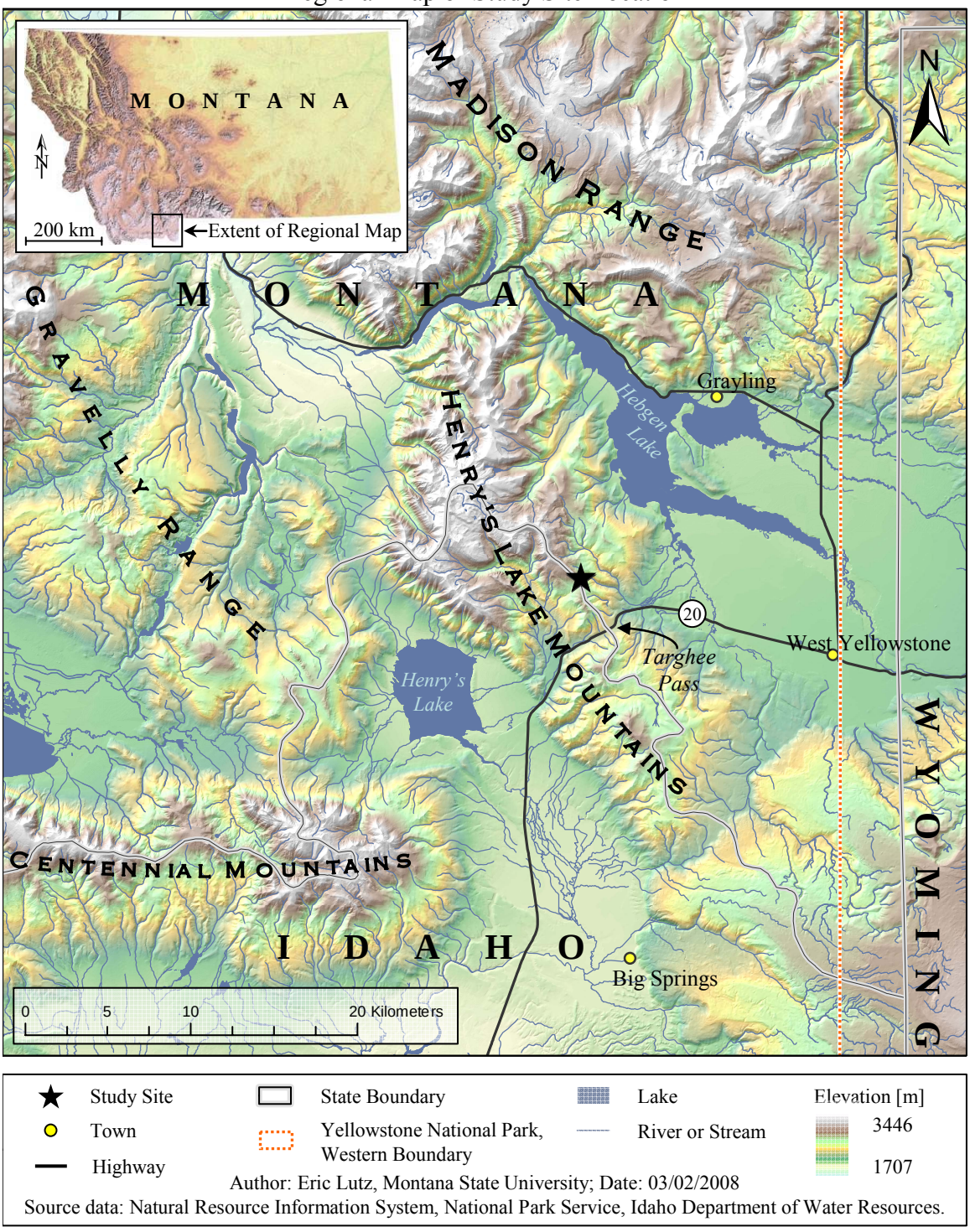

Figure 3. The Lionhead study sites (44˚ 42’ N; 111˚ 17’ W) are located in southwestern Montana at the Lionhead area, approximately 15 kilometers west-northwest of West Yellowstone, Montana, U.S.A. The study sites are located near the continental divide which doubles as the Idaho - Montana state boundary.

stretch approximately 35 kilometers along a south-southeast to north-northwest trajectory, comprising a section of the Continental Divide and serving as a section of the state boundary between Idaho and Montana. More specifically, the study site lies toward the southern end of the Lionhead ridgeline, where it descends toward Targhee Pass (Figure 4).

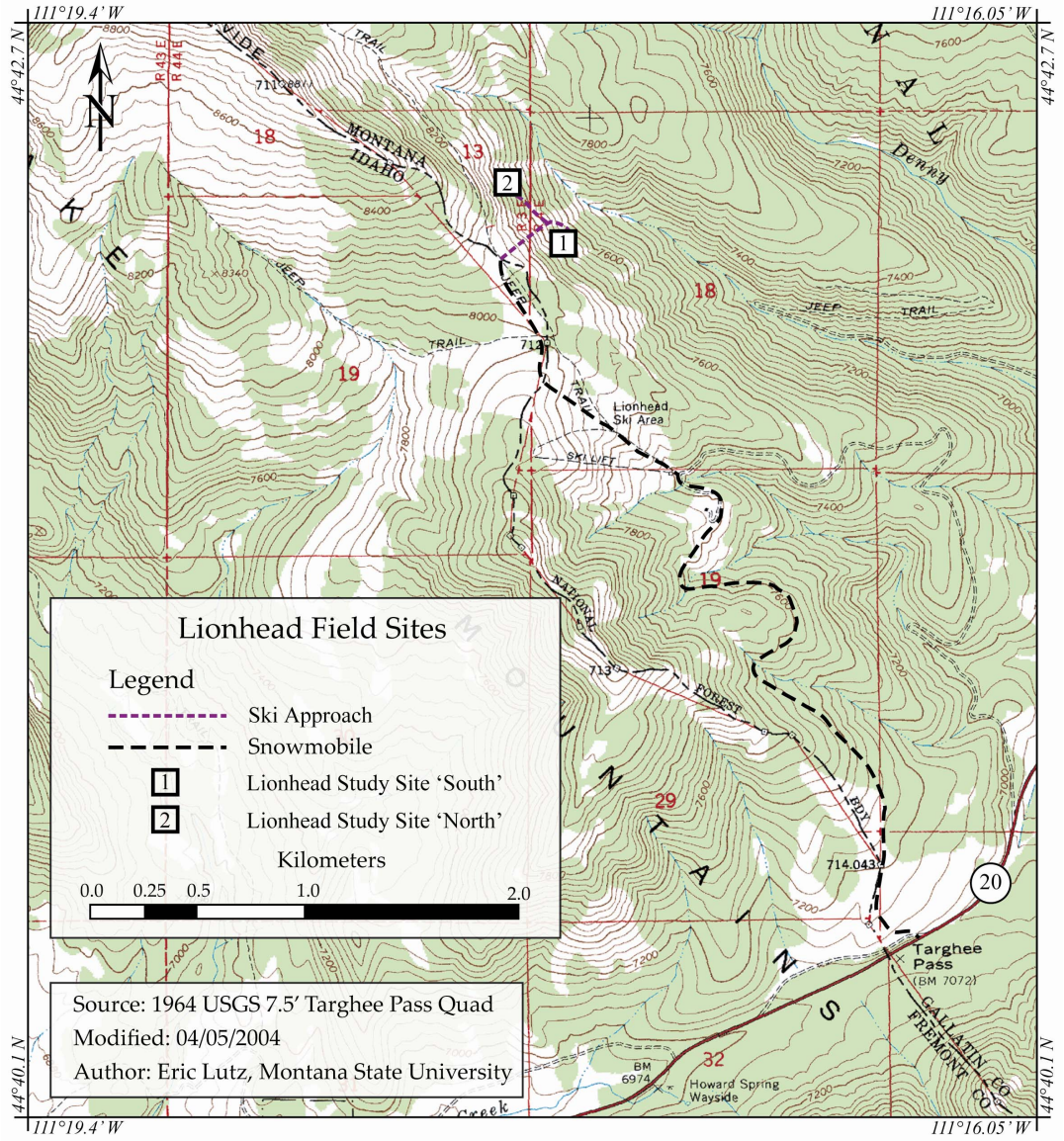

Figure 4. The Lionhead study sites (44° 42' N; 111° 17' W) were accessed from Targhee Pass (lower right corner). I examine data collected at Lionhead 'South' study site. Both study sites face approximately northeast.

In winter, the study site is most efficiently accessed by snowmobiling up the main Lionhead ridge from Targhee Pass to a meadow on top of the ridge. The site itself is then approached from above by skis (Figure 4). In summer, automobile access is permitted on U. S. Forest Service roads to the base of the Lionhead Ski Area, a slope formerly operated as a small ski area. From there an ATV track serves as a hiking trail up the ridge.

Basins on both sides of the range contain artificially dammed lakes (Henry's Lake in Idaho and Hebgen Lake in Montana), vast lodgepole pine (*Pinus contorta*) forests, rangelands, and small towns that have grown as a direct result of tourism associated with year-round outdoor recreation (Figure 5). The town of West Yellowstone (Montana) lies 15 kilometers east of Lionhead (Figure 3) and serves as the western gateway to Yellowstone National Park. Highway 20 crosses the Henry's Lake Mountains at Targhee Pass, connecting southeastern Idaho to southwestern Montana and Yellowstone National Park.

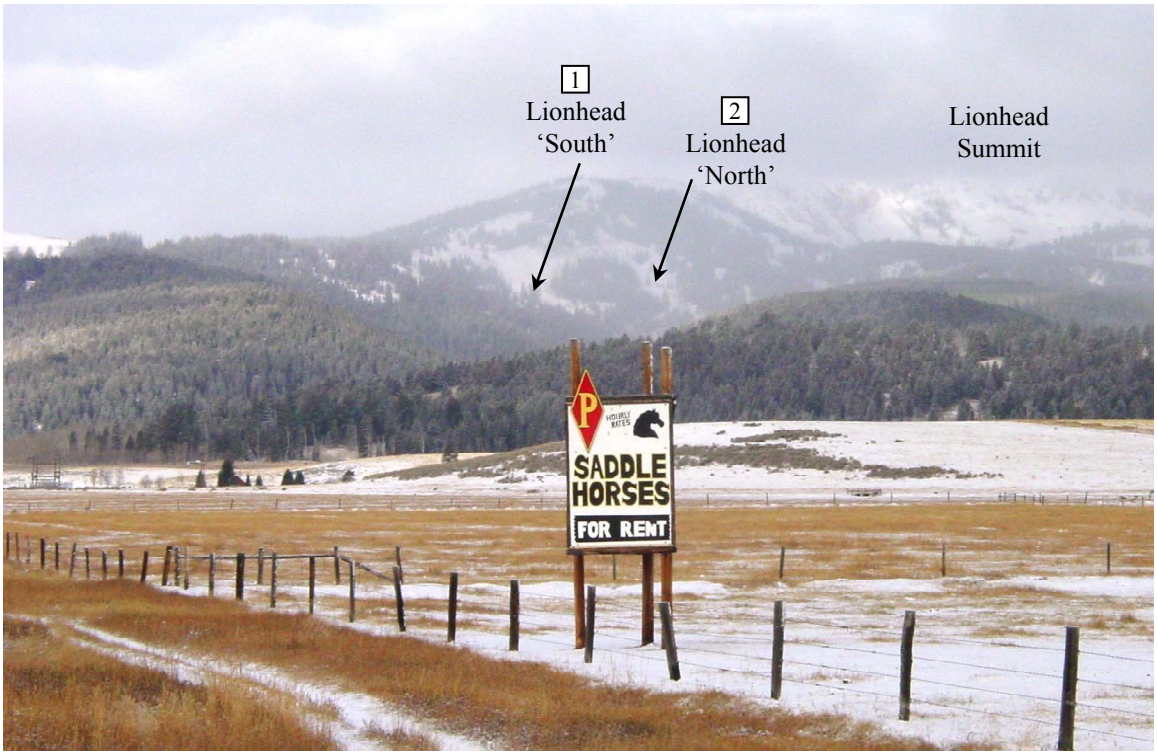

Figure 5. The Lionhead study sites are visible from Highway 20, about 10 km west of West Yellowstone. Several ecotypes exist within a few hundred vertical meters, progressing upward from rangeland (foreground) through montane forests, into alpine regions on Lionhead.

Geology: This range is composed of Precambrian (Archean ~ 3800 to 2500 mya), high-grade metamorphic, basement material overlain by Paleozoic Era (542 to 251 mya), sedimentary rocks (USGS, 1998). During orogenesis, the uplifted sedimentary rocks eroded from the northern portion of the range, exposing the basement material, while in the southern portions of the range the sedimentary rocks remain intact. The main Lionhead formation, including the study area, is composed of Mississippian bedrock (354 to 323 mya, within the Carboniferous (354-290 mya)) (USGS, 1998). Just south of the study area, along the access route, progressively younger Paleozoic bedrock formations are present; Pennsylvanian (323 to 290 mya) and Permian (290 – 248 mya) formations still cover the Mississippian (USGS, 1998). Further south still, Cenozoic volcanic rock

associated with the Yellowstone volcanic complex, cover these formations (USGS, 1998).

Geomorphology: The study site is situated on the steep side of an escarpment[4], approximately 100 m below its crest. The upper portion of the slope features sparsely vegetated outcroppings of sedimentary rock (which run parallel to the escarpment). Thicker soils have developed further down the scarp slope, below the outcroppings and in broad gullies and depressions, as well as on the relatively flat dip slope. Where avalanches frequently occur, the largest plants are trembling aspen (*Populus tremuloides*) and sagebrush (*Artemisia tridentata*), while an open montane forest has become established on parts of the slope that are not affected by avalanche processes.

The study site itself is relatively planar. Slope angles range between 24-29° and slope aspect ranges from 34° to 49° or north to northeast. Exposed bedrock is present in the upper left (looking up-slope) portion of the slope, indicating the soil present elsewhere on the site may be quite thin. The effort required to set steel rebar during a field survey confirmed this, requiring a sledge hammer to drive steel rebar more than 20 cm into the sub-surface, blocky parent material. The study site is lightly covered by rock debris ranging in size from fist to small boulders. Some of this detritus, particularly the larger pieces, probably originates from the previously described outcrop higher up on the slope and has rolled down the slope or as been carried down by snow avalanches. The

[4] An escarpment is a geological formation that generally results from the erosion of tilted strata. The relatively low-angle slope parallel with strata is referred to as the dip slope and the steep slope is referred is the scarp or scarp face.

smaller particles may originate locally from the colluvium (sub soil) through a combination of bio- and cryo-turbation.

The soil parent material is a loamy-colluvium, which typically is derived from shales, limestones or sandstones (NRCS, 2006). As a result of the nature of the parent material, topography and the montane climate, soils here can be described as cryochrepts and cryoborolls (NRCS, 2006). Both of these subgroups are characterized by frost-related processes and, on steep slopes, influenced by frost-creep.

Vegetation: At the mountain range-scale, the vegetation at the study area varies dramatically with elevation. Lower elevations maintain closed and open montane forest. At prominent points at higher elevations sub-alpine and alpine vegetation can be found. In the transitional zone between these ecotypes, large grassy openings mosaic with dense coniferous forest and occasional aspen stands.

The study site is located in a montane forest opening. The surrounding forest is composed primarily of two tree species ranging in height from 1 m to 30 m. Douglas-Fir (*Pseudotsuga menziesii*) is abundant, including two prominent trees at the base of the slope which protrude into the slope's viewshed. Subalpine fir (*Abies lasiocarpa*) is also present, primarily north of and up-slope of the study site. Several trees have trunk diameters greater than 0.5 m and crown diameters greater than 5 m.

Vegetation within the study site is relatively uniform, composed primarily of sub-alpine grasses, forbs, and small shrubs. Woody plants taller than 0.5 m which persisted into the winter (and thereby likely influenced the snowpack dynamics) included small coniferous trees and sage brush.

Fauna: Prominent fauna in the region include black bear (*Ursus americanus*), coyote (*Canis latrans)*, elk (*Cervus canadensis)*, mule deer (*Odocoileus hemionus*) and white-tail deer (*Odocoileus virginianus*), various squirrel (ground squirrels, red squirrels, chipmunks, and possibly marmots), various raptors and song birds, and possibly grizzly bear (*Ursus arctos*) (MFWP, 2009). Black bear tracks were found near the study site. The study site itself is regularly crossed by elk, evident from tracks along a game trail, droppings, and browsing damage in autumn, and damaged wooden posts with elk hair on them near the game trail. The effect of burrowing mammals is extensive and clearly evident in spring, after snowmelt. Given that in winter those large mammals listed above are either hibernating (bears) or have migrated to lower elevations (ungulates), and that dogs were not allowed to join us on field days, no obvious snowpack disturbance was inflicted by animals.

Climate: The Henry's Lake Mountain range is on the western fringe of the Rocky Mountains and is situated in the intermountain climate, between the maritime and continental climates of North America (Mock and Birkeland, 2000). Southwestern Montana can experience weather extremes associated with both climates, most notably the warmer, moist air masses from the Pacific and cold, dry air from the Arctic, respectively.

The mid-latitude Westerlies are the prevailing upper level winds which carry relatively warm, moist air masses from the Pacific, located more than 1000 km to the west. With the exception of thunder showers, most precipitation in this region results from dynamic mixing of air masses along the polar front which often positions itself over

Montana in winter. Undulations in the position of the jet stream allow for troughs of dense, cold air masses to extend southward from the Arctic and for ridges of warmer mid-latitude air masses to move northward. The relative positions of the air masses can result in divergence of upper level air and the ascension of warm surface air (a surface low) which leads to cyclogenesis and possibly precipitation. Warm-, cold- and occluded-fronts bring large variations in air temperature and wind direction, as well as precipitation. In contrast to weather associated with cyclogenesis, a polar high pressure system can hold cold, dry air over southwest Montana for several days at a time, often resulting in temperature inversions and fog in the basins neighboring the Henry's Lake Mountains.

Before the moist air from the Pacific Ocean can reach this highland region, the air must pass over extensive mountain ranges, resulting in orographic precipitation. The drier air then flows over vast expanses of dry valleys and rugged terrain before being orographically lifted by the mountain ranges associated with the Rockies. Hence, in comparison with coastal regions, this area is dry.

Micro-Climate: Due to its northeast orientation and steep pitch, the study site experiences highly oblique direct sunlight, especially in winter. Trees surrounding the site experience fairly intense direct sunlight on their south-facing sides. The ridgeline and open forest on the upper slope shelter the site from westerly ridge-top winds. A relatively cold and calm micro-climate persists throughout winter on this slope, frequently fostering surface hoar formation. As a result, several recent snow studies

examining buried surface hoar - related instabilities have utilized this slope (Landry, 2002; Landry et al., 2004; Birkeland, et al., 2004; Logan, 2005; Logan et al., 2007).

Site Preparation and Maintenance

The Lionhead study site was prepared for this research in the autumn of 2003 by Spencer Logan and me. It consisted of a 31 m x 31 m square sampling area (961 m^2), located in a forest opening (Figure 6). The site contained five plots, including a large cross-plot spanning the site and four square plots nested between the arms of the cross-plot.

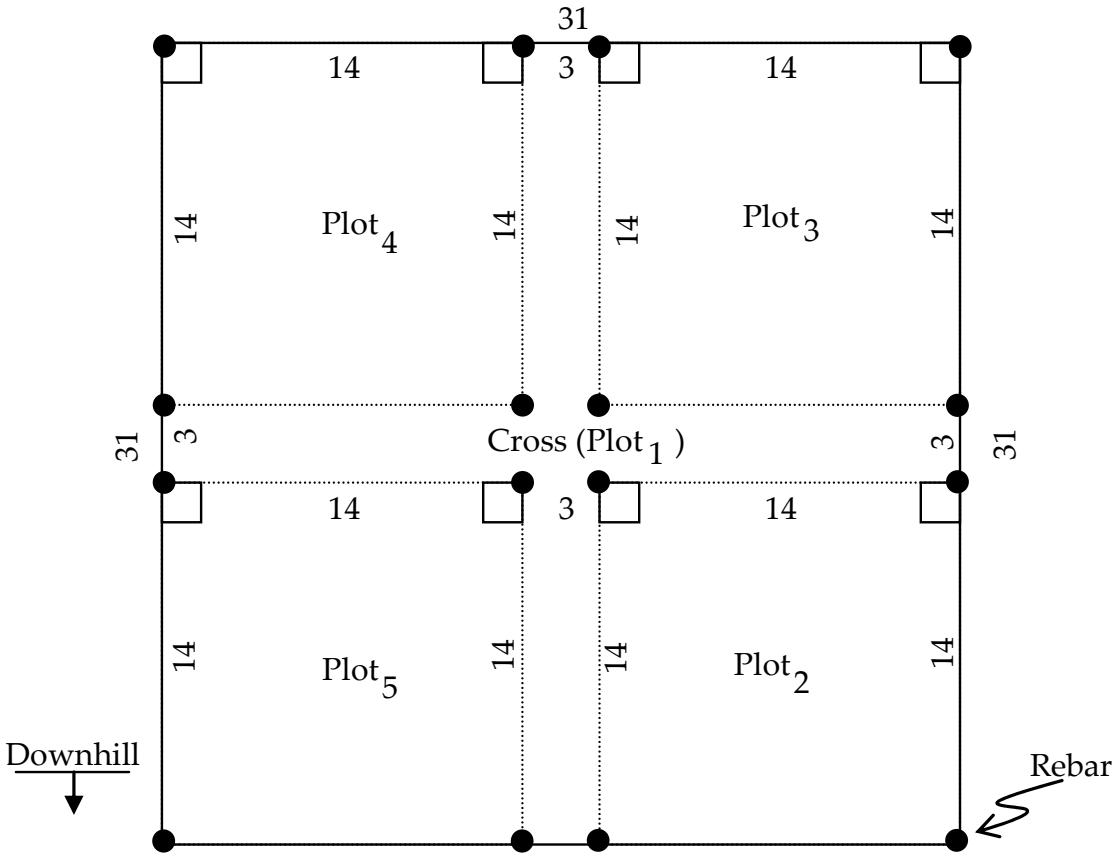

Figure 6. Study site. Small boxes by rebar indicate plot corners that were squared using triangulation during field survey. Distances are in meters.

The sides of the site were oriented parallel to the slope's fall-line, using an inclinometer. Plot dimensions were plotted using multiple survey tapes, starting at the top of the site (black arrows in Figure 7). For each square plot, the upper corners were plotted as 90° corners, using triangulation of survey tapes (small, solid-line boxes in Figure 6). The bottom transect of each square plot was measured last, indicating whether the plots were close to square (Figure 7).

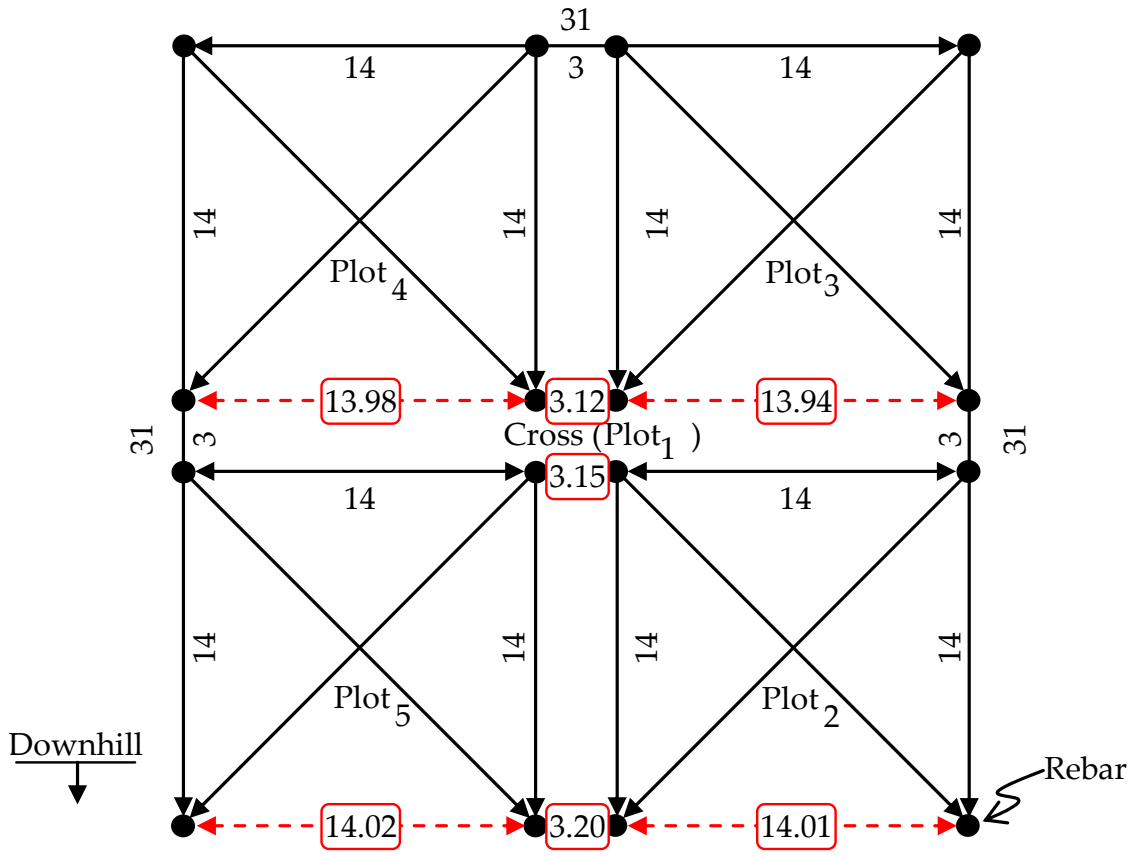

Figure 7. Closing measurements of all five plots are shown in red boxes along dotted arrows. Black arrows across the plots represent triangulated survey tapes. Distances are in meters.

If the slope was perfectly planar and measurements accurate, the closing transects (dotted red arrows in Figure 7) would equal 14 m. In actuality the length of closing runs

deviated by no more than - 0.06 m or a combined angular divergence of 0.12°. Whether caused by terrain or measurement error, these discrepancies were negligible.

The corners of each plot were marked with rebar that were between 0.6 – 1 m long. To aid in locating the corners in winter, wood posts were secured to the corner markers using steel wire (Figure 8).

Figure 8. Attaching wooden posts to rebar in October, 2004.

To deter backcountry enthusiasts (skiers, snowboarders and snowmobilers) from disturbing the snowpack within the field site, cautionary signs with an informative description of the study and contact information were posted strategically around the perimeter of the site (Figure 9). Periodically throughout the winter the signs and posts

were inspected and when necessary repaired and extended higher up in the snowpack. In summer all corner markers and signs were repaired and reset.

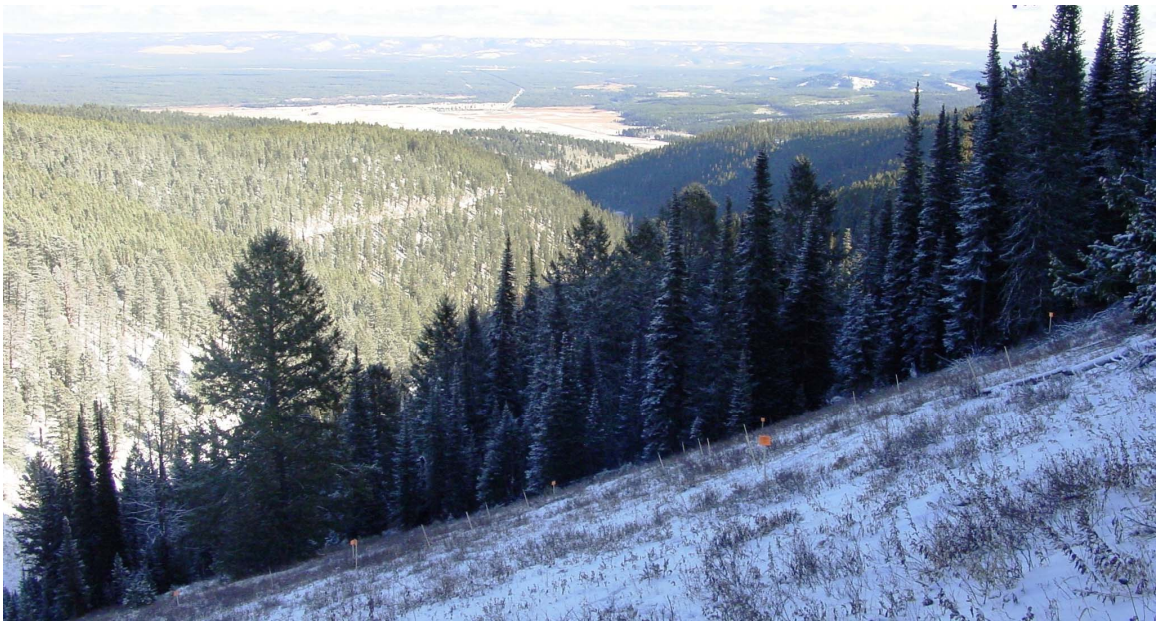

Figure 9. An example of a prepared site, with rebar, wooden posts, and cautionary signs posted. This particular study site, Lionhead North, was compromised when half the site was entrained by an avalanche that initiated at an outcrop above.

Snowpack Observations

Snowpack observations at the site began once a testable surface hoar layer had formed and been covered (and preserved) by snowfall. I examined four types of collected snowpack information: shear strength, microstructural resistance, perpendicular snow depth, and standard snow pit observations (Figure 10). At each observation, the local slope-oriented surface coordinates were recorded (Figure 11).

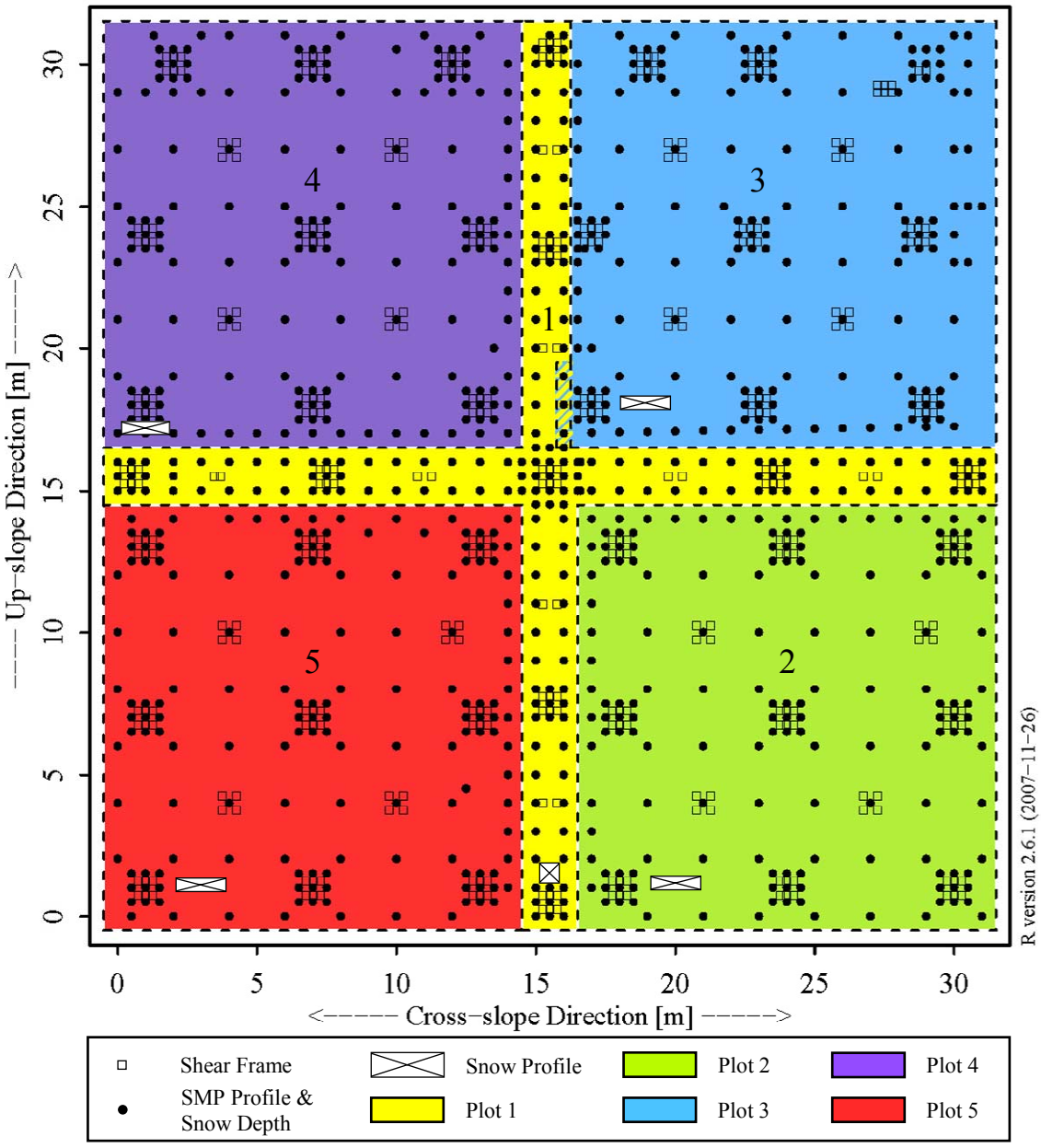

Figure 10. Sample layout includes five plots (colored regions), sampled during five field days spanning three weeks. I examined four types of collected observations, totaling five manual snow profiles, 352 shear frame tests (open squares) and 824 SMP and depth profiles (solid dots).

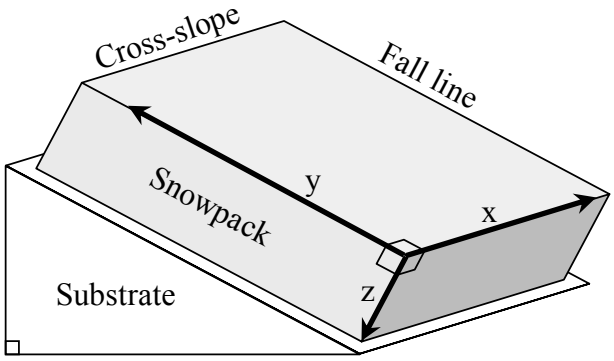

Figure 11. The local coordinate system consisted of three axes: a slope-normal z-axis with origin at the snow surface was used to analyze slab and weak layer dimensions, a cross-slope x-axis and an up-slope y-axis.

Sampling Layout

The sample layout evolved from a scheme used on a pilot study in the previous winter (2003-2004), described by Logan (2005). All observations were registered on a local coordinate system, such that the x- and y-axes were cross- and up-slope axes, and the z-axis was slope-normal with origin at the snow surface (Figure 11). The layout was developed primarily for geostatistical analysis of SMP profiles and for pit-to-plot analysis of SMP and shear frame measurements. Using basic geostatistical analysis, a sample scheme with a balance between short and long point-pair distances was identified (Figure 12.). Each plot contained nine clusters of observations at 0.5 m spacing. The sample spacing resulted in more than 100 pair distances in each 0.5 m lag distance (Figure 12). This helped ensure that geostatistics produced from the sampled area were representative.

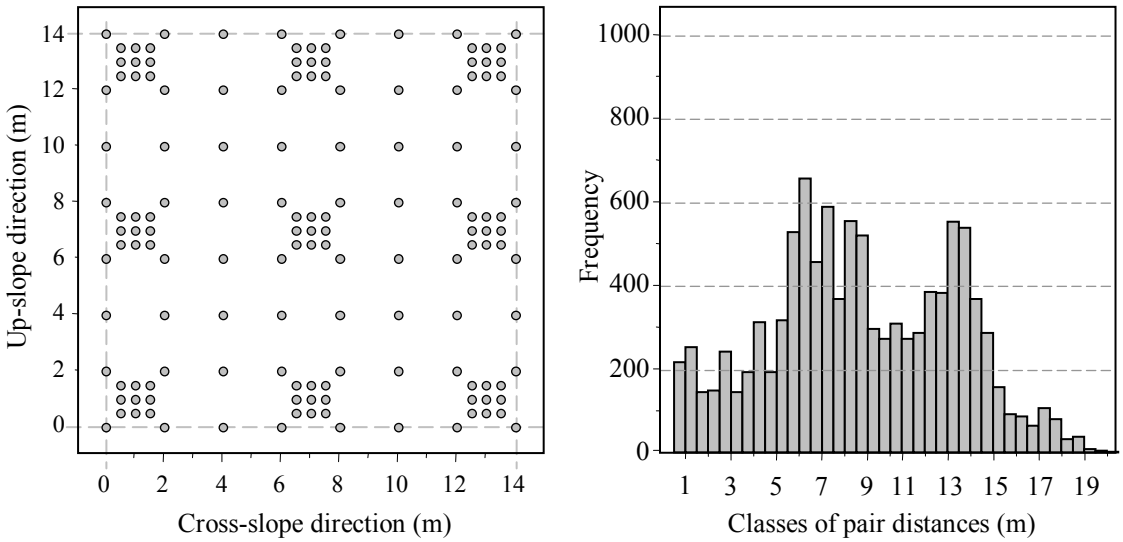

Figure 12. SMP profile sample layout for one 14 m x 14 m plot (left) results in a full coverage of lag distances, evident in the fact that there are no drastic drops in frequency of pair distances.

Random sampling was considered. Kronholm and Birkeland (2007) found that random sampling of an existing spatial pattern produced more accurate estimates of the existing spatial structure, as defined using a variogram, than did samples collected on a grid layout. We deemed it operationally impractical to randomly sample a slope and simultaneously obtain spatial coordinate information. Hence, I proposed the applied layout, which was later compared with other layouts, including random layouts, by Kronholm and Birkeland (2007) and was found to be more effective at characterizing local spatial structure than other tested grid layouts.

On February 28, 2005, three weeks after a surface hoar layer was buried, we sampled the large cross spanning the entire site (Figure 10, Plot 1). This allowed for slope-scale trends of snow properties in the up-slope and cross-slope directions to be identified at the beginning of the study. Thereafter, on March 1, 8, 14 and 21, the nested

plots (Plots 2 through 5) were consecutively sampled. This section describes the main measurement techniques as well as the sampling strategy and sequence.

The relative locations of snow observations were recorded using a slope-oriented coordinate system that was anchored to the wooden posts and rebar that had been set along the site perimeter before snowfall (Figures 6 and 8). Sample locations were identified on the snow surface by pulling and offsetting survey tapes between wooden posts. Sample surface locations were positioned to a relative accuracy of +/- 0.1 m, and an estimated absolute accuracy of +/- 0.25 m.

Each plot contained nine main clusters, each including six shear frame tests and nine SMP profiles within a 1 m^2 surface area. Because of the intensive bench preparation that occurs for shear frame testing, clusters are referred to as 'pits' in this dissertation. Four additional small pits were spaced between the main pits, each including four shear frame tests and a single SMP profile. Additional SMP profiles were located throughout the plot on a grid with 1 m spacing (Figure 10).

Field Work Progression

Due to the large number of observations and the significant travel and setup times, field days were executed very efficiently. The field crew carpooled from Bozeman (Montana) around 4:45 am and arrived at Targhee Pass around 6:15 am. Snowmobiles were used to bring the crew and equipment 4.5 km up the Lionhead ridge. Avalanche danger was assessed on site through local observations of avalanche activity, weather conditions, snow properties, and regional observations and regional forecast information. When a safe route was identified to the field site, which is approximately 100 m below

where the snowmobiles were parked on the ridge, the site was accessed by skis. Conditions were reassessed at the field site throughout the course of the day.

Upon safe arrival at the field site, site preparation required about 45 minutes to an hour. The SMP operator assembled the SMP and allowed the sensor to cool to below 0° C before beginning test profiles. This reduced temperature-dependent poor quality signals and snow melting and refreezing on the probe. Depending on snow and weather conditions, silicon gel was applied to the sensor tip to prevent moisture from entering the sensor chamber. The stability test operator conducted trial shear frame tests and stability tests (e.g. the Stuffblock test (Birkeland and Johnson, 1999) and the Quantified Loaded Column test (Landry et al., 2001)) to determine if there was an interesting weak layer present and, if so, which test was best suited for measuring its strength. One or two workers located and dug out the corner posts, which were then used as anchors for survey tapes that were pulled out across the plot.

As soon as the survey tapes were in place, the SMP, snow depth and shear strength measurements were then carefully coordinated. The SMP operator began measurements across the lowest transect, and then worked his way progressively upslope. The SMP profile holes were subsequently used for snow height measurements, using a centimeter delineated probe, as well as for establishing the locations of the stability test pits. The SMP operator and snow height observer were careful not to disturb the snow within the stability pits by maintaining their footing a safe distance from measurement locations. Because the weak layer was buried 20 cm to 55 cm below a soft, fairly

uncohesive slab, we estimated that a safe working distance equal to twice the slab height would be adequate.

Field workers utilized different media for logging observations, including map-based note taking, tabular note taking in field books, and tabular note taking in spreadsheet programs on personal digital assistant (PDA). While the latter was most convenient, poor cold weather performance and PDA crashes that resulted in data loss steered us back to analog note taking.

Once all observations were obtained, typically 6 to 8 hours after starting the measurements, all equipment was dismantled and packed up. Large snow piles and deep pits adjacent to neighboring plots were leveled to minimize differential deposition or ablation during subsequent storms. Typically we were back at the vehicle by sundown, and arriving in Bozeman between 19:00 and 21:00.

Manual Snow Profile

A manual snow profile, including hand hardness, crystal type and size, layer thickness, and a temperature profile, was performed at the bottom of the plot (Figure 10), using standard methods (Greene et al., 2004). Snow profiles are conducted to record several important stratigraphic characteristics of the snowpack, including snow hardness, grain form, grain size and temperature. The two structural properties of snow that are most commonly associated with snowpack strength are hardness and density.

Snow hardness was measured using the hand-hardness test (Greene et al., 2004). Because the stratigraphic weakness involved a buried surface hoar layer under a thin layer (e.g., 5 – 10 mm) of small grained facets, this type of observation was not helpful in

determining properties of either layer of interest. For thin and subtle stratigraphic features, the SMP has proved very useful in determining average hardness of thin weak layers, as well as microstructural hardness characteristics (Pielmeier and Schneebeli, 2003). Hence the collection and analysis of snow hardness information recorded by the SMP as penetration resistance profiles was central in this study.

Snow temperature has been shown to inversely affect the shear strength of faceted crystals and melt-freeze grains (Perla et al., 1982; Jamieson and Johnston, 2001). Snow temperature is measured using calibrated electronic thermometers at 5 cm or 10 cm increments. This data is useful for determining the temperature-induced vapor pressure gradients that are present within the snowpack and, hence, the types of metamorphism that may be active.

Grain characteristics play an important role in the structure, texture and strength of the snowpack. In addition, they provide important information about the type of metamorphism that previously or currently affects the snowpack. Although the Chinese identified the hexagonal geometry of snow crystals more than 2000 years ago, the first accurate systematic classification of snow crystals was developed in the 19th century using micro-photography (Gubler, 1999). Indisputably, the most significant photographic documentation of snow crystals was conducted by Bentley (1931), who documented over 6000 snow crystals using micro-photography (Nakaya, 1938). In the 1920's and 1930's Japanese researchers pioneered investigations into the behavior, mechanics and physical properties of snow (e.g., Nakaya, 1938; Daisuke Kuroiwa, in Wakahama, 1985).

The crystal habit of snow and ice was first scientifically described by Nakaya (1938), who classified artificial and natural snow crystals using three criteria, including crystal form, the formation temperature and the percent supersaturation relative to ice (Gubler, 1999). The International Classification for Seasonal Snow on the Ground (Colbeck et al., 1990) is the basis for the grain form and size observations in this study.

Grain form information has been shown to be invaluable for assessing shear strength (Perla et al., 1982; Föhn et al., 1998; Jamieson and Johnston, 2001). For a given density, faceted crystals and depth hoar possess substantially lower shear strength values than precipitation particles, decomposing fragments and rounded grains (Jamieson and Johnston, 2001). Grain size inversely affects shear strength for rounded grains, faceted crystals and melt-freeze grains (Perla et al., 1982). This can be explained by the fact that small grains possess greater surface area available for contact and bonding with adjacent grains, as well as a smaller displacement volume.

In this study, snow density measurements were limited to slab density observations at each cluster (pit) of shear frame measurements. Stratigraphic profiles of snow density were not performed for two reasons. As with hand hardness tests, volumetric density measurements require a relatively thick (i.e., several centimeters) sample for accurate values. Previous studies of strength properties of thin persistent weak layers such as buried surface hoar have not focused on density measurements (e.g., Jamieson and Johnston, 1999), largely because they can not be accurately sampled using volumetric density samplers (Jamieson and Schweizer, 2000). Even for newly developed surface hoar layers (still present on the surface) with crystals $\geq$ 5 mm, Föhn (2001)

recorded fairly high average densities (e.g., 132 kg m^{-3}) and suspected measurement error.

A second more fundamental reason for not conducting density profiles was that more stratigraphic information pertinent to snow strength could be obtained using the SMP. In the absence of micro-penetrometry technology, temporal or stratigraphic changes in snow density are commonly used to estimate snowpack strength. Many studies have shown snow density to positively affect strength and snow stability (Mellor, 1975; Perla et al., 1982; Jamieson, 1995, in Conway and Wilbour, 1999; Jamieson and Johnston, 2001), and comparisons of the density of different failure layers show that denser layers are typically stronger (McClung and Schaerer, 1993). However, the relationship between snow density and strength is not deterministic but rather a coincidental side-effect of microstructural properties (Shapiro et al., 1997). Given the availability of SMP technology, this study focused on acquiring large numbers of SMP profiles, instead of density profiles.

Shear Frame Test

Approximately 70 shear frame measurements quantified the *in-situ* shear strength of the targeted buried surface hoar weak layer at each plot, totaling 352 tests. Shear frame tests were preferred over column-type stability tests because additional buried surface hoar layers existed in the soft slab above the targeted weak layer which complicated the performance and interpretation of column tests. Using a 250 cm^2 shear frame, we followed standard operating procedure (Greene et al., 2004) (Figure 13).

Figure 13. Kalle Kronholm performing a shear frame measurement.

The shear frame test measures, *in-situ*, the amount of force needed to shear an isolated weak layer or *Gleitschicht* within the snowpack, (Perla and Beck, 1983). Pielmeier (2003) stated Eugster (1938) first developed a shear frame technique, while others have stated that Roch was its founder (DeQuervain, 1951, in Jamieson and Johnston 2001:59). In either case, the shear frame test has been used extensively for avalanche research purposes and for avalanche forecasting (e.g., Schleiss and Schleiss, 1970, in Jamieson and Johnston, 2001).

The shear frame was positioned within 5 mm of the boundary between the weak layer and the super-stratum (Perla and Beck, 1983). *Gleitschicht*-parallel force was then

applied in the down-slope direction using a force gauge attached to the shear frame at a pull-rate that was within the range of brittle fracture (e.g., 1s) (Jamieson and Johnston 2001:60).

The shear strength measured with a 250 cm^2 frame τ_{250} (Pa) is generally defined as the pull-generated shear force at failure F_{fail} divided by the tested area A_{frame} such that,

$$\tau_{250} = \frac{F_{fail}}{A_{frame}}$$

A more complete definition of shear strength incorporates the shear component of the force exerted by the experimental setup $\tau_{expt.}$ which is dependent on the slope angle α. $\tau_{expt.}$ accounts for the weight of the shear frame and the snow within the shear frame during the experiment, such that,

$$\tau_{expt.} = \frac{g \sin\alpha (m_{frame} + m_{expt.\,snow})}{A_{frame}}$$

Most studies disregard $\tau_{expt.}$ because it is small in comparison with typical shear strength values; however it becomes more influential when calculating stability indices involving light slabs. Combining the two previous equations, the total shear stress at failure τ_{∞} can be summarized as follows:

$$\tau_{total} = (\tau_{250} + \tau_{expt.})$$

A value of the shear strength independent of the frame area, τ_{∞}, was calculated by multiplying by a size-correction parameter, developed from measurements using shear frames of different sizes (Sommerfeld, 1984; Föhn, 1987), such that,

$$\tau_{\infty} = \tau_{total} \times 0.65$$

For the remainder of this manuscript, the terms 'shear strength' and 'τ_∞' are used synonymously.

Three components of slab stress were calculated: the vertical stress V_{slab}, the slope-normal stress N_{slab}, and the shear stress τ_{slab}. These stresses were calculated from slab mass m_{slab} (kg) values, which was derived from slab density measurements, and the slope-normal and shear stresses also utilized slope angle α, such that,

$$V_{slab} = gm_{slab}$$

$$N_{slab} = gm_{slab}\cos(\alpha)$$

$$\tau_{slab} = gm_{slab}\sin(\alpha)$$

Snowpack stability (S) was estimated as the ratio between shear strength (τ_∞) and slab stress (Conway and Abrahmson, 1984; Föhn, 1987),

$$S = \frac{\tau_\infty}{\tau_{Slab}}$$

A third variable calculated from the shear frame tests was the residual shear strength τ_{resid},

$$\tau_{resid} = \tau_\infty - \tau_{slab}$$

The residual shear strength (τ_{resid}) value quantifies the amount of additional force needed to reduce S to a value of 1, or hypothetically needed to cause shear failure. Sommerfeld (1984) used principally the same equation to estimate the additional slab load and new snow depth (assuming a pre-defined new snow density) that a stratigraphic weakness can support. Both τ_{resid} and Sommerfeld's (1984) "additional load" quantitatively describe the residual strength of the weak layer. While S can be used to

describe changes in the ratio of shear strength (τ_{∞}) to stress (τ_{slab}), changes in τ_{resid} describe changes in the difference between shear strength (τ_{∞}) and stress (τ_{slab}).

SnowMicroPen (SMP) Resistance Profile

I recorded 824 slope-normal hardness profiles using the SnowMicroPen (SMP) Serial No. 9-9. In this study SMP profiles served two main purposes, including stratigraphic delineation and microstructural characterization of the super-stratum weak layer complex, which included the weak layer and the 5 mm of adjacent slab. The methodologies relating to SMP signal processing and analysis are addressed in the following section.

SMP Profile Processing

Prior to SMP signal processing, the raw SMP data is downloaded as *.pnt files from the SMP controller using an OmniDrive USB Pro memory card reader in conjunction with the executable command-line based program *MMCREAD*. The files can be viewed and exported into ASCI files using *PeneWin32* (Version 4.1.0), a graphics software developed specifically for SMP data. Many statistical software packages are available for analyzing one or both of the file types, including R, S-Plus, SAS, IDL, MATLAB, etc. This study focused on developing code in R (R Development Core Team, 2008), which is a robust, cost-free, statistical software package available on the internet.

Pre-processing consisted of three main steps. Before calculating microstructural properties from SMP profiles, profiles were examined for usability, based on the presence

(or absence) of the weak layer and the signal quality of each profile. Then, the noise component of the resistance signal was estimated using non-parametric estimates, before a rupture-picking routine could be applied for microstructural estimates. These methods are described in the following sections.

Weak Layer Presence

I examined SMP profiles to determine if the weak layer was present and where on the slope the weak layer was not present. In most cases, weak layer presence could easily be determined (Table 1). In some instances it was more difficult to determine because of weak layer abnormalities (i.e., extremely thin or located adjacent to abnormal layers). Of the 824 recorded SMP profiles, 806 profiles (97.8%) exhibited the weak layer and 18 profiles (2.2%) did not definitively contain the weak layer (Table 1).

Table 1. Summary of weak layer presence in SMP profiles, determined through manual examination of profiles. For the purpose of this study, 'assumed present' refers to the profiles that definitely and very likely exhibit the weak layer and 'assumed not present' refers to the profiles that definitely and very likely exhibit no weak layer properties.

Plot	SMP No. Obs.	Definitely Present		Very Likely Present		Very Likely Not Present		Definitely Not Present		Assumed Present		Assumed Not Present	
		Count	%	Count	%	Count	%	Count	%	Count	%	Count	%
1	183	179	97.8	3	1.6	0	0.0	1	0.5	182	99.5	1	0.5
2	157	157	100.0	0	0.0	0	0.0	0	0.0	157	100.0	0	0.0
3	165	154	93.3	1	0.6	0	0.0	10	6.1	155	93.9	10	6.1
4	163	159	97.5	2	1.2	0	0.0	2	1.2	161	98.8	2	1.2
5	156	147	94.2	4	2.6	4	2.6	1	0.6	151	96.8	5	3.2
Total	824	796	96.6	10	1.2	4	0.5	14	1.7	806	97.8	18	2.2

SMP Signal Quality

Potential Causes of Poor Signal Quality: When the SMP is in perfect working order, mechanical and electrical interactions between the SMP and the external

environment can cause signal problems. Water can freeze in the sensor chamber or tip canal, reducing the signal micro-variance. Water enters the sensor chamber in one of two obvious manners: 1. water vapor within the chamber can condense when the instrument cools in the field, 2. snow on the probe can melt (from exposure to warm air or compression in the mechanical cog drive) and run down the probe to the tip where it is pulled up into the tip canal through capillary action. Silicon can hinder the latter occurrence, but excessive silicon in the tip canal may diminish signal micro-variance. The newer SMP models, such as the model 9.9 which I used, contain a rubber o-ring that hinders liquid water from entering the tip canal but may thereby also influence micro-variance through its elastic properties.

Slightly over-tightening the sensor tip causes the neck of the sensor tip to pitch slightly off center which may cause either friction within the canal, uneven force distribution at the o-ring, or torque on the sensor itself. In any event, this results in a change of micro-variance and in some instances a drastic change in mean resistance values (Figure 14). Conversely, an under-tightened sensor tip introduces obvious erratic signals. Snow grains, in particular dry small facets, can wedge or pin themselves behind the sensor head, between the sensor tip, o-ring and probe fulcrum edge, affecting micro-variance and mean resistance to varying degrees. Static caused by dry wind-blown snow can cause large-scale trends in profiles (Sturm et al., 2004).

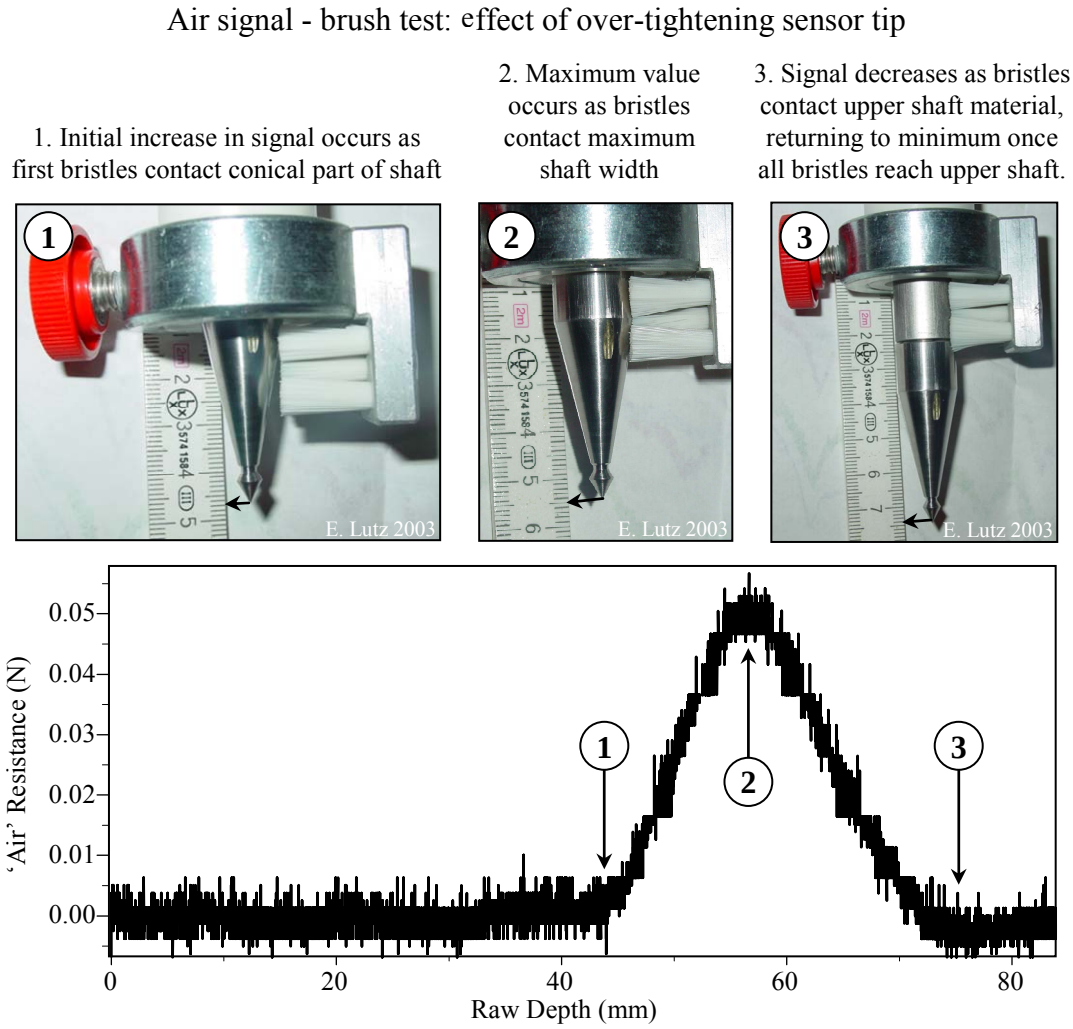

Figure 14. The apparent effects of over-tightening the sensor tip can be dramatic. In this example the sensor tip was intentionally slightly over-tightened. It is strong evidence that over-tightening caused either the shaft of the sensor tip or the sensor itself to contact the conus.

Signal quality can be greatly compromised by internal instrumental problems as well. A worn tooth or ice-clogged trough on either the cog wheel or probe causes the probe to either jostle, vibrate, slow down-and-then-surge, or it causes an unknown electrical issue (surge due to power draw, for example). Regardless of which phenomenon is occurring, ultimately these problems introduce spikes in the signal. When a worn tooth exists on the probe, spikes occur systematically at the same location

in multiple profiles (Figure 15). If the cog-wheel is damaged, the spikes appear periodically within each profile at a repeating distance equal to the circumference of the cog wheel.

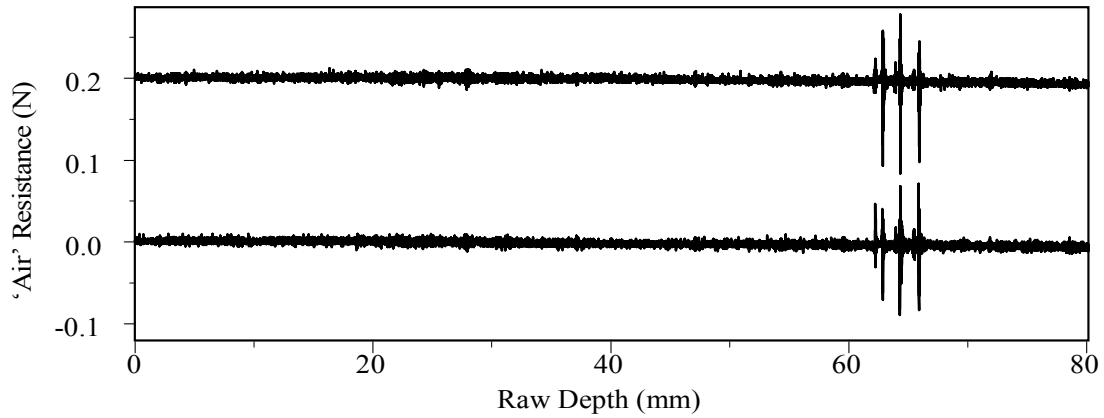

Figure 15. Two SMP air profiles (one of which is offset by + 0.2 N) illustrate the effects of a worn tooth, or rather set of teeth, on the probe shaft approximately 6.5 cm from the probe's starting position. A worn tooth on the cog-wheel results in similar errors that repeat periodically in profile.

Tooth wear may be accentuated when snow is not properly cleared from the teeth before they pass through the drive, which can result in ice build-up between the teeth and an increase of play in the cog-wheel system. While the provided brush mount removes much of the snow, manually cleaning the threads with a paint brush every time the probe retracts greatly improves performance.

Electrical factors can influence the signal as well. I witnessed that profiles recorded while the instrument is still cooling down often contain a trend, likely due to differential cooling in the quartz sensor (Figure 16). Worn transmission cables compromise accurate signal transmission, sometimes resulting in the complete loss of micro-variance information and adding significant trends in mean values (Figure 17).

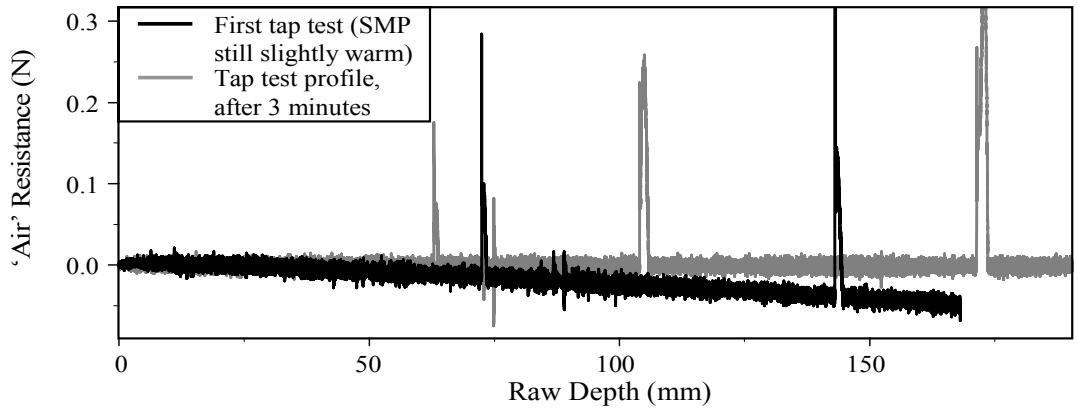

Figure 16. The black signal was recorded a few minutes after the SMP was unpacked and set up, and contained an obvious trend. The grey signal was recorded 3 minutes later and is perfectly level. Spikes in resistance are tap tests (see below).

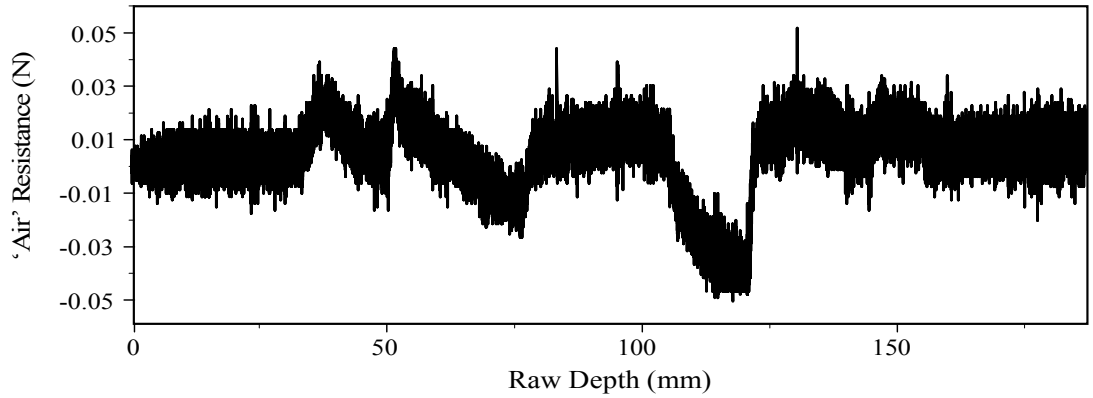

Figure 17. Air signal containing large deviations in mean hardness as a result of damaged cables. The sensor tip was removed to eliminate sensor tip-interactions as a possible cause. During a series of air tests, the cables were lightly bent, allowing for "soft spot" to be found.

As designed, the cables experience significant bending at their exit point at the top of the probe and at the controller. Faulty transmissions at these 'soft spots' may only occur when the worn cables are draped in a particular position, resulting in unpredictable errors. While the delicate nature of these cables lends to the high instrumental precision, it is difficult to utilize the instrument extensively throughout a field season (i.e., 2,000 to

3,000 profiles) without anticipating that, despite careful handling, parts do become worn.[5] Lastly, slight surges in electrical current, related to the battery power source, have influenced the force resolution in earlier SMP models. A magnetic ring and coil have been inserted into the controller which has reduced these effects (Schneebeli, pers. com., 2005).

SMP Signal Quality Control and Management in the Field: In addition to proper handling, diligence is required to limit the problems that can cause poor quality signals. The following techniques were developed over the course of the pilot study (2003-2004 season) and proved very useful in the main field season (2004-2005):

1. The SMP was cooled slowly over several hours prior to sampling. This was accomplished by placing the SMP in a backpack with a down jacket around it, and then placing the SMP outside. Cooling it slowly limited the chance for moisture to condense inside the sensor chamber in the early morning and lessened the cool down time necessary to eliminate signal drift (Figure 16).
2. Before sampling, several air profiles were performed. During each test, very small taps (< 0.02 N) were exerted on the tip, using a finger nail (hard, but harmless). Taps in clean signals return immediately to zero while in dampening signals (see next section) they return more gradually to zero, which influences microstructural estimates (see Figure 21).
3. Air profiles with tap tests were repeated several times a day, throughout the day.

5 R. Wetter clearly advised, "Cables should be handled in a very gentle way. It's a high-precision instrument with very sensitive parts to it." (SLF, Davos-Dorf, May 25, 2005)

4. The SMP was always held in the same orientation to the slope. In my experience, normal mechanical vibrations associated with the cog drive can vary considerably, depending on the instrument's orientation (i.e., whether the probe teeth are riding over the cog wheel or passing below it).
5. To ensure that snow did not get compressed by the cog system, in addition to utilizing the snow-removing bristle brush, the operator manually cleaned the threads with a paint brush after every profile, as the probe retracted.
6. Air pocket tests were also performed to test for trends in the signal.
7. In 2004, I designed and built a simple, white carrying case for less than $ 4.00. This made safe packing easier. The case could also be mounted on the SMP on relatively warm sunny days, to help keep the probe cool, thereby greatly reducing the amount of snow clinging to the probe as it retracts (Figure 18).
8. I replaced the standard short bipod poles with adjustable ski poles, reducing weight and providing better and more comfortable reach.

Figure 18. SMP retro-fitted with PVC packing container, which doubled as a shading device, as well as adjustable ski poles which aided in long reaches.

Classification of SMP Signal Quality: Diligence is required to limit the problems that can cause poor quality signals. Despite best efforts, a small number of profiles in any SMP campaign will likely contain poor quality resistance signals. If included in the analysis, these profiles can compromise the microstructural interpretation of the snowpack, especially for small (e.g., n <= 10) datasets.

To safeguard against false interpretations, at the outset of this analysis the signal quality of all SMP profiles was determined. The signal quality was characterized on the basis of three types of signal errors, including artificial trends, dampened micro-variance,

and a combination of the two (Table 2). The signal quality determines the potential use of a profile in microstructural and stratigraphic analysis.

Table 2. SMP signal quality classes.

Signal Quality Class	Signal Problem	Useable for micro-structural estimates (f_m, L, & σ_{micro}) & microstructure-based layer delineation	Useable for mean resistance - based layer delineation	Correction
C1	None	Yes	Yes	Not necessary
C2	Artificial offset or trend (linear or not)	Yes	Yes, if correctable No, if not correctable	Offset or de-trend may be possible
C3	Dampened micro-variance	No	Yes	Not possible
C4	Both C2 and C3	No	Yes, if C2 component of error is correctable	Not possible

Class 1 signals possess perfect character (Figures 19 to 21). Class 2 signals possess artificial trends that may be corrected using trend fits or simple offsets (Figures 16, and 19.2).

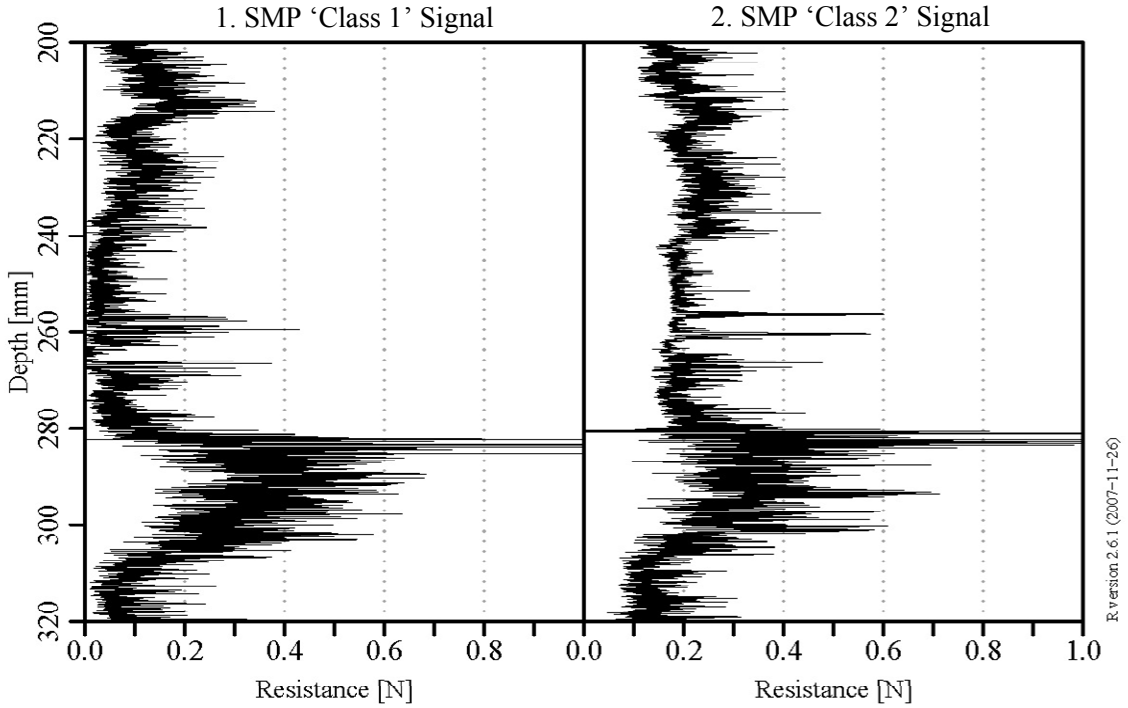

Figure 19. Comparison of (1) a normal 'Class 1' signal and (2) a 'Class 2' signal with an artificial trend that at this window extent appears to be a simple offset.

While some microstructural estimates, such as the mean rupture force (f_m) and the structural element length (L) are not directly affected by uncorrected Class 2 signals, estimates that depend on absolute force values, such as resistance statistics and the deflection at rupture (which is not applied in this study but is described by Johnson and Schneebeli (1999) and Marshall and Johnson (in review)), are adversely affected.

Class 3 signals exhibit a dampened micro-variance but maintain reasonable mean resistance values (Figure 20.2, and Figure 21.2). In the context of bond failures, Class 3 signals can possess greatly decreased rupture rates (Figure 21.2). Class 4 signals possess both artificial trends and hampered micro-variance. Class 3 and 4 signals can be used to delineate distinct transitions that are a function of mean hardness but, because the micro-variance information is corrupt, they cannot be used for microstructural analysis.

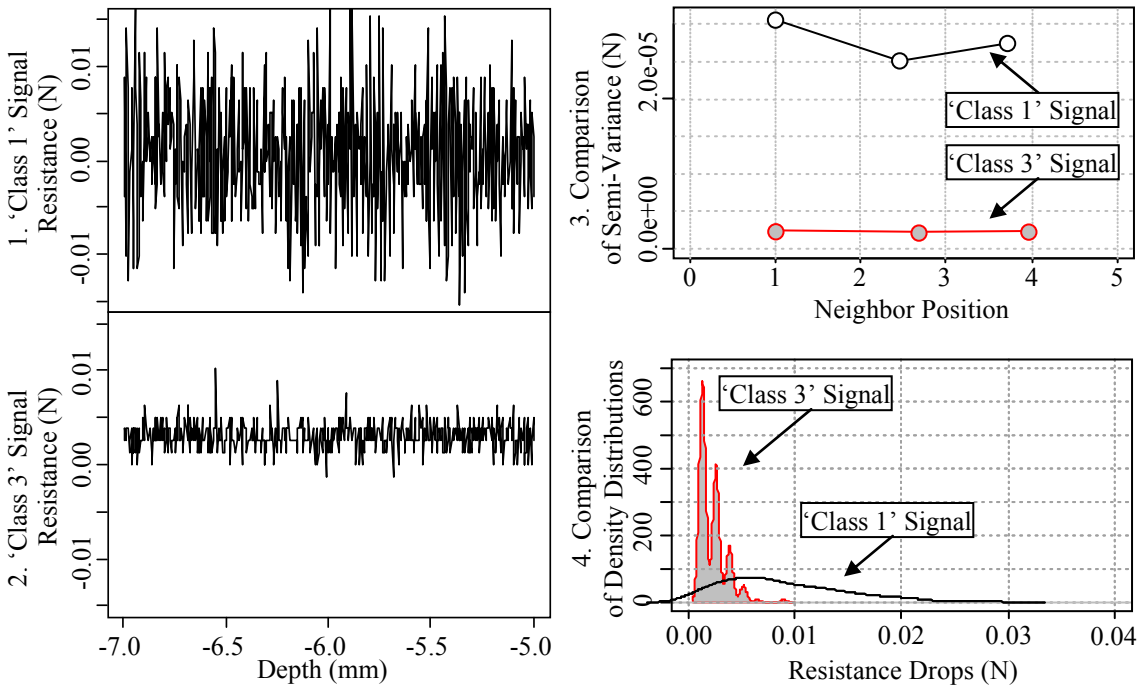

Figure 20. Comparison of open air segments from SMP profiles possessing (1) Class 1 and (2) Class 3 signals. (3) Semi-variance analysis of these two samples and (4) density distributions of the first derivative of resistance illustrate discrepancies in micro-variance.

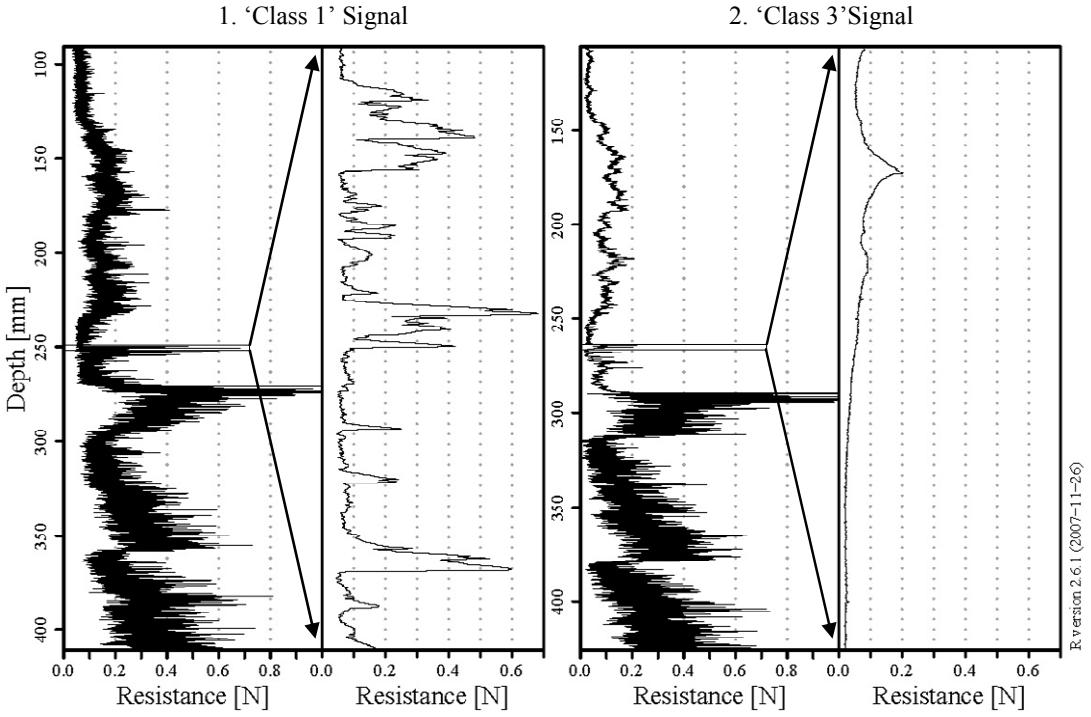

Figure 21. Comparison of weak layer segments from SMP profiles possessing (1) Class 1 and (2) Class 3 signals. Insets in (1) and (2) represent 3 mm segments originating from within the buried surface hoar layer. Note the high degree of artificial smoothing in the Class 3 signal as well as the absences of instantaneous drops (far right).

Of the 824 SMP profiles recorded during this field campaign, 781 profiles (94.8%) possessed Class 1 and 2 signals, jointly referred to as 'Good Quality' profiles, while the remaining 43 profiles (5.2 %) exhibited Class 3 and 4 characteristics and are grouped as 'Poor Quality' profiles (Table 3).

Table 3. Signal quality classes of SMP profiles, listed by plot. Counts and percentages of profiles used in and excluded from this analysis are listed on the columns on the right.

Plot	SMP No. Obs.	Class 1		Class 2		Class 3		Class 4		Good Quality (C1's and 2's)		Poor Quality (C3's and 4's)	
		Count	%	Count	%	Count	%	Count	%	Count	%	Count	%
1	183	171	93.4	10	5.5	0	0.0	2	1.1	181	**98.9**	2	**1.1**
2	157	131	83.4	0	0.0	26	16.6	0	0.0	131	**83.4**	26	**16.6**
3	165	156	94.5	7	4.2	0	0.0	2	1.2	163	**98.8**	2	**1.2**
4	163	163	100.0	0	0.0	0	0.0	0	0.0	163	**100.0**	0	**0.0**
5	156	143	91.7	0	0.0	12	7.7	1	0.6	143	**91.7**	13	**8.3**
Total	824	764	92.7	17	2.1	38	4.6	5	0.6	781	**94.8**	43	**5.2**

Plot 4 contained the cleanest dataset with all 163 profiles maintaining perfect signal characteristics. Most of the poor quality profiles originated from Plots 2 and 5. These compromised profiles often occurred in sequence (Figure 22).

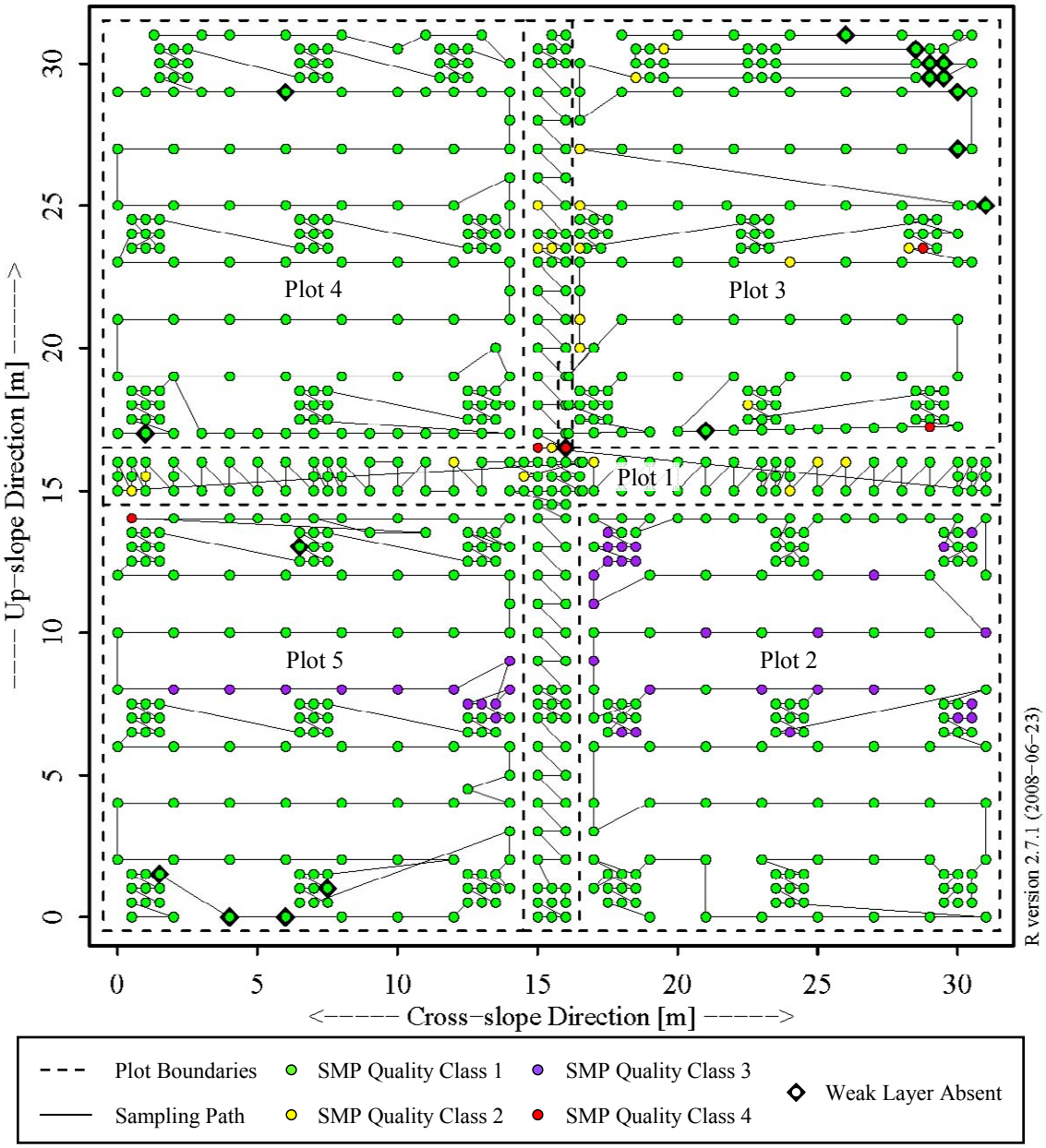

Figure 22. SMP signal quality classes. Black diamonds behind points indicate weak layer absence. Black lines indicate sequential order of profiles, generally executed in an up-slope sequence.

Considering the weak layer presence and signal quality, the total number of profiles available for microstructural analysis is limited to 760 profiles (Table 4). Plots 1 and 4 contain the greatest number and percentage of profiles available for microstructural analysis. Of the 781 profiles with signal quality adequate for microstructural analysis, 21 profiles did not exhibit the weak layer (Table 4).

Table 4. Counts and percentages of profiles grouped by signal quality and weak layer presence.

Plot	SMP No. Obs.	Good Quality and Weak Layer Present		Good Quality and Weak Layer Absent		Poor Quality and Weak Layer Present		Poor Quality and Weak Layer Absent	
		Count	%	Count	%	Count	%	Count	%
1	183	180	98.4	1	0.5	1	0.5	1	0.5
2	157	131	83.4	0	0.0	26	16.6	0	0.0
3	165	152	92.1	11	6.7	2	1.2	0	0.0
4	163	160	98.2	3	1.8	0	0.0	0	0.0
5	156	137	87.8	6	3.8	13	8.3	0	0.0
Total	824	760	92.2	21	2.5	42	5.1	1	0.1

To summarize, in determining the presence or absence of the weak layer across the slope, I utilized all 824 profiles. For the microstructural analysis of the weak layer, I excluded 64 profiles (21 good quality profiles did not contain the weak layer, 42 profiles contained the weak layer but possessed poor signal quality and 1 profile possessed poor signal quality and did not contain the weak layer).

Signal Noise Estimation

Deducing microstructural estimates from SMP profiles required estimates of instrumental noise – signal fluctuations not associated with mechanical interactions between the sensor tip and the snowpack. By examining the micro-variances of four types of SMP resistance signals, including open air, air pocket, soft surface snow and

weak layer snow (Figure 23), basic noise values were estimated. Fifty-five SMP profiles from plots 1 through 5 contained all four segment types.

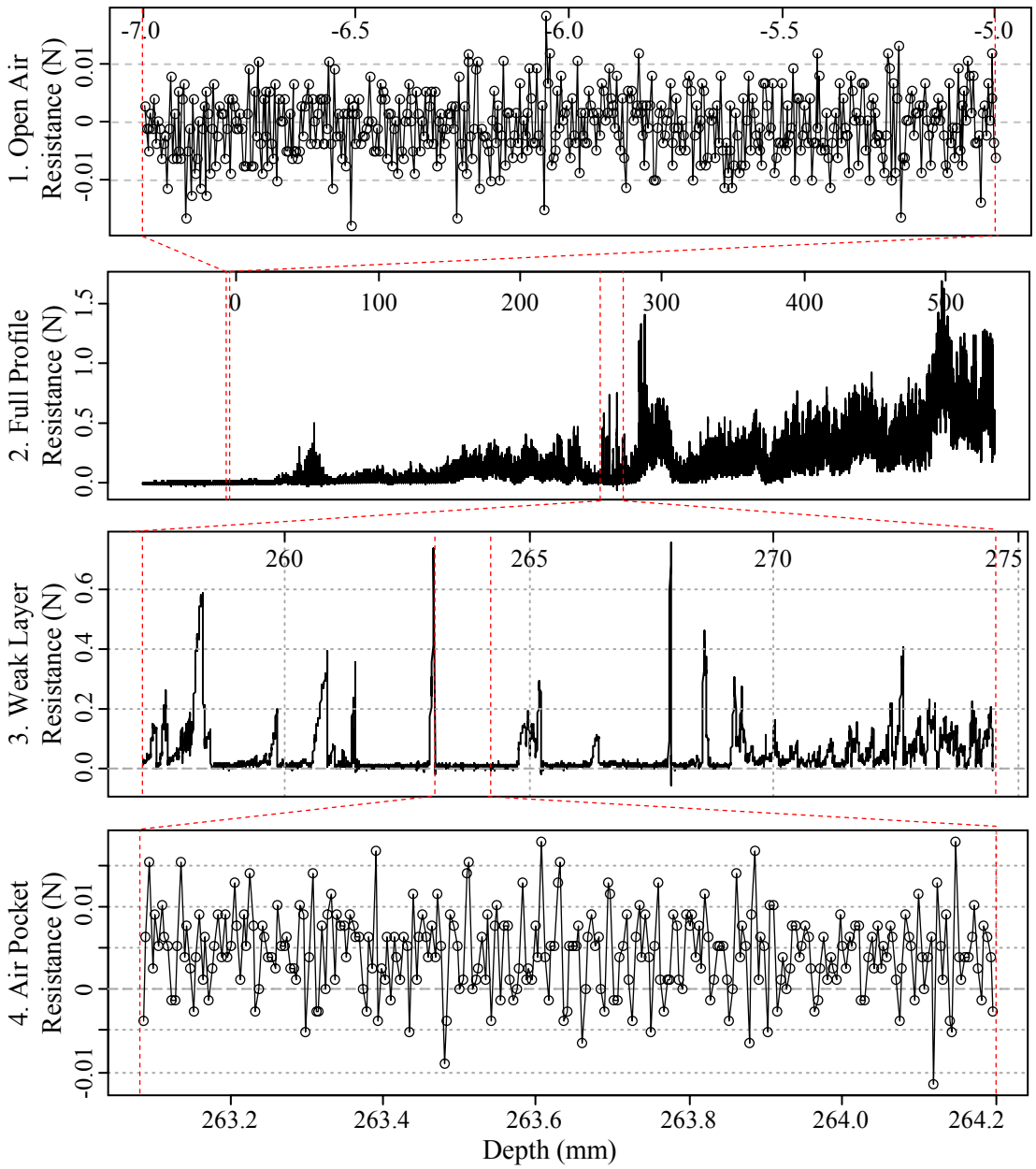

Figure 23. Example of sample segments of raw force values from Profile # 131 on plot 4, including (1) open air, (2) full profile, (3) weak layer, and (4) air pocket within weak layer. Note how similar the open air (1) and air pocket (4) signals appear.

The open air signal, recorded directly before the sensor tip enters the snowpack, quantifies instrumental noise in the absence of tip-grain and probe-snowpack interactions. In all 55 SMP profiles, open air signals were obtained from a 2 mm segment located 5 mm above the snow surface (Figure 23.1 and 23.2).

Analyzing noise of air pocket signals was useful because it indicated how much variation existed in the signal when the probe was submerged in the snowpack but the sensor tip was not interacting with structures. This likely occured when the tip moved through an opening between structures. The spaces were either pre-existing or they were created when the tip ruptured large structures which fell away from the tip into pore spaces. The 55 SMP profiles examined in the comparison were selected because they all contain air pocket segments within the weak layer (Figure 23.3). These short (e.g., 0.1 to 3 mm) 'flat line' segments exhibited no obvious autocorrelation or trends and often possessed mean resistance values near 0 N (Figure 23.4).

To confirm that SMP signals recorded in snow samples were not composed primarily of noise, the micro-variance of snow samples was also estimated. For all 55 SMP profiles, the soft snow segments were obtained from a 2 mm segment located 5 mm below the snow surface, and the buried surface hoar segments were defined using the manually delineated weak layer boundaries (Figure 23.3).

Non-Parametric Micro-Variance Estimation: For each segment type, the differences between local minima and the preceding maxima were pooled and their frequency distribution plotted (Figure 24). Since all four segment types possessed non-normal distributions with positive skew (Figure 22), parametric estimates, such as the

mean and standard deviation, were not useful descriptors. More valuable were non-parametric estimates, such as the median and the 99th percentile of drop values.

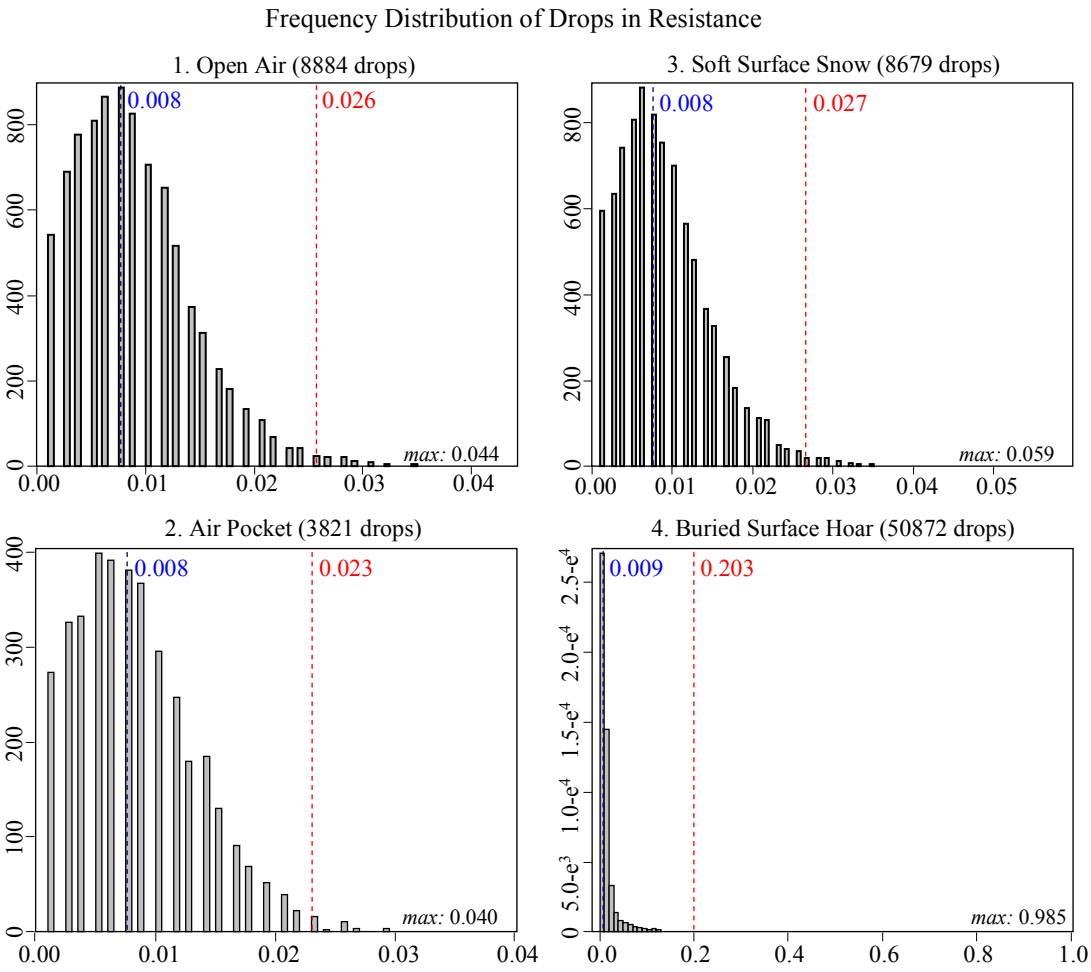

Figure 24. Frequency (y-axis) distribution of drop in resistance (x-axis, [N]) in four types of SMP segments, derived from (1) open air, (2) air pockets, (3) soft surface snow, (4) buried surface hoar. Values in parentheses indicate the total count of drops observed in each segment type. Blue and red dotted lines indicate median and 99th percentile values respectively. Note the different scales on the plots.

Median drop values were indistinguishable for open air, air pocket and soft surface snow samples (Figure 24.1 through 24.3). The median drop in resistance for the buried surface hoar measurements was 0.001 N greater than that of the other segments (Figure 24.4), presumably due to tip-grain interactions. This indicates that the SMP

signal obtained from air and soft snow samples possessed numerous drops in resistance that were indistinguishable from, and may be related to, instrumental noise.

Evaluation of the upper tail of the frequency distributions, specifically the 99th percentiles, revealed discrepancies between the segment types (Figure 24). The 99th percentile of all drop values from air pocket samples was 0.023 N (Figure 24.2), 0.003 N smaller than that of open air samples (Figure 24.1). This indicates that, in the absence of tip-grain interactions, less variance occured when the probe was penetrating the snowpack than when it was moving through open air. This finding was statistically confirmed by conducting a paired Wilcoxon Rank Sum test (Figure 25).

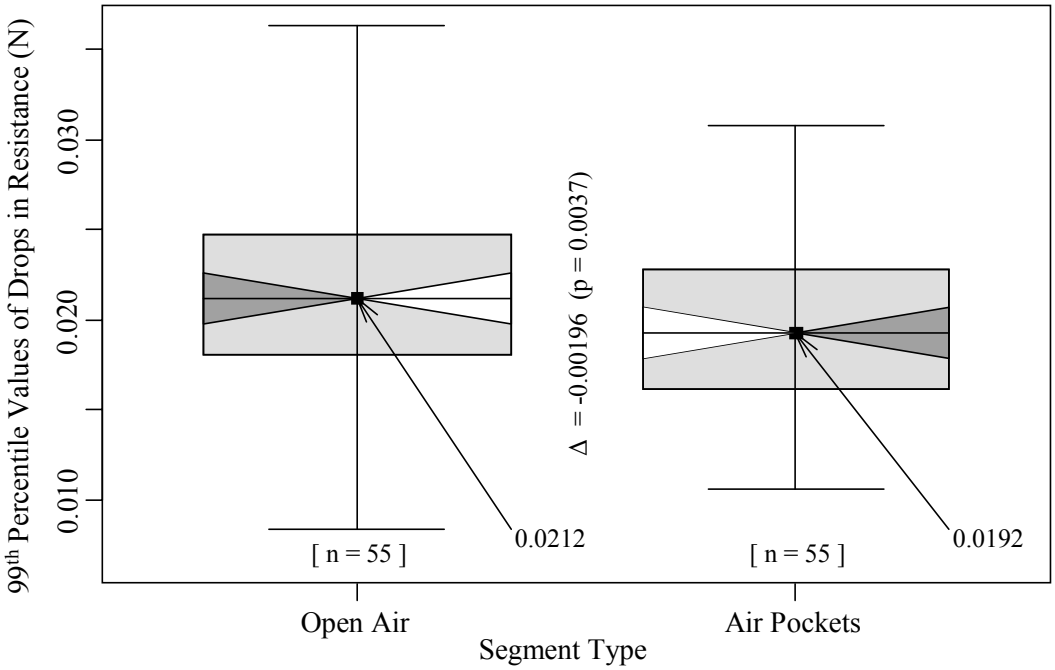

Figure 25. Boxplot comparison of 99th percentile resistance drop values from paired open air and air pocket samples. A significant (p = 0.0037) difference in centrality was identified using the paired Wilcoxon Rank Sum test.

The paired Wilcoxon Rank Sum test identified that a significant (p = 0.0037) difference in centrality existed between the 99th percentile values of open air and air

pocket values from the 55 examined SMP profiles (Figure 25). The median of the 99th percentile values of resistance drops within air pockets was 0.002 N smaller than it was in open air samples (Figure 25). This difference is slightly larger than to the instrumental precision of 0.0013 N, indicating that the SMP can distinguish force recordings between these sample types at this force resolution. Clearly, recording force at a higher resolution may allow for better differentiation between the sample types.

A probable explanation is that, through continuous contact with the penetrometer probe, the snowpack dampens mechanical vibrations generated by the motor or cogs that may otherwise cause the tip to oscillate, which in turn cause variations in the force signal.[6] Considering that the available contact area of the probe is several magnitudes greater than that of the sensor tip itself, the probe likely absorbs vibrations while the penetrometer moves through snow, reducing the vibrations affecting the sensor and thereby reducing instrumental noise.[7,8] This is further examined in the section on semi-variance signal analysis in Appendix F.

The largest drop values in the soft surface snow (quantified as the 99th percentile) were 0.0013 N greater than those of open air samples (Figure 26). This indicates that, while much of the signal is indistinguishable, a small number of recorded drops in the soft surface snow were larger. This was probably due to tip-grain interactions. This

---

[6] Such effects are probably most pronounced in data obtained from early SMP versions that did not yet have rubber o-rings integrated in the sensor tip – cone system.

[7] For example, at a depth of 20 cm, 1.57 x 10^{-2} m^2 of the shaft's surface area is submerged in the snowpack, while the sensor tip offers only 3.9 x 10^{-5} m^2 of surface area– a difference of three orders of magnitude.

[8] Future research could definitively test this hypothesis by recording SMP profiles with multiple 2 cm air pockets dug out at 10 cm or 20 cm intervals throughout the profiles. One should see the background variance in the artificially created air pockets decrease at greater depths in the snowpack. Jerry Johnson (pers. comm., 2008) suggested a controlled test where the probe is run through a block of elastic foam to quantify how much instrumental noise can be removed through dampening of the probe.

difference is identical to the instrumental precision of 0.0013 N, which indicates that lower resolution force recordings would fail to differentiate these sample types (air and soft new snow). The largest drop values recorded in the buried surface hoar samples (Figure 24.4), quantified as the 99th percentile, were an order of magnitude greater than those of the other three segment types. This discrepancy was clearly due to tip-grain interactions dominated by the rupture of structures.

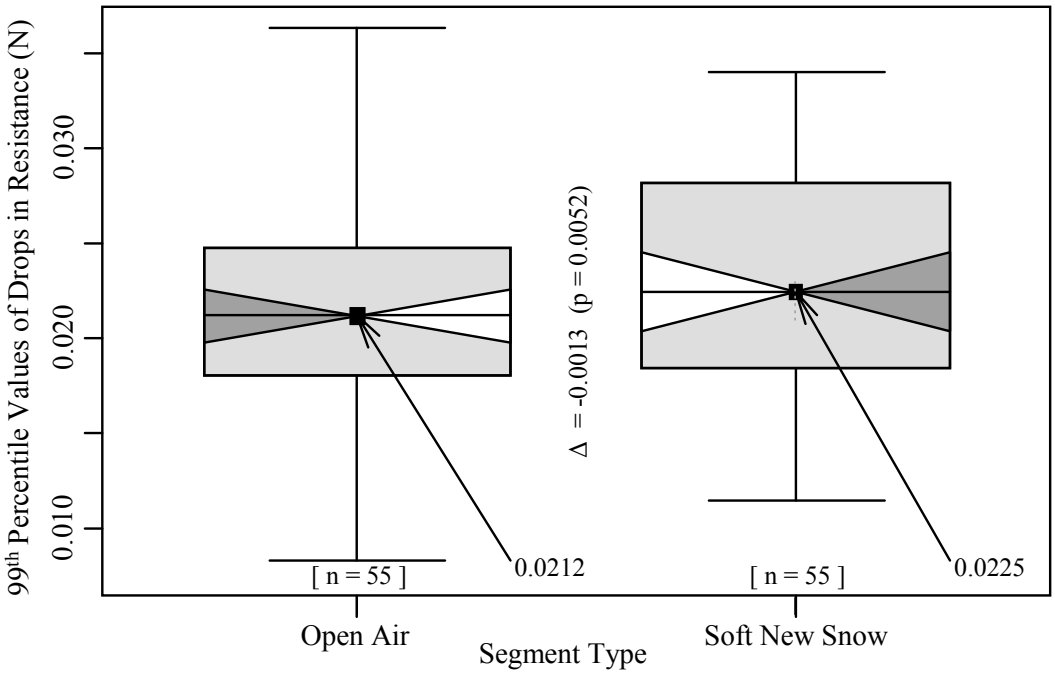

Figure 26. Boxplot comparison of 99th percentile resistance drop values from paired open air and soft new snow samples. A significant (p = 0.0052) difference in centrality was identified using the paired Wilcoxon Rank Sum test.

Rupture Picking Routing

Until recently, three main approaches have been utilized to define and select microstructural ruptures in SMP resistance profiles. Johnson and Schneebeli (1999) derived drop values from local minima and maxima and excluded drop values smaller than a pre-defined threshold value. Kronholm (2004) applied a slope-dependent

threshold to eliminate gradual drops in resistance from the microstructural analysis. This method relies heavily on consistent sensor tip performance. Instrumental problems can cause unpredictable subtle changes in signal quality that alter the slope value of drops in resistance, irrespective of snow type. To compensate for this, Kronholm (2004) shifted the threshold value from -2 $N \cdot mm^{-1}$ to -1 $N \cdot mm^{-1}$ when he deemed it appropriate. While the -2 $N \cdot mm^{-1}$ threshold filtered out instantaneous (i.e. occurring over one depth increment, 0.004 mm) drops in resistance smaller than 0.008 N, dropping the threshold to -1 $N \cdot mm^{-1}$ included all instantaneous drops larger than 0.004 N.

Sturm et al. (2004) applied a similar type of threshold. Initially, they corrected for linear drifting and signal chatter, and then subtracted the corrected signal from a fairly extensive (1 mm span width) local spline fit to deduce the 'sawtooth' residuals from which all drops in resistance greater than a certain force threshold were included in the microstructural analysis as ruptures.[9] Both studies assumed all remaining drop values to be ruptures.

Recently, Marshall and Johnson (in review) have proposed a dynamic rupture selection process that allows for the threshold to shift as a function of the maximum rupture force (f_{max}) within a given sample. In a sensitivity analysis of threshold selection, Marshall and Johnson (in review) found that by defining the threshold values as a percentage of the maximum rupture force (f_{max}) of a given snow type or sample, a constant relationship is maintained between the microstructural properties of eight

9 Sturm et al. (2004) do not state the exact threshold value they utilized. However, Figure 3b in Sturm et al. (2004:15) indicates that the threshold excluded most drops smaller than 0.006 N; occasional larger drops were excluded as well, indicating they may have used a rate dependent threshold.

different snow types. They suggest that setting the threshold value to 10 % of the maximum rupture value appears to be a reasonable starting point. At lower percentages, the differences between snow types become less distinct, while at values greater than 20 % the comparisons between snow types become more difficult due to increasing variance in their relationships between the maximum rupture force (f_{max}) and the microstructural parameters. In addition, this technique ensures that in very soft snow (e.g., mean resistance <= 0.02 N) the threshold value will not exclude all interactions below a defined threshold value (since the threshold value itself is defined by the sample).

I opted to apply Johnson and Schneebeli's (1999) static threshold to drop values derived from local maxima and minima. Based on the micro-variance values recorded in the air pocket segments, I defined a rupture as an abrupt decrease in resistance equal to or greater than the 0.0231 N in the raw signal, or 0.032 N once the values have been corrected for the normal force and tip friction. Hence, only a portion of the drops in resistance recorded in this surface hoar layer qualified as ruptures to be used for microstructural estimations (Figure 27).

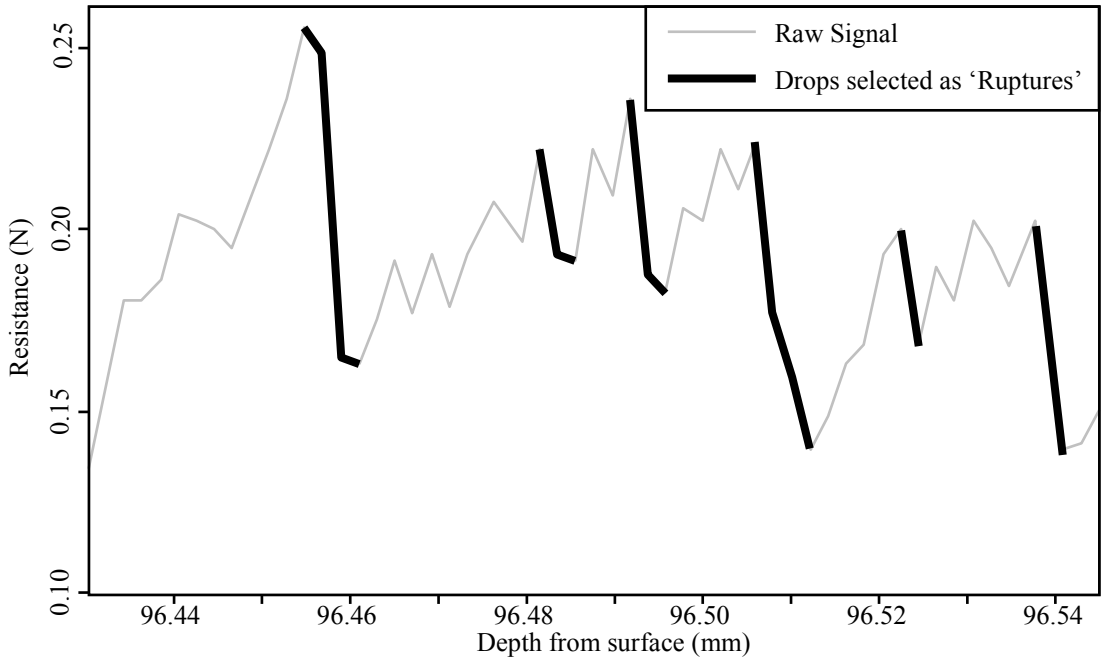

Figure 27. Example of rupture selection in a short (ca. 0.11 mm) segment of a SMP resisatnce profile. Based on the noise estimation and threshold selection criteria, drops in resistance greater than 0.023 N in the raw signal were selected as 'ruptures' (bold black). The remaining saw-tooth signature (grey line) is interpreted as noise. Based on these ruptures, the signal is further modified (Figure 28).

Microstructural Model Overview

Microstructural properties were estimated using Marshall and Johnson's (in review) micro-mechanical model, whereby estimates were derived from rupture size and frequency information recorded within SMP profiles. Marshall and Johnson's (in review) micromechanical model modifies Johnson and Schneebeli's (1999) model by accounting for limitations of the one-dimensional force signal and its force and depth resolution. The modifications include: (1) Accounting for simultaneous ruptures, (2) Building on Sturm et al.'s (2004) approach, the deflection at rupture δ is calculated exactly, (3) δ is calculated using individual rupture forces, (4) A force digitization error at rupture is

corrected. Cumulatively, these modifications improve the accuracy of microstructural estimates in simulations (Marshall and Johnson, in review).

The basic code for Marshall and Johnson's (in review) microstructural estimates was provided by Hans-Peter Marshall. I converted the code from MatLab to R macro language and modified how the digitization error correction is applied. For a noise-free signal, Marshall and Johnson (in review) use the slope of the raw signal immediately following ruptures to calculate the actual rupture values (Figure 28). However, because the SMP signal contains a substantial noise component, the resulting correction values are susceptible to erratic slope values caused by signal noise. More specifically, the noise can cause an overestimation of rupture forces (Figure 28).

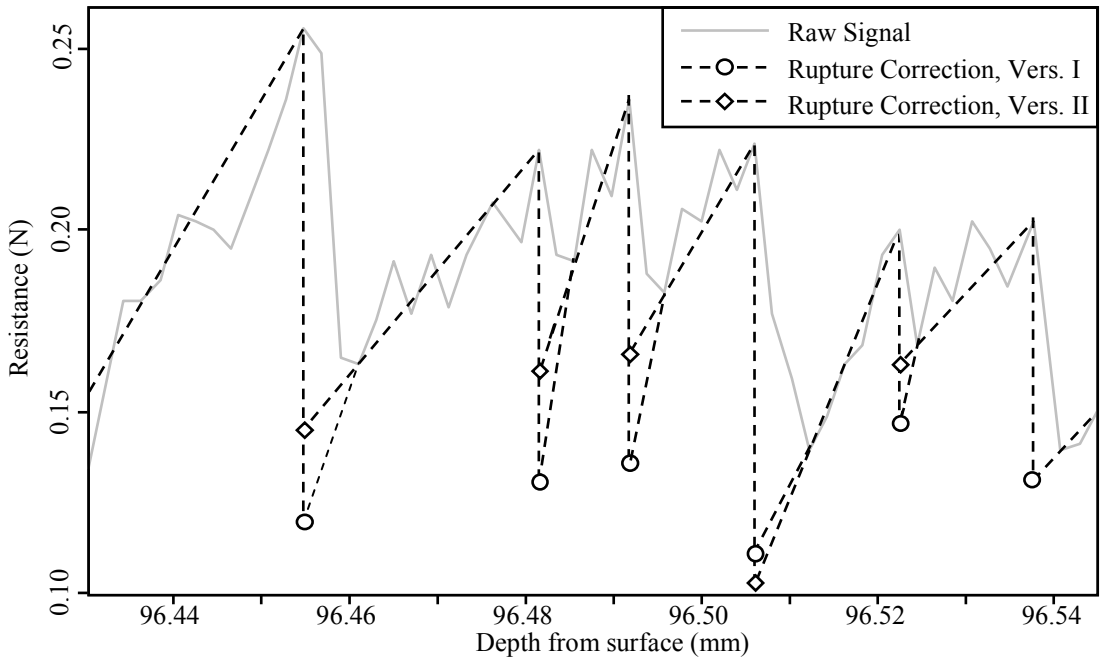

Figure 28. Two possible applications of Marshall and Johnson's (in review) digitization error applied to a short (ca. 0.11 mm) segment of SMP signal (grey line). One method utilized the rate of change of immediate subsequent loads (dotted line with circles) and the other, as applied in this study, utilized the subsequent load defined by the rupture and the next maximum (dotted line with diamonds). If noise was absent, both correction methods would produce identical results.

I incorporated a second algorithm that calculates the digitization error correction based on the average slope of each subsequent load, from the base of each rupture to the following peak (Figure 28). If the signal contained no noise, the two algorithms would produce the same corrections. However, given that noise is present, I made the assumption that the slope of the resistance values between immediate neighbors is less accurate than the average slope of a loading event.

Microstructural Estimates

Prior to microstructural estimation, the penetration force recorded in the vertical direction F_z was transformed into the force normal to the tip surface F. Johnson and Schneebeli (1999) and Marshall and Johnson (in review) define F as,

$$F = \frac{F_z}{\sin\theta(1+\mu\cot\theta)} = \frac{F_z}{\sin\theta+\mu\cos\theta}$$

where θ is the half angle of the cone (30°) and μ describes the friction coefficient between the sensor tip and the ice structures (i.e., 0.25, after Mellor (1975), in Kronholm, 2004). Several microstructural estimates can be derived from F, six of which were examined in this work and are described in greater detail below.

Rupture Force Characteristics (f_m, f_{max}, f_{cv}): The amount of force required to cause an individual element to rupture is termed the rupture force f (Johnson and Schneebeli, 1999). For a given profile segment of length z (mm), the mean rupture force f_m (N) is the sum of the rupture values divided by the number of ruptures N_f,

$$f_m = \frac{\sum_{i=1}^{N_f} f_i}{N_f}$$

f_m has been identified as a useful indicator of snow strength or stability (Kronholm, 2004; Sturm et al., 2004; Pielmeier and Schweizer, 2007; Lutz et al., 2008a, Pielmeier and Marshall, 2008).

I also examined the maximum rupture force f_{max}, which is pertinent because it is correlated with F_{max}, which has been correlated with shear strength of buried surface hoar (Birkeland et al., 2004; Lutz et al., 2007). Unlike F_{max}, however, f_{max} is unaffected by signal offsets or trends (Class 2 SMP signals).

As previously mentioned, individual values of f are dependent on processes that can not be determined using the current technology or micro-mechanical models, such as the relative orientation of the individual grains to the sensor tip surface, which undoubtedly influences the recorded resistance. Hence, as an individual value of f, f_{max} can vary substantially between adjacent profiles and with sample size. Despite this limitation in its interpretation, I rationalize that a population of f_{max} values, derived from several adjacent SMP profiles, can be used to obtain a typical f_{max} value for a surface hoar layer in a given spatial extent. This value is particularly useful because f_{max} is unaffected by resistance-based threshold values and hence can be easily compared with other studies using different threshold values.

Previous studies have utilized profile-oriented calculations of the texture index TI (Schneebeli et al., 1999) and the coefficient of variation of force F_{cv} (Pielmeier, 2003; Lutz et al. 2005, 2007) to discern weak layers such as buried surface hoar. F_{cv} is the standard deviation of resistance normalized by the mean resitance:

$$F_{cv} = \frac{\sqrt{\frac{1}{N_F}\sum_{i=1}^{N_F}(F_i - F_m)^2}}{F_m}$$

whereby F_m is the mean resistance and N_F is the number of resistance recordings in the sampled signal segment. I divided the standard deviation of f by f_m to calculate the coefficient of variation of rupture force f_{cv} as an index of texture:

$$f_{cv} = \frac{\sqrt{\frac{1}{N_f}\sum_{i=1}^{N_f}(f_i - f_m)^2}}{f_m}$$

Unlike TI and F_{cv}, f_{cv} is unaffected by near zero or negative values of F_m, which can occur in soft layers or Class 2 signals, respectively. By definition, f is always associated with relative drops in resistance and hence f and f_m cannot change signs. Also, it is not possible for f_m to approach 0 N because f is determined using a pre-defined threshold value. Unlike f_m, which cannot drop below the pre-defined threshold value, F_m can approach 0 N in soft snow, or, if a slight trend is present in the signal (e.g., Class 2 signal), F_m can drop below 0 N (Figure 29.1). As a result, F_{cv} can become a very large positive or negative value in magnitude (Figure 29.2), which is unrealistic and difficult to interpret. Because TI is derived in part from F_{cv} , TI also exhibits these erratic values (Figure 29.3). Because f_m remains positive and cannot approach zero (Figure 29.4), f_{cv} is robust against these influences (Figure 29.5). A comparison of the three micro-variance based texture estimates (TI, F_{cv} and f_{cv}) revealed that f_{cv} is more effective than TI and F_{cv} at differentiating the surface hoar layer from the adjacent soft small-grained facets above and below the surface hoar layer (Figure 29). For the pupose of this study, only the upper

transition (Figure 29.5, demarcated with arrow), between the surface hoar layer and facets above the surface hoar layer, is of direct interest, since this was the observed shear interface.

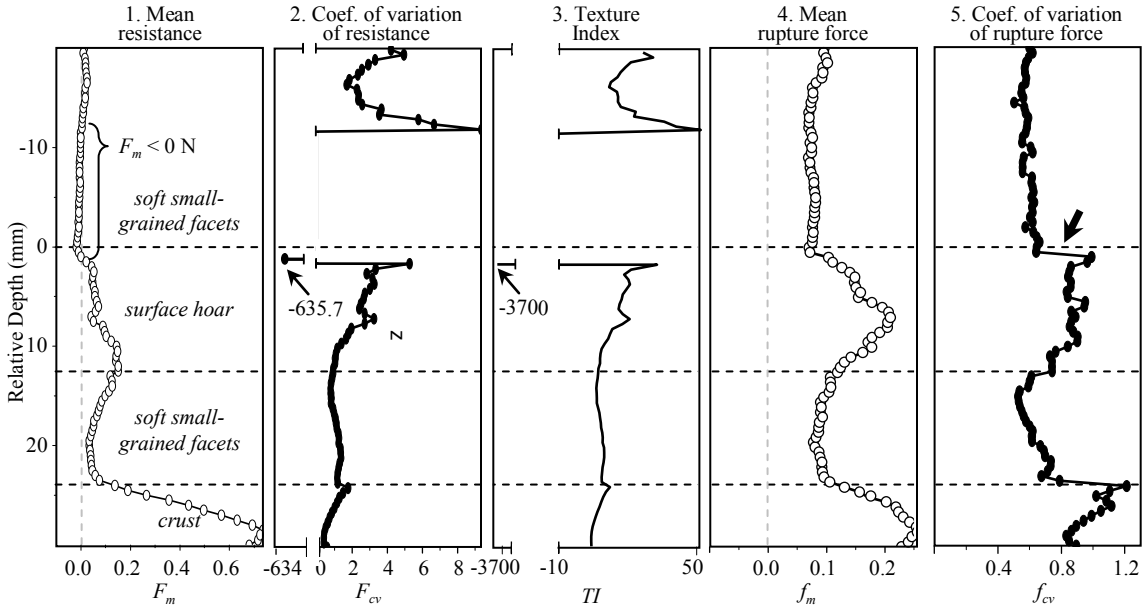

Figure 29. Comparison of micro-variance based texture indices (derived for Profile #12 at Plot 4) in their ability to differentiate surface hoar, soft small-grained facets, and a crust. (1) F_m dropped slightly below 0 N at relative depths between -13 - 2 mm (primarily within soft small grained facets). (2) F_{cv} and (3) TI became extremely small. (4) f_m cannot drop to 0 N and hence (5) f_{cv} can distinguish the upper boundary of the weak layer without being affected by low or negative F_m values. Based on the manually delineated transitions (dashed horizontal lines), (4) f_m and (5) f_{cv} more effectively distinguished the surface hoar from adjacent facets than did (1) F_m, (2) F_{cv}, or (3) TI. The transition that was examined extensively for my dissertation is demarcated with an arrow in (5). A crust 1 cm below the surface hoar layer is also evident in the data.

Structural Element Length Characteristics (L, L_{max}): Structural element length L (mm) describes the mean dimension of snow microstructures based on the number of ruptures recorded within a given volume of penetrated snow. Conceptually it is related to Gubler's (1978) 'fundamental unit'. Johnson and Schneebeli (1999) assume the structural elements occupy a cubical colume L^3, such that L is the cubic root of the average volume occupied by structures,

$$L = \sqrt[3]{\frac{\pi r^2 z}{N_f}}$$

whereby r is the radius of the sensor tip (2.5 mm), z is the vertical extent of the sample (which for this study is held constant at 5 mm) and N_f is the total number of ruptures identified within the sample. Hence, L is inversely proportional to the cubic root of rupture frequency.

Sturm et al. (2004) assumed spherical volumes that result in slightly larger estimates of structural element lengths. In this study I applied the former, which, assuming r and z are held constant, can be converted to spherical volumetric estimates by multiplying by a factor of 1.24. In either case, several studies have identified that L is correlated with grain size and possibly with stability (e.g., Pielmeier et al., 2006; Pielmeier and Schweizer, 2007).

The maximum structural element length L_{max} was also calculated, since it is unaffected by the threshold-dependent rupture picking routine and because it estimates the largest possible structure or void space between structures. Unlike L, which is a good indicator of average structure sizes (since it is derived from an average), L_{max} does not correspond with the exact dimension of the largest distance between structures or bonds, since it is unknown how the actual microstructure was configured in relation to the tip. However, L_{max} is likely a better indicator of large pore spaces than is L but is highly dependent on applied window size (sample extent) z.

Micro-Strength (σ_{micro}): As defined by Johnson and Schneebeli (1999) the micro-strength σ_{micro} ($N \cdot mm^{-2}$) defines the following relationship between strength and structure,

$$\sigma_{micro} = \frac{f_m}{L^2}$$

This estimate recognizes an increase in f_m or a decrease in L will result in stronger microstructure. Conversely a decrease of f_m or an increase in L results in a decrease of σ_{micro}. Absolute values of σ_{micro} should not be over-interpreted as true strength values, since L is calculated under the assumption of microstructural isotropy, which is probably inaccurate for surface hoar layers. Despite this limitation, σ_{micro} does effectively describe changes in stability. Lutz et al. (2008a) and Pielmeier and Marshall (2008) identified σ_{micro} as effectively differentiating stable and unstable conditions of weak layers.

Stratigraphic Sampling Approaches of SMP Profiles

An important component of the microstructural analysis is the stratigraphic sampling approach. Three types of stratigraphic sampling approaches were tested in this study, the last of which was chosen for the dissertation. Basic concepts of these approaches are summarized in Table 5 and illustrated in Figure 30.

Table 5. General information regarding the stratigraphic sampling approaches. Results presented in this documentation highlight approach 3.

Sample approach	Sample extent (mm)	Resample	Uses exact manual boundaries?	Pros	Cons
1. *Discrete Layer*	h_{wl} (3 – 20)	No	Yes	- All weak layer data utilized	- A priori boundaries - Results influenced by changing sample size (dep. on h_{wl})
2. *Median of Multiple Windows*	5	Yes, median of multiple samples	Yes	- All weak layer data utilized - Constant sample size allows for consistent comparisons	- A priori boundaries
3. *Continuum Sampled at f_{cv} Extremes*	5	No	No	- Exact boundaries not needed - Objectifies and automates delineation (based on logical (e.g. textural) prop.) - Constant sample size allows for consistent comparisons	- Potentially erratic, since only 1 sample

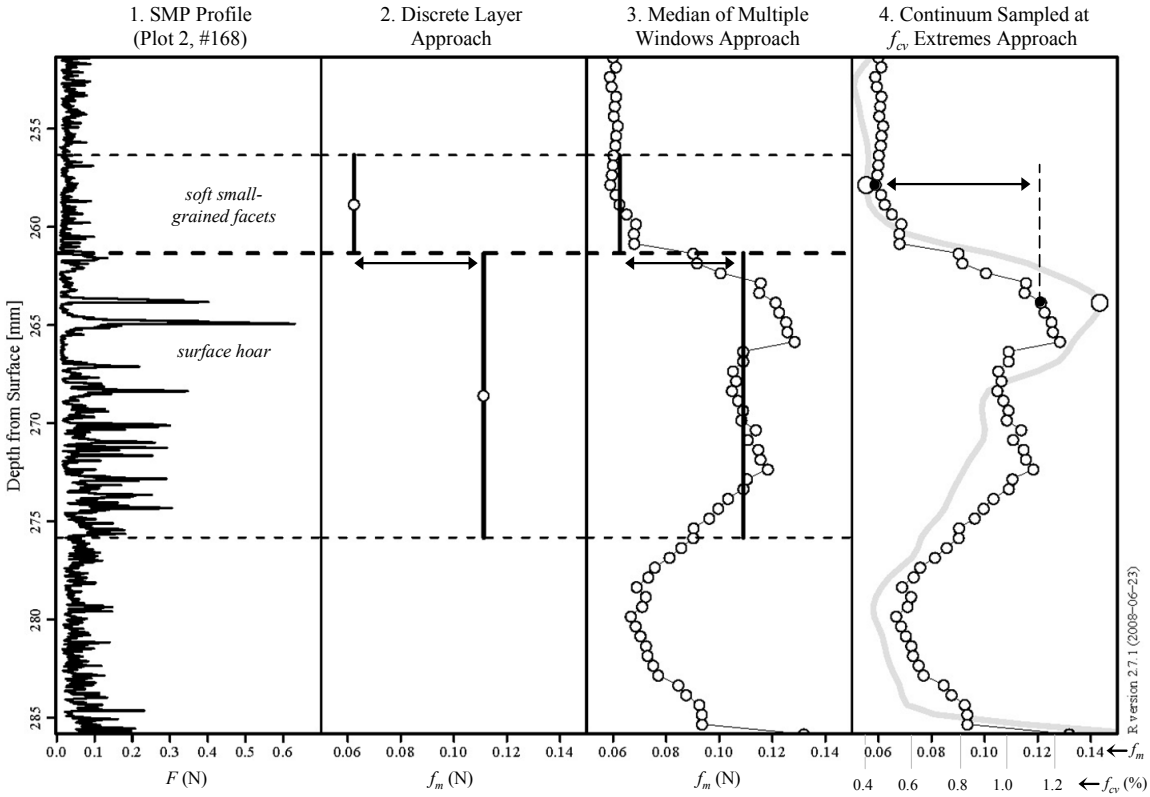

Figure 30. Stratigraphic approaches of calculating a weak layer's mean rupture force (f_m). The raw resistance profile (1) was used to manually delineate the boundaries of the weak layer (bold, dashed horizontal line). f_m of the weak layer was derived using (2) the discrete layer approach, (3) the median of multiple moving-windows approach, each derived from 5 mm windows, and (4) a single f_m value derived from a 5 mm window located at the local maximum of f_{cv} (also derived from 5 mm moving windows). This study utlized results produced from the third technique.

Discrete Layer Approach: Most SMP studies have utilized discrete layer-based analysis when analyzing stratigraphic properties (e.g. Birkeland et al., 2004; Kronholm, 2004). This technique necessitates manual delineation of all layers of interest. Using the boundaries, a resistance profile is segmented into discrete layers which are treated as independent samples, from which microstructural estimates are derived (Figure 30.2). In this study, two signal criteria assisted in manually delineating the buried surface hoar layer in the SMP profiles:

1. The load and fracture signature typical of large hoar crystals interacting with the sensor tip (Johnson and Schneebeli, 1999; Schneebeli et al., 1999). While the absolute values of the load and rupture pairs can vary signficiantly, typically the the resistance drops close to 0 N between loads. Thus, variations in the resistance signal appear to be largely caused by individual structures. In contrast, in small grained equilibrium snow, resistance will rarely near 0 N between loads, since far more structures are often in contact with the sensor tip than in more porous snow types.

2. A flat line signal indicative of the air in coarse, but low density snow, typically between large hoar crystals. When such segments were present in this dataset, they varied between 0.1 mm and 3 mm in length.

These criteria could be safely assumed since the adjacent layers were small facets which produced more frequent variations in resistance that were typically a magnitude smaller than those recorded in the surface hoar layer. In addition, Birkeland et al. (2004) found that slight displacements of the boundary locations (e.g., 5% thinning of the weak layer) did not significantly affect statistical analysis. The slab thickness (h_{slab}) was derived directly from the depth to the weak layer. The snow surface was delineated manually.

For the super-stratum, the 5 mm segment directly above the weak layer was also sampled, as it is the stratigraphic location where the base of the shear frame was located. For each profile, differences between these adjacent samples were calculated for each variable and are referred to as step-changes (horizontal two-sided arrow in Figure 30.2).

Building conceptually on the moving-window application of Lutz et al. (2007), two additional sampling approaches were considered, both of which utilize moving-window estimates but varying in their degree of automation or need for manually delineated transitions (Table 5). For both methods, microstructural estimates were produced from 5 mm signal extents (or 'windows') that are offset by 0.5 mm. Although sometimes redundant, this sampling scheme more reliably produces local minima and maxima values than do moving-windows with larger windows or smaller overlaps.

Median of Multiple Windows Approach: This sampling approach utilized the *a priori* knowledge of manually delineated layer boundaries to resample the profile-oriented microstructural estimates. For a given microstructural estimate (f_m, for example) the median value of all moving window samples between the upper and lower boundaries of the weak layer was obtained (Figure 30.3). While for some estimates, the values were very similar to those produced by using the discrete layer-based approach, dimensional estimates such as L and L_{max} can be significantly different. Although this also requires manual delineation, estimates are derived consistently from the same sample extents (5 mm), potentially increasing comparability. The same procedure was applied for deriving estimates of the adjacent 5 mm of super-strata.

Continuum Approach: Automated Sampling using f_{cv} Extremes: Since the SMP measures very small increments along a profile, layer boundaries that typically are considered discrete features (e.g., when using the hand-hardness test) are more accurately recorded as gradual transitions (Birkeland et al., 2004). For any microstructural estimate,

a discrete layer, such as the buried surface hoar layer, is not described by a single value (as in the disctere layer approach) but rather by a sequence of values (white dots in Figure 30.3 and 30.4). This allows for the bed surface-weak layer-slab complex to be treated as a continuum of estimates, containing extreme values and transitions of varying degrees of abruptness. Because estimates are derived from SMP segments of a constant extent (5 mm in this study), estimates are easily compared and a degree of automation can be brought into the stratigraphic analysis.

To derive microstructural properties from stratigraphic features or transitions, the continuous moving-window microstructural estimates were sampled using local extreme values in a texture profile. This basic methodology builds on those developed by Lutz et al. (2005 and 2007). They utilized local extremes and transitions of F_m and F_{cv} to locate stratigraphic boundaries. I utilized variations in texture, quantified with f_{cv}, instead of F_m, since in this dataset, F_m remained fairly constant between the surface hoar and super-stratum.

Several studies have identified the usefulness of F_{cv} for distinguishing buried surface hoar layers from adjacent strata (e.g., Pielmeier, 2003; Lutz et al., 2007). In general, transitions between layers are often associated with local maxima of F_{cv} (Lutz et al., 2005). Thin surface hoar layers, which possess larger textures than adjacent strata, typically contain one local maxima of F_{cv} near the middle of the surface hoar layer (Lutz et al., 2007). As described previously, F_{cv} is affected by values near zero or negative, which makes automated interpretation difficult. Instead of F_{cv} or TI, three robust indicators of texture were considered: N_f, L, and f_{cv}. After comparative testing, f_{cv} was

chosen over L and N_f because it differentiated both the super- and sub-strata boundaries more consistently than the other two estimates did.

Using an automated routine, the maximum f_{cv} value within the weak layer or the adjacent 5 mm of slab was identified (Figure 30.4). Then the first minimum (trough) value above was identified. At both of these stratigraphic depths, the microstructural profiles (f_m, f_{max}, f_{cv}, L, L_{max}, and σ_{micro}) were sampled and the step-changes between these estimates calculated (horizontal arrows in Figure 30.4). Since shear failure was consistently initiated at the upper weak layer boundary, the substrata and lower step-change were not examined here.

Comparison of Stratigraphic Sampling Approaches: A comparison of micro-strength (σ_{micro}) properties of the weak layer, produced using the three stratigraphic sampling approaches, is described by Lutz et al. (2008b). All three approaches produced similar spatial datasets and nearly identical temporal results. The *discrete layer* and *median of multiple windows* approaches possessed higher degrees of spatial dependence. Values produced by all three approaches correlated with spatial patterns in weak layer thickness (h_{wl}) and shear strength (τ_∞), indicating that all three sampling approaches capture pertinent microstructural information.

The three tested microstructural sampling approaches produced the same finding: micro-strength (σ_{micro}) decreased significantly following an increase in slab load. The decrease in micro-strength (σ_{micro}) was accompanied by a significant decrease of stability, derived from shear frame measurements of strength. The *continuum* approach that utilized the local maximum of f_{cv} to sample the microstructural properties of the weak

layer produced very similar results while utilizing significantly less resistance information (for each SMP profile, microstructural estimates of the surface hoar layer were obtained from only a single 5 mm window). Most importantly, this approach is the most objective and can be automated without precisely manually delineating the weak layer. Hence, for the purpose of this study, results from the third approach, the *continuum* approach with automated sampling at f_{cv} extremes, were examined in greater detail.

In summary, the main SMP analysis was conducted using several methods of signal processing, microstructural sampling and stratigraphic sampling techniques that for each stratigraphic location resulted in 18 datasets (Figure 31). Extensive testing was done using a 0.025 mm micro-filter that applied a gaussian smooth to reduce noise between immediate neighbors in the resitance signals. This dissertation focuses on the findings produced by one set of methods, as highlighted in Figure 31.

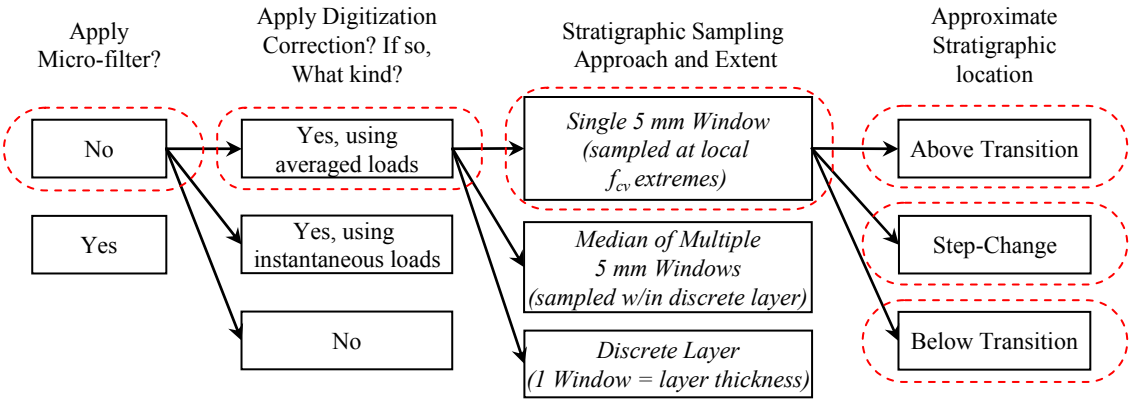

Figure 31. Processing and sampling options applied within this study are represented as boxes. Arrows indicate possible options when the first option of a given column is selected. Hence, for each of the three stratigraphic locations (right) 18 sets of results were produced. The main analysis focused on the circled options.

Stratigraphic Visualization of SMP Subsets

For a given spatial subset of SMP measurements, microstructural profiles were aggregated based on a stratigraphic reference location (Figure 32). At each successive depth increment, boxplot statistics were calculated from the aggregated values, resulting in profile-oriented boxplot statistics, which could then be used to visually compare stratigraphic characteristics of microstructural estimates derived from different groups SMP profiles (Figure 32).

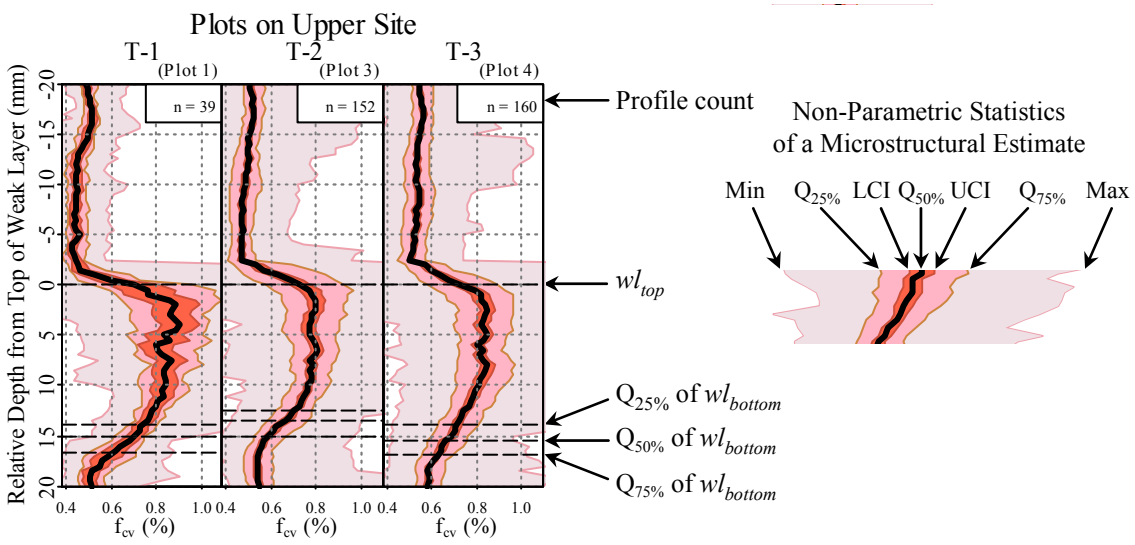

Figure 32. Example of stratigraphic visualization. In this example, f_{cv} is compared for plots on the upper half of the study site ('Upper Site'), using all available profiles. Non-parametric statistics included extreme values, the first-, second- and third- quartiles ($Q_{25\%}$, $Q_{50\%}$, and $Q_{75\%}$), and the lower and upper confidence intervals (LCI and UCI). Depth values are relative to the manually delineated upper boundary of weak layer (solitary black dotted line). The triplet of black dotted lines marks the median and inter-quartile range of the weak layer's manually delineated lower boundary.

An important aspect to profile aggregation was choosing an appropriate stratigraphic reference technique. Different types of reference locations were tested and are briefly described in Appendix A. The relative amount of spread present at important stratigraphic locations, such as the top of the weak layer, indicated how well a given

approach aligned the profiles. Because the weak layer's upper boundary fractured easily during shear frame tests and was considered the most relevant to snowpack instability, the upper boundary of the weak layer was utilized as the stratigraphic reference location.

Thickness of Main Stratigraphic Features

At each SMP profile, the slope-normal snow height $h_{snowpack}$ was recorded to the nearest centimeter using a delineated avalanche probe (Figure 33). The probe was inserted directly into the hole made by the SMP to measure the snow depth. The slope-normal slab thickness h_{slab} was equal to the depth from the snow surface to the top of the weak layer, as derived from SMP profiles. The slope-normal weak layer thickness h_{wl} was derived through manual delineation of SMP profiles.

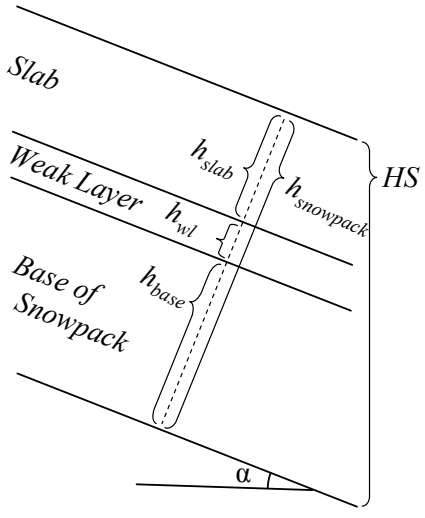

Figure 33. The five main stratigraphic features (left) include the vertical snow depth *HS* and the slope-normal measures $h_{snowpack}$, h_{slab}, h_{wl}, and h_{base}.

Lastly, the slope-normal height of the weak layer above the ground, referred to as the base height h_{base}, was obtained by subtracting the sum of the slab and weak layer thickness (h_{slab} and h_{wl}, respectively) from $h_{snowpack}$ (Figure 33). Vertical snow depth *HS*

was calculated for the spatial transformation of SMP profiles from the slope-normal coordinate system to the terrain model for radiation modeling.

Weather Station

In late autumn of 2004, Karl Birkeland, Kalle Kronholm and I established a weather station approximately 14 m upslope from the study site (Figure 34). Snow depth, solar radiation, air temperature and wind were recorded throughout the winter. A Campbell Scientific CR-10X data logger recorded measurements at 10 minute intervals. The weather station provided data that could be used to estimate local weather conditions during the surface hoar formation period.

Figure 34. Weather station upslope of the study site, with one of the numerous cautionary signs posted on the site perimeter, asking backcountry enthusiast to avoid disturbing the study site. As evident in this photo taken directly following a snowfall event in mid December, 2005, the instruments needed routine cleaning to ensure accurate data was collected throughout the season.

Snow Depth

Snow depth was measured hourly using a Campbell Scientific Sonic Ranger 50M-45. This instrument emits sonic pulses and measures time travel, which is then converted to sensor distance to snow surface with an accuracy of ±1 cm or 0.4% of the distance to the target (which ever is greater) (Campbell Scientific, 2003). Because the speed of sound is dependent on air temperature, the instrument necessitates coincident air temperature measurements to correct for air temperature dependent variations. The snow depth measurements were utilized to pin-point when the surface hoar layer was buried by subsequent snowfall.

Shortwave Radiation

LI-COR Li-200 pyranometers measured incoming and outgoing global shortwave radiation. Global shortwave radiation includes direct and diffuse shortwave radiation, the product of solar radiation, measured as $W \cdot m^{-2}$. The logger recorded hourly averages. This instrument typically has a measurement error of +/- 5 % of the maximum daylight when measuring unobstructed daylight (Campbell Scientific, 1997). However, conditions at the study site were not optimal. Because of the weather station's location on the slope, the sensor experienced tree shade intermittently for much of the day, including during the noon hour. This made it difficult to estimate the maximum incoming global shortwave radiation or to compare it with modeled global shortwave radiation on the site.

Another important factor is that most of the data collected with the pyranometer was influenced by a cosine (i.e., Lambertian) response or effect (Iqbal, 1983). This means that the accuracy of the recorded values may be compromised due to a high angle of

incidence between the sensor surface (normal vector) and the incoming direct shortwave radiation. Kalle Kronholm installed the pyranometer and oriented it parallel to the slope so that the recorded radiation values would correspond directly with the orientation of the study slope (pers. comm., Kronholm, 2004). Yet, tilted at 27° and facing northeast (NE 44°), the sensor surface was highly oblique to incoming direct shortwave radiation.

Using vector analysis of the sun's position and the pyranometer's orientation, I estimated that in January the angle of incidence remained greater than 80° for all but 2.25 hours of the day, between 9:00 and 11:15 (Figure 35). Although the instrument is cosine corrected to an angle of incidence of 80°, at such high angles of incidence the measurement error of the LI-COR 200 increases from 3% to over 10% (LI-COR, 2005).

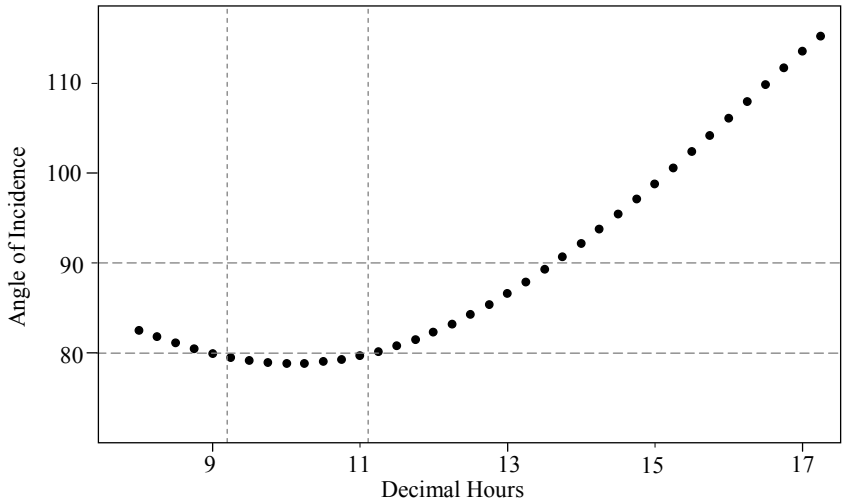

Figure 35. The modeled angle of incidence between the sensor surface-normal vector and incoming direct shortwave radiation at the study site on January 21, 2005. Note that for all times before 9:10 am and after 11:05 am this angle was greater than 80°, outside the range of cosine corrected angles.

Air Temperature

A Campbell Scientific 107 Temperature Probe recorded hourly average air temperature in Celsius degrees. Every 24 hours the minimum and maximum

temperatures were also logged. This instrument has an accuracy of +/- 0.5° C in the relevant temperature range (-35° C to +50° C) (Campbell Scientific, 2004a).

Wind Speed and Direction

A MetOne 034A wind sensor measured wind speed and direction. Wind speed was recorded to an accuracy of ± 0.12 $m \cdot s^{-1}$ of wind speeds under 10.1 $m \cdot s^{-1}$ and ± 1.1 % of the wind speed for wind speeds greater than 10.1 $m \cdot s^{-1}$ (Campbell, 2004b). Wind direction was recorded to an accuracy of ± 4°. Every ten minutes, the logger saved basic statistics of wind speed and direction to memory, including the minimum, maximum and standard deviation of wind speed and the mean and standard deviation of azimuthal wind direction. The wind direction was initially calculated using azimuthal vector components, which enables the calculation of standard deviation when values of wind direction switch between the first and second quadrants (the NE and NW quadrants).

Terrain and Vegetation Observations

Substrate Elevation Survey

Topography and tree information was collected during summer and autumn 2005 and 2006 with help from Patricia 'Trish" Jenkins and my wife, Rachel Lutz-Mountain. Using a Nikon DTM-500 total station, we collected approximately 2300 elevation points within the study site and several hundred surrounding the site (Figure 36). For each observation, three-dimensional coordinates of the ground surface were recorded relative to the base location, which was marked with rebar.

Measurements were taken at 1 m intervals along slope-parallel transects. Adjacent transects were spaced 0.5 m apart in the fall-line and staggered 0.5 m in the cross-slope direction. Flagging approximate survey locations increased survey time by approximately 20 % but guaranteed point sampling would be consistent and adequate (Figure 36). This method ensured an average point-spacing of 0.7 m on the slope-plane and resulted in a median point density (intensity) of 2.2 points / m^2 and a median point spacing of 0.61 m, in the horizontal plane. Rebar marking plot corners were also surveyed as reference points to enable the snow observations to be spatially linked to the terrain model.

Figure 36. Flagging approximate survey locations increased survey time by approximately 20 % but guaranteed point sampling was consistent and adequate. Inset: garments shaded the tripod base to reduce surficial thawing which, as I learned through initial experience, can cause systematic error.

Prior to the total station-based survey, we tested a terrestrial laser ranging system in collaboration with Thad Wasklewicz at another field site to determine if this would be

an accurate and efficient method of obtaining a high resolution elevation data set. Unfortunately, low density vegetative cover, such as grass, hindered the laser from reaching the substrate, resulting in a poor quality surface model. Terrestrial laser ranging would only be viable if a multi-return laser system (records last pulse returns) was employed.

Vegetation Survey

Within the study site, we mapped significant woody plants such as sage brush and coniferous trees taller than 0.4 m, during the elevation survey. This was necessary because these plants persist into winter and may influence snowpack dynamics. Vegetation heights were measured on the reflector staff's ruler and logged in the field book with the corresponding ground survey point identification number.

Along the perimeter of the study area, all trees within 30 m of the perimeter were surveyed. I applied two different techniques to survey tree base locations, including total station measurements and three-dimensional triangulation from known (surveyed) positions on the slope using survey tapes and inclinometer readings. Tree heights were determined using inclinometer readings from known (surveyed) positions (trees were assumed to be plumb). Crown radii were visually estimated to the nearest meter.

I classified trees in three form categories described through simple mathematical functions as linear-, near linear-, or rounded-form. A typical subalpine fir that is narrow with a pointed peak was classified as a linear cone, while a broad Douglas fir with the same radius had more volume near its peak and exhibited a rounded form (non-linear). In instances where trees were closely positioned and shared the majority of their canopy

space, I considered the group of trees one object and their form was considered in its entirety.

3D Reconstruction of Terrain, Vegetation and Snowpack

The three-dimensional reconstruction of the terrain, vegetation and snowpack methodologies are grouped into three parts. First, the basic elevation models are described, along with the three-dimensional reconstruction of the rebar and wooden corner posts which later link the terrain models with the snow observations. Second, the snow surface model development is described. Lastly, the transformation of the snow observations to their appropriate surface and depth locations is described and illustrated.

The described methods were applied to each plot individually because the substrate, vegetation, and snowpack characteristics within each of the five plots varied. Hence, while only described once here, these methods were applied five times, once for each plot. All interpolations in this section were calculated using ArcMap's Geostatistical Wizard. The Arc extension ET Geo Wizard vers. 9.7 for ArcGIS ver 9.2 (copyright Tchoukanski, 12/18/2007) greatly expedited several conversions and links between vector and raster based datasets.

Base Layers and Reference Points

The survey elevation data was used to create three grid format elevation models and 3D Shapefiles of the wooden corner posts. These datasets served as the foundation for the snowpack reconstruction.

High Resolution Substrate Elevation Model. Universal kriging is a geostatistical interpolation method that incorporates two types of spatial structure into the interpolation formula, including a trend surface and the modeled autocorrelation of residuals. The root-mean-square prediction errors ranged between 0.04 – 0.05 m for the five separate plots, calculated through cross-validation. In cross-validation, individual elevation points are withheld sequentially from the interpolation and compared with estimated values until each data point has been withheld and compared with modeled values. The elevation possessed different spatial properties in all five plots (Figure 6), thereby justifying that the ground surface in all five plots be modeled separately (Figure 37).

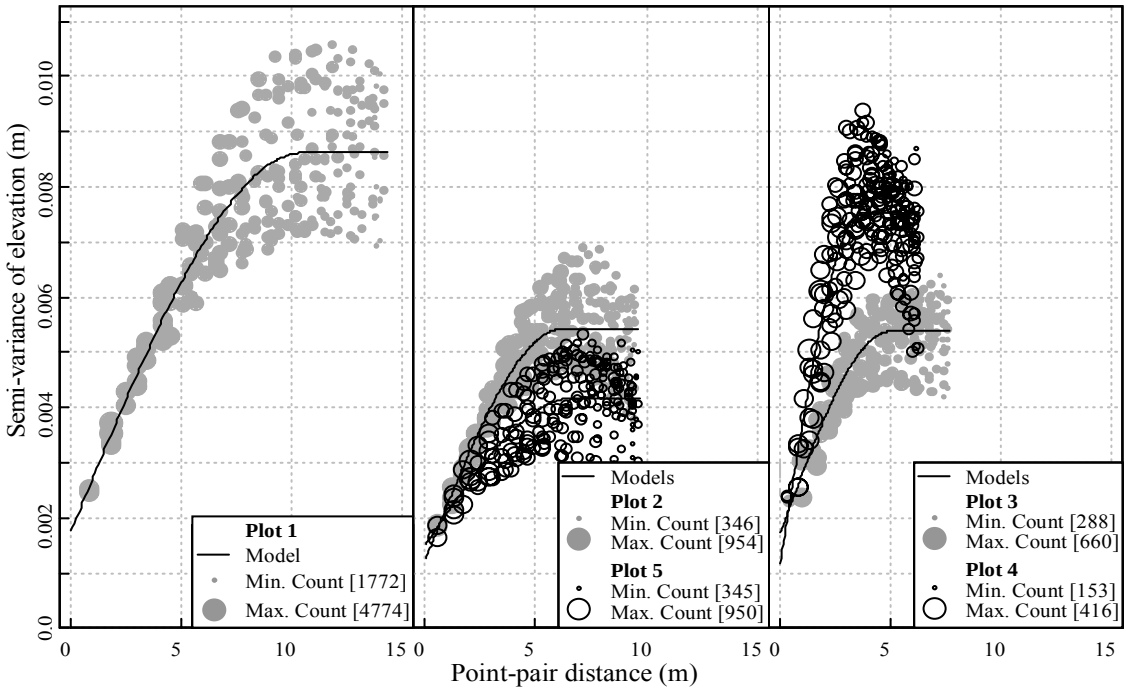

Figure 37. Variograms of residuals from second-order polynomial trend fit to surveyed elevation values. Plot 1 has the greatest sill value because it spans the entire slope and hence incorporates greater variations in terrain than the other plots. Note that while the lower plots (plots 2 and 5) have very similar spatial structure, the upper plots (plots 3 and 4) are quite different, whereby plot 4 possessed greater local variability and a hole effect.

Although the entire site could have been treated as a single dataset and been interpolated into one substrate elevation model, the prediction error would overall be greater, since various spatial structures in the different plots could not be accounted for as accurately. Hence, by sub-dividing the survey data into five groups, each extending at least two meters beyond a given plot's spatial extent, the substrate of each plot could be more accurately modeled (since that of other plots could be ignored).

High Resolution Vegetation Surface Model. Vegetation heights, which were linked with the surveyed horizontal coordinates <x,y>, were interpolated across the site using a third-degree inverse weighted distance interpolation. Cells adjacent to vegetation were forced through a height value of zero. The interpolated vegetation height was then added to the substrate model to create the vegetation surface model.

Smoothed Substrate Elevation Model. A smoothed substrate elevation model was generated for use in modeling the snow surface, using a first-order local polynomial interpolation. This model utilized both local and global (plot-scale) polynomial fits, whereby local polynomial fits accounted for 40 % of the final estimate and global (plot-scale) polynomial fits accounted for 60 % of the estimate. Despite the significant smoothing that this method applies to the input values, the mean and root-mean-square prediction errors were below 0.02 m and 0.07 m, respectively.

3D Reconstruction of Wooden Corner Posts. The wooden posts attached to rebar marking the plot corners served as the main link between the snow observations and the terrain model. The three-dimensional reconstruction was made possible using the

surveyed <xyz> coordinates of the rebar, the slope angles estimates α_{est} derived from the smoothed substrate elevation model, and snow depth observations $h_{snowpack}$. Given that the wooden posts and the snow depth measurements were oriented perpendicular to the slope, the <xyz> coordinates of the wooden posts at the snow surface could be estimated as follows:

$$z_{snow\,surface} = z_{rebar\,base} + \left(h_{snowpack} \times \cos(\alpha_{est})\right)$$

$$y_{snow\,surface} = y_{rebar\,base} + \left(h_{snowpack} \times \sin(\alpha_{est})\right)$$

$$x_{snow\,surface} = x_{rebar\,base}$$

The <x> coordinate was held constant since it was assumed that a difference in the fall-line orientation between the rebar and snow surface was negligible.

Snow Surface Models

The most accurate snow surface model would be obtained by surveying the snow surface with survey equipment or with a terrestrial laser ranging system (Joerg et al., 2006). However, neither option was operationally feasible during the winter field campaign. The alternative was to reconstruct the snow surface using the terrain elevation observations and the perpendicular snow depth observations. Three grid format snow surface models were generated, including the vertical snow height, and the approximate and refined snow surface elevation models.

Approximate Snow Surface Elevation Model: As a first step toward positioning the surface locations of the snow observations, an approximate snow surface model was generated using a third-order global polynomial interpolation. The model surface

intersects all relevant reference points (wooden posts at snow surface) as well as all positions along the shortest paths between wooden posts in three-dimensional space.

Vertical Snow Height Model: First, the slope-normal snow depth observations were transformed from their slope-plane coordinate system to the terrain's <xy> coordinate system using ArcMap's Spatial Adjust Tool (projection transformation option) to anchor the datasets to the <xy> coordinates of the snow surface at the wooden posts. The transformation errors for Plots 2 through 5 (the square corner plots) varied between 0.02 – 0.06 m, indicating that the shape of the coordinate systems in winter (on the snow surface) very closely matched the snow-free plot geometry in the horizontal plane (Table 6). Plot 1 possessed a slightly higher root-mean-square prediction error of 0.08 m which, considering the 31 m x 31 m span, is negligible.

Table 6. Spatial Transformation Errors of Snow Observations.

	Plot 1	Plot 2	Plot 3	Plot 4	Plot 5
Root-mean-square error (m)	0.080	0.062	0.024	0.017	0.058

The slope-normal snow depth was then estimated across the plot by applying simple kriging interpolation. Simple kriging is ideal for modeling spatial patterns that exhibit no trend surfaces and can be explained through the population mean and the modeled semi-variance of residuals of the mean. For all five plots, the snow depth possessed no plot-scale trends and, hence, simple kriging was ideal.

The vertical snow height *HS* was then estimated:

$$HS = \frac{h_{snowpack}}{\cos(\alpha_{DEM})}$$

Refined Snow Surface Elevation Model: The refined snow surface elevation model is the sum of the smoothed substrate elevation model and the estimated vertical snow height. For the spatial transformation of snow observations from the planar to refined snow surface models, slope angle and exposition of the refined snow surface were generated as grids.

Spatial Transformation of Snow Observations to Refined Snow Surface

The spatial information needed to transformation snow observations to their appropriate surface and depth positions was calculated in a grid-based environment. Recall that the snow observations had already been transformed onto the approximate snow surface elevation model. To accurately reposition the snow observations from the approximate snow surface elevation model to the refined snow surface elevation model, a three-dimensional transformation was required (Figures 38 and 39). While a z-axis offset

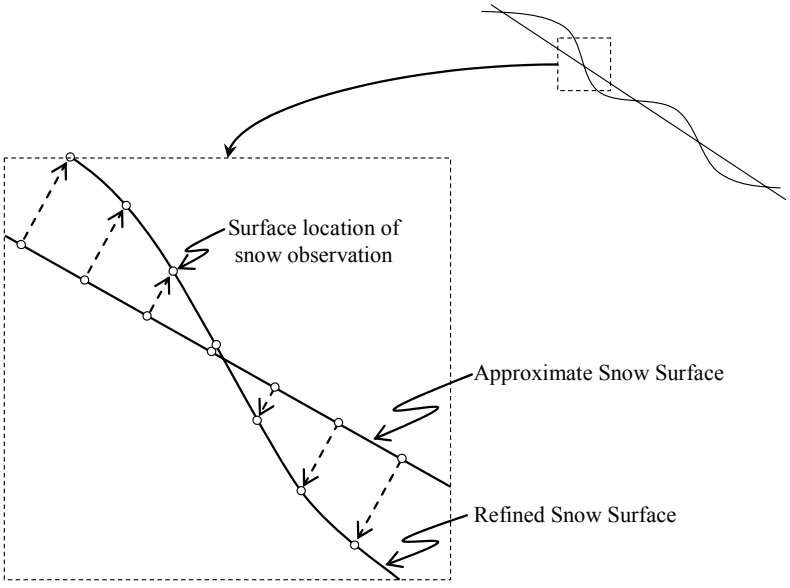

Figure 38. Hypothetical depiction of the approximate and refined snow surfaces (upper right hand corner) with the appropriate transformation of surface locations of snow observations.

would have been much simpler, it would result in uneven spacing of snow observations along the slope-plane axes, which did not occur in the field because the survey tapes were pulled taut on the slope plane.

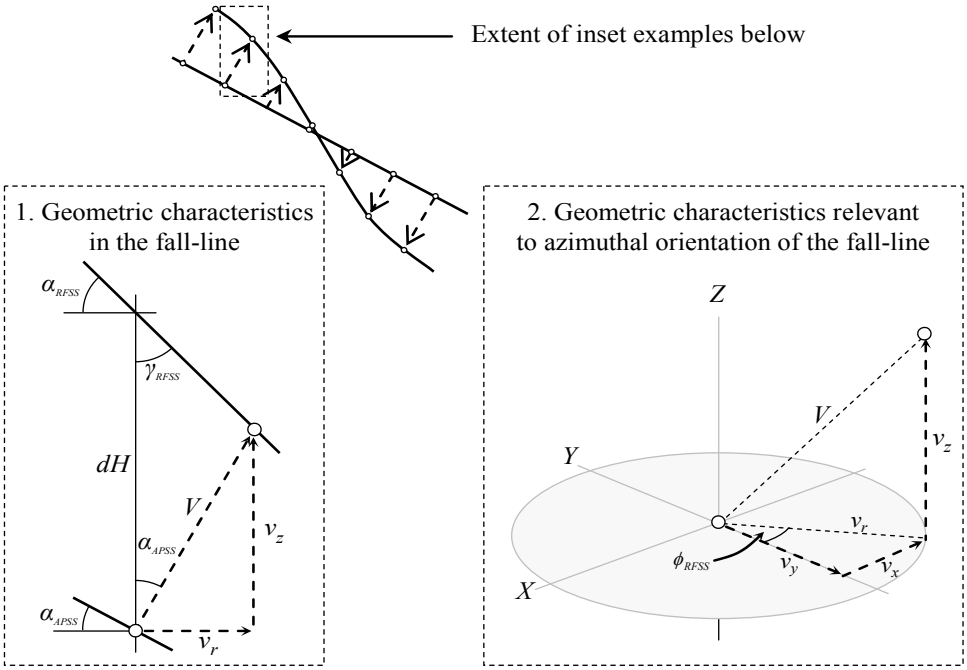

Figure 39. Geometric components of transformation from the approximate snow surface to the refined snow surface. The x- and y-axes in the slope azimuthal orientation represent the cross- and up-slope directions, respectively. Sub-scripts *'APSS'* and *'RFSS'* refer to the approaixmate and refined snow surface models, respectively.

Trigonometry was applied to estimate the direction and distance a point (a snow observation) must travel perpendicular from the reference plane (the approximate snow surface) until it reaches the destination plane (the refined snow surface) (Figure 38). In addition to the <xyz> coordinates of the snow observations located on the approximate snow surface, several topographic values were utilized, including the slope angle α_{APSS} and exposition ϕ_{APSS} of the approximate snow surface, the slope angle α_{RFSS} of the

refined snow surface, and the difference between the snow surface models, *dH* (Figure 39).

The length of the offset vector *V* is described,

$$V = \sin(\gamma_{RFSS}) \times \left(\frac{dH}{\sin(180 - (\alpha_{APSS} + \gamma_{RFSS}))} \right)$$

whereby γ_{RFSS} is the complimentary angles of α_{RFSS}. The z-component v_z and the radial-component v_r of offset *V* (Figure 39.1), were calculated as follows,

$$v_z = V \times \cos(\alpha_{APSS})$$

$$v_r = V \times \sin(\alpha_{APSS})$$

The radial component v_r was further reduced to its horizontal components v_x and v_y (Figure 39.2), such that,

$$v_y = v_r \times \cos(\phi_{APSS})$$

$$v_x = v_r \times \sin(\phi_{APSS})$$

Lastly, the grid format components v_x, v_y, and v_z were added to the attribute table of the snow observations Shapefile. They were then added to the existing <xyz> coordinates of snow observations, resulting in the <xyz> coordinates of snow observations at the refined snow surface (Figure 39.2).

Spatial Reconstruction of Stratigraphic Features

Once the surface locations of snow observations were determined, the stratigraphic depth of various observations could be calculated. At the surface location of each SMP profile, the slope angle α_{RFSS} and exposition ϕ_{RFSS} were utilized to determine

the slope-normal trajectory that was followed during SMP and snow depth measurements. The bottom of the snow depth measurements was determined using a similar method as applied for calculating the offset vector *V*. In this instance, the offset vector *P* describes a snow depth profile of length $h_{snowpack}$. The three-dimensional offset vector components were calculated as follows,

$$p_z = h_{snowpack} \times \cos(\alpha_{RFSS})$$

$$p_r = h_{snowpack} \times \sin(\alpha_{RFSS})$$

$$p_x = p_r \times \sin(\phi_{RFSS})$$

$$p_y = p_r \times \cos(\phi_{RFSS})$$

The p_{xyz} values were subtracted from the <x,y,z> surface locations, resulting in the <xyz> bottom locations of profiles. A good indication of the accuracy of the reconstruction was whether or not the profile bottoms were near the underlying terrain surface. Visual inspection of depth probes indicated that the bases were typically within 10 cm of ground surface. SMP profiles maintain the same orientation as the snow depth probes but do not reach the ground. The three-dimensional location of the weak layer was interpolated across the slope using the <xyz> locations of the weak layer in the three-dimensionally oriented SMP profiles (Figure 40).

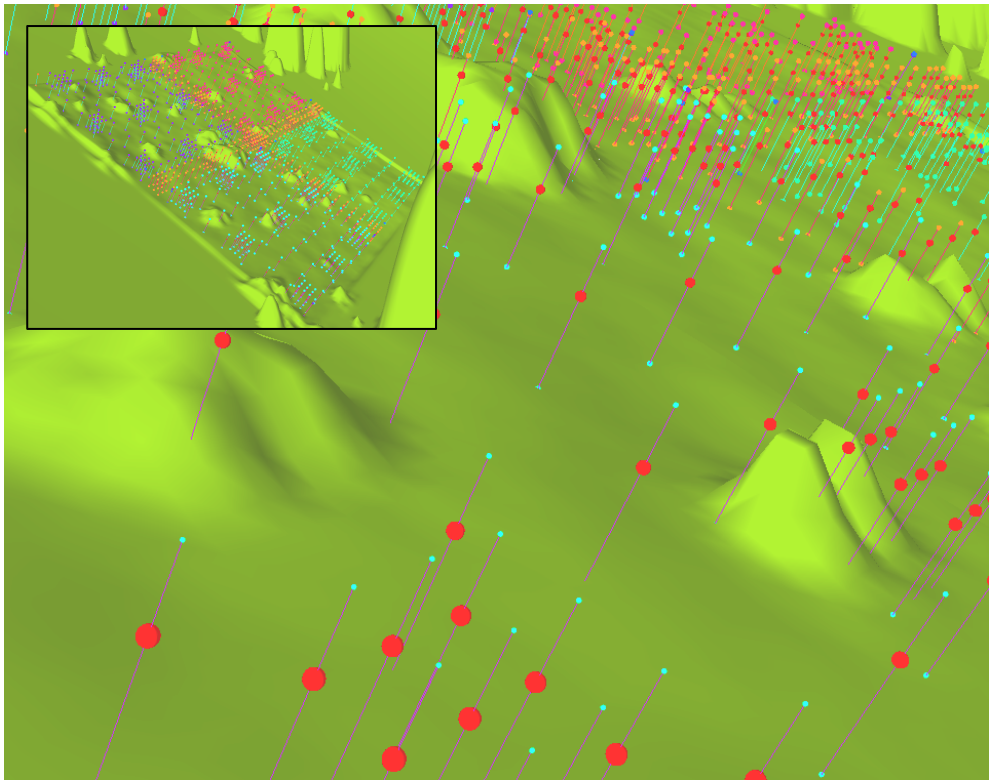

Figure 40. Surface represents terrain covered with small bushes. Lines are 3D representations of snow depth profiles. Green dots represent the top and bottom of snow depth profiles and red spheres represent the location of the weak layer, as located using paired SMP profiles.

Universal kriging was applied for all plots; accept for the cross-slope transect of Plot 1 which necessitated ordinary kriging. Using a mosaic function, the grid surfaces of the five plots were blended together (with distance-weighted averaging in overlapping areas) to form a single surface that represents the location of the weak layer. Another option for modeling the previous snow surface that existed during surface hoar formation was to subtract the slab from the existing surface. The former was preferred because it relied on dimensional information that is independent of the previous spatial transformations, thus ensuring that the slab thickness (h_{slab}) is not influenced by potential errors in previous transformations. This surface model corresponds approximately with

the old snow surface at the time of surface hoar formation. It was utilized for modeling the environmental conditions at the time of surface hoar formation.

Shear frame measurements were transformed to the appropriate stratigraphic depth by replacing $h_{snowpack}$ with slab thickness (h_{slab}) in the previously mentioned offset formulas and transformations. Snow properties derived from the SMP and shear frame tests could then be interpolated across the site for visual analysis.

The vertical slab thickness was generated across the slope using two methods. First, the elevation of the old snow surface was subtracted from that of the new snow surface. Second, slope corrected slab thickness at the SMP profiles was interpolated across the slope. The two results are comparable. The former was chosen for simplicity (one less interpolation necessary).

Incorporation of Basin-Scale Elevation Model

The landscape surrounding the study site was incorporated into the study site surface models in order to model environmental variables. This was done by integrating USGS 30 m resolution digital elevation models with the above described models. While this elevation information is far less resolved than that of the site survey, it is adequate for modeling adjacent ridgelines that obstruct the solar path (relevant to modeling direct shortwave radiation) and influence sky visibility (relevant to modeling longwave and diffuse shortwave radiation). To accurately integrate these models of different accuracy and resolution, three surface zones were established, in which different interpolation methods were used (Figure 41).

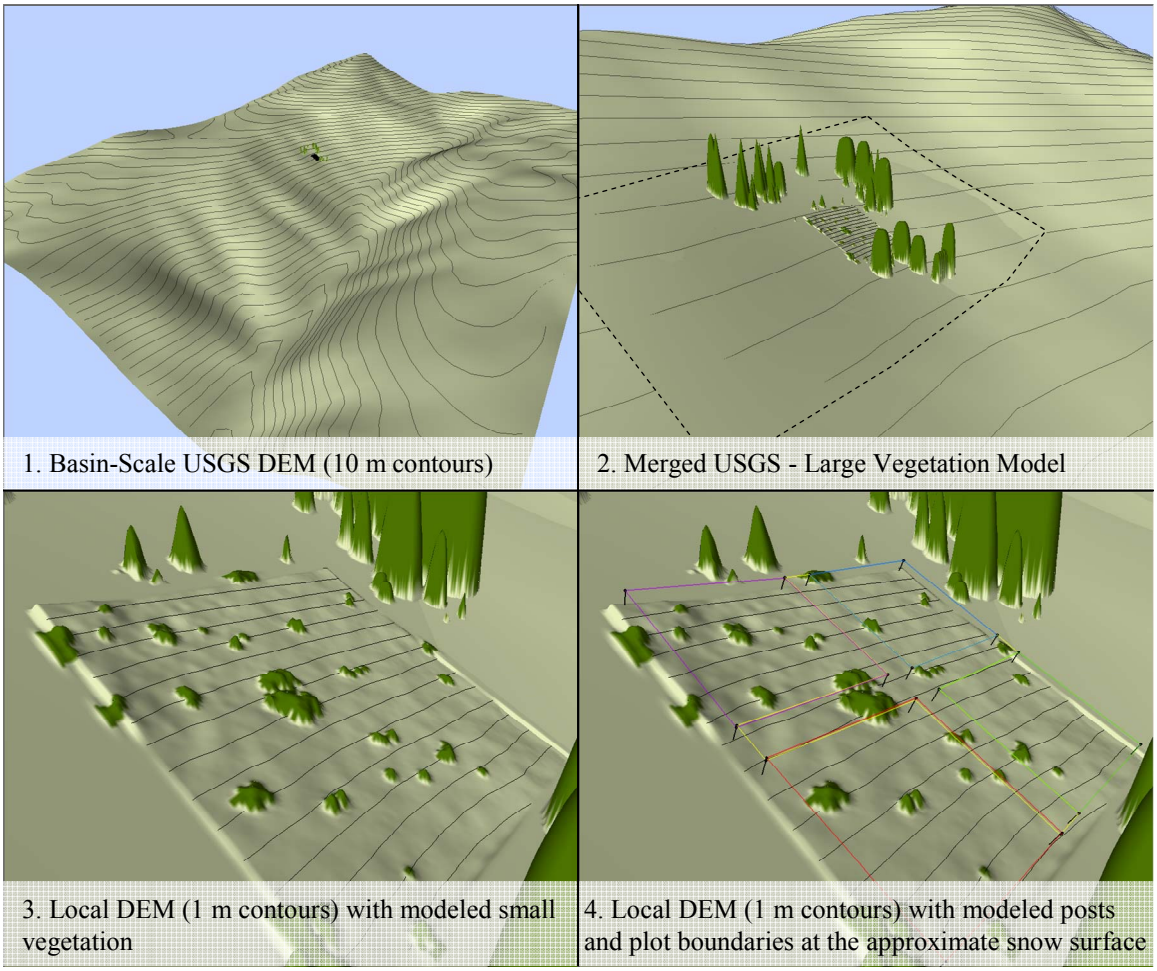

Figure 41. Elevation model consisted of basin-scale (USGS) DEM, a local high-resolution DEM, and a zonal merged DEM, which encorporated the USGS data with tree base elevations (dotted line represents outer extent of this model).

Although the entire site could have been treated as a single dataset and been interpolated into one substrate elevation model, the prediction error would overall be greater, since various spatial structures in the different plots could not be accounted for as accurately. Hence, by sub-dividing the survey data into five groups, each extending at least two meters beyond a given plot's spatial extent, the substrate of each plot could be more accurately modeled (since that of other plots could be ignored).

The first zone corresponded with the study site itself, which extended 2 m beyond the study site corners and utilized only the survey data to create the surface using kriging interpolation (Figure 41.3 and 41.4). The second zone corresponded with a transition between site survey data to USGS grid (30 m^2) values (Figure 41.2). In this zone USGS grid values and survey data of the tree bases near the site were used in a local polynomial interpolation of the ground. The tree surface model was then added to this surface. The third zone utilized USGS grid values that were linearly interpolated (Figure 41.1).

Radiation Modeling

In addition to topographic characteristics and proximity of vegetation buried within the snowpack, two additional environmental properties were modeled: longwave and shortwave (solar) radiation. Both types of radiation affect snow surface temperature and surface hoar growth and preservation. An important input for both incoming longwave radiation and diffuse shortwave radiation is the percent of hemispheric viewshed that is not obstructed by terrain or vegetation, referred to the sky visibility $v_{\%}$. Methods for estimating radiation are proceeded by the applied methods for estimating sky visibility.

Hemispheric Sky Visibility ($v_{\%}$)

As input for the incoming longwave and the diffuse shotwave component of the global radiation fluxes, $v_{\%}$ was estimated using two techniques: a GIS-based model and optical measurements using the Solar Pathfinder. While the GIS-approach utilized a high-resolution (0.25 m) terrain and vegetation model to calculate estimates, results were

highly dependent on the accuracy of the modeled topography and tree geometry. Since only the trees within 30 m of the site's perimeter could be efficiently surveyed and modeled, and because the model assumed trees to be solid objects, the GIS model accuracy was unknown. For this reason, optical field measurements were made to calculate $v_{\%}$ at 45 reference locations on the study site. Both methods are described in detail in the following sections. The observed $v_{\%}$ values were tabulated and spatially linked with the GIS modeled $v_{\%}$ in ArcMap, allowing for a comparison of their results, using linear regression and a scatterplot.

GIS Model of $v_{\%}$: The grid-based GIS model was written in Arc Macro Language (AML) and implements a modified viewshed analysis in ArcInfo Workstation vers. 9.2. This model was conceptually similar to that presented by Dozier and Frew (1990) with the distinction that the hemisphere was modeled with higher resolution and that the input terrain model included individual trees.

The sky above the study site (hemispherical viewshed) was partitioned into altitudinal (horizontal) and azimuthal (vertical) bands (Figure 42). The angular resolution was set to 5° for altitudinal bands and 2° for azimuthal bands. For each 0.25 m grid cell in the study site, the model calculated how much of the sky view was obstructed by adjacent surfaces, as percentage values of a hemisphere. Hence, on a flat treeless surface all cells possess 100% sky visibility and 0% sky obstruction. A planar treeless surface, inclined 30°, experiences approximately 80% sky visibility, while with abundant trees present sky visibility could be reduced to below 10%. The study area contained steep

topography coupled with neighboring trees, which resulted in approximately 30 % variation of $v_{\%}$ across the site (Figure 43).

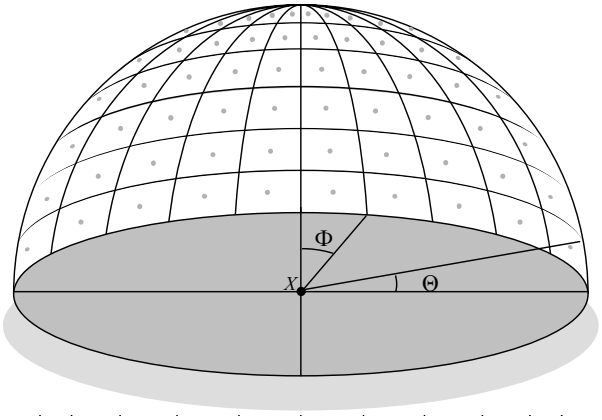

Figure 42. The hemispherical viewshed was divided into altitudinal and azimuthal bands each of Θ and Φ degrees respectively. For a given observation point *X*, the visibility of the center of each resulting hemispheric cell (gray dots) is tested. The graphic contains fewer cells than the model.

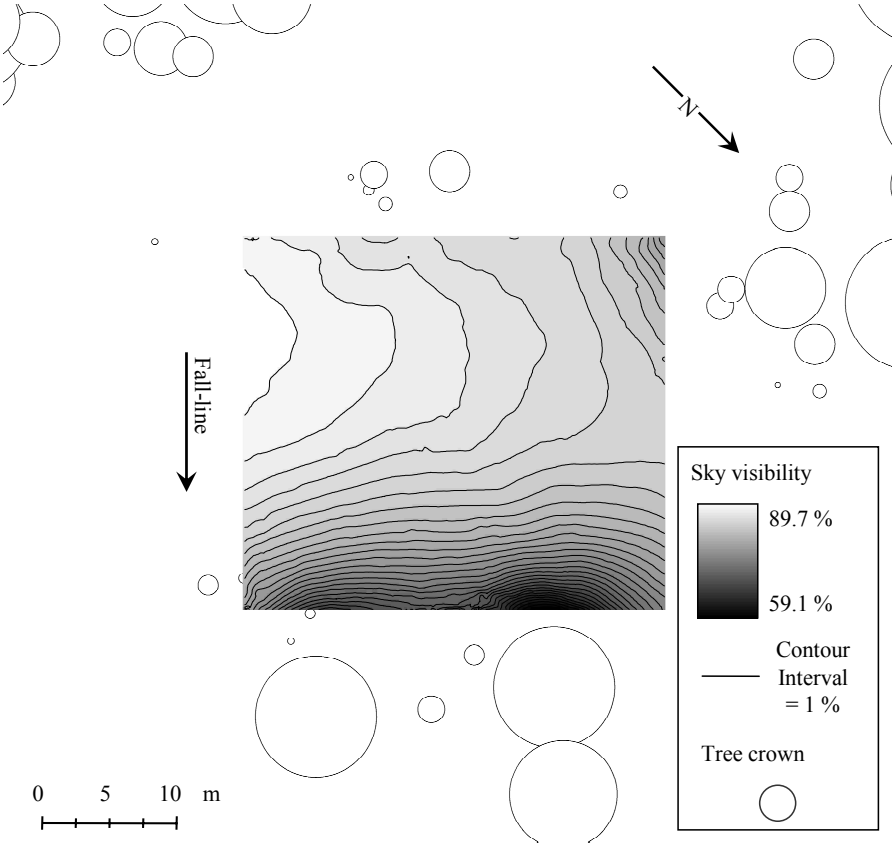

Figure 43. Map of the GIS model of $v_{\%}$. Dark areas possess low sky visibility and light areas possess high sky visibility. Tree crowns are represented proportionally as circles.

Field Observations of $v_{\%}$. Field observations were made using a modified Solar Pathfinder (Figure 44.1) in combination with a mounted digital camera and the fisheye image analysis software Gap Light Analyzer (GLA, Frazer et al. (1999)). Solar Pathfinder is designed to estimate site-specific shade and daily insolation values as a function of $v_{\%}$, geographic and solar data. It is nearly identical to the German-made Horizontoscope (Tonne, 1999). Although primarily used in the solar energy industry to determine solar panel placement, these instruments have been applied in riparian ecology (Platts et al., 1987; Ringold et al., 2003), forest ecology (Brang, 1998), and snow studies (Höller, 2001).

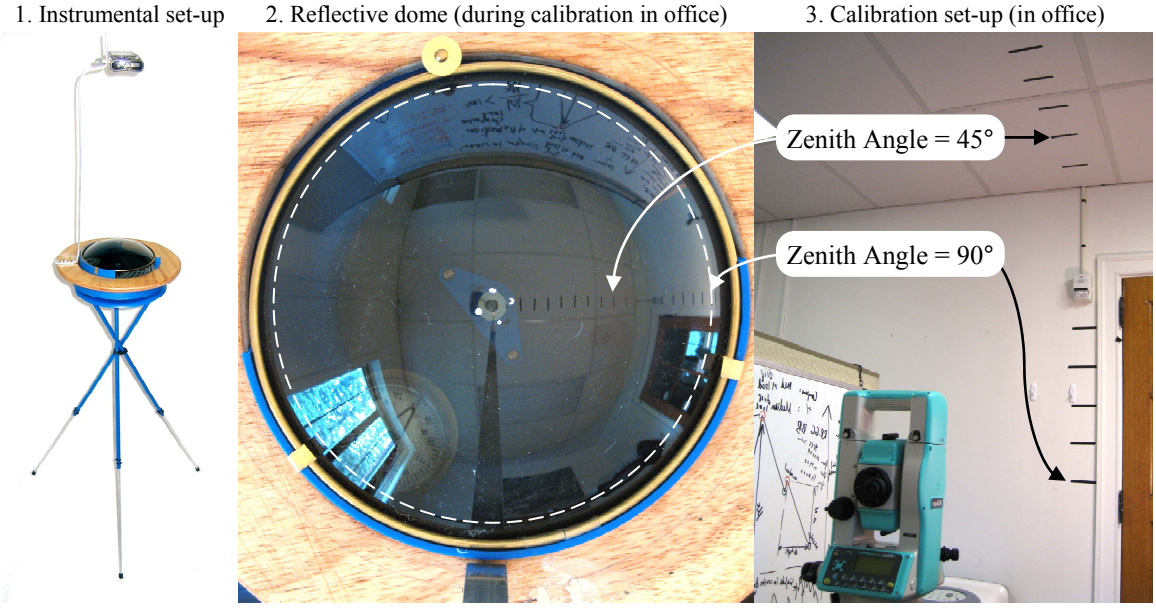

Figure 44. (1) Solar pathfinder with mono-pod and lightweight digital camera mounted. (2) Digital image of reflective dome, acquired in office during calibration; superimposed dotted white line represents the 180° hemisphere, distal of which the reflected image is partially distorted. (3) Altitudinal projection for dome calibration, established with total station in office.

Analogue and digital circular fisheye photography have been widely used for canopy estimations (e.g., Anderson, 1964; Rich, 1990; Englund et al., 2000; Frazer et al.,

2001). Although such techniques are more accurate than the Solar Pathfinder (Teti and Pike, 2005), they were not feasible because of the associated high capital cost. The materials for the modified technique described below cost approximately $240 USD, in comparison to several thousand for professional fisheye instrumentation. Like circular fisheye lenses, the Solar Pathfinder can be used to estimate canopy cover for the entire hemispherical viewshed. Other field instruments such as spherical densitometers and LIA-2000 cannot quantify canopy cover within 30° of the horizon.

Traditionally the user looks down at the Solar Pathfinders polycarbonate dome and outlines the reflected projection of the surroundings onto a plate located below the translucent dome. More recently, the software package Solar Pathfinder Assistant Ver 3.0 was developed to process digital photos taken of the projected viewshed, increasing efficiency. However, no literature is available quantifying the accuracy of the technique or software. In addition, a 5° discrepancy appeared to exist between the edge of the base plate used to estimate the angular height of reflected objects and the edge of the dome's undistorted reflection. Hence, to limit potential errors, I developed a mono-pod camera mount that consistently allowed accurate measurements to be taken in a short time period (Figure 44.1).

The light-weight aluminum mono-pod greatly expedited camera positioning in the field and enabled consistent images to be recorded. The mono-pod was secured to a custom fit laminated wooden ring that fits on the Solar Pathfinder's tripod using non-magnetic hardware, which was important to allow for proper azimuthal orientation in the

field (Figure 44.2 and 44.3). This set-up kept the camera at the optimal focal length and in the middle of the projection, which was important for post-processing of photos.

Once the mono-pod was constructed, I calibrated the reflective polycarbonate dome using an altitudinal projection in an office space (Figure 44.3). A total station was used to locate successive 5° altitudinal increments up to 75° (the steepest angle the total station could shoot) (Figure 44.3). Nadir was located using a plumb (since total stations cannot measure vertical trajectories) and the increments between 75° and 90° were calculated using trigonometry. The Solar Pathfinder was then set up in place of the total station, so that the photographed reflected image was at the center of the office-space projection (Figure 44.2). Looking through the digital camera, the ideal focal distance from dome to camera lens was predetermined by identifying the distance at which the horizontal trajectory (0° altitudinal or 90° zenith angle) was visible on the edge of the dome's reflection (Figure 44.2).

Then, using Microsoft Office Picture Manager and Excel, I tabulated the radial distance (in pixels) of each 5° altitudinal trajectory (from the center of the projection). A polynomial function nearly perfectly ($r^2 = 0.99994$) described the altitudinal position of a pixel in an image as a function of its radial distance from the image center, to an accuracy of +/- 0.5°. This information was tabulated in a calibration file that was later used in GLA to calculate $v_{\%}$.

On October 11, 2007, 50 digital images were taken across the study site and at the weather station location using the above described modified Solar Pathfinder approach. The images were recorded approximately 0.8 m to 1 m above ground level, depending on

tripod positioning. Using survey tapes attached to the plot corner posts, the observations were carefully distributed across the site such that each photograph corresponded with the locations where a cluster (pit) of SMP and shear frame measurements were taken during the 2005 winter field season (Figure 10). The unit was set up on its tripod, leveled, oriented to magnetic north and corrected for declination (the latter was important for solar analysis). Using a 5-second timer allowed me sufficient time to trigger the camera and then crouch down to the ground so that I did not obstruct any of the photographed reflections (Figure 45.1).

Image post-processing is easiest when photos are taken on cloudy days. This allows for bright pixels to be allocated to sky and dark pixels to sky obstructions. During the field day, the predicted bad-weather unfortunately cleared, which meant many images contained dark blue sky, which complicated the image analysis.

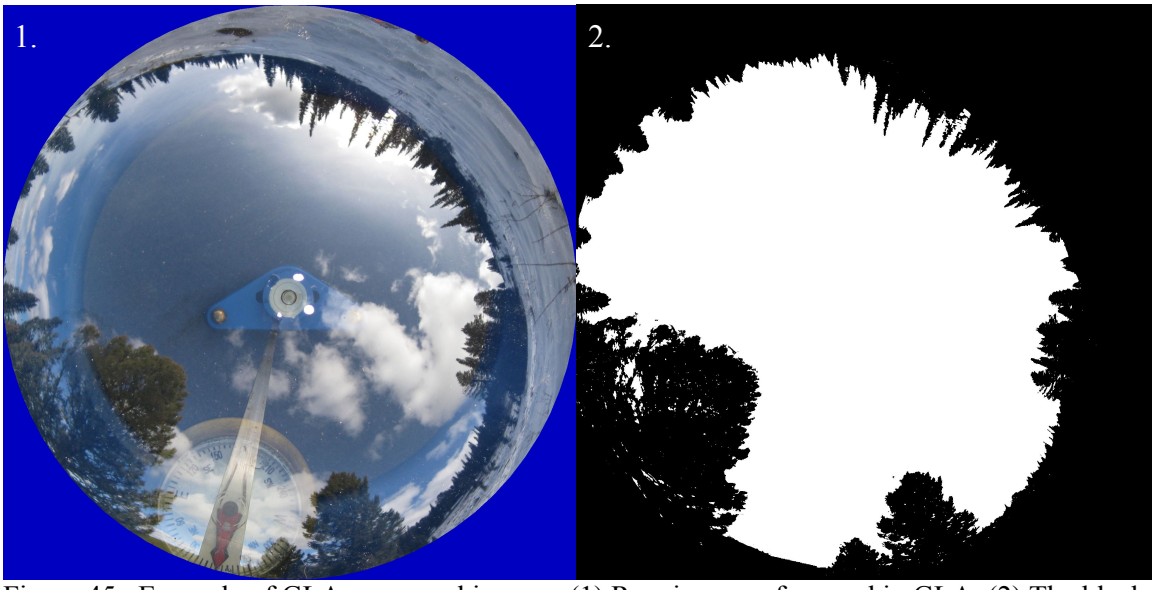

Figure 45. Example of GLA processed images. (1) Raw image referenced in GLA. (2) The black and white processed image indicating obstruction (black) and visible sky (white). This image was taken at the base of the study site, where two Douglas-Fir trees downhill of the study site protrude significantly into the viewshed.

The photos were cropped and oriented for analysis in Gap Light Analyzer (GLA) Vers. 2.0, a cost-free hemispheric image analysis software package available on the internet (Frazer et al., 1999). Using pixel value-based filters and manual delineation, the tree line was selected in each image and the unobstructed sky visibility was calculated from pixels with a value of 255 (Figure 45). In certain instances, when the filters could not differentiate surface types, manual delineation was necessary. This included snow on the ground, which was bright like clouds, and occasionally dark patches of blue sky as sky, which resembled coniferous trees. For a detailed description of GLA, refer to Frazer et al. (1999, 2001).

Comparison of GIS Modeled and Observed Sky Visibility ($v_{\%}$): With the exception of areas directly next to trees (white dots in Figure 46) on average the GIS model overestimated $v_{\%}$ (underestimated sky obstruction) by approximately 12 %. This is likely because distant tree stands that were not modeled in the GIS actually obstructed peripheral sky areas fairly uniformly at positions across the site. The reason that locations directly adjacent to trees do not have this offset is because the trees were modeled as solid bodies, which they are not in reality. The results are convincing enough to warrant using both datasets in the analysis of spatial patterns across the study site. Limitations of both methods are discussed in Appendix B.

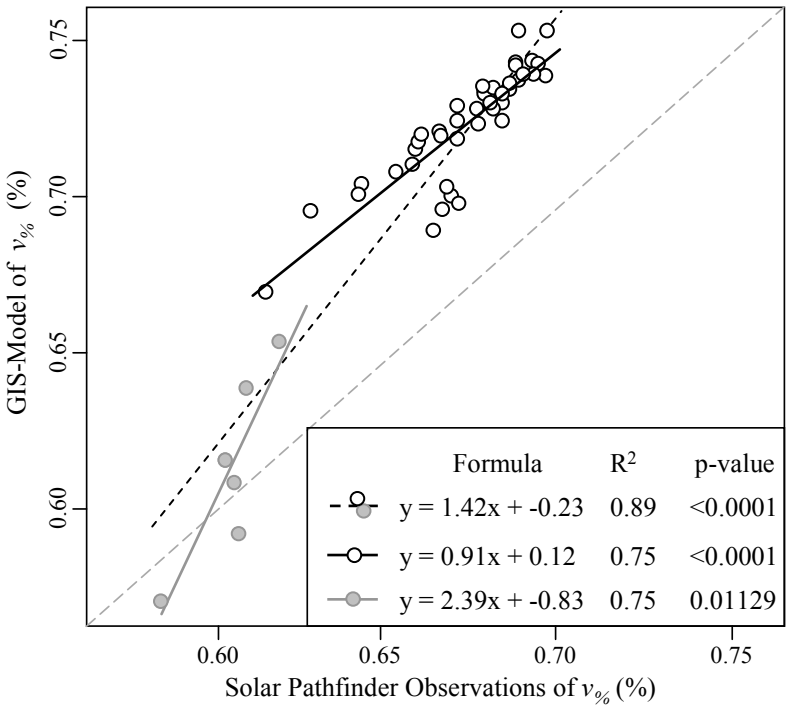

Figure 46. The GIS-based model explained 89% of the variation in observed $v_{\%}$, as quantified with the Pathfinder (all points, dotted black line). When only observations not adjacent to trees were included (white dots) and observations directly adjacent to trees excluded (solid grey dots), the fit neared a 1:1 ratio (solid black line).

Modeling Longwave Radiation

In the absence of shortwave (solar) radiation, the snow surface temperature is mainly controlled by the difference between incoming and outgoing longwave radiation fluxes ($L_{\downarrow}$ and $L_{\uparrow}$, respectively), referred to as the net longwave flux L_{net}:

$$L_{net} = L_{\uparrow} - L_{\downarrow}$$

Negative values of L_{net} indicate surface cooling and positive values indicate surface warming. Utilizing field observations and cited emissivity values, $L_{\uparrow}$ can be estimated across the entire study site and L_{net} can be estimated at the weather station. A brief overview of longwave radiation lays foundation for these estimates.

The Stefan-Boltzmann law states that a black body radiates energy across its surface proportionally to the fourth power of the body's thermodynamic (absolute) temperature *T*. The Stefan-Boltzmann constant of proportionality σ is equal to 5.67×10^{-8} $W \cdot m^{-2} K^{-4}$. Natural surfaces are more accurately described as gray bodies that radiate only a portion of the radiative flux, described through their emissivity ε.

Estimating Incoming Longwave Radiation ($L_{\downarrow}$): For an unobstructed surface, the incoming longwave flux $L_{\downarrow}$ is a function of the atmospheric emissivity ε_{air} and temperature T_{air}, such that,

$$L_{\downarrow} = \varepsilon_{air} \sigma T_{air}^4$$

For a forest opening, where trees partially obscure the sky view, ε_{tree} and tree temperature T_{tree} are incorporated,

$$L_{\downarrow} = (1 - v_{\%}) \varepsilon_{tree} \sigma T_{veg}^4 + v_{\%} \varepsilon_{air} \sigma T_{air}^4$$

Whereby $v_{\%}$ and 1- $v_{\%}$ are percentages of the hemispheric viewshed occupied by sky and vegetation, respectively. Because $v_{\%}$ is largely an inverse function of tree proximity, $v_{\%}$ possessed unique values across the study site. T_{tree} was set equal to T_{air}, as proposed by Bader and Weilenmann (1992) and Höller (2001) for snow-free canopies, reducing the equation to,

$$L_{\downarrow} = \sigma T_{air}^4 \left[(1 - v_{\%}) \varepsilon_{tree} + v_{\%} \varepsilon_{air} \right]$$

This assumption seemed reasonable. Although solar radiation warmed the trees during the day, under clear sky conditions the tree surfaces cooled throughout the night and likely equaled T_{air} before sunrise. For the purpose of this estimation (to identify

possible trends in net flux that may account for spatial patterns in surface hoar development), this assumption was conservative by nature. Any resulting spatial pattern evident in the incoming longwave flux ($L\downarrow$) under this assumption would only be greater if the trees were actually warmer than the air.

$L_{\downarrow}$ was estimated at locations across the study site as defined in the previous equation, utilizing the GIS-based model of $L\downarrow$ and the Solar Pathfinder derived field estimates of $L\downarrow$.

Following Gubler and Rychetnik (1991) and Höller (2001), tree emissivity ε_{tree} was set to 0.94 and sky emissivity ε_{air} was set to 0.70. Cirrus and cirrostratus clouds were observed on the afternoon of January 20 during field work and were also noted in weather observations at the West Yellowstone Airport on other days during surface hoar formation period. Because clear sky conditions dominated at night time, it was assumed that a relatively low emissivity could be applied. T_{air} was obtained from weather station measurements on January 20 and was treated as spatially constant across the study site.

Estimating Outgoing Longwave Radiation ($L\uparrow$): The outgoing longwave flux $L_{\uparrow}$ was estimated at the weather station location using snow surface temperature T_{snow} and a snow emissivity ε_{snow} of 1 (after Bader and Weilenmann, 1992):

$$L_{\uparrow} = \varepsilon_{snow}\sigma T_{snow}^{4}$$

Unlike T_{air}, which was recorded continuously at the weather station, T_{snow} was observed in manual snow pits. Hence, concurrent data during the surface hoar formation

period is limited to the morning of January 20. This was the second morning in the 7 day period during which surface hoar formed.

Estimating Net Longwave Radiation (L_{net}): The net longwave radiation flux at the snow surface - atmosphere interface L_{net} was deduced by subtracting $L_{\uparrow}$ from $L_{\downarrow}$. Because T_{snow} was sampled at the snow profile adjacent to the weather station and because T_{snow} likely varied across the study site, L_{net} cannot be easily calculated across the site. However, since $L_{\downarrow}$ is known across the study site, differences in the cooling potential can still be identified.

Global Shortwave Radiation

Incoming global shortwave radiation, which is the sum of diffuse and direct solar radiation, was estimated across the slope at 15-minute intervals for the duration of January 21, 2005. The outputs of this model indicated spatially what parts of the study site experience the greatest amounts of shortwave radiation and the time at which those values occur. There were two main parts to these calculations. The first component entailed modeling the shortwave radiation at the weather station, where pyranometer recordings could be used to verify the model results. The second component took the calculated 15-minute interval shortwave radiation values and plugged them into the GIS model to estimate spatial patterns in shortwave radiation, over the course of a day.

Bird Model of Global Shortwave Radiation (I): The Bird Clear Sky Model was applied to estimate clear sky direct beam, hemispherical diffuse, and the total hemispherical (global) shortwave radiation for a horizontal surface I_H in Watts m^{-2} (Bird

and Hulstrom, 1981). An Excel macros-based implementation of the Bird Clear Sky Model by Myers (2004) was available through the Renewable Resource Data Center (RReDC), a branch of the National Renewable Energy Laboratory (NREL). This spreadsheet format greatly expedited the calculations and enabled simple modifications of the model. Extensive advice was offered by Daryl Myers (Pers. Comm., 2005) regarding general information such as model application and accuracy, as well as several suggestions for sources of atmospheric input data.

The model produces several estimates of solar irradiance during clear sky conditions, including diffuse and direct irradiance on horizontal surfaces, defined as I_{ah} and I_{dh} respectively, as well as the direct irradiance on a surface oriented perpendicular to the solar rays I_{db}. Daily variations of I_{ah} and I_{dh} are largely a function of atmospheric extinction of extraterrestrial solar irradiation I_o (Figure 47). Atmospheric extinction is

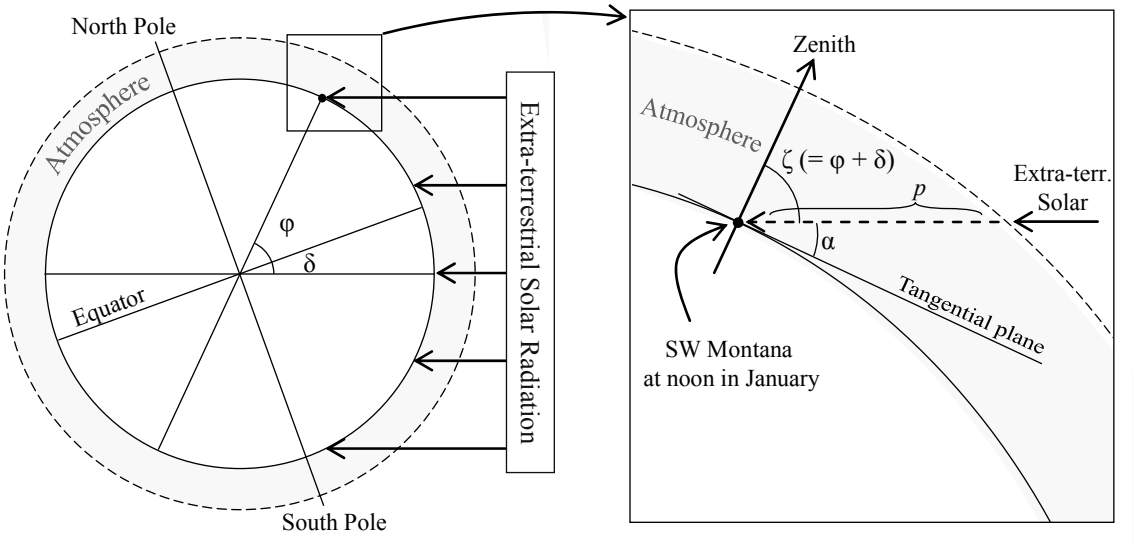

Figure 47. Overview of earth's orientation to incoming solar radiation at high noon in January (left) and relationships between the zenith angle (ζ), solar altitude (α), and atmospheric path length (p) in Montana at that time (right). Note that even at high noon, when p is at its daily minimum, significant atmospheric extinction occurs.

dependent on air mass M, atmospheric thickness (which is largely a function of the sun's zenith angle ζ), and multiple atmospheric transmission factors (Bird and Hulstrom, 1981).

Bird and Hulstrom (1981) calculated incoming solar radiation as follows:

$$I_{ah} = \frac{I_o \cos(\zeta)(0.76)T_o T_w T_{UM} T_A \left[0.5(1-T_R)+B_a(1-T_{AS})\right]}{[1-M+M^{1.02}]}$$

$$I_{db} = I_o(0.9662)T_R T_o T_{UM} T_w T_A$$

$$I_{dh} = I_{db}\cos(\xi)$$

Transmittance factors for ozone absorptance T_O, water vapor absorptance T_w, uniformly mixed gases (carbon dioxide and oxygen) absorptance T_{UM}, aerosol absorptance and scattering T_A, Rayleigh scattering T_R, and aerosol scattering T_{AS} are described in detail by Bird and Hulstrom (1981) and in the Excel spreadsheet by Myres (2004). Diffuse irradiance I_{ah} incorporates the ratio of forward scatter to the total scatter B_a, which was set to 0.85. Lastly, the global shortwave irradiance on a horizontal surface I_H is equal to the portion of I_{ah} and I_{dh} absorbed by the surface, a function of surface and atmospheric albedo, r_g and r_s respectively:

$$I_H = \frac{(I_{dh}+I_{ah})}{(1-r_g r_s)}$$

The snow surface albedo r_g was set to a 0.9. The atmospheric albedo r_s is defined by Bird and Hulstrom (1981) and in the Excel spreadsheet by Myres (2004).

In addition to latitude, longitude and time of day, four types of information are utilized to calculate the transmission factors, including the local atmospheric pressure, precipitable water, aerosol, and ozone contents (Table 7). Atmospheric pressure was calculated from aviation weather reports recorded at the West Yellowstone Airport. The

difference in atmospheric pressure between the airfield and the study site was estimated as an inverse function of elevation change.

Table 7. Atmospheric Data Sources

Variable	Distributor	Data Type	Station Name	U.S.A.F ID
Atmospheric pressure (mbar)	National Climatic Data Center (NCDC, branch of NOAA);	DATSAV3 Global Surface; Hourly Data; Aviation weather reports (METAR routine and selected special)	West Yellowstone, MT.	726763
Precipitable Water Content (cm)	National Solar Radiation Data Base (NSRDB), RReDC, NREL	NSRDB / NREL format; Hourly integrated atmospheric variables	Dillon, MT.	726796
			Bozeman G.F., MT.	726797
			Idaho Falls, ID.	725785
Optical aerosol depth (unitless)	National Solar Radiation Data Base (NSRDB), RReDC, NREL	NSRDB / NREL format; Hourly integrated atmospheric variables	Dillon, MT.	726796
			Bozeman G.F., MT.	726797
			Idaho Falls, ID.	725785
Ozone content (cm)	National Solar Radiation Data Base (NSRDB), RReDC, NREL	NSRDB / NREL format; Hourly integrated atmospheric variables	Dillon, MT.	726796
			Bozeman G.F., MT.	726797
			Idaho Falls, ID.	725785

Hourly values of precipitable water and ozone contents and aerosol depth were available at three weather stations in Southwestern Montana and Idaho (Table 7, Appendix C). All three stations are located within 120 to 150 km of the study site. Detailed information about the sensors, data, and data processing is available in NREL (2007) Given the large-scale uniformity of these atmospheric conditions, values from all three stations could be averaged based on proximity to the study site. Appendix C details the atmospheric data and corresponding stations.

The Bird model was run at 15 minute increments throughout January 21, 2005. Although several input parameters were only available as daily or hourly estimates,

significant changes in incoming global shortwave radiation at time increments of 15 minutes or less occur due to the sun's position above the horizon, which affects the path length and associated atmospheric transmittance.

GIS Application of Bird Model: The tabulated results from the Bird model were imported in ArcInfo Workstation 9.2 and integrated into an arc macro language (AML) based spatial-temporal model that I wrote which maps the diffuse, direct and global shortwave radiation across the study site over the course of a day. The model was run for January 21, a fairly warm, clear day during the surface hoar formation (and persistence) period.

In the model script, at each 15 minute time-step, a discrete hillshade analysis detects areas that are shaded from direct sunlight and allocates an I_{db} value of zero to cells within those areas. For non-shaded cells, the wattage of direct shortwave radiation as experienced on variable terrain I_{ds} is calculated by considering the relationship between the slope orientation and the trajectory of the incoming direct radiation I_{db}. Across variable terrain, relative intensity was defined as the cosine of the angle of incidence φ, the angle between an incoming solar ray i and the surface normal vector s at the point of incidence. Since both i and s vary (over space or time), it was most practical to calculate relative intensity using three-dimensional vector components of i and s (Lutz, 2003). The absolute intensity at the terrain surface I_{ds} was defined as a function of I_{db} and the relative intensity, such that:

$$I_{ds} = I_{db} \times \left(\frac{i_x s_x + i_y s_y + i_z s_z}{\sqrt{i_x^2 + i_y^2 + i_z^2}\sqrt{s_x^2 + s_y^2 + s_z^2}} \right)$$

Whereby i_x, i_y, i_z are the x-, y-, and z- components of the incoming solar direct radiation vector of strength I_{db} and t_x, t_y, t_z are the x-, y-, and z- components of the slope normal vector s. To model diffuse shortwave radiation in mountainous terrain, Wilson and Gallant (2000) recognize the need to account for sky visibility obstructed by terrain and trees. At each time-step, the diffuse global shortwave radiation on the slope I_{as} is calculated by multiplying the Bird estimate of diffuse shortwave radiation I_{ah} with the percentage unobstructed hemispheric viewshed $v_{\%}$:

$$I_{as} = I_{ah} \times v_{\%}$$

The modeled global shortwave irradiance at each grid cell on the snow surface I_s was then the sum of I_{as} and I_{ds}. The model did not consider reflection from adjacent trees and slopes. After running the model iteratively in 15 minute increments over the course of the selected day, four grid outputs were generated, including:

1. The maximum global shortwave (diffuse and direct solar) radiation I_{max} ($W \cdot m^{-2}$) experienced at each cell location during the day.
2. The time at which maximum global shortwave (diffuse and direct solar) radiation occurred t_{Imax}. This variable was useful for quality control and may prove useful for future analysis. However, this variable was not used in the main analysis.
3. The total global shortwave (diffuse and direct solar) radiation experience over the course of the day $\sum I$ ($MJ \cdot m^{-2}$).
4. The cumulative exposure time to direct shortwave radiation $\sum t_I$ (Hrs.).

Solar Pathfinder Application of Bird Model: For each sky observation location the global shortwave radiation was estimated at 15 minute intervals using the tabulated

results from the Bird model in conjunction with sun path information derived from the Solar Pathfinder imagery. For each image, the solar path across the hemispheric projection was generated using GLA (Figure 48).

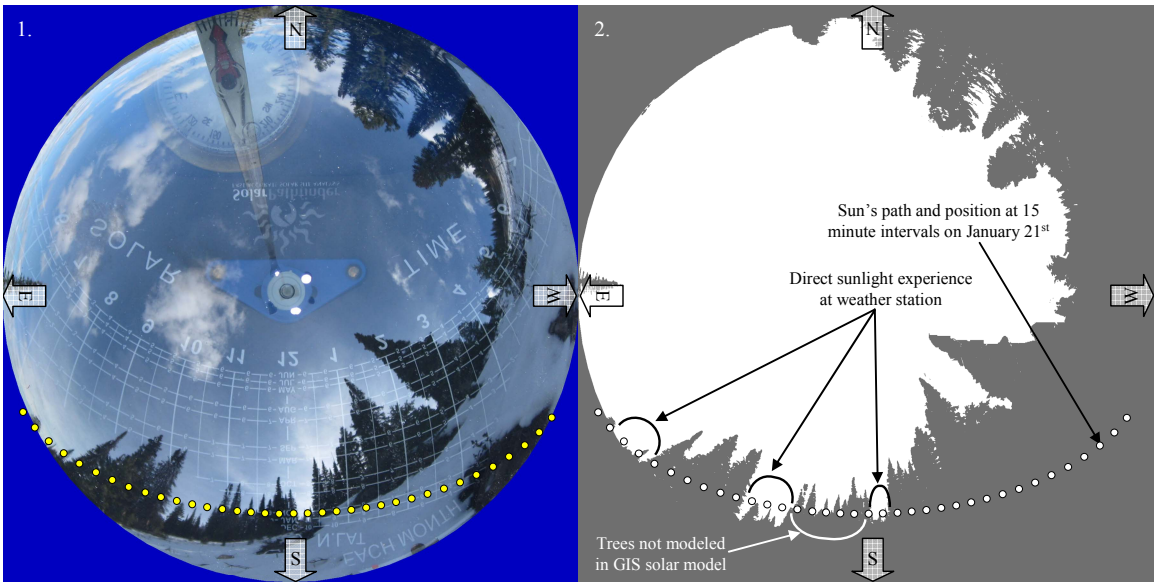

Figure 48. The sun's path across the weather station's hemispheric viewshed on January 21. (1) Photograph oriented to north with solar path super-imposed. (2) The weather station experiences direct shortwave radiation for only three short periods on this day as a result of the sun's low path and the presence of trees near the study site. A distant group of trees that is not modeled in the GIS model but is accounted for in the Solar Pathfinder application (white bracket) blocks direct sunlight before the noon hour.

At 15 minute increments along the sun's trajectory, the sun path visibility was estimated as an approximate percentage using the Solar Pathfinder imagery (100% and 0% denote no and complete obstruction for a 15 minute period). To obtain the direct shortwave radiation encountered on the surface, these values were multiplied with the Bird estimate of direct beam solar radiation before accounting for the angle of incidence. Unlike the GIS model, this method accounted for shading from all visible trees (not just those within a 30 m perimeter of the study site) and allowed for partial shading from direct sunlight (not just 0% and 100% shading). As implemented by Wilson and Gallant

(2000) and in the above described GIS model, at each location of the site and at each point in time, I_{as} was calculated by multiplying I_{ah} by $v_{\%}$. Unlike the GIS model, this method accounted for sky obstruction caused by all visible trees, including those located more than 30 m from the site perimeter.

Comparison of GIS and Solar Pathfinder Applications of Global Shortwave Radiation: A qualitative comparison of the GIS and Solar Pathfinder estimates revealed clear similarities and differences between the modeled and measured values (Figure 49). In the absence of trees, both techniques produced very similar global shortwave radiation estimates. Unlike the GIS model, the Solar Pathfinder method accounted for shading from all visible trees (not just those within a 30 m perimeter of the study site) and allowed for partial shading from direct sunlight (not just 0% and 100% shading).

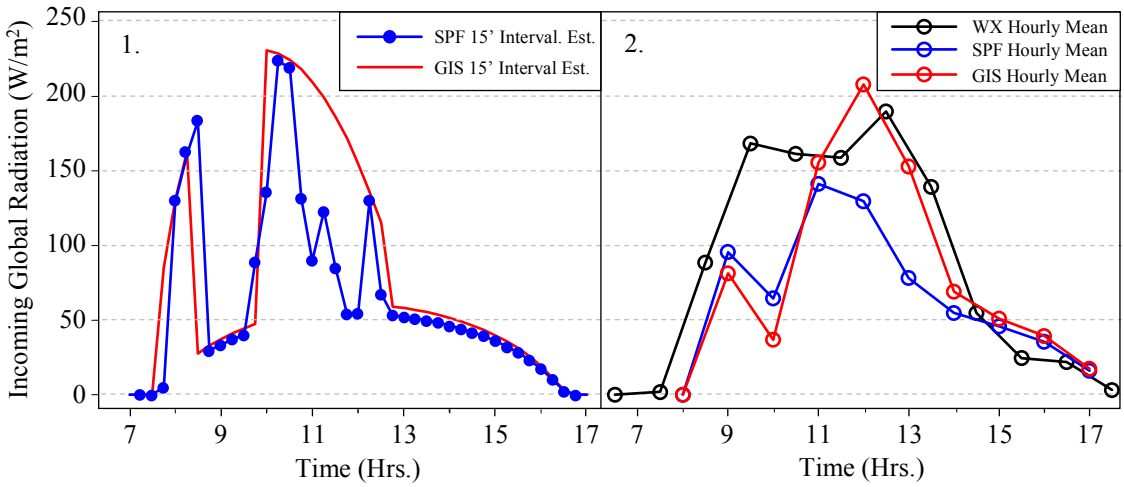

Figure 49. Comparison of global shortwave radiation information at weather station location. (1) Comparison of the Solar Pathfinder (SPF) and GIS applications of Bird estimates reveals that the GIS model overestimates incoming direct radiation, as a result of fewer and thinner tree shadows. (2) Comparison of hourly means of Bird estimates with the weather station values shows that all three information types possess two maximums caused by spacing between tree shadows and that the Bird estimates are generally smaller than pyranometer values, possibly due to the absence of reflected light of adjacent areas.

Comparison of Estimated and Measured Global Shortwave Radiation: To assess the accuracy of the Bird estimates, global radiation values estimated using the GIS and Pathfinder methods were compared with the raw pyranometer data. The comparison revealed similarities and differences between the estimates and the measured values (Figure 49.2).

Both information types began with very similar values until the first tree shadow was encountered around 9:00, at which point the estimates produced much lower values. At this hour, the pyranometer measurements should not be affected by Cosine Effect (Figure 35). Hence, it is is likely that the GIS and optical estimates exaggerated the shading effects of tree shadows. In reality, the shadows were probably less discrete. These low values, as well as those estimated at mid-day using the Solar Pathfinder, were likely caused by an underestimated diffuse component. Since the hillside was slightly convex in its entirety, it is possible that additional solar radiation was reflected off of the snowpack onto the site.

Spatial Analysis

All explicit and implicit spatial analysis methods described below were applied to all variables representing snowpack properties in each of the five plots. These methods can be categorized into two groups: geostatistics and pit-to-plot analysis. Based on spatial patterns and variability identified in snowpack properties at initial conditions (at Plot 1), the temporal analysis was then addressed.

Geostatistical Analysis

Geostatistical analysis identified significant spatial patterns in snowpack properties and attempted to quantify the predictability of snow properties on the slope. Variables were tested for two components of spatial structure, including spatial trends and positive autocorrelation. Because of the large number of spatial datasets, the spatial analysis was automated using a macro script I wrote and implemented in R. This expedited the model fitting process and ensured that model fitting was objectively conducted. In addition to the description provided here, Fotheringham and Brunsdon (2002) and O'Sullivan and Unwin (2002) provide overviews and Cressie (1993) describes spatial analysis techniques thoroughly.

Trend Surface Fitting: For each stratigraphic and microstructural variable at each plot, eleven trend surfaces were calculated using linear and polynomial regressions models (Table 8). Kronholm (2004), Logan (2005), and Lutz et al. (2007) found global spatial regression modeling useful for describing simple slope-scale trends of snowpack properties which could then be de-trended in order to further analyze local spatial variations. When no significant ($p <= 0.05$) spatial trend existed for a given variable, the mean of the variable was considered its best fit trend surface model. When only one trend fit was significant ($p <= 0.05$) it was selected as the best model. When multiple trend fits were significant ($p <= 0.05$), the most significant model was selected.

Table 8. Eleven spatial trend surface models. $\beta_{0\text{-}i}$ are coefficients, *x* and *y* are coordinate observations (Figure 11), $\mu(z)$ is the predicted local mean, μ is the global mean. The R syntax *I( )* is an identify function that allows normal mathematical symbols within model expressions.

Trend Id.	Mathematical Model	Examples of R Syntax
0	$\mu(z) = \mu$	z ~ mean(z)
1	$\mu(z) = \beta_0 + \beta_1 x$	z ~ x
2	$\mu(z) = \beta_0 + \beta_1 y$	z ~ y
3	$\mu(z) = \beta_0 + \beta_1 x + \beta_2 y$	z ~ x + y
4	$\mu(z) = \beta_0 + \beta_1 xy$	z ~ x:y *or* I(x*y)
5	$\mu(z) = \beta_0 + \beta_1 x + \beta_2 y + \beta_3 xy$	z ~ x*y *or* ~ x + y + x:y
6	$\mu(z) = \beta_0 + \beta_1 x^2$	z ~ I(x^2)
7	$\mu(z) = \beta_0 + \beta_1 y^2$	z ~ I(y^2)
8	$\mu(z) = \beta_0 + \beta_1 x + \beta_2 x^2$	z ~ x + I(x^2)
9	$\mu(z) = \beta_0 + \beta_1 y + \beta_2 y^2$	z ~ y + I(y^2)
10	$\mu(z) = \beta_0 + \beta_1 x + \beta_2 y + \beta_3 x^2 + \beta_4 y^2 + \beta_5 yx$	z ~ x + y + I(x^2) + I(y^2) + I(x*y)

Semi-Variance Modeling: Semi-variance analysis tested for spatial autocorrelation of the residuals from the best fit trend surface models. When spatial autocorrelation was evident in a semi-variogram (i.e., semi-variance increased with lag distance, until a sill threshold value was reached) then a spherical semi-variogram model was fitted to empirical semi-variograms using an automated weighted least squares function in R that iteratively tested a spherical function against the empirical variogram until the best fit was accomplished. Exponential models were also tested. However, the calculated standard errors for these models were significantly higher than those of the spherical models. A detailed description of the weighted least squares function is provided by Cressie (1993). The modeled semi-variogram dimensions, including the range, partial sill, nugget, and nugget-sill ratio were tabulated.

Spatial Interpolations: The trend surface and semi-variance information were used to interpolate two types of prediction maps of snow observations, presented in pairs in the results section. Interpoaltions of local mean values were generated using *gstat* and *geoR* packages in R. For each dataset, the selected interpolation method (plot mean, regression, ordinary kriging, or universal kriging) is presented in the geostatistical tables in the Results section. This type of interpolation, referred to as a prediction map, depicts spatial patterns of average values.

The second type of interpolation incorporated random values (noise) into the previously described interpolation. Using the R statistical package *RandomFields*, noise was defined within the interpolation using semi-variance structure and variance information. For any given dataset, *RandomFields* will generate slightly different values with every simulation, because of its random component. The purpose of presenting these simulations in the Results was to illustrate how spatial patterns in local mean values can be obscured by noise in the observations.

Pit-to-Plot Analysis

Pit-to-plot analysis quantifies how well a predefined subset or 'pit' of observations represents the observations of an entire plot. In other words, it tests spatial subsets of a dataset against the population as a whole, to see which and how many subsets are statistically representative of the conditions encountered on the entire plot. Landry (2002), Landry et al. (2004) and Logan (2005) have applied this methodology in snowpack stability studies.

Each plot contained nine pits that were tested (Figure 50). Significant differences in central tendency between pit and plot values were identified and quantified using the non-parametric Wilcoxon Rank-Sum Test (Wilcoxon, 1945), also referred to as the

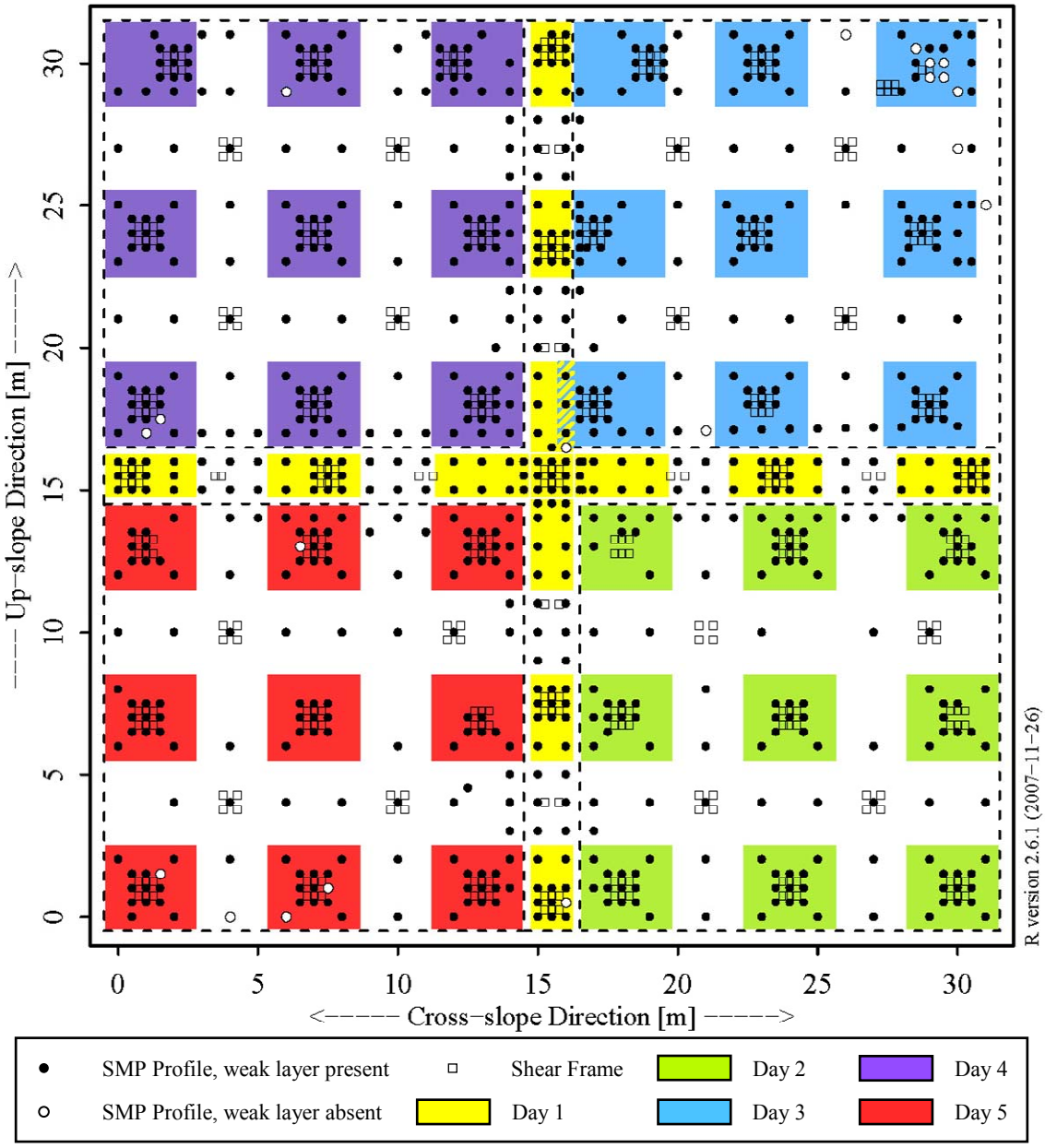

Figure 50. Pit subsets are representated as colored regions in all five plots. Each plot contained nine pits that were utilized as plot subsets for pit-to-plot representativity testing and weighted least squares regression between snow properties and with environmental estimates.

Mann-Whitney Test (Mann and Whitney, 1947). Landry (2002), Landry et al. (2004) and Logan (2005) tested values within one pit against all observations within the plot, including observations from the pit of interest. Unlike the methods applied in these studies, I tested the values within one pit against all other observations within the plot (*excluding observations from the pit of interest*). While this generally increases the apparent variability when small sample sizes are used, including the test pit's values within the population values biases the result toward spatial uniformity.

I also apply the Kolmogorov-Smirnov Test in a pit-to-plot analysis to test which and how many pits maintain a distribution that is representative of (or not significantly different than) the plot's distribution (Conover, 1971). More specifically, it estimates whether a significant difference in the cumulative distributions of two groups of data are different. Like the Wilcoxon (Mann-Whitney) Test, the Kolmogorov-Smirnov Test is a non-parametric rank-based test. The pit-to-plot ratios for central tendency P_{Wilco} and distribution P_{KS} describe the plot's variability and are equal to the percentage of representative pits:

$$P = \frac{\#\ Representative\ pits}{Total\ \#\ pits}$$

A high pit-to-plot ratio indicates plot uniformity. Low ratio values indicate high variability which, due to the spatial subsetting, is indicative of a pronounced spatial pattern which may limit the plot-scale predictive strength of individual pits. This fairly simple technique is useful to estimate how well one's observations can be extrapolated across a slope, in particular for practical situations when large datasets can not be attained

for geostatistical analysis. Hence, this approach and its results can have obvious implications for backcountry and operational settings.

Temporal Analysis

Selection of Temporal Sequences

The temporal analysis examined changes in snowpack properties that occurred over time. To conclusively state that differences between two groups of observations were due solely to temporal changes, one must show that the two groups originated from the same population and possessed the same spatial attributes at initial conditions. Otherwise, the difference between the groups may be the result of a spatial phenomenon.

Based on the spatial analysis of snowpack and environmental properties, up-slope trends were identified in several variables. All five plots contained these trends, with Plot 1 possessing the most significant trends due to its larger spatial extent. This finding challenged our ability to identify temporal changes, because it violated the assumption that the study site can be treated as a single population. A sensible solution was developed to deal with this situation.

First, the up-slope orientation of prominent trends in snowpack and environmental variables was considered. For example, $v_{\%}$ and h_{wl} were significantly greater on upper portions of the slope than they were on lower portions of the slope. This was evident in the geostatistical analysis of individual observations and of pit means from Plot 1. In contrast, few variables possessed cross-slope trends and when so, only very slight in magnitude.

Considering these patterns, the study site was segmented into an upper and lower site. The upper site was characterized as having greater sky visibility and thicker surface hoar, while the lower site possessed a thinner weak layer and lower sky visibility. Because cross-slope trends were minimal, it was thought that differences between the lower plots (Plots 2 and 5) could be attributed to changes over time. Likewise, differences between the upper plots (Plots 3 and 4) could largely be considered temporal changes. This approach was utilized for datasets with small sample sizes, such as the slab loads, which were observed once at each snow pit, equaling nine observations per plot.

There was still a degree of uncertainty in the interpretation of the results, because it was unknown whether the snowpack properties at the outer corners of the site (e.g., (*x, y*) coordinates = (0, 0), (31, 0), (31, 31), and (0, 31)) were similar to observations at the outer extents of Plot 1 (e.g., (*x,y*) coordinates = (15.5, 0), (31, 15.5), (15.5, 31), and (0, 15.5)). Hence, for relatively large datasets, such as SMP and shear strength observations, a more conservative temporal analysis was made by limiting the datasets to those observations directly adjacent to Plot 1 (Figure 51). This reduced the comparison to the column subsets near the center of the study site, each containing three pits.

Because adjacent columns spanned the same up-slope extent of the slope, any spatial variations due to up-slope trends were experienced in all subsets. Significant differences could hence be attributed to temporal changes. Temporal changes in median values of observations were quantified using the Wilcoxon Rank-Sum (Mann Whitney) Test (Wilcoxon, 1945; Mann and Whitney, 1947) and in distribution using the

Kolmogorov-Smirnov Test (Conover, 1971). Results from the same analysis using cross-slope rows were excluded because they could not be conclusively interpreted, due to the uphill spatial trends.

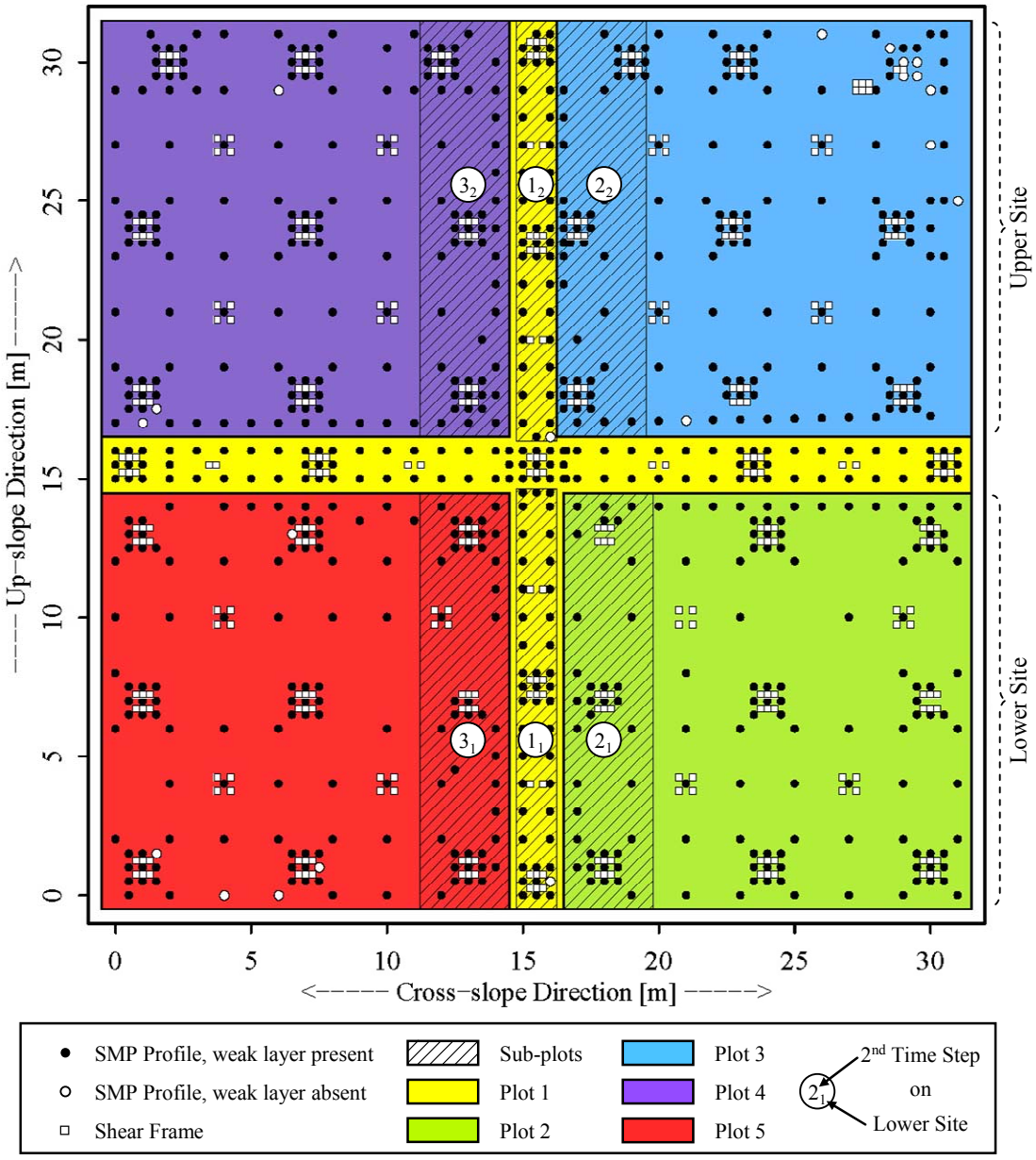

Figure 51. Conservative approach to temporal analysis utilized upslope oriented sub-plots.

Boxplot Representations

All boxplots have graphical features to help illustrate statistical properties of each group and relationships between adjacent groups in the temporal analysis. Whiskers represent the range. Boxes represent the inter-quartile range. Triangles on the sides of boxes represent approximate lower and upper 95 % non-parametric confidence intervals as calculated in R, such that,

$$\pm error = \pm 1.58 \times \frac{I.Q.R.}{\sqrt{n}}$$

Where *I.Q.R.* is the inter-quartile range and *n* is the sample size. Similar estimations are described by Chambers et al. (1983) and McGrill (1978). When significant differences existed between adjacent groups, as calculated with the Wilcoxon Rank-Sum (Mann Whitney) Test, the confidence triangles were colored white, otherwise they were colored grey. Vertical text between groups described the change in median values, along with p-values when differences were significant ($p <= 0.05$).

Snowpack Associations

Internal relationships between snowpack properties as well as relationships between snowpack properties and environmental properties were examined at each plot using scatterplots, weighted least squares regression of pit observations, and comparisons of boxplot series. Relationships were examined at 8 spatial extents, including the entire site, individual plots (Figure 6), and the cross- and up-slope transects of Plot 1, independent of each other.

The weighted least squares regression was deemed a reasonable method for determining linear fits with this particular dataset. First, because both the shear frame and SMP measurements were destructive, they could not be paired spatially on the same unit of snow. Hence, it was not possible to determine if a relationship existed between the variances of the two types of observations, based on individual pairs of observations.

Given that the observations were placed in tightly spaced local grids, it was possible to estimate the local variance of both types of observations. Hence, as an alternative to mixed effect modeling, a weighted least squares regression could be run using pit means of a variable as the predictor, and the inverse of pit-variances as the weights. By including the inverse variance as a weight in this model, the least squares fit is determined in part by weighting pits with lower variance more than those with greater variance.

Data Archive

All field observations have been archived digitally (DVD format) with the Department of Earth Sciences, at Montana State University, Bozeman, MT. The contact information for obtaining this data, at the time of this publication, is as follows:

Department of Earth Sciences
Montana State University
P. O. Box 173480
Bozeman, MT 59717-3480
Location: 200 Traphagen
Tel: (406) 994-3331
Fax: (406) 994-6923
Email: earthsciences@montana.edu

The main data components include:

1. SMP profiles with surface coordinates.
2. Shear frame observations with surface coordinates.
3. Long- and shortwave radiation estimates at pit coordinates.
4. Weather station measurements.
5. Manual snow profiles.

RESULTS

Results Overview

Following an overview of the weak layer formation and meterological conditions during its formation and persistence, the spatial and temporal results are presented in separate sections. Then, external and internal associations involving environmental and snowpack properties are presented. Lastly, the pit-to-plot representativity results are presented.

Snowpack Development

By the second week of January 2005, early season instabilities associated with a 50 cm depth hoar base had diminished after several small snow storms had incrementally loaded the existing snowpack with more than 1 m of new snow. Then, during the second half of January, a diurnal cycle of relatively warm days with light cloud cover and cool clear nights developed. The presence of hollow columnar surface hoar was observed on January 20. Surface hoar crystal height was typically 4 to 8 mm but in some instances was up to 15 mm. The crystals consisted of open-sided columns, approximately 2 to 4 mm in width, with distinct scrolling on both columnar edges (Figure 52.2 and 52.3). All slope aspects near the site were densely covered.

Five days later (January 25, 2005) the surface hoar had grown into a unique combination of two crystal types "perched" one on top of the other: relatively large plates (approximately 15 mm tall) had 'sprouted' from the tops of the hollow columnar

forms witnessed five days prior, now decomposed into apparently solid stems (Figure 52.1).

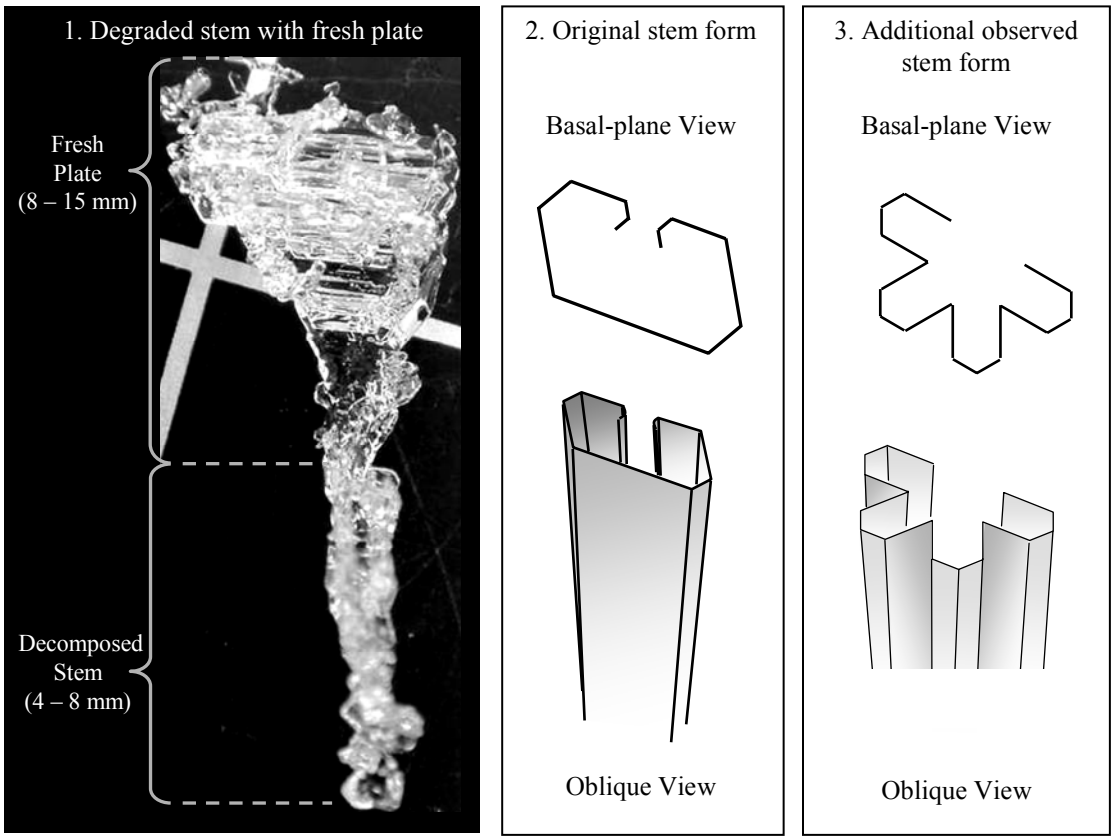

Figure 52. (1) Photograph of surface hoar crystal, taken on 15th February, approximately 3 weeks after crystal formation and 10 days after burial, stem and plate structures are evident. (2) Enlarged illustration of initial hollow columnar crystal form with scrolling edges on one side, as it was observed on January 20 before plate growth or stem degradation occurred. (3) Additional hollow crystal form observed on January 20.

The surface hoar persisted on the surface for another 11 days before being capped off by 10 cm of new snow accumulating between February 5 and 7. Between February 12 and 14 another 20 cm new snow accumulated, further ensuring the persistence of the buried surface hoar. When field sampling began on February 28, 2005, the slab contained approximately 50 mm snow water equivalent. Between the sampling of Plots 3

and 4 (March 8 to 14) approximately 4 mm water equivalent accumulated as 5 cm new snow. On March 20, one day prior to the sampling of Plot 5, approximately 30 mm of water equivalent accumulated as approximately 23 cm of new snow.

Meteorological Conditions during Surface Hoar Formation

The surface hoar formation period can be divided into two clear time periods. The first period included the formation of the hollow columns observed on January 20. The second formation period occurred between January 20 – 25, during which the plates formed. The following two sections describe meteorological conditions at the study during these periods which are relevant to surface hoar formation.

First Period of Surface Hoar Formation: We observed small hollow columnar surface hoar crystals on January 20. Because these delicate, elaborate surface hoar crystals exhibited no degradation (rounding), and because of weather conditions, it was assumed that these crystals had formed within two days of their observation. The meteorological conditions on January 19 and preceding days were mostly clear with a night time breeze, recorded as an 10-minute average wind speed of 0 – 2 $m \cdot s^{-1}$ with maximum gusts below 10 $m \cdot s^{-1}$ (Figure 53.1). Winds were primarily out of the east or northeast, which corresponded approximately with an up-slope movement and was likely associated with a regional wind (Figure 53.2). Temperatures were mild but remained below 0°C (Figure 53.3).

With no snow temperature sensors, the only available information regarding snow temperature was recorded at snow pits. On January 20 at 10:00 am the snow surface

temperature was -2 °C, approximately 2 degrees cooler than the air temperature at 1.5 m. Outgoing global shortwave radiation (reflected off the snow surface) was significantly larger than incoming global shortwave radiation on January 19 (Figure 53.4, arrow).

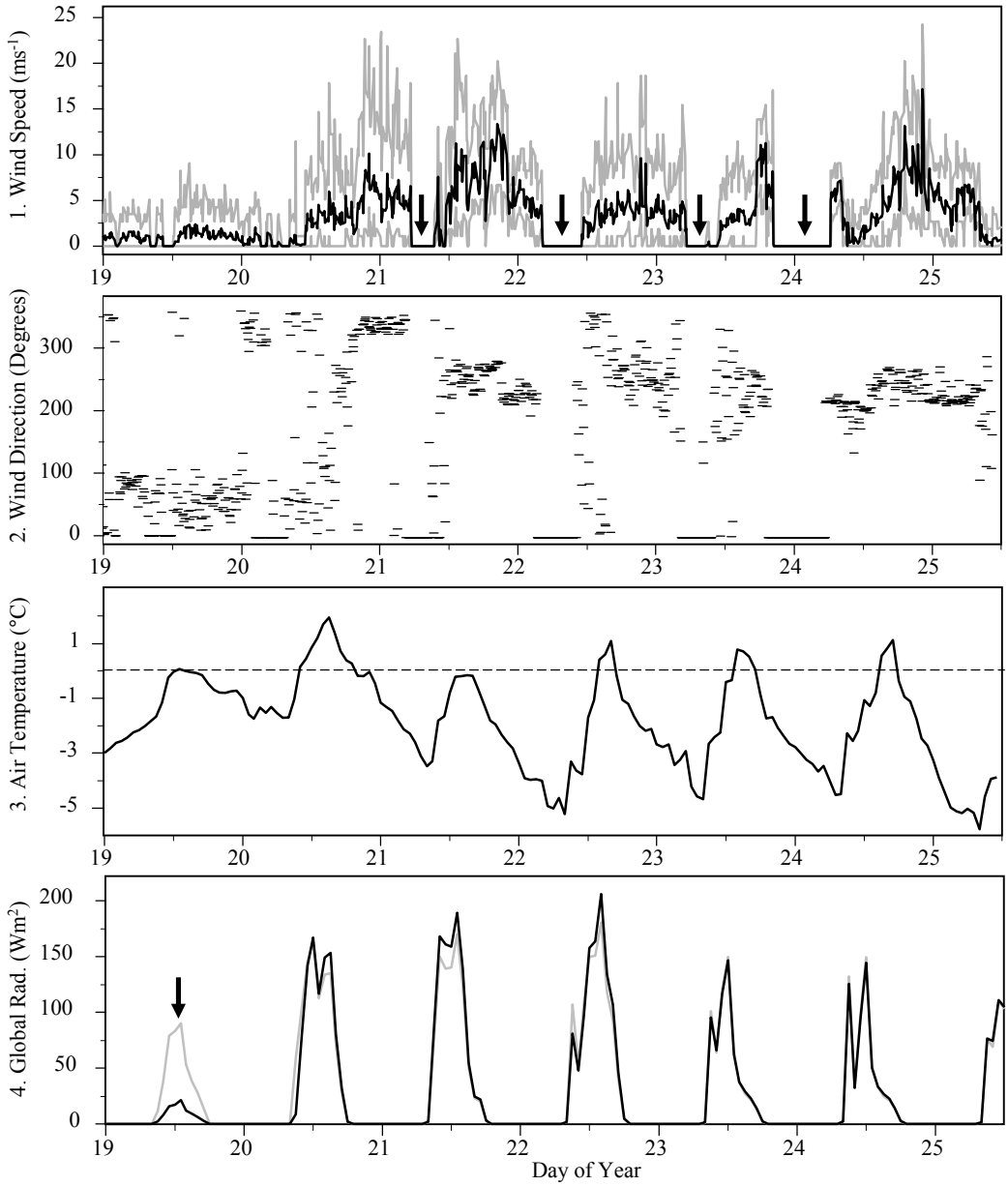

Figure 53. Meteorological conditions at the study site between January 19 – 25, the surface hoar formation period. (1) The 10-minute minimum, average and maximum wind speeds (m·s-1) (grey, black, and grey lines, respectively) with arrows indicating calm periods. (2) Wind direction (azimuthal degrees). (3) T_{air} (°C). (4) Incoming and outgoing global shortwave radiation ($W \cdot m^{-2}$) (black and grey lines, respectively) with arrow indicating possible snow accumulation on sensor.

This may have been instrumental error caused by surface hoar crystals forming on the upward facing pyranometer, which would influence the incoming global shortwave measurements.

Second Surface Hoar Formation Period: The second period of surface hoar formation occurred between January 20 - 25, when plates sprouted from the tops of the thin columns. It is not known precisely when during these four days the plates formed. However, the meteorological data can be used to identify distinct diurnal meteorological patterns associated with the crystal growth.

Between January 20 - 24, the average wind speed varied considerably, between 0-18 $m \cdot s^{-1}$ and the maximum wind speeds reached 24 $m \cdot s^{-1}$(Figure 53.1). Winds were generally strongest in the evening and subsided by sunrise. Early morning hours were completely calm (thick arrows, Figure 53.1). Around noon an up-slope breeze began and steadily increased. By mid-afternoon the wind had switched directions and was moving cross- or down-slope (Figure 53.2), reaching a maximum average wind speed of 18 $m \cdot s^{-1}$ around 22:00. Winds began to subside by midnight and by sunrise the air was completely calm once again.

During this second surface hoar formation period, maximum daytime T_{air} was between 1° to 3° C and nighttime T_{air} dropped to -5° C. A clear diurnal fluctuation pattern existed, with daily minimums occurring at early morning and maximums occurring in the afternoon (Figure 53.3). In total T_{air} varied by only 8 °C during these six days. The sky was typically clear, evident through the consistent global shortwave radiation readings (Figure 53.4).

Meteorological Conditions during Surface Hoar Persistence

Surface hoar had fully formed by January 26 and remained exposed on the surface until the snowfall event 10 days later (Figure 54). During this period, daytime air temperatures regularly exceeded 0° C and nighttime lows varied between -5 to -10° C.

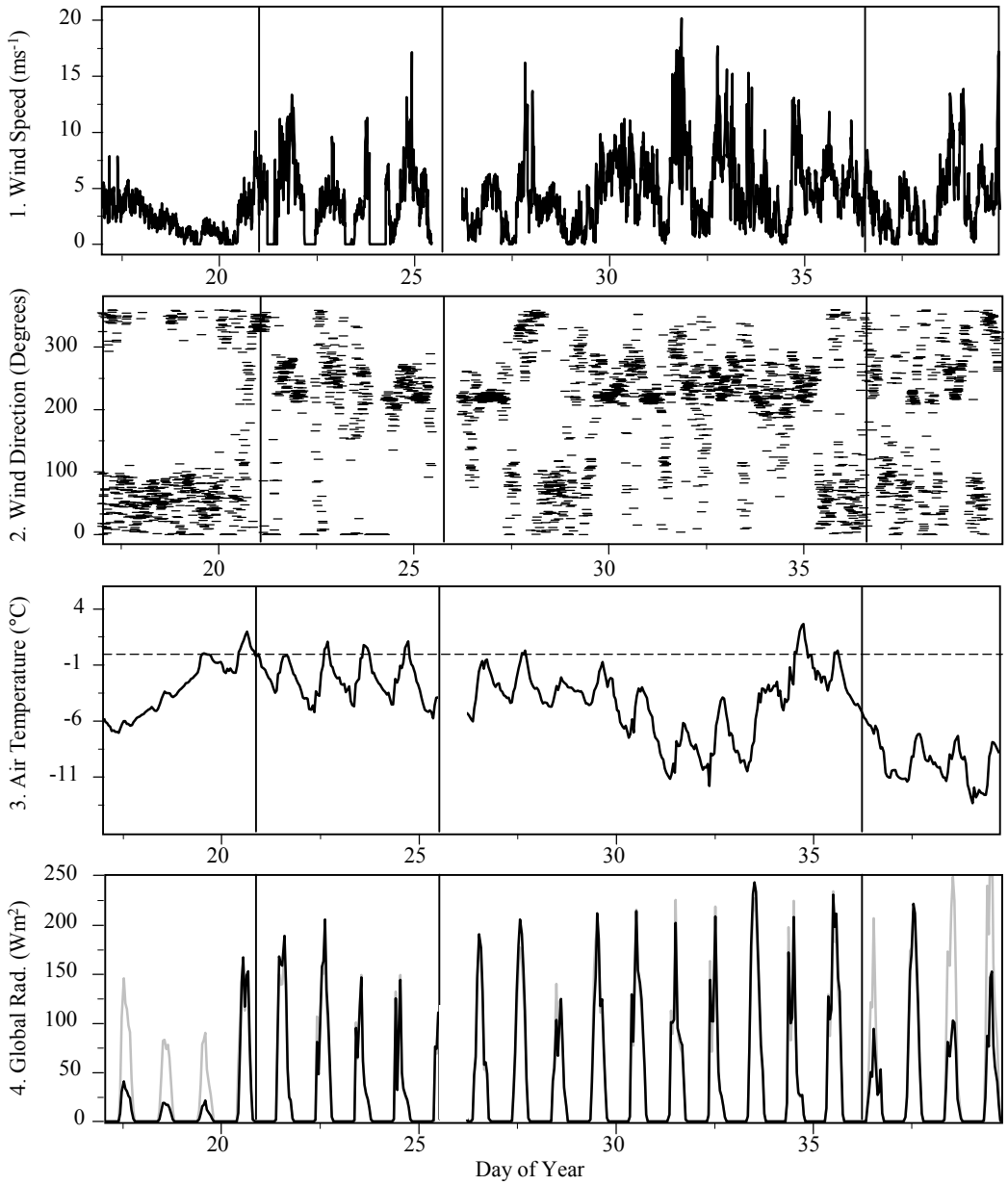

Figure 54 Meteorological conditions at the study site between January 19 –February 10, 2005. (1) Wind speeds ($m \cdot s^{-1}$). (2) Wind direction (azimuthal degrees). (3) T_{air} (°C). (4) Incoming and outgoing global shortwave radiation ($W \cdot m^{-2}$) (black and grey lines, respectively).

Average wind speeds were similar to those of previous days but were not necessarily diurnal (Figure 54.1). There were periods of sustained 5 to 10 $m \cdot s^{-1}$ wind events. Air temperatures rarely rose above 0 °C during the persistence period but did on one occasion reach 3 °C (Figure 54.3). Clear and partially cloudy conditions persisted throughout the period, evident by the consistently high peaks in incoming global shortwave radiation (Figure 54.2).

The surface hoar layer was finally capped off by 10 cm of new snow accumulating between February 5 (Figure 55, arrow) and 9. Between February 12 and 14 another 20 cm new snow accumulated, further ensuring the persistence of the buried surface hoar (Figure 55).

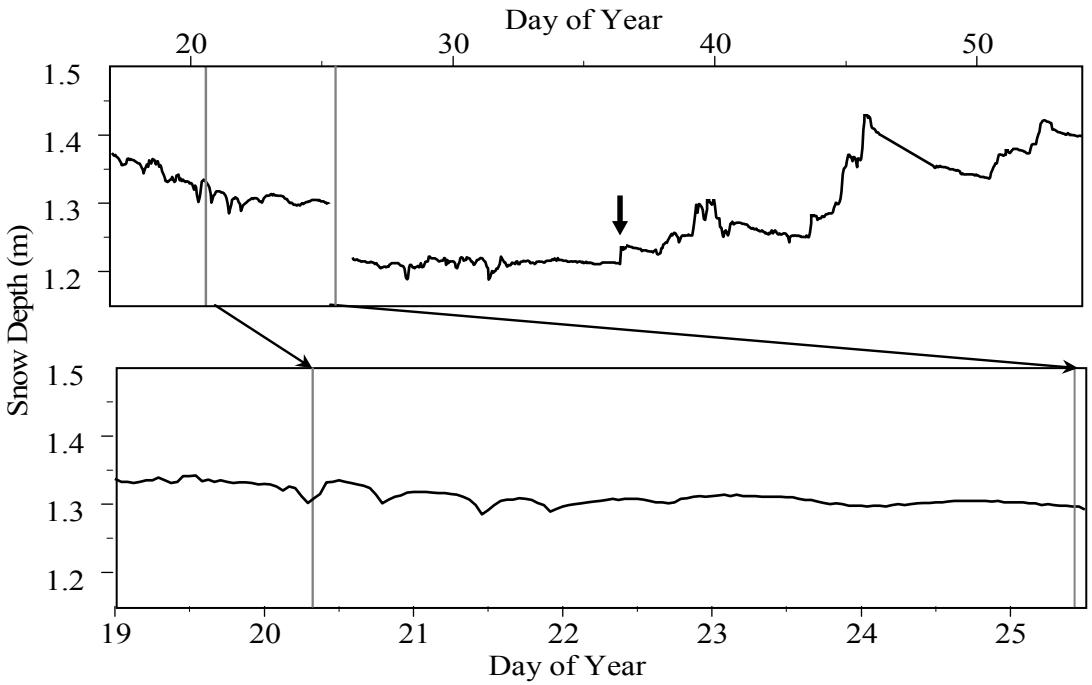

Figure 55. Snow depth at the weather station, from mid January to late February, 2005. Note the systematic error possibly associated with temperature fluctuations or surface conditions, and the 7 cm offset that occurred while maintaining the site on January 25. The first snowfall that buried the surface hoar layer began on February 5 (arrow).

Spatial Analysis

Topography

Slope angle (Figure 56.1) and azimuthal orientation (Figure 56.2), derived from the snow surface elevation model, quantify topographic characteristics of the site. Slope angle varied between 25° and 29° with the steepest sections limited to a cross slope band at the top of the site and a convexity at the base of Plot 5 (Figure 56.1). Moving across the site from the left to right side, the azimuthal orientation changed from 34° to 47° East of North (Figure 56.2).

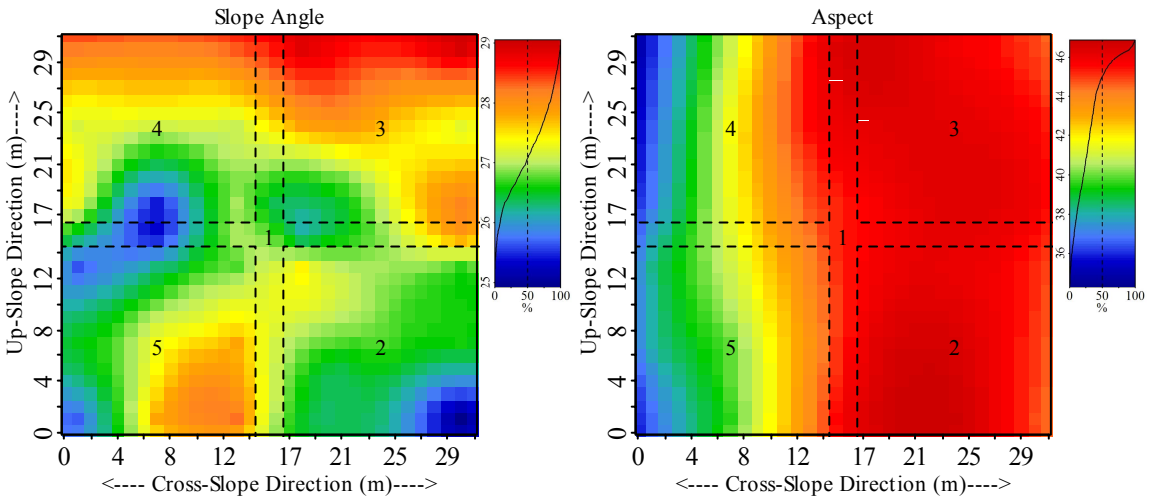

Figure 56. (1) Slope angle and (2) azimuthal orientation of the snow surface during the surface hoar formation period, derived from the high resolution elevation model. Black line on color scale indicates cumulative distribution of grid values.

On-Site Vegetation

Large bushes may have been near the weak layer, as indicated by the dark blue areas in the prediction map depicting the depth to nearest object (Figure 57.1). By February, snowfall and snowpack creep likely pushed small vegetation (sage brush and coniferous saplings) toward the ground and away from the weak layer, though it is

possible individual branches affected some small portions of the weak layer. A cross-slope trend in the depth to the nearest object is present on the site, whereby Plots 4 and 5 possess smaller depth values than Plots 2 and 3. This is solely due to a spatial pattern in h_{base}. Horizontal (Euclidean) distance to small vegetation was also mapped (Figure 57.2).

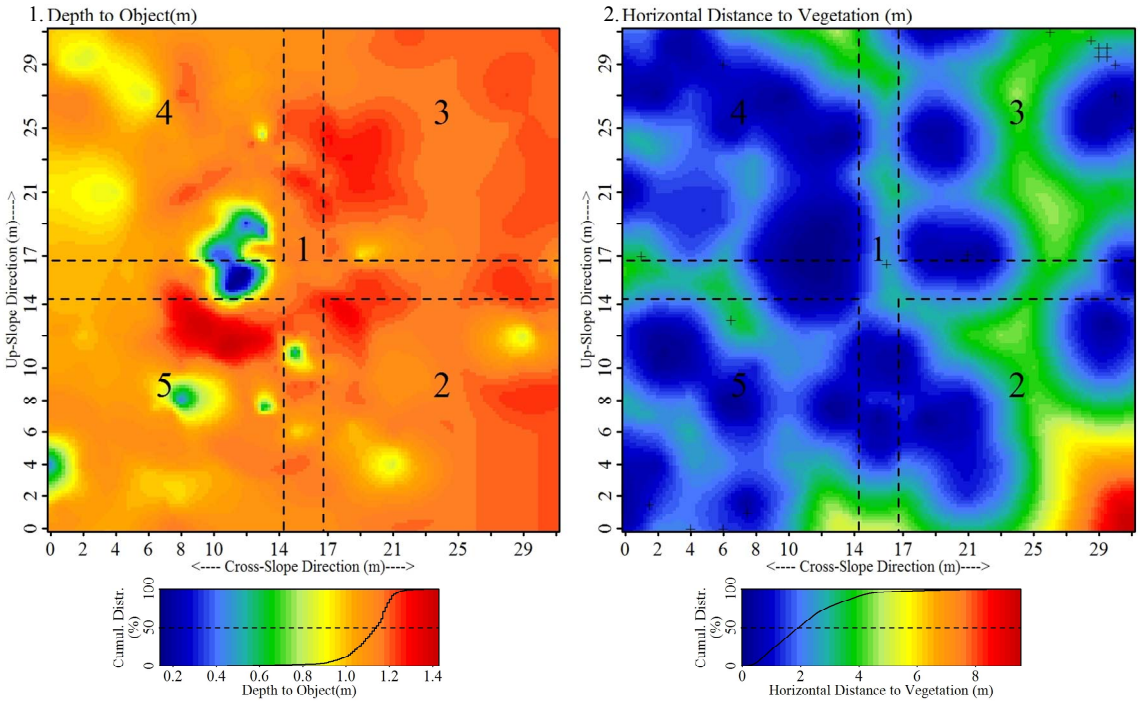

Figure 57. (1) Depth (m) to nearest object (top of vegetation or ground) from weak layer position. In parts, the weak layer was only 14 cm above the summer vegetation heights. (2) Euclidean distance (m) to small vegetation on the site, with color ramp scaled by non-parametric percentile values. '+' represent the 18 of 824 SMP profiles that did not contain the weak layer

Radiation Estimates

Hemispheric Sky Visibility ($v_{\%}$): Sky visibility was highly spatially correlated in the optical- and GIS-based estimates (Table 9 and Figure 58). More than 42 % to 43 % of the sky viewshed was obstructed on the lower slope. The mid to upper left portion of the site experienced at least 10 % greater sky visibility than the base of the slope. A wider range of $v_{\%}$ values existed in the GIS model (18.5 %) than in the optical values

(11.3 %). The lower visibility at the base of the slope in the GIS model was due to the trees being modeled as solid objects and the higher values experienced further up-slope are a result of distant obstructions (e.g., trees and nearby ridges) being excluded from the GIS model. Visually, both models possessed very similar spatial patterns.

Table 9. Spatial patterns of radiation and topographic estimates. Variables were estimated using the optical Solar Pathfinder (S.P.F.) and G.I.S.techniques.

Variable	Estimate Type	Interpolation Method	Regression Component			Variogram Component			Model Error	
			Formula	p-value	r^2	Range (m)	Nugget	Sill	$\sigma_{pred.err}$	$m_{pred.err}$
$v_{\%}$	*S.P.F.*	Universal	10	1.5E-20	0.92	13.20	0.0E+00	6.5E-05	8.4E-06	2.1E-05
	G.I.S.	Universal	10	9.0E-21	0.92	149.19	0.0E+00	9.6E-04	1.0E-05	2.6E-05
$L\downarrow$	*S.P.F.*	Universal	10	1.5E-20	0.92	13.20	0.0E+00	3.6E-01	4.6E-02	1.1E-01
	G.I.S.	Universal	10	8.3E-22	0.93	9889.05	0.0E+00	3.2E+02	5.1E-02	1.3E-01
I_{max}	*S.P.F.*	Universal	8	2.8E-11	0.68	2726.66	3.3E+01	1.2E+04	7.6E+00	6.0E+01
	G.I.S.	Universal	8	1.5E-11	0.69	2660.92	3.3E+01	1.2E+04	8.1E+00	6.3E+01
$\sum I$	*S.P.F.*	Universal	10	7.3E-09	0.68	214.80	8.6E-03	1.3E-01	2.5E-03	1.4E-02
	G.I.S.	Universal	10	1.1E-11	0.77	257.80	7.1E-03	2.8E-01	3.4E-03	1.4E-02
$\sum t_I$	*S.P.F.*	Universal	2	5.1E-04	0.25	5.88	7.2E-02	9.8E-02	3.4E-03	9.9E-02
	G.I.S.	Universal	3	2.3E-12	0.73	309.43	2.6E-02	6.1E-01	4.3E-03	4.1E-02
$Slope_{slope}$	*G.I.S.*	Universal	7	1.6E-05	0.35	9.40	0.0E+00	4.9E-01	8.0E-02	2.1E-01
$Aspect_{slope}$	*G.I.S.*	Universal	8	2.6E-17	0.83	1119.24	8.3E-01	8.2E+01	1.5E-01	1.4E+00

* 'Formula' refers to best-fit regression model, as defined in Table 8.

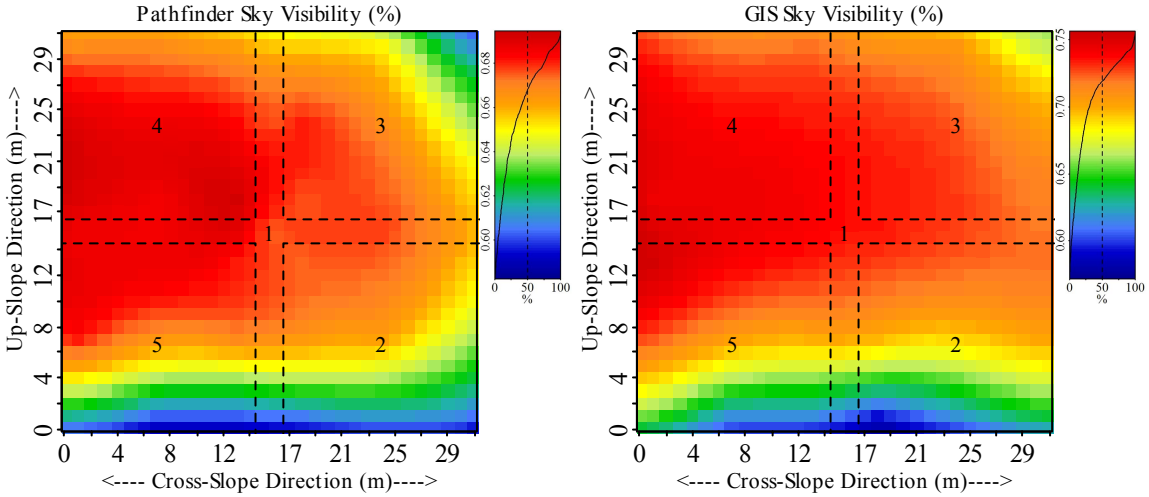

Figure 58. $v_{\%}$ estimates interpolated from (1) optical field measurements and from (2) the GIS model. 1 m resolution. Black line on color scale indicates cumulative distribution of grid values.

Incoming Longwave Radiation ($L\downarrow$): The prediction maps for $L_{\downarrow}$ (Figures 59 and 60), calculated using two different T_{air} values (-1.7° C and -5.2° C) from early morning

conditions measured at the weather station during the surface hoar formation period, mirror the spatial pattern of $v_{\%}$ (Figure 58). At the site-scale, the pattern can be described as a concave form, whereby $L_{\downarrow}$ is greatest at the slope base and along the right and upper edges of the site (Figures 59 and 60). Logically, the spatial variation of $L_{\downarrow}$ is nearly identical for both T_{air} values since, in both circumstances, T_{air} is defined as spatially constant. Estimates for T_{air} = -5.2° C can be derived by multiplying $L_{\downarrow}$ for T_{air} = -1.7° C by a factor of 0.95. The total range of $L_{\downarrow}$ for T_{air} = -1.7° C is slightly larger than when T_{air} = -5.2° C (by a factor of 1.05).

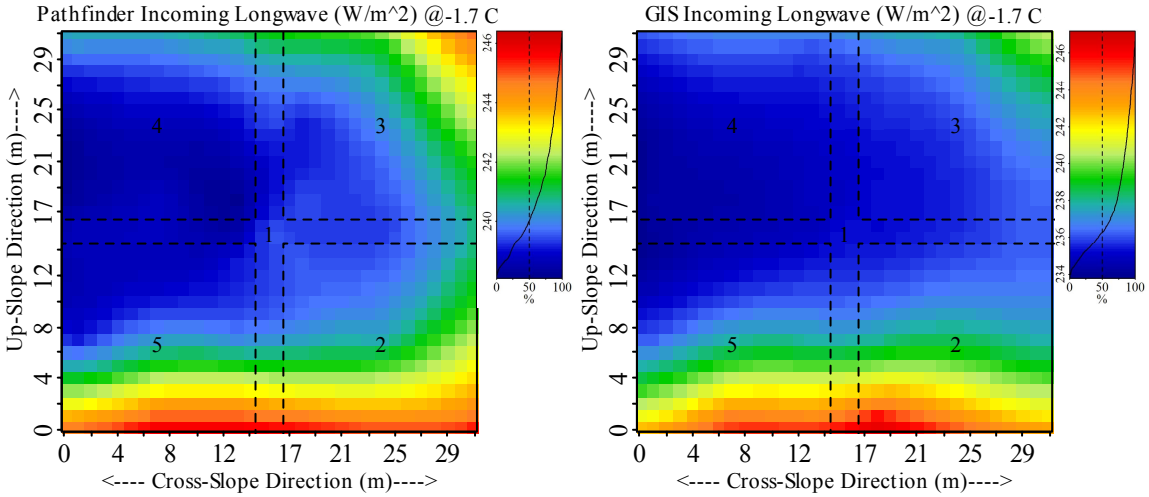

Figure 59. Estimated incoming longwave flux ($L_{\downarrow}$) with air temperature set to -1.7° C, derived from (1) optical field measurements and from (2) the GIS model. 1 m resolution. Black line on color scale indicates cumulative distribution of grid values.

The lowest $L_{\downarrow}$ estimates are located near the middle of the site in Plot 4, where $v_{\%}$ was greatest, and the greatest $L_{\downarrow}$ values are located at the base of the slope, where down-slope trees greatly reduced $v_{\%}$ (Figure 58). For T_{air} = -1.7° C, $L_{\downarrow}$ varies across the site by 8.3 $W \cdot m^{-2}$ using the Pathfinder estimates and 13.5 $W \cdot m^{-2}$ when using the GIS estimates. For T_{air} = -5.2° C, the range of $L_{\downarrow}$ is slightly smaller (by a factor of 0.094).

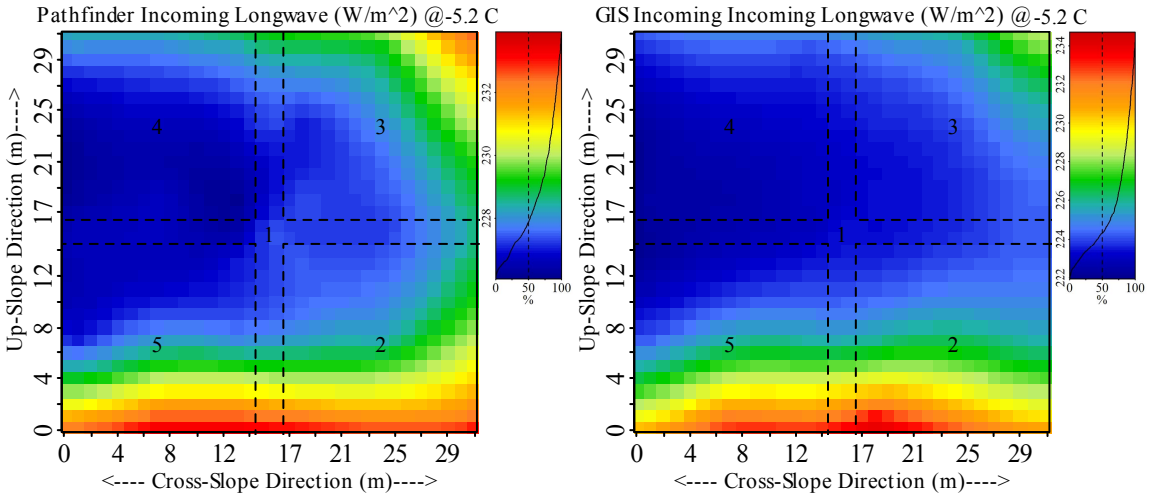

Figure 60. Estimated incoming longwave flux ($L_{\downarrow}$) with air temperature set to -5.2° C, derived from optical field measurements (left) and from the GIS model (right). 1 m resolution. Black line on color scale indicates cumulative distribution of grid values.

Three estimates of incoming global shortwave radiation during clear sky conditions were calculated for both Solar Pathfinder and GIS methods, including the maximum global shortwave radiation (I_{max}) (Figure 61), the cumulative global shortwave radiation ($\sum I$) (Figure 62), and the total exposure time to direct shortwave radiation ($\sum t_I$) (and Table 9). All three estimates account for complex terrain, including the effects of varying topography and vegetation and temporal changes in solar radiation due to atmospheric conditions and sun position.

Maximum Global Shortwave Radiation (I_{max}): Prediction maps of I_{max} on January 21 indicate that the right half of the site (Plots 2 and 3) experienced maximum global shortwave radiation values that were 85 $W \cdot m^{-2}$ greater than those experienced on the left half of the site (Plots 4 and 5) (Figure 61). If an albedo value of 90 % is assumed, this translates to an 8.5 $W \cdot m^{-2}$ spatial variation of absorbed solar radiation, which is coincidentally quite similar to the site-scale variation experienced in $L_{\downarrow}$. Although the

GIS model of I_{max} (Figure 61.2) estimated higher values than the Pathfinder method (Figure 61.1) due to limited effects from tree shadows, both models possessed very similar spatial patterns.

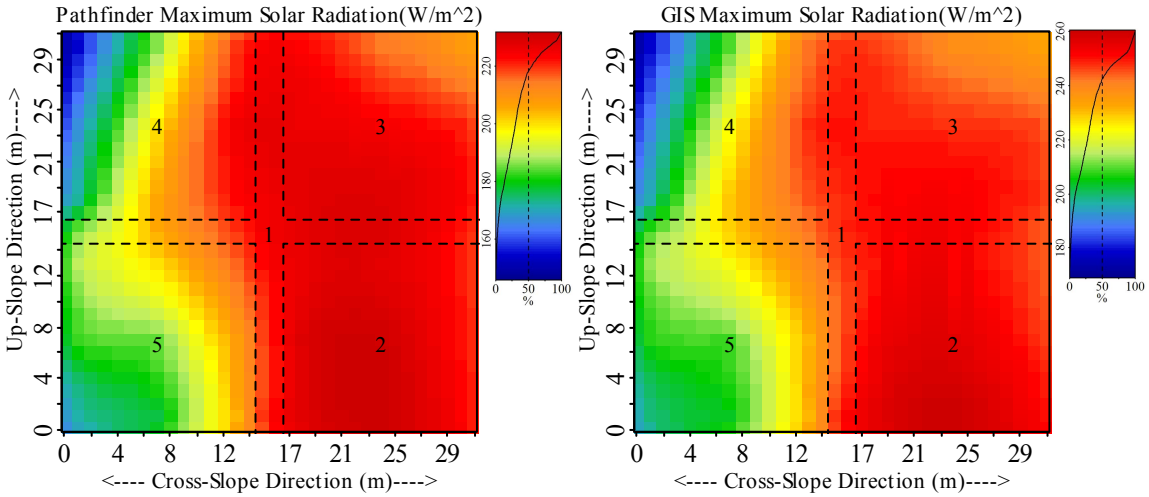

Figure 61. Estimated maximum global shortwave radiation ($W \cdot m^{-2}$), derived from (1) optical pathfinder measurements and from (2) the GIS model. 1 m resolution. Black line on color scale indicates cumulative distribution of grid values.

Total Global Shortwave Radiation ($\sum I$): Prediction maps of $\sum I$ indicated that cumulatively over the course of a clear sky day, Plot 2 received the greatest amount of solar energy and that the outer corners of the remaining plots recieved the smallest amount of solar energy (Figure 62). While the GIS model produced significantly higher values than the Pathfinder method, the spatial patterns of both estimates are quite similar. Compared to results presented by Feick et al. (2007), both methods produce values at the minimum observed values, well within the surface hoar preservation regime observed by Feick et al. (2007).

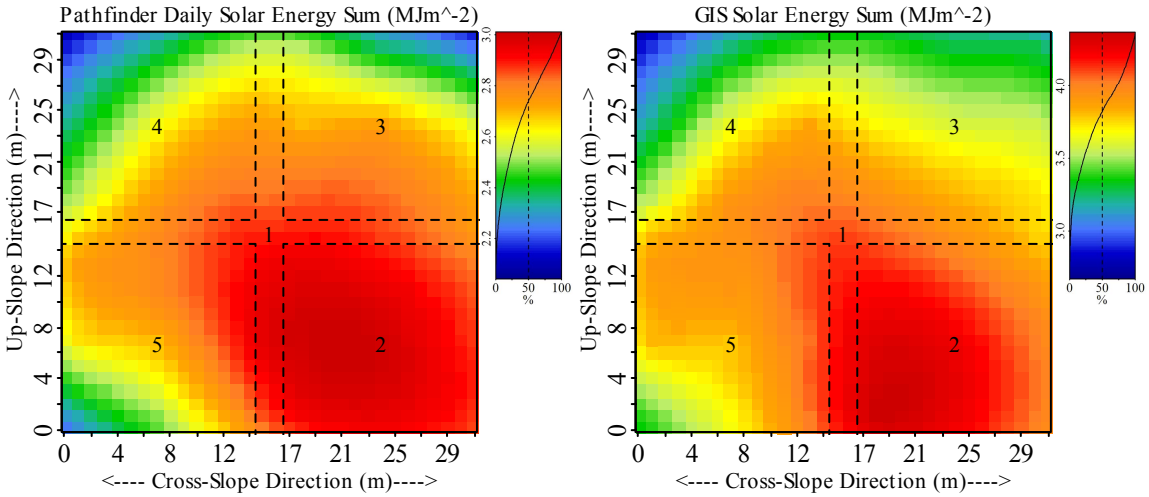

Figure 62. Daily cumulative global shortwave radiation ($MJ \cdot m^{-2}$), derived from (1) Pathfinder measurements and from (2) the GIS model. 1 m resolution. Black line on color scale indicates cumulative distribution of grid values.

Cumulative Exposure Time ($\sum t_l$): Distinct patterns existed across the site in the modeled cumulative global shortwave exposure time ($\sum t_l$). The Solar Pathfinder calculations indicated that the lower slope was exposed to direct sunlight only three quarters of an hour longer than the upper site (Figure 63). The GIS calculations indicated a larger discrepancy in exposure times across the site, with the trend running diagonally from the

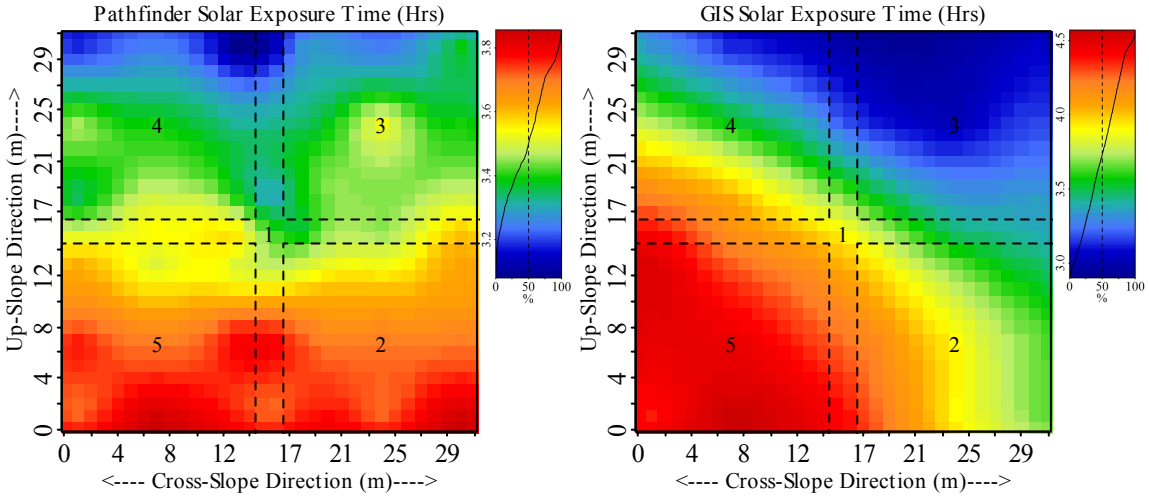

Figure 63. Cumulative exposure time to direct shortwave radiation $\sum t_l$. (hrs), derived from Pathfinder measurements (left) and from the GIS model (right). 1 m resolution. Black line on color scale indicates cumulative distribution of grid values.

upper right to lower left corners (Figure 63). The GIS model was likely less accurate because modeled trees were treated as solid objects and distant trees were not included in the model.

Weak Layer Presence and Absence

Eighteen of the 824 SMP profiles (2.2 %) did not contain the weak layer in either the raw signal or in the microstructural estimates of these profiles (Figure 64). Nine of these profiles were located directly where a ski track had been cut through the outer corner of Plot 3 in January. This track was observed after the surface hoar had formed, but before the final snowfall event that occurred before sampling began. It was clearly identified in the field by the shear frame and SMP operators while sampling Plot 3.

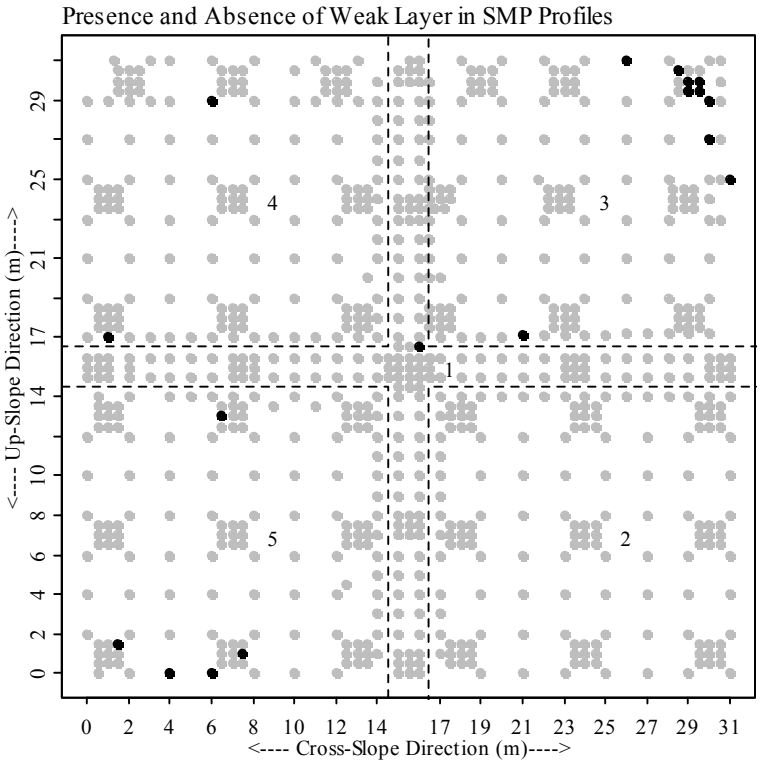

Figure 64. For 824 SMP profiles, the weak layer was identified in 806 profiles (gray dots) and was absent from 18 profiles (black dots), half of which were caused by a ski track located at the outer corner of Plot 3.

Wilcoxon Rank-Sum (Mann-Whitney) Tests tested for significant relationships between weak layer absence and the vertical and horizontal proximity to vegetation. For this comparison, profiles associated with the ski track disturbance were excluded. The results show that weak layer absence was not associated with horizontal proximity to vegetation (Figure 65.1). Profiles with no weak layer were significantly closer to the ground than profiles containing the weak layer (Figure 65.2). However, the weak layer was identified in one SMP profile where the weak layer was only 0.07 m above the modeled vegetation (Figure 65.2).

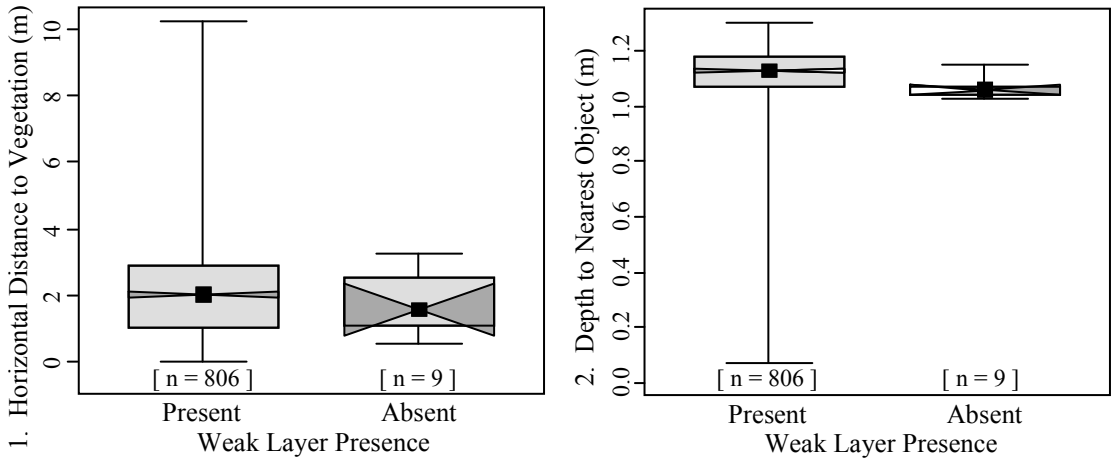

Figure 65. (1) Horizontal proximity to buried vegetation and (2) vertical proximity to buried vegetation or ground, grouped by weak layer presence and absence. Boxplot properties described on page 137.

SMP-Derived Stratigraphic Estimates

Slope-Normal Weak Layer Thickness (h_{wl}): A significant slope-scale trend existed in h_{wl} (Figure 33) from the lower right corner to the upper left corner, evident in Plots 1, 2, and 5 independently and when all plots are grouped as a single dataset (Table

10, Figures 66 and 67). This pattern was recognized in the field during shear frame measurements. The weak layer was thickest in Plot 4 and thinnest in Plot 2.

Table 10. Spatial patterns of h_{wl}. Estimates derived from SMP measurements are in millimeters.

h_{wl} (mm)	Interpolation Method	Regression Component			Variogram Component			Model Error	
Areal Extent		Formula	p-value	r^2	Range (m)	Nugget	Sill	$\sigma_{pred.err}$	$m_{pred.err}$
Plot1: Up-Slope	Universal	7	8.03E-14	0.47	1.76	0.14	3.05	0.41	1.33
Plot1: Cross-Slope	Ordinary	0	NA	NA	6.54	4.10	5.18	0.06	4.60
Plot1	Universal	3	1.29E-11	0.25	2.57	2.60	4.28	0.16	3.59
Plot2	Universal	10	1.14E-13	0.37	4.99	2.78	3.83	0.12	3.42
Plot3	Regression	1	3.26E-02	0.03	NA	NA	NA	0.04	0.20
Plot4	Universal	5	3.67E-02	0.05	4.04	4.03	4.73	0.09	4.61
Plot5	Regression	3	2.58E-07	0.19	NA	NA	NA	0.05	0.27
All Plots	Universal	10	1.16E-40	0.22	3.51	3.69	4.43	0.10	4.27

* 'Formula' refers to best-fit regression model, as defined in Table 8.

The majority of the variation of h_{wl} can be explained by the up-slope trend surface. However, a subtle but significant cross-slope trend was also present. Two distinct characteristics indicate that this pattern was a spatial phenomenon and was not related to weak layer thinning over the sampling period. First, the absolute values and trend characteristics of the four square plots closely mimic values observed in the adjacent arms of Plot 1. Second, although Plot 4 was sampled two weeks after Plot 2, the weak layer at Plot 4 was at least twice as thick as that of Plot 2, indicating that despite the passage of time the weak layer on the upper slope was distinctly thicker (Figure 66). Because this appeared to be a spatial phenomenon, a prediction map was also produced using all observations from all five plots together (Figure 67).

The semi-variance analysis showed that the weak layer thickness (h_{wl}) at Plots 1, 2, and 4 was locally correlated to distances of 2.6 m, 5.0 m, and 4.0 m respectively (Table 10 and Figure 68). Plots 3 and 5 however, possessed no autocorrelation of h_{wl} and were best described by simple trend surfaces.

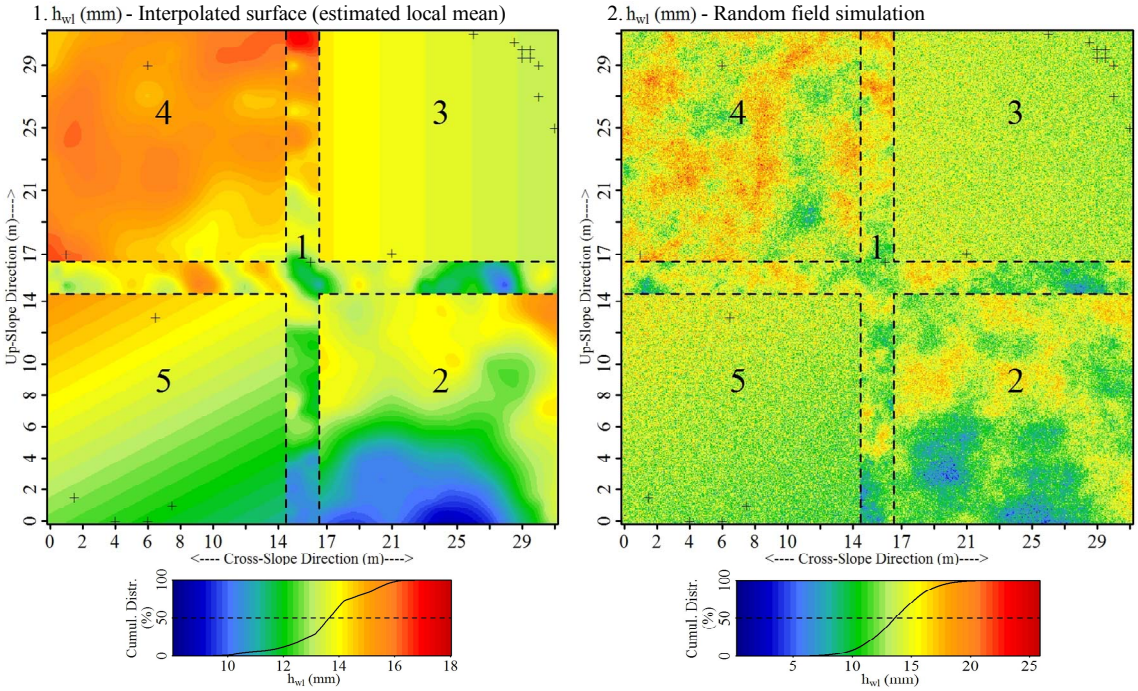

Figure 66. Spatial interpolations of h_{wl} (mm) for Plots 1 – 5. (1) Interpolated surfaces of local mean values (Table 10). (2) Random field simulation incorporates randomness based on semi-variance (Figure 68). '+' indicates location where weak layer was absent in SMP profiles.

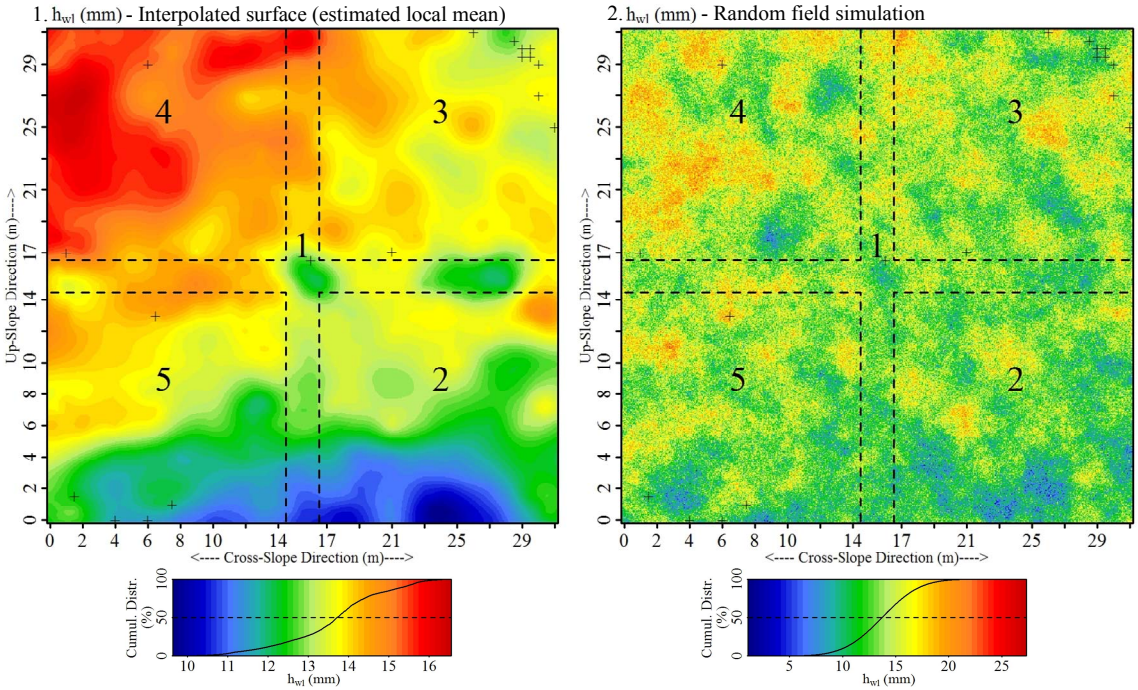

Figure 67. Spatial interpolations of h_{wl} (mm) for all SMP data. (1) Interpolated surface of local mean values (Table 10). (2) Random field simulation incorporates randomness, based on semi-variance (Figure 69). '+' indicates locations where weak layer was absent in SMP profiles.

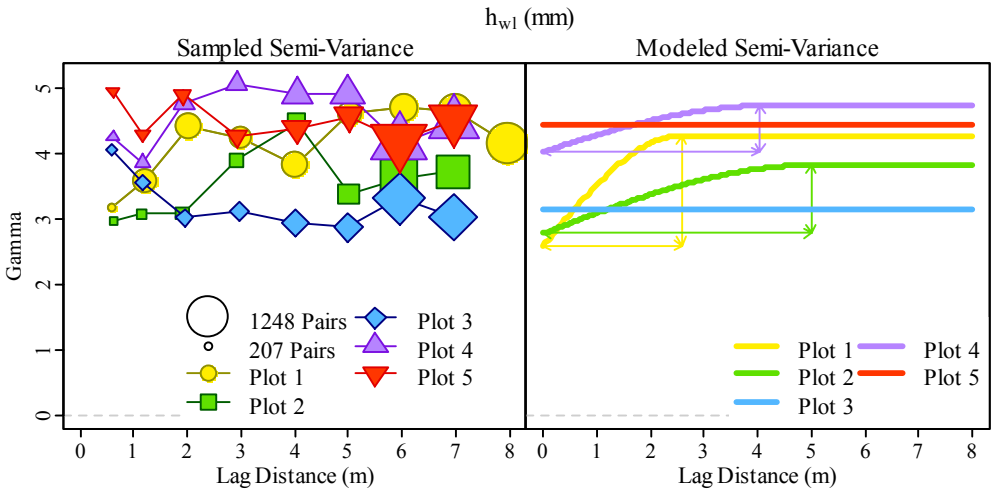

Figure 68. Sample (left) and model (right) variograms of h_{wl} (mm).

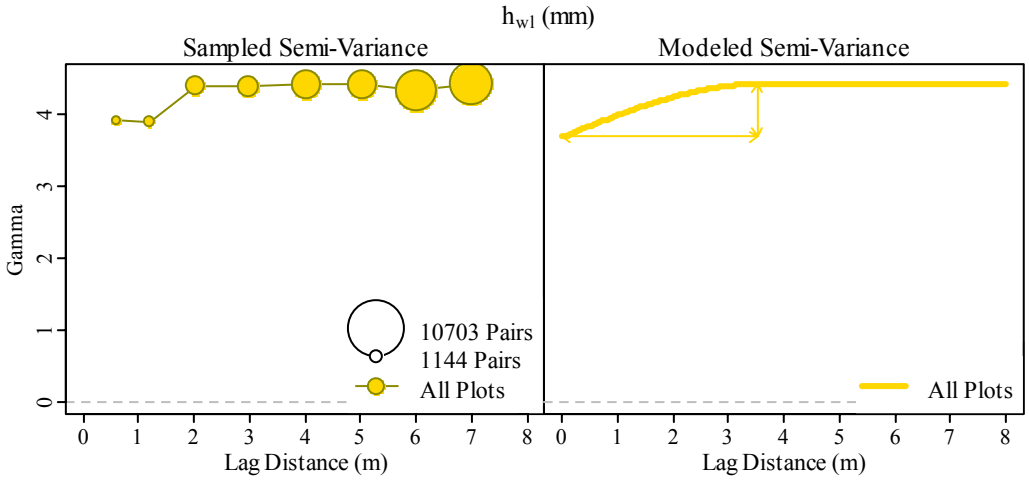

Figure 69. Sample (left) and model (right) variograms of h_{wl} (mm).

Slope-Normal Base Height (h_{base}): The left portion of the study site (Plots 4 and 5) possessed a shallower base (h_{base}, Figure 33) than average and contained slight cross-slope trends (Figure 70). Base height values were greater in Plot 1 than in Plots 4 and 5 in the areas where these plots contacted each other, possibly associated with basal thinning (Figure 70). Plots 2 and 3 had concave and convex base height patterns, respectively (Figure 70). At the study site h_{base} was slightly smaller than the recorded

snow depth (1.2 m) at the weather station (ca. 14 m up-slope of Plot 3) before the surface hoar was buried. The 0.1 to 0.2 m discrepancy could be the result of base settlement and spatial variations in h_{base}.

Table 11. Spatial patterns of snowpack, base, weak layer and slab thickness. Estimates derived from SMP measurements are in millimeters, while those involving probe measurements are in centimeters.

Variable	Areal Extent	Interpolation Method	Regression Component			Variogram Component			Model Error	
			Formula*	p-value	r^2	Range (m)	Nugget	Sill	$\sigma_{pred.err}$	$m_{pred.err}$
h_{base} (cm)	$Plot1_{Up\text{-}Slope}$	Ordinary	0	NA	NA	4.47	7.87	20.37	0.80	11.81
	$Plot1_{Cross\text{-}Slope}$	Universal	8	4.07E-05	0.20	5.61	16.41	21.28	0.38	18.91
	Plot1	Universal	8	2.97E-06	0.14	5.07	12.23	21.49	0.61	15.68
	Plot2	Universal	3	1.02E-06	0.17	3.28	15.02	22.69	1.04	20.42
	Plot3	Universal	10	1.60E-03	0.13	1.82	24.28	29.07	0.83	29.70
	Plot4	Universal	1	1.26E-14	0.32	7.46	26.89	39.89	0.87	32.08
	Plot5	Universal	6	1.15E-08	0.20	4.98	18.90	24.00	0.51	22.24
h_{slab} (mm)	$Plot1_{Up\text{-}Slope}$	Universal	2	2.80E-05	0.18	1.05	13.36	40.75	3.77	29.90
	$Plot1_{Cross\text{-}Slope}$	Universal	8	4.96E-07	0.27	1.86	4.64	56.97	6.94	25.70
	Plot1	Universal	10	3.19E-08	0.22	1.54	0.00	50.40	8.59	22.54
	Plot2	Universal	10	2.13E-13	0.37	2.52	0.00	84.06	16.47	40.13
	Plot3	Universal	10	2.35E-09	0.29	1.69	1.07	63.50	16.77	45.73
	Plot4	Universal	10	1.51E-04	0.15	2.25	0.00	209.93	48.86	112.39
	Plot5	Universal	8	6.08E-06	0.15	1.46	0.00	127.15	33.75	94.59
$h_{snowpack}$ (cm)	$Plot1_{Up\text{-}Slope}$	Universal	7	4.7E-02	0.05	4.14	6.85	20.55	0.94	11.17
	$Plot1_{Cross\text{-}Slope}$	Universal	8	1.6E-03	0.13	7.69	15.67	21.82	0.36	18.01
	Plot1	Universal	8	3.6E-04	0.09	4.95	11.60	22.28	0.692	15.375
	Plot2	Universal	10	2.3E-09	0.33	1.11	12.17	22.74	1.51	22.63
	Plot3	Universal	9	9.6E-04	0.09	2.45	27.58	33.24	0.71	33.08
	Plot4	Universal	1	3.2E-12	0.27	1.86	19.02	43.19	4.40	37.79
	Plot5	Universal	6	2.5E-07	0.19	0.45	18.93	25.39	0.48	25.45

* 'Formula' refers to best-fit regression model, as defined in Table 8.

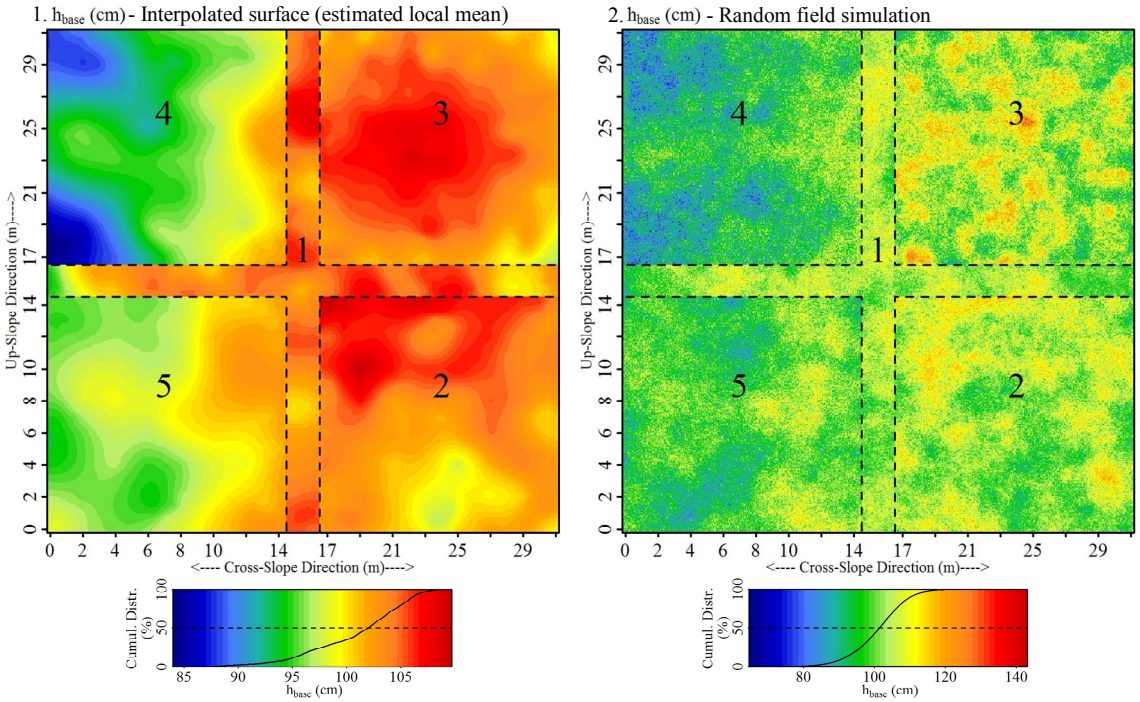

Figure 70. Spatial interpolations of h_{base} (cm) for Plots 1 – 5. (1) Interpolated surfaces of local mean values, utilizing chosen interpolation method (Table 11). (2) Random field simulation incorporates randomness, based on semi-variance values in Figure 71 (below).

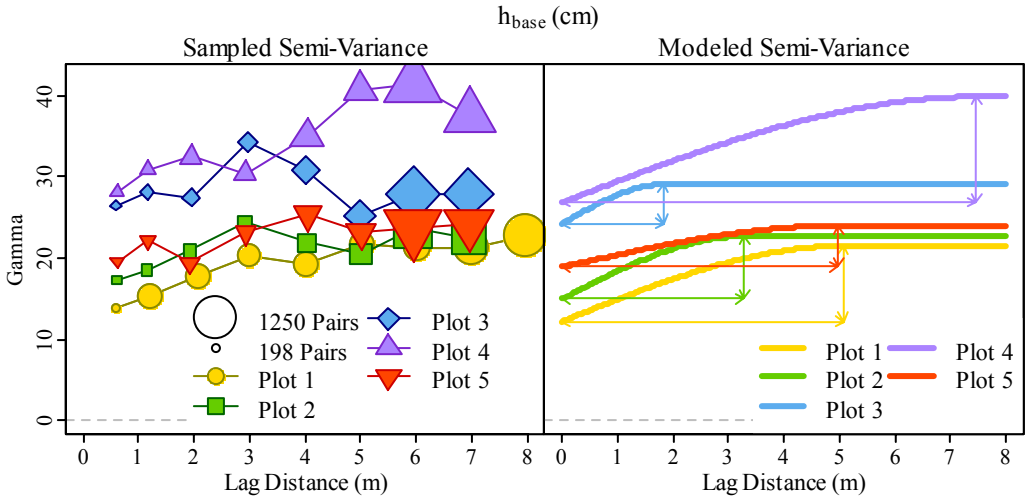

Figure 71. Sample (left) and model (right) variograms of h_{base} (cm).

Slope-Normal Slab Thickness (h_{slab}): The large difference in slab thickness (h_{slab}, Figure 33) between Plot 5 and the other plots was because of the large snowfall event that

occurred between the last two sampling days (Table 11, Figure 72). Slab thinning over time was evident as a discrete decrease in slab thickness (h_{slab}) between Plots 2 and 3, which were sampled one week apart. Plot 4 possesses a slightly greater slab thickness (h_{slab}) than Plot 3 due to a small snowfall event.

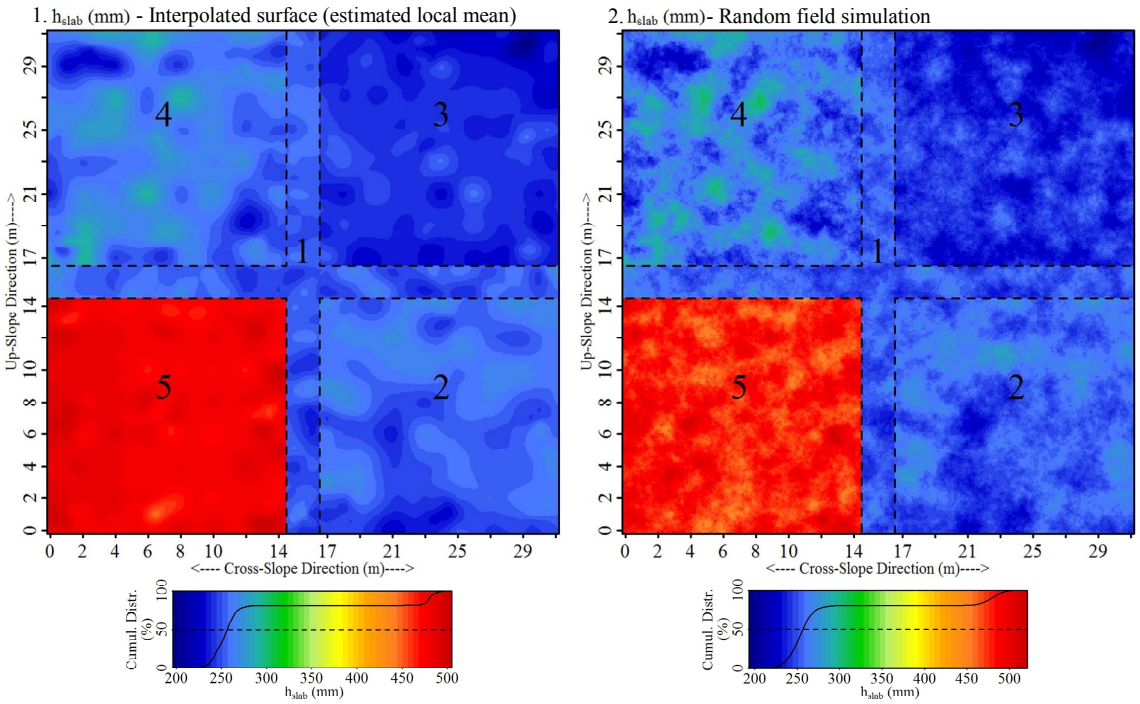

Figure 72. Spatial interpolations of h_{slab} (mm) for Plots 1 – 5. (1) Interpolated surfaces of local mean values, utilizing chosen interpolation method (Table 11). (2) Random field simulation incorporates randomness, based on semi-variance values in Figure 73(below).

All five plots exhibit a high degree of spatial dependence at distances below 2.4 m (Figure 73). A remarkable degree of spatial correlation exists between Plots 1 and 4, evident through the matching of small variations in slab thickness (h_{slab}) along adjacent plot edges (Figure 73). Given that these adjacent prediction maps were generated using only the observations from their respective plots, this observation indicates that the applied sampling scheme very effectively estimated a natural phenomenon.

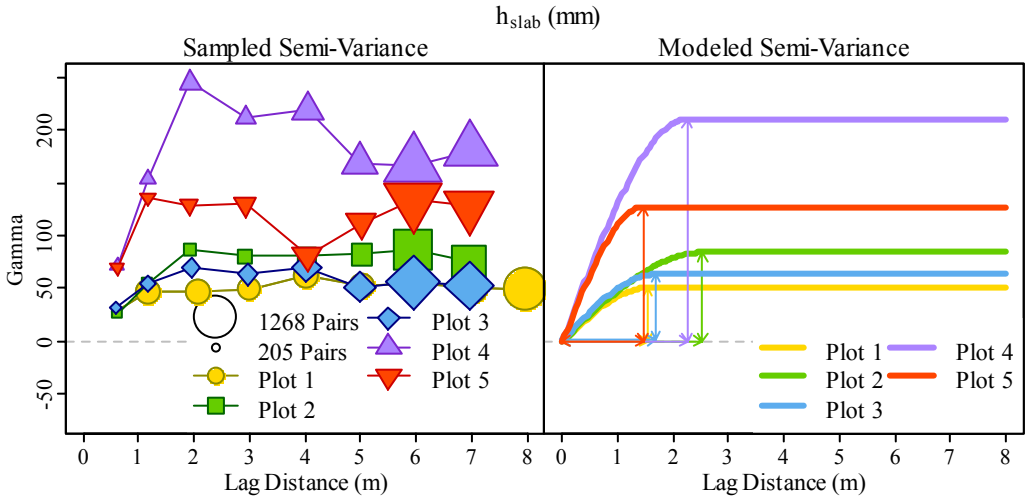

Figure 73. Sample (left) and model (right) variograms of h_{slab} (mm).

The upper portion of Plot 2 possessed larger h_{slab} values than the adjacent arms of Plot 1 (Figure 72). Since h_{slab} values were derived directly from SMP measurements, it is highly unlikely that this was due to measurement error, such as systematic error of the SMP orientation on the upper portion of Plot 2.[10] Hence, it is likely a real spatial discrepancy coincided with the plot alignment. Wind-related re-deposition did not occur between the two sampling days. Plot 4 possessed the greatest plot-scale variability. This could be related to differential slab densification, which results in divergence of h_{slab} over time. It may also be a direct result of Plot 4 having a higher degree of topographical variability than the other square plots (Figure 37).

[10] Error due to the SMP being oriented 10° oblique from the surface-normal position would result in only a 1.5 % increase of stratigraphic units, such as h_{slab}.

Shear Frame - Related Variables

Load - Related Variables: Prominent spatial patterns exist in all slab stresses (Table 12, Figures 74 - 81). The slab's V_{slab} is derived from HSW_{slab}. The corresponding normal- and shear- stresses, N_{slab} and τ_{slab}, were dependent on patterns in the V_{slab} and slope angle.

Table 12. Spatial patterns of slab-related loads. Formula Ids refer to Table 8.

Variable	Areal Extent	Interpolation Method	Regression Component			Variogram Component			Model Error	
			Formula*	p-value	r^2	Range (m)	Nugget	Sill	$\sigma_{pred.err}$	$m_{pred.err}$
HSW_{slab} (mm)	$Plot1_{Up\text{-}Slope}$	Universal	9	6.27E-07	0.56	13.18	0.00	5.12	0.31	0.72
	$Plot1_{Cross\text{-}Slope}$	Universal	8	6.64E-03	0.25	14.12	0.00	9.35	0.52	1.24
	Plot1	Universal	9	5.43E-07	0.35	10.80	0.00	5.40	0.38	0.93
	Plot2	Universal	5	1.59E-24	0.82	9.88	0.00	4.19	0.43	1.08
	Plot3	Universal	10	5.00E-14	0.65	11.67	0.00	1.07	0.16	0.26
	Plot4	Universal	10	8.50E-16	0.71	8.30	0.00	1.81	0.29	0.58
	Plot5	Universal	10	2.23E-08	0.49	9.78	0.00	3.69	0.42	0.99
V_{slab} (Pa)	$Plot1_{Up\text{-}Slope}$	Universal	9	6.27E-07	0.56	13.55	0.00	501.96	29.60	68.78
	$Plot1_{Cross\text{-}Slope}$	Universal	8	6.64E-03	0.25	12.11	0.00	762.29	49.87	117.46
	Plot1	Universal	9	5.43E-07	0.35	12.54	0.00	590.79	35.94	87.19
	Plot2	Universal	5	1.59E-24	0.82	9.88	0.00	403.28	41.15	103.55
	Plot3	Universal	10	5.00E-14	0.65	11.67	0.00	102.53	15.31	25.09
	Plot4	Universal	10	8.50E-16	0.71	8.29	0.00	173.66	27.56	56.16
	Plot5	Universal	10	2.23E-08	0.49	9.73	0.00	353.92	40.12	95.43
N_{slab} (Pa)	$Plot1_{Up\text{-}Slope}$	Universal	9	1.56E-06	0.53	13.29	0.00	389.25	23.39	54.37
	$Plot1_{Cross\text{-}Slope}$	Universal	8	8.14E-04	0.33	12.20	0.00	682.22	44.31	104.37
	Plot1	Universal	10	1.69E-06	0.41	12.36	0.00	510.99	32.31	78.31
	Plot2	Universal	5	1.19E-22	0.79	9.82	0.00	344.46	35.37	88.98
	Plot3	Universal	10	2.79E-12	0.61	8.82	0.00	67.46	13.46	22.05
	Plot4	Universal	10	7.31E-13	0.64	9.16	0.00	176.48	25.39	51.57
	Plot5	Universal	10	1.37E-06	0.42	11.09	0.00	322.77	31.79	76.04
τ_{slab} (Pa)	$Plot1_{Up\text{-}Slope}$	Universal	9	6.69E-10	0.70	12.52	0.00	99.11	6.32	14.70
	$Plot1_{Cross\text{-}Slope}$	Universal	6	1.05E-04	0.35	12.69	0.00	135.92	8.46	19.93
	Plot1	Universal	10	1.02E-13	0.66	12.23	0.00	129.94	8.31	20.13
	Plot2	Universal	10	1.01E-32	0.91	7.92	0.00	44.75	6.32	14.97
	Plot3	Universal	3	8.52E-23	0.77	9.68	0.00	36.72	4.82	9.97
	Plot4	Universal	10	1.28E-23	0.83	4.23	2.18	25.24	7.25	18.80
	Plot5	Universal	3	2.13E-20	0.74	9.40	0.00	94.15	9.98	25.28

* 'Formula' refers to best-fit regression model, as defined in Table 8.

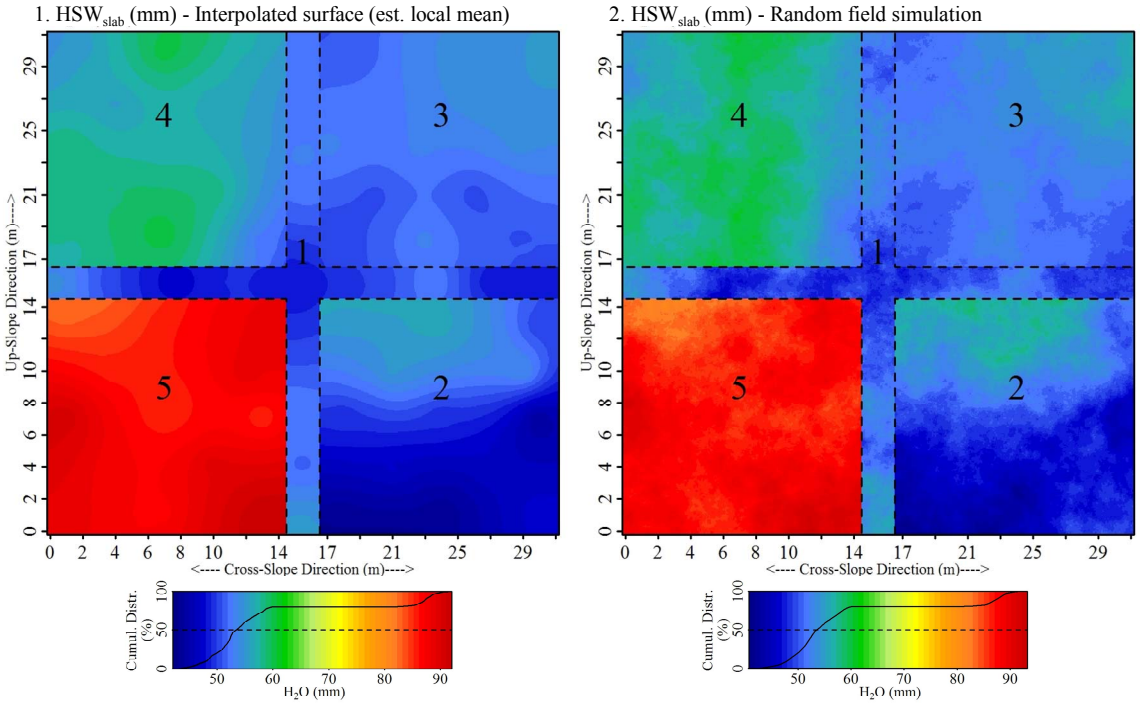

Figure 74. Spatial interpolations of HSW_{slab} (mm). Interpolated surfaces of local mean values, utilizing chosen interpolation method (Table 12). (2) Random field simulation incorporates randomness, based on semi-variance values in Figure 75.

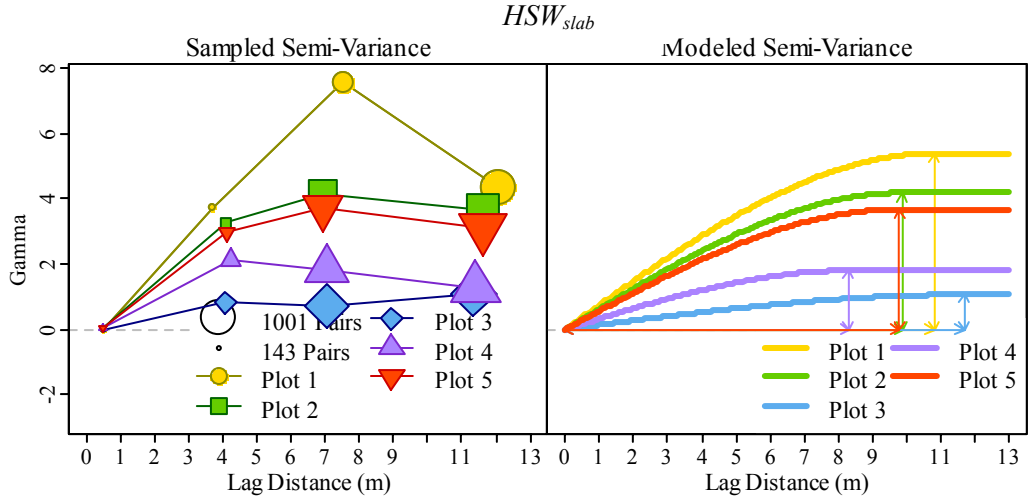

Figure 75. Sample (left) and model (right) variograms of HSW_{slab} (mm).

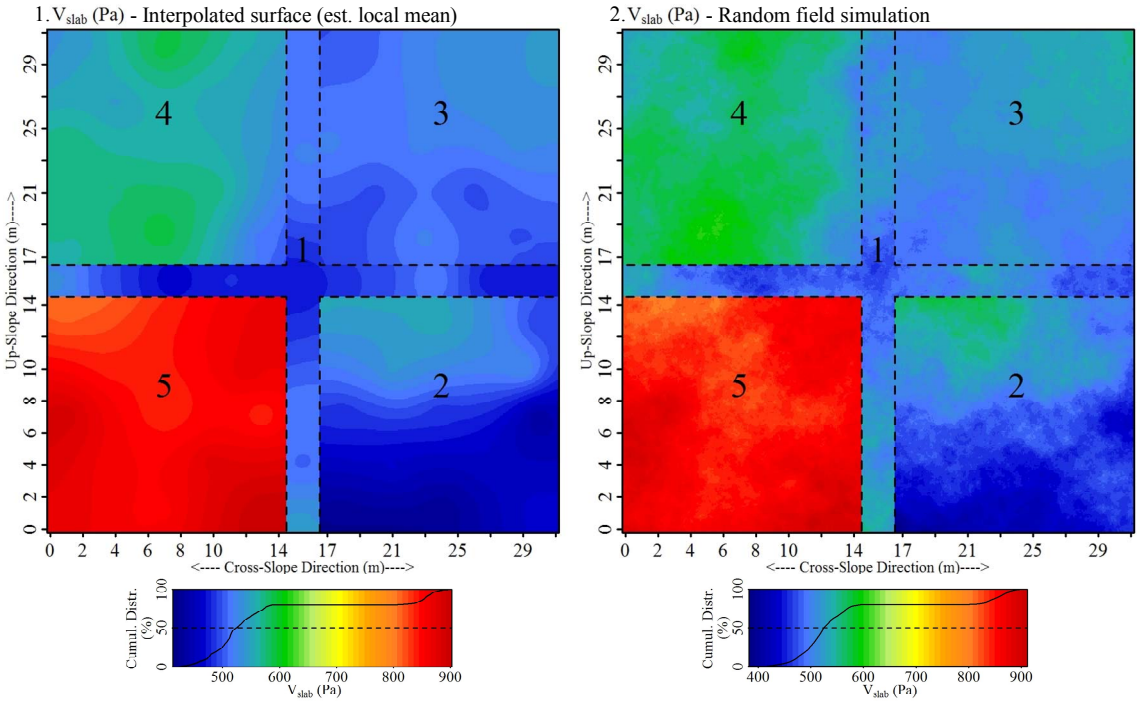

Figure 76. Spatial interpolations of V_{slab} (Pa). Interpolated surfaces of local mean values, utilizing chosen interpolation method (Table 12). (2) Random field simulation incorporates randomness, based on semi-variance values in Figure 77.

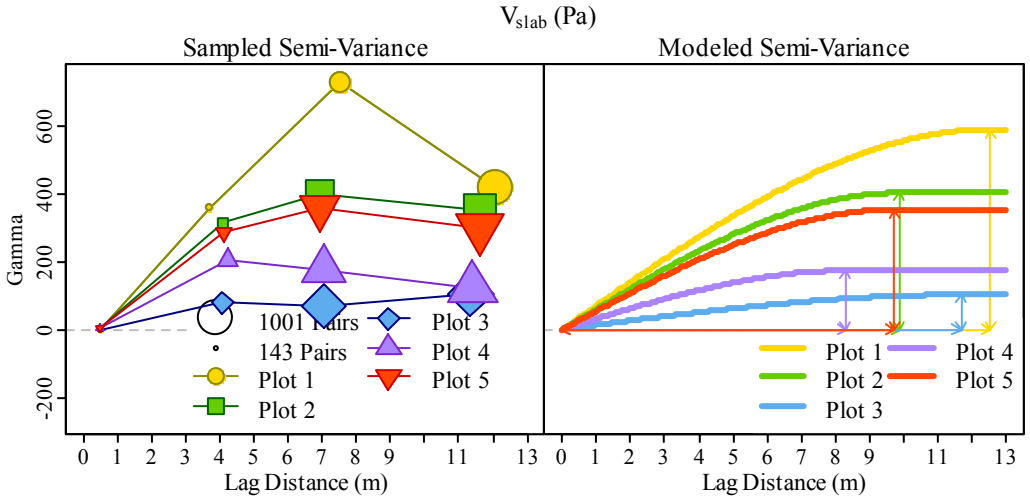

Figure 77. Sample (left) and model (right) variograms of V_{slab} (Pa).

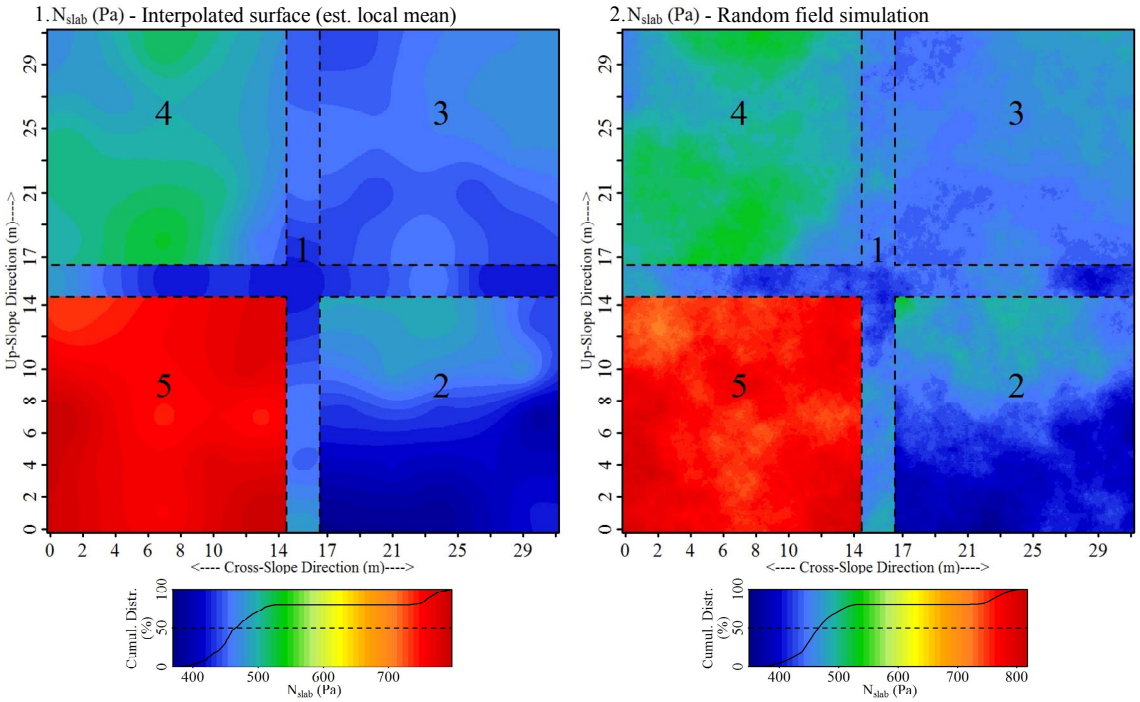

Figure 78. Spatial interpolations of N_{slab} (Pa). Interpolated surfaces of local mean values, utilizing chosen interpolation method (Table 12). (2) Random field simulation incorporates randomness, based on semi-variance values in Figure 79.

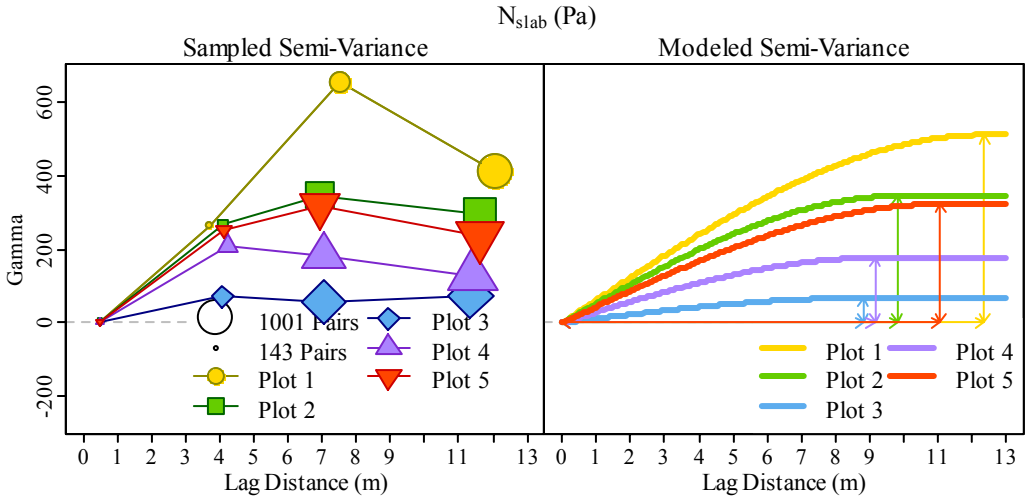

Figure 79. Sample (left) and model (right) variograms of N_{slab} (Pa).

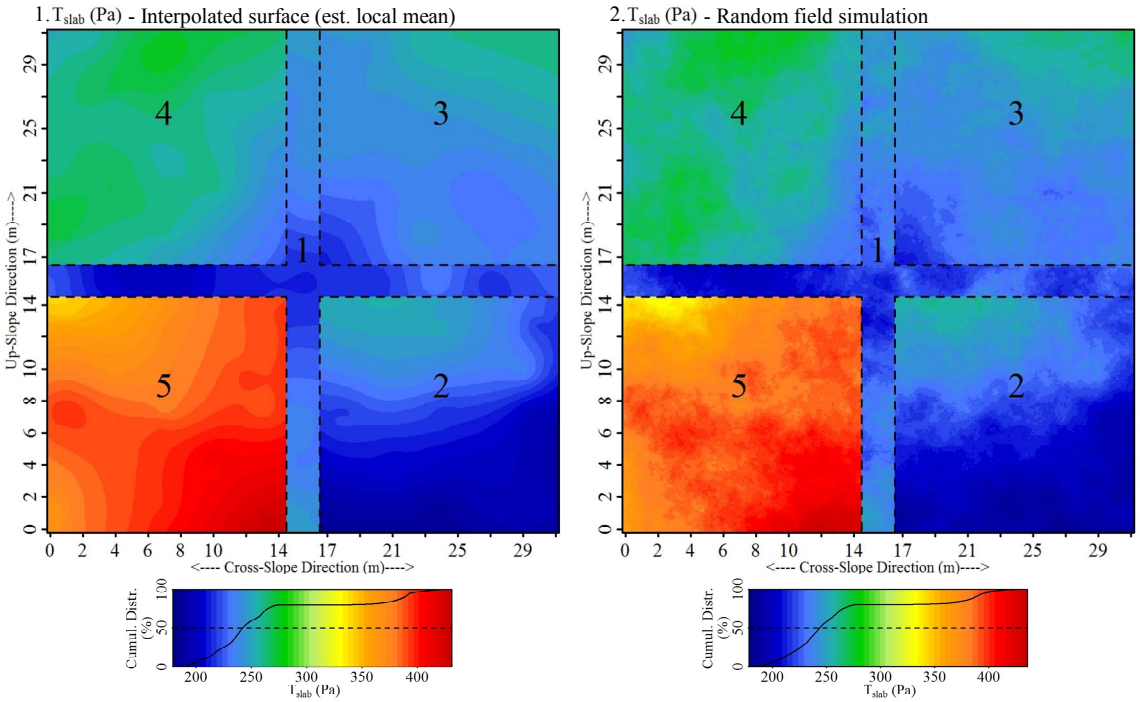

Figure 80. Spatial interpolations of τ_{slab} (Pa). Interpolated surfaces of local mean values, utilizing chosen interpolation method (Table 12). (2) Random field simulation incorporates randomness, based on semi-variance values in Figure 81.

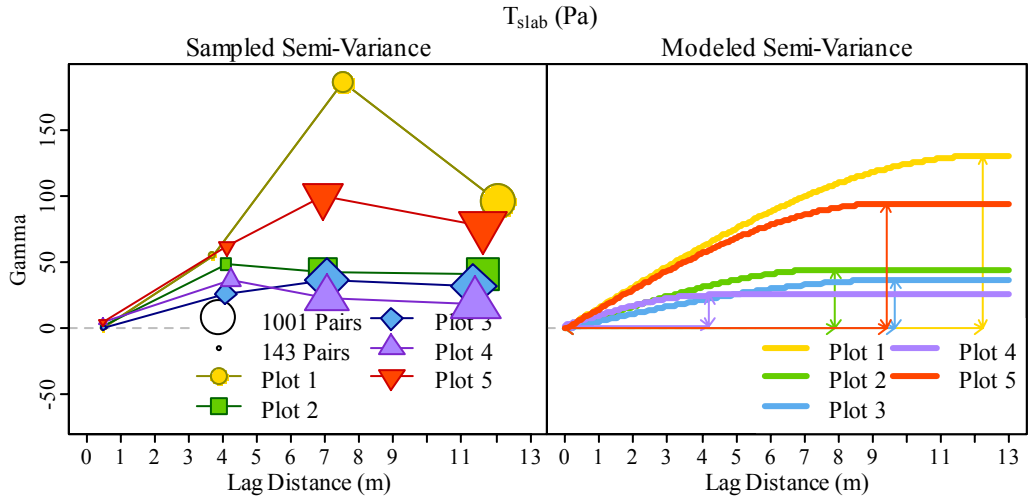

Figure 81. Sample (left) and model (right) variograms of τ_{slab} (Pa).

The map of V_{slab} indicates that Plot 2 possessed a greater load than Plot 1, despite being measured on consecutive days with no snowfall occurring overnight (Figure 80).

This discrepancy is related to the spatial pattern observed in HSW_{slab} and slope angle. All slab stresses were greatest at Plot 5, which was sampled after a significant snowfall event. Plot 2 had the greatest site-scale variability (sill value).

A high-degree of local spatial dependence existed, evident in nugget values of '0' (Figures 75, 77, 79 and 81). This was caused by the assumption that all shear frame measurements within a given pit had the same slab water equivalency, which in actuality was measured at only one central location at each pit.

Shear Strength (τ_∞): A significant trend of τ_∞ existed at Plot 1 comprised primarily of an up-slope weakening, as well as a subtle cross-slope trend. These patterns closely mimiced that of h_{wl} (Table 13, Figure 82). This trend of τ_∞ was also faintly evident at Plots 2, 3, and 5, further supporting the inverse spatial relationship with h_{wl}, indicating that τ_∞ decreased as h_{wl} increased up-slope (Shear Strength (τ_∞) ~ Weak Layer Thickness (h_{wl}, page 248).

Table 13. Spatial patterns of shear strength (τ_∞).

τ_∞ (N)	Interpol.	Regression Component			Variogram Component			Model Error	
Areal Extent	Method	Formula*	p-value	r^2	Range (m)	Nugget	Sill	$\sigma_{pred.err}$	$m_{pred.err}$
Plot1 Up-Slp	Universal	2	8.67E-03	0.18	3.76E+00	1.04E+04	1.46E+04	6.56E+02	1.40E+04
Plot1 Cross-Slp	Ordinary	0	NA	NA	5.99E+00	8.06E+03	9.14E+03	7.83E+01	8.90E+03
Plot1	Universal	2	3.12E-03	0.12	3.73E+00	8.57E+03	1.18E+04	4.74E+02	1.13E+04
Plot2	Universal	3	1.57E-02	0.12	4.10E+00	5.38E+03	7.97E+03	5.11E+02	7.69E+03
Plot3	Ordinary	0	NA	NA	7.11E+00	8.50E+03	1.15E+04	3.17E+02	1.03E+04
Plot4	Ordinary	0	NA	NA	4.23E+00	1.25E+04	2.28E+04	1.70E+03	2.01E+04
Plot5	Universal	2	7.77E-03	0.10	4.10E+00	1.16E+04	1.82E+04	1.25E+03	1.71E+04

* 'Formula' refers to best-fit regression model, as defined in Table 8.

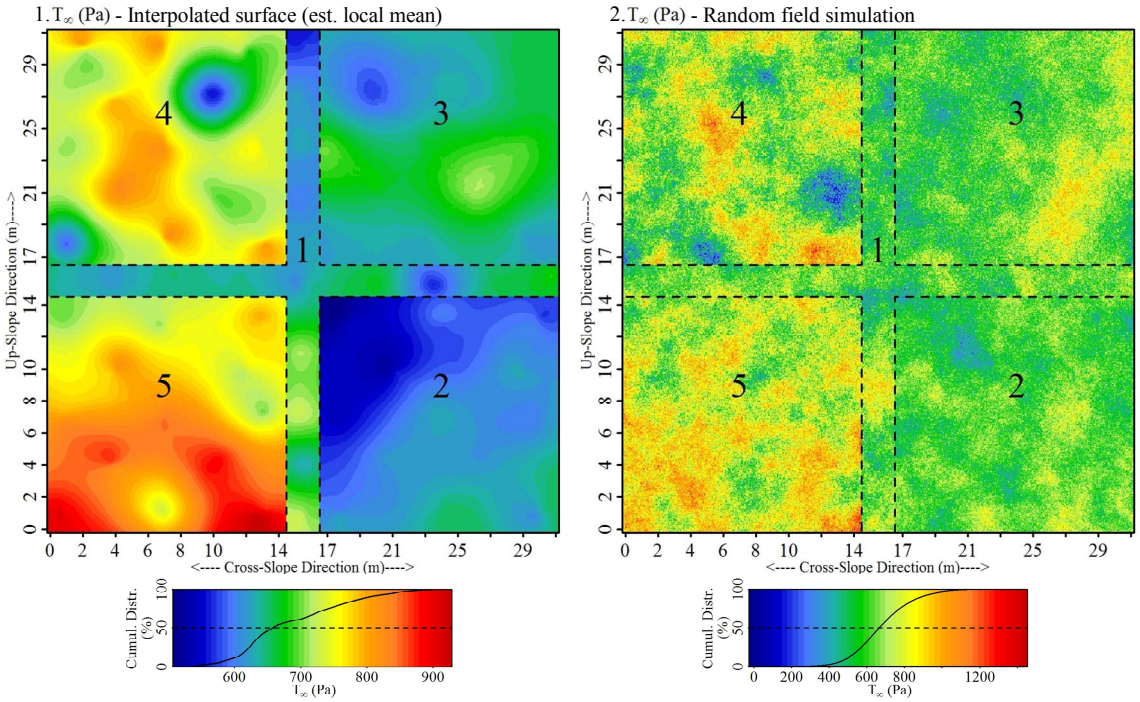

Figure 82. Spatial interpolations of shear strength (τ_∞) (Pa). Interpolated surfaces of local mean values, utilizing chosen interpolation method (Table 13). (2) Random field simulation incorporates randomness, based on semi-variance values in Figure 83.

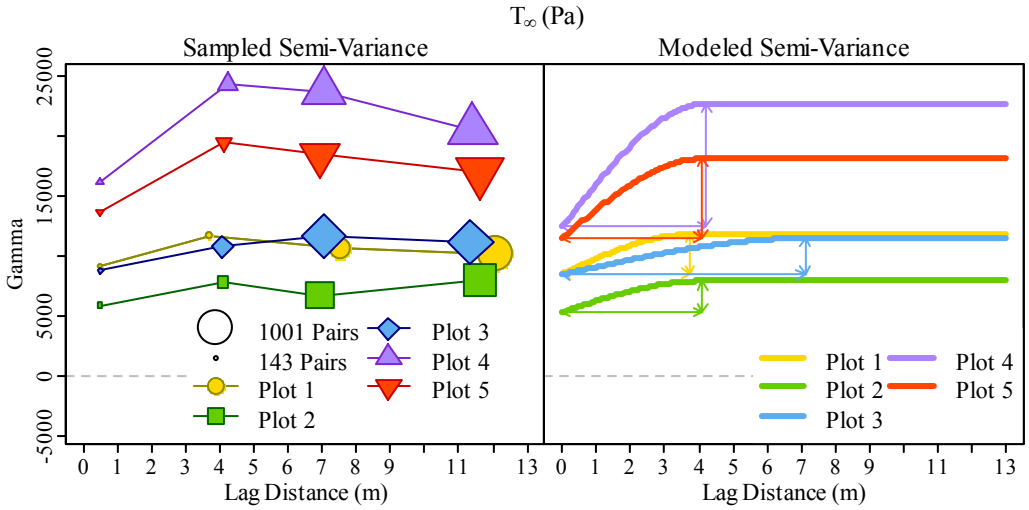

Figure 83. Sample (left) and model (right) variograms of shear strength (τ_∞) (Pa).

Based on the nugget and sill values of τ_∞ sample variograms at Plots 3 and 4, it is clear that local spatial dependency existed at all five plots to distances of 3.5 m and in the

case of Plot 3, up to 7 m (Figure 83). However, because of the small number of point pairs present at 1 to 3 m distances, it is not possible to assertain whether range values shorter than 3.5 m existed in actuality (Figure 83, right).

Residual Shear Strength (τ_{resid}): Trend analysis revealed up-slope trends at Plots 1, 2 and 5, which indicates that residual shear strength (τ_{resid}) decreased in the up-slope direction (Figure 84). Hence a smaller load would be needed to cause the weak layer to fail at the top of the slope. In the semi-variance analysis, τ_{resid} maintained very consistent range values, varying from 3.7 to 4.6 m at the five plots (Figure 85, Table 14).

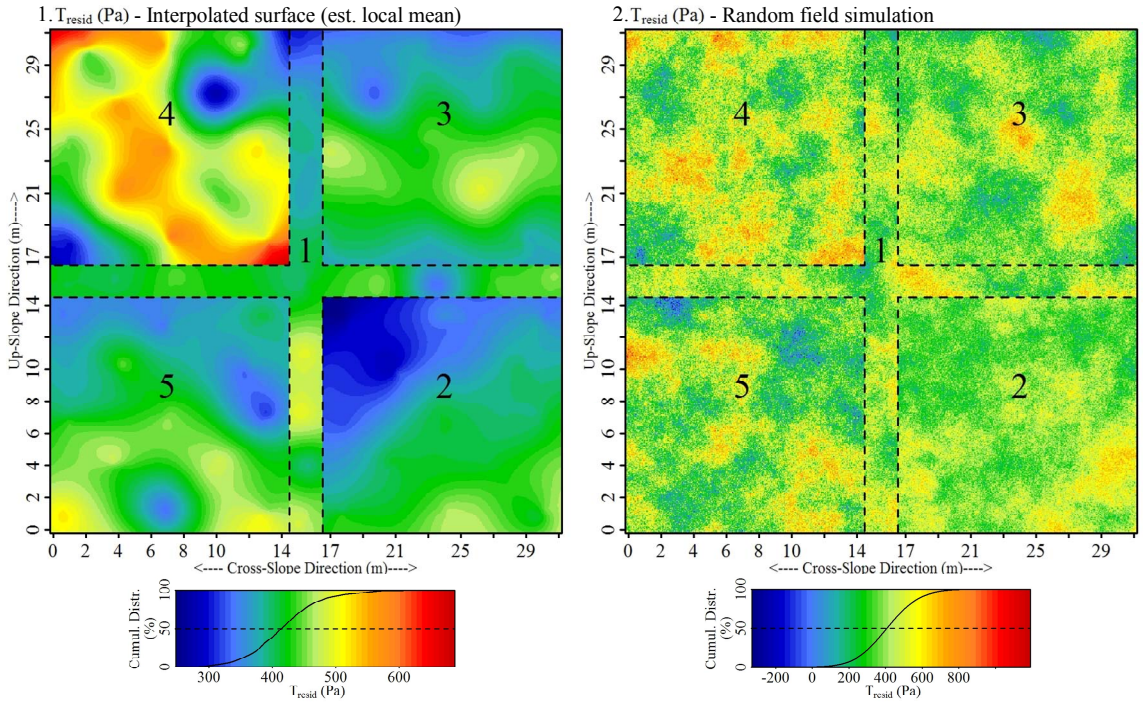

Figure 84. Spatial interpolations of residual shear strength (τ_{resid}) (Pa). Interpolated surfaces of local mean values, utilizing chosen interpolation method (Table 14). (2) Random field simulation incorporates randomness, based on semi-variance values in Figure 85.

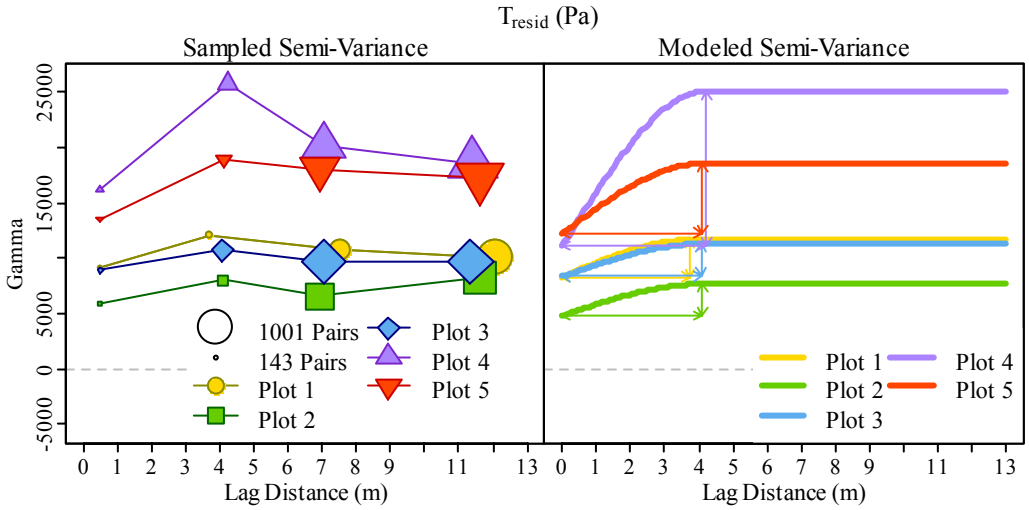

Figure 85. Sample (left) and model (right) variograms of residual shear strength (τ_{resid}) (Pa).

Table 14. Spatial patterns of residual shear strength (τ_{resid}).

τ_{resid} (N) Areal Extent	Interpol. Method	Regression Component			Variogram Component			Model Error	
		Formula*	p-value	r^2	Range (m)	Nugget	Sill	$\sigma_{pred.err}$	$m_{pred.err}$
Plot1 Up-Slp	Universal	7	4.77E-03	0.20	3.76E+00	1.04E+04	1.44E+04	6.37E+02	1.39E+04
Plot1 Cross-Slp	Ordinary	0	NA	NA	4.60E+00	7.91E+03	9.74E+03	1.87E+02	9.31E+03
Plot1	Universal	7	2.14E-03	0.13	3.73E+00	8.29E+03	1.16E+04	4.92E+02	1.10E+04
Plot2	Universal	3	6.09E-05	0.25	4.10E+00	4.82E+03	7.66E+03	5.80E+02	7.28E+03
Plot3	Universal	9	2.94E-02	0.10	4.07E+00	8.33E+03	1.13E+04	6.61E+02	1.12E+04
Plot4	Universal	5	2.69E-02	0.13	4.23E+00	1.11E+04	2.51E+04	3.46E+03	2.22E+04
Plot5	Universal	2	4.28E-02	0.06	4.10E+00	1.22E+04	1.85E+04	1.17E+03	1.76E+04

* 'Formula' refers to best-fit regression model, as defined in Table 8.

As with τ_{∞}, Plot 2 possessed the lowest sill value and Plot 4 possessed the greatest sill and partial sill values for τ_{resid}, indicating that spatial structure became more pronounced but the scale of structure remained unchanged. A decrease in sill values between plots 4 and 5 may be evidence of convergence.

Stability Index (*S*): As with τ_{resid}, *S* possessed more pronounced spatial patterns than τ_{∞} (Figure 86). The spatial patterns in Plots 3 and 4 appear to be well correlated with each other. Both of these findings are likely due to the high degree of

autocorrelation present in the observed slab characteristics. Semi-variance analysis of the four similarly sampled square plots (Plots 2 through 5) revealed interesting changes in spatial patterns over time (Figure 87).

Before the sampling of Plot 5, local and plot-scale variance of *S* increased over time, evident as increases of variogram nugget and sill values between Plots 2, 3, and 4. Simultaneously, variogram ranges remained between 4.07 and 4.23 m.

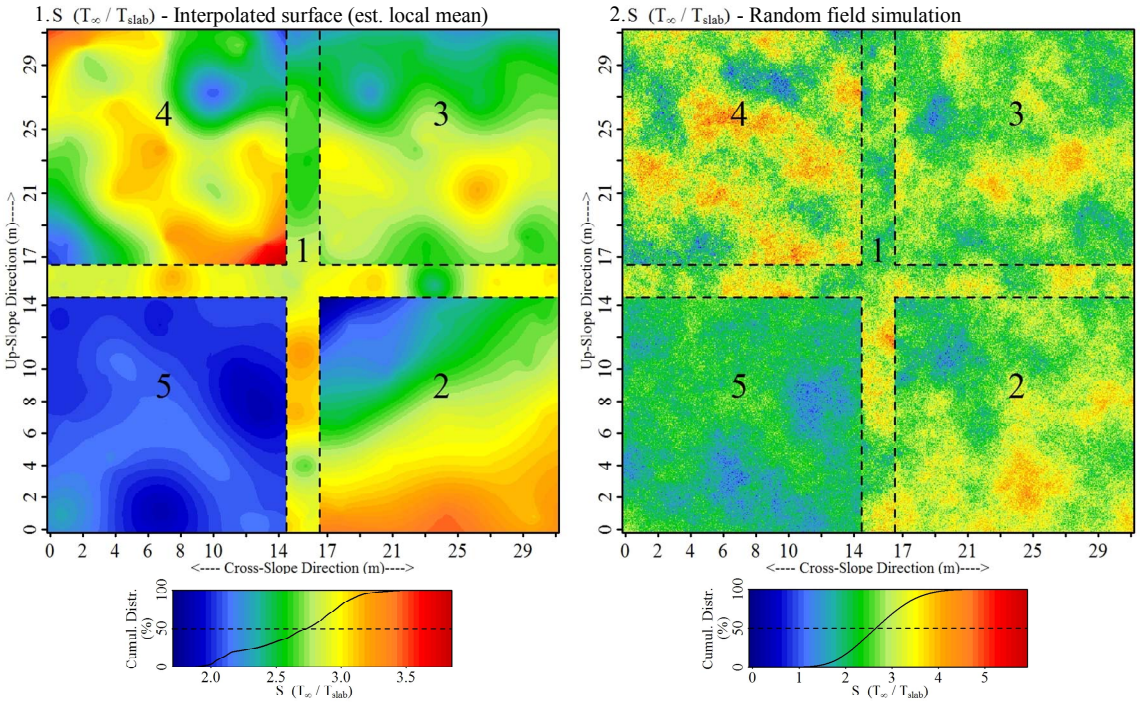

Figure 86. Spatial interpolations of stability (*S*). Interpolated surfaces of local mean values, utilizing chosen interpolation method (Table 15). (2) Random field simulation incorporates randomness, based on semi-variance values in Figure 87.

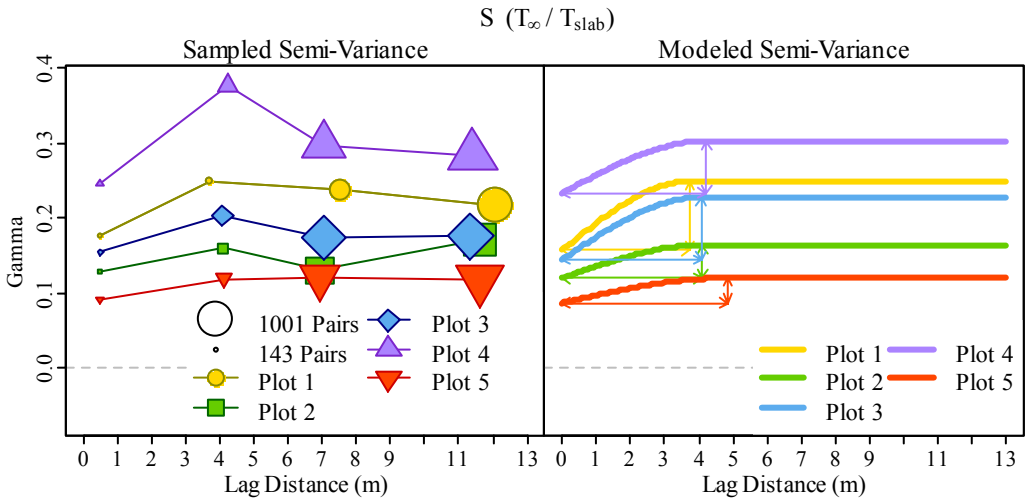

Figure 87. Sample (left) and model (right) variograms of stability (*S*).

Table 15. Spatial patterns of stability (*S*).

S Areal Extent	Interpolation Method	Regression Component			Variogram Component			Model Error	
		Formula	p-value	r^2	Range (m)	Nugget	Sill	$\sigma_{pred.err}$	$m_{pred.err}$
Plot1 Up-Slp	Universal	7	2.40E-03	0.23	3.77E+00	1.92E-01	2.95E-01	1.72E-02	2.75E-01
Plot1 Cross-Slp	Ordinary	0	NA	NA	7.17E+00	1.63E-01	2.52E-01	8.45E-03	2.10E-01
Plot1	Universal	7	7.05E-04	0.16	3.74E+00	1.57E-01	2.49E-01	1.45E-02	2.27E-01
Plot2	Universal	5	4.67E-10	0.50	4.10E+00	1.20E-01	1.64E-01	9.25E-03	1.62E-01
Plot3	Universal	9	5.18E-03	0.14	4.07E+00	1.44E-01	2.28E-01	1.90E-02	2.18E-01
Plot4	Universal	5	2.39E-03	0.19	4.23E+00	2.33E-01	3.03E-01	5.30E-02	4.03E-01
Plot5	Ordinary	0	NA	NA	4.85E+00	8.66E-02	1.20E-01	4.37E-03	1.12E-01

* 'Formula' refers to best-fit regression model, as defined in Table 8.

Spatial properties changed after the loading event that preceded Plot 5. Local- and plot-scale variance of *S* decreased substantially and the distance to which observations are correlated across the slope (i.e., the variogram range) increased to 4.85 m (Figure 87, right). This means that after the loading event, observations become less variable and that the distance between dissimilar observations becomes larger.

Microstructural Estimates of Weak Layer

Rupture Force Characteristics (f_m, f_{max}, f_{cv}): The f_m and f_{max} properties of the weak layer at Plots 2 and 5 on the lower slope possessed pronounced spatial structure (Table 16, Figures 88 - 91). On the upper slope, the estimates were devoid of spatial structure at the scale of observation, other than a trend surface of f_{max} at Plot 3 (Table 16). Otherwise lacking spatial trends or autocorrelation, these plots were best described through central tendency and spread, as presented in the temporal analysis.

Table 16. Spatial patterns of f_m (N) and f_{max}(N) and f_{cv} (%) of the weak layer.

Variable	Areal Extent	Interpol. Method	Regression Component			Variogram Component			Model Error	
			Formula	p-value	r^2	Range (m)	Nugget	Sill	$\sigma_{pred.err}$	$m_{pred.err}$
f_m (N)	Plot1 Up-Slp	Mean	0	NA	NA	NA	NA	NA	0.0E+00	2.7E-02
	Plot1 Cross-Slp	Ordinary	0	NA	NA	8.2E+00	6.1E-04	6.5E-04	1.3E-06	6.3E-04
	Plot1	Ordinary	0	NA	NA	7.4E+00	6.7E-04	7.7E-04	4.6E-06	7.3E-04
	Plot2	Universal	5	3.2E-02	0.07	2.7E+00	5.9E-04	6.4E-04	8.8E-06	6.5E-04
	Plot3	Mean	0	NA	NA	NA	NA	NA	0.0E+00	2.6E-02
	Plot4	Mean	0	NA	NA	NA	NA	NA	0.0E+00	2.8E-02
	Plot5	Universal	4	4.6E-02	0.03	2.8E+00	3.3E-04	6.5E-04	5.3E-05	5.6E-04
f_{max} (N)	Plot1 Up-Slp	Regression	9	3.5E-02	0.08	NA	NA	NA	1.3E-02	5.6E-02
	Plot1 Cross-Slp	Ordinary	0	NA	NA	5.7E+00	4.3E-02	6.2E-02	1.1E-03	5.1E-02
	Plot1	Ordinary	0	NA	NA	9.7E+00	7.3E-02	9.0E-02	7.3E-04	8.0E-02
	Plot2	Universal	4	6.1E-04	0.09	1.3E+00	9.9E-03	6.9E-02	1.3E-02	6.0E-02
	Plot3	Regression	2	3.4E-02	0.03	NA	NA	NA	5.8E-03	2.8E-02
	Plot4	Mean	0	NA	NA	NA	NA	NA	0.0E+00	2.7E-01
	Plot5	Ordinary	0	NA	NA	5.5E+00	3.5E-02	3.7E-02	7.4E-05	3.7E-02
f_{cv} (%)	Plot1 Up-Slp	Ordinary	0	NA	NA	2.3E+00	3.5E-02	6.3E-02	2.6E-03	5.1E-02
	Plot1 Cross-Slp	Mean	0	NA	NA	NA	NA	NA	0.0E+00	1.6E-01
	Plot1	Ordinary	0	NA	NA	5.2E+00	3.4E-02	4.5E-02	6.6E-04	4.0E-02
	Plot2	Regression	4	2.6E-05	0.13	NA	NA	NA	4.5E-03	2.1E-02
	Plot3	Mean	0	NA	NA	NA	NA	NA	0.0E+00	1.9E-01
	Plot4	Mean	0	NA	NA	NA	NA	NA	0.0E+00	1.9E-01
	Plot5	Regression	6	2.0E-02	0.04	NA	NA	NA	3.7E-03	1.9E-02

* 'Formula' refers to best-fit regression model, as defined in Table 8.

The absence of spatial patterns on the upper slope may be a direct result of the weak layer structures being larger (due to the thicker weak layer). Since the selected sampling technique utilized only a single 5 mm segment to estimate the weak layer

characteristics (where f_{cv} was at it's local maximum) at areas of the slope where the weak layer was thick, a proportionally smaller segment of the weak layer was represented in the 5 mm segment.

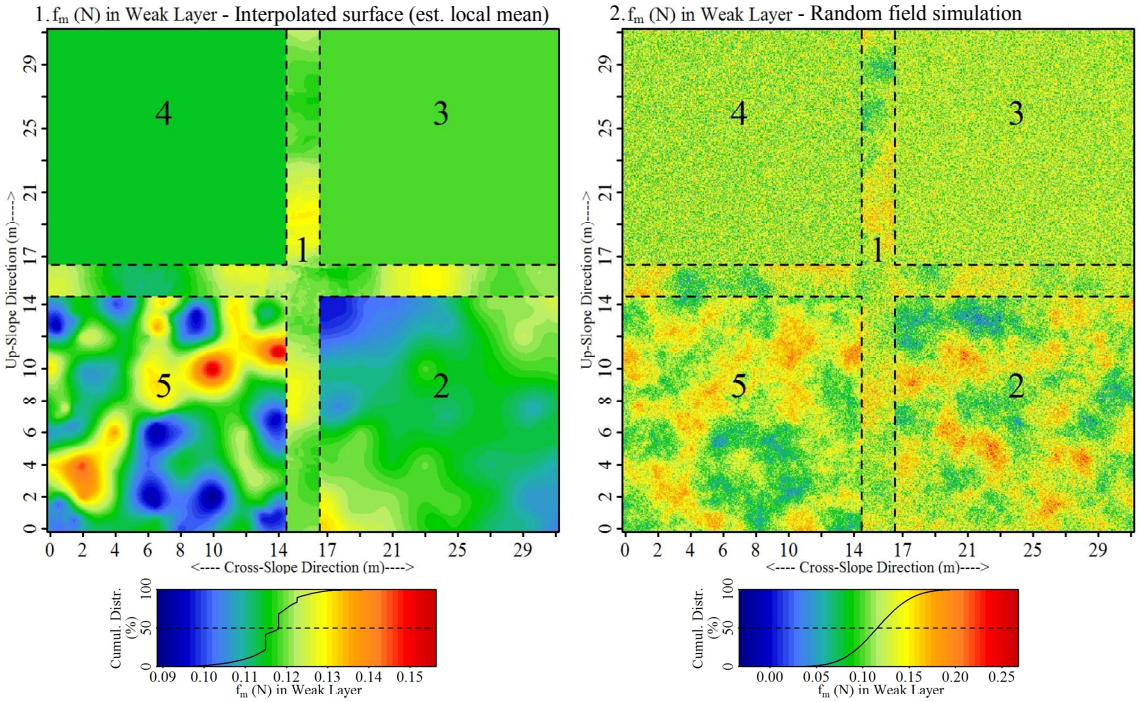

Figure 88. Spatial interpolations of f_m of the weak layer. Interpolated surfaces of local mean values, utilizing chosen interpolation method (Table 16). (2) Random field simulation incorporates randomness, based on semi-variance values in Figure 89.

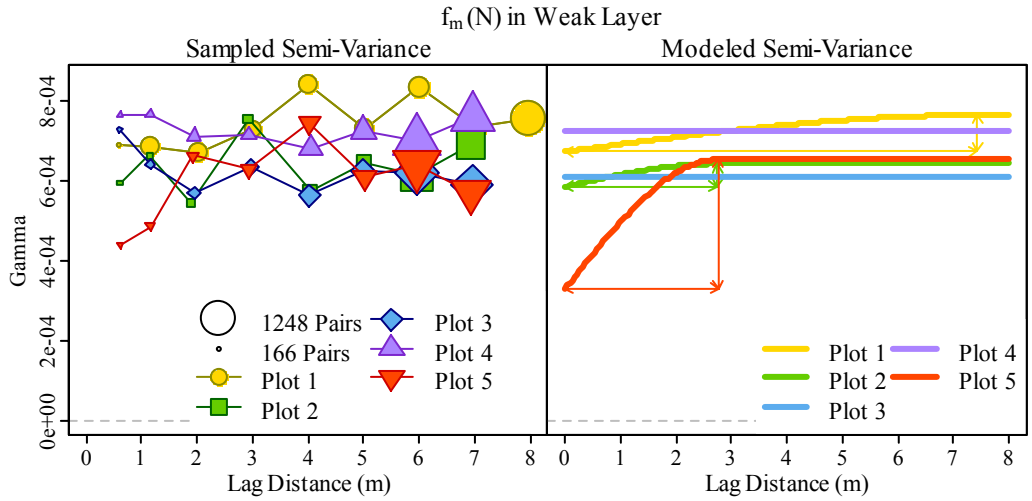

Figure 89. Sample (left) and model (right) variograms of f_m of the weak layer.

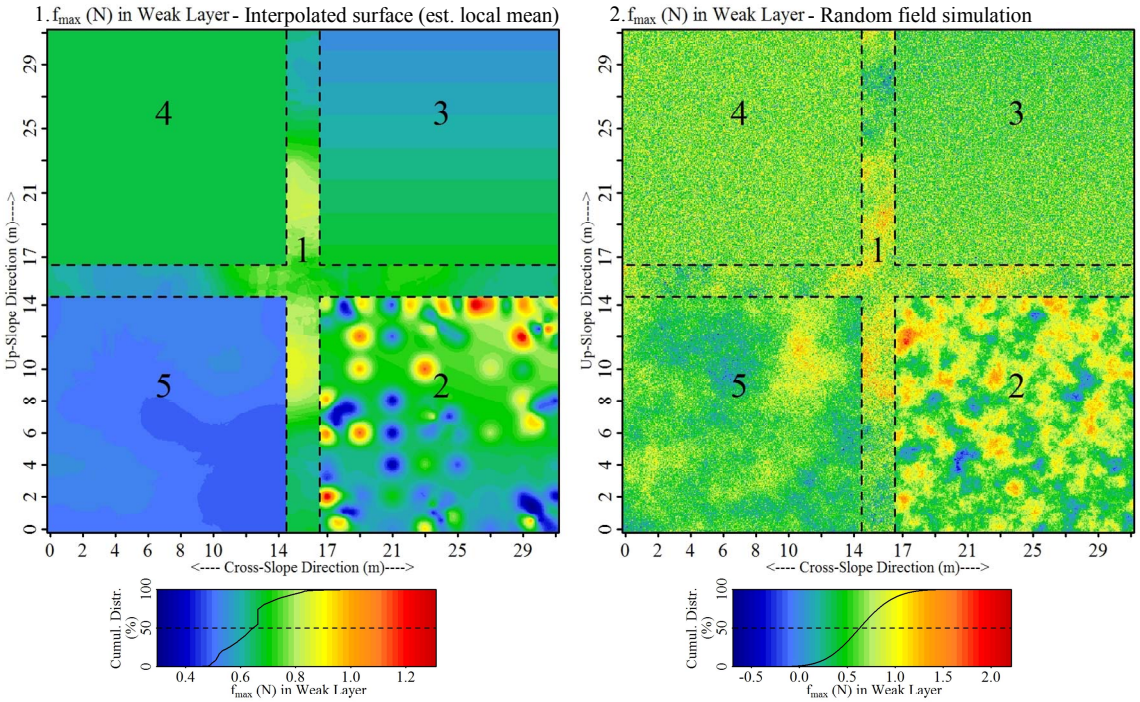

Figure 90. Spatial interpolations of f_{max} of the weak layer. Interpolated surfaces of local mean values, utilizing chosen interpolation method (Table 16). (2) Random field simulation incorporates randomness, based on semi-variance values in Figure 91.

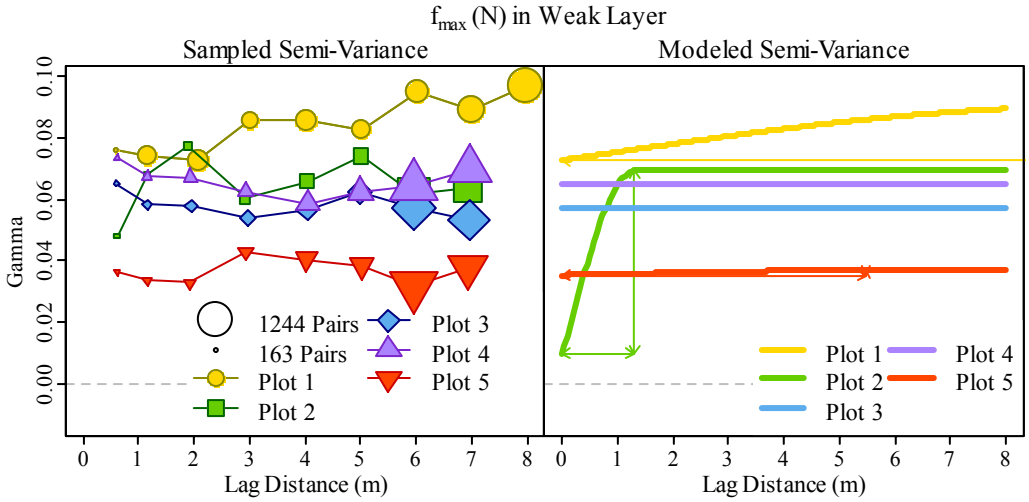

Figure 91. Sample (left) and model (right) variograms of f_{max} of the weak layer.

Micro-variance of rupture force, described by f_{cv}, had less spatial structure than f_m or f_{max}. (Table 16, Figures 92 and 93). Besides Plot 1 and its up-slope transect, all plots were void of autocorrelation (Figure 93), indicating that f_{cv} was not locally correlated at

the scale of observation. For f_m, f_{max}, and f_{cv}, the semi-variance characteristics indicate that Plot 5 had lower sill values than the other plots. Plot 5 also had the largest partial sill value of f_m.

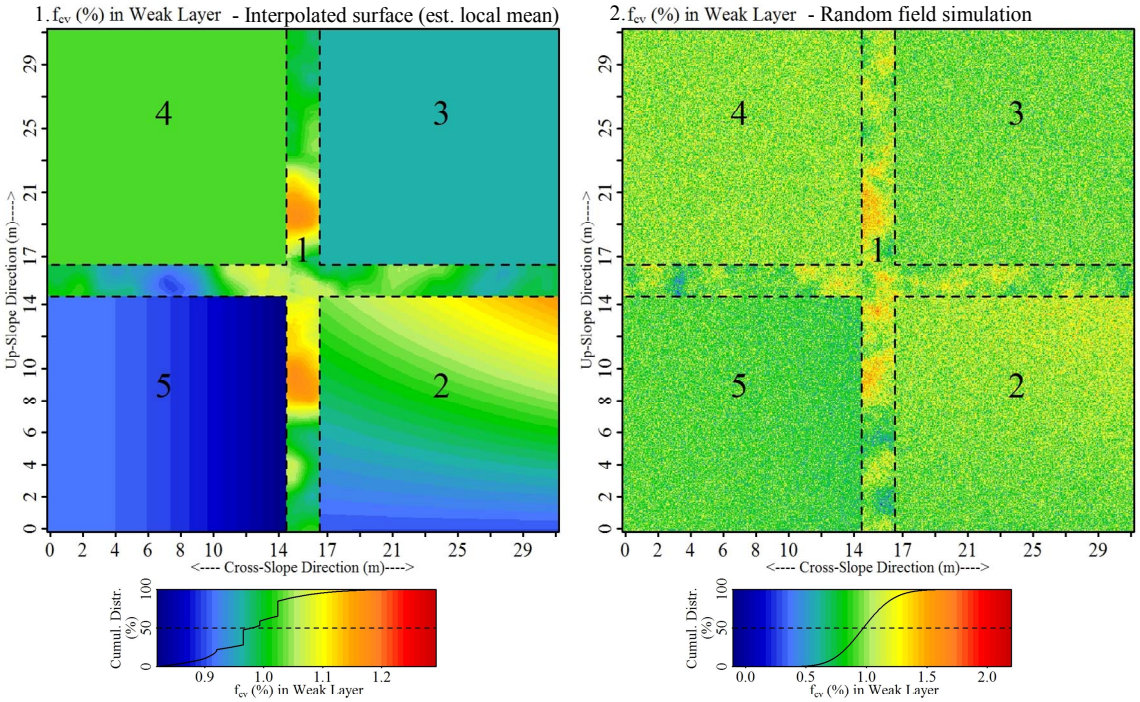

Figure 92. Spatial interpolations of f_{cv} of the weak layer. Interpolated surfaces of local mean values, utilizing chosen interpolation method (Table 16). (2) Random field simulation incorporates randomness, based on semi-variance values in Figure 93.

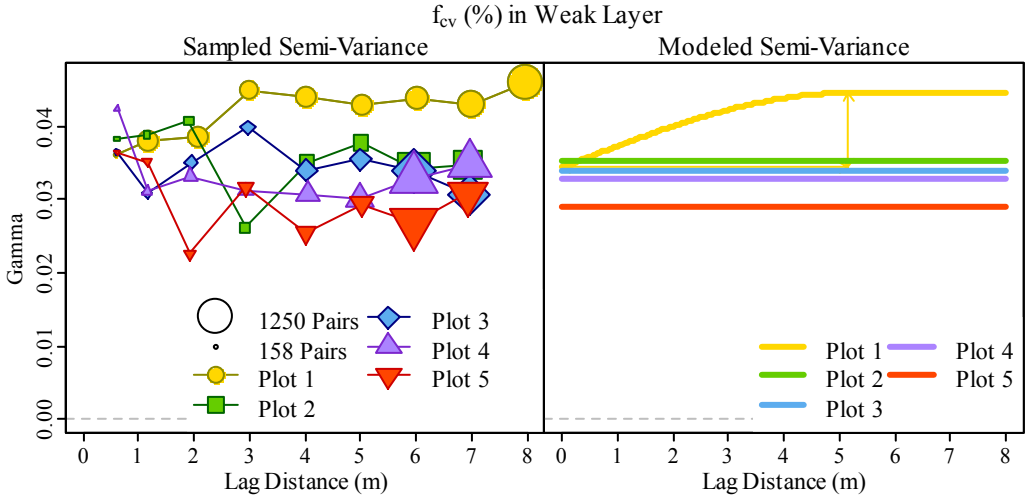

Figure 93. Sample (left) and model (right) variograms of f_{cv} of the weak layer.

Structural Element Length Characteristics (L, L_{max}): Mean structural element length (L) possessed no autocorrelation at Plots 3, 4, and 5 and very small partial sill values at the remaining plots (Table 17, Figures 94 - 97). This means that these plots have fairly uniform variability of L across each plot. In contrast, L_{max} possessed fairly pronounced autocorrelation at Plots 1, 3, and 5.

Table 17. Spatial patterns of L and L_{max} of the weak layer.

Variable	Areal Extent	Interpol. Method	Regression Component			Variogram Component			Model Error	
			Formula*	p-value	r^2	Range (m)	Nugget	Sill	$\sigma_{pred.err}$	$m_{pred.err}$
L	Plot1 Up-Slp	Regression	7	9.0E-04	0.12	NA	NA	NA	6.7E-03	2.9E-02
	Plot1 Cross-Slp	Ordinary	0	NA	NA	3.0E+00	2.3E-02	3.7E-02	1.3E-03	3.1E-02
	Plot1	Universal	7	1.3E-03	0.06	1.4E+02	3.7E-02	7.0E-02	4.2E-04	3.9E-02
	Plot2	Regression	4	1.2E-07	0.20	NA	NA	NA	3.1E-03	1.5E-02
	Plot3	Ordinary	0	NA	NA	9.4E-01	3.5E-02	3.7E-02	4.6E-05	3.7E-02
	Plot4	Regression	9	9.6E-10	0.23	NA	NA	NA	4.0E-03	2.4E-02
	Plot5	Mean	0	NA	NA	NA	NA	NA	0.0E+00	2.6E-01
L_{max}	Plot1 Up-Slp	Universal	7	2.5E-02	0.06	3.8E+00	7.8E-02	1.0E-01	2.0E-03	9.2E-02
	Plot1 Cross-Slp	Ordinary	0	NA	NA	1.8E+00	4.1E-02	6.7E-02	2.7E-03	5.9E-02
	Plot1	Universal	7	1.6E-02	0.03	3.5E+00	6.3E-02	8.6E-02	2.0E-03	7.6E-02
	Plot2	Regression	7	1.9E-03	0.07	NA	NA	NA	5.1E-03	2.6E-02
	Plot3	Ordinary	0	NA	NA	9.4E-01	2.8E-02	8.8E-02	1.0E-02	8.0E-02
	Plot4	Regression	9	3.0E-05	0.13	NA	NA	NA	5.8E-03	3.3E-02
	Plot5	Ordinary	0	NA	NA	3.9E+00	8.7E-02	1.0E-01	1.6E-03	9.9E-02

* 'Formula' refers to best-fit regression model, as defined in Table 8.

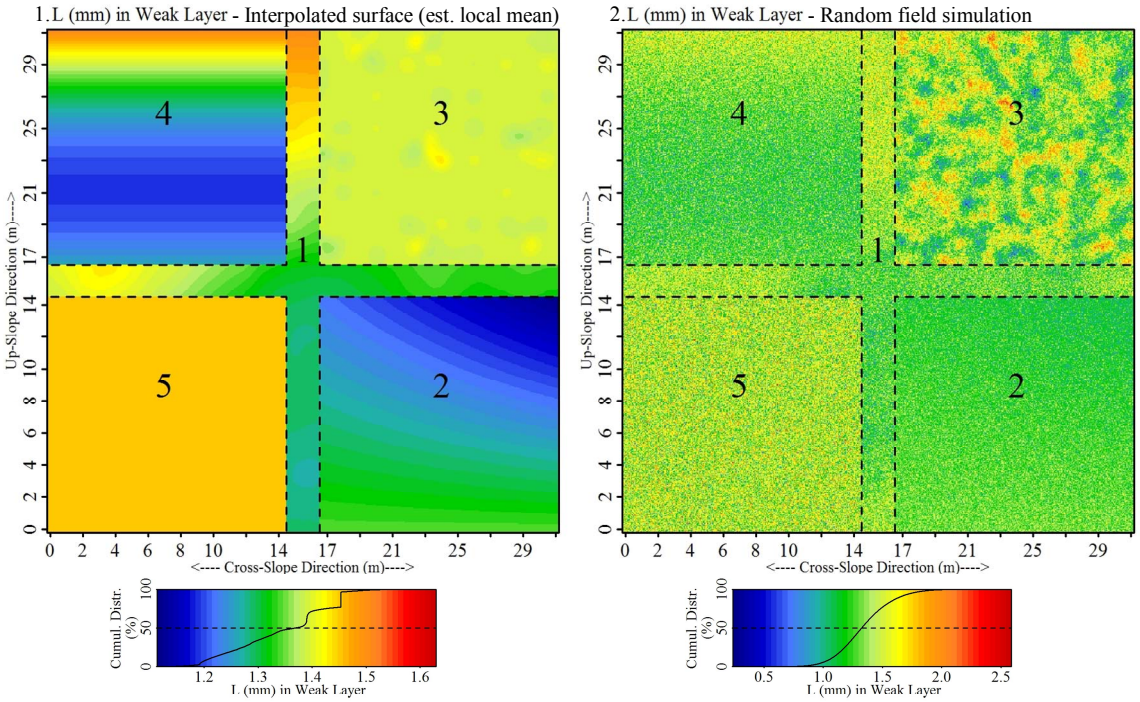

Figure 94. Spatial interpolations of *L* of the weak layer. Interpolated surfaces of local mean values, utilizing chosen interpolation method (Table 17). (2) Random field simulation incorporates randomness, based on semi-variance values in Figure 95.

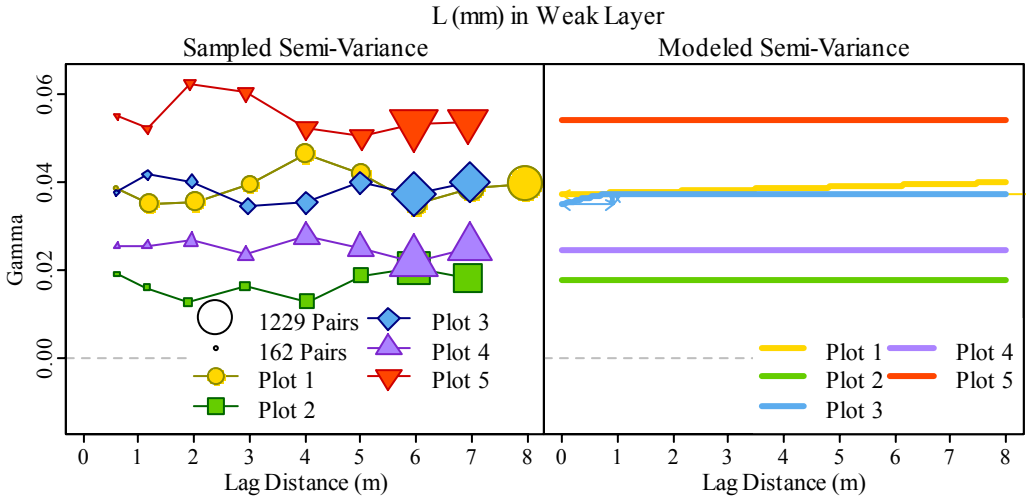

Figure 95. Sample (left) and model (right) variograms of *L* of the weak layer.

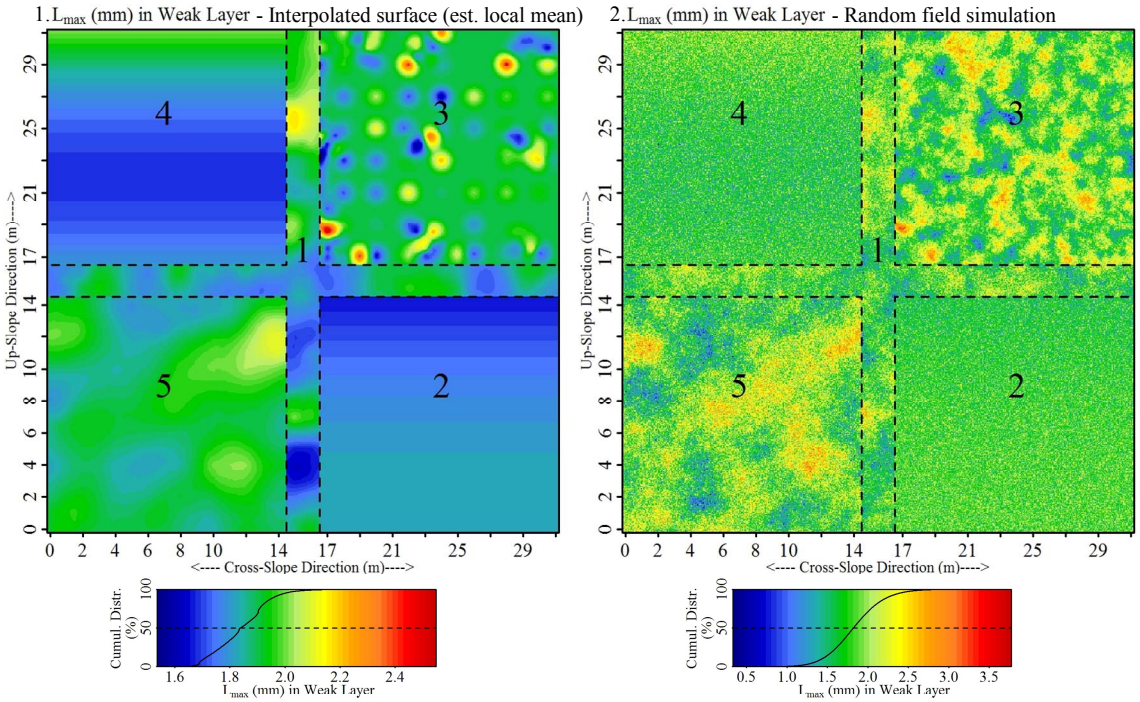

Figure 96. Spatial interpolations of L_{max} of the weak layer. Interpolated surfaces of local mean values, utilizing chosen interpolation method (Table 17). (2) Random field simulation incorporates randomness, based on semi-variance values in Figure 97.

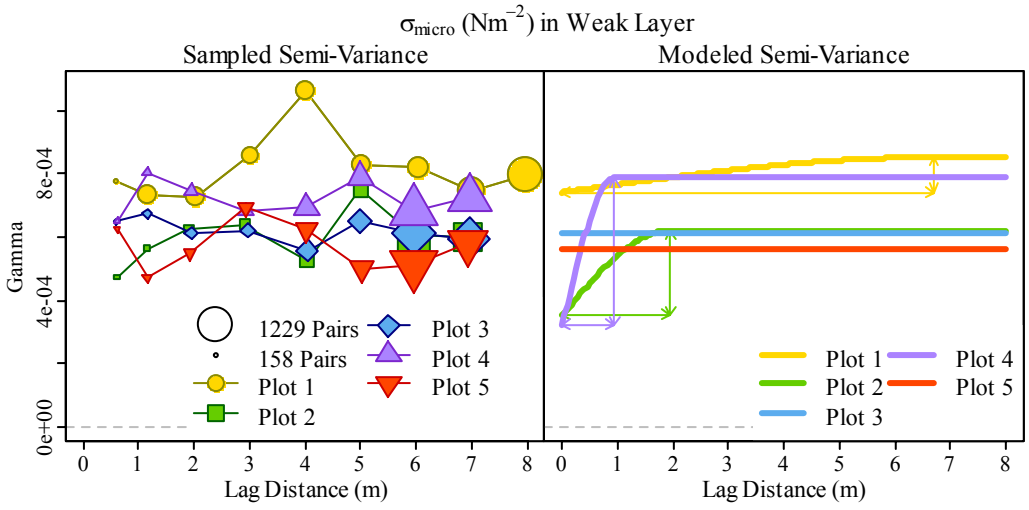

Figure 97. Sample (left) and model (right) variograms of L_{max} of the weak layer.

<u>Micro-Strength (σ_{micro}):</u> Plots 2 and 4 possessed pronounced autocorrelation of σ_{micro} at short distances, while Plots 3 and 5 indicated none (Table 18, Figures 98 and 99).

A zone of high micro-strength (σ_{micro}) was present at the top of Plot 2, which may be associated with the larger load that was estimated here.

Table 18. Spatial patterns of σ_{micro} of the weak layer.

σ_{micro} (N·mm^{-2})	Interpolation Method	Regression Component			Variogram Component			Model Error	
Areal Extent		Formula*	p-value	r^2	Range (m)	Nugget	Sill	$\sigma_{pred.err}$	$m_{pred.err}$
Plot1 Up-Slp	Regression	7	4.9E-02	0.04	NA	NA	NA	9.9E-04	4.2E-03
Plot1 Cross-Slp	Ordinary	0	NA	NA	6.3E+00	6.4E-04	7.4E-04	6.2E-06	7.0E-04
Plot1	Ordinary	0	NA	NA	6.7E+00	7.4E-04	8.5E-04	6.1E-06	8.0E-04
Plot2	Universal	4	1.5E-03	0.08	1.9E+00	3.5E-04	6.2E-04	4.2E-05	5.8E-04
Plot3	Mean	0	NA	NA	NA	NA	NA	0.0E+00	2.5E-02
Plot4	Universal	7	4.2E-02	0.03	9.4E-01	3.2E-04	7.9E-04	7.6E-05	7.3E-04
Plot5	Mean	0	NA	NA	NA	NA	NA	0.0E+00	2.5E-02

* 'Formula' refers to best-fit regression model, as defined in Table 8.

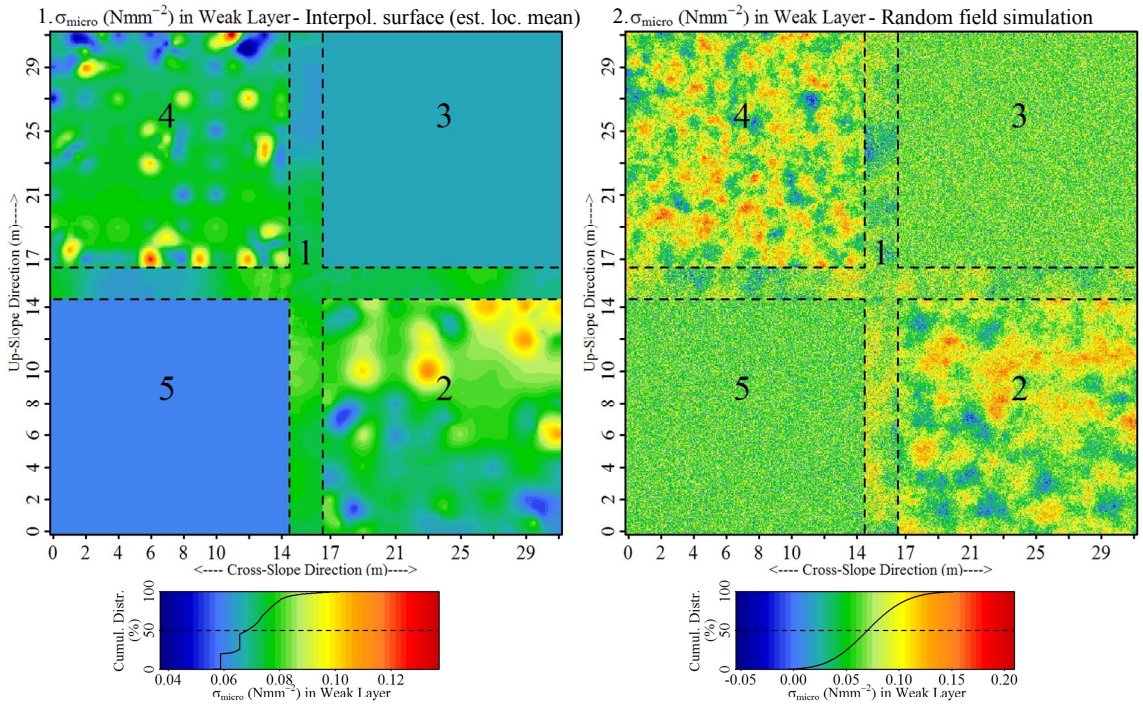

Figure 98. Spatial interpolations of σ_{micro} of the weak layer. Interpolated surfaces of local mean values, utilizing chosen interpolation method (Table 18). (2) Random field simulation incorporates randomness, based on semi-variance values in Figure 99.

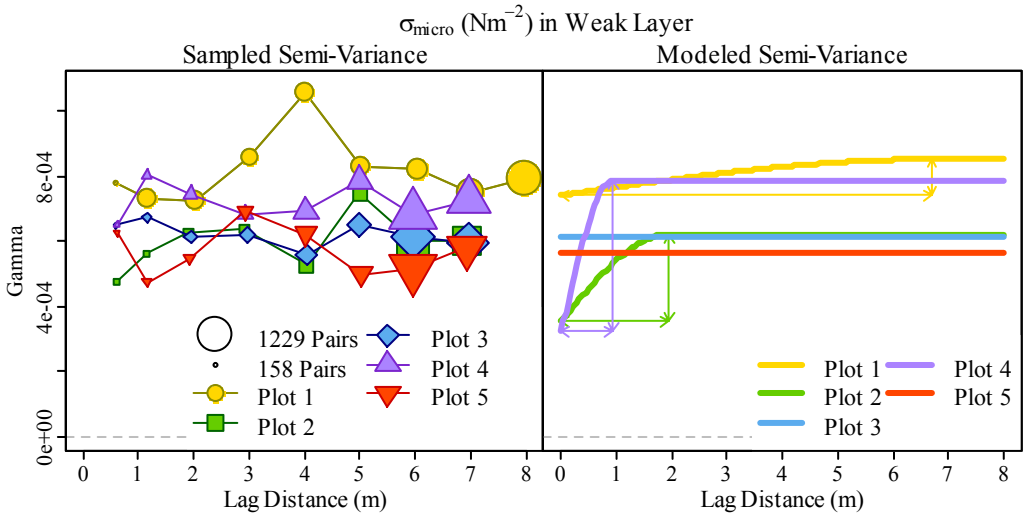

Figure 99. Sample (left) and model (right) variograms of σ_{micro} of the weak layer.

Microstructural Estimates of the Super-Stratum

Rupture Force Characteristics (f_m, f_{max}, f_{cv}): Local spatial structure of f_m and f_{max} of the slab were more pronounced than those of the weak layer (Figures 100 - 105, Table 19).

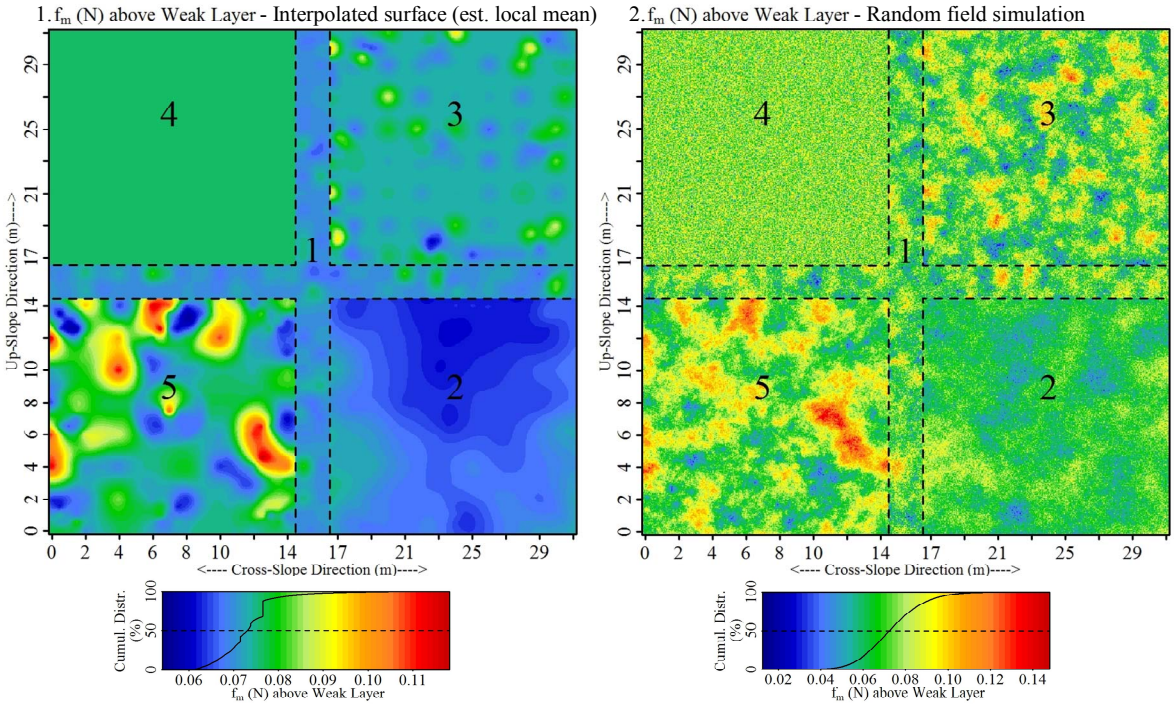

Figure 100. Spatial interpolations of f_m of the super-stratum. Interpolated surfaces of local mean values, utilizing chosen interpolation method (Table 19). (2) Random field simulation incorporates randomness, based on semi-variance values in Figure 101.

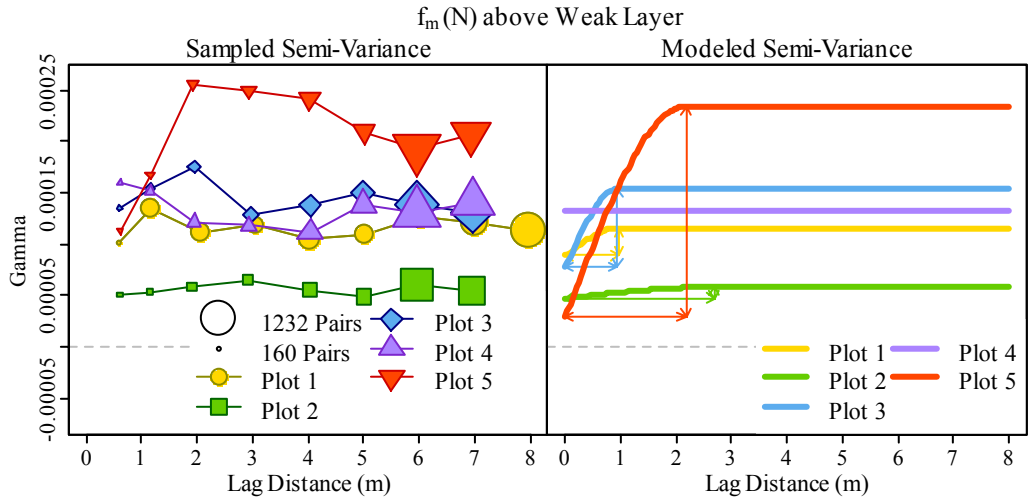

Figure 101. Sample (left) and model (right) variograms of f_m of the super-stratum.

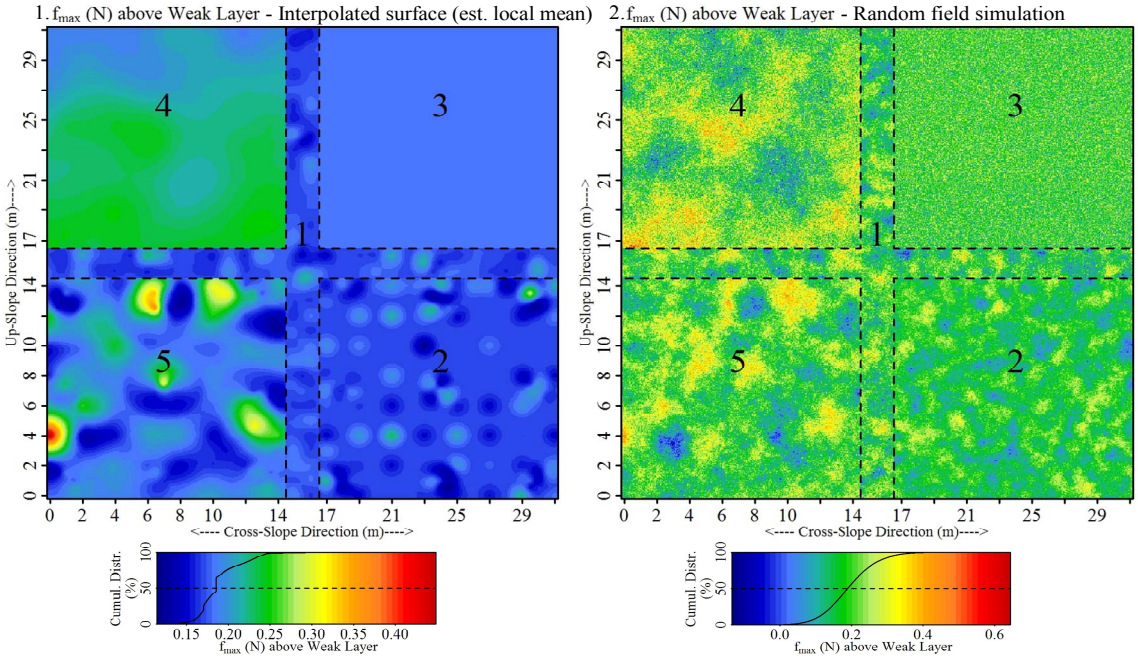

Figure 102. Spatial interpolations of f_{max} of the super-stratum. Interpolated surfaces of local mean values, utilizing chosen interpolation method (105, Table 19).). (2) Random field simulation incorporates randomness, based on semi-variance values in Figure 103.

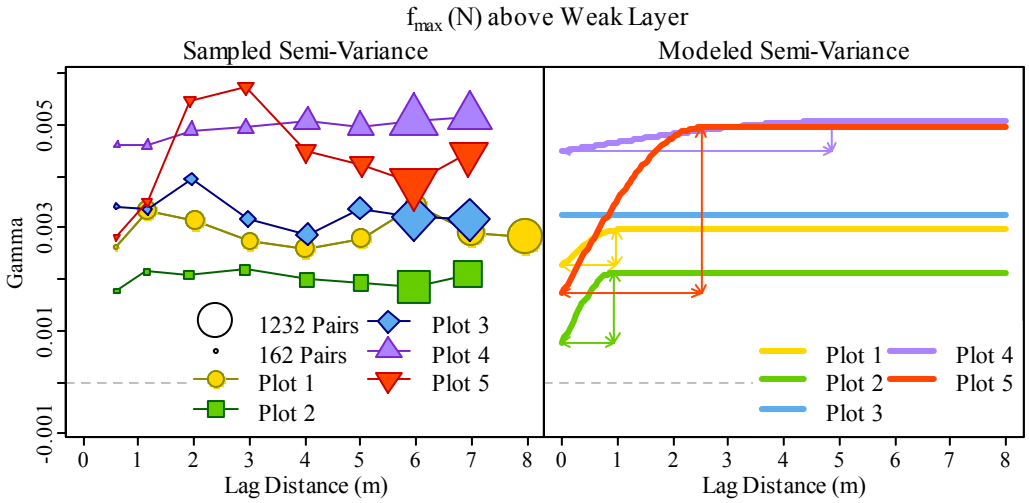

Figure 103. Sample (left) and model (right) variograms of f_{max} of the super-stratum.

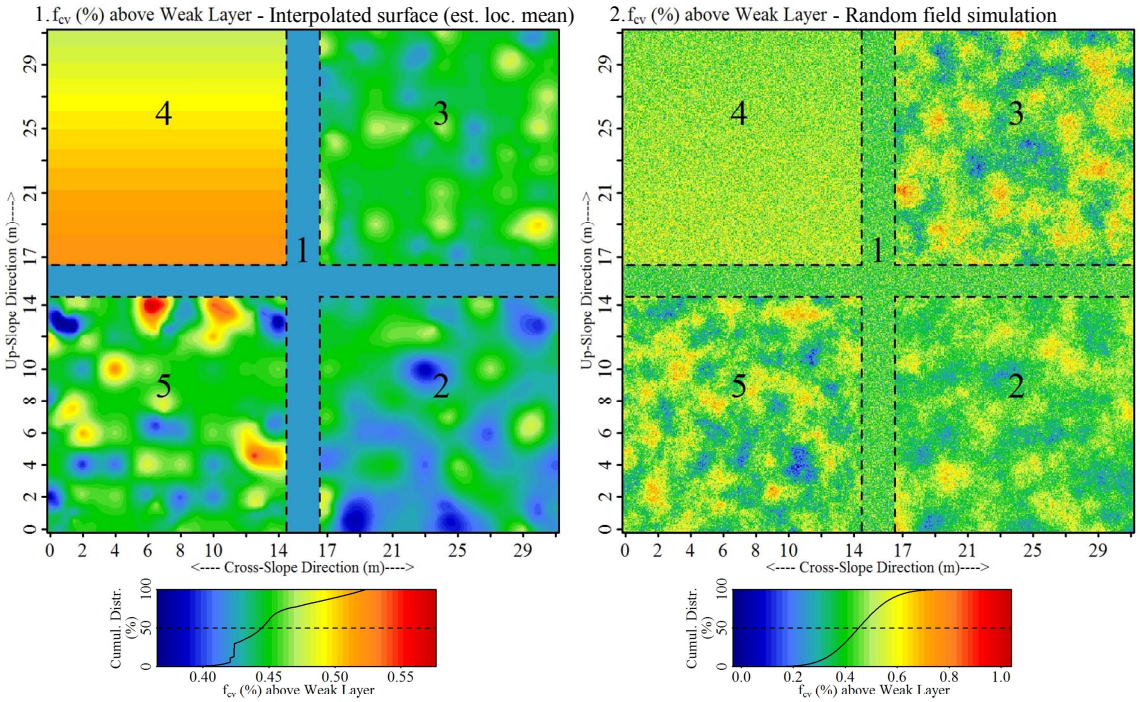

Figure 104. Spatial interpolations of f_{cv} of the super-stratum. Interpolated surfaces of local mean values, utilizing chosen interpolation method (105, Table 19).). (2) Random field simulation incorporates randomness, based on semi-variance values in Figure 105.

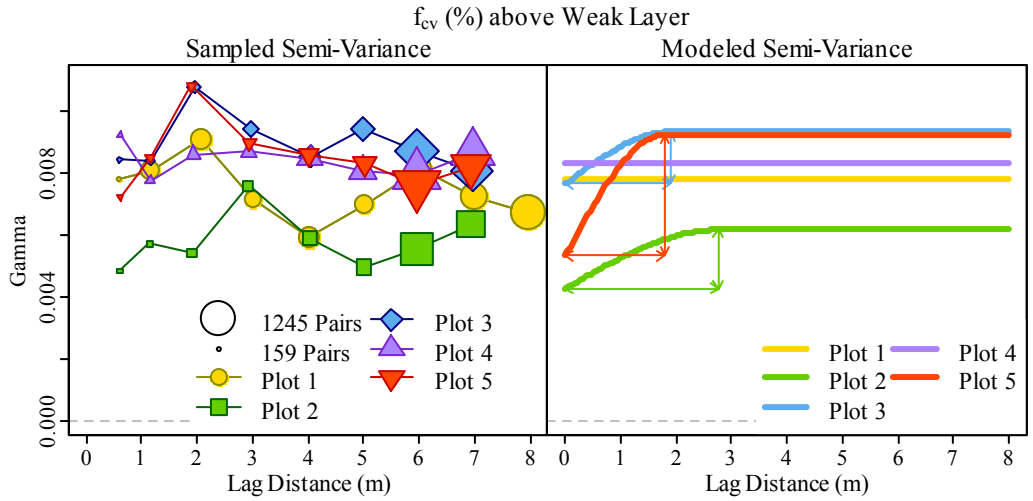

Figure 105. Sample (left) and model (right) variograms of f_{cv} of the super-stratum.

Table 19. Spatial patterns of f_m (N), f_{max} (N) and f_{cv} (%) of the super-stratum.

Variable	Areal Extent	Interpol. Method	Regression Component			Variogram Component			Model Error	
			Formula*	p-value	r^2	Range (m)	Nugget	Sill	$\sigma_{pred.err}$	$m_{pred.err}$
f_m (N)	Plot1 Up-Slp	Ordinary	0	NA	NA	1.22	0.0E+00	1.1E-04	2.2E-05	6.3E-05
	Plot1 Cross-Slp	Mean	0	NA	NA	NA	NA	NA	0.0E+00	1.3E-02
	Plot1	Ordinary	0	NA	NA	0.96	8.9E-05	1.2E-04	1.9E-06	1.1E-04
	Plot2	Universal	10	3.5E-03	0.13	2.68	4.7E-05	5.8E-05	1.7E-06	5.9E-05
	Plot3	Ordinary	0	NA	NA	0.94	7.8E-05	1.5E-04	9.9E-06	1.5E-04
	Plot4	Mean	0	NA	NA	NA	NA	NA	0.0E+00	1.3E-02
	Plot5	Ordinary	0	NA	NA	2.18	2.9E-05	2.3E-04	4.6E-05	1.6E-04
f_{max} (N)	Plot1 Up-Slp	Universal	7	4.6E-02	0.05	0.94	1.7E-03	2.5E-03	8.6E-05	2.4E-03
	Plot1 Cross-Slp	Ordinary	0	NA	NA	0.94	1.4E-03	3.3E-03	2.6E-04	2.8E-03
	Plot1	Ordinary	0	NA	NA	0.97	2.3E-03	3.0E-03	4.8E-05	2.9E-03
	Plot2	Ordinary	0	NA	NA	0.93	7.8E-04	2.1E-03	2.1E-04	2.0E-03
	Plot3	Mean	0	NA	NA	NA	NA	NA	0.0E+00	6.1E-02
	Plot4	Universal	7	4.8E-03	0.05	4.86	4.5E-03	5.1E-03	5.4E-05	4.9E-03
	Plot5	Ordinary	0	NA	NA	2.50	1.7E-03	4.9E-03	5.9E-04	3.8E-03
f_{cv} (%)	Plot1 Up-Slp	Mean	0	NA	NA	NA	NA	NA	0.0E+00	8.0E-02
	Plot1 Cross-Slp	Mean	0	NA	NA	NA	NA	NA	0.0E+00	9.1E-02
	Plot1	Mean	0	NA	NA	NA	NA	NA	0.0E+00	9.1E-02
	Plot2	Ordinary	0	NA	NA	2.76	4.3E-03	6.2E-03	2.5E-04	5.8E-03
	Plot3	Ordinary	0	NA	NA	1.90	7.7E-03	9.3E-03	1.4E-04	9.2E-03
	Plot4	Regression	7	2.1E-02	0.03	NA	NA	NA	1.9E-03	9.4E-03
	Plot5	Ordinary	0	NA	NA	1.79	5.4E-03	9.3E-03	5.7E-04	8.7E-03

* 'Formula' refers to best-fit regression model, as defined in Table 8.

Structural Element Length Characteristics (L, L_{max}): Pronounced spatial structure of L and L_{max} was present within the super-stratum at all plots except Plot 4 (Table 20, Figures 106 - 109). As with f_m and f_{max}, the greatest plot-scale variability of L and L_{max} occurred in Plot 5 (Figures 107 and 109).

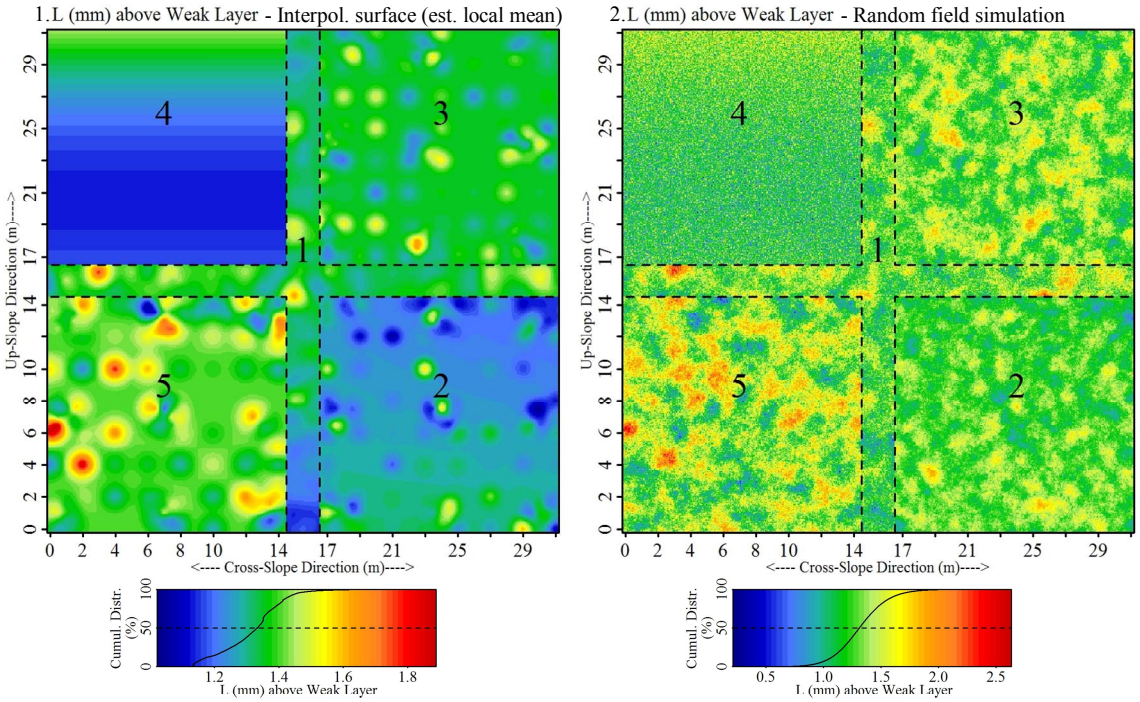

Figure 106. Spatial interpolations of *L* of the super-stratum. Interpolated surfaces of local mean values, utilizing chosen interpolation method (Table 20). (2) Random field simulation incorporates randomness, based on semi-variance values in Figure 107.

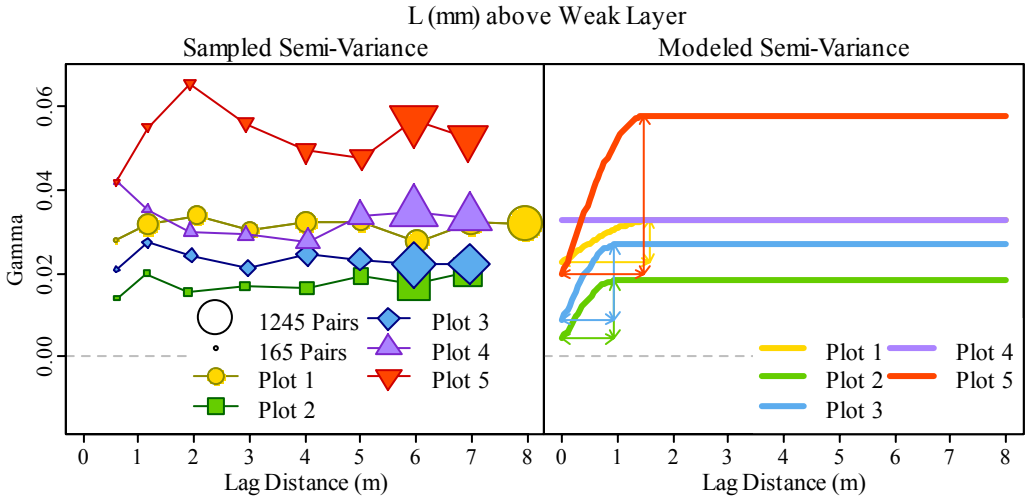

Figure 107. Sample (left) and model (right) variograms of *L* of the super-stratum.

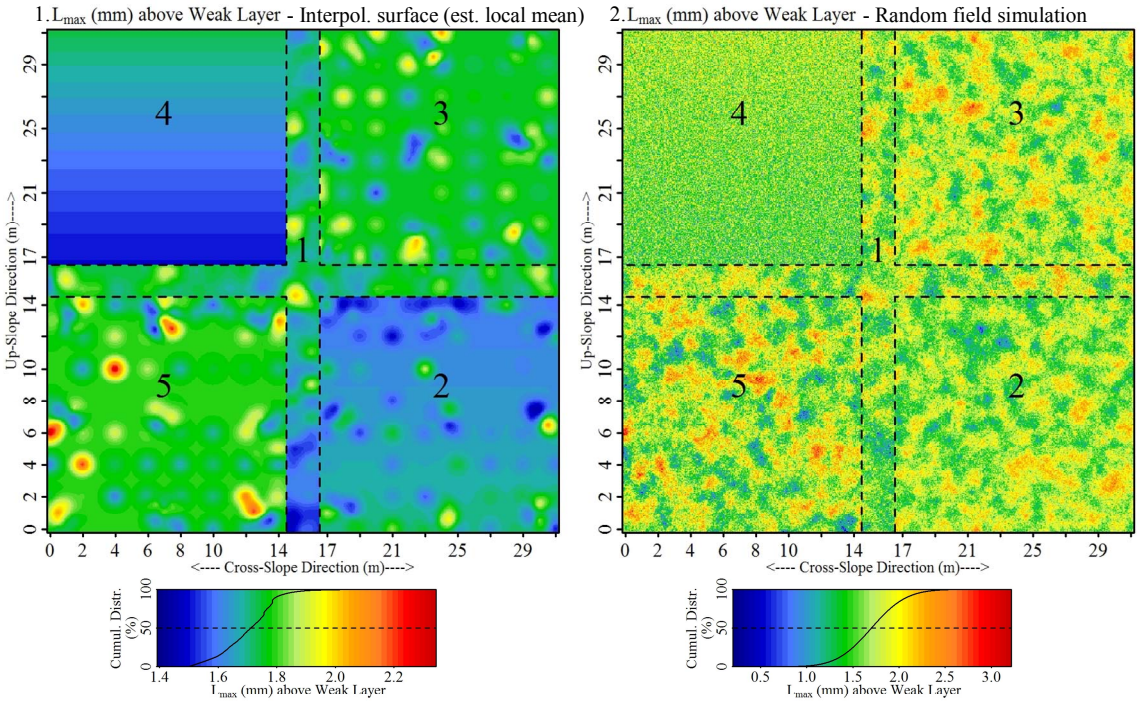

Figure 108. Spatial interpolations of L_{max} of the super-stratum. Interpolated surfaces of local mean values, utilizing chosen interpolation method (Table 20). (2) Random field simulation incorporates randomness, based on semi-variance values in Figure 109.

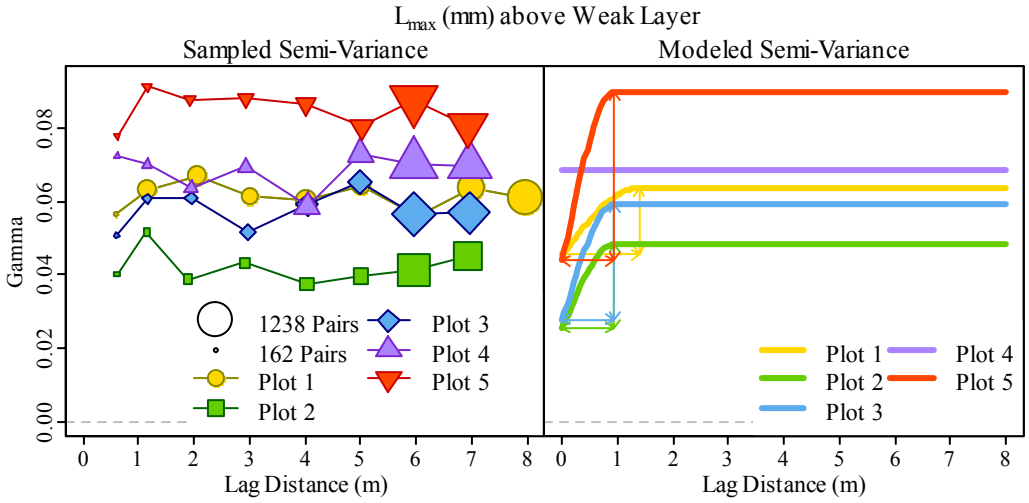

Figure 109. Sample (left) and model (right) variograms of L_{max} of the super-stratum.

Table 20. Spatial patterns of L and L_{max}(mm).

Variable	Areal Extent	Interpol. Method	Regression Component			Variogram Component			Model Error	
			Formula*	p-value	r^2	Range (m)	Nugget	Sill	$\sigma_{pred.err}$	$m_{pred.err}$
L	Plot1 Up-Slp	Universal	9	1.1E-02	0.10	130.06	2.7E-02	5.4E-02	4.0E-04	2.9E-02
	Plot1 Cross-Slp	Ordinary	0	NA	NA	164.71	2.5E-02	9.3E-02	2.0E-04	2.7E-02
	Plot1	Universal	9	3.9E-03	0.06	1.56	2.3E-02	3.2E-02	1.0E-03	3.1E-02
	Plot2	Universal	4	4.4E-04	0.09	0.93	4.4E-03	1.8E-02	2.6E-03	1.7E-02
	Plot3	Ordinary	0	NA	NA	0.94	8.9E-03	2.7E-02	3.0E-03	2.4E-02
	Plot4	Regression	9	1.3E-07	0.18	NA	NA	NA	4.7E-03	2.8E-02
	Plot5	Ordinary	0	NA	NA	1.48	2.0E-02	5.7E-02	7.0E-03	5.1E-02
L_{max}	Plot1 Up-Slp	Ordinary	0	NA	NA	1.68	2.3E-02	6.6E-02	5.1E-03	4.8E-02
	Plot1 Cross-Slp	Regression	8	2.0E-02	0.08	NA	NA	NA	8.9E-03	3.6E-02
	Plot1	Universal	9	1.5E-02	0.05	1.39	4.6E-02	6.4E-02	1.8E-03	6.1E-02
	Plot2	Universal	2	1.8E-02	0.04	0.93	2.6E-02	4.8E-02	2.9E-03	4.7E-02
	Plot3	Ordinary	0	NA	NA	0.94	2.8E-02	5.9E-02	4.4E-03	5.6E-02
	Plot4	Regression	7	3.3E-04	0.08	NA	NA	NA	5.5E-03	2.8E-02
	Plot5	Ordinary	0	NA	NA	0.93	4.4E-02	9.0E-02	6.1E-03	8.5E-02

* 'Formula' refers to best-fit regression model, as defined in Table 8.

Micro-Strength (σ_{micro}): Based on the mean prediction error, the micro-strength (σ_{micro}) was least effectively estimated at Plot 4 (Table 21). This was also the only plot that possessed no positive spatial autocorrelation (nugget was equal to the sill, Figure 111). In contrast, the plot-scale variability of micro-strength (σ_{micro}) at Plot 5 was largely resolved at small distances (Figure 111). Considering differences in range values, on the lower slope, the distance at which observations were correlated increased between Plot 2 and 5.

Table 21. Spatial patterns of σ_{micro} of the super-stratum.

σ_{micro} ($N \cdot mm^{-2}$)	Interpolation Method	Regression Component			Variogram Component			Model Error	
Areal Extent		Formula	p-value	r^2	Range (m)	Nugget	Sill	$\sigma_{pred.err}$	$m_{pred.err}$
Plot1 Up-Slp	Universal	2	1.9E-02	0.06	1.02	1.2E-04	1.6E-04	3.9E-06	1.6E-04
Plot1 Cross-Slp	Ordinary	0	NA	NA	5.46	1.5E-04	1.8E-04	1.9E-06	1.7E-04
Plot1	Universal	2	5.3E-03	0.04	5.74	1.6E-04	1.9E-04	2.0E-06	1.8E-04
Plot2	Ordinary	0	NA	NA	0.93	4.5E-05	1.3E-04	1.3E-05	1.2E-04
Plot3	Ordinary	0	NA	NA	0.94	1.2E-04	1.4E-04	1.4E-06	1.4E-04
Plot4	Regression	9	1.6E-05	0.13	NA	NA	NA	4.5E-04	2.7E-03
Plot5	Ordinary	0	NA	NA	1.86	1.2E-04	3.1E-04	3.4E-05	2.7E-04

* 'Formula' refers to best-fit regression model, as defined in Table 8.

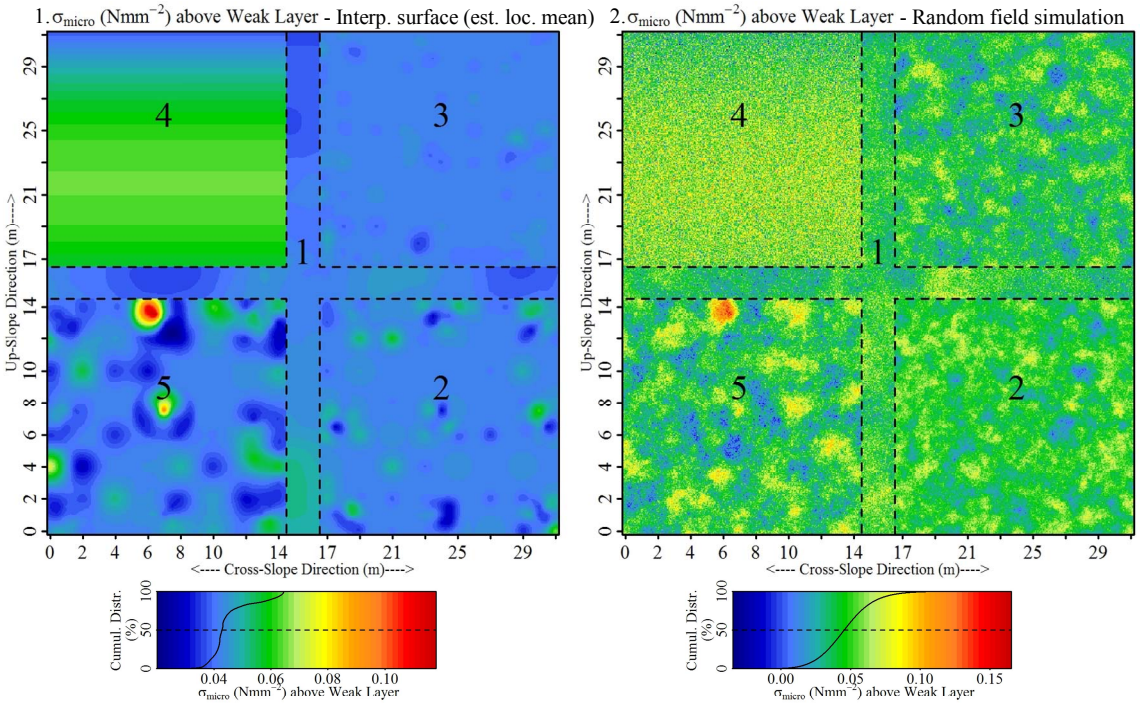

Figure 110. Spatial interpolations of σ_{micro} of the super-stratum. Interpolated surfaces of local mean values, utilizing chosen interpolation method (Table 21). (2) Random field simulation incorporates randomness, based on semi-variance values in Figure 111.

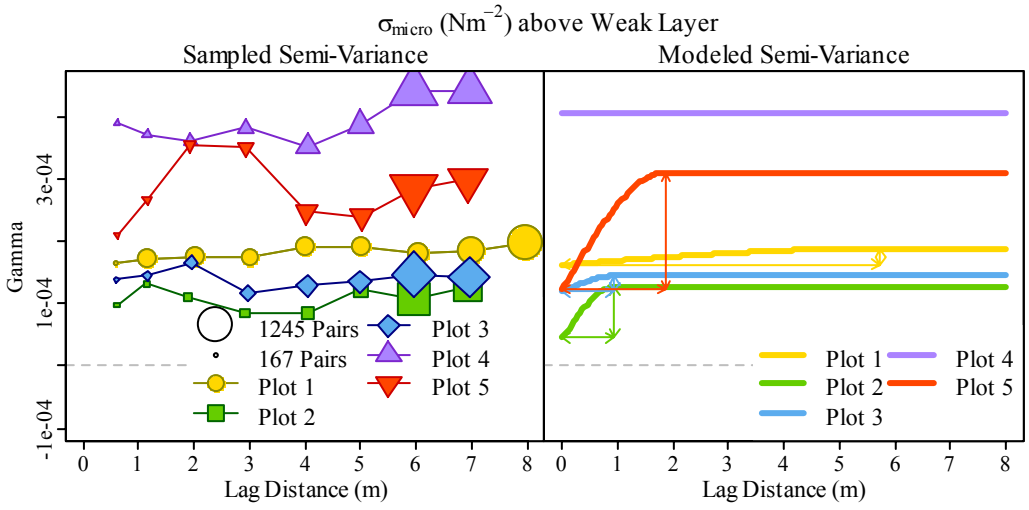

Figure 111. Sample (left) and model (right) variograms of σ_{micro} of the super-stratum.

Step-Changes of Microstructural Estimates

Step-Changes of Rupture Force Characteristics (Δf_m, Δf_{max}, Δf_{cv}): As a direct result of the spatial structure inherent to f_m within the weak layer, the step-change of the mean rupture force (Δf_m) had a similar patterns at Plots 2 and 5 (Figure 112). In the prediction maps, dark blue zones on these plots represent areas where differences in rupture force between the super-stratum and the weak layer are minimal. Plot 5 had the greatest predictive strength for Δf_m, possessing the smallest nugget value and largest sill value (Figure 113). In contrast, Plot 5 also possessed the smallest sill values for step-change of f_{max}. These observations illustrate that after the large loading event plot-scale variability of the step-changes in f_m increased significantly, while step-changes of f_{max} decreased significantly.

Table 22. Spatial patterns of Δf_m (N) and Δf_{max}(N) and Δf_{cv} (%).* 'Formula' defined in Table 8.

Variable	Areal Extent	Interpol. Method	Regression Component			Variogram Component			Model Error	
			Formula*	p-value	r^2	Range (m)	Nugget	Sill	$\sigma_{pred.err}$	$m_{pred.err}$
Δf_m (N)	Plot1 Up-Slp	Ordinary	0	NA	NA	1.26	4.1E-04	6.9E-04	3.0E-05	6.4E-04
	Plot1 Cross-Slp	Mean	0	NA	NA	NA	NA	NA	0.0E+00	2.4E-02
	Plot1	Ordinary	0	NA	NA	3.91	5.0E-04	5.9E-04	6.3E-06	5.6E-04
	Plot2	Universal	5	4.0E-02	0.06	3.15	5.1E-04	6.8E-04	2.4E-05	6.5E-04
	Plot3	Mean	0	NA	NA	NA	NA	NA	0.0E+00	2.6E-02
	Plot4	Ordinary	0	NA	NA	0.94	6.3E-04	7.7E-04	8.0E-06	7.6E-04
	Plot5	Ordinary	0	NA	NA	2.85	3.3E-04	8.3E-04	8.5E-05	6.4E-04
Δf_{max} (N)	Plot1 Up-Slp	Ordinary	0	NA	NA	2.08	8.4E-02	1.1E-01	1.7E-03	1.0E-01
	Plot1 Cross-Slp	Ordinary	0	NA	NA	130.01	3.9E-02	6.6E-02	1.1E-04	4.2E-02
	Plot1	Universal	8	4.1E-02	0.04	4.62	6.0E-02	7.4E-02	1.2E-03	6.8E-02
	Plot2	Universal	4	1.6E-03	0.08	1.46	2.7E-02	6.9E-02	7.9E-03	6.3E-02
	Plot3	Regression	2	3.2E-02	0.03	NA	NA	NA	5.6E-03	2.8E-02
	Plot4	Mean	0	NA	NA	NA	NA	NA	0.0E+00	2.7E-01
	Plot5	Ordinary	0	NA	NA	3.71	3.2E-02	3.7E-02	3.6E-04	3.6E-02
Δf_{cv} (%)	Plot1 Up-Slp	Ordinary	0	NA	NA	2.01	4.4E-02	7.2E-02	2.7E-03	6.3E-02
	Plot1 Cross-Slp	Ordinary	0	NA	NA	0.94	6.6E-03	2.8E-02	3.5E-03	2.1E-02
	Plot1	Ordinary	0	NA	NA	1.71	2.2E-02	4.7E-02	2.8E-03	3.8E-02
	Plot2	Regression	4	8.4E-04	0.08	NA	NA	NA	4.6E-03	2.2E-02
	Plot3	Mean	0	NA	NA	NA	NA	NA	0.0E+00	1.9E-01
	Plot4	Ordinary	0	NA	NA	1.91	3.4E-02	3.6E-02	3.4E-05	3.6E-02
	Plot5	Mean	0	NA	NA	NA	NA	NA	0.0E+00	1.8E-01

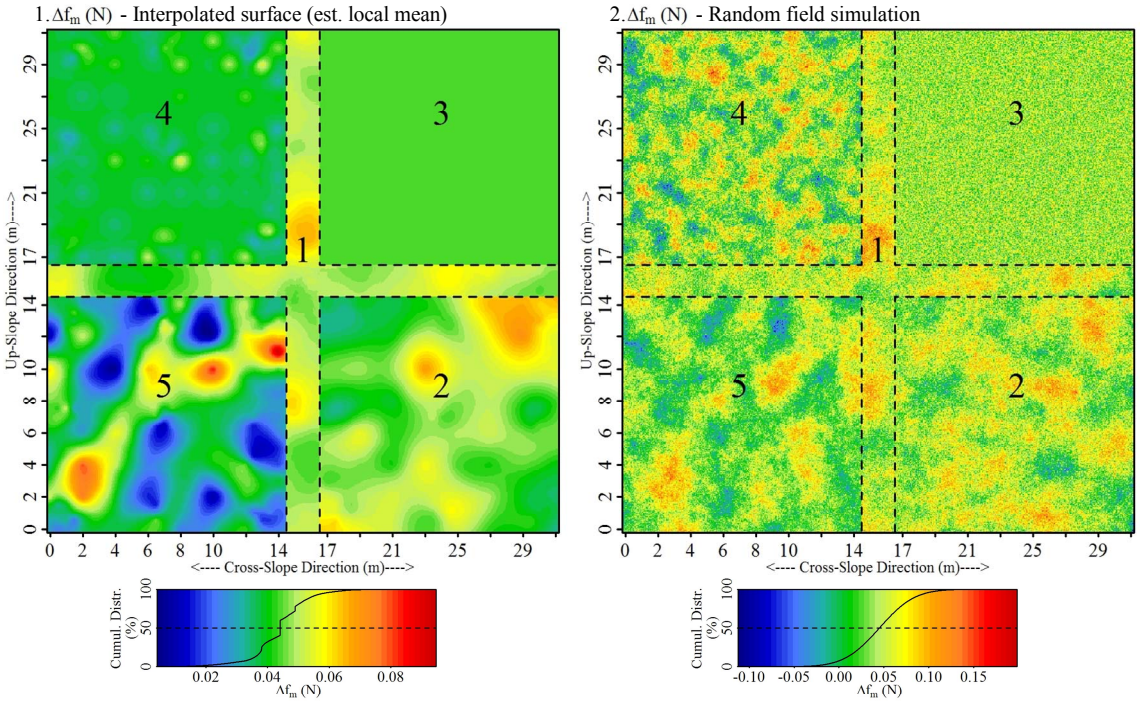

Figure 112. Spatial interpolations of Δf_m (N). Interpolated surfaces of local mean values, utilizing chosen interpolation method (Table 22). (2) Random field simulation incorporates randomness, based on semi-variance values in Figure 113.

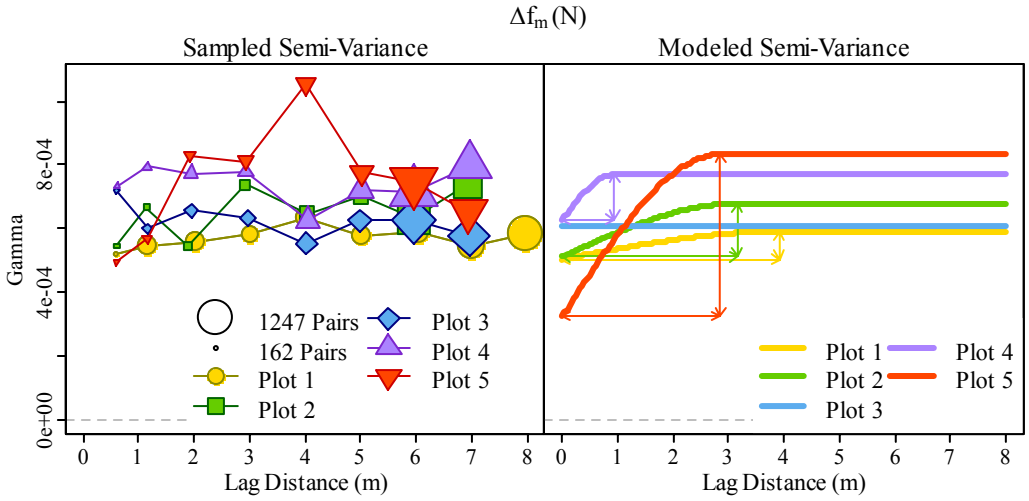

Figure 113. Sample (left) and model (right) variograms of Δf_m (N).

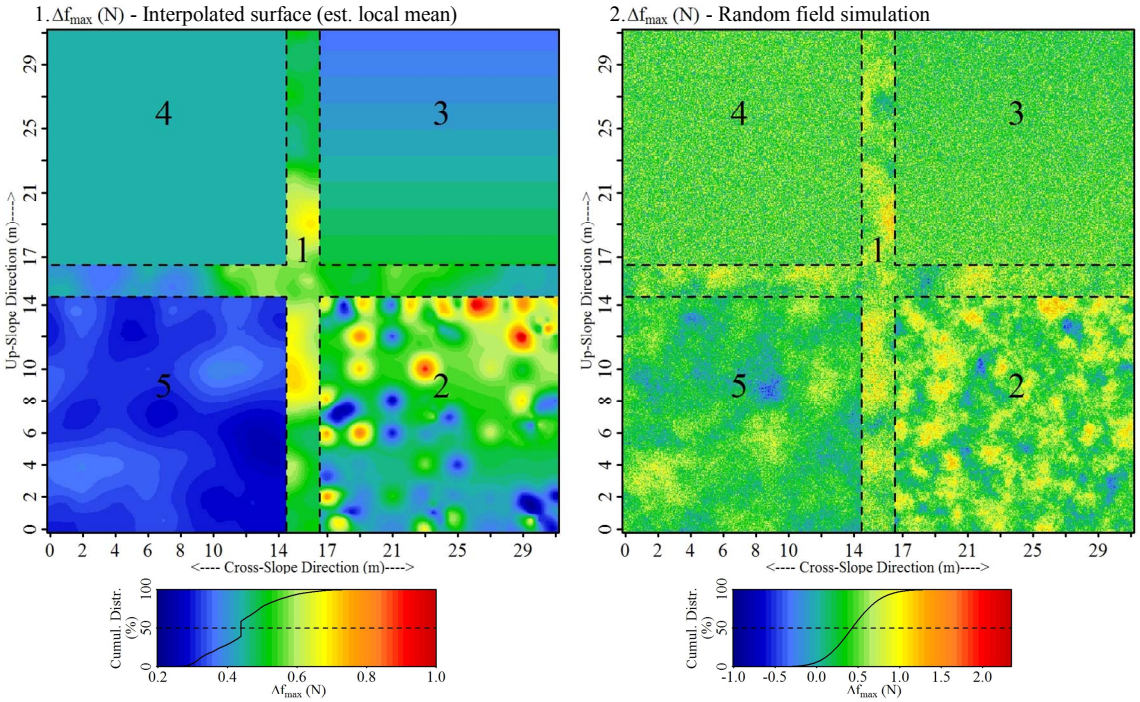

Figure 114. Spatial interpolations of Δf_{max} (N). Interpolated surfaces of local mean values, utilizing chosen interpolation method (Table 22). (2) Random field simulation incorporates randomness, based on semi-variance values in Figure 115.

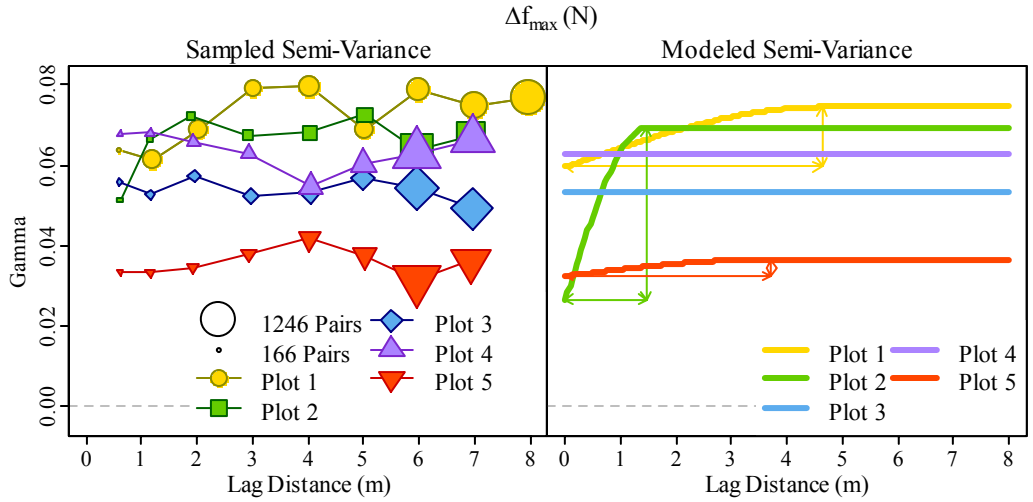

Figure 115. Sample (left) and model (right) variograms of Δf_{max} (N).

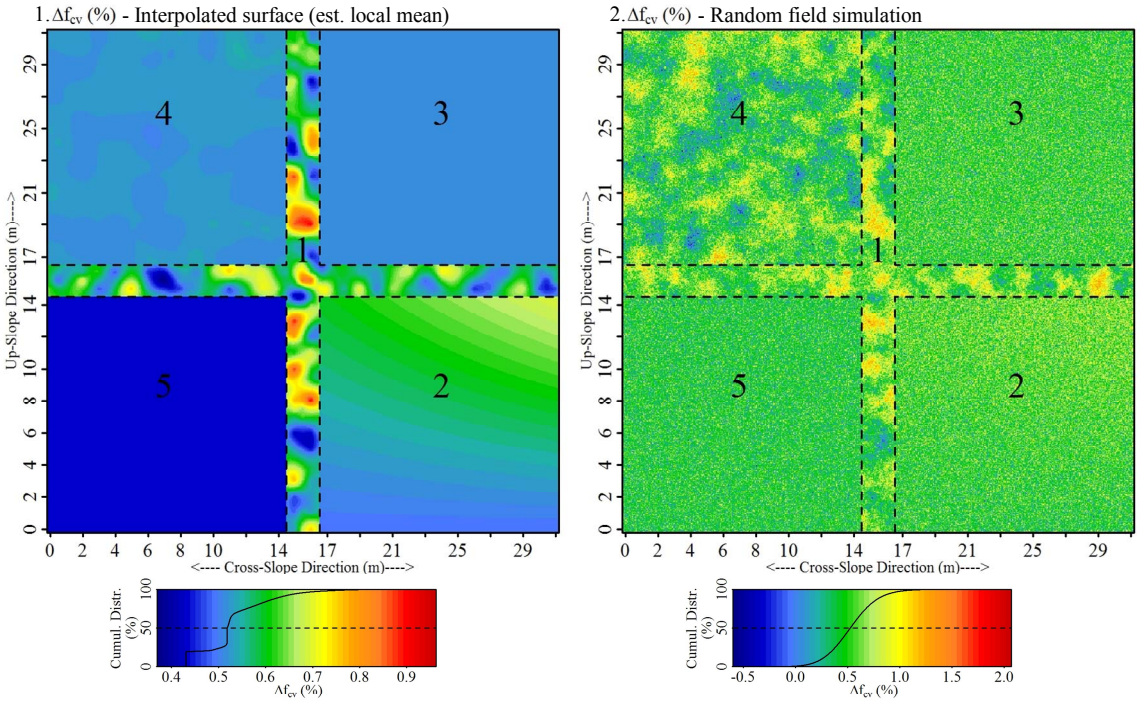

Figure 116. Spatial interpolations of Δf_{cv} (%). Interpolated surfaces of local mean values, utilizing chosen interpolation method (Table 22). (2) Random field simulation incorporates randomness, based on semi-variance values in Figure 117.

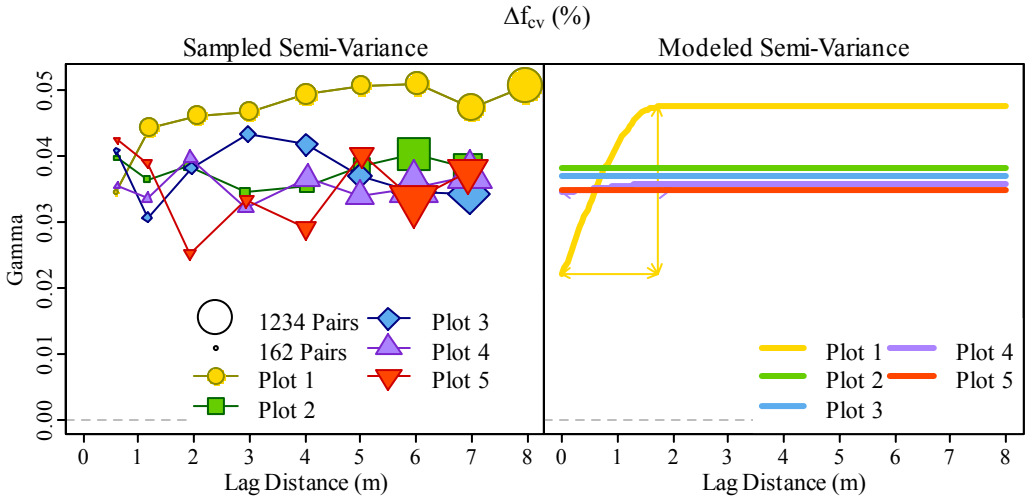

Figure 117. Sample (left) and model (right) variograms of Δf_{cv} (%).

Regarding Δf_{cv}, Plot 1 possessed the largest step-changes in micro-variance with pronounced local spatial structure (large values in Figure 116, and low nugget value and

large partial sill in Figure 117) while plot 5 possessed the smallest step-changes with no spatial structure whatsoever (small values in Figure 116, and no autocorrelation structure in Figure 117).

Step-Changes of Structural Element Length Characteristics (ΔL, ΔL_{max}):

Pronounced spatial patterns were present in the step-changes of mean and maximum structural element lengths (ΔL and ΔL_{max}) that were not related to spatial patterns in either stratum independently (Table 23, Figures 118 through 121). This indicates that the patterns were a result of both layers properties. Plot 5 had a large zone of small step-change values, indicating that, at this area of the slope, the difference in structural element size between super-stratum and weak layer was smallest. These zones of stratigraphic uniformity did not coincide with areas of low shear strength (τ_∞). Plot 5 also had the highest plot-sclae variance of ΔL and ΔL_{max}.

Table 23. Spatial patterns of ΔL and ΔL_{max}(mm).

Variable	Areal Extent	Interpol. Method	Regression Component			Variogram Component			Model Error	
			Formula *	p-value	r^2	Range (m)	Nugget	Sill	$\sigma_{pred.err}$	$m_{pred.err}$
ΔL (mm)	Plot1 Up-Slp	Regression	9	5.0E-04	0.16	NA	NA	NA	7.5E-03	3.0E-02
	Plot1 Cross-Slp	Ordinary	0	NA	NA	1.45	1.5E-02	2.9E-02	1.8E-03	2.5E-02
	Plot1	Regression	9	7.6E-04	0.08	NA	NA	NA	1.0E-02	2.3E-02
	Plot2	Regression	8	4.3E-02	0.05	NA	NA	NA	4.3E-03	2.3E-02
	Plot3	Universal	4	3.0E-02	0.03	1.40	3.5E-02	4.0E-02	4.0E-04	4.0E-02
	Plot4	Regression	1	8.8E-03	0.04	NA	NA	NA	4.2E-03	2.1E-02
	Plot5	Ordinary	0	NA	NA	7.38	7.3E-02	8.4E-02	7.1E-04	8.0E-02
ΔL_{max} (mm)	Plot1 Up-Slp	Regression	9	1.2E-02	0.10	NA	NA	NA	1.1E-02	4.8E-02
	Plot1 Cross-Slp	Ordinary	0	NA	NA	0.94	5.0E-02	7.8E-02	2.7E-03	7.3E-02
	Plot1	Regression	10	1.1E-04	0.14	NA	NA	NA	1.9E-02	5.0E-02
	Plot2	Mean	0	NA	NA	NA	NA	NA	0.0E+00	2.7E-01
	Plot3	Mean	0	NA	NA	NA	NA	NA	0.0E+00	3.1E-01
	Plot4	Ordinary	0	NA	NA	0.94	3.5E-02	8.7E-02	8.2E-03	8.1E-02
	Plot5	Ordinary	0	NA	NA	3.36	1.3E-01	1.6E-01	4.3E-03	1.5E-01

* 'Formula' refers to best-fit regression model, as defined in Table 8.

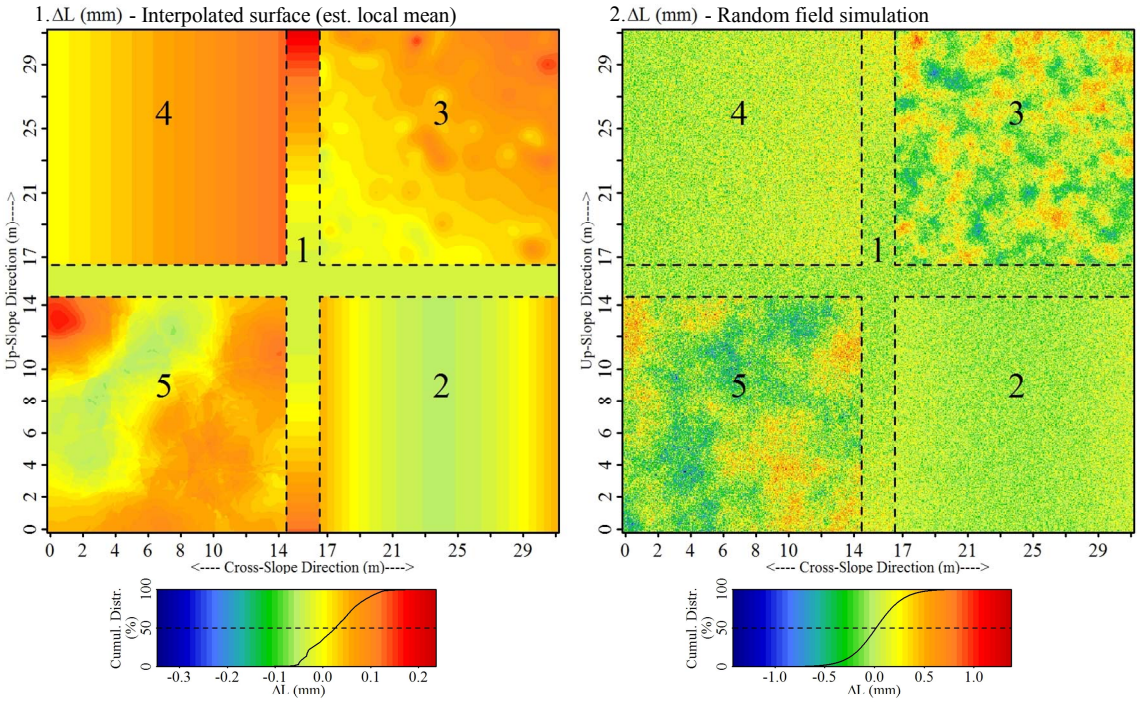

Figure 118. Spatial interpolations of ΔL (mm). Interpolated surfaces of local mean values, utilizing chosen interpolation method (Table 23). (2) Random field simulation incorporates randomness, based on semi-variance values in Figure 119.

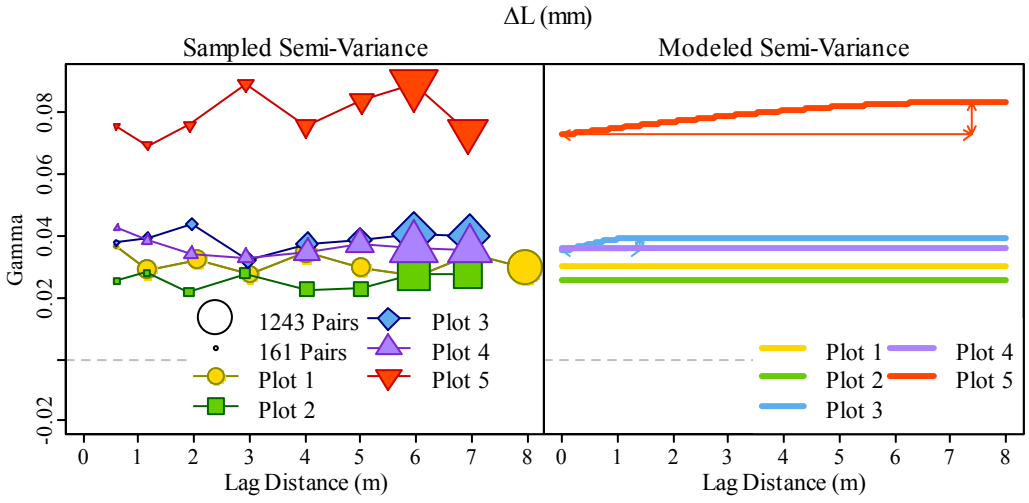

Figure 119. Sample (left) and model (right) variograms of ΔL (mm).

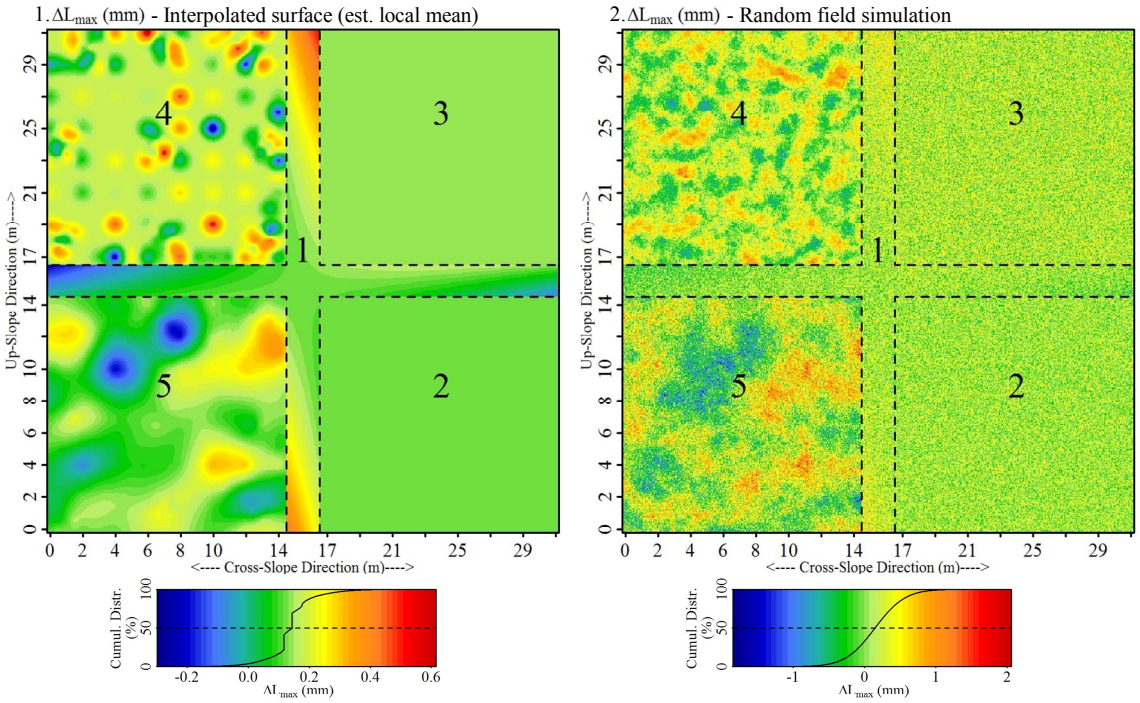

Figure 120. Spatial interpolations of ΔL_{max} (mm). Interpolated surfaces of local mean values, utilizing chosen interpolation method (Table 23). (2) Random field simulation incorporates randomness, based on semi-variance values in Figure 121.

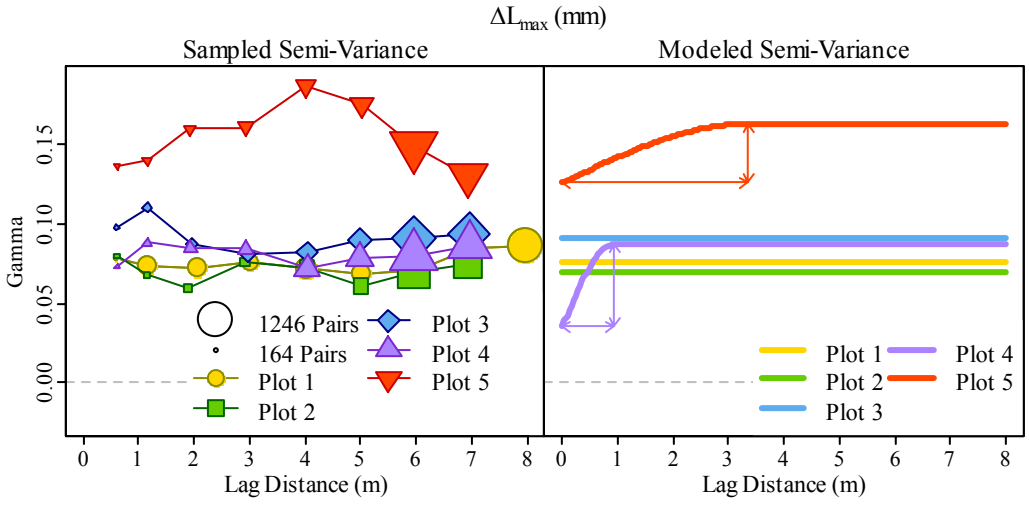

Figure 121. Sample (left) and model (right) variograms of ΔL_{max} (mm).

Step-Change of Micro-Strength ($\Delta\sigma_{micro}$): Plot 2 possessed the minimum and maximum values of step-change of micro-strength ($\Delta\sigma_{micro}$, the difference between the

super-stratum and weak layer micro-strength) for the entire site (Figure 122). However, a general increase in plot-scale $\Delta\sigma_{micro}$ was evident through the typical increase in sill values from Plot 1 through Plot 4 (Figure 123). Although $\Delta\sigma_{micro}$ values remained similar at Plot 5, a large decrease in the plot-scale variance occurred at Plot 5.

Table 24. Spatial patterns of $\Delta\sigma_{micro}$.

$\Delta\sigma_{micro}$ ($N{\cdot}mm^{-2}$) Areal Extent	Interpolation Method	Regression Component			Variogram Component			Model Error	
		Formula*	p-value	r^2	Range (m)	Nugget	Sill	$\sigma_{pred.err}$	$m_{pred.err}$
Plot1 Up-Slp	Regression	10	4.1E-02	0.13	NA	NA	NA	4.6E-03	9.1E-03
Plot1 Cross-Slp	Mean	0	NA	NA	NA	NA	NA	0.0E+00	2.1E-02
Plot1	Ordinary	0	NA	NA	5.71	5.0E-04	5.2E-04	1.1E-06	5.2E-04
Plot2	Universal	5	2.1E-02	0.07	1.14	0.0E+00	7.6E-04	1.8E-04	6.4E-04
Plot3	Mean	0	NA	NA	NA	NA	NA	0.0E+00	2.4E-02
Plot4	Ordinary	0	NA	NA	0.94	3.2E-04	9.8E-04	1.2E-04	8.9E-04
Plot5	Ordinary	0	NA	NA	2.57	4.5E-04	6.3E-04	2.3E-05	5.9E-04

* 'Formula' refers to best-fit regression model, as defined in Table 8.

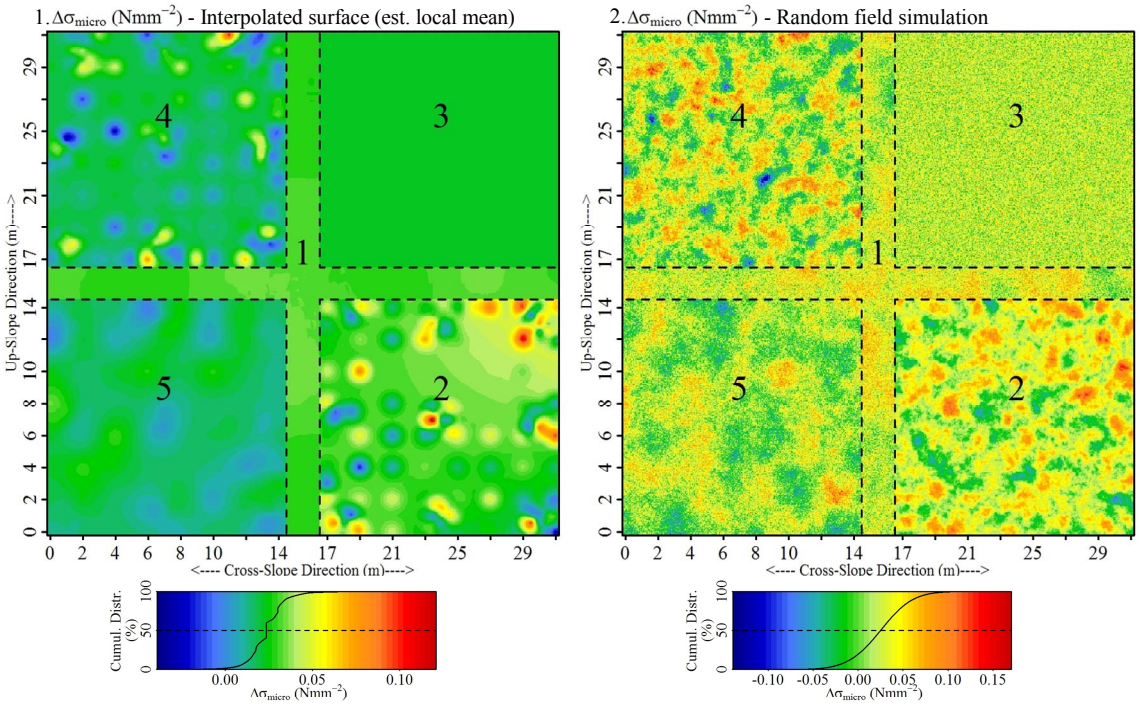

Figure 122. Spatial interpolations of $\Delta\sigma_{micro}$ ($N{\cdot}mm^{-2}$). Interpolated surfaces of local mean values, utilizing chosen interpolation method (Table 24). (2) Random field simulation incorporates randomness, based on semi-variance values in Figure 123.

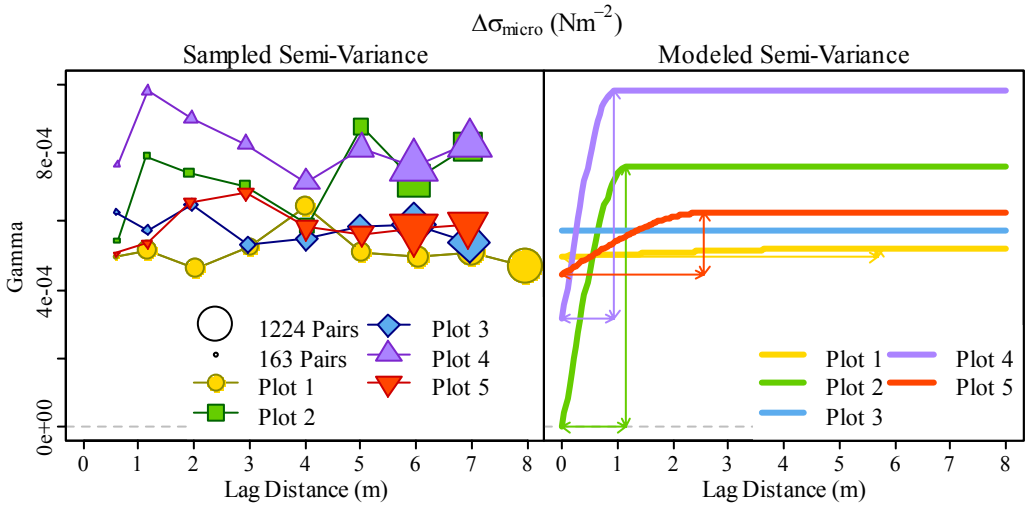

Figure 123. Sample (left) and model (right) variograms of σ_{micro} (N·mm^{-2}).

Temporal Results

Overview

The temporal analysis focused on changes in snow properties between adjacent plots in the cross-slope direction (Methods: Temporal Analysis, page 134). As identified in the previous spatial analysis section, a large up-slope trend of h_{wl} and τ_{∞} hindered definitive temporal comparisons between adjacent up-slope plots. For SMP variables and shear strength and stability variables, up-slope oriented sub-plots were compared (Figure 51, page 136). For load related variables, which were derived from shear frame pit observations (including HSW_{slab}, V_{slab}, N_{slab}, τ_{slab}), sub-plot comparisons resulted in too small populations sizes for statistical tests. Hence, only plot comparisons were conducted for these variables.

Shear Frame - Related Variables

Slab Water Equivalent (HSW_{slab}): At the upper site, HSW_{slab} increased significantly at the second time-step due to a small snowfall event (Table 25 and Figure 124.1). On the lower site a large change at the second time-step was associated with both snowfall events that preceded Plot 5 sampling (Figure 124.2). A decrease in minimum values of HSW_{slab} existed between Plots 1 and 2. This decrease in load was related to the spatial pattern described in the spatial analysis.

Table 25. Non-parametric tests of differences in central tendency (Wilcoxon Rank-Sum) and distribution (Kolmogorov-Smirnov) for slab load related variables. Bold signifies significant ($p \leq 0.05$) differences. Observations are grouped by plot for the upper and lower sites separately.

Variable	Part of Study Site	Plots Involved	Time-Step (Days)	Wilcoxon Rank-Sum: Change in Centrality?		Kolmogorov-Smirnov: Change in Distribution?	
				p-value	Δ Median	p-value	D-statistic
HSW_{slab} (mm)	Upper-Slope	1* → 3	8	7.77E-01	7.25E-01	4.84E-01	0.46
		3 → 4	6	**7.86E-05**	**4.31E+00**	**5.00E-06**	**0.92**
	Lower-Slope	1* → 2	1	1.93E-01	-3.01E+00	6.64E-02	0.69
		2 → 5	20	**1.65E-05**	**3.82E+01**	**1.92E-07**	**1.00**
V_{slab} (Pa)	Upper-Slope	1* → 3	8	7.77E-01	7.11E+00	4.84E-01	0.46
		3 → 4	6	**7.86E-05**	**4.22E+01**	**5.00E-06**	**0.92**
	Lower-Slope	1* → 2	1	1.93E-01	-2.95E+01	6.64E-02	0.69
		2 → 5	20	**1.65E-05**	**3.75E+02**	**1.92E-07**	**1.00**
N_{slab} (Pa)	Upper-Slope	1* → 3	8	9.07E-01	9.81E+00	7.56E-01	0.38
		3 → 4	6	**4.33E-05**	**3.92E+01**	**3.09E-05**	**0.92**
	Lower-Slope	1* → 2	1	2.11E-01	-2.45E+01	1.97E-01	0.62
		2 → 5	20	**1.57E-05**	**3.33E+02**	**4.52E-06**	**1.00**
τ_{slab} (Pa)	Upper-Slope	1* → 3	8	6.92E-01	1.97E+00	7.68E-01	0.37
		3 → 4	6	**1.03E-03**	**1.79E+01**	**2.87E-03**	**0.69**
	Lower-Slope	1* → 2	1	1.57E-01	-1.68E+01	6.64E-02	0.69
		2 → 5	20	**1.65E-05**	**1.72E+02**	**1.92E-07**	**1.00**

* In upper and lower slope 'Plots' comparisons, Plot 1 contained transect arm adjacent to both related plots.

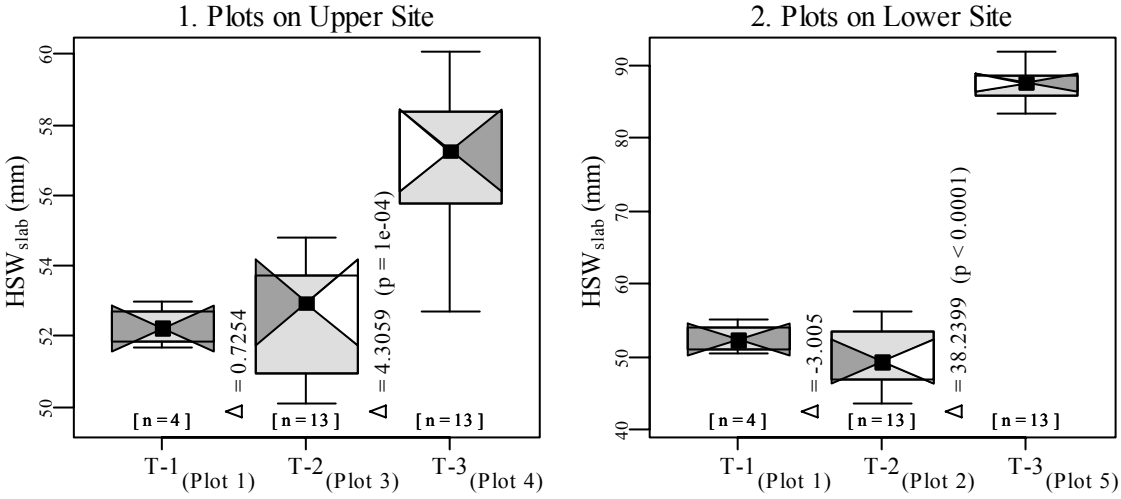

Figure 124. Boxplots illustrating changes of HSW_{slab} (mm) on the (1) upper and (2) lower slope, using all pit observations in Plots 2 through 5. Boxplot properties described on page 137.

Slab Stresses (V_{slab}, N_{slab}, τ_{slab}): On the upper site, a significant increase of the slab vertical-, normal- and shear stresses (V_{slab}, N_{slab} and τ_{slab}, respectively) occurred at the second time-step (Table 25 and Figures 125 - 127). This was related to a small snowfall event between the third and fourth sampling days which caused the signficaint increase of HSW_{slab} (Figure 124.1).

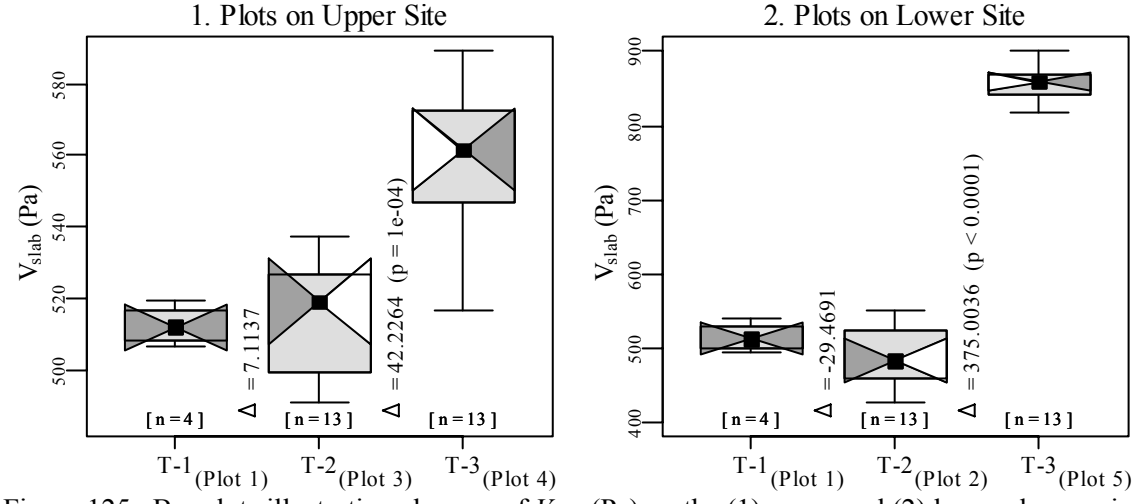

Figure 125. Boxplots illustrating changes of V_{slab} (Pa) on the (1) upper and (2) lower slope, using all pit observations in Plots 2 through 5. Boxplot properties described on page 137.

Two changes were evident on the lower site. An insignificant decrease of the three slab stresses occurred between Plots 1 and 2 (Table 25 and Figures 125 - 127) associated with a similar change of HSW_{slab}. Large significant increases of all three slab stresses were observed at the second time-step, which were the cumulative result of both snowfall events that preceded the sampling of Plot 5.

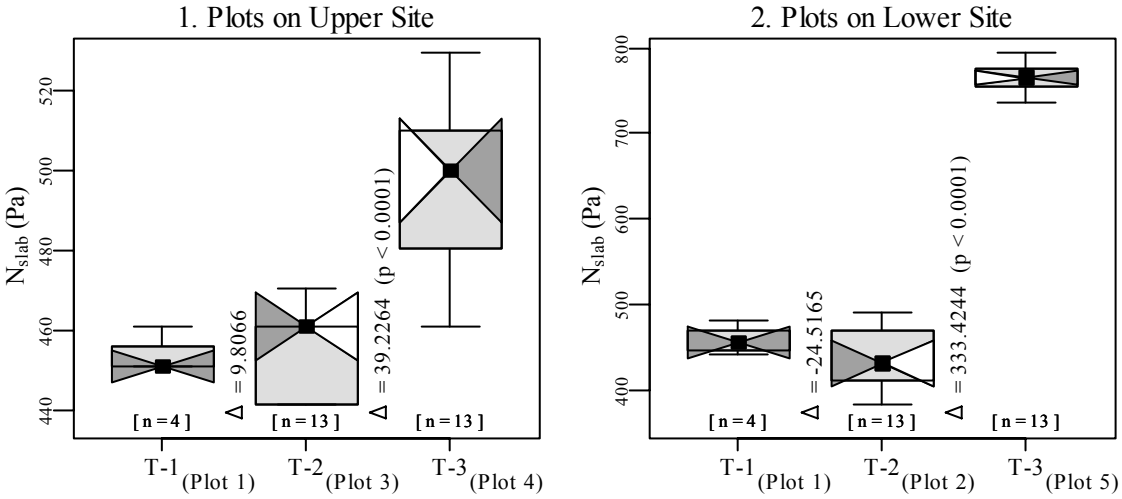

Figure 126. Boxplots illustrating changes of N_{slab} (Pa) on the (1) upper and (2) lower slope, using all pit observations in Plots 2 through 5. Boxplot properties described on page 137.

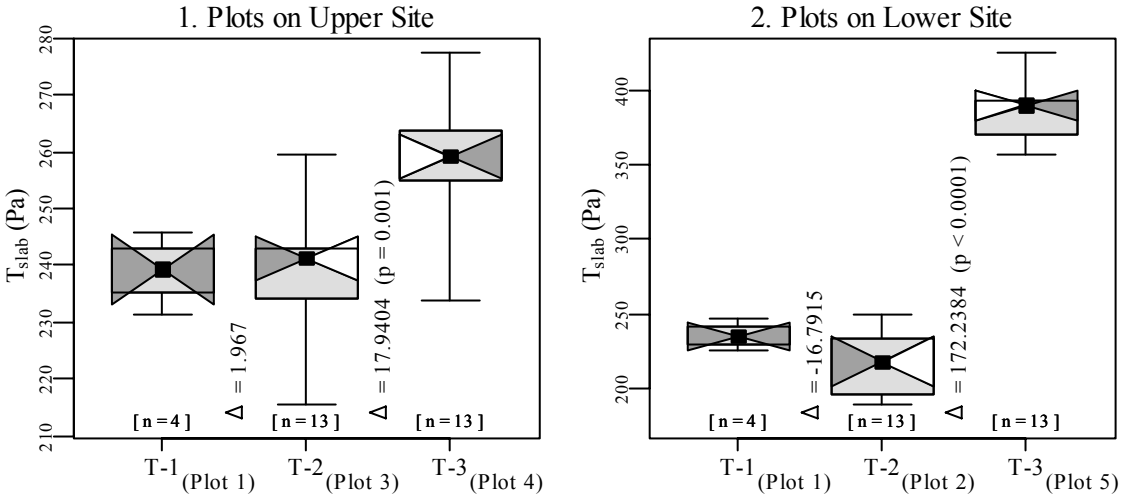

Figure 127. Boxplots illustrating changes of τ_{slab} (Pa) on the (1) upper and (2) lower slope, using all pit observations in Plots 2 through 5. Boxplot properties described on page 137.

Shear Strength (τ_∞): On the upper site, τ_∞ increased significantly at the second time-step. Strengthening at the second time-step was significant, with a change in median value of 100 Pa (Table 26 and Figure 128). This indicates an average daily strengthening of 17 Pa·day^{-1} occurred during this later time-step. At the first time-step, changes between sub-plots were statistically insignificant but there is some evidence ($p = 0.15$) that τ_∞ may have increased by 67 Pa, which would equate to an approximate rate of strengthening of 8 Pa·day^{-1}.

Table 26. Non-parametric tests of differences in central tendency and distribution of τ_∞, between sub-plots on upper (I) and lower (II) site. Bold signifies significant ($p \leq 0.05$) change.

Shear Strength τ_∞ (Pa)	Slope Extent	Plots Involved	Time-Step (Days)	Wilcoxon Rank-Sum: Change in Centrality?		Kolmogorov-Smirnov: Change in Distribution?	
				p-value	Δ Median	p-value	D-statistic
I. Upper-Slope	Sub-plots	1 → 3	8	1.5E-01	66.67	1.0E-01	0.40
		3 → 4	6	**2.2E-02**	**100.21**	5.6E-02	0.44
II. Lower-Slope	Sub-plots	1 → 2	1	**7.7E-04**	**-184.25**	**1.0E-03**	**0.64**
		2 → 5	20	**6.5E-06**	**255.32**	**1.3E-05**	**0.78**

* In upper and lower slope 'Plots' comparisons, Plot 1 contained transect arm adjacent to both related plots.

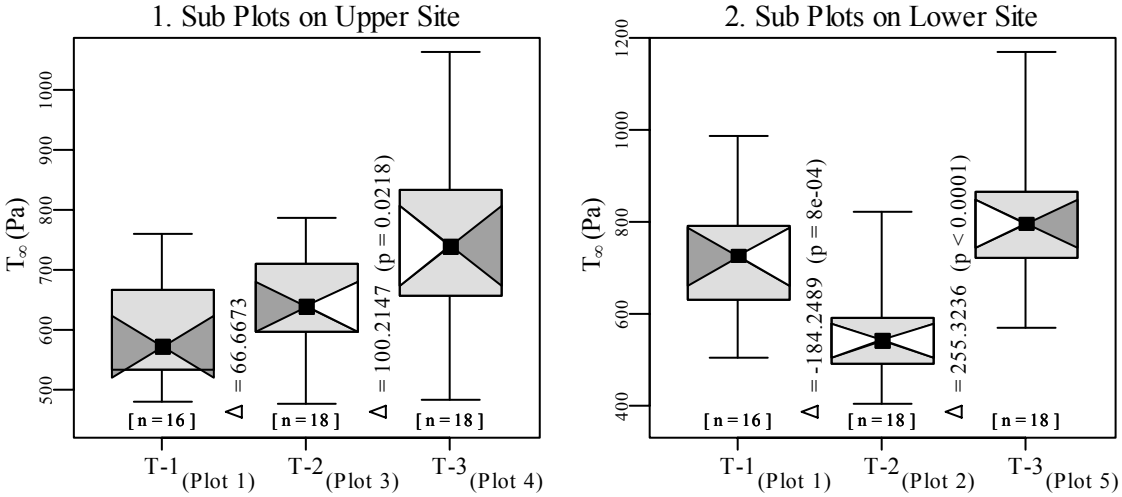

Figure 128. Boxplots illustrating changes in τ_∞ on the (1) upper and (2) lower slope, using observations in sub-plots. Boxplot properties described on page 137.

On the lower site, the first time-step possessed a significant decrease of τ_∞ (Table 26, Figure 128). Given that Plots 1 and 2 were sampled on consecutive days, it is unlikely that this change was temporally based. The surface hoar may have been weaker at Plot 2 than at Plot 1 due to a spatial discrepancy in load-related strengthening. A change of 184 Pa occurred over the 20 day period. This equated to an approximate rate of strengthening of 9.2 Pa·day^{-1}.

Residual Shear Strength (τ_{resid}): There was some evidence (p = 0.1 and 0.06) that τ_{resid} increased at both time-steps on the upper site. The apparent increase of τ_{resid} over time on the upper site would equate to 10.4 Pa·day^{-1} and 12.7 Pa·day^{-1} for the two time-steps. Yet, these changes were not significant (Table 27 and Figure 129).

Table 27. Non-parametric tests of differences in central tendency and distribution of τ_{resid}, between sub-plots on upper (I) and lower (II) site. Bold signifies significant ($p \leq 0.05$) change.

τ_{resid} (Pa)	Slope Extent	Plots Involved	Time-Step (Days)	Wilcoxon Rank-Sum: Change in Centrality?		Kolmogorov-Smirnov: Change in Distribution?	
				p-value	Δ Median	p-value	D-statistic
I. Upper-Slope	Sub-plots	1 → 3	8	1.01E-01	8.33E+01	1.02E-01	3.96E-01
		3 → 4	6	5.56E-02	7.62E+01	1.32E-01	3.89E-01
II. Lower-Slope	Sub-plots	1 → 2	1	**2.84E-03**	**-1.71E+02**	**3.62E-03**	**5.83E-01**
		2 → 5	20	9.67E-02	8.88E+01	1.32E-01	3.89E-01

* In upper and lower slope 'Plots' comparisons, Plot 1 contained transect arm adjacent to both related plots.

On the lower site τ_{resid} decreased significantly at the first time-step (Table 27 and Figure 129.2). The second time-step on the lower site contained no significant change of τ_{resid}, unlike τ_∞. This lack of change for τ_{resid} shows that the difference between τ_∞ and τ_{slab} did not change between the two days. So, despite significant strengthening, evident through an increase of τ_∞ over the 20 day period (between the sampling of Plots 2 and 5),

the significant increase of τ_{slab} (due to the snowfall event preceding Plot 5 sampling) caused τ_{resid} to remain unchanged.

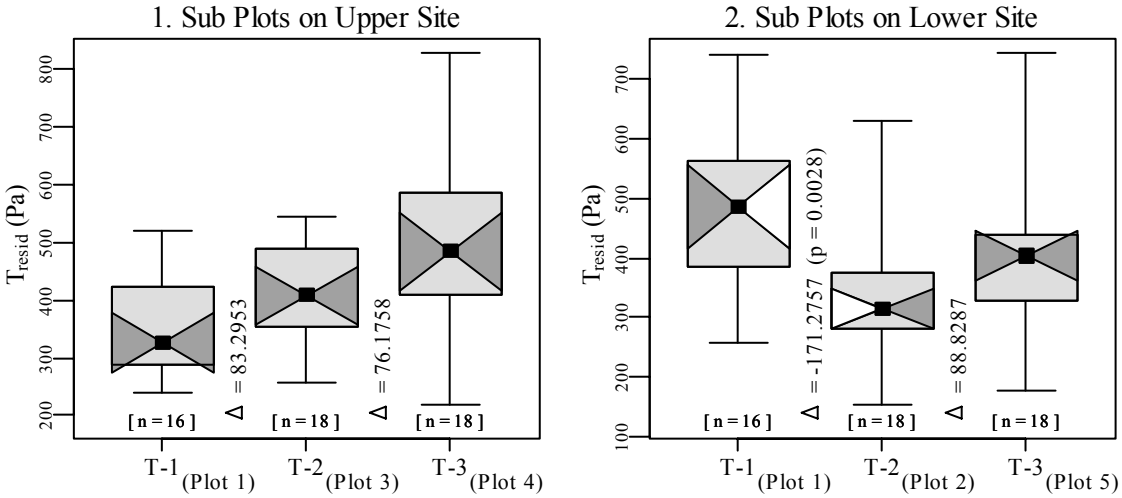

Figure 129. Boxplots illustrating changes in τ_{resid} on the (1) upper and (2) lower slope, using observations in sub-plots. Boxplot properties described on page 137.

Stability Index (*S*): Examining the upper site, *S* appeared to increase at both time-steps. However, at these 8 and 6 day intervals the changes were statistically insignificant (Table 28 and Figure 130). The lower site possessed a near opposite trend (Table 28 and Figure 130). The significant decrease in stability between Plots 1 and 2 resulted from significantly lower τ_{∞} at Plot 2. The significant decrease of *S* between plots 2 and 5 can be attributed to the significant increase in τ_{slab}, that was caused by both snowfall events.

Table 28. Non-parametric tests of differences in central tendency and distribution of *S* between sub-plots on upper (I) and lower (II) site. Bold signifies significant ($p \leq 0.05$) change.

S	Slope Extent	Plots Involved	Time-Step (Days)	Wilcoxon Rank-Sum: Change in Centrality?		Kolmogorov-Smirnov: Change in Distribution?	
				p-value	Δ Median	p-value	D-statistic
I. Upper-Slope	Sub-plots	1 → 2	8	5.6E-02	0.43	1.0E-01	0.40
		2 → 5	6	1.9E-01	0.19	5.0E-01	0.28
II. Lower-Slope	Sub-plots	1 → 3	1	**2.6E-02**	-0.57	**3.5E-02**	0.47
		3 → 4	20	**1.2E-03**	-0.48	**1.8E-03**	0.61

* In upper and lower slope 'Plots' comparisons, Plot 1 contained transect arm adjacent to both related plots.

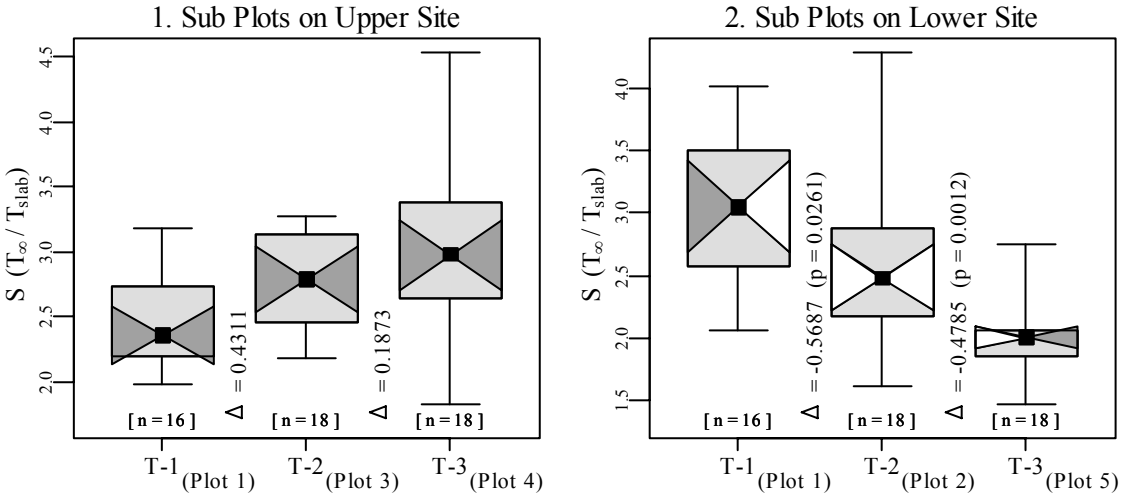

Figure 130. Boxplots illustrating changes in *S* on the (1) upper and (2) lower slope, using observations in sub-plots. Boxplot properties described on page 137.

SMP - Related Stratigraphic Estimates

Slope-Normal Weak Layer Thickness (h_{wl}): On the upper site, h_{wl} appeared to decrease and then increase. This nonsensical observation may be the result of a spatial dataset containing a spatial trend being viewed as a temporal sequence. As described previously, h_{wl} possessed a highly significant spatial pattern. At initial conditions it was determined that, in addition to the prominent up-slope trend of h_{wl}. the weak layer was slightly thinner on the right side of the slope than on the left side. Hence, it could be expected that, if no change occurred in h_{wl} over time, the temporal analysis h_{wl} would show a decrease at the first time-step and then an increase on the second time-step. This is what was observed at the upper site (Figure 131 and Table 29).[11] On the lower slope, no significant differences existed between the three involved Plots (Figure 131).

[11] Since the development of these methods, more effective spatio-temporal patterns have been applied by Trautman et al. (2006), Hendrix and Birkeland (2008) and Lutz and Trautman (in prep).

Minimum h_{wl} values at Plot 1 were far smaller than those at Plot 2 and 5. This may be evidence of a stronger weak layer at Plot 1 than at Plot 2.

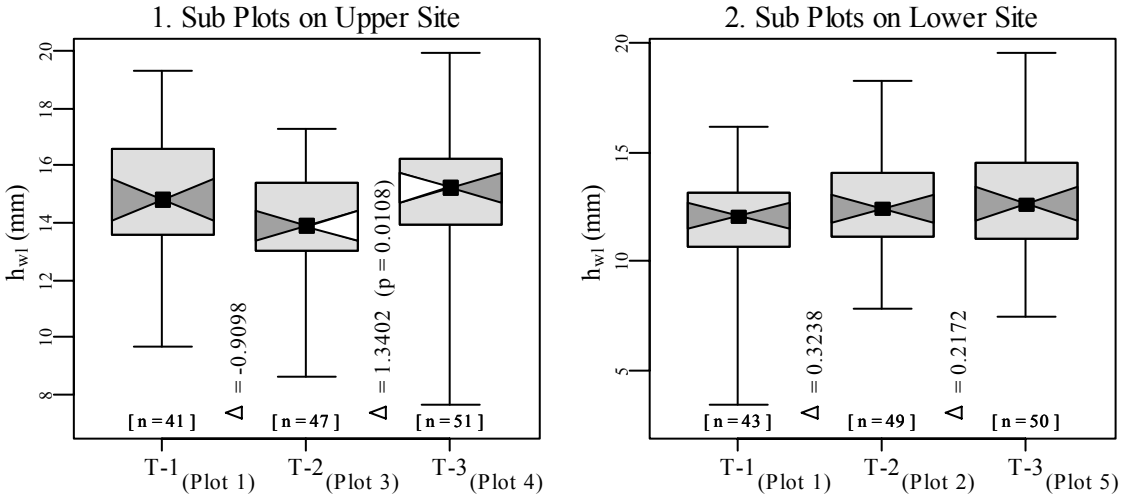

Figure 131. Boxplots illustrating changes in h_{wl} on the (1) upper and (2) lower slope, using observations in sub-plots. Boxplot properties described on page 137.

Table 29. Non-parametric tests of differences in central tendency and distribution of h_{wl}, between sub-plots on upper (I) and lower (II) site. Bold signifies significant ($p \leq 0.05$) change.

h_{wl} (mm)	Slope Extent	Plots Involved	Time-Step (Days)	Wilcoxon Rank-Sum: Change in Centrality?		Kolmogorov-Smirnov: Change in Distribution?	
				p-value	Δ Median	p-value	D-statistic
I. Upper-Slope	Sub-plots	1 → 3	8	8.6E-02	-9.1E-01	9.0E-02	0.26
		3 → 4	6	**1.1E-02**	**1.3E+00**	**4.3E-02**	**0.28**
II. Lower-Slope	Sub-plots	1 → 2	1	3.4E-01	3.2E-01	4.2E-01	0.18
		2 → 5	20	7.0E-01	2.2E-01	7.4E-01	0.14

* In upper and lower slope 'Plots' comparisons, Plot 1 contained transect arm adjacent to both related plots.

Slope-Normal Base Thickness (h_{base}): On the upper site, both time-steps indicated decreases of h_{base}, the latter of which was significant (Table 30 and Figure 132). This decrease of h_{base} may indicate thinning of the snowpack base. On the upper site, a 2.4 cm or 2.3 % decrease in base height (h_{base}) appeared to have occurred over the 6 day period. The lower site also indicated thinning occurred during the second time-step (Table 30 and Figure 132). A small (i.e., 0.7 cm) but significant increase of h_{base} between sub-plots of

Plots 1 and 2 indicates that a slight local spatial pattern may have existed (not at the scale of adjacent plots but rather at the scale of adjacent sub-plots).

Table 30. Non-parametric tests of differences in central tendency and distribution of h_{base}, between sub-plots on upper (I) and lower (II) site. Bold signifies significant ($p \leq 0.05$) change.

h_{base} (cm)	Slope Extent	Plots Involved	Time-Step (Days)	Wilcoxon Rank-Sum: Change in Centrality?		Kolmogorov-Smirnov: Change in Distribution?	
				p-value	Δ Median	p-value	D-statistic
I. Upper-Slope	Sub-plots	1 → 3	8	2.8E-01	-3.1E+00	2.6E-01	0.21
		3 → 4	6	**3.4E-03**	**-2.4E+00**	**2.0E-02**	**0.31**
II. Lower-Slope	Sub-plots	1 → 2	1	**4.8E-02**	**7.3E-01**	**4.3E-02**	**0.28**
		2 → 5	20	**7.9E-04**	**-2.3E+00**	**1.0E-02**	**0.32**

* In upper and lower slope 'Plots' comparisons, Plot 1 contained transect arm adjacent to both related plots.

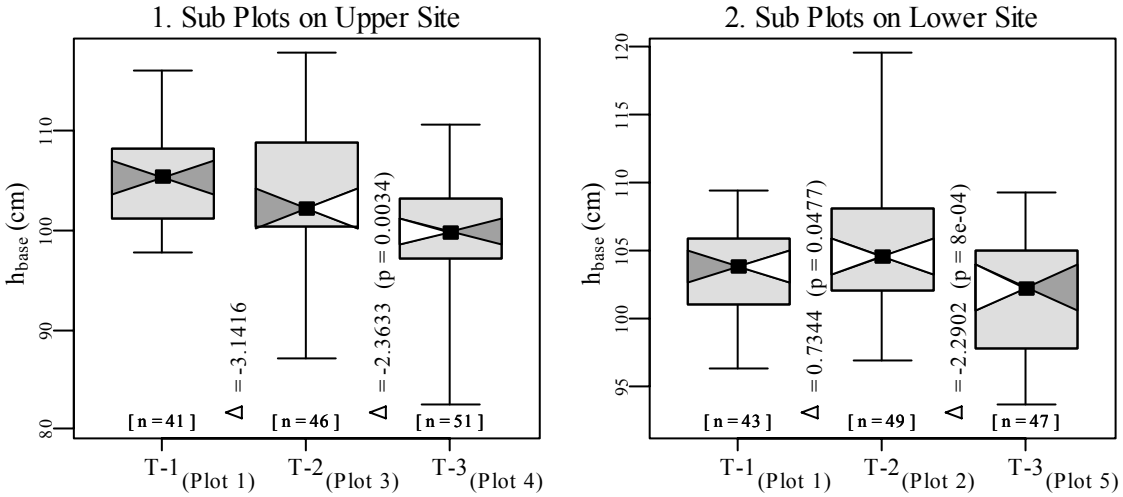

Figure 132. Boxplots illustrating changes in h_{base} on the (1) upper and (2) lower slope, using observations in sub-plots. Boxplot properties described on page 137.

Slope-Normal Slab Thickness (h_{slab}): Significant changes in h_{slab} occurred at both time-steps on both the upper and lower site (Table 31). On the upper site, h_{slab} decreased significantly at the first time-step (Figure 133). This was likely caused by settling of the slab over this eight day period. A significant increase of h_{slab} occurred at the second time-step. This was associated with the small loading event between these sampling days.

Table 31. Non-parametric tests of differences in central tendency and distribution of h_{slab}, between sub-plots on upper (I) and lower (II) site. Bold signifies significant ($p \leq 0.05$) change.

h_{slab} (mm)	Slope Extent	Plots Involved	Time-Step (Days)	Wilcoxon Rank-Sum: Change in Centrality?		Kolmogorov-Smirnov: Change in Distribution?	
				p-value	Δ Median	p-value	D-statistic
I. Upper-Slope	Sub-plots	1 → 3	8	**7.3E-12**	**-1.3E+01**	**7.2E-13**	**7.6E-01**
		3 → 4	6	2.1E-10	1.4E+01	**1.1E-09**	**6.3E-01**
II. Lower-Slope	Sub-plots	1 → 2	1	**4.4E-03**	**6.1E+00**	**7.6E-03**	**3.4E-01**
		2 → 5	20	**1.0E-17**	**2.2E+02**	**-2.2E-16**	**1.0E+00**

***** In upper and lower slope 'Plots' comparisons, Plot 1 contained transect arm adjacent to both related plots.

On the lower site, h_{slab} increased significantly at both time-steps (Table 31 and Figure 133). The first increase in median h_{slab} of 5-6 mm was probably due to a spatial pattern, given that it did not snow between these sampling days. The second increase, a 223 mm change of median h_{slab}, was caused by the large snowfall event.

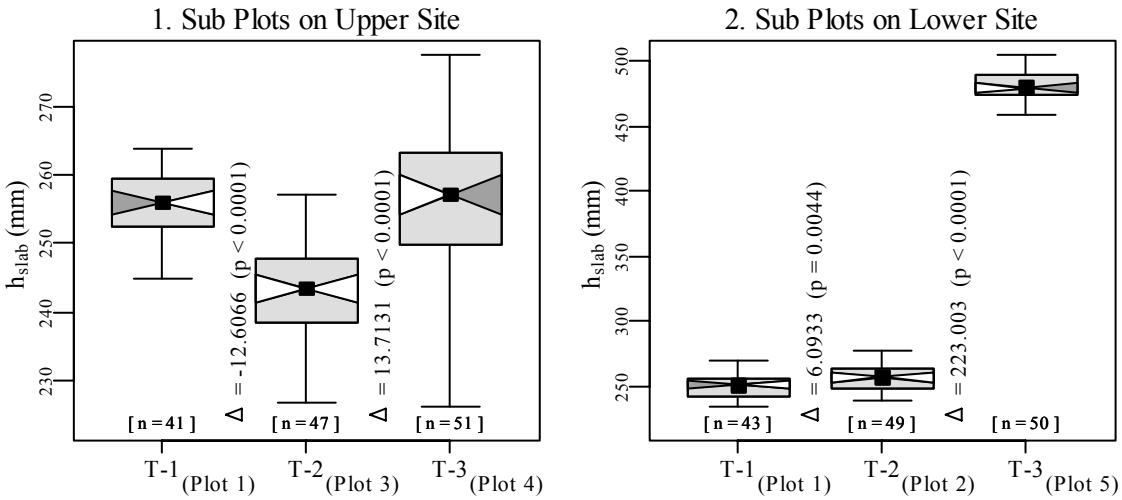

Figure 133. Boxplots illustrating changes in h_{slab} on the (1) upper and (2) lower slope, using observations in sub-plots. Boxplot properties described on page 137.

Microstructural Estimates of Weak Layer

Mean Rupture Force (f_m): On the upper site, f_m did not change significantly at the first time-step (Table 32 and Figure 134). At the second time-step a significant decrease

in f_m occurred between the sub-plots of Plots 3 and 4. The decrease of the residual bond strength at Plot 4 may be related to a small snowfall event which proceeded that sampling day. No significant change of f_m occurred on the lower site (Table 32 and Figure 134). This lack of change is similar to what was observed for τ_{resid}.

Table 32. Non-parametric tests of differences in central tendency and distribution of f_m, between sub-plots on upper (I) and lower (II) site. Bold signifies significant ($p \leq 0.05$) change.

f_m	Slope Extent	Plots Involved	Time-Step (Days)	Wilcoxon Rank-Sum Test: Change in Centrality?		Kolmogorov-Smirnov Test: Change in Distribution?	
				p-value	Δ Median	p-value	D-statistic
I. Upper-Slope	Sub-plots	1 → 3	8	1.1E-01	-4.9E-03	3.4E-01	0.166
		3 → 4	6	8.9E-01	-2.1E-03	8.1E-01	0.078
II. Lower-Slope	Sub-plots	1 → 2	1	1.8E-01	-1.1E-02	2.7E-01	0.218
		2 → 5	20	9.3E-01	5.4E-03	3.4E-01	0.202

* In upper and lower slope 'Plots' comparisons, Plot 1 contained transect arm adjacent to both related plots.

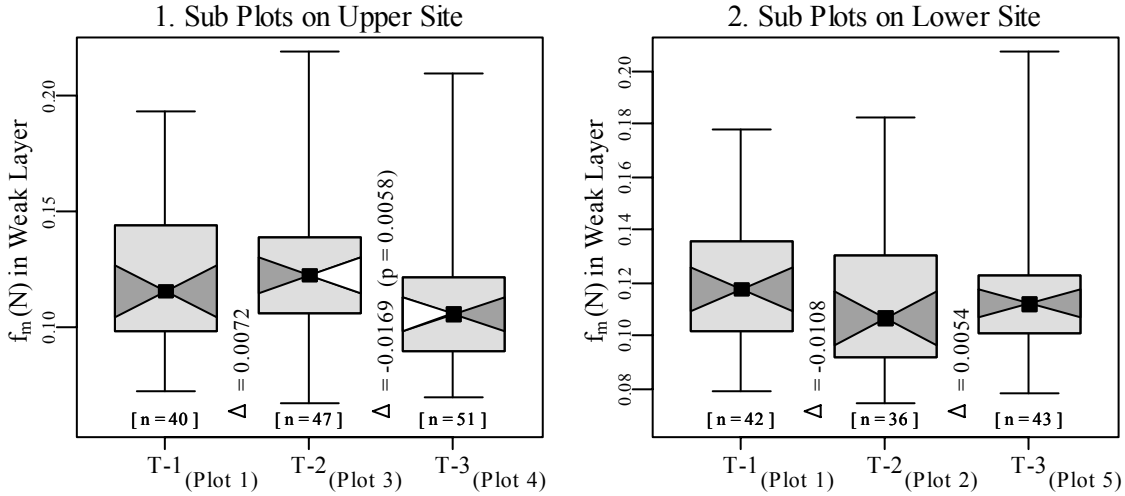

Figure 134. Boxplots illustrating changes in f_m on the (1) upper and (2) lower slope, using observations in sub-plots. Boxplot properties described on page 137.

Maximum Rupture Force (f_{max}): In contrast to f_m, f_{max} decreased significantly on the lower site between Plots 2 and 5 (Table 33 and Figure 135). This indicates that while f_m remained unchanged, f_{max} shifted to lower values. It is likely that this difference in f_{max}

was related to the loading event that occurred directly before Plot 5 was sampled. No significant changes in f_{max} of the weak layer occurred on the upper site (Figure 135).

Table 33. Non-parametric tests of differences in central tendency and distribution of f_{max}, between sub-plots on upper (I) and lower (II) site. Bold signifies significant ($p \leq 0.05$) change.

f_{max} (N)	Slope Extent	Plots Involved	Time-Step (Days)	Wilcoxon Rank-Sum Test: Change in Centrality?		Kolmogorov-Smirnov Test: Change in Distribution?	
				p-value	Δ Median	p-value	D-statistic
I. Upper-Slope	Sub-plots	1 → 3	8	5.5E-01	-1.0E-01	2.1E-01	0.220
		3 → 4	6	1.0E+00	2.9E-02	5.1E-01	0.158
II. Lower-Slope	Sub-plots	1 → 2	1	1.6E-01	-1.3E-01	2.7E-01	0.218
		2 → 5	20	**5.1E-03**	**-1.5E-01**	**5.0E-02**	**0.295**

* In upper and lower slope 'Plots' comparisons, Plot 1 contained transect arm adjacent to both related plots.

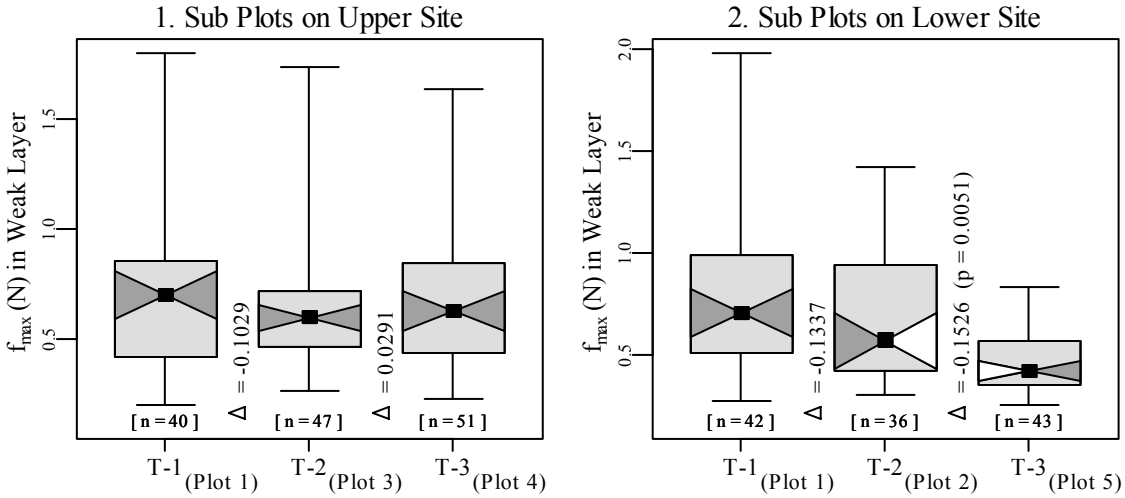

Figure 135. Boxplots illustrating changes in f_{max} on the (1) upper and (2) lower slope, using observations in sub-plots. Boxplot properties described on page 137.

Rupture Force Coefficient of Variation (f_{cv}): No significant change of the coefficient of variation of rupture force (f_{cv}) within the weak layer occurred on the upper site (between Plots 3 and 4) (Table 34 and Figure 136), despite aging and strengthening. On the lower site, f_{cv} decreased significantly between Plots 2 and 5 (Table 34 and Figure

136). This indicates that the micro-variance became smaller (or the ruptures values became more uniform) directly after the loading event.

Table 34. Non-parametric tests of differences in central tendency and distribution of f_{cv}, between plots and sub-plots on upper (I) and lower (II) site. Bold signifies significant ($p \leq 0.05$) change.

f_{cv}	Slope Extent	Plots Involved	Time-Step (Days)	Wilcoxon Rank-Sum Test: Change in Centrality?		Kolmogorov-Smirnov Test: Change in Distribution?	
				p-value	Δ Median	p-value	D-statistic
I. Upper-Slope	Sub-plots	1 → 3	8	1.3E-01	-8.2E-02	7.5E-02	0.266
		3 → 4	6	1.3E-01	5.6E-02	3.3E-01	0.184
II. Lower-Slope	Sub-plots	1 → 2	1	1.9E-01	-8.0E-02	3.5E-01	0.202
		2 → 5	20	**1.6E-03**	**-1.2E-01**	**5.2E-03**	**0.378**

* In upper and lower slope 'Plots' comparisons, Plot 1 contained transect arm adjacent to both related plots.

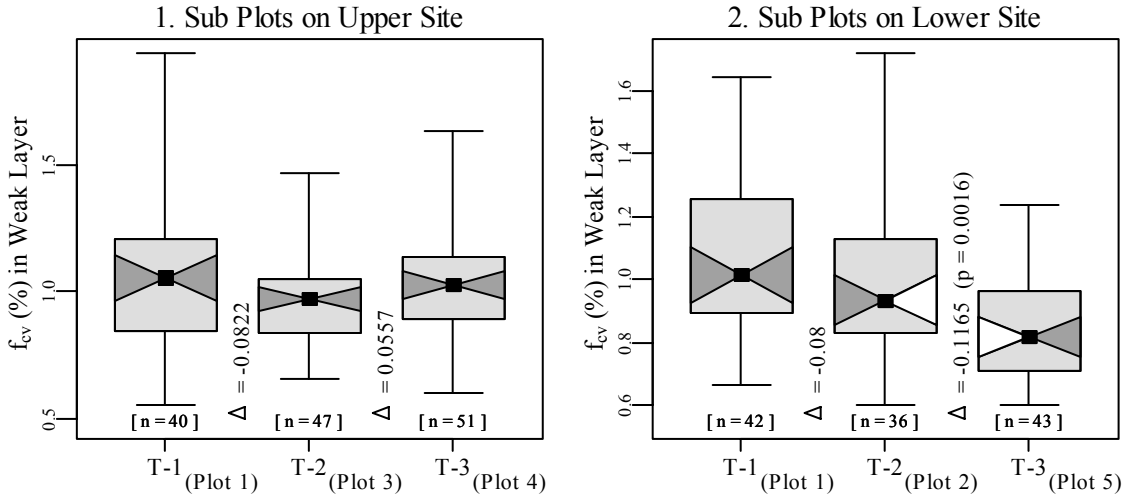

Figure 136. Boxplots illustrating changes in f_{cv} on the (1) upper and (2) lower slope, using observations in sub-plots. Boxplot properties described on page 137.

Structural Element Length Characteristics (L, L_{max}): On the upper and lower sites, no significant changes occurred in L during the first time-step. On the upper site there was a significant decrease in L between Plots 3 and 4 (Table 35 and Figure 137). A probable cause for this observation is that deformation within the weak layer over this sampling period resulted in more closely spaced structures. On the lower site, a

significant increase of microstructural element lengths (*L)* occurred within the weak layer between Plots 2 and 5 (Table 35 and Figure 137).

Table 35. Non-parametric tests of differences in central tendency and distribution of L and L_{max}, between sub-plots on upper (I) and lower (II) site. Bold signifies significant ($p \leq 0.05$) change.

Variable	Slope Extent	Plot Extent	Plots Involved	Time-Step (Days)	Wilcoxon Rank-Sum Test: Change in Centrality?		Kolmogorov-Smirnov Test: Change in Distribution?	
					p-value	Δ Median	p-value	D-statistic
L	I. Upper-Slope	Sub-plots	1 → 3	8	4.1E-01	-6.5E-02	6.0E-01	0.164
			3 → 4	6	**1.3E-02**	**-1.1E-01**	**1.6E-02**	**0.315**
	II. Lower-Slope	Sub-plots	1 → 2	1	4.0E-01	3.3E-02	3.8E-01	0.206
			2 → 5	20	**6.1E-04**	**1.2E-01**	**4.7E-03**	**0.393**
L_{max}	I. Upper-Slope	Sub-plots	1 → 3	8	1.7E-01	-1.6E-01	2.3E-01	0.224
			3 → 4	6	2.8E-01	-6.1E-02	3.6E-01	0.187
	II. Lower-Slope	Sub-plots	1 → 2	1	6.7E-01	-9.7E-03	5.4E-01	0.183
			2 → 5	20	**4.4E-03**	**1.7E-01**	**2.4E-02**	**0.335**

* In upper and lower slope 'Plots' comparisons, Plot 1 contained transect arm adjacent to both related plots.

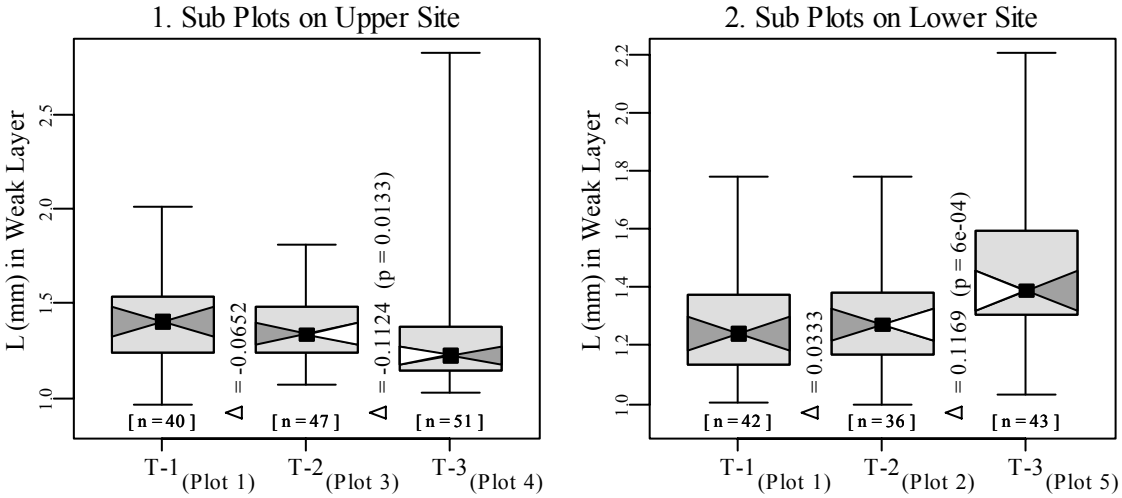

Figure 137. Boxplots illustrating changes in L on the (1) upper and (2) lower slope, using observations in sub-plots. Boxplot properties described on page 137.

The maximum structural element length (L_{max}) possessed similar characteristics to L (Table 35). A slight decrease of L_{max} appeared to occur at the upper site, though no change was significant (Figure 138). The significant increases of L and L_{max} on the lower

site between Plots 2 and 5 (Figure 138) were likely related to the significant loading event.

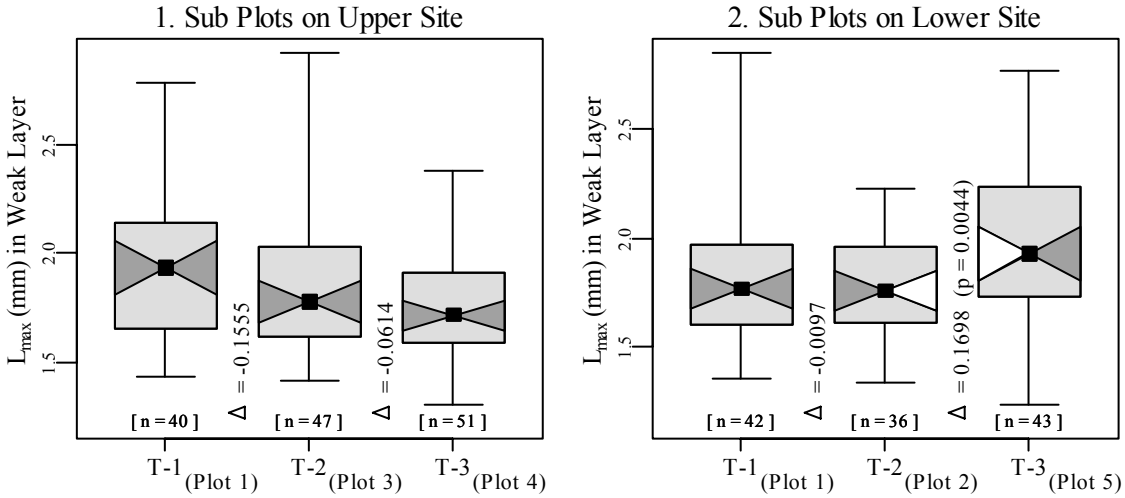

Figure 138. Boxplots illustrating changes in L_{max} on the (1) upper and (2) lower slope, using observations in sub-plots. Boxplot properties described on page 137.

Micro-Strength (σ_{micro}): Examining the upper and lower slopes separately revealed temporal patterns in σ_{micro} (Table 36 and Figure 139). On the upper site, no significant change of σ_{micro} occurred between Plots 3 and 4 at the sub-plot scale. Evidently, the significant decrease of L was offset by small f_m values, which may have been associated with the small loading event that occurred before Plot 4 was sampled.

Table 36. Non-parametric tests of differences in central tendency and distribution of σ_{micro}, between sub-plots on upper (I) and lower (II) site. Bold signifies significant ($p \leq 0.05$) change.

σ_{micro} (N·mm^{-2})	Slope Extent	Plots Involved	Time-Step (Days)	Wilcoxon Rank-Sum Test: Change in Centrality?		Kolmogorov-Smirnov Test: Change in Distribution?	
				p-value	Δ Median	p-value	D-statistic
I. Upper-Slope	Sub-plots	1 → 3	8	1.7E-01	-1.6E-01	2.3E-01	0.224
		3 → 4	6	2.8E-01	-6.1E-02	3.6E-01	0.187
II. Lower-Slope	Sub-plots	1 → 2	1	6.7E-01	-9.7E-03	5.4E-01	0.183
		2 → 5	20	**4.4E-03**	**1.7E-01**	**2.4E-02**	**0.335**

* In upper and lower slope 'Plots' comparisons, Plot 1 contained transect arm adjacent to both related plots.

On the lower slope, a large significant decrease in σ_{micro} occurred between sub-plots of Plots 2 and 5 (Figure 139). This significant decrease of σ_{micro} was the result of L increasing significantly.

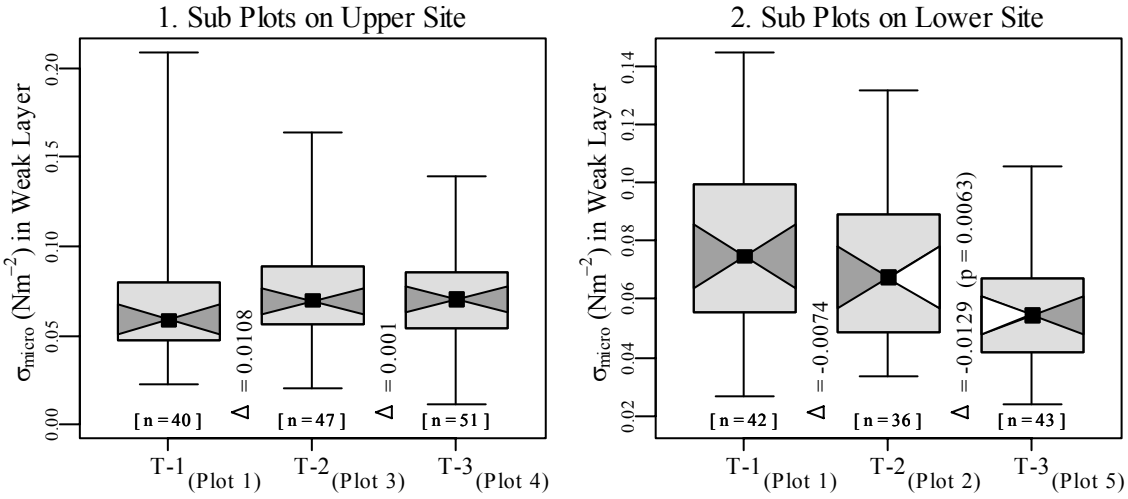

Figure 139. Boxplots illustrating changes in σ_{micro} on the (1) upper and (2) lower slope, using observations in sub-plots. Boxplot properties described on page 137.

Microstructural Estimates of Super-stratum

Mean Rupture Force (f_m): Significant increases of f_m of the super-stratum occurred on the upper site at the first time-step and on the lower site at the second time-step (Table 37 and Figure 140). The later of these changes indicates that the residual strength of the super-stratum increased, despite a larger slab load. This may have been possible due to the small and numerous structures. As with f_m of the weak layer, f_m of the super-stratum decreased initially between Plots 1 and 2 on the lower site. The drop in f_m may be the result of weaker microstructure at Plot 2 resulting from the lighter slab load at Plot 2, which could have hindered deformation within the super-stratum.

Table 37. Non-parametric tests of differences in central tendency and distribution of f_m, between sub-plots on upper (I) and lower (II) site. Bold signifies significant ($p \leq 0.05$) change.

f_m (N)	Slope Extent	Plots Involved	Time-Step (Days)	Wilcoxon Rank-Sum Test: Change in Centrality?		Kolmogorov-Smirnov Test: Change in Distribution?	
				p-value	Δ Median	p-value	D-statistic
I. Upper-Slope	Sub-plots	1 → 3	8	**3.5E-02**	**3.3E-03**	6.1E-02	0.27
		3 → 4	6	8.4E-02	5.1E-03	7.1E-02	0.25
II. Lower-Slope	Sub-plots	1 → 2	1	2.8E-01	-3.1E-03	2.9E-01	0.21
		2 → 5	20	**6.5E-03**	**8.6E-03**	**9.1E-03**	**0.36**

* In upper and lower slope 'Plots' comparisons, Plot 1 contained transect arm adjacent to both related plots.

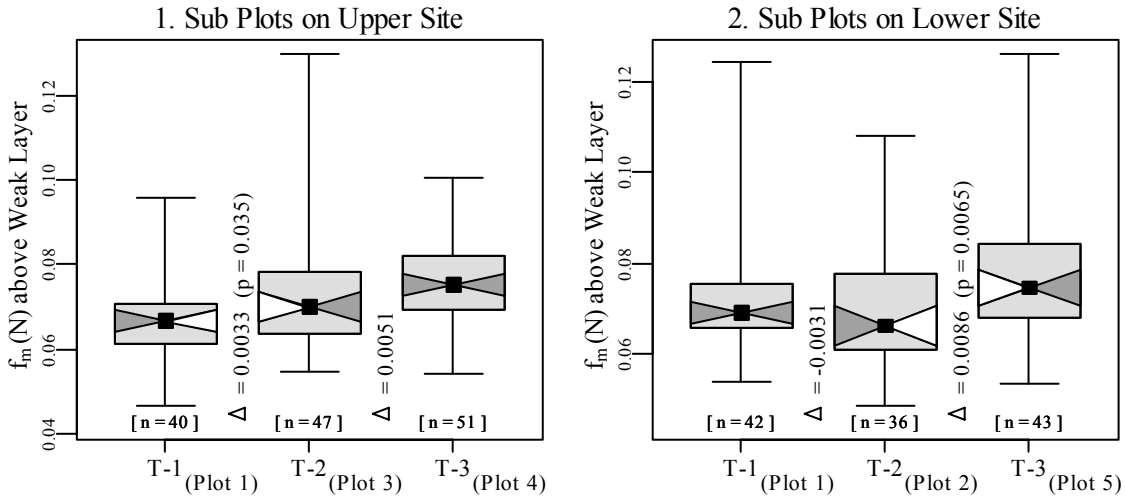

Figure 140. Boxplots illustrating changes in f_m on the (1) upper and (2) lower slope, using observations in sub-plots. Boxplot properties described on page 137.

Maximum Rupture Force (f_{max}): The upper site experienced an increase in f_{max} of the super-stratum (or slab) at the second time-step, which indicates strengthening occurred (Table 38 and Figure 141). The lower site experienced no significant change in f_{max} of the slab at either time-step (Table 38 and Figure 141).

Table 38. Non-parametric tests of differences in central tendency and distribution of f_{max}, between sub-plots on upper (I) and lower (II) site. Bold signifies significant ($p \leq 0.05$) change.

f_{max} (N)	Slope Extent	Plots Involved	Time-Step (Days)	Wilcoxon Rank-Sum Test: Change in Centrality?		Kolmogorov-Smirnov Test: Change in Distribution?	
				p-value	Δ Median	p-value	D-statistic
I. Upper-Slope	Sub-plots	1 → 3	8	1.1E-01	1.6E-02	2.1E-01	0.22
		3 → 4	6	**4.1E-03**	**4.5E-02**	**4.3E-04**	**0.40**
II. Lower-Slope	Sub-plots	1 → 2	1	3.7E-01	-1.1E-02	5.7E-01	0.18
		2 → 5	20	1.8E-01	2.3E-02	8.2E-02	0.28

* In upper and lower slope 'Plots' comparisons, Plot 1 contained transect arm adjacent to both related plots.

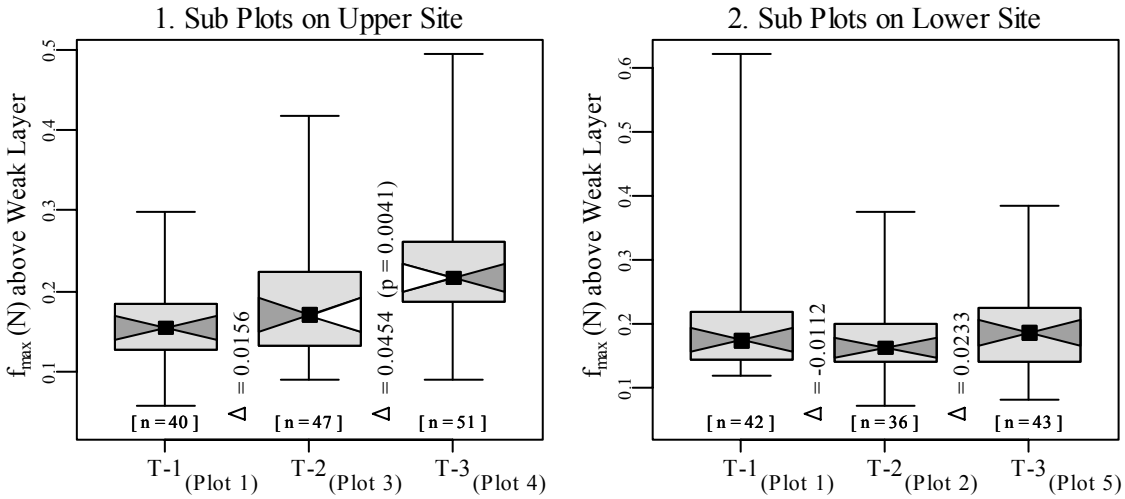

Figure 141. Boxplots illustrating changes in f_{max} on the (1) upper and (2) lower slope, using observations in sub-plots. Boxplot properties described on page 137.

Rupture Force Coefficient of Variation (f_{cv}): On the upper site, a significant increase of f_{cv} of the super-stratum occurred between Plot 3 and 4 (Table 39 and Figure 142). This indicates that micro-variance of the super-stratum increased over time. No significant change occurred in f_{cv} of the super-stratum on the lower site (Table 39, Figure 142). This indicates that either f_{cv} was unaffected by aging and changes in load or, more likely, that an increase in f_{cv} associated with aging was countered by a decrease associated with loading, resulting in no change.

Table 39. Non-parametric tests of differences in central tendency and distribution of f_{cv}, between sub-plots on upper (I) and lower (II) site. Bold signifies significant ($p \leq 0.05$) change.

f_{cv}	Slope Extent	Plots Involved	Time-Step (Days)	Wilcoxon Rank-Sum Test: Change in Centrality?		Kolmogorov-Smirnov Test: Change in Distribution?	
				p-value	Δ Median	p-value	D-statistic
I. Upper-Slope	Sub-plots	1 → 3	8	6.2E-02	2.6E-02	1.8E-01	0.23
		3 → 4	6	**4.4E-03**	**6.0E-02**	**7.2E-03**	**0.33**
II. Lower-Slope	Sub-plots	1 → 2	1	4.1E-01	8.3E-06	4.2E-01	0.19
		2 → 5	20	3.0E-01	2.2E-02	6.7E-01	0.15

* In upper and lower slope 'Plots' comparisons, Plot 1 contained transect arm adjacent to both related plots.

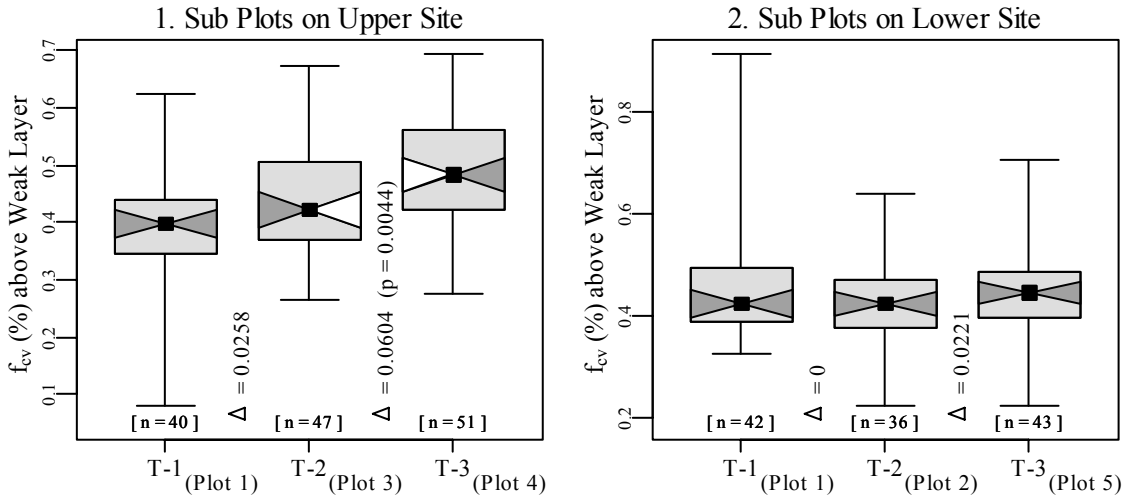

Figure 142. Boxplots illustrating changes in f_{cv} on the (1) upper and (2) lower slope, using observations in sub-plots. Boxplot properties described on page 137.

Structural Element Length (L): A significant change occurred on the second time-step at both the upper and lower sites (Table 40). At the upper site, L of the super-stratum became significantly smaller. This was likely due to an increase in bonds per unit volume or a possible densification (Figure 143). In both cases, strengthen would result from this decrease in structure size.

Table 40. Non-parametric tests of differences in central tendency and distribution of *L,* between sub-plots on upper (I) and lower (II) site. Bold signifies significant ($p \leq 0.05$) change.

L (mm)	Slope Extent	Plots Involved	Time-Step (Days)	Wilcoxon Rank-Sum Test: Change in Centrality?		Kolmogorov-Smirnov Test: Change in Distribution?	
				p-value	Δ Median	p-value	D-statistic
I. Upper-Slope	Sub-plots	1 → 3	8	3.6E-01	2.3E-02	5.0E-01	0.18
		3 → 4	6	**2.1E-06**	**-1.8E-01**	**5.0E-05**	**0.47**
II. Lower-Slope	Sub-plots	1 → 2	1	9.2E-01	-4.3E-03	9.9E-01	0.10
		2 → 5	20	**1.1E-03**	**1.7E-01**	**8.6E-03**	**0.37**

* In upper and lower slope 'Plots' comparisons, Plot 1 contained transect arm adjacent to both related plots.

On the lower site, *L* of the super-stratum became larger when an additional load was added (Figure 143). Both of these significant changes in *L* of the super-stratum were also observed in *L* of the weak layer. These findings highlight the idea that structural changes due to aging or loading events are not limited to weak layers and can be quantified throughout the snowpack using the SMP.

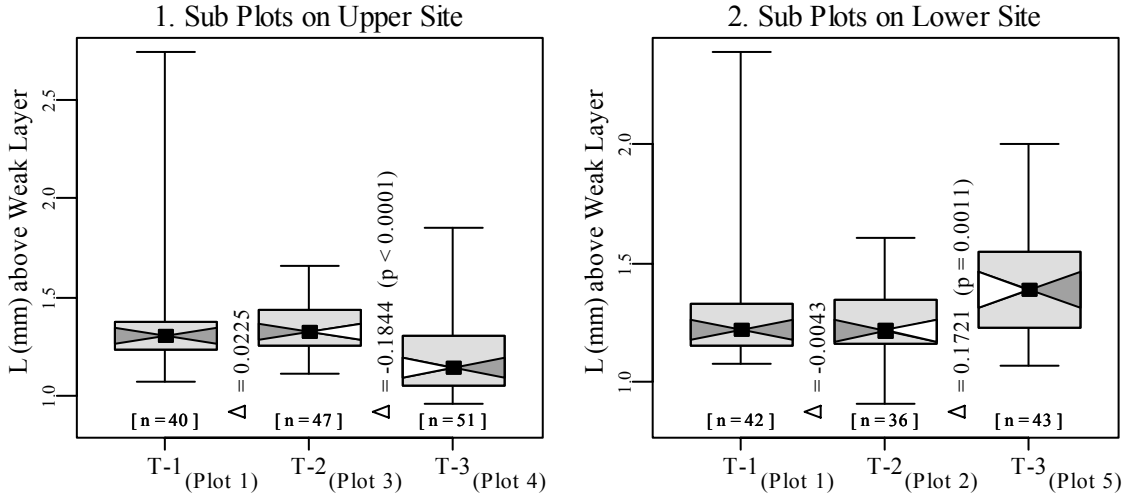

Figure 143. Boxplots illustrating changes in *L* on the (1) upper and (2) lower slope, using observations in sub-plots. Boxplot properties described on page 137.

Maximum Structural Element Length (L_{max}): Similar changes in L_{max} were evident as for *L*, with one additional change: a significant increase in L_{max} also occurred between

Plots 1 and 3 on the upper site (Table 41 and Figure 144). This change cannot be rationalized by loading or aging.

Table 41. Non-parametric tests of differences in central tendency and distribution of L_{max}, between sub-plots on upper (I) and lower (II) site. Bold signifies significant ($p \leq 0.05$) change.

L_{max} (mm)	Slope Extent	Plots Involved	Time-Step (Days)	Wilcoxon Rank-Sum Test: Change in Centrality?		Kolmogorov-Smirnov Test: Change in Distribution?	
				p-value	Δ Median	p-value	D-statistic
I. Upper-Slope	Sub-plots	1 → 3	8	**4.6E-02**	**1.1E-01**	8.6E-02	0.27
		3 → 4	6	**3.7E-04**	**-2.1E-01**	**9.7E-04**	**0.40**
II. Lower-Slope	Sub-plots	1 → 2	1	9.5E-01	2.2E-02	8.2E-01	0.14
		2 → 5	20	**5.0E-03**	**1.2E-01**	6.1E-02	0.30

* In upper and lower slope 'Plots' comparisons, Plot 1 contained transect arm adjacent to both related plots.

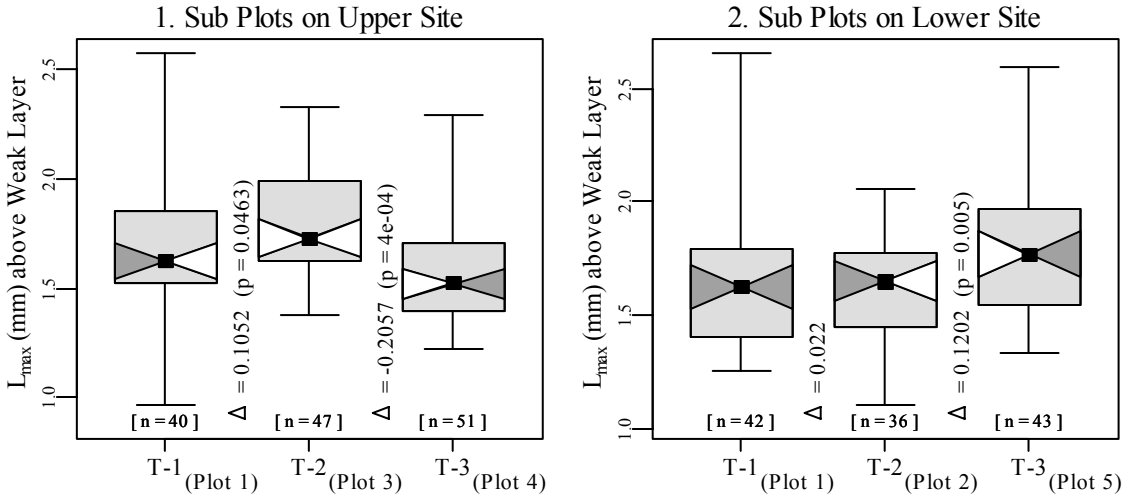

Figure 144. Boxplots illustrating changes in L_{max} on the (1) upper and (2) lower slope, using observations in sub-plots. Boxplot properties described on page 137.

Micro-Strength (σ_{micro}): On the upper site, σ_{micro} increased significantly at the second time-step (Table 42 and Figure 145). These large σ_{micro} values were the result of the decrease in L (the root of the denominator of σ_{micro}) as well as the increase in f_m (the numerator of σ_{micro}), both of which are assumed to be associated with microstructural strengthening. A good indicator that the slab's σ_{micro} is less critical to weak layer strength

and snowpack stability than the weak layer's σ_{micro} is that the decreases in σ_{micro} of the weak layer were larger and more significant than those of the super-stratum.

Table 42. Non-parametric tests of differences in central tendency and distribution of σ_{micro}, between sub-plots on upper (I) and lower (II) site. Bold signifies significant ($p \leq 0.05$) change.

σ_{micro} ($N \cdot mm^{-2}$	Slope Extent	Plots Involved	Time-Step (Days)	Wilcoxon Rank-Sum Test: Change in Centrality?		Kolmogorov-Smirnov Test: Change in Distribution?	
				p-value	Δ Median	p-value	D-statistic
I. Upper-Slope	Sub-plots	1 → 3	8	5.9E-01	-3.9E-04	7.3E-01	0.15
		3 → 4	6	**7.0E-05**	**2.1E-02**	**1.7E-04**	**0.42**
II. Lower-Slope	Sub-plots	1 → 2	1	5.2E-01	-2.4E-03	7.1E-01	0.15
		2 → 5	20	1.9E-01	-5.6E-03	**4.8E-02**	**0.30**

* In upper and lower slope 'Plots' comparisons, Plot 1 contained transect arm adjacent to both related plots.

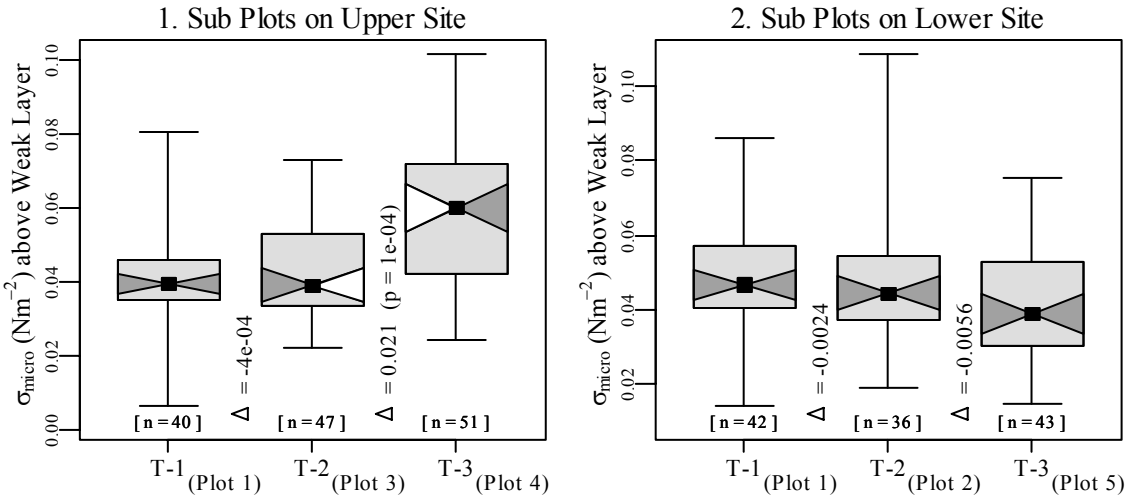

Figure 145. Boxplots illustrating changes in σ_{micro} on the (1) upper and (2) lower slope, using observations in sub-plots. Boxplot properties described on page 137.

Step-Changes in Microstructural Estimates

While absolute values of microstructural estimates are important for ascertaining layer properties, step-changes in these properties and temporal changes of step-changes may also play a critical role in stratigraphic weaknesses and instabilities and in their evolution over time. In these results, a 'step-change' refers to the difference between the

weak layer and super-stratum estimates; a positive value step-change indicates the weak layer possessed a higher value than the super-stratum. To aid in this analysis, stratigraphic visualizations accompany each estimate.

Step-Change of Mean Rupture Force (Δf_m): The mean rupture force (f_m) was generally greater within the weak layer than it was in the super-stratum, resulting in positive Δf_m values (Figure 146). On average, f_m is 0.03 N to 0.05 N greater within the weaker layer than in the super-stratum. (Figure 147). Only rarely is f_m of the super-stratum greater than f_m of the weak layer, evident in box tails of Δf_m reaching below 0 N (Figure 147).

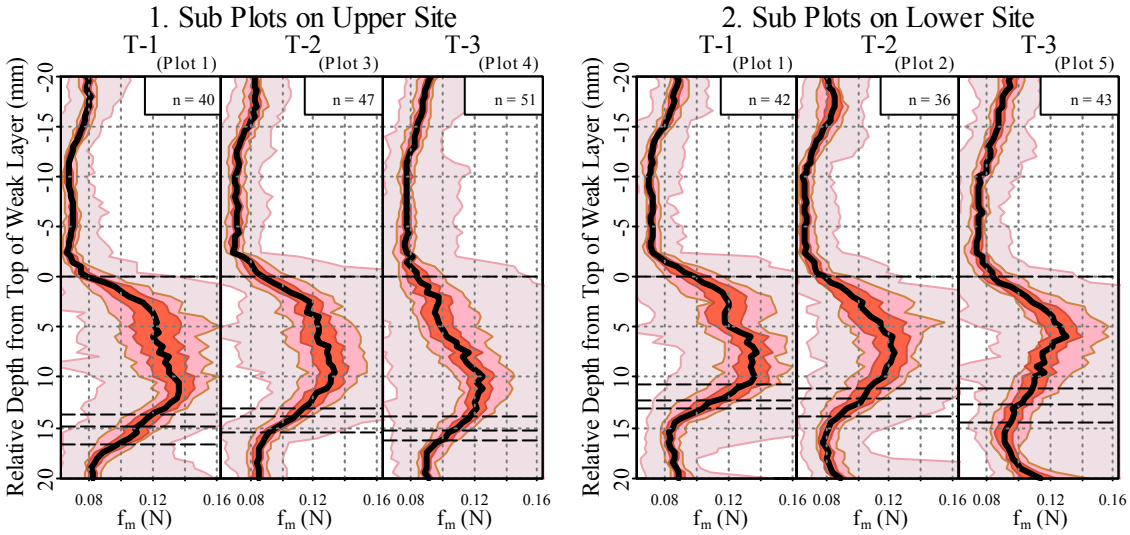

Figure 146. Stratigraphic visualizations of f_m on the (1) upper and (2) lower site summarized for sub-plot spatial extents. Graphic features defined in Figure 32 on page 89

Examining the upper site as a temporal dataset, we see a significant decrease occurred in the step-change of f_m at the second time-step (between Plots 3 and 4) (Table 43 and Figure 147). This change indicates that between these two plots the stratigraphic difference in f_m became smaller. This change toward stratigraphic conformity is due to f_m

increasing significantly within the super-stratum and decreasing significantly within the weak layer (Figure 146).

Table 43. Non-parametric tests of differences in central tendency and distribution of Δf_m, between sub-plots on upper (I) and lower (II) site. Bold signifies significant ($p \leq 0.05$) change.

Δf_m	Slope Extent	Plots Involved	Time-Step (Days)	Wilcoxon Rank-Sum Test: Change in Centrality?		Kolmogorov-Smirnov Test: Change in Distribution?	
				p-value	Δ Median	p-value	D-statistic
I. Upper-Slope	Sub-plots	1 → 3	8	3.4E-01	-2.9E-03	4.7E-01	0.173
		3 → 4	6	**1.8E-02**	**-2.2E-02**	**3.5E-02**	**0.279**
II. Lower-Slope	Sub-plots	1 → 2	1	3.0E-01	-9.9E-03	2.9E-01	0.214
		2 → 5	20	1.3E-01	-4.8E-03	3.1E-01	0.207

* In upper and lower slope 'Plots' comparisons, Plot 1 contained transect arm adjacent to both related plots.

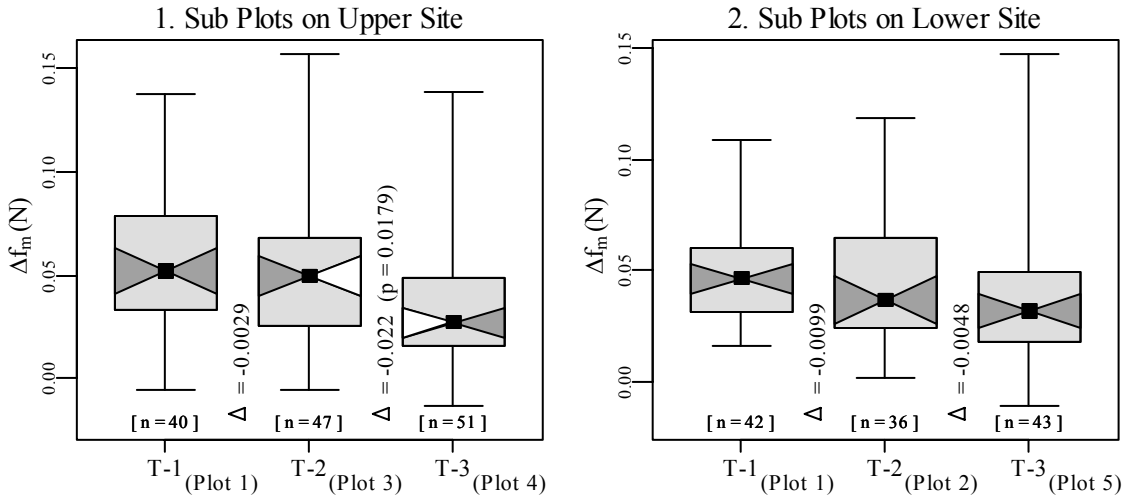

Figure 147. Boxplots illustrating changes in Δf_m on the (1) upper and (2) lower slope, using observations in sub-plots. Boxplot properties described on page 137.

Examining the sub-plots on the lower sites as a temporal dataset, we see no significant decreases in the step-change of f_m (Table 43 and Figure 147). The slight decrease in Δf_m was due to the significant increase of f_m within the super-stratum, which coincided with the loading event. This decrease in the difference between the super-stratum and weak layer's f_m values was statistically insignificant but may be evidence of

step-changes in f_m positively relating to stability. Pielmeier et al. (2006) identified a similar relationship with the step-change of the mean penetration F_m, which is an aggregated measure of force closely related to f_m.

Step-Change of Maximum Rupture Force (Δf_{max}): The maximum rupture force (f_{max}) was generally greater within the weak layer than in the super-stratum (Figure 148), normally resulting in positive values of Δf_{max} (Figures 149 and Table 44). Exceptions to this generality indicate that some SMP profiles recorded greater f_{max} values in super-stratum than in the weak layer. This demonstrates the need for more than one SMP profile to be recorded in any event. On the upper site, no significant change occurred in Δf_{max} (Table 44). This means that despite a week of aging between both these time-steps and a small loading event during the second time-step, step-changes in f_{max} remained unchanged.

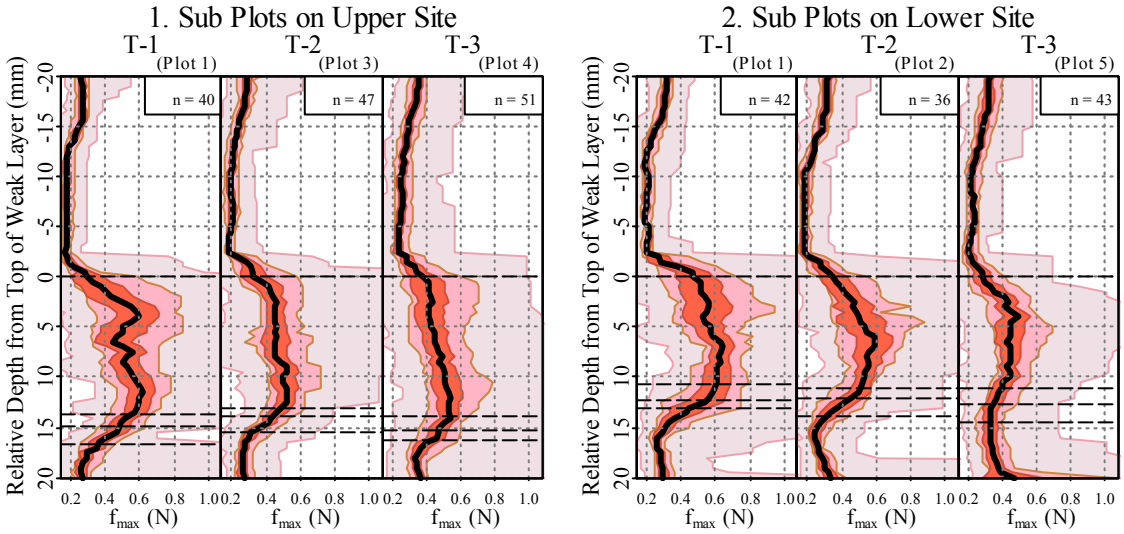

Figure 148. Stratigraphic visualizations of f_{max} on the (1) upper and (2) lower site summarized for sub-plot spatial extents. Graphic features defined in Figure 32 on page 89

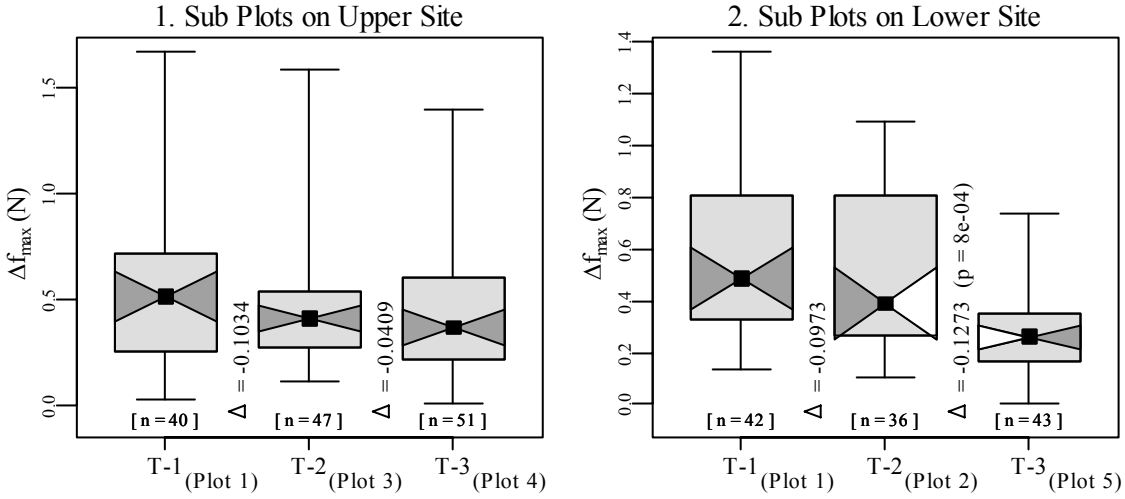

Figure 149. Boxplots illustrating changes in Δf_{max} on the (1) upper and (2) lower slope, using observations in sub-plots. Boxplot properties described on page 137.

Table 44. Non-parametric tests of differences in central tendency and distribution of Δf_{max}, between sub-plots on upper (I) and lower (II) site. Bold signifies significant ($p \leq 0.05$) change.

Δf_{max} (N)	Slope Extent	Plots Involved	Time-Step (Days)	Wilcoxon Rank-Sum Test: Change in Centrality?		Kolmogorov-Smirnov Test: Change in Distribution?	
				p-value	Δ Median	p-value	D-statistic
I. Upper-Slope	Sub-plots	1 → 3	8	2.8E-01	-1.0E-01	9.0E-02	0.259
		3 → 4	6	5.1E-01	-4.1E-02	3.9E-01	0.174
II. Lower-Slope	Sub-plots	1 → 2	1	1.8E-01	-9.7E-02	3.1E-01	0.210
		2 → 5	20	**8.3E-04**	**-1.3E-01**	**5.9E-03**	**0.374**

* In upper and lower slope 'Plots' comparisons, Plot 1 contained transect arm adjacent to both related plots.

A very different situation existed on the lower site (Table 44, Figures 148 and 149). A large significant decrease in the Δf_{max} occurred as a result of a decrease of the weak layer's f_{max} values. The step-change analysis allowed us to see that as a stratigraphic weakness progressed to a less stable condition (due to loading), the stratigraphic difference in f_{max} became subdued.

Step-Change of Rupture Force Coefficient of Variation (Δf_{cv}): The coefficient of variation of the rupture force (f_{cv}) consistently reached a maximum value within the weak

layer and very effectively differentiated the adjacent small grain facets from the surface hoar stratum (Figures 150 and 151). In all 760 SMP profiles, f_{cv} was larger in the weak layer than in the super-stratum, evident through positive Δf_{cv} values in the boxplots (Figure 151).

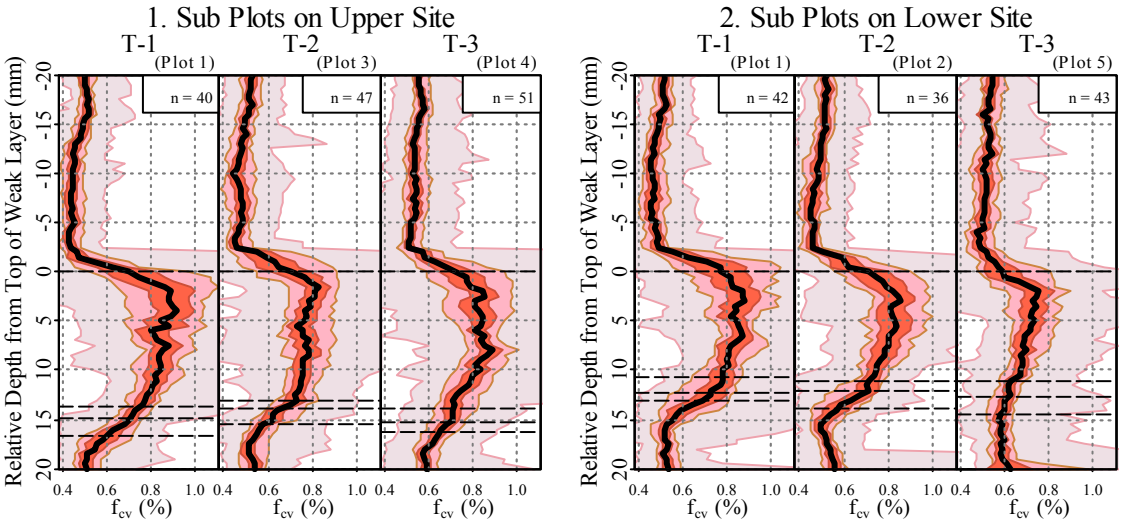

Figure 150. Stratigraphic visualizations of f_{cv} on the (1) upper and (2) lower site summarized for sub-plot spatial extents. Graphic features defined in Figure 32 on page 89.

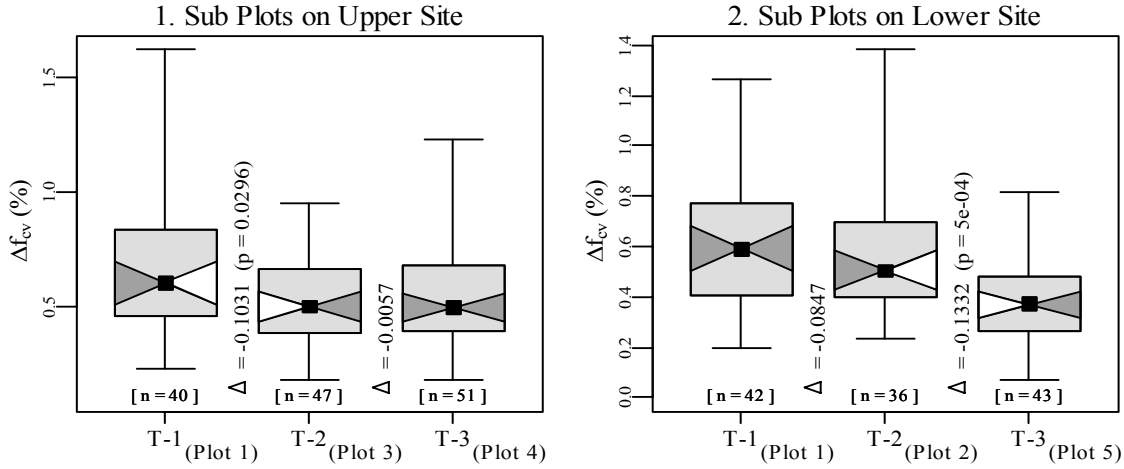

Figure 151. Boxplots illustrating changes in Δf_{cv} on the (1) upper and (2) lower slope, using observations in sub-plots. Boxplot properties described on page 137.

A significant decrease in the Δf_{cv} occurred on the upper site between Plots 1 and 3 (Figure 151 and Table 45). This decrease of Δf_{cv} was due to a larger increase of f_{cv} in the super-stratum than in the weak layer. A possible physical reason for this change is that enough time passed between these two field days to allow internal changes to occur within the snowpack. Metamorphism could lead to a decrease in the textural differences between adjacent strata.

Table 45. Non-parametric tests of differences in central tendency and distribution of Δf_{cv}, between sub-plots on upper (I) and lower (II) site. Bold signifies significant ($p \leq 0.05$) change.

Δf_{cv}	Slope Extent	Plots Involved	Time-Step (Days)	Wilcoxon Rank-Sum Test: Change in Centrality?		Kolmogorov-Smirnov Test: Change in Distribution?	
				p-value	Δ Median	p-value	D-statistic
I. Upper-Slope	Sub-plots	1 → 3	8	**3.0E-02**	**-1.0E-01**	8.3E-02	0.262
		3 → 4	6	9.5E-01	-5.7E-03	9.5E-01	0.096
II. Lower-Slope	Sub-plots	1 → 2	1	3.8E-01	-8.5E-02	2.2E-01	0.230
		2 → 5	20	**4.7E-04**	**-1.3E-01**	**4.5E-03**	**0.382**

* In upper and lower slope 'Plots' comparisons, Plot 1 contained transect arm adjacent to both related plots.

On the lower site there was a significant decrease in the step-change of f_{cv} between Plots 2 and 5 (Figure 151 and Table 45). This indicates that the difference in micro-variance between adjacent strata became smaller or, in other words, that the micro-variance became more uniform across the strata. f_{cv} became smaller in the weak layer, resulting in more similar values (Δf_{cv} becomes smaller). This is likely associated with the loading event.

Step-Change of Structural Element Length (ΔL): The mean structural element length (L) of the weak layer and the super-stratum were indistinguishable in most profiles at all five plots (Figure 152 and Table 46), evident through typical step-change values near 0.0 mm (Figure 153). The only significant change in the step-change of the

structural element length (ΔL) occurred at the second time step on the upper site (Table 46, Figure 153). This may be associated with larger structures at Plot 4 than at Plot 3, or with the small loading event that preceded Plot 4 sampling.

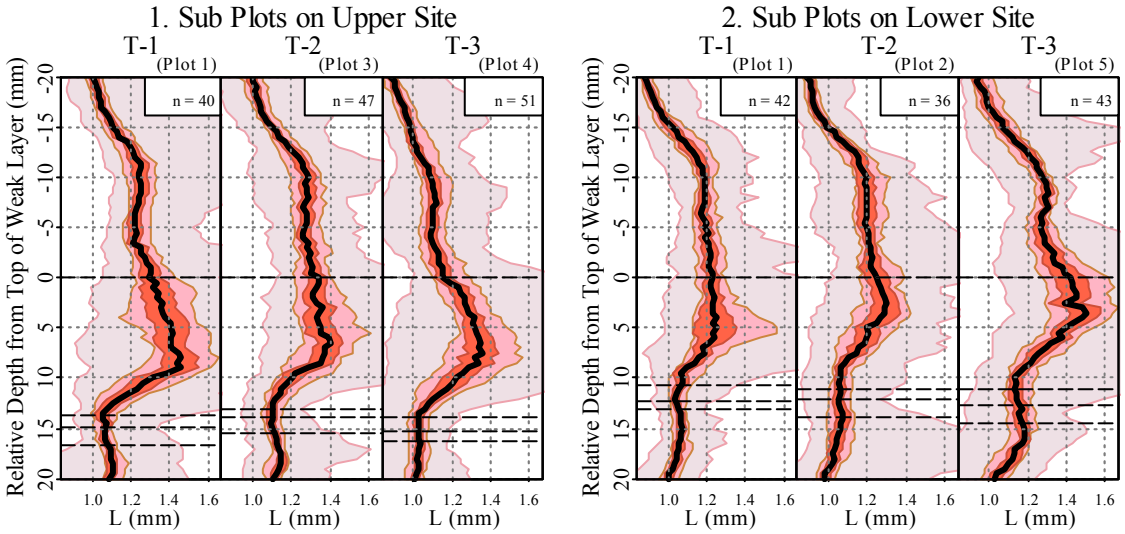

Figure 152. Stratigraphic visualizations of L on the (1) upper and (2) lower site summarized for sub-plot spatial extents. Graphic features defined in Figure 32 on page 89.

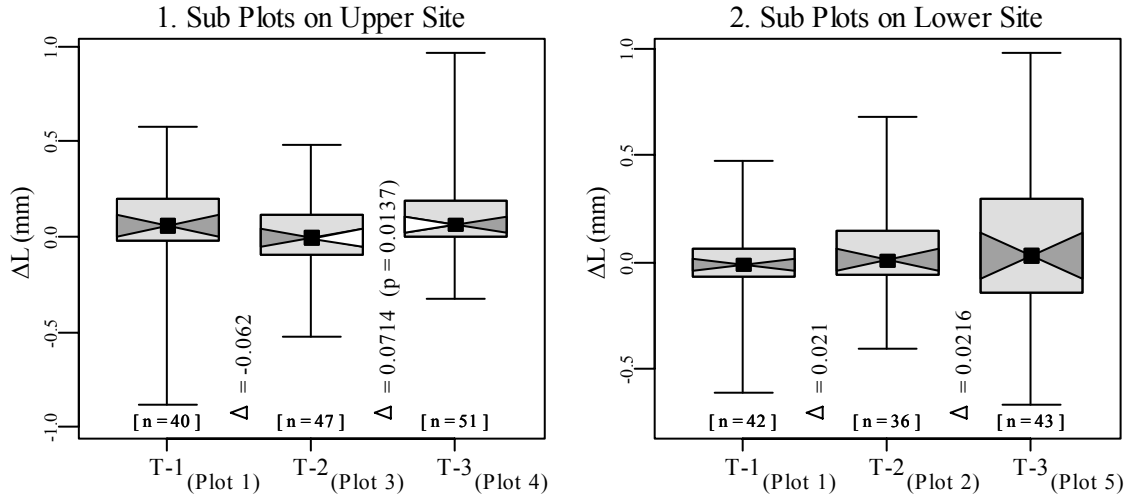

Figure 153. Boxplots illustrating changes in ΔL on the (1) upper and (2) lower slope, using observations in sub-plots. Boxplot properties described on page 137.

Table 46. Non-parametric tests of differences in central tendency and distribution of ΔL, between sub-plots on upper (I) and lower (II) site. Bold signifies significant ($p \leq 0.05$) change.

ΔL (mm)	Slope Extent	Plots Involved	Time-Step (Days)	Wilcoxon Rank-Sum Test: Change in Centrality?		Kolmogorov-Smirnov Test: Change in Distribution?	
				p-value	Δ Median	p-value	D-statistic
I. Upper-Slope	Sub-plots	1 → 3	8	1.6E-01	-6.2E-02	2.7E-01	0.214
		3 → 4	6	**1.4E-02**	**7.1E-02**	**1.7E-02**	**0.313**
II. Lower-Slope	Sub-plots	1 → 2	1	3.3E-01	2.1E-02	3.6E-01	0.210
		2 → 5	20	7.2E-01	2.2E-02	4.4E-01	0.196

* In upper and lower slope 'Plots' comparisons, Plot 1 contained transect arm adjacent to both related plots.

Step-Change of Maximum Structural Element Length (ΔL_{max}): The maximum structural element length (L_{max}) of the weak layer and the super-stratum were only slightly better differentiated than L (Figures 154 and 155). However, like L it still often possessed negative step-change values (larger L_{max} values in super-stratum than in weak layer). On the upper slope, there was a significant decrease of ΔL_{max} from Plot 1 to Plot 3, indicating that the difference in maximum structural element size between the super-stratum and weak layer became smaller.

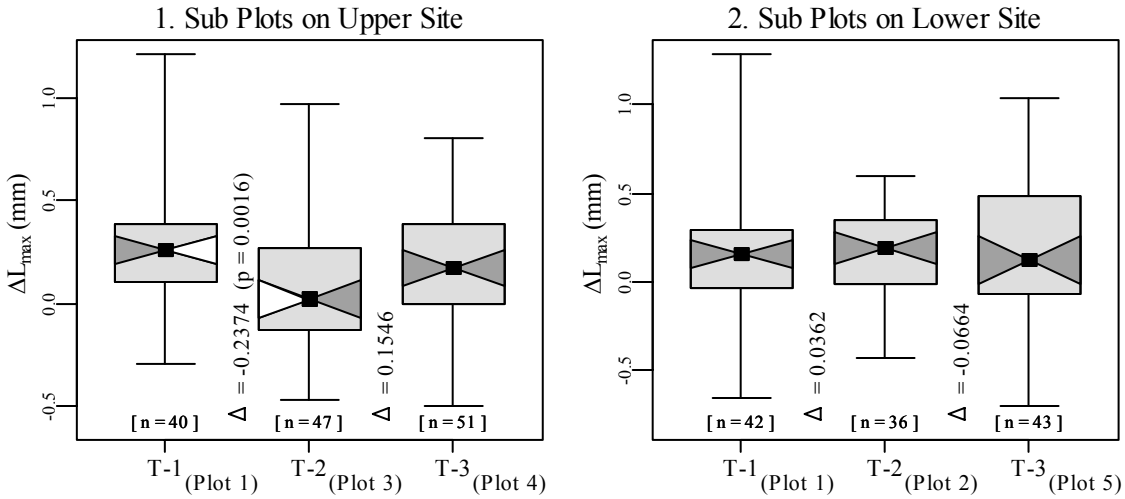

Figure 154. Boxplots illustrating changes in ΔL_{max} on the (1) upper and (2) lower slope, using observations in sub-plots. Boxplot properties described on page 137.

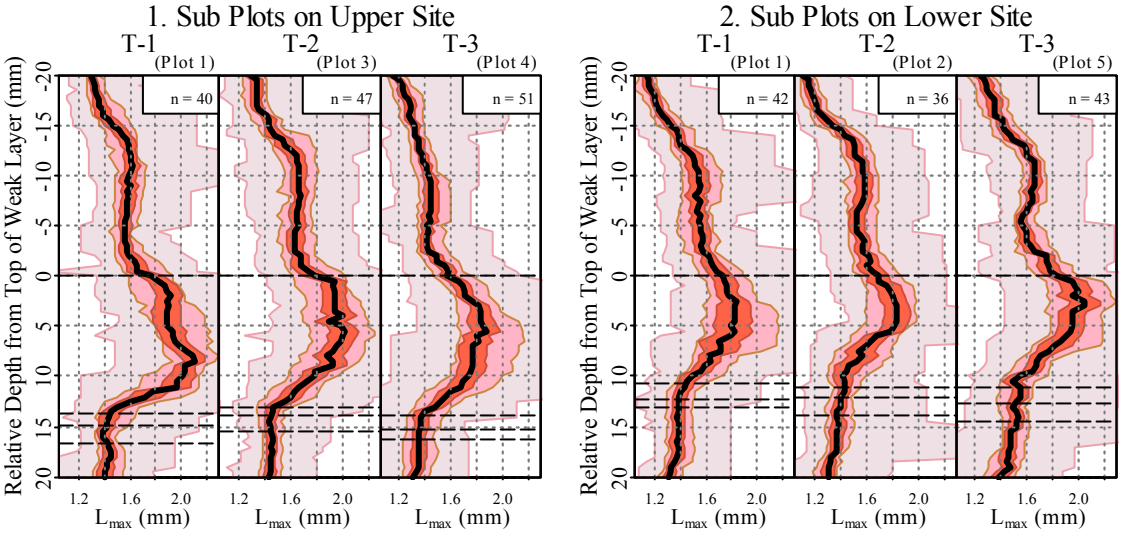

Figure 155. Stratigraphic visualizations of L_{max} on the (1) upper and (2) lower site summarized for sub-plot spatial extents. Graphic features defined in Figure 32 on page 89.

Table 47. Non-parametric tests of differences in central tendency and distribution of ΔL_{max}, between sub-plots on upper (I) and lower (II) site. Bold signifies significant ($p \leq 0.05$) change.

ΔL_{max} (mm)	Slope Extent	Plots Involved	Time-Step (Days)	Wilcoxon Rank-Sum Test: Change in Centrality?		Kolmogorov-Smirnov Test: Change in Distribution?	
				p-value	Δ Median	p-value	D-statistic
I. Upper-Slope	Sub-plots	1 → 3	8	**1.6E-03**	**-2.4E-01**	**2.0E-03**	**0.399**
		3 → 4	6	6.2E-02	1.5E-01	9.1E-02	0.251
II. Lower-Slope	Sub-plots	1 → 2	1	7.2E-01	3.6E-02	9.1E-01	0.127
		2 → 5	20	1.0E+00	-6.6E-02	3.8E-01	0.205

* In upper and lower slope 'Plots' comparisons, Plot 1 contained transect arm adjacent to both related plots.

Step-Change of Micro-Strength ($\Delta\sigma_{micro}$): The micro-strength (σ_{micro}) was generally greater within the weak layer than in the super-stratum, evident through positive step-change values of micro-strength ($\Delta\sigma_{micro}$) (Figures 156 and 157). As with ΔL and ΔL_{max}, there were instances were the step-change value was negative. However, unlike these other estimates, the weak layer signature of σ_{micro} appeared more complex (Figure 157). The base of the weak layer was generally much stronger than the top, and for Plot 3, 4, and 5 there was a trough or local minimum value present in the middle

portion of the weak layer. This was likely the middle of the surface hoar layer, where few structures were available to break, L was large, and f_m could be relatively small.

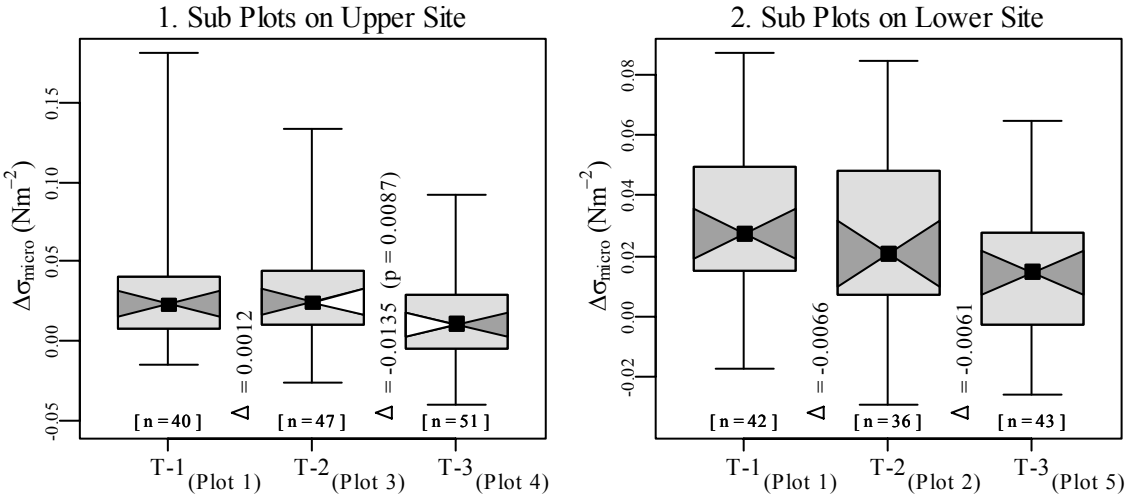

Figure 156. Boxplots illustrating changes in $\Delta\sigma_{micro}$ on the (1) upper and (2) lower slope, using observations in sub-plots. Boxplot properties described on page 137.

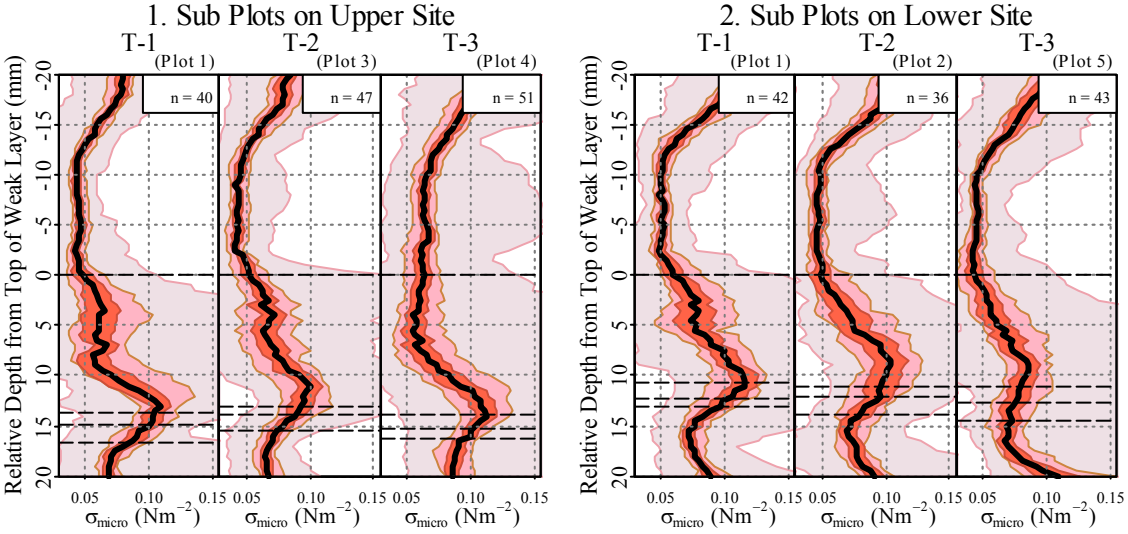

Figure 157. Stratigraphic visualizations of σ_{micro} on the (1) upper and (2) lower site summarized for sub-plot spatial extents. Graphic features defined in Figure 32 on page 89.

On the upper site, $\Delta\sigma_{micro}$ decreased significantly during the second time-step (Table 48, Figure 156). This change toward stratigraphic uniformity was caused by a relative strengthening of the super-stratum. Conversely, the slight decrease in $\Delta\sigma_{micro}$ on

the lower slope, though insignificant, was the result of a relative weakening of the weak layer (Figure 157).

Table 48. Non-parametric tests of differences in central tendency and distribution of $\Delta\sigma_{micro}$ between sub-plots on upper (I) and lower (II) site. Bold signifies significant ($p \leq 0.05$) change.

$\Delta\sigma_{micro}$ (N·mm^{-2})	Slope Extent	Plots Involved	Time-Step (Days)	Wilcoxon Rank-Sum Test: Change in Centrality?		Kolmogorov-Smirnov Test: Change in Distribution?	
				p-value	Δ Median	p-value	D-statistic
I. Upper-Slope	Sub-plots	1 → 3	8	7.6E-01	1.2E-03	9.4E-01	0.105
		3 → 4	6	**8.7E-03**	**-1.4E-02**	**1.5E-02**	**0.307**
II. Lower-Slope	Sub-plots	1 → 2	1	2.8E-01	-6.6E-03	2.3E-01	0.226
		2 → 5	20	8.1E-02	-6.1E-03	**2.8E-02**	**0.319**

* In upper and lower slope 'Plots' comparisons, Plot 1 contained transect arm adjacent to both related plots.

External Snowpack Associations

Weak Layer Thickness (h_{wl}) ~ Radiation Estimates

Weak Layer Thickness (h_{wl}) ~ Hemispheric Sky Visibility ($v_{\%}$): Significant positive correlations were identified between $v_{\%}$ and h_{wl} (Part I of Table 49, and Figure 158). GIS-derived $v_{\%}$ at Plots 1, 2 and 5 accounted for 47 %, 74 %, and 80 % of plot-scale variability of pit-derived mean h_{wl}, respectively. The correlations identified across Plot 1 and its up-slope transect were the result of a single, high-leverage point, while correlations at Plots 2 and 5 have more robust fits. When all 45 pits are grouped as a single population, 52 % of the site-scale variability of pit-derived mean h_{wl} is accounted for by a significant relationship with $v_{\%}$. All four of these significant relationships also existed with Solar Pathfinder radiation estimates, albeit with slightly smaller explanatory strengths (Table 49).

Table 49. Significant weighted least squares linear regression fits between h_{wl} and environmental estimates derived from Solar Pathfinder and GIS-methods (left and right respectively). Weights defined as the inverse of pit variance of h_{wl}. Bold signifies significant ($p \leq 0.05$) fit.

Variable	Areal Extent	~ *f*(Solar Pathfinder Estimate) p-value	r^2	b	m	~ *f*(GIS Estimate) p-value	r^2	b	m
$h_{wl} \sim v_{\%}$	Site	**4.0e-07**	**0.43**	**-10.46**	**36.03**	**6.8e-09**	**0.52**	**-3.92**	**24.53**
	Plot1	**1.7e-02**	**0.42**	**-11.78**	**37.20**	**1.0e-02**	**0.47**	**-3.63**	**23.29**
	Plot2	**8.0e-03**	**0.66**	**-12.64**	**38.85**	**2.8e-03**	**0.74**	**-3.67**	**23.93**
	Plot5	**3.5e-03**	**0.73**	**-5.15**	**28.28**	**1.1e-03**	**0.80**	**-1.18**	**21.07**
$h_{wl} \sim L\downarrow$	Site	**4.0e-07**	**0.43**	**130.65**	**-0.49**	**6.6e-09**	**0.52**	**91.98**	**-0.33**
	Plot1	**1.7e-02**	**0.42**	**133.93**	**-0.50**	**8.6e-03**	**0.48**	**89.12**	**-0.32**
	Plot2	**8.0e-03**	**0.66**	**139.52**	**-0.53**	**3.0e-03**	**0.74**	**90.00**	**-0.32**
	Plot5	**3.5e-03**	**0.73**	**105.62**	**-0.38**	**1.8e-03**	**0.77**	**80.27**	**-0.28**
$h_{wl} \sim I_{max}$	Site	**1.1e-02**	**0.13**	**19.39**	**-0.03**	**2.4e-03**	**0.18**	**21.19**	**-0.03**
	Plot2	1.2e-01	0.30	43.29	-0.13	**3.3e-02**	**0.50**	**49.06**	**-0.14**
$h_{wl} \sim \sum t_I$	Site	**2.3e-02**	**0.11**	**17.22**	**-1.11**	**7.4e-04**	**0.22**	**17.79**	**-1.19**
	Plot1	7.3e-01	0.01	14.48	-0.44	**2.7e-03**	**0.57**	**21.40**	**-2.22**
	Plot5	**1.5e-02**	**0.59**	**24.07**	**-2.83**	9.3e-01	0.00	12.61	0.15
$h_{wl} \sim \sum I$	Site	**1.2e-03**	**0.21**	**21.70**	**-3.00**	**1.2e-07**	**0.46**	**24.57**	**-2.86**
	Plot1	**3.2e-02**	**0.35**	**33.74**	**-7.33**	**9.0e-05**	**0.77**	**30.57**	**-4.36**
	Plot4	3.0e-01	0.15	18.80	-1.31	**5.0e-02**	**0.44**	**20.80**	**-1.50**

p-value := significance level; r^2 := explanatory strength; b = y-intercept; m = coefficient (slope)

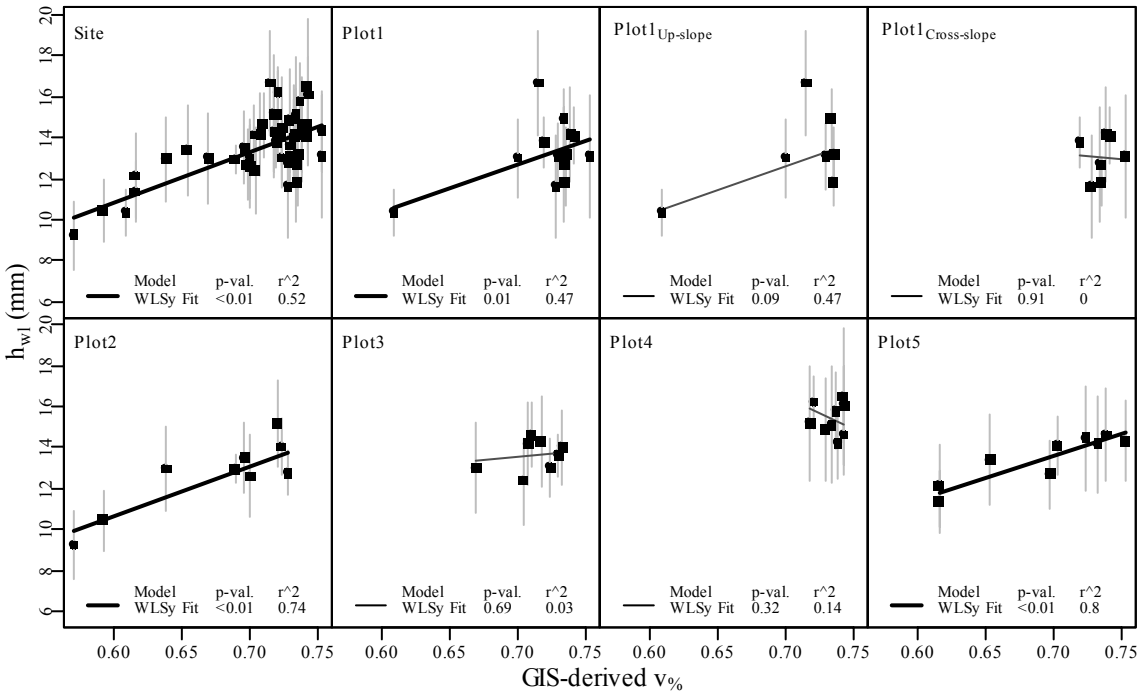

Figure 158. Relationship between pit-average h_{wl} and GIS derived $v_{\%}$, fitted using weighted least squares regression with weights defined as the inverse of pit variance of h_{wl}. Slightly weaker correlations exist between h_{wl} and Solar Pathfinder derived $v_{\%}$.

Weak Layer Thickness (h_{wl}) ~ Incoming Longwave Radiation ($L\downarrow$): Significant negative correlations were identified between $L\downarrow$ and h_{wl} at Plots 1, 2, and 5, and the entire site (Table 49). The significance and explanatory strength of the associations are identical to those of $v_{\%}$, since $v_{\%}$ was the spatial determinant in estimating $L\downarrow$. However, $L\downarrow$ has a physical basis for determining surface hoar growth. Areas that receive smaller amounts of incoming longwave radiation at night are more likely to cool, which will foster surface hoar formation. The significant inverse relationships identified here statistically support this physical rationale (Figure 159). No significant relationships existed at Plots 3 and 4 on the upper site, where h_{wl} possessed weak autocorrelation (Plot 4) or appeared spatially random (Plot 3).

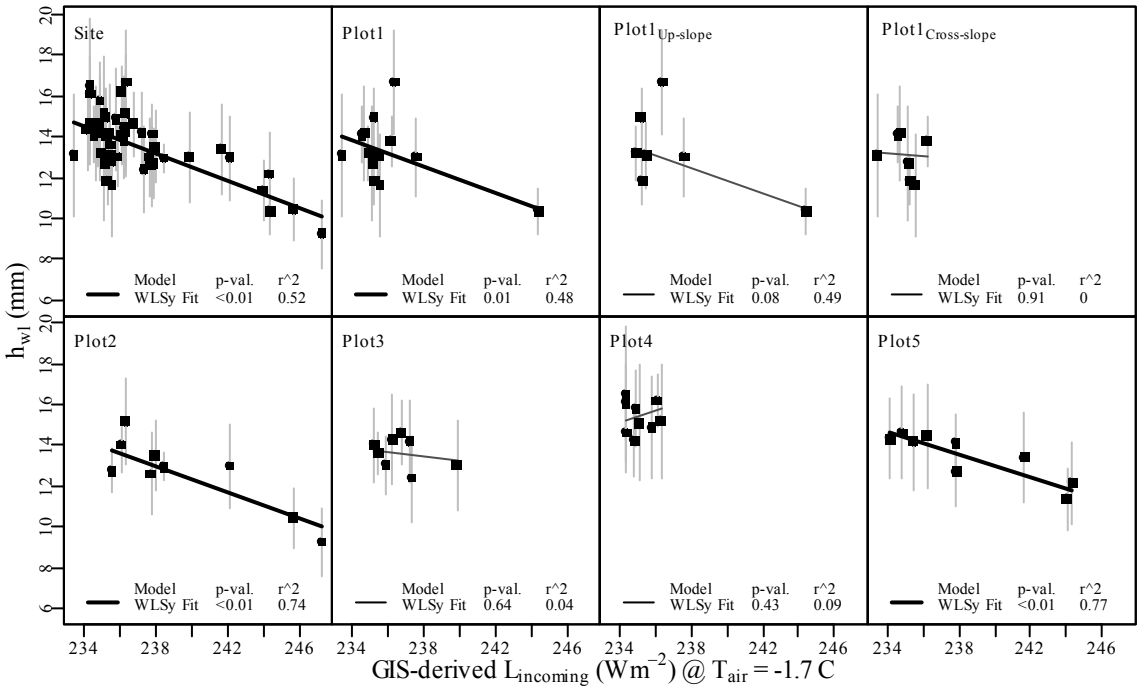

Figure 159. Relationship between pit-average h_{wl} and GIS-derived $L\downarrow$, fitted using weighted least squares regression, with weights defined as the inverse of pit variance of h_{wl}. Slightly weaker correlations exist between h_{wl} and Solar Pathfinder derived $L\downarrow$.

Weak Layer Thickness (h_{wl}) ~ Maximum Global Shortwave Radiation (I_{max}):

Significant inverse linear relationships existed between the GIS-derived I_{max} and h_{wl} at Plot 1 and 2, and for the entire site (Table 49, Figure 160). Solar Pathfinder-derived I_{max} correlated significantly with h_{wl} only when all plots were grouped together (Table 49). The significance and explanatory strength of the identified associations between h_{wl} and I_{max} were lower than those identified with $L\downarrow$. No significant correlations were present on the upper slope at Plots 3 and 4.

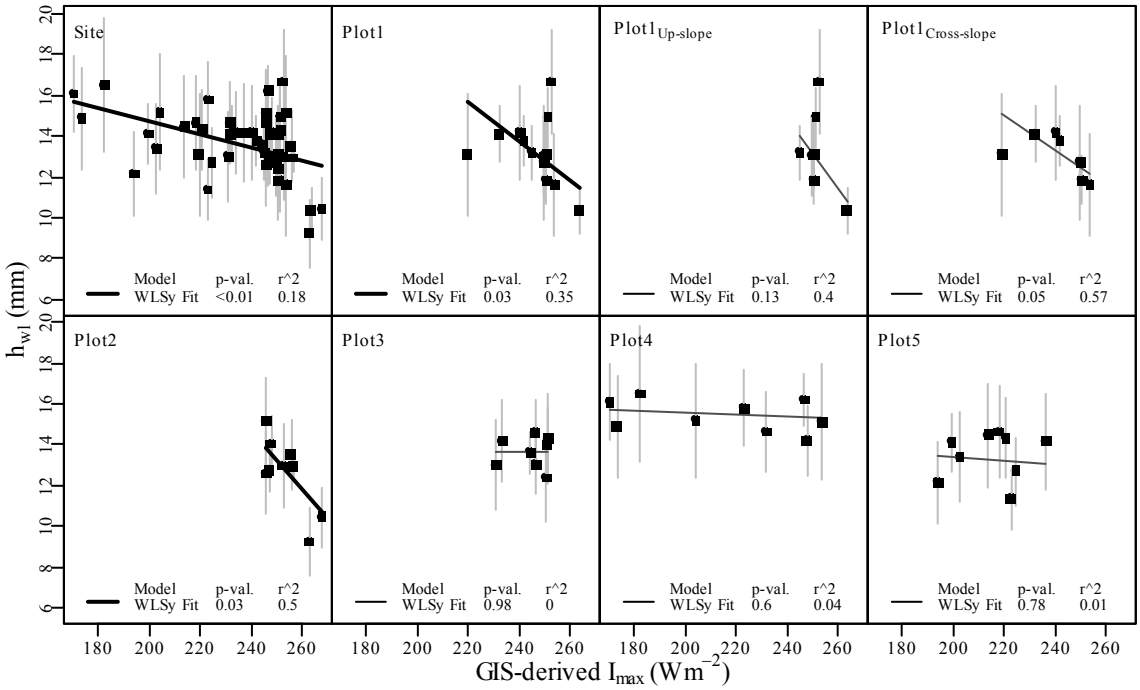

Figure 160. Relationship between pit-average h_{wl} and GIS-derived I_{max}, fitted using weighted least squares regression, with weights defined as the inverse of pit variance of h_{wl}. Slightly weaker correlations exist between h_{wl} and Solar Pathfinder derived I_{max}.

Weak Layer Thickness (h_{wl}) ~ Cumulative Exposure Time ($\sum t_l$): Significant inverse linear relationships existed between the $\sum t_l$ and h_{wl} at Plots 1 and 2 and for the entire site using either the GIS- or Solar Pathfinder results (Table 49, Figures 161 and 162). While all significant correlations possessed negative slopes, there were

discrepancies between the GIS and Solar Pathfinder in identifying significant correlations. The GIS estimates were significantly correlated with h_{wl} at Plot 1 and at the up-slope transect of Plot 1 (Table 49). The Solar Pathfinder estimates were not significant at Plot 1 but rather at Plot 5.

These discrepancies are not trivial and can be rationalized by a general deficiency of the GIS model, where shadows from distant trees were not accounted for and trees themselves were modeled as solid bodies. I speculate that this error in the GIS model resulted in a spatial pattern that coincidentally increased the correlations with the spatial pattern of h_{wl}. A strong indicator of a real correlation existed when both methods indicated similar associations. When the results from the two estimate types deviated from each other, the GIS estimates were, for the above described reasons, considered more likely to contain error.

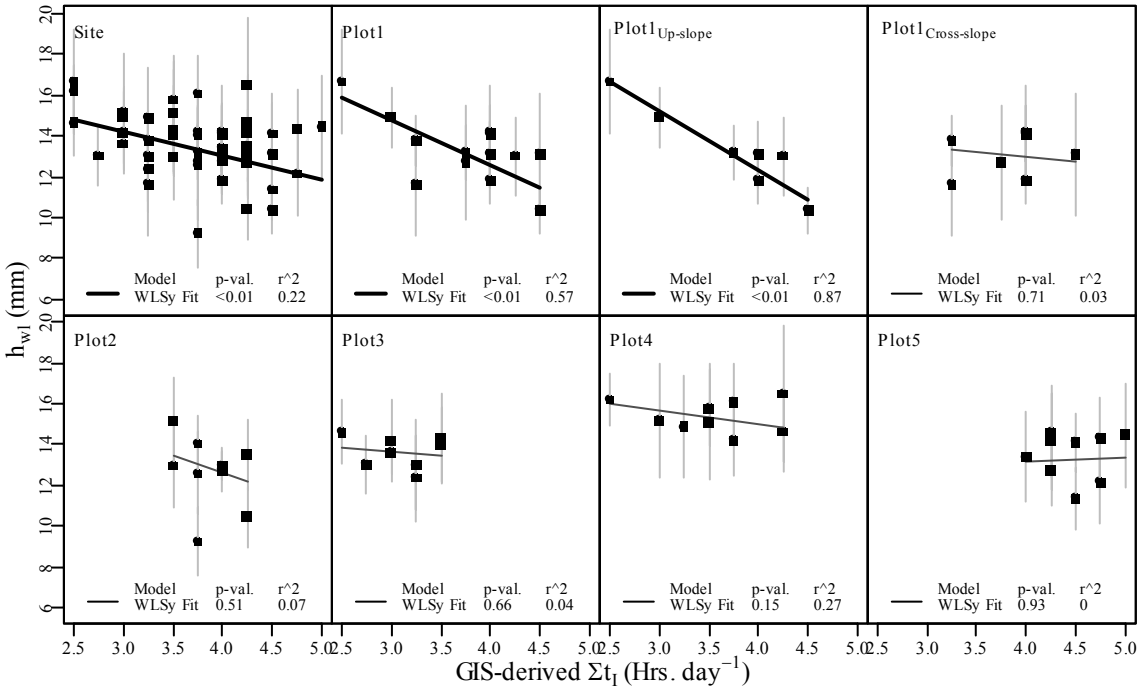

Figure 161. Relationship between pit-average h_{wl} and GIS-derived $\sum t_I$, fitted using weighted least squares regression, with weights defined as the inverse of pit variance of h_{wl}.

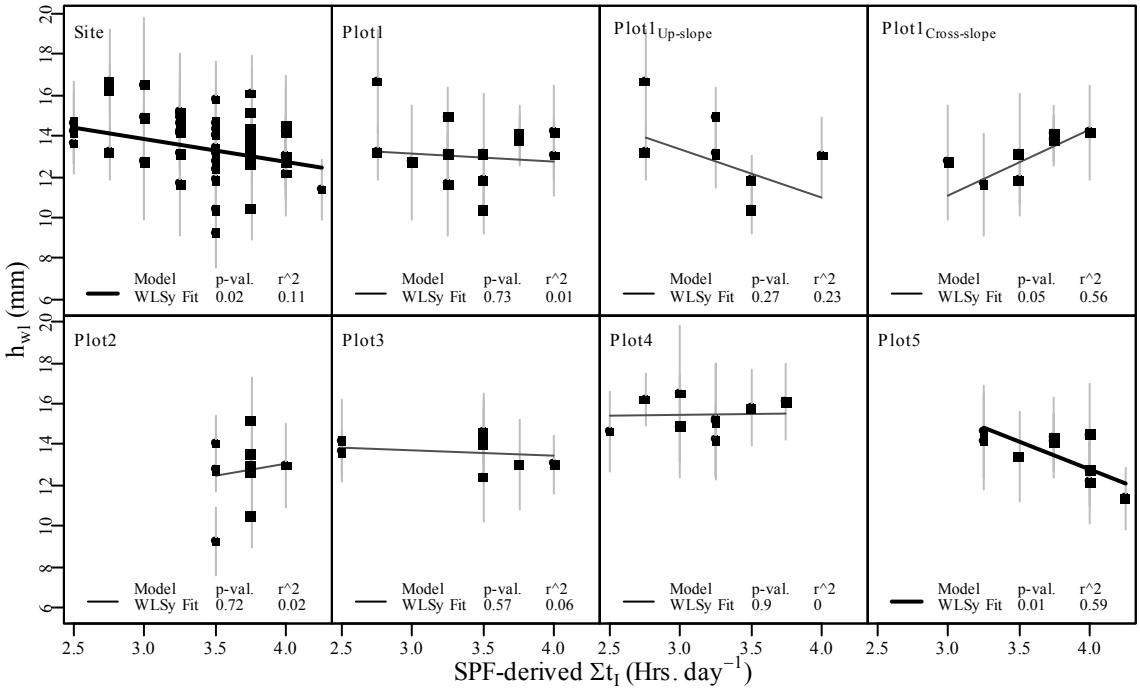

Figure 162. Relationship between pit-average h_{wl} and Solar Pathfinder-derived $\sum t_I$, fitted using weighted least squares regression, with weights defined as the inverse of pit variance of h_{wl}.

$\underline{h_{wl} \sim \sum I}$: Significant inverse linear relationships existed between the $\sum I$ and h_{wl} (Table 49). At Plot 1 and for the entire site, the GIS-estimates accounted for 43% and 77% of variability of pit-mean h_{wl}, respectively. Solar Pathfinder estimates possessed approximately half the explanatory power (Table 49). Additionally, the GIS-estimates across the up-slope transect of Plot 1 were highly correlated with h_{wl}, accounting for 93 % of the pit-mean variability of h_{wl}. A less significant ($p = 0.05$) inverse relationship also existed at plot 4 (Table 49).

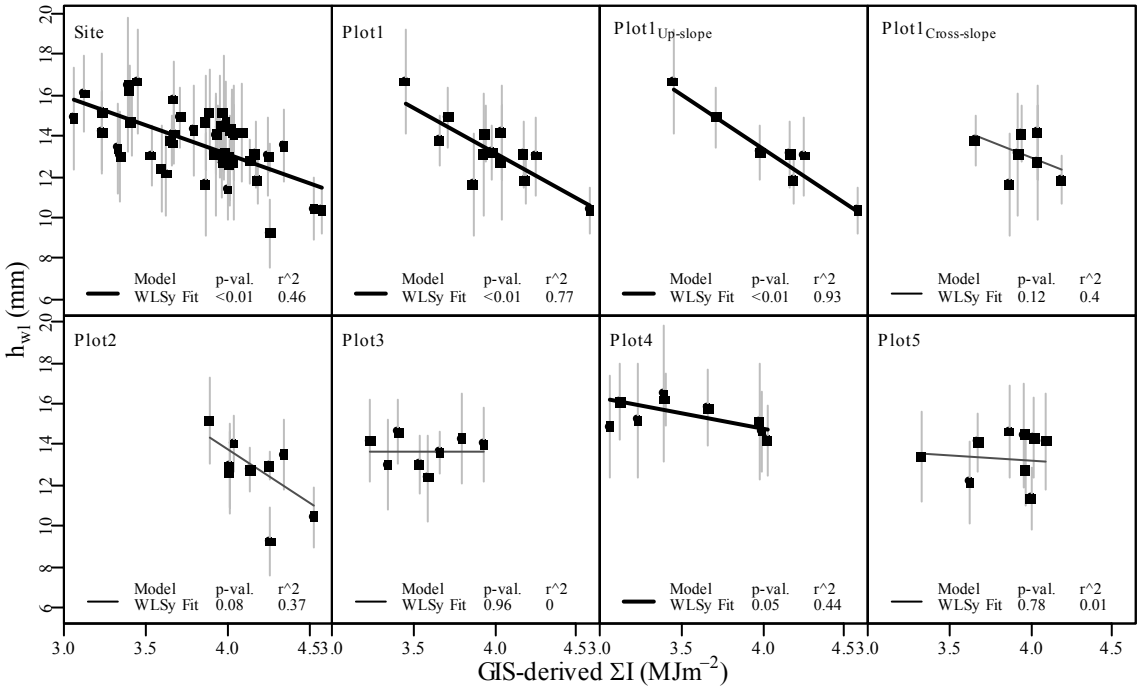

Figure 163. Relationship between pit-average h_{wl} and GIS-derived $\sum I$, fitted using weighted least squares regression, with weights defined as the inverse of pit variance of h_{wl}.

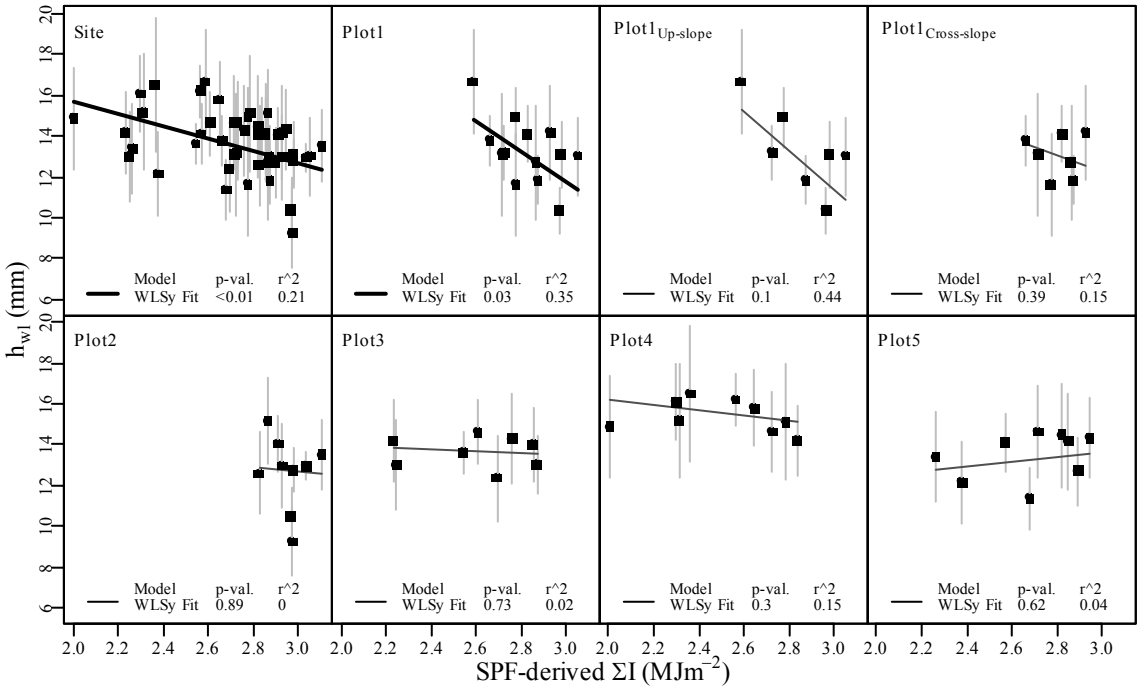

Figure 164. Relationship between pit-average h_{wl} and Solar Pathfinder-derived $\sum I$, fitted using weighted least squares regression, with weights defined as the inverse of pit variance of h_{wl}.

Shear Strength (τ_∞) ~ Radiation Estimates

No significant linear correlations were identified between τ_∞ and $v_{\%}$ or $L\downarrow$. However, the global shortwave radiation estimates did show associations at individual plots (Table 50). $\sum t_I$ was significantly correlated at all three spatial extents of Plot 1, indicating that areas that were exposed for long time periods to the sun possessed stronger shear strength (τ_∞) (Table 50, Figure 165). $\sum I$ also possessed significant positive correlations with high explanatory strength at Plot 1 and its up-slope transect (Table 50, Figure 166).

Table 50. Significant weighted least squares linear regression fits between τ_∞ and environmental estimates derived from Solar Pathfinder and GIS-methods (left and right columns respectively). Weights defined as the inverse of pit variance of τ_∞. Bold signifies significant ($p \leq 0.05$) fit.

	Areal	~ *f*(Solar Pathfinder Estimate)				~ *f*(GIS Estimate)			
	Extent	p-value	r^2	b	m	p-value	r^2	b	m
$\tau_\infty \sim I_{max}$	Site	**1.9e-03**	**0.21**	**998.7**	**-1.6**	**2.3e-03**	**0.20**	**1028.3**	**-1.6**
$\tau_\infty \sim \sum t_I$	Plot1	**3.5e-03**	**0.73**	**161.2**	**136.0**	**4.6e-02**	**0.46**	**402.8**	**63.8**
	$Plot1_{Up\text{-}Slope}$	**8.0e-03**	**0.93**	**141.5**	**149.9**	**2.7e-02**	**0.84**	**328.1**	**92.8**
	$Plot1_{Cross\text{-}Slope}$	**3.3e-02**	**0.82**	**-159.9**	**219.3**	6.0e-01	0.10	499.0	33.8
$\tau_\infty \sim \sum I$	Plot1	**2.4e-02**	**0.54**	**-317.6**	**341.7**	**4.2e-02**	**0.47**	**-7.5**	**165.8**
	$Plot1_{Up\text{-}Slope}$	**5.3e-03**	**0.95**	**-486.5**	**401.4**	**3.8e-02**	**0.81**	**-89.9**	**188.9**

p-value := significance level; r^2 := explanatory strength; b = y-intercept; m = coefficient (slope)

These findings indicate that at the slope-scale, variations in pit-estimates of τ_∞ could largely be explained by spatial patterns of $\sum t_I$ and $\sum I$. Lastly, I_{max} was not significantly correlated with any individual plot but was significantly inversely correlated at the site-scale (Table 50). Although it was significantly correlated when all plots were considered together, it only accounted for 20 % of the variability between shear frame pit-means. This relationship is a false association, as it compares τ_∞, which changed significantly over time, with a spatial variable.

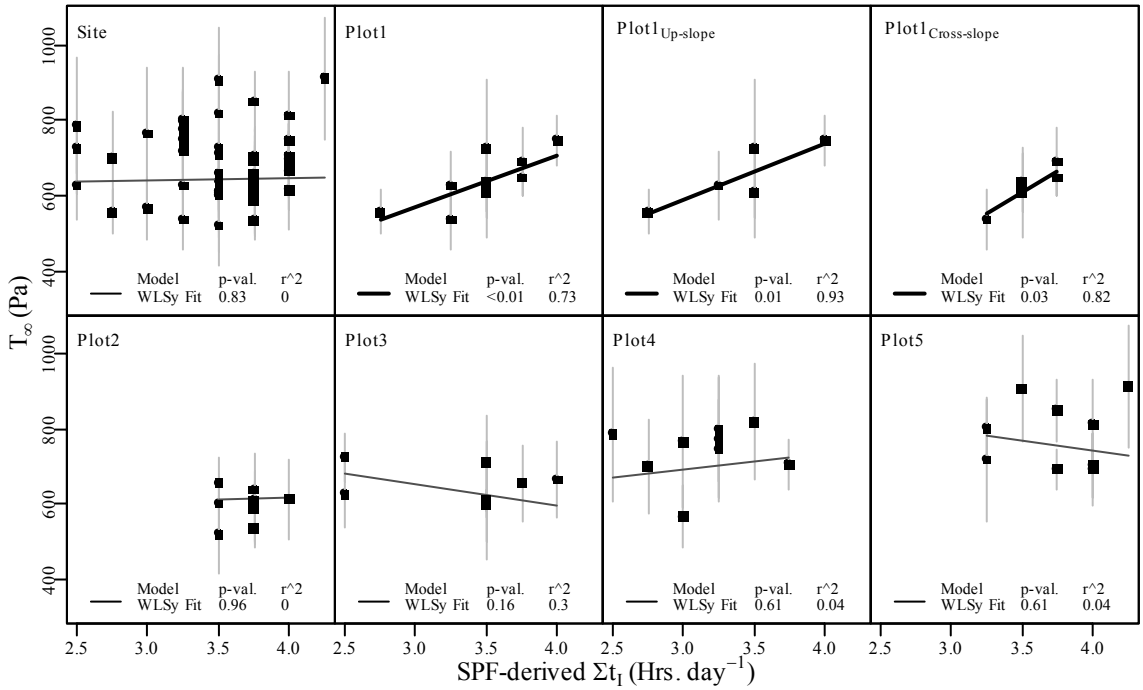

Figure 165. Relationship between pit-average τ_∞ and Solar Pathfinder-derived $\sum t_I$, fitted using weighted least squares regression, with weights defined as the inverse of pit variance of τ_∞.

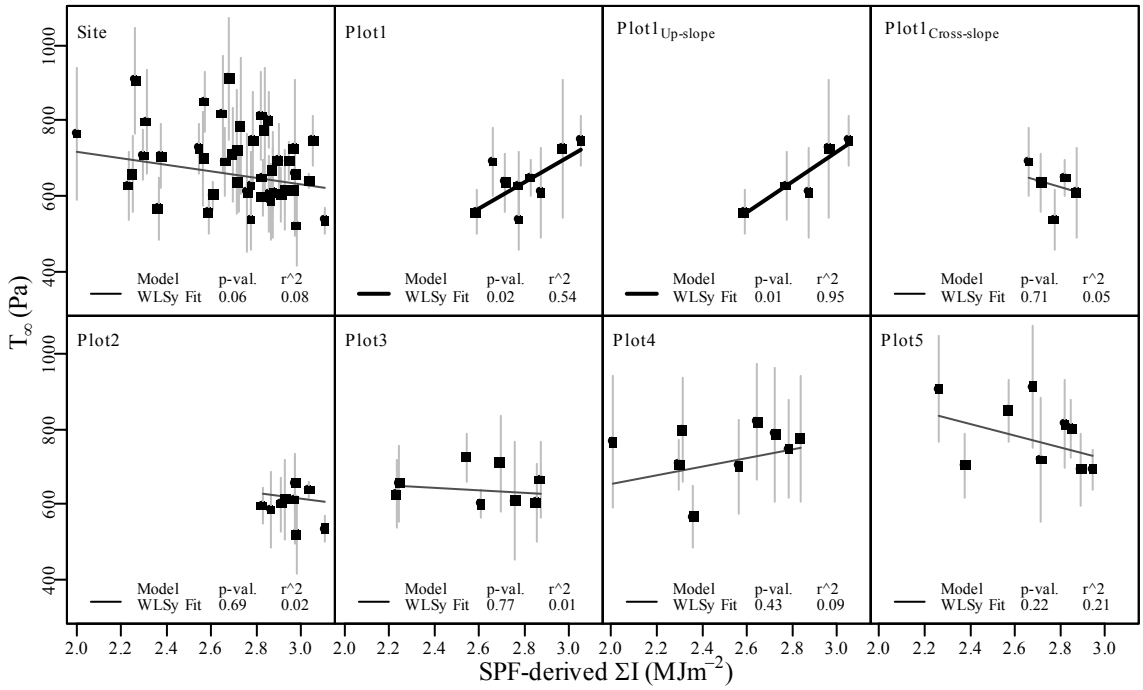

Figure 166. Relationship between pit-average τ_∞ and Solar Pathfinder-derived $\sum I$, fitted using weighted least squares regression, with weights defined as the inverse of pit variance of τ_∞.

Residual Shear Strength (τ_{resid}) ~ Radiation Estimates

No significant linear correlations were identified between τ_{resid} and $v_{\%}$ or $L\downarrow$. The global shortwave radiation estimates did show logical associations (Table 51, Figures 167 and 168). $\sum t_I$ and $\sum I$ were significantly correlated with τ_{resid} at Plot 1, indicating that areas that were exposed for longer time periods to the sun or to cumulatively more radiation possessed greater residual shear strength (τ_{resid}) (Table 51). These findings indicate that slope-scale variations of τ_{resid} pit-estimates were explained by spatial patterns of $\sum t_I$ and $\sum I$.

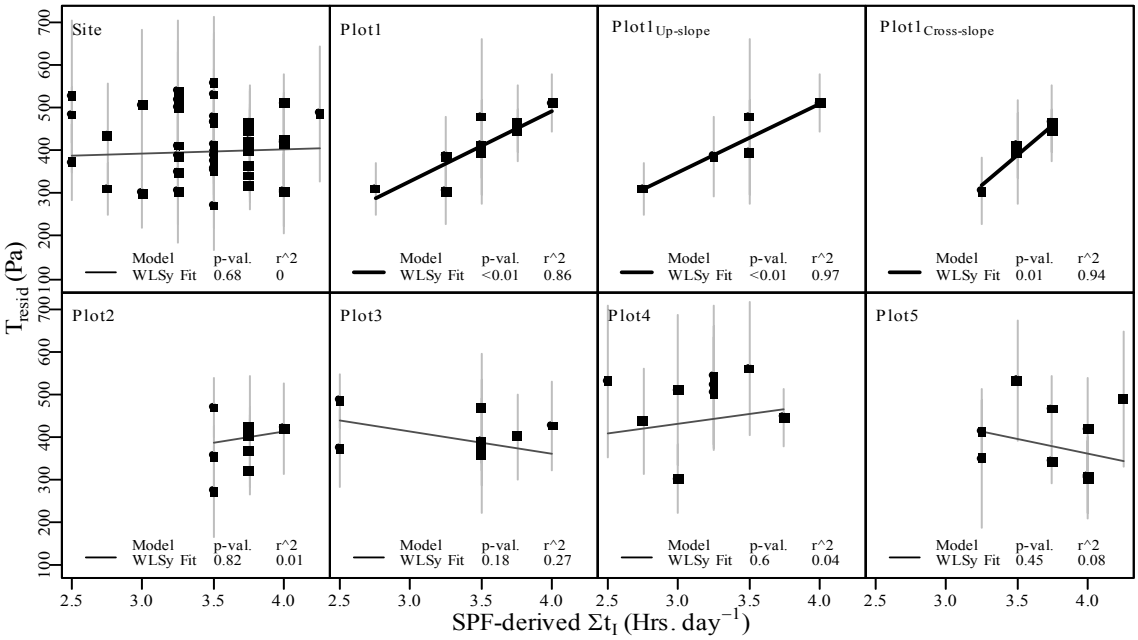

Figure 167. Relationship between pit-average τ_{resid} and Solar Pathfinder-derived $\sum tI$, fitted using weighted least squares regression, with weights defined as the inverse of pit variance of τ_{resid}.

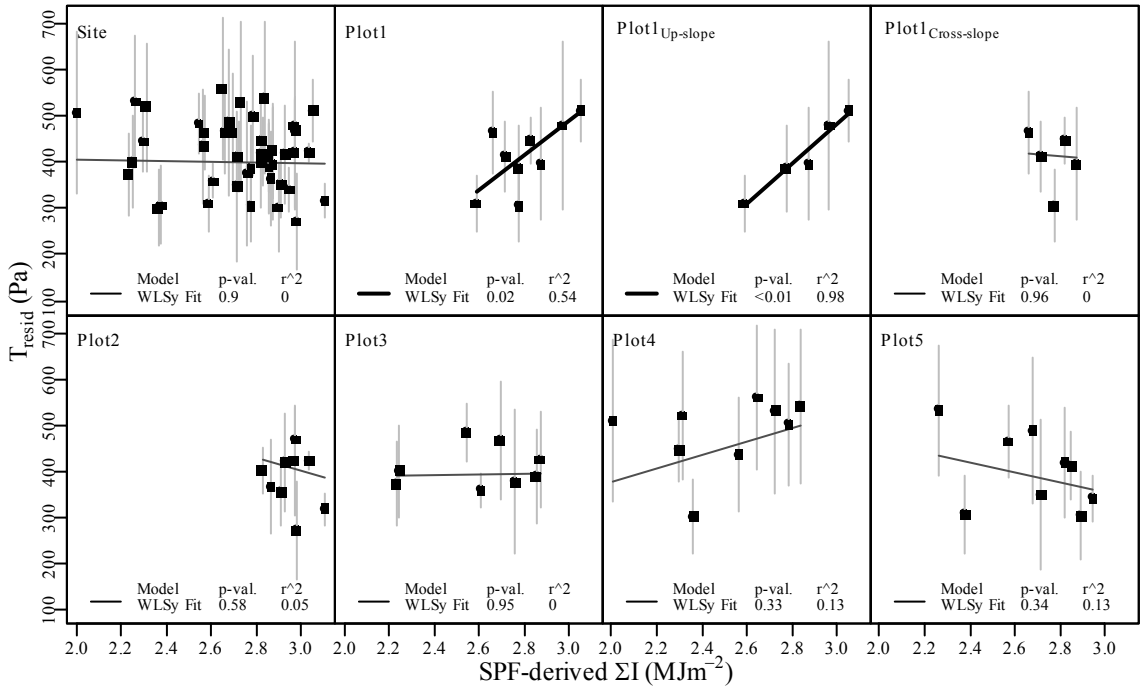

Figure 168. Relationship between pit-average τ_{resid} and Solar Pathfinder-derived $\sum I$, fitted using weighted least squares regression, with weights defined as the inverse of pit variance of τ_{resid}.

Table 51. Significant weighted least squares linear regression fits between τ_{resid} and radiation estimates derived from Solar Pathfinder and GIS-methods (left and right respectively). Weights defined as the inverse of pit variance of $\tau_{resid,}$ Bold signifies significant ($p \leq 0.05$) fit.

Variable	Areal Extent	~ *f*(Solar Pathfinder Estimate)				~ *f*(GIS Estimate)			
		p-value	r^2	b	m	p-value	r^2	b	m
$\tau_{resid} \sim \sum t_I$	Plot1	**3.1E-04**	**0.86**	**-1.6E+02**	**1.6E+02**	**1.8E-02**	**0.57**	**1.2E+02**	**7.9E+01**
	$Plot1_{Up\text{-}Slope}$	**2.1E-03**	**0.97**	**-1.3E+02**	**1.6E+02**	**1.4E-02**	**0.90**	**6.3E+01**	**1.0E+02**
	$Plot1_{Cross\text{-}Slope}$	**7.2E-03**	**0.94**	**-5.7E+02**	**2.7E+02**	5.2E-01	0.15	2.3E+02	4.7E+01
$\tau_{resid} \sim \sum I$	Plot1	**2.4E-02**	**0.54**	**-6.3E+02**	**3.7E+02**	**3.2E-02**	**0.51**	**-3.2E+02**	**1.9E+02**
	$Plot1_{Up\text{-}Slope}$	**9.1E-04**	**0.98**	**-8.0E+02**	**4.3E+02**	**2.3E-02**	**0.86**	**-3.9E+02**	**2.0E+02**

p-value := significance level; r^2 := explanatory strength; b = y-intercept; m = coefficient (slope)

Stability Index (*S*) ~ Radiation Estimates

Correlations that incorporated all pits from all five plots were not valued in this analysis. Such correlations would falsely identify a relationship between *S* and radiation variables, when in fact two snowfall events, which occurred between the sampling of Plots 3 and 5, influenced pit-derived *S* values over time. The other 7 spatial groupings

were examined. One significant (p = 0.05) relationship at Plot 2 accounted for 45 % of the pit-mean variability of *S*, indicating that at Plot 2 *S* was positively influenced by $v_{\%}$ and negatively influenced by $L\downarrow$ (Figures 169 and 170, and Table 52). At Plot 1, significant positive correlations existed between *S* and the total exposure time and cumulative global shortwave radiation estimates. This was a direct result of the correlations between these radiation estimates and τ_∞ (Figure 169). The latter of these estimates also was positively correlated at Plot 3 (Table 52).

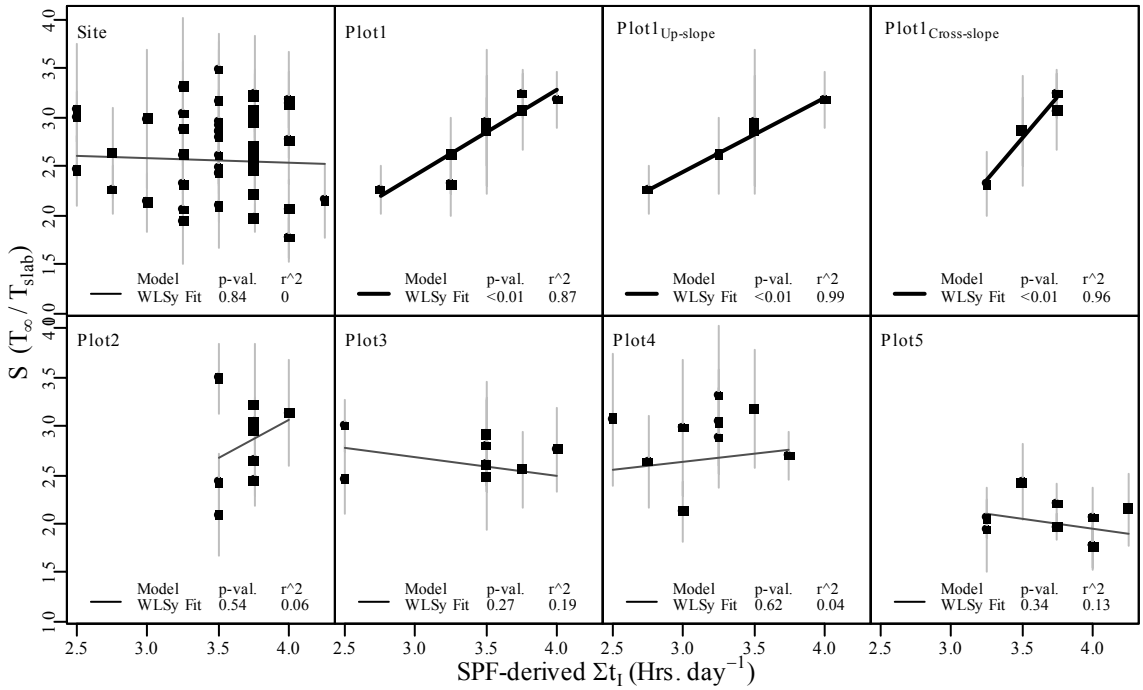

Figure 169. Relationship between pit-average *S* and Solar Pathfinder-derived $\sum t_I$, fitted using weighted least squares regression, with weights defined as the inverse of pit variance of *S*.

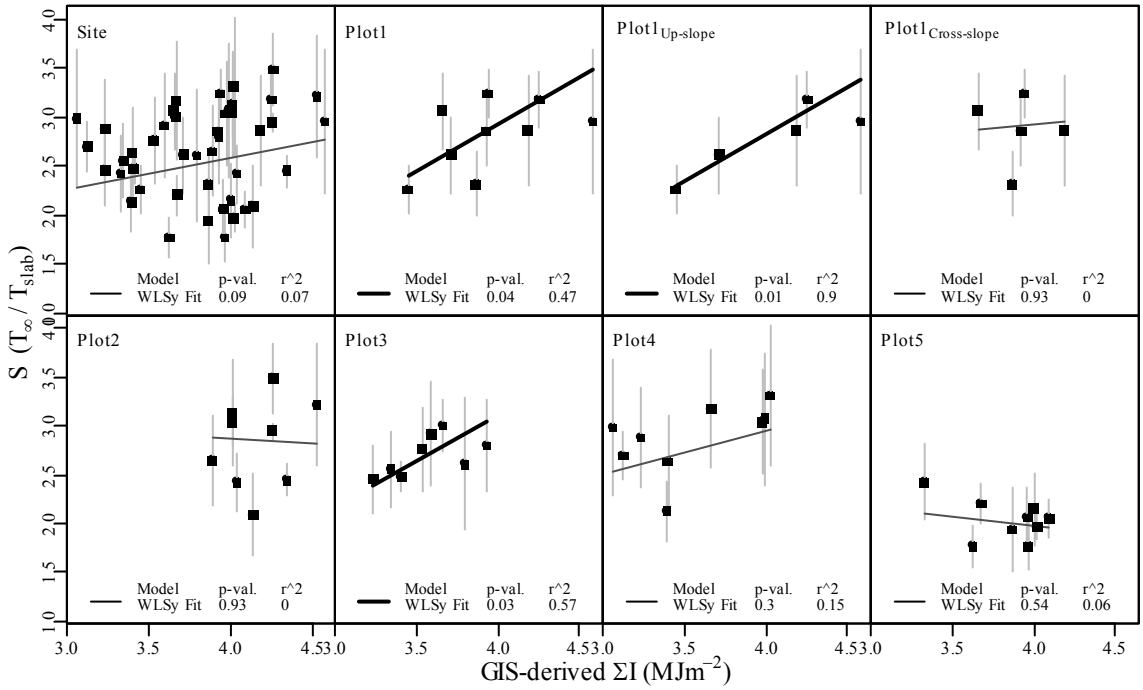

Figure 170. Relationship between pit-average *S* and Solar Pathfinder-derived $\sum I$, fitted using weighted least squares regression, with weights defined as the inverse of pit variance of *S*.

Table 52. Significant weighted least squares linear regression fits between *S* and environmental estimates derived from Solar Pathfinder and GIS-methods (left and right columns respectively). Weights defined as the inverse of pit variance of *S*. Bold signifies significant ($p \leq 0.05$) fit.

	Areal	~ *f*(Solar Pathfinder Estimate)				~ *f*(GIS Estimate)			
	Extent	p-value	r^2	b	m	p-value	r^2	b	m
$S \sim v_{\%}$	Plot2	6.4E-02	0.41	9.43	-10.03	**5.0E-02**	**0.45**	**7.44**	**-6.67**
$S \sim L\downarrow$	Plot2	6.4E-02	0.41	-29.84	0.14	**4.8E-02**	**0.45**	**-18.98**	**0.09**
$S \sim I_{max}$	Site	**3.7E-04**	**0.26**	**0.45**	**0.01**	**2.7E-04**	**0.27**	**0.16**	**0.01**
$S \sim \sum t_I$	Site	8.4E-01	0.00	2.70	-0.04	**3.4E-02**	**0.10**	**3.39**	**-0.21**
	Plot1	**2.3E-04**	**0.87**	**-0.20**	**0.87**	**9.8E-03**	**0.64**	**1.21**	**0.45**
	$Plot1_{Up\text{-}Slope}$	**2.2E-04**	**0.99**	**0.21**	**0.75**	**4.9E-03**	**0.95**	**1.10**	**0.48**
	$Plot1_{Cross\text{-}Slope}$	**3.9E-03**	**0.96**	**-3.16**	**1.70**	4.5E-01	0.20	1.67	0.33
$S \sim \sum I$	Plot1	**4.6E-02**	**0.46**	**-2.24**	**1.81**	**4.3E-02**	**0.47**	**-0.88**	**0.95**
	$Plot1_{Up\text{-}Slope}$	**3.4E-05**	**1.00**	**-2.87**	**1.98**	**1.3E-02**	**0.90**	**-1.03**	**0.96**
	Plot3	5.6E-01	0.06	1.86	0.30	**2.9E-02**	**0.57**	**-0.64**	**0.94**

p-value := significance level; r^2 := explanatory strength; b = y-intercept; m = coefficient (slope)

Weak Layer Microstructure ~ Radiation Estimates

Significant negative correlations between f_m and $\sum t_I$ existed at Plots 4 and 5 (Table 53), signifying that at each of these plots exposure time to direct shortwave radiation

negatively influenced f_m (Figure 171). This means that microstructural residual strength was larger where exposure time to direct shortwave radiation was limited. This relationship is logical, if large structures produce greater f_m values.

Table 53 Significant weighted least squares linear regression fits between rupture force of weak layer (f_m and f_{max}) and radiation estimates derived from Solar Pathfinder and GIS-methods (left and right columns respectively). Weights defined as the inverse of pit variance of f_{max} of weak layer. Bold signifies significant ($p \leq 0.05$) fit.

	Areal	~ *f*(Solar Pathfinder Estimate)				~ *f*(GIS Estimate)			
	Extent	p-value	r^2	b	m	p-value	r^2	b	m
$f_m \sim \sum t_I$	Plot4	**1.6E-02**	**0.59**	**1.5E-01**	**-1.1E-02**	6.7E-01	0.03	1.1E-01	2.0E-03
	Plot5	**1.2E-02**	**0.62**	**1.8E-01**	**-1.8E-02**	4.6E-01	0.08	1.4E-01	-7.9E-03
$f_{max} \sim v_{\%}\downarrow$	Plot4	**1.4E-02**	**0.60**	**-2.3E+00**	**4.3E+00**	1.2E-01	0.32	-2.3E+00	4.0E+00
$f_{max} \sim L\downarrow$	Plot4	**1.4E-02**	**0.60**	**1.5E+01**	**-5.9E-02**	**4.8E-02**	**0.45**	**1.4E+01**	**-5.6E-02**

p-value := significance level; r^2 := explanatory strength; b = y-intercept; m = coefficient (slope)

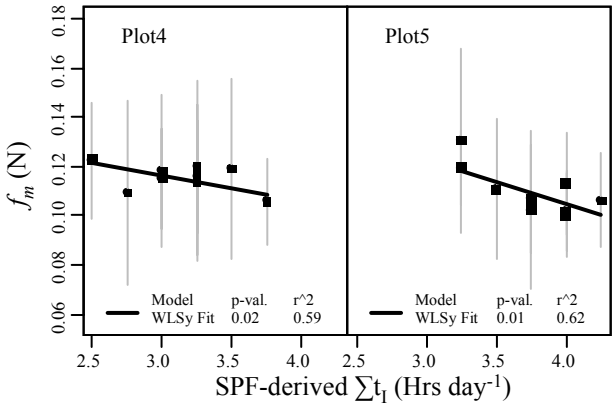

Figure 171. For Plots 4 and 5, relationship between f_m and Solar Pathfinder-derived $\sum t_I$, fitted using weighted least squares regression, with weights defined as the inverse of pit variance of f_m.

At Plot 4, f_{max} was negatively correlated with $L\downarrow$ (Table 53). This indicates that maximum rupture force (f_{max}) was greatest where $v_{\%}$ was highest and $L\downarrow$ smallest (Figure 172). Since weak layer thickness (h_{wl}) held the same associations with these radiation estimates, it is likely that the larger f_{max} values were associated with larger surface hoar structures.

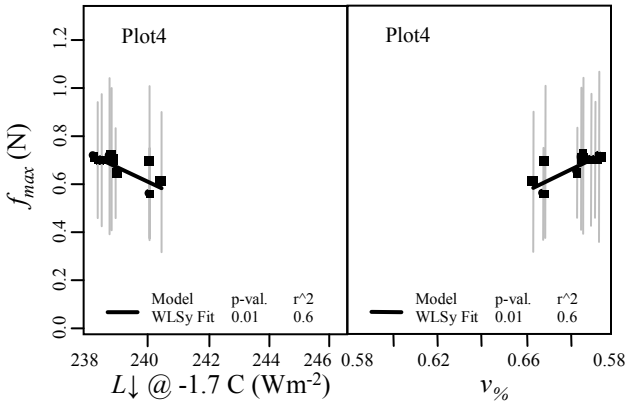

Figure 172. For Plots 4, relationship between f_{max} and Solar Pathfinder-derived $L\downarrow$ and $v_{\%}$ fitted using weighted least squares regression, with weights defined as the inverse of pit variance of f_{max}.

As with f_{max}, a negative correlation existed between $L\downarrow$ and f_{cv} at Plot 4 (Table 53). This indicates that micro-variance of the rupture force (f_{cv}) was greatest where $v_{\%}$ was highest and $L\downarrow$ smallest (Figure 172). As with h_{wl}, it is likely that the larger f_{cv} values were associated with larger surface hoar structures.

At the up-slope transect of Plot1, f_{cv} was negatively correlated with $L\downarrow$, and I_{max}. It was positively associated with h_{wl}, indicating that where the surface hoar was largest and $L\downarrow$, and I_{max} small, f_{cv} was larger (Table 54). Since weak layer thickness (h_{wl}) holds the similar associations with radiation estimates, it is likely that larger f_{cv} values were

Table 54 Significant weighted least squares linear regression fits between f_{cv} of weak layer and environmental estimates derived from Solar Pathfinder and GIS-methods (left and right columns respectively). Weights defined as the inverse of pit variance of f_{cv} of weak layer. Bold signifies significant ($p \leq 0.05$) fit.

	Areal	~ *f*(Solar Pathfinder Estimate)				~ *f*(GIS Estimate)			
	Extent	p-value	r^2	b	m	p-value	r^2	b	m
$f_{cv} \sim v_{\%}$	$Plot1_{Up\text{-}Slope}$	**8.9E-03**	**0.78**	**-2.1E-01**	**1.9E+00**	**3.3E-02**	**0.63**	**3.4E-01**	**9.9E-01**
$f_{cv} \sim L\downarrow$	$Plot1_{Up\text{-}Slope}$	**8.9E-03**	**0.78**	**7.2E+00**	**-2.6E-02**	**3.6E-02**	**0.62**	**4.2E+00**	**-1.3E-02**
$f_{cv} \sim I_{max}$	$Plot1_{Up\text{-}Slope}$	**7.0E-03**	**0.80**	**4.3E+00**	**-1.4E-02**	**1.2E-02**	**0.75**	**3.4E+00**	**-9.2E-03**
$f_{cv} \sim \sum I$	Plot3	**3.4E-02**	**0.55**	**7.2E-01**	**9.5E-02**	1.6E-01	0.29	7.2E-01	6.9E-02
$f_{cv} \sim \sum t_I$	Plot2	**2.9E-02**	**0.52**	**2.3E+00**	**-3.5E-01**	7.8E-01	0.01	8.3E-01	3.8E-02
	Plot5	3.7E-01	0.12	6.9E-01	4.7E-02	**2.9E-02**	**0.52**	**3.8E-01**	**1.1E-01**

p-value := significance level; r^2 := explanatory strength; b = y-intercept; m = coefficient (slope)

associated with larger surface hoar structures. Additional associations appeared in Plot 2, 3, and 5, however they were limited to only one of the two methods (Pathfinder or GIS) and possessed irrational (positive and negative) signs of the linear coefficients (Table 54).

Several associations existed between L and radiation estimates (Table 55). Plots 2 and 4 possessed logical inverse correlations with $\sum t_I$ and $\sum I$ that were significant. Positive correlations existed between L and $L\downarrow$ (and negative associations with $v_{\%}$), indicating that on these plots L was larger where $L\downarrow$ was greater. This counter-intuitive relationship, coupled with the logical relationships with solar radiation estimates, indicates that solar radiation may have played a more important role in spatial pattern of L than did the longwave estimates. L_{max} was not correlated with any radiation estimates.

Table 55 Significant weighted least squares linear regression fits between L of weak layer and environmental estimates derived from Solar Pathfinder and GIS-methods (left and right columns respectively). Weights defined as the inverse of pit variance of L of weak layer. Bold signifies significant ($p \leq 0.05$) fit.

	Areal	~ *f*(Solar Pathfinder Estimate)				~ *f*(GIS Estimate)			
	Extent	p-value	r^2	b	m	p-value	r^2	b	m
$L \sim v_{\%}$	Plot2	**9.6E-03**	**0.64**	**2.5E+00**	**-1.9E+00**	**8.3E-03**	**0.65**	**2.0E+00**	**-1.1E+00**
	Plot4	**1.4E-02**	**0.60**	**6.8E+00**	**-8.1E+00**	7.1E-02	0.39	7.3E+00	-8.2E+00
$L \sim L\downarrow$	Site	**3.1E-03**	**0.18**	**-3.0E+00**	**1.8E-02**	**8.2E-03**	**0.14**	**-1.2E+00**	**1.1E-02**
	Plot2	**9.6E-03**	**0.64**	**-5.1E+00**	**2.6E-02**	**8.9E-03**	**0.65**	**-2.5E+00**	**1.5E-02**
	Plot4	**1.4E-02**	**0.60**	**-2.5E+01**	**1.1E-01**	6.7E-02	0.40	-2.1E+01	9.5E-02
$L \sim I_{max.}$	Plot2	1.8E-01	0.24	-4.3E-01	7.4E-03	**3.4E-02**	**0.50**	**-8.4E-01**	**8.3E-03**
$L \sim \sum I$	Plot1	**7.3E-03**	**0.50**	**2.5E+00**	**-3.9E-01**	**2.8E-03**	**0.57**	**2.1E+00**	**-1.7E-01**
	$Plot1_{Up\text{-}Slope}$	7.6E-02	0.50	2.4E+00	-3.7E-01	**1.9E-02**	**0.70**	**2.1E+00**	**-1.7E-01**
	$Plot1_{Cross\text{-}Slope}$	**1.6E-02**	**0.72**	**3.2E+00**	**-6.6E-01**	**3.5E-02**	**0.62**	**2.4E+00**	**-2.7E-01**
$L \sim \sum t_I$	Plot1	7.3E-01	0.01	1.4E+00	-1.9E-02	**5.8E-03**	**0.51**	**1.7E+00**	**-8.8E-02**
	$Plot1_{Up\text{-}Slope}$	2.9E-01	0.22	1.7E+00	-9.2E-02	**1.1E-02**	**0.76**	**1.7E+00**	**-9.8E-02**

p-value := significance level; r^2 := explanatory strength; b = y-intercept; m = coefficient (slope)

Micro-strength (σ_{micro}) was negatively correlated with $L\downarrow$ at Plots 3 and 4 indicating that strength was greatest where incoming longwave radiation ($L\downarrow$) was lowest (Table 56). However, I_{max} was positively associated with σ_{micro} at Plots 1 and 3, which would be expected if the surface hoar structure was strengthened by solar radiation.

Table 56 Significant weighted least squares linear regression fits between σ_{micro} of weak layer and environmental estimates derived from Solar Pathfinder and GIS-methods (left and right columns respectively). Weights defined as the inverse of pit variance of σ_{micro} of weak layer. Bold signifies significant ($p \leq 0.05$) fit.

	Areal	~ *f*(Solar Pathfinder Estimate)				~ *f*(GIS Estimate)			
	Extent	p-value	r^2	b	m	p-value	r^2	b	m
$\sigma_{micro} \sim v_{\%}$	Plot3	**2.7E-02**	**0.59**	**-7.0E-02**	**2.1E-01**	**1.4E-02**	**0.66**	**-9.3E-02**	**2.2E-01**
	Plot4	**6.2E-03**	**0.68**	**-5.5E-01**	**9.2E-01**	**1.6E-02**	**0.58**	**-6.8E-01**	**1.0E+00**
$\sigma_{micro} \sim L\downarrow$	Plot3	**2.7E-02**	**0.59**	**7.4E-01**	**-2.8E-03**	**1.4E-02**	**0.67**	**7.9E-01**	**-3.1E-03**
	Plot4	**6.2E-03**	**0.68**	**3.0E+00**	**-1.2E-02**	**2.2E-02**	**0.55**	**3.0E+00**	**-1.3E-02**
$\sigma_{micro} \sim I_{max}$	Plot3	**6.3E-03**	**0.74**	**-6.6E-02**	**6.0E-04**	**6.6E-03**	**0.73**	**-1.0E-01**	**6.8E-04**
$\sigma_{micro} \sim \sum I$	Plot3	**1.9E-02**	**0.63**	**7.5E-03**	**2.3E-02**	**7.2E-03**	**0.73**	**-4.1E-02**	**3.0E-02**
$\sigma_{micro} \sim \sum t_I$	Plot1	9.2E-01	0.00	6.9E-02	6.4E-04	**3.3E-02**	**0.35**	**4.1E-02**	**8.1E-03**
	Plot4	5.0E-01	0.07	4.4E-02	8.3E-03	**2.1E-03**	**0.76**	**5.6E-03**	**1.9E-02**

p-value := significance level; r^2 := explanatory strength; b = y-intercept; m = coefficient (slope)

Internal Snowpack Associations

In this section, causal relationships between snowpack properties relevant to weak layer strength and snowpack stability are described.

Shear Strength (τ_∞) ~ Weak Layer Thickness (h_{wl})

Significant inverse linear relationships were identified between h_{wl} and τ_∞ on the upper slope at Plots 3 and 4, when the pit-scale variance of h_{wl} was included as a weight in the regression (Table 57). These relationships indicate that, on the upper slope, shear strength (τ_∞) of the weak layer was greater where the weak layer was thinner. A logical reason for this relationship is that at any given shear stress larger surface hoar crystals experienced greater torque than smaller surface hoar crystals; assuming bond characteristics are similar, a thicker surface hoar layer will rupture under less stress than a thin surface hoar layer. All other plots possessed no significant relationship between these observations types, although the sign of the fitted lines were also negative for Plots 1, 2, and 5 (Figure 173).

Table 57. Associations between pit-estimates of τ_∞ and h_{wl}, quantified with weighted least squares linear regression. Bold signifies significant ($p \leq 0.05$) fit.

	Areal	WLS, *wts* = 1/pit variance (h_{wl})				WLS, *wts* = 1/pit variance(τ_∞)			
	Extent	p-value	r^2	b	m	p-value	r^2	b	m
$\tau_\infty \sim h_{wl}$	Site	6.6E-01	0.00	621.5	3.91	9.7E-01	0.00	638.5	0.32
	Plot1	3.2E-01	0.14	819.2	-12.39	4.1E-01	0.10	811.9	-12.82
	$Plot1_{Up\text{-}Slope}$	2.9E-01	0.35	894.3	-18.67	1.1E-01	0.62	1106.2	-32.21
	$Plot1_{Cross\text{-}Slope}$	9.5E-02	0.66	192.8	34.39	6.1E-02	0.74	86.7	40.90
	Plot2	4.9E-01	0.07	725.7	-9.60	3.0E-01	0.15	833.2	-17.05
	Plot3	9.1E-02	0.35	1332.2	-48.96	**2.8E-02**	**0.52**	**1364.2**	**-52.12**
	Plot4	7.1E-02	0.39	1439.7	-45.03	**2.0E-02**	**0.56**	**2102.9**	**-88.59**
	Plot5	4.6E-01	0.08	1080.9	-21.30	9.4E-01	0.00	788.5	-2.29

p-value := significance level; r^2 := explanatory strength; b = y-intercept; m = coefficient (slope)

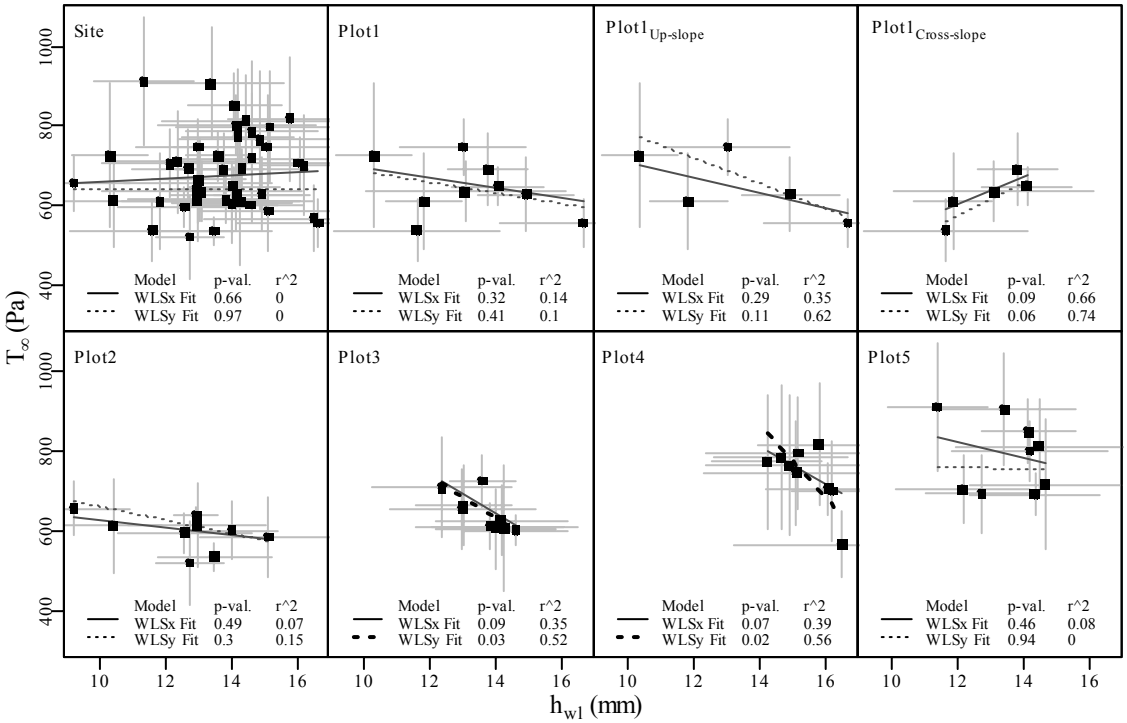

Figure 173. Relationship between pit-scale τ_∞ and h_{wl}. Linear models fitted using weighted least squares regression with weights defined as the inverse of pit variance of τ_∞ and h_{wl}.

These findings are quite perplexing, since Plots 3 and 4 were the only plots that did not contain spatial trends of τ_∞ yet h_{wl} did contain trends at both these sites. In addition, h_{wl} did not possess any spatial autocorrelation Plot 3. It is possible that a common spatial structure exists for both these variables at a different scale of

observation. This would allow for them to be correlated yet appear to have different spatial structures.

Shear Strength (τ_∞) ~ Slab Stresses

At the plot-scale, no significant relationship was evident between τ_∞ and τ_{slab}. However, there were significant positive relationships between τ_∞ and the slab's V_{slab} and N_{slab} components at Plot 5 (Table 58). The latter relationship was also present at Plot 3 (Figure 174). These relationships indicate that at these points in time, the weak layer shear strength (τ_∞) was greatest where N_{slab} was greatest. This is evidence that load positively influenced strengthening at the scale of the shear frame observations.

Table 58. Significant weighted least squares linear regression fits between τ_∞ and slab stresses. Weights defined as the inverse of pit variance of τ_∞. Bold signifies significant ($p \leq 0.05$) fit.

	Areal Extent	WLS, *wts* = 1/pit variance (τ_∞) p-value	r^2	b	m
$\tau_\infty \sim \tau_{slab}$	Site	**1.2E-05**	**0.36**	**4.4E+02**	**8.3E-01**
$\tau_\infty \sim V_{slab}$	Site	**5.3E-06**	**0.39**	**4.4E+02**	**3.9E-01**
	Plot5	**4.2E-02**	**0.47**	**-9.6E+02**	**2.0E+00**
$\tau_\infty \sim Norm_{slab}$	Site	**4.7E-06**	**0.39**	**4.4E+02**	**4.3E-01**
	Plot3	**4.7E-02**	**0.45**	**-6.0E+02**	**2.7E+00**
	Plot5	**3.9E-02**	**0.48**	**-1.2E+03**	**2.6E+00**

p-value := significance level; r^2 := explanatory strength; b = y-intercept; m = coefficient (slope)

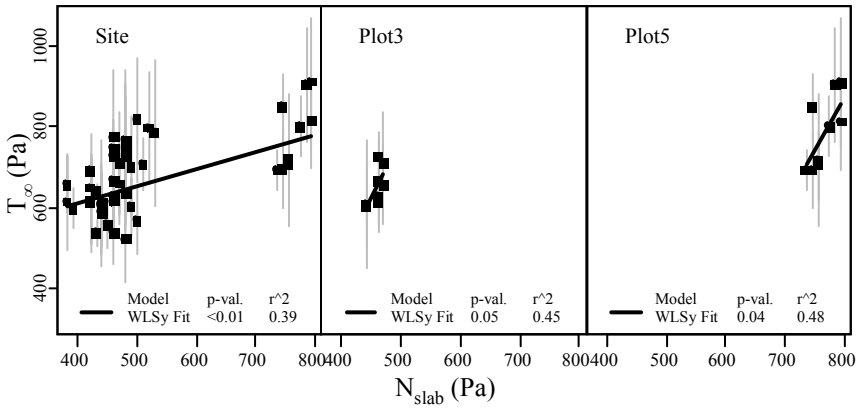

Figure 174. Significant correlations between τ_∞ and N_{slab}. Linear models fitted using weighted least squares regression with weights defined as the inverse of pit variance of τ_∞.

Shear Strength (τ_∞) ~ Weak Layer Microstructural Estimates

No statistically significant relationship was identified between τ_∞ and f_m, f_{max}, and L using the continuum approach with automated sampling using f_{cv} (Table 59). This lack of correlation was likely due to the different phenomena being observed. While the SMP measures rupture force of microstructures under a slab load, shear frame tests quantify rupture force of an aggregate of bonds that have rebounded elastically.

Table 59. Significant weighted least squares linear regression fits between τ_∞ and microstructural estimates of the weak layer. Weights defined as the inverse of pit variance of τ_∞ (left) and that of the SMP estimate (right). Bold signifies significant ($p \leq 0.05$) fit.

	Areal	WLS, *wts* = 1/pit variance($Estimate_{SMP}$)				WLS, *wts* = 1/pit variance (τ_∞)			
	Extent	p-value	r^2	b	m	p-value	r^2	b	m
$\tau_\infty \sim f_{max}$	Site	**6.6E-03**	**0.16**	**876.2**	**-313.4**	**4.5E-03**	**0.17**	**878.2**	**-384.5**
$\tau_\infty \sim f_{cv}$	Site	**2.2E-03**	**0.20**	**1216.4**	**-550.3**	**3.2E-02**	**0.10**	**994.0**	**-363.0**
$\tau_\infty \sim L_{max}$	Plot3	6.0E-02	0.42	1428.1	-415.7	**1.3E-02**	**0.61**	**1488.0**	**-451.9**
$\tau_\infty \sim \sigma_{micro}$	Site	**1.5E-02**	**0.13**	**894.8**	**-3205.3**	1.7E-01	0.04	739.5	-1372.0
	Plot2	9.4E-01	0.00	587.2	152.7	**4.1E-02**	**0.47**	**337.5**	**3564.9**

p-value := significance level; r^2 := explanatory strength; b = y-intercept; m = coefficient (slope)

The maximum structural element L_{max} was significantly correlated with τ_∞ at Plot 3 when the regression was weighted using the pit-variance of τ_∞. This fit explained 61 % of the variance in the pit-estimates of τ_∞ and indicates that at Plot 3, τ_∞ was smaller when L_{max} was larger.

Shear Strength (τ_∞) ~ Super-stratum Microstructural Estimates

Statistically significant positive relationships were identified between τ_∞ and f_m and f_{max} of the adjacent super-stratum when all pits are pooled together (Table 60). As was indicated in the temporal analysis, this inherently depicts the correlation between shear strengthening and bond strengthening in the 5 mm above the weak layer, where the shear frame was positioned. A less significant ($p = 0.04$) negative association was

present between these variables at Plot 2. While this may be a statistical anomaly, it is possible that τ_∞ was weaker where f_m of the super-stratum was greater because the shear frame may have more effectively transferred shear force across the 5 mm thick prepped surface down into the weak layer when the internal bonds within the super-stratum were stronger (recorded as large f_m values) which would result in an easier shear.

Table 60. Significant weighted least squares linear regression fits between τ_∞ and microstructural estimates of super-stratum. Weights defined as the inverse of pit variance of τ_∞ (left) and that of SMP estimate (right). Bold signifies significant ($p \leq 0.05$) fit.

	Areal	WLS, *wts* = 1/pit variance($Estimate_{SMP}$)				WLS, *wts* = 1/pit variance (τ_∞)			
	Extent	p-value	r^2	b	m	p-value	r^2	b	m
$\tau_\infty \sim f_m$	Site	**4.2E-06**	**0.39**	**-1.4E+02**	**11589.3**	**2.8E-02**	**0.11**	**356.2**	**4.1E+03**
	Plot2	4.1E-01	0.10	2.2E+02	5636.7	**4.4E-02**	**0.46**	**1346.7**	**-1.1E+04**
$\tau_\infty \sim f_{max}$	Site	**4.5E-03**	**0.17**	**3.5E+02**	**1817.9**	**3.3E-02**	**0.10**	**441.7**	**1.1E+03**
$\tau_\infty \sim f_{cv}$	Site	**8.3E-02**	**0.07**	**3.7E+02**	**700.2**	2.3E-01	0.03	458.3	4.2E+02
$\tau_\infty \sim L$	Site	8.8E-01	0.00	7.0E+02	-24.1	**1.8E-02**	**0.12**	**230.6**	**3.1E+02**
	Plot2	**7.8E-03**	**0.66**	**-1.3E+02**	**570.6**	1.8E-01	0.24	-157.0	6.1E+02
$\tau_\infty \sim L_{max}$	$Plot1_{Cross\text{-}Slope}$	6.0E-02	0.74	-1.5E+03	1177.8	**2.8E-02**	**0.84**	**-1829.1**	**1.4E+03**
	Plot2	**5.2E-03**	**0.70**	**-2.5E+02**	**511.6**	**3.7E-04**	**0.85**	**-570.6**	**7.0E+02**
	Plot3	**6.7E-04**	**0.83**	**1.6E+03**	**-567.1**	**1.2E-04**	**0.89**	**1754.1**	**-6.3E+02**
	Plot5	**4.2E-02**	**0.47**	**-6.5E+02**	**802.9**	2.8E-01	0.16	-167.6	5.2E+02
$\tau_\infty \sim S$	Plot2	**2.4E-02**	**0.54**	**9.4E+02**	**-8143.6**	**1.7E-02**	**0.58**	**1142.2**	**-1.2E+04**

p-value := significance level; r^2 := explanatory strength; b = y-intercept; m = coefficient (slope)

Several spatial extents possessed positive correlations between L or L_{max} and τ_∞. This indicates that larger structures would be associated with greater shear strengths, which, for intact surface hoar, is counter-intuitive. This may be a good indication that the microstructural estimates derived from the super-stratum are unrelated to the shear frame results, despite the frame being positioned within this stratum.

Significant negative associations between the super-stratum's micro-strength (σ_{micro}) and τ_∞ existed at Plot 2. This association was the direct result of the previously described association with f_m and L. Finally, a significant positive association between the micro-variance f_{cv} at the slope-scale indicates that micro-variance was greatest where

the shear strength (τ_∞) was greatest. This supports Lutz et al.'s (2007) observation that micro-variance increases as a weak layer ages and strengthens.

Shear Strength (τ_∞) ~ Step-Changes of Microstructural Estimates

Step-change in rupture force (Δf_m) held a significant positive correlation with τ_∞ at Plot 2 (Table 61). This indicates that a greater step-change in rupture force (Δf_m) from the super-stratum to the weak layer was associated with stronger shear strengths. For all pits pooled together, a significant negative correlation existed between step-changes of f_m or f_{max} and τ_∞, This may well have been a temporal relationship. The step-change in f_m was greatest on the right side of the slope (Plots 2 and 3) and smallest on the left side of the slope (Plots 4 and 5). Given that Plots 4 and 5 were the last two plots sampled, these plots also had the highest shear strengths.

Table 61. Significant weighted least squares linear regression fits between τ_∞ and step-changes of microstructural estimates. Weights defined as the inverse of pit variance of τ_∞ (left) and that of SMP estimate (right). Bold signifies significant ($p \leq 0.05$) fit.

	Areal	WLS, *wts* = 1/pit variance($Estimate_{SMP}$)				WLS, *wts* = 1/pit variance (τ_∞)			
	Extent	p-value	r^2	b	m	p-value	r^2	b	m
$\tau_\infty \sim \Delta f_m$	Site	**2.3E-02**	**0.11**	**802.0**	**-3032.8**	**4.2E-02**	**0.09**	**760.3**	**-2651.8**
	Plot2	9.8E-02	0.34	448.5	3410.3	**3.3E-02**	**0.50**	**318.0**	**6425.2**
$\tau_\infty \sim \Delta f_{max}$	Site	**2.3E-04**	**0.27**	**874.7**	**-459.9**	**4.7E-04**	**0.25**	**844.0**	**-463.2**
$\tau_\infty \sim \Delta f_{cv}$	Site	**7.3E-04**	**0.24**	**978.0**	**-593.4**	**8.4E-03**	**0.15**	**859.9**	**-413.8**
$\tau_\infty \sim \Delta L$	Plot2	3.9E-01	0.11	580.2	-268.7	**3.6E-03**	**0.72**	**601.8**	**-578.3**
$\tau_\infty \sim \Delta L_{max}$	$Plot1_{Cross\text{-}Slope}$	6.7E-02	0.73	677.8	-682.2	**3.5E-02**	**0.82**	**675.1**	**-665.3**
$\tau_\infty \sim \Delta \sigma_{micro}$	Site	**1.0E-03**	**0.22**	**787.6**	**-4827.4**	9.0E-02	0.07	689.0	-1694.5
	Plot2	2.4E-01	0.19	525.6	2294.9	**5.8E-03**	**0.69**	**483.9**	**3816.6**

p-value := significance level; r^2 := explanatory strength; b = y-intercept; m = coefficient (slope)

Significant negative correlation existed between τ_∞ and ΔL and Plot 2 and ΔL_{max} at the upper-transect of Plot 1. This indicates that as the difference in structural element length (ΔL) increased between the adjacent strata, the shear strength (τ_∞) decreased. At Plot 2 and the up-slope transect of Plot 1, these linear relationships describe 72 % and 78

% of the variance between pit-estimates of τ_∞, respectively. Significant negative relationships also existed between τ_∞ and $\Delta\sigma_{micro}$ and f_{cv}, indicating that as the differences in micro-strength (σ_{micro}) and micro-variance (f_{cv}) increased between the adjacent strata, the shear strength (τ_∞) decreased.

Residual Shear Strength (τ_{resid}) ~ Weak Layer Thickness (h_{wl})

As with τ_∞, significant inverse linear relationships were identified between h_{wl} and τ_{resid} on the upper slope at Plots 3 and 4 (Table 62, Figure 175). On the upper slope, τ_{resid} increased with decreasing h_{wl}.

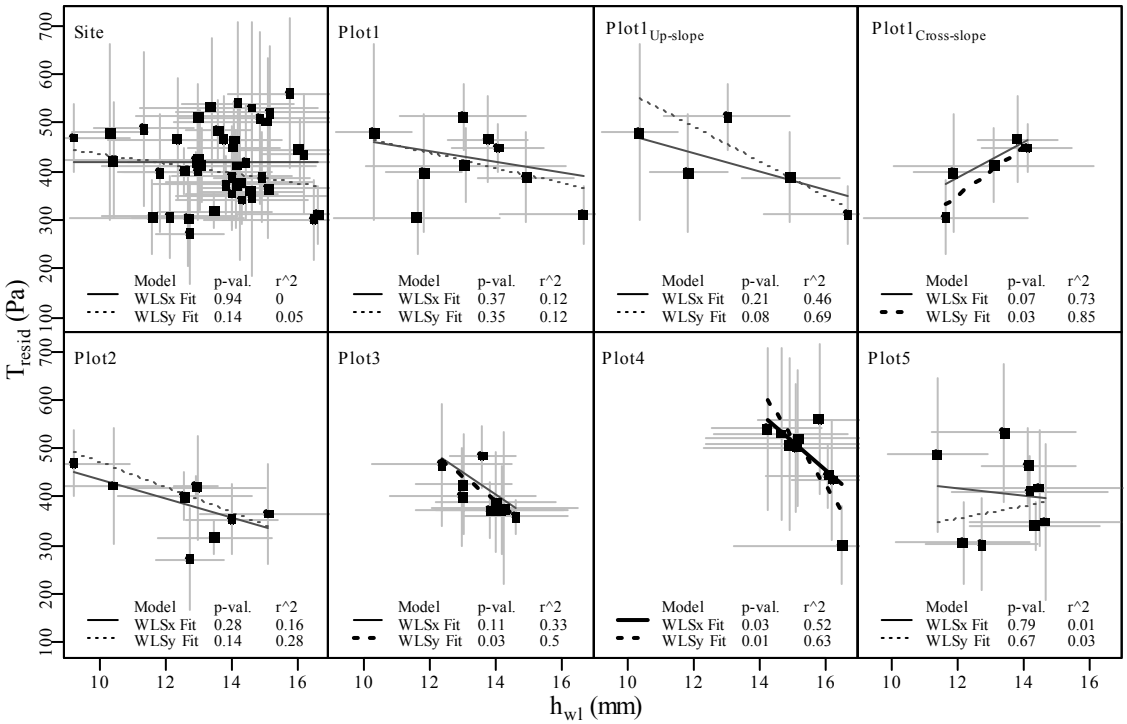

Figure 175. Relationship between pit-scale τ_{resid} and h_{wl}. Linear models fitted using weighted least squares regression with weights defined using the inverse of pit variance of τ_{resid} and h_{wl}.

Table 62. Associations between pit-estimates of shear strength (τ_∞) and weak layer thickness (h_{wl}), quantified with weighted least squares linear regression. Bold signifies significant ($p \leq 0.05$) fit.

	Areal Extent	WLS, *wts* = 1/pit variance($Estimate_{SMP}$) p-value	r^2	b	m	WLS, *wts* = 1/pit variance (τ_∞) p-value	r^2	b	m
$\tau_{resid} \sim h_{wl}$	Site	9.39E-01	0.00	426.02	-0.53	1.42E-01	0.05	534.56	-9.98
	Plot1	3.71E-01	0.12	569.27	-10.62	3.55E-01	0.12	625.16	-15.56
	$Plot1_{Up\text{-}Slope}$	2.11E-01	0.46	668.56	-19.29	8.09E-02	0.69	919.63	-35.76
	$Plot1_{Cross\text{-}Slope}$	6.66E-02	0.73	-52.42	36.65	**2.60E-02**	**0.85**	**-264.33**	**51.24**
	Plot2	2.80E-01	0.16	626.29	-19.10	1.42E-01	0.28	726.51	-25.46
	Plot3	1.07E-01	0.33	1048.14	-45.81	**3.24E-02**	**0.50**	**1104.01**	**-50.83**
	Plot4	**2.82E-02**	**0.52**	**1365.60**	**-56.88**	**1.10E-02**	**0.63**	**1995.72**	**-98.37**
	Plot5	7.94E-01	0.01	501.15	-6.98	6.67E-01	0.03	211.28	12.15

p-value := significance level; r^2 := explanatory strength; b = y-intercept; m = coefficient (slope)

Residual Shear Strength (τ_{resid}) ~ Slab Stresses

At the plot-scale, no significant relationship existed between τ_{resid} and all slab stresses (τ_{slab}, V_{slab} and N_{slab}).

Residual Shear Strength (τ_{resid}) ~ Weak Layer Microstructural Estimates

Few statistically significant relationships were identified between τ_{resid} and microstructural estimates of the weak layer (Table 63). The lack of correlation was likely due to the different phenomena being observed. Despite both variables estimating residual strength of the weak layer, τ_{resid} does not account for elastic strength of the weak layer. While the SMP measures rupture force of microstructures while under a slab load, shear frame tests quantify rupture force of an aggregate of bonds that have rebounded elastically. The maximum structural element L_{max} was significantly correlated with τ_{resid} at Plot 3 when the regression was weighted using the pit-variance of $L_{max,}$ This fit explained 49 % of the variance in the pit-estimates of τ_{resid} and indicates that on Plot 3 τ_{resid} was smaller when L_{max} was larger.

Table 63. Significant weighted least squares linear regression fits between τ_{resid} and microstructural estimates of the weak layer. Weights defined as the inverse of pit variance of τ_{resid} (left) and that of the SMP estimate (right). Bold signifies significant ($p \leq 0.05$) fit.

Relationship	Areal Extent	WLS, *wts* = 1/pit variance($Estimate_{SMP}$) p-value	r^2	b	m	WLS, *wts* = 1/pit variance (τ_∞) p-value	r^2	b	m
$\tau_{resid} \sim f_{max}$	Site	**1.42E-02**	**0.13**	**260.40**	**252.64**	**4.5E-03**	**0.17**	**878.2**	**-384.5**
$\tau_{resid} \sim L_{max}$	Plot3	6.0E-02	0.42	1428.1	-415.7	**3.59E-02**	**0.49**	**1151.63**	**-402.16**
$\tau_{resid} \sim \sigma_{micro}$	Site	**1.5E-02**	**0.13**	**894.8**	**-3205.3**	**4.72E-02**	**0.09**	**289.30**	**1561.72**

p-value := significance level; r^2 := explanatory strength; b = y-intercept; m = coefficient (slope)

Residual Shear Strength (τ_{resid}) ~ Super-stratum Microstructural Estimates

Statistically significant positive relationships were identified between τ_{resid} and f_m and f_{max} of the adjacent super-stratum when all pits are pooled together (Table 64). As was indicated in the temporal analysis, this inherently depicts the correlation between shear strengthening and bond strengthening in the 5 mm above the weak layer, where the shear frame was position. At Plot 3, a significant negative correlation existed between τ_{resid} and L_{max}. This logical relationship was not present at any other plot. In fact, on Plots 2 and 5 positive correlations between L or L_{max} and τ_{resid} existed. This indicates that larger structures were correlated with greater shear strengths, which is counter-intuitive. This may be a good indication that the microstructural estimates derived from the super-stratum are unrelated to the shear frame results, despite the frame being positioned within this stratum.

Significant negative associations between the super-stratum's micro-strength (σ_{micro}) and τ_∞ existed at Plot 2. This association was the direct result of the previously described association with f_m and L. τ_{resid} decreased as σ_{micro} increased. This inverse relationship may indicate that when the super-stratum was harder the shear frame transferred energy more effectively into the surface hoar layer, resulting in lower observed shear strength (τ_∞) values.

Table 64. Significant weighted least squares linear regression fits between τ_{resid} and microstructural estimates of super-stratum. Weights defined as the inverse of pit variance of τ_{resid} (left) and that of SMP estimate (right). Bold signifies significant ($p \leq 0.05$) fit.

Relationship	Areal Extent	WLS, *wts* = 1/pit variance($Estimate_{SMP}$)				WLS, *wts* = 1/pit variance (τ_{∞})			
		p-value	r^2	b	m	p-value	r^2	b	m
$\tau_{resid} \sim f_m$	Site	**1.28E-04**	**0.29**	**-165.25**	**8140.7**	9.51E-01	0.00	392.69	95.9
$\tau_{resid} \sim f_{max}$	Site	**2.19E-03**	**0.20**	**141.17**	**1508.0**	8.29E-02	0.07	265.95	750.2
$\tau_{resid} \sim L$	Plot2	**2.66E-03**	**0.75**	**-704.62**	**853.6**	6.94E-02	0.40	-692.29	870.5
$\tau_{resid} \sim L_{max}$	$Plot1_{Cross\text{-}Slope}$	6.96E-02	0.72	-1864.54	1263.3	**1.56E-02**	**0.89**	**-2544.41**	**1631.9**
	Plot2	**2.15E-04**	**0.87**	**-939.31**	**800.7**	**7.18E-05**	**0.91**	**-958.32**	**804.1**
	Plot3	**2.98E-03**	**0.74**	**1305.27**	**-513.6**	**6.15E-04**	**0.83**	**1464.84**	**-607.2**
	Plot5	**2.91E-02**	**0.52**	**-1108.99**	**845.5**	2.32E-01	0.20	-532.45	515.1
$\tau_{resid} \sim \sigma_{micro}$	Plot2	**3.42E-02**	**0.50**	**845.87**	**-10911.5**	**2.14E-02**	**0.55**	**971.59**	**-13194.5**

p-value := significance level; r^2 := explanatory strength; b = y-intercept; m = coefficient (slope)

Residual Shear Strength (τ_{resid}) ~ Step-Changes of Microstructural Estimates

Step-change in rupture force (Δf_m) had a significant positive correlation with τ_{resid} at Plot 2 (Table 65). This indicates that at Plot 2 a greater step-change in rupture hardness from the super-stratum to the weak layer was associated with stronger shear strengths. For all pits pooled together, a significant negative correlation existed between step-changes of f_m or f_{max} and $\tau_{resid,}$ This may well indicate a temporal relationship. The step-change in f_m was greatest on the right side of the slope (Plots 2 and 3) and smallest on the left side of the slope (Plots 4 and 5). Given that Plots 4 and 5 were the last two plots to be sampled, these plots also had the highest shear strengths.

Significant negative correlation existed between τ_{resid} and ΔL at Plot 1 and Plot 2, as well as between τ_{resid} and ΔL_{max} at Plot 1 (Table 65). τ_{resid} and $\Delta\sigma_{micro}$ was also negatively correlated at Plot 2 (Table 65). This means that over these spatial extents, as ΔL and $\Delta\sigma_{micro}$ increased, τ_{resid} decreased. This indicates that larger differences in element size and micro-strength (σ_{micro}) may have fostered easier shear fracture on these plots.

Table 65. Significant weighted least squares linear regression fits between τ_{resid} and step-changes of microstructural estimates. Weights defined as the inverse of pit variance of τ_{resid} (left) and that of SMP estimate (right). Bold signifies significant ($p \leq 0.05$) fit.

Relationship	Areal Extent	WLS, *wts* = 1/pit variance($Estimate_{SMP}$)				WLS, *wts* = 1/pit variance (τ_{∞})			
		p-value	r^2	b	m	p-value	r^2	b	m
$\tau_{resid} \sim \Delta f_m$	Plot2	1.01E-01	0.34	162.99	4854.48	**1.89E-02**	**0.57**	**48.17**	**7612.28**
$\tau_{resid} \sim \Delta L$	Site	4.73E-01	0.01	408.27	121.11	**4.56E-03**	**0.17**	**404.88**	**-258.61**
	Plot1	2.27E-01	0.20	409.09	-406.38	**2.84E-02**	**0.52**	**421.98**	**-627.36**
	$Plot1_{Cross\text{-}Slope}$	**3.65E-02**	**0.81**	**376.63**	**-904.36**	7.57E-02	0.70	397.64	-829.07
	Plot2	6.49E-01	0.03	358.53	-198.29	**1.35E-02**	**0.61**	**386.12**	**-589.63**
$\tau_{resid} \sim \Delta L_{max}$	$Plot1_{Cross\text{-}Slope}$	**3.30E-02**	**0.82**	**467.94**	**-792.95**	**1.91E-02**	**0.88**	**470.83**	**-804.62**
$\tau_{resid} \sim \Delta \sigma_{micro}$	Plot2	3.98E-01	0.10	306.53	2324.75	**1.78E-02**	**0.58**	**265.90**	**3894.10**

p-value := significance level; r^2 := explanatory strength; b = y-intercept; m = coefficient (slope)

Stability Index (S) ~ Slab Stresses

At the site scale, a clear inverse relationship existed between S and slab stresses, largely due to the snowfall event that resulted in higher stress values at Plot 5 (Table 66, Figure 176). At the plot-scale, S also possessed inverse relationships with slab stresses at Plot 2. The association with τ_{slab} was also present at Plot 1.

Table 66. Significant weighted least squares linear regression fits between S and slab stresses. Weights defined as the inverse of pit variance of S. Bold signifies significant ($p \leq 0.05$) fit.

Relationship	Areal Extent	WLS, *wts* = 1/pit variance(τ_{∞})			
		p-value	r^2	b	m
$S \sim \tau_{slab}$	Site	**1.7E-12**	**0.69**	**4.0E+00**	**-5.2E-03**
	Plot1	**3.1E-02**	**0.51**	**6.7E+00**	**-1.7E-02**
	Plot2	**1.9E-02**	**0.57**	**6.5E+00**	**-1.7E-02**
$S \sim V_{slab}$	Site	**2.0E-11**	**0.65**	**3.9E+00**	**-2.3E-03**
	Plot2	**3.2E-02**	**0.50**	**6.7E+00**	**-8.0E-03**
$S \sim N_{slab}$	Site	**4.4E-11**	**0.64**	**3.9E+00**	**-2.5E-03**
	Plot2	**3.8E-02**	**0.48**	**6.7E+00**	**-8.9E-03**

p-value := significance level; r^2 := explanatory strength; b = y-intercept; m = coefficient (slope)

This is logical, since the denominator of S is slab shear stress. With the exception of Plot 5, all other spatial extents also possessed negative relationships between S and τ_{slab}, however they were statistically insignificant. The apparent lack of association

between *S* and slab stresses at Plot 5 are due to the positive associations between τ_∞ and slab stresses identified at Plot 5.

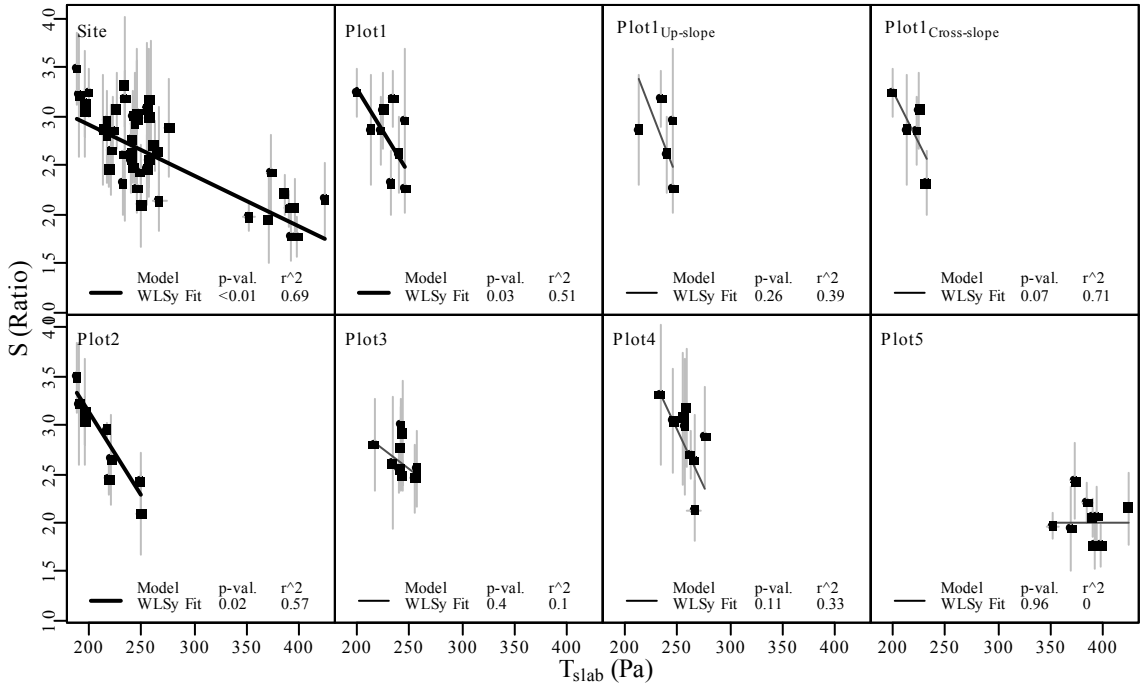

Figure 176. Significant correlations between *S* and τ_{slab}. Linear models were fitted using weighted least squares regression with weights defined using the inverse of pit variance of τ_{slab}.

Stability Index (*S*) ~ Weak Layer Microstructural Estimates

At Plot 2 and for all pits grouped together, significant positive linear relationships existed between *S* and f_m and f_{max}. This relationship is easily rationalized, considering that f_m is essentially an indicator of the residual bond strength, which should be positively correlated with stability. Conversely, an inverse relationship existed between *S* and f_m at the up-slope transect of Plot 1 (Table 67). A logical association where a decrease of stability is accompanied by an increase of f_m can be explained by larger crystals producing large f_m values and shearing more easily than small crystals.

At Plot 3 and for all pits grouped together, significant negative correlations existed between S and L and L_{max}, indicating that where microstructures were larger the stability was smaller (Table 67). However, Plot 2 possessed a significant positive association, which is counter-intuitive. Lastly, when all pits are grouped together, positive correlations are present between S and σ_{micro} and f_{cv}. This last significant result indicates that stability and micro-strength (σ_{micro}) were positively correlated when all pits, from all five days, are analyzed together.

Table 67. Significant weighted least squares linear regression fits between S and microstructural estimates of the weak layer. Weights defined as the inverse of pit variance of S (left) and that of SMP estimate (right). Bold signifies significant ($p \leq 0.05$) fit.

Relation-ship	Areal Extent	WLS, *wts* = 1/pit variance($Estimate_{SMP}$) p-value	r^2	b	m	WLS, *wts* = 1/pit variance (S) p-value	r^2	b	m
$S \sim f_m$	Site	**5.7E-03**	**0.16**	**0.13**	**21.28**	6.1E-02	0.08	0.81	15.48
	$Plot1_{Cross\text{-}Slope}$	**4.1E-02**	**0.80**	**6.79**	**-31.60**	**2.9E-02**	**0.84**	**6.45**	**-28.94**
	Plot2	**4.0E-02**	**0.47**	**-1.33**	**37.27**	**5.0E-02**	**0.45**	**-1.82**	**42.29**
$S \sim f_{max}$	Site	**8.3E-08**	**0.49**	**0.67**	**3.20**	**7.6E-04**	**0.23**	**1.12**	**2.43**
$S \sim L$	Site	2.2E-01	0.04	3.75	-0.80	**2.3E-06**	**0.41**	**5.09**	**-1.85**
	Plot2	**4.8E-02**	**0.45**	**-2.13**	**3.89**	5.7E-01	0.05	4.13	-1.04
	Plot3	**3.8E-02**	**0.48**	**6.98**	**-3.10**	**3.4E-02**	**0.50**	**6.73**	**-2.92**
$S \sim L_{max}$	Site	1.2E-01	0.06	4.56	-1.02	**1.4E-02**	**0.13**	**5.86**	**-1.74**
$S \sim \sigma_{micro}$	Site	**2.9E-04**	**0.27**	**1.13**	**22.15**	**6.2E-08**	**0.50**	**0.86**	**25.36**

p-value := significance level; r^2 := explanatory strength; b = y-intercept; m = coefficient (slope)

Stability Index (S) ~ Super-stratum Microstructural Estimates

Several correlations between S and microstructural estimates of the super-stratum mimic those within the weak layer itself. As with the weak layer's mean rupture force (f_m) at the up-slope transect of Plot 1, a significant negative relationship existed between the super-stratum's f values and S when pits from all plots are grouped together (Table 68). This counter-intuitive correlation resulted from two temporal processes that differentiate the pits collected at Plot 5 from the other pits, resulting in a negative association. As with the weak layer, a significant negative relationship existed within the

super-stratum, between *S* and *L* at Plot 3 and when all pits were grouped together (Table 68). Also, Plot 2 possessed the counter-intuitive positive association between *L* and *S*. Lastly, a significant negative relationship existed between *S,* and σ_{micro} and f_{cv}. Four significant correlations, three of which were positive, existed between *S* and L_{max}.

Table 68. Significant weighted least squares linear regression fits between *S* and microstructural estimates of super-stratum. Weights defined as the inverse of pit variance of *S* (left) and that of SMP estimate (right). Bold signifies significant ($p \leq 0.05$) fit.

Relation-ship	Areal Extent	WLS, *wts* = 1/pit variance(*Estimate*$_{SMP}$) p-value	r^2	b	m	WLS, *wts* = 1/pit variance (*S*) p-value	r^2	b	m
$S \sim f_m$	Site	1.9E-01	0.04	1.5	16.1	**7.0E-03**	**0.16**	**4.7**	**-30.3**
$S \sim L$	Site	9.5E-02	0.06	4.2	-1.2	**3.9E-03**	**0.18**	**5.5**	**-2.2**
	Plot2	**7.7E-04**	**0.82**	**-5.5**	**6.6**	**1.3E-02**	**0.61**	**-6.2**	**7.2**
$S \sim L_{max}$	Plot1$_{Cross\text{-}Slope}$	1.2E-01	0.61	-8.8	6.5	**2.7E-02**	**0.85**	**-14.8**	**9.8**
	Plot2	**7.2E-05**	**0.91**	**-7.3**	**6.1**	**1.2E-03**	**0.80**	**-4.6**	**4.4**
	Plot3	5.7E-02	0.43	5.7	-1.7	**7.5E-03**	**0.66**	**6.8**	**-2.4**
	Plot5	**2.8E-02**	**0.52**	**-2.1**	**2.3**	2.2E-01	0.21	-0.3	1.3
$S \sim \sigma_{micro}$	Plot2	**3.8E-02**	**0.48**	**6.2**	**-79.5**	5.3E-02	0.43	6.1	-75.7

p-value := significance level; r^2 := explanatory strength; b = y-intercept; m = coefficient (slope)

Stability Index (*S*) ~ Step-Changes of Microstructural Estimates

Step-changes in f_m were significantly correlated with τ_∞ through a negative relationship at Plot 1 and at the up-slope transect of Plot 1, indicating that at Plot 1 a greater difference in rupture hardness from the super-stratum to the weak layer was associated with lower stability. A positive relationship was present between *S* and Δf_m and Δf_{max} when all pits across the site were tested together, indicating that lower stability was associated with smaller step-changes in f_m. These site-scale correlations describe relationships that were caused by temporal processes (loading of the weak layer).

Significant negative correlation existed between *S* and *L* and L_{max} at Plot 1, the cross-slope transect of Plot 1, and when all pits were tested together (Table 69). This

indicates that as the difference in L increased between the adjacent strata, the stability decreased.

Significant positive relationships also existed between S and the step-changes of σ_{micro} at the site-scale (all pits tested together), indicating that spatial and temporal variability of S is positively associated with increases of $\Delta\sigma_{micro}$. Within Plot 1, Δf_{cv} was negatively correlated with stability, indicating that within this extent, larger step-changes in micro-variance between the super-stratum and the weak layer are associated with lower stability.

Table 69. Significant weighted least squares linear regression fits between S and step-changes of microstructural estimates. Weights defined as the inverse of pit variance of S (left) and that of SMP estimate (right). Bold signifies significant ($p \leq 0.05$) fit.

Relation-ship	Areal Extent	WLS, *wts* = 1/pit variance($Estimate_{SMP}$) p-value	r^2	b	m	WLS, *wts* = 1/pit variance (*S*) p-value	r^2	b	m
$S \sim \Delta f_m$	Site	**1.6E-02**	**0.13**	**1.9**	**17.1**	**4.7E-04**	**0.25**	**1.5**	**24.3**
	Plot1	**1.4E-02**	**0.60**	**4.1**	**-25.4**	1.3E-01	0.30	4.0	-22.8
	$Plot1_{Cross\text{-}Slope}$	**2.3E-02**	**0.86**	**4.2**	**-26.5**	**3.1E-02**	**0.83**	**4.3**	**-28.3**
$S \sim \Delta f_{max}$	Site	**3.8E-06**	**0.40**	**1.4**	**2.9**	**9.2E-04**	**0.23**	**1.6**	**2.4**
$S \sim \Delta f_{cv}$	Plot1	**4.8E-02**	**0.45**	**4.5**	**-3.1**	2.8E-01	0.17	3.9	-1.9
$S \sim \Delta L$	Site	2.7E-01	0.03	2.7	-1.0	**2.7E-05**	**0.34**	**2.7**	**-2.4**
	Plot1	**3.2E-02**	**0.50**	**2.9**	**-3.5**	**2.8E-03**	**0.74**	**2.9**	**-4.2**
	$Plot1_{Cross\text{-}Slope}$	**2.7E-02**	**0.85**	**2.7**	**-5.8**	**3.0E-02**	**0.83**	**2.8**	**-5.6**
$S \sim \Delta L_{max}$	$Plot1_{Cross\text{-}Slope}$	**2.5E-02**	**0.85**	**3.2**	**-4.4**	**3.3E-02**	**0.83**	**3.3**	**-4.7**
$S \sim \Delta\sigma_{micro}$	Site	**1.8E-03**	**0.20**	**2.1**	**21.7**	**2.8E-07**	**0.46**	**1.9**	**25.7**

p-value := significance level; r^2 := explanatory strength; b = y-intercept; m = coefficient (slope)

Weak Layer Microstructural Estimates ~ Slab Stresses

At the slope-scale, including data from all five plots, clear inverse relationships existed between the three slab stresses and f_m and f_{max} (Table 70). This indicates that under different slabs loads, regardless of space and time, the residual strength of bonds and structures was smallest when the slab stresses were greatest.

Table 70. Associations between slab stresses and pit-estimates of weak layer microstructural estimates, quantified with weighted least squares linear regression. Bold signifies significant ($p \leq 0.05$) fit.

Significant Relationship		Spatial Extent	p-value	r^2	b	m
$f_m \sim$	V_{slab}	Site	**8.5E-03**	**0.15**	**1.3E-01**	**-2.2E-05**
		Plot2	**2.6E-02**	**0.53**	**1.7E-01**	**-1.3E-04**
	N_{slab}	Site	**9.7E-03**	**0.15**	**1.3E-01**	**-2.5E-05**
		Plot2	**2.2E-02**	**0.55**	**1.8E-01**	**-1.5E-04**
	τ_{slab}	Site	**5.4E-03**	**0.17**	**1.3E-01**	**-5.1E-05**
		Plot1 Cross-Slope	**1.3E-02**	**0.90**	**-4.5E-02**	**7.8E-04**
		Plot2	**4.7E-02**	**0.45**	**1.6E-01**	**-2.2E-04**
		Plot3	**3.4E-02**	**0.50**	**2.4E-01**	**-4.9E-04**
$f_{max} \sim$	V_{slab}	Site	**4.4E-11**	**0.64**	**9.1E-01**	**-5.4E-04**
	N_{slab}	Site	**7.6E-11**	**0.63**	**9.1E-01**	**-6.1E-04**
	τ_{slab}	Site	**9.6E-12**	**0.66**	**9.1E-01**	**-1.2E-03**
		Plot1 Up-Slope	**3.0E-02**	**0.84**	**1.9E+00**	**-5.0E-03**
		Plot3	**3.0E-02**	**0.51**	**1.7E+00**	**-4.6E-03**
$f_{cv} \sim$	V_{slab}	Site	**1.1E-04**	**0.30**	**1.1E+00**	**-2.9E-04**
	N_{slab}	Site	**9.0E-05**	**0.30**	**1.1E+00**	**-3.3E-04**
	τ_{slab}	Site	**2.5E-04**	**0.27**	**1.1E+00**	**-6.1E-04**
$L \sim$	V_{slab}	Site	**6.9E-03**	**0.16**	**1.1E+00**	**3.2E-04**
		Plot2	**4.9E-02**	**0.45**	**1.8E+00**	**-1.1E-03**
	N_{slab}	Site	**7.4E-03**	**0.16**	**1.1E+00**	**3.6E-04**
	τ_{slab}	Site	**5.9E-03**	**0.16**	**1.1E+00**	**7.2E-04**
		Plot2	**2.6E-02**	**0.53**	**1.8E+00**	**-2.4E-03**
$\sigma_{micro} \sim$	V_{slab}	Site	**2.8E-05**	**0.34**	**8.9E-02**	**-4.0E-05**
		Plot3	**1.7E-02**	**0.58**	**2.5E-01**	**-3.6E-04**
	N_{slab}	Site	**4.5E-05**	**0.32**	**8.9E-02**	**-4.4E-05**
	τ_{slab}	Site	**5.3E-06**	**0.39**	**9.1E-02**	**-9.3E-05**
		Plot3	**9.5E-04**	**0.81**	**1.9E-01**	**-5.3E-04**

When Plot 2 was examined separately, the same relationship was observed, indicating that a similar relationship can exist over space at one point in time (Table 70, Figure 177). Of particular interest in this comparison is the magnitude of the changes occurring. Across Plot 2, the total variation of slab-generated vertical stress was 124 Pa (Min: 426 Pa, Max: 550 Pa), which equates to a difference of about 12.6 mm water equivalent or 1.14 kg (2.5 lbs) applied to a 30 cm^2 surface area (the area of a standard

stability test). The weighted least squares linear fit estimated that for every 1 Pa added to the vertical load, f_m decreased by 0.00013 N.

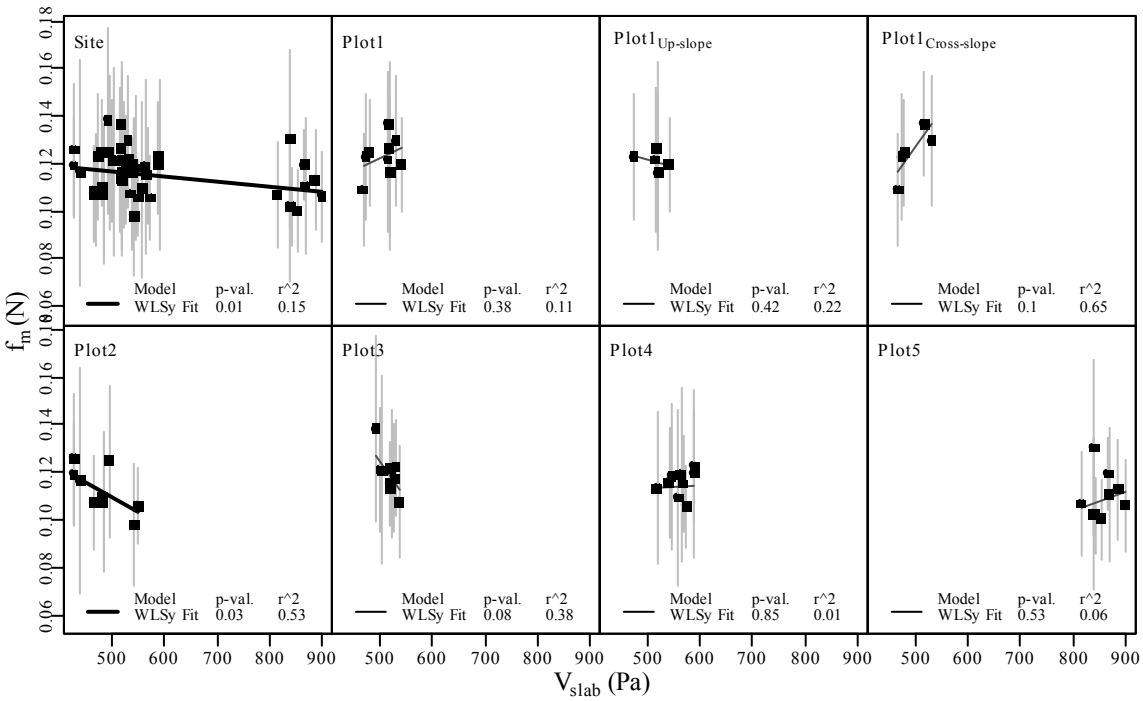

Figure 177. Significant correlations between f_m and V_{slab}. Linear models were fitted using weighted least squares regression with weights defined using the inverse of pit variance of V_{slab}.

Plot 3 also possessed inverse relationships between τ_{slab} and f_m and f_{max}. The results from Plots 2 and 3 may be good indications of weak zone development. On these plots, large slab stresses coincide with low rupture forces that correspond with microstructural residual strength, resulting in potential weak zones that may be more susceptible to failure than adjoining areas. A clear rationale can be made as to why the other plots did not contain this association. Over time, areas with greater slab load will experience additional deformation and strengthening. Hence, as a snowpack stabilizes after a loading event, areas with the greatest stress will experience the most deformation and hence strengthening. So the residual strength of individual structures is initially

inversely proportional to slab stress but with time should be positively affected by slab stress.

At the site-scale, micro-variance f_{cv} also was inversely related to slab stresses, indicating that larger stress was associated with smaller micro-variance (Table 70). Depending on whether observations from individual plots or from the entire site were examined, different relationships existed between slab load and L. At the site-scale, L is positively correlated with slab-stresses. Under an increased load some bonds within the weak layer may have begun to fail or were so close to failing their rupture could not be differentiated from instrumental noise. With fewer ruptures being recognized by the penetrometer within a set volume, L increased. Regardless of whether bonds already failed or were so small that the SMP could no longer recognize them, in both circumstances fewer discernable structures existed when the load was increased.

An opposite relationship was evident at one point in time at Plot 2, whereby L decreased with increasing load (Table 70). This relationship over space may be the result of the load-related deformation. Over time, areas with larger loads would potentially cause greater deformation which, in turn resulted in smaller distances between bonds or structures. σ was inversely related to load at the site-scale and at the plot-scale at Plot 3. As load increased, σ decreases.

Super-stratum Microstructural Estimates ~ Slab Stresses

When all data from the study site were examined together, f_m was inversely proportional to all slab stresses (Table 71). Unlike for the weak layer, it appears that f_m of the super-stratum increased with an increased load. Conversely, as within the weak layer,

the super-stratum at Plot 2 possessed positive correlations between f_m and slab stresses, suggesting that greater load caused local strengthening.

Table 71. Associations between slab stresses and pit-estimates of super-stratum microstructural estimates, quantified with weighted least squares linear regression. Bold signifies significant ($p \leq 0.05$) fit.

Significant Relationship		Spatial Extent	p-value	r^2	b	m
$f_m \sim$	V_{slab}	Site	**2.8E-02**	**0.11**	**6.1E-02**	**1.4E-05**
		Plot2	**1.3E-02**	**0.61**	**8.8E-02**	**-4.8E-05**
	N_{slab}	Site	**2.9E-02**	**0.11**	**6.1E-02**	**1.6E-05**
		Plot2	**1.5E-02**	**0.59**	**8.9E-02**	**-5.5E-05**
	τ_{slab}	Site	**2.6E-02**	**0.11**	**6.1E-02**	**3.2E-05**
		Plot2	**7.6E-03**	**0.66**	**8.6E-02**	**-9.5E-05**
$L \sim$	V_{slab}	Plot1	**2.2E-03**	**0.76**	**3.0E+00**	**-3.4E-03**
		Plot1 Up-Slope	**4.8E-02**	**0.78**	**2.9E+00**	**-3.1E-03**
		Plot2	**7.9E-03**	**0.66**	**1.9E+00**	**-1.2E-03**
		Plot3	**3.9E-02**	**0.48**	**2.3E+00**	**-1.9E-03**
	N_{slab}	Plot1	**3.1E-03**	**0.74**	**3.0E+00**	**-3.7E-03**
		Plot1 Up-Slope	**3.2E-02**	**0.83**	**2.9E+00**	**-3.5E-03**
		Plot2	**8.7E-03**	**0.65**	**1.9E+00**	**-1.4E-03**
	τ_{slab}	Plot1	**2.3E-02**	**0.55**	**2.5E+00**	**-5.3E-03**
		Plot2	**7.1E-03**	**0.67**	**1.8E+00**	**-2.4E-03**
		Plot3	**3.8E-02**	**0.48**	**2.0E+00**	**-2.5E-03**
$L_{max} \sim$	V_{slab}	Plot1	**1.2E-02**	**0.61**	**3.2E+00**	**-3.0E-03**
		Plot1 Up-Slope	**1.6E-02**	**0.89**	**3.3E+00**	**-3.1E-03**
		Plot2	**6.9E-03**	**0.67**	**2.2E+00**	**-1.3E-03**
	N_{slab}	Plot1	**2.5E-02**	**0.54**	**3.1E+00**	**-3.1E-03**
		Plot1 Up-Slope	**7.7E-03**	**0.93**	**3.3E+00**	**-3.7E-03**
		Plot2	**9.4E-03**	**0.64**	**2.3E+00**	**-1.4E-03**
		Plot3	**3.2E-02**	**0.50**	**3.7E+00**	**-4.2E-03**
	τ_{slab}	Plot1	**1.3E-02**	**0.61**	**2.9E+00**	**-5.0E-03**
		Plot2	**2.4E-03**	**0.75**	**2.2E+00**	**-2.6E-03**
$\sigma_{micro} \sim$	V_{slab}	Plot1	**1.3E-02**	**0.61**	**-4.7E-02**	**1.7E-04**
		Plot1 Cross-Slope	**3.0E-02**	**0.84**	**-1.3E-02**	**1.1E-04**
	N_{slab}	Plot1	**7.8E-03**	**0.66**	**-4.6E-02**	**1.9E-04**
		Plot1 Cross-Slope	**2.0E-02**	**0.87**	**-7.8E-03**	**1.1E-04**

Unlike the fits involving the weak layer, the relationship involving the super-stratum at Plot 2 involved a shallow slope which means that for a given change in slab stress, the corresponding change in f_m is smaller than it was in the weak layer. This is

logical, given that in the small grained super-stratum the slab force is distributed over more structures, resulting in a small change of the residual strength of structures.

All significant relationships between the structural element length (L) of the super-stratum and the slab load were positive associations. The only correlation between σ_{micro} of the super-stratum and slab load was at Plot 1, where σ_{micro} was positively associated with slab load.

Step-Changes of Microstructural Estimates ~ Slab Stresses

Step-changes of mean and maximum rupture force (Δf_m and Δf_{max}) were negatively correlated with load when all plots were considered together (Table 72). This indicates that large loads caused differences of f_m between adjacent strata to become smaller. Lutz et al. (2008a) confirmed this observation using a dataset from 2008. Plot 1 possessed an inverse association, indicating that, at one point in time, the step-change in f_m was larger where the load was greater. This was expected because the added stress would cause additional deformation that would result in stronger structures with greater associated rupture forces. However, given how small the difference in slab load is across the slope, it is more likely that this different in Δf_m was due to pre-existing spatial patterns in Δf_m.

Step-changes of mean and maximum microstructural element length (ΔL and ΔL_{max}) were consistently and positively associated with slab load at Plot 1 and it's individual transects. Large loads were associated with large differences in L and L_{max}. Step-changes of micro-strength ($\Delta\sigma_{micro}$) were negatively associated with load at the site-scale and for Plots 1 and 3, which shows that differences in micro-strength ($\Delta\sigma_{micro}$)

between the slab and weak layer became smaller when the load was greater. The opposite was observed at Plot 5.

Table 72. Associations between slab stresses and pit-estimates of step-changes of microstructural estimates, from the adjacent super-stratum to the weak layer, quantified with weighted least squares linear regression. Bold signifies significant ($p \leq 0.05$) fit.

Significant Relationship		Spatial Extent	p-value	r^2	b	m
Δf_m -	V_{slab}	Site	**5.5E-04**	**0.25**	**6.0E-02**	**-3.3E-05**
		Plot1	**1.7E-02**	**0.58**	**-8.6E-02**	**2.7E-04**
	N_{slab}	Site	**6.4E-04**	**0.24**	**6.0E-02**	**-3.7E-05**
		Plot1	**2.9E-02**	**0.52**	**-8.6E-02**	**3.0E-04**
	τ_{slab}	Site	**3.6E-04**	**0.26**	**6.0E-02**	**-7.3E-05**
		Plot1	**1.6E-02**	**0.59**	**-4.7E-02**	**4.3E-04**
		Plot1 Cross-Slope	**2.2E-02**	**0.87**	**-1.2E-01**	**8.0E-04**
Δf_{max} -	V_{slab}	Site	**1.5E-10**	**0.62**	**7.0E-01**	**-5.0E-04**
	N_{slab}	Site	**2.7E-10**	**0.61**	**7.0E-01**	**-5.6E-04**
	τ_{slab}	Site	**3.0E-11**	**0.65**	**7.0E-01**	**-1.1E-03**
		Plot1 Up-Slope	**2.6E-02**	**0.85**	**1.8E+00**	**-5.6E-03**
Δf_{cv} -	V_{slab}	Site	**8.5E-04**	**0.23**	**6.6E-01**	**-2.6E-04**
		Plot1	**4.0E-02**	**0.47**	**-5.0E-01**	**2.1E-03**
	N_{slab}	Site	**7.9E-04**	**0.23**	**6.6E-01**	**-3.0E-04**
	τ_{slab}	Site	**1.4E-03**	**0.21**	**6.5E-01**	**-5.6E-04**
		Plot1	**2.2E-02**	**0.55**	**-2.7E-01**	**3.6E-03**
ΔL -	V_{slab}	Plot1	**1.9E-03**	**0.77**	**-1.3E+00**	**2.5E-03**
		Plot1 Cross-Slope	**7.1E-03**	**0.94**	**-1.2E+00**	**2.5E-03**
	N_{slab}	Plot1	**5.9E-03**	**0.69**	**-1.3E+00**	**2.8E-03**
		Plot1 Cross-Slope	**1.6E-02**	**0.89**	**-1.2E+00**	**2.7E-03**
	τ_{slab}	Plot1	**8.7E-04**	**0.81**	**-9.1E-01**	**4.2E-03**
		Plot1 Up-Slope	**2.4E-02**	**0.86**	**-1.3E+00**	**5.7E-03**
		Plot1 Cross-Slope	**3.4E-02**	**0.82**	**-8.9E-01**	**4.1E-03**
ΔL_{max} -	V_{slab}	Plot1	**4.4E-03**	**0.71**	**-2.1E+00**	**4.6E-03**
		Plot1 Up-Slope	**3.0E-02**	**0.84**	**-2.3E+00**	**4.9E-03**
	N_{slab}	Plot1	**1.3E-02**	**0.61**	**-2.0E+00**	**4.9E-03**
		Plot1 Up-Slope	**3.0E-02**	**0.83**	**-2.3E+00**	**5.6E-03**
	τ_{slab}	Plot1	**8.7E-03**	**0.65**	**-1.4E+00**	**6.8E-03**
$\Delta\sigma_{micro}$ -	V_{slab}	Site	**2.7E-05**	**0.34**	**4.4E-02**	**-3.6E-05**
		Plot3	**4.6E-02**	**0.46**	**1.9E-01**	**-3.3E-04**
	N_{slab}	Site	**4.2E-05**	**0.33**	**4.4E-02**	**-4.0E-05**
		Plot5	**5.0E-02**	**0.45**	**-1.4E-01**	**2.0E-04**
	τ_{slab}	Site	**6.4E-06**	**0.38**	**4.5E-02**	**-8.4E-05**
		Plot1 Up-Slope	**4.4E-02**	**0.79**	**1.2E-01**	**-4.2E-04**
		Plot3	**3.0E-03**	**0.74**	**1.5E-01**	**-5.4E-04**

Weak Layer Microstructural Estimates ~ Weak Layer Thickness (h_{wl})

Significant positive correlations between L of the weak layer and h_{wl} were identified at Plot 1 and at Plot 1's up-slope transect (Figure 178). Both these spatial extents contained the largest range of h_{wl} values of any individual plot. This means that the length of microstructural elements, as estimated using an individual 5 mm segment of the weak layer and selected automatically using the local maximum of f_{cv}, was correlated with the thickness of the buried surface hoar layer itself. This relationship is logical, since the thickness of a buried surface hoar layer is largely determined by the size of individual crystals. This finding shows that the selected estimation procedure (5 mm moving-window) and selected sampling technique (local maxima of f_{cv}) appears to produce relevant information that, in this instance, spans microstructural and stratigraphic scales.

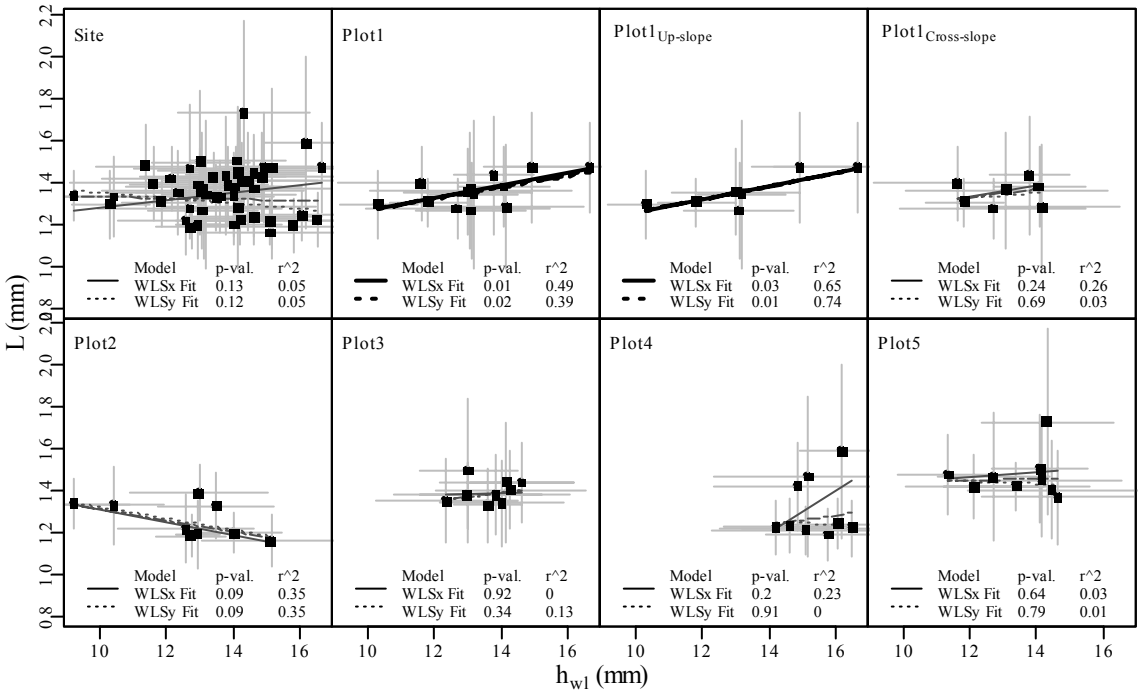

Figure 178. L of the weak layer, as a function of weak layer thickness (h_{wl}).

No significant correlations existed between h_{wl} and L_{max}, σ_{micro} or f_{cv}. A weak positive correlation was identified between f_m and h_{wl} at Plot 5, and a negative correlation between f_{max} and h_{wl} on Plot 1's cross-plot. It is difficult to justify these relationships, as the two correlations possess opposed signs.

Pit-to-Plot Representativity

Overview

Pit-to-plot tests of representativity for the main snow strength and stability variables were summarized in graphic and tabular forms. Graphics depict which pits within a given plot are not representative of their respective plots, in terms of their central tendency and distribution, as tested using the Wilcoxon Rank Sum test and the Kolmogorov-Smirnoff Test, respectively. This format facilitates comprehending spatial patterns in uniformity, more effectively than do tables alone.

Shear Frame Derived Variables

Shear Strength (τ_∞): Plot 1 contained three pits that were not representative of the plot median or distribution (Table 73). Two of these pits were at opposite ends of the up-slope transect (Figure 179). The pit with significantly stronger τ_∞ values was near the base of the slope and the pit with significantly weaker τ_∞ values was at the top. These discrepancies were the result of the up-slope trend in τ_∞ quantified in the geo-statistical analysis. A third pit at Plot 1, located on the right arm, possessed significantly weaker τ_∞ values.

A spatial pattern existed in pit representativity of τ_∞ on the remaining four plots. Spanning the upper slope, Plots 3 and 4 were quite uniform, evident in that eight out of nine pits were representative of their respective plots, in both their median values and distributions (Table 73 and Figure 179).

Conversely, on the lower slope, Plots 2 and 5 contained several pits that were not representative of their respective plots (Figure 179). There were two unrepresentative pits at Plot 5, where the pit with above average τ_∞ was at the base of the plot (red circle, Figure 179) and a pit with below-average τ_∞ values at the top of the plot (blue circle, Figure 179). Two unrepresentative pits containing proportionally more shear strength (τ_∞) observations with small values than their respective plot distribution (as established with Kolmogorov-Smirnov Test) were at the middle or top of Plots 2 and 5 (blue squares in Figure 179). Hence, on the lower slope, we see fewer representative pits or a lesser degree of uniformity. These unrepresentative pits on the lower slope coincided with spatial patterns in τ_∞, whereby τ_∞ decreased from the lower right to upper left corners of these plots. These findings illustrate how results from pit-to-plot analysis were significantly influenced by spatial trends in the observed phenomenon.

Table 73. Frequency and percentage of pits that are representative of respective plots in for τ_∞.

		Wilcoxon –Rank Sum Test (tests centrality)				Kolmogorov-Smirnov Test (tests distribution)			
	T_∞	Pits are statistically* representative of plot		Pits are statistically* unrepresentative of plot		Pits are statistically* representative of plot		Pits are statistically* unrepresentative of plot	
Plot	Date	Freq.	(Plot %)	Freq.	(Plot %)	Freq.	(Plot %)	Freq.	(Plot %)
1	28.02.2005	6	67	3	33	7	78	2	22
2	1.03.2005	8	89	1	11	6	67	3	33
3	8.03.2005	8	89	1	11	8	89	1	11
4	14.03.2005	8	89	1	11	8	89	1	11
5	21.03.2005	7	78	2	22	8	89	1	11

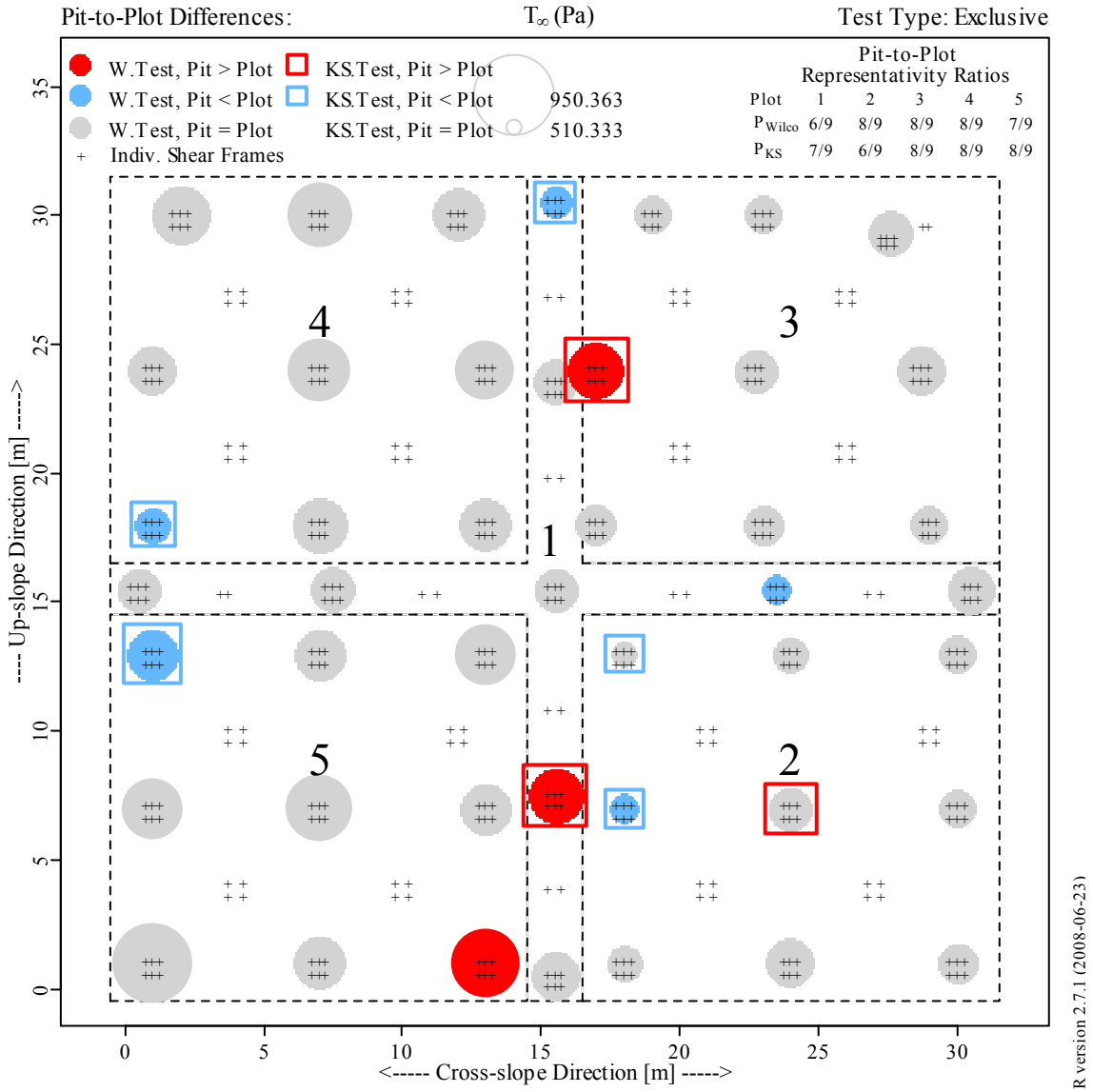

Figure 179. Pit-to-plot representativity of τ_∞ across the slope. Black dotted lines are plot boundaries. Circle size represents the pit-derived median of τ_∞. Blue and red circles indicate significantly lower and higher median values, based on the Wilcoxon Rank Sum test. Blue and red squares indicate significantly different distributions, with blue and red indicating if pit observations where generally lower than or higher than plot observations, based on the Kolmogorov-Smirnov test.

The results from the upper and lower slopes can be considered separately to detect any changes in representativity that may have occurred over time. On the upper slope, pit representativity did not change between Plots 3 and 4. On the lower slope, changes were

not definitive: the pit-to-plot ratios for central tendency P_{Wilco} decreased from 8/9 to 7/9 and the pit-to-plot ratios for distribution P_{KS} increased from 6/9 to 8/9.

Residual Shear Strength (τ_{resid}): As with τ_{∞}, Plot 1 contained three pits that were not representative of either the plot median or distribution (Table 74), two of which reinforce the geo-statistical findings that quantified an up-slope trend in τ_{resid} (Figure 180). A third pit at Plot 1, located on the right arm, possessed significantly weaker τ_{resid} values. A similar pattern existed in pit representativity of τ_{resid} on the remaining four plots as did for τ_{∞}. Spanning the upper slope, Plots 3 and 4 are quite uniform, evident in that 16 of 18 pits were representative plot median and distributions values (Table 74 and Figure 180).

Table 74. Frequency and percentage of pits that are representative of respective plots in for τ_{resid}.

		Wilcoxon -Rank Sum Test (tests centrality)				Kolmogorov-Smirnov Test (tests distribution)			
	τ_{resid}	Pits are statistically* representative of plot		Pits are statistically* unrepresentative of plot		Pits are statistically* representative of plot		Pits are statistically* unrepresentative of plot	
Plot	Date	Freq.	(Plot %)	Freq.	(Plot %)	Freq.	(Plot %)	Freq.	(Plot %)
1	28.02.2005	6	67	3	33	7	78	2	22
2	1.03.2005	6	67	3	33	6	67	3	33
3	8.03.2005	8	89	1	11	8	89	1	11
4	14.03.2005	8	89	1	11	8	89	1	11
5	21.03.2005	6	67	3	33	7	78	2	22

* Both tests are non-parametric two-sided tests with a 'significant' difference based on a 95 % confidence level.

Conversely, on the lower slope, six pits were not representative of their respective plots (Figure 180). Three unrepresentative pits existed at Plot 2, whereby the pit with above average τ_{resid} was at the base of the plot (red circle, Figure 180) and a pits with below-average τ_{resid} values were at the middle or top of the plot (blue circle, Figure 180). A similar pattern at Plot 5 was obscured by a single pit with lower than average values at the base of the plot. Hence, on the lower slope, fewer representative pits existed,

indicating a lesser degree of uniformity. As observed for Plot 1, these unrepresentative pits on the lower slope largely coincided with up-slope trends in τ_{resid}. These findings illustrate how results from pit-to-plot analysis were significantly influenced by spatial trends in the observed phenomenon.

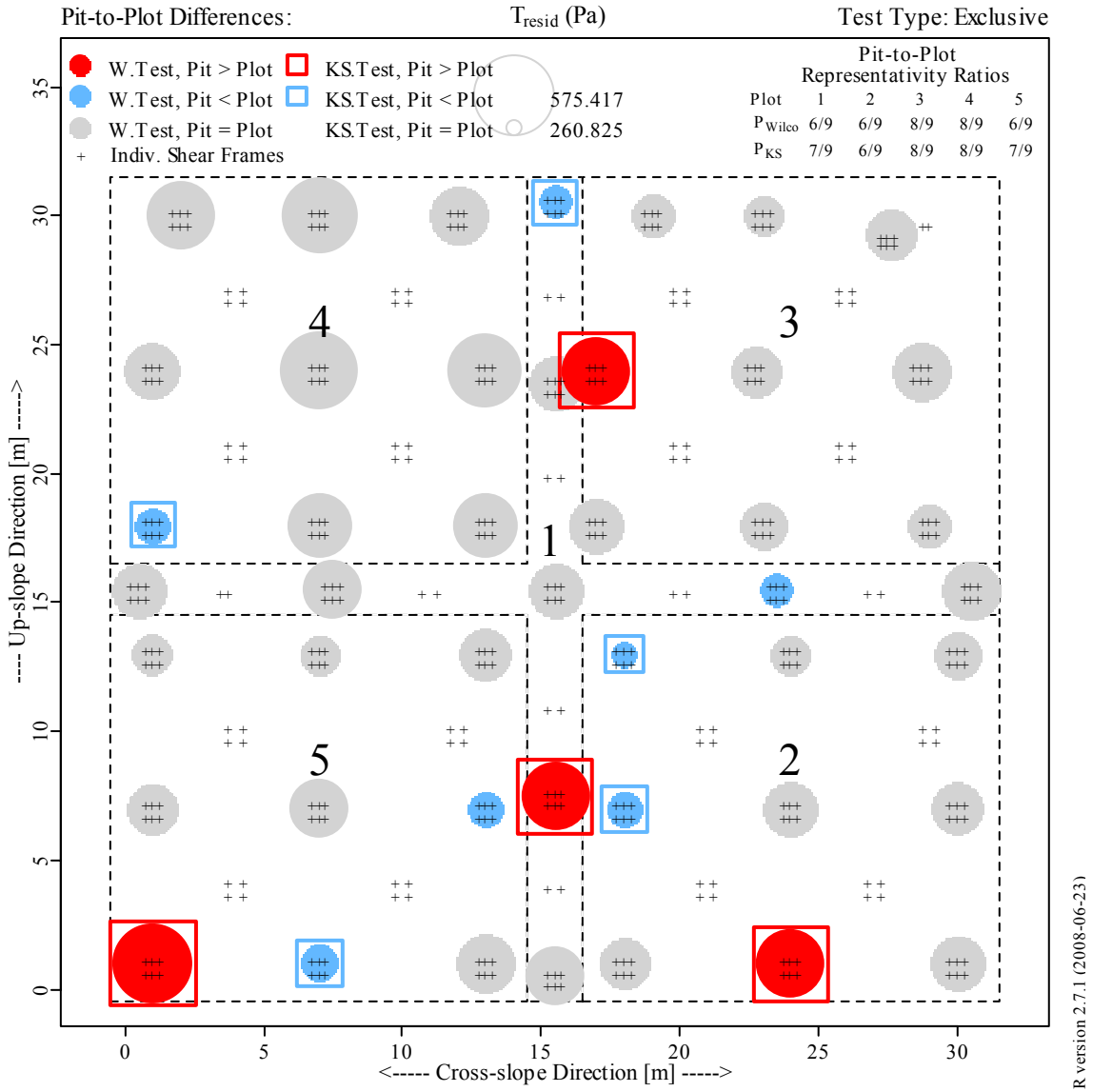

Figure 180. Pit-to-plot representativity of τ_{resid} across the slope. Black dotted lines are plot boundaries. Circle size represents the pit-derived median of τ_{resid}. Blue and red circles indicate significantly lower and higher median values, based on the Wilcoxon Rank Sum test. Blue and red squares indicate significantly different distributions, with blue and red indicating if pit observations where generally lower than or higher than plot observations, based on the Kolmogorov-Smirnov test.

As for τ_∞, the results from the upper and lower slopes were considered separately to detect possible changes in representativity that may have occurred over time. No changes occurred on the upper slope. On the lower slope, changes were not definitive: the pit-to-plot ratios for central tendency P_{Wilco} stayed at 6/9 and the pit-to-plot ratios for distribution P_{KS} increased slightly from 6/9 to 7/9.

Stability Index (S): A total of 13 pits were unrepresentative of S at their respective plots, in terms of their median value or distribution (Table 75). Seven of these pits were positively associated with pits that were unrepresentative for τ_∞, which is logical since τ_∞ is the numerator in S (Figure 181). An additional six pits across the site were unrepresentative of S, despite being representative of τ_∞. Two of these pits existed at Plot 2 and corresponded with a plot-scale trend of τ_{slab}.

Viewed as a single time sequence, pit representativity of S was lowest at the beginning and end of the sampling period (Table 75). This may be due to the slope-scale trends, or it may indicate that, over time, areas became more uniform until a loading event, which occurred between Plots 4 and 5.

Table 75. Frequency and percentage of pits that are representative of respective plots in for S.

		Wilcoxon -Rank Sum Test				Kolmogorov-Smirnov Test			
	S	Pits are statistically* representative of plot		Pits are statistically* unrepresentative of plot		Pits are statistically* representative of plot		Pits are statistically* unrepresentative of plot	
Plot	Date	Freq.	(Plot %)	Freq.	(Plot %)	Freq.	(Plot %)	Freq.	(Plot %)
1	28.02.2005	6	67	3	33	5	56	4	44
2	1.03.2005	5	56	4	44	5	56	4	44
3	8.03.2005	9	100	0	0	8	89	1	11
4	14.03.2005	8	89	1	11	8	89	1	11
5	21.03.2005	6	67	3	33	7	78	2	22

* Both tests are non-parametric two-sided tests with a 'significant' difference based on a 95 % confidence level.

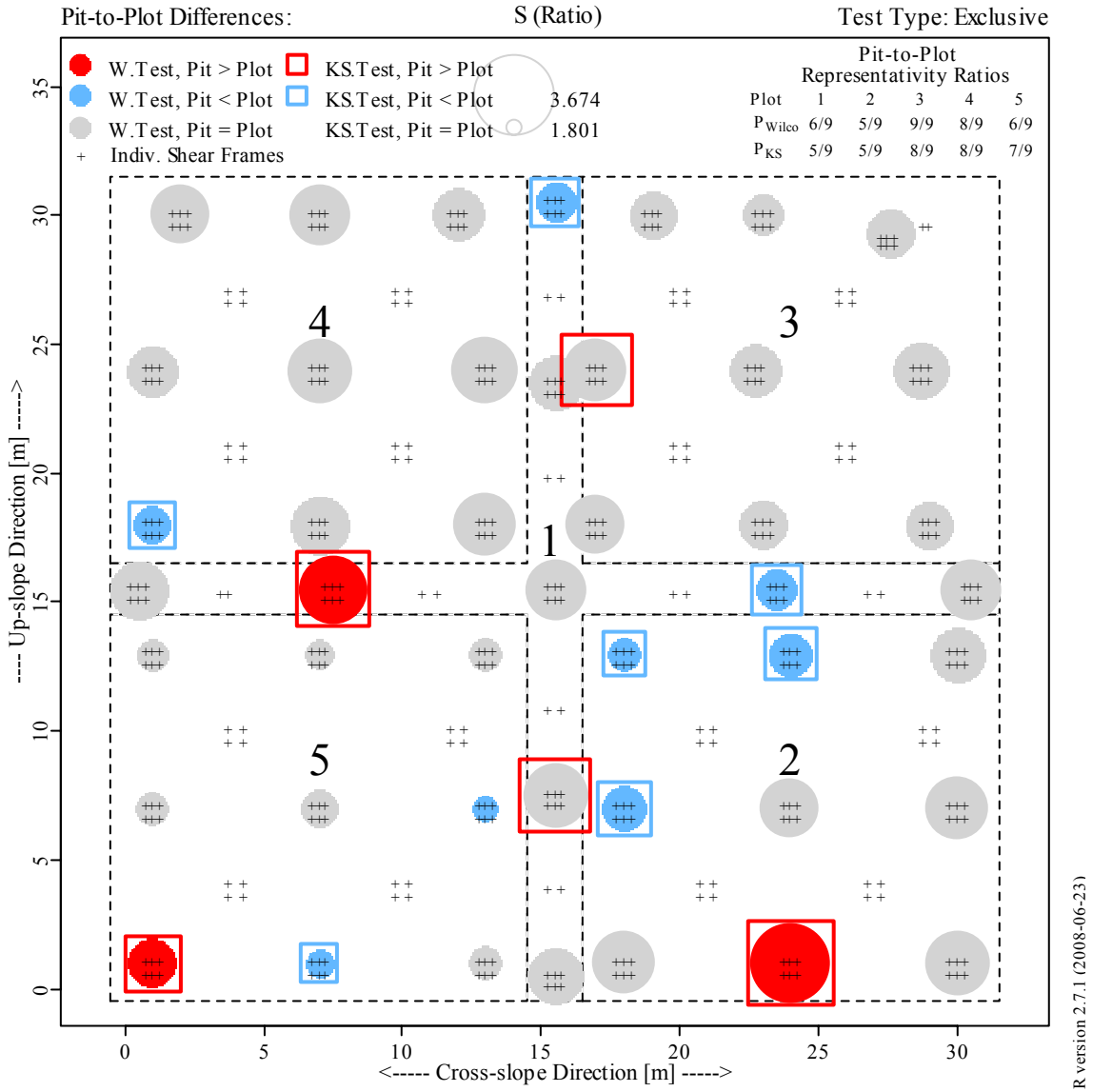

Figure 181. Pit-to-plot representativity of *S* across the study site. Black dotted lines are plot boundaries. Circle size represents the pit-derived median of *S*. Blue and red circles indicate significantly lower and higher median values, based on the Wilcoxon Rank Sum test. Blue and red squares indicate significantly different distributions, with blue and red indicating if pit observations where generally lower than or higher than plot observations, based on the Kolmogorov-Smirnov test.

Weak Layer Thickness (h_{wl})

Five pits across Plot 1 were unrepresentative of h_{wl} (Figure 76). Because there was a pronounced up-slope trend in h_{wl}, pits located along the up-slope transect produced

h_{wl} estimates that were significantly different from plot estimates (Figure 182). All four subsequent plots showed a similar pattern at smaller spatial extents; unrepresentative pits possessing a thinner than normal weak layer were never located at the top portion of a plot.

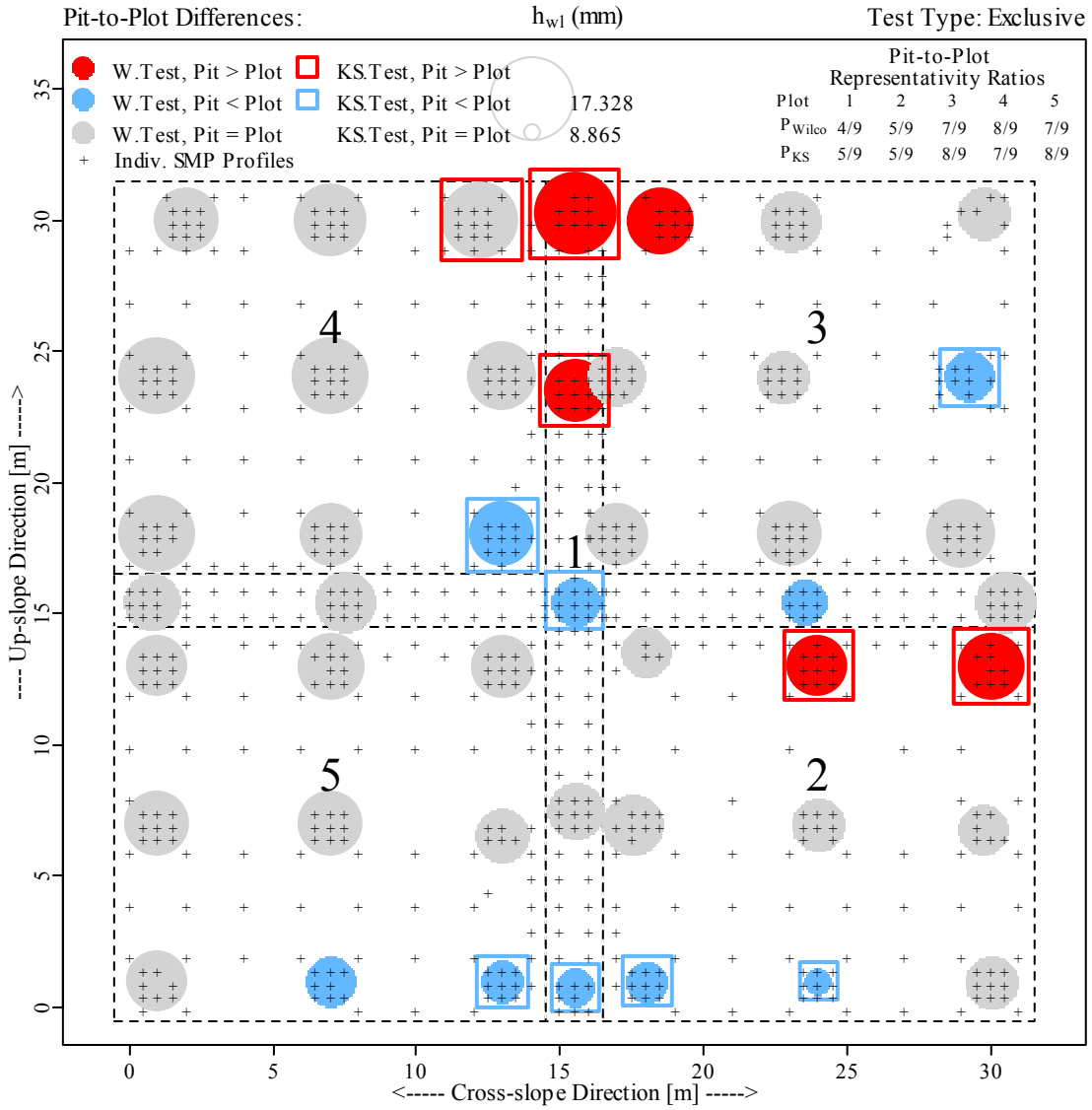

Figure 182. Pit-to-plot representativity of h_{wl} across the study site. Black dotted lines are plot boundaries. Circle size represents the pit-derived median of h_{wl}. Blue and red circles indicate significantly lower and higher median values, based on the Wilcoxon Rank Sum test. Blue and red squares indicate significantly different distributions, with blue and red indicating if pit observations where generally lower than or higher than plot observations, based on the Kolmogorov-Smirnov test.

Table 76. Frequency and percentage of pits that are representative of respective plots in for h_{wl}.

		Wilcoxon -Rank Sum Test				Kolmogorov-Smirnov Test			
	h_{wl}	Pits are statistically* representative of plot		Pits are statistically* unrepresentative of plot		Pits are statistically* representative of plot		Pits are statistically* unrepresentative of plot	
Plot	Date	Freq.	(Plot %)	Freq.	(Plot %)	Freq.	(Plot %)	Freq.	(Plot %)
1	28.02.2005	4	44	5	56	5	56	4	44
2	1.03.2005	5	56	4	44	5	56	4	44
3	8.03.2005	8	89	1	11	8	89	1	11
4	14.03.2005	8	89	1	11	7	78	2	22
5	21.03.2005	7	78	2	22	8	89	1	11

* Both tests are non-parametric two-sided tests with a 'significant' difference based on a 95 % confidence level.

The opposite held true for pits that possessed thicker than average weak layer values. These findings reinforce the geostatistical findings that an up-slope trend existed in weak layer thickness (h_{wl}) across the site (Spatial Analysis: SMP-Derived Stratigraphic Estimates, page 155). It also exemplifies that, when a spatial trend exists in a snow property, a large portion of pits will be unrepresentative.

Microstructural Estimates of Weak Layer

Rupture Force Characteristics (f_m, f_{max}, f_{cv}): Pit estimates of the weak layer's rupture force were considerably uniform at all plots, with a total of four unrepresentative pits for f_m and f_{max} for the entire site (Figure 183, Table 77).

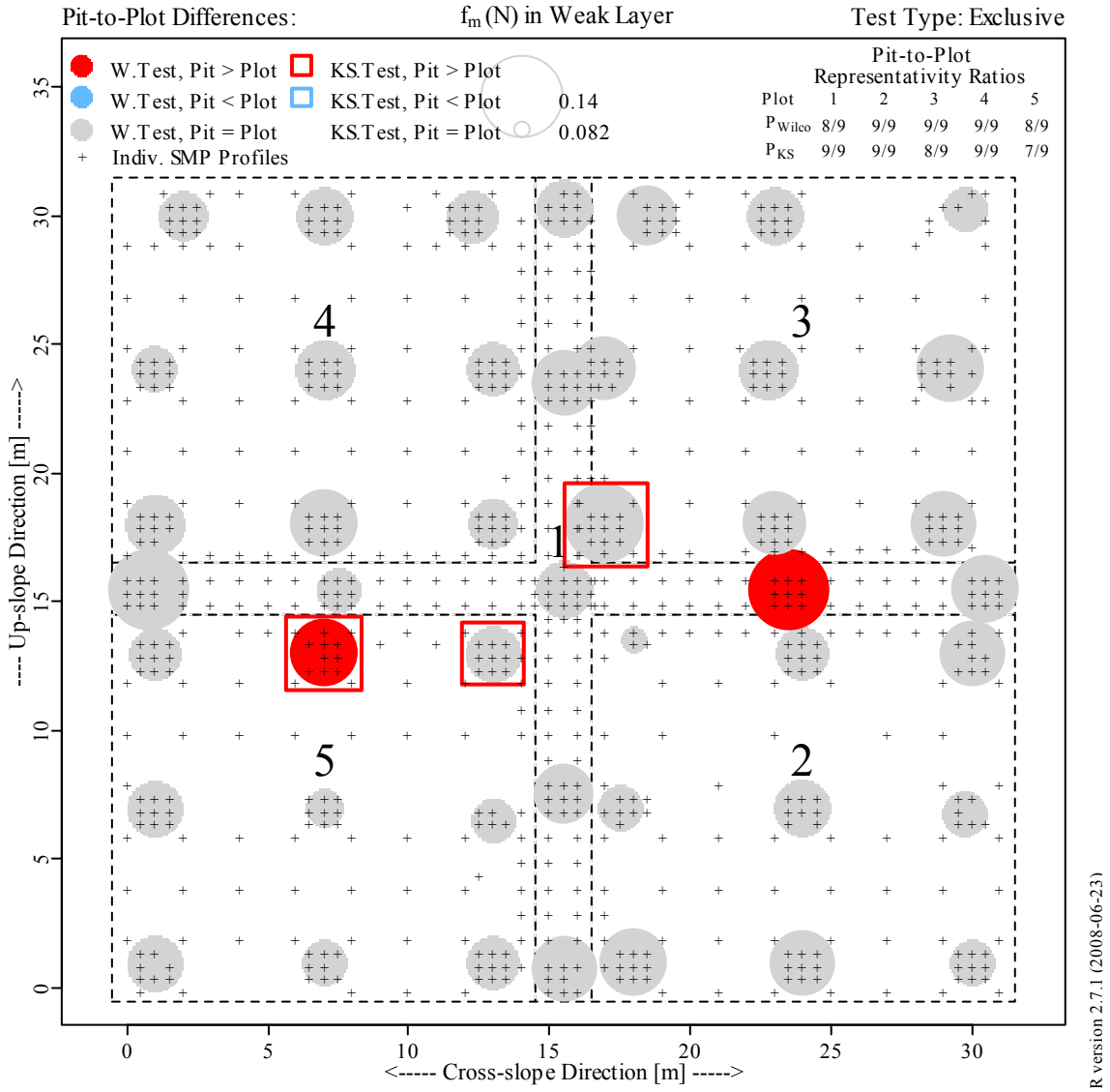

Figure 183. Pit-to-plot representativity of f_m across the study site. Black dotted lines are plot boundaries. Circle size represents the pit-derived median of f_m. Blue and red circles indicate significantly lower and higher median values, based on the Wilcoxon Rank Sum test. Blue and red squares indicate significantly different distributions, with blue and red indicating if pit observations where generally lower than or higher than plot observations, based on the Kolmogorov-Smirnov test.

Table 77. Frequency and percentage of pits that are representative of respective plots in for f_m and f_{max} of the weak layer.

Weak Layer		Wilcoxon -Rank Sum Test				Kolmogorov-Smirnov Test			
		Pits are statistically* representative of plot		Pits are statistically* unrepresentative of plot		Pits are statistically* representative of plot		Pits are statistically* unrepresentative of plot	
	f_m								
Plot	Date	Freq.	(Plot %)	Freq.	(Plot %)	Freq.	(Plot %)	Freq.	(Plot %)
1	28.02.2005	8	89	1	11	9	100	0	0
2	1.03.2005	9	100	0	0	9	100	0	0
3	8.03.2005	9	100	0	0	8	89	1	11
4	14.03.2005	9	100	0	0	9	100	0	0
5	21.03.2005	8	89	1	11	7	78	2	22
	f_{max}								
Plot	Date	Freq.	(Plot %)	Freq.	(Plot %)	Freq.	(Plot %)	Freq.	(Plot %)
1	28.02.2005	8	89	1	11	8	89	1	11
2	1.03.2005	7	78	2	22	8	89	1	11
3	8.03.2005	9	100	0	0	9	100	0	0
4	14.03.2005	9	100	0	0	9	100	0	0
5	21.03.2005	9	100	0	0	9	100	0	0
	f_{cv}								
Plot	Date	Freq.	(Plot %)	Freq.	(Plot %)	Freq.	(Plot %)	Freq.	(Plot %)
1	28.02.2005	8	89	1	11	9	100	0	0
2	1.03.2005	7	78	2	22	8	89	1	11
3	8.03.2005	9	100	0	0	9	100	0	0
4	14.03.2005	9	100	0	0	9	100	0	0
5	21.03.2005	9	100	0	0	8	89	1	11

* Both tests are non-parametric two-sided tests with a 'significant' difference based on a 95 % confidence level.

Structural Element Length Characteristics (L, L_{max}): A total of four pits were unrepresentative of their respective plots, in terms of their median value of L, their distribution of L, or both (Table 78). Seven of these pits possessed higher than average L values, five of which were located at the top of Plots 1, 4 and 5. This pattern supports the observtaion that L increased with h_{wl} (Figure 184). Four unrepresentative pits at Plot 2 indicated that L increased in the down-slope direction. While this is not in consistent with the rest of the site, it does support the geostatistical analysis, which quantified the primary spatial pattern in L as being a trend surface that increased in the down-slope direction.

Table 78. Frequency and percentage of pits that are representative of respective plots in for L and L_{max} of the weak layer.

Structural Element Length of Weak Layer		Wilcoxon -Rank Sum Test				Kolmogorov-Smirnov Test			
		Pits are statistically* representative of plot		Pits are statistically* unrepresentative of plot		Pits are statistically* representative of plot		Pits are statistically* unrepresentative of plot	
	L								
Plot	Date	Freq.	(Plot %)	Freq.	(Plot %)	Freq.	(Plot %)	Freq.	(Plot %)
1	28.02.2005	8	89	1	11	8	89	1	11
2	1.03.2005	6	67	3	33	5	56	4	44
3	8.03.2005	9	100	0	0	9	100	0	0
4	14.03.2005	5	56	4	44	7	78	2	22
5	21.03.2005	8	89	1	11	9	100	0	0
	L_{max}								
Plot	Date	Freq.	(Plot %)	Freq.	(Plot %)	Freq.	(Plot %)	Freq.	(Plot %)
1	28.02.2005	9	100	0	0	9	100	0	0
2	1.03.2005	8	89	1	11	9	100	0	0
3	8.03.2005	8	89	1	11	9	100	0	0
4	14.03.2005	8	89	1	11	9	100	0	0
5	21.03.2005	9	100	0	0	9	100	0	0

* Both tests are non-parametric two-sided tests with a 'significant' difference based on a 95 % confidence level.

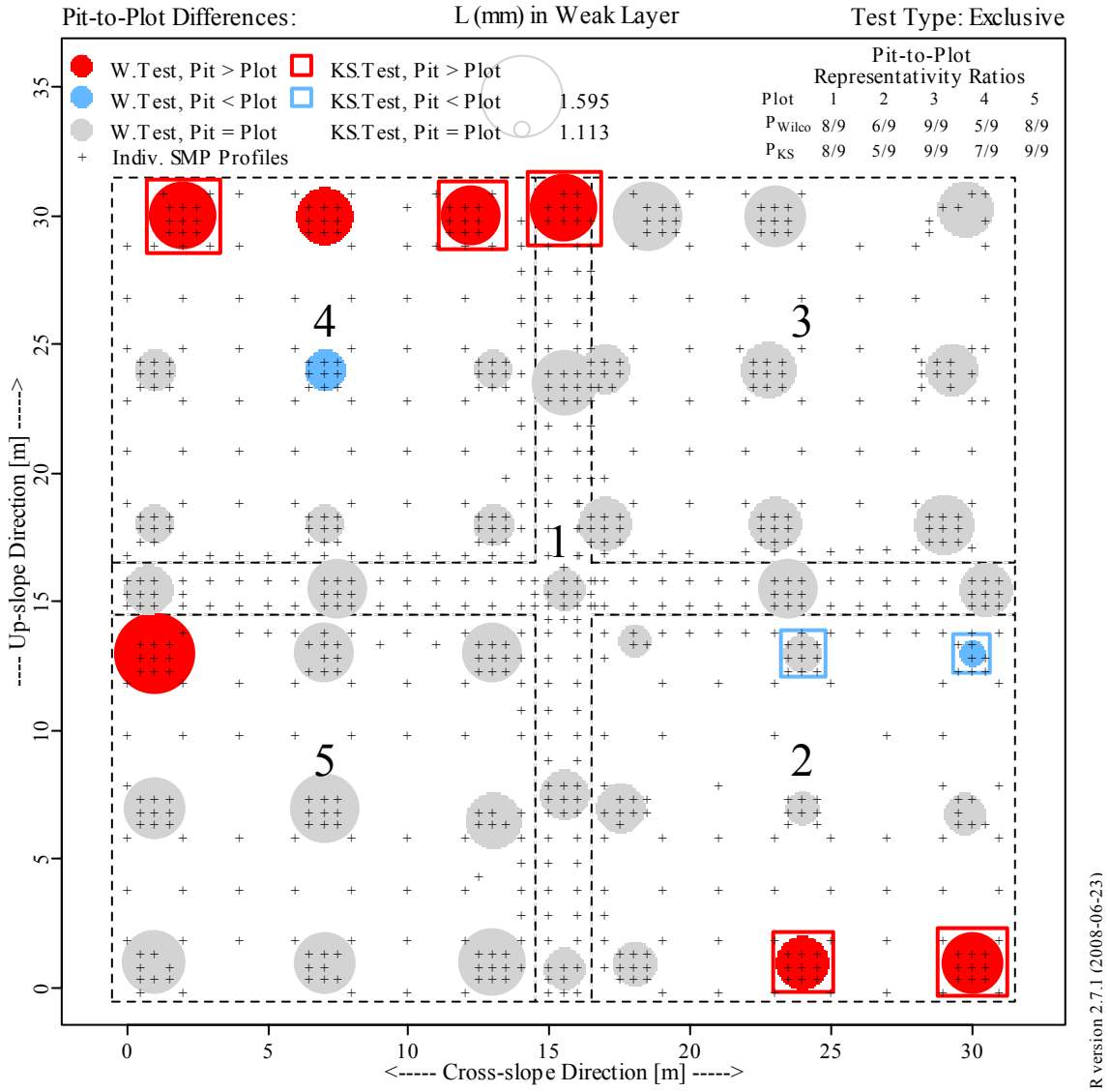

Figure 184. Pit-to-plot representativity of *L* across the study site. Black dotted lines are plot boundaries. Circle size represents the pit-derived median of *L*. Blue and red circles indicate significantly lower and higher median values, based on the Wilcoxon Rank Sum test. Blue and red squares indicate significantly different distributions, with blue and red indicating if pit observations where generally lower than or higher than plot observations, based on the Kolmogorov-Smirnov test.

Micro-Strength (σ_{micro}): All pits at Plot 1 were representative of the median and distribution of σ_{micro} across Plot 1. At Plot 2, one pit at the base possessed below average *S* values and one pit at the top possessed above average σ_{micro} values (Figure 184). Plot 3

contained one pit with above average σ_{micro}, located adjacent to the center of Plot 1 (Figure 184). This higher strength value may have been the result of local disturbance of the snow, as the pit was unintentionally placed 0.5 m closer to Plot 1 then planned (Figure 184). The three remaining unrepresentative pits all possessed lower than average S values and were located at the top portion of Plots 4 and 5 (Figure 184).

As a result of σ_{micro} being derived from f_m and L, most of the six unrepresentative pits can be explained through pits that were unrepresentative of L or f_m. Four pits with below average σ_{micro} values coincided with pits that had above-average L values. One pit with above average σ_{micro} values corresponded with a pit possessing above average f_m values (Figure 185).

Table 79. Pit-to-plot representativity of σ_{micro} in the weak layer.

σ_{micro}		Wilcoxon -Rank Sum Test				Kolmogorov-Smirnov Test			
		Pits are statistically* representative of plot		Pits are statistically* unrepresentative of plot		Pits are statistically* representative of plot		Pits are statistically* unrepresentative of plot	
Plot	Date	Freq.	(Plot %)	Freq.	(Plot %)	Freq.	(Plot %)	Freq.	(Plot %)
1	28.02.2005	9	100	0	0	9	100	0	0
2	1.03.2005	7	78	2	22	7	78	2	22
3	8.03.2005	8	89	1	11	9	100	0	0
4	14.03.2005	8	89	1	11	7	78	2	22
5	21.03.2005	8	89	1	11	7	78	2	22

* Both tests are non-parametric two-sided tests with a 'significant' difference based on a 95 % confidence level.

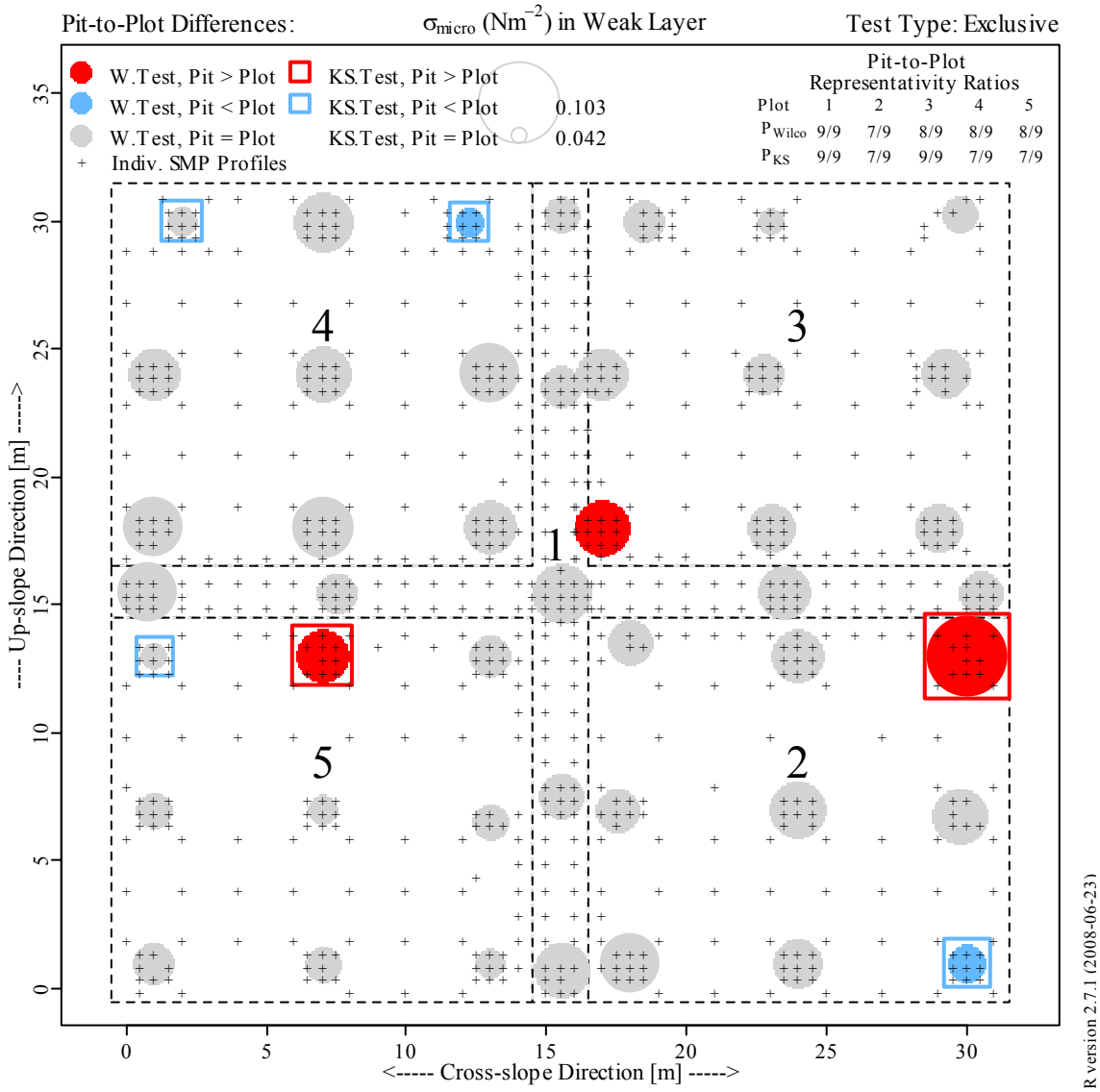

Figure 185. Pit-to-plot representativity of σ_{micro} across the study site. Blue and red circles indicate significantly lower and higher median values, based on the Wilcoxon Rank Sum test. Blue and red squares indicate significantly different distributions, with blue and red indicating if pit observations where generally lower than or higher than plot observations, based on the Kolmogorov-Smirnov test.

Synopsis of Test for Pit-to-Plot Representativity

At Plots 1 and 5, pits that were unrepresentative of their plot in describing τ_∞ coincided with unrepresentative pits of f_m, L, or σ_{micro}. σ_{micro} appears to overcompensate for structure. This was evident at Plot 1, where all pits appeared representative of the plot

as a whole. Based on the shear frame, S and h_{wl} values I expected a decreasing trend of σ_{micro} in the up-slope direction, which is not evident in this pit-based analysis of σ_{micro}.

Application of the pit-to-plot analysis using this dataset exemplifies that representativity was greatly affected by spatial trends. If trends were more pronounced on one portion of the slope than another (in this instance, the lower slope had more pronounced spatial trends in h_{wl} and τ_{∞}) then, on that portion of the slope, pits would be less representative, regardless of changes occurring over time.

DISCUSSION

General Meteorological Conditions during Surface Hoar Formation and Persistence

Weak Layer Formation

The surface hoar was composed of thin columnar bases and broad, plate-like leaves (Figure 52), which formed under different meteorological conditions influencing the crystal growth regime (Jamieson and Schweizer, 2000). While it is unknown the exact time of day when both portions of the surface hoar layer formed, general differences in meteorological conditions could be identified.

During the first growth period (between January 19 and 20), winds were light (Figure 53.1). Light winds have been shown to foster surface hoar formation through turbulent transfer of water vapor (Colbeck, 1987; Hachikubo and Akitaya, 1997; Cooperstein, 2008). Hachikubo and Akitaya (1997) recorded winds of 1.5 – 2.6 $m \cdot s^{-1}$ at 1 m above the snow surface during surface hoar formation, which very closely matches conditions recorded during the first surface hoar formation period. The absence of moderate or strong winds may have also fostered the development of the necessary temperature gradient at the snow surface. Moderate or strong winds can cause the surface to warm through the increase sensible heat flux (Nyberg, 1939; Colbeck, 1987; Hachikubo and Akitaya, 1997). Because, regardless of time of day, the winds were consistently out of the one direction (northeast) (Figure 53.2), it is likely they were regional winds.

The second surface hoar formation period (between January 20 - 24) was dominated by a diurnal pattern that was probably associated with solar-induced warming. An up-slope breeze developed as day time temperatures increased and then switched to cross and down-slope winds by late afternoon (Figure 53.2). Winds varied considerably but were generally strongest in the evening and subsided by sunrise, with complete calm (indicated by arrows in Figure 53.1) dominating the early morning hours.

Based on Colbeck (1987) and Hachikubo and Akitaya (1997), the wind conditions were probably most conducive to turbulent vapor transfer in the early morning hours, when a light breeze existed, but before complete calm began. Colbeck (1987:11) rationalized that not only light winds but "irregularity in the flow would increase turbulence and promote the growth of surface hoar". Periodic air movement resupplies vapor to the boundary layer without causing a temperature gradient to be diminished, as would occur under sustained winds (Colbeck, 1987). The 10-minute minimum and maximum recorded wind speed values (gray lines in Figure 53.1) indicated that when there was any wind at all, it varied considerably during this second surface hoar formation period.

Air temperatures at 1.5 m above the snow surface never dropped below -5° C during both surface hoar formation periods (Figure 53.3). This observation contrasts with observations by Kobayashi (1961), who found wedge-shaped surface hoar to form at temperatures between -10° and -21° C (in Schweizer and Jamieson, 2000). The discrepancy in temperature values may be related to differences in the height of temperature measurements above the snow surface.

Clear sunny weather (Figure 53.4), temperatures near 0° C (Figure 53.3), sustained winds of 5-10 $m \cdot s^{-1}$ and strong gusts (e.g., 24 $m \cdot s^{-1}$) (Figure 53.1) were experienced during the formation period. The windy conditions may have also been partially responsible for the spatial patterns in the surface hoar thickness (h_{wl}).

The observations also indicate that, despite multiple years of field observations by forecasters and researchers indicating that this slope was well protected from wind, the Lionhead study site can experience sustained winds and strong gusts. The field site was selected largely because it is located several hundred meters below the ridge line, where winds were observed to be mild. However, as the weather data shows, moderate winds were frequent (Figure 53.1). For this observation time period, the winds were always lightest in the early to mid-morning, and were strongest in the late evening. When winds follow this diurnal pattern with strong winds occurring during late evening hours, field observers would rarely be present at the time when winds were strongest. This highlights the importance of constant weather station observations.

Weak Layer Persistence

The surface hoar was exposed to atmospheric conditions for at least 11 days after its formation, before being buried by a small snowfall event that began on February 5 (indicated by arrow in Figure 55). During this persistence period, daytime air temperatures regularly exceeded 0° C (Figure 54.3), wind speeds reached 10 $m \cdot s^{-1}$ (Figure 54.1), and global shortwave radiation of more than 200 $W \cdot m^{-2}$ (Figure 54.4) was experienced. These observations show clearly that on a northeast-facing slope, surface

hoar can remain intact on the surface for many days, despite direct shortwave radiation, high winds, and relatively warm air temperatures.

Because the study site did experience winds at the weather station, the air flow patterns at the study site itself cannot be assumed to have been spatially uniform. Potential spatial patterns in winds may have resulted in trends of sensible heat flux and vapor transport across the study site, both of which would influence growth and persistence of surface hoar.

Weak Layer Presence and Absence

Eighteen of the 824 SMP profiles (2.2 %) did not contain the weak layer (Figure 64). In nine of these 18 profiles, the weak layer was likely absence due to a ski track that had been cut through the outer corner of Plot 3 in January (Figure 64).

Of the nine remaining profiles with no observable weak layer (not related to the ski track), five were located where the weak layer was fairly thin: at the base of Plot 5 and the center of Plot 1 (compare Figure 64 with Figures Figure 66.1 Figure 67.1). This is a good indication that, in these instances, the absence of the weak layer may have been related to the weak layer being very thin. The weak layer may have been present but not registered by the SMP sensor tip because the layer was so thin that the tip was simultaneously in contact with microstructures from adjacent layers. It is unclear then, why the weak layer was discernable in SMP profiles obtained from other areas of the study site where the weak layer was even thinner (e.g. lower portion of Plot 2).

The remaining 4 profiles lacking the weak layer segment were not associated with thin weak layer zones or with the ski track. These may have been caused by localized

disturbances such as small snowball 'rollers' that could have fallen from up-slope trees and rolled down the slope during or after the small snowfall event that first buried the surface hoar layer. In this instance, the weak layer could be compressed by the snowball's track or, if the slab was very thin, the snowball could crush the weak layer in its track.

Another possible cause for the weak layer absence from two of the four remaining profiles was weak layer deformation caused by slab creep. Two profiles were located directly at the lower edge of Plots 3 and 4. The slab on these two plots had been separated from adjacent portions of the slope on their inside edges when troughs were formed during the sampling of Plot 1. It is possible that the slab crept more at the lower edge of these plots where the slab was unhindered from down-slope movement, resulting in greater shear deformation at the base of these plots. This, in turn, could have resulted in thinner weak layer values as derived from SMP measurements. While possible, under this rationale one might expect the weak layer to be consistently thinner at the base of these plots.

The Wilcoxon Rank-Sum (Mann-Whitney) Test results showed that weak layer absence was not associated with horizontal proximity to vegetation (Figure 65.1). Profiles with no weak layer were significantly closer to the ground than profiles containing the weak layer (Figure 65.2). However, this difference between the two groups was due to a thinner base (Figure 70), and not due directly to proximity to vegetation. Further evidence that promixmity to vegetation did not influence the presence or absence of the weak layer is that the weak layer was discernable in an SMP

profile where the weak layer was only 0.07 m above the modeled vegetation (Figure 65.2). This is a good indication that proximity to buried vegetation did not determine the weak layer's presence.

Spatial Associations between Radiation and Surface Hoar

Surface Hoar Thickness (h_{wl}) Associated with Radiation

Associations between the modeled long- and shortwave radiation and the observed surface hoar thickness (h_{wl}) were prominent at Plots 1, 2 and 5 (Table 49). Associations were generally more significant at the lower plots than at the upper plots (Table 49) because the modeled radiation patterns were more distinct on the lower portion of the site (e.g. incoming longwave radiation ($L\downarrow$), Figures 59and 60). This indicates that associations between the thickness of the buried surface hoar layer (h_{wl}) and incoming radiation can be identified for fairly small extents (e.g., 14 m) when local spatial patterns are distinct.

Weak layer thickness (h_{wl}) was inversely affected by modeled incoming longwave and shortwave radiation. While the former hinders crystal growth, the latter can degrades crystals. Unfortunately, since the longwave and global shortwave radiation estimates had similar spatial patterns across the study site, it is impossible to discern, in this dataset, if one is more responsible for the variations in weak layer thickness (h_{wl}) (due to their co-linearity). However, it is likely that both longwave and shortwave estimates are responsible for creating the pattern in surface hoar thickness (h_{wl}), based on the three following observations: 1. correlations for both types of radiation were significant (Table

49), 2. all significant correlations are logical (Table 49), and 3. when the albedo of global shortwave radiation is accounted for (multiply values in Figures 61and 62 by 0.1, assuming an albedo of 90%), the magnitude of the spatial variations of absorbed radiation is similar for both longwave and shortwave estimates.

The inverse relationship between modeled incoming longwave flux ($L\downarrow$) and the surface hoar layer thickness (h_{wl}) (Table 49, Figure 159) supports previous associations identified by Gubler and Rychetnik (1991) and Höller (2001). Because the study site was situated on an inclined surface in a forest opening, trees below the study site affected sky visibility in the opening much more than trees above the site. On a horizontal slope, based on simple geometry, tree proximity and shape would be the primary cause for spatial variations in sky visibility ($v_{\%}$). However, on an inclined slope, such as this study site, trees standing below the site occupy a much greater portion of the visible hemisphere than do trees standing above a site. This was clearly evident in the spatial models of sky visibility ($v_{\%}$) at this study site (Figure 58). Hence, for a forest opening on an inclined slope, surface hoar growth is expected to be greatest up-slope of the middle of the opening.[12]

The thickness of the buried surface hoar layer (h_{wl}) was negatively correlated with maximum global shortwave radiation (I_{max}, Figure 160), cumulative global shortwave radiation ($\sum I$, Figures 163 and 164), and cumulative exposure time to direct shortwave radiation ($\sum I_t$, Figures 161 and 162) (Table 49). Compared to cumulative global shortwave radiation results presented by Feick et al. (2007), both the GIS-based and Solar

[12] Conversely, an individual tree or small group of trees on an open mountain-side would reduce sky visibility up-slope of the trees more than down-slope of the trees. Hence, surface hoar growth can be expected to be greater down-slope of the tree(s) than up-slope of the tree(s)

Pathfinder-based estimation methods used in this study produced cumulative global shortwave radiation values ($\sum I$) that coincide with the minimum values observed by Feick et al. (2007) and thereby fall within the surface hoar preservation regime observed by Feick et al. (2007).

Previous studies comparing sites with different aspects have correlated surface hoar growth with site aspect (Cooperstein et al., 2004; Cooperstein, 2008). Cooperstein (2008) found that during surface hoar formation periods, surface hoar crystals grew up to four times larger on north aspects than on south aspects. In my work, which examined surface hoar on a Northeast-facing slope, I found that the surface hoar layer thickness (h_{wl}) varied by a factor of seven (3-22 mm) within the 31 x 31 m study site, and is inversely correlated with short and longwave radiation.

My findings support Gubler and Rychetnik's (1991) assertion that surface hoar formation will be most productive in places where both shading and sky visibility factors are coupled together. In addition, for the northern hemisphere it can be emphasized that these micro-climatic factors are most frequently coupled on northern-aspects, as illustrated by a conceptual diagram in Figure 186. On a northeast-facing aspect night-time sky visibility (Figure 186.1) and day-time shading (Figure 186.2) coincide near the center of the site and together encourage cool surface temperatures throughout the night and day.

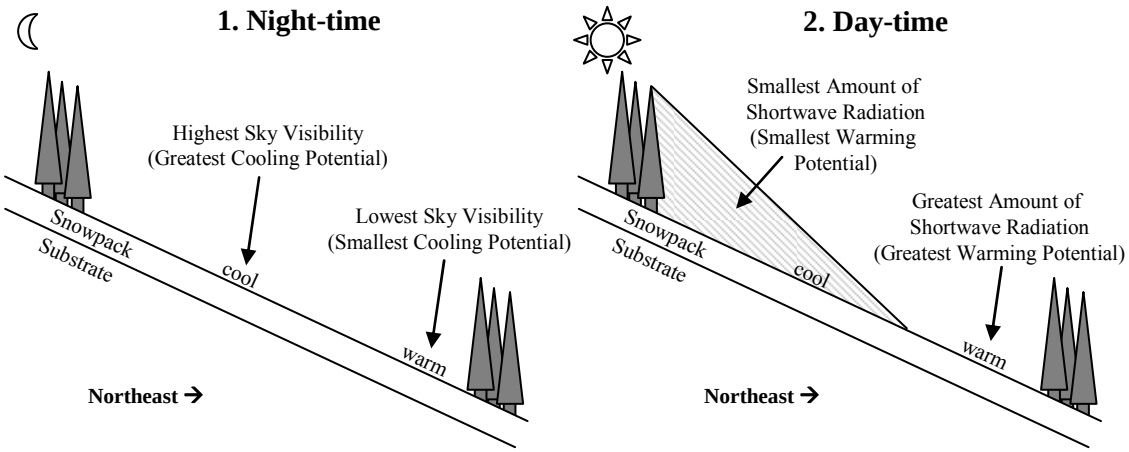

Figure 186. Hypothetical differences in (1) night-time and (2) day-time patterns in surface temperature on a northeast-facing (right) slope in the northern hemisphere.

On south-facing aspects these factors do not coincide in space (Figure 187). The center of the opening has the highest cooling potential at night (Figure 187.1) which may foster surface hoar growth. However, during the day this area is exposed to direct sunlight (Figure 187.2), potentially destroying developed surface hoar.

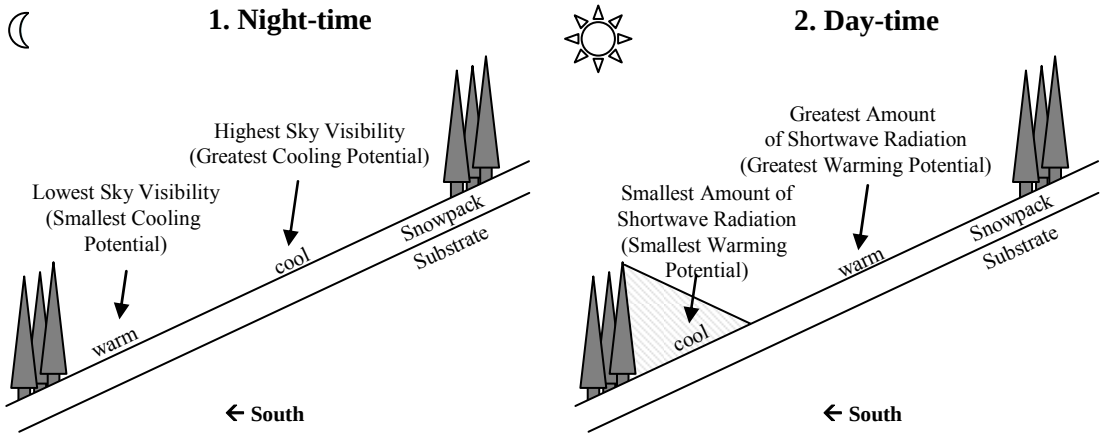

Figure 187. Hypothetical differences in (1) night-time and (2) day-time patterns in surface temperature on a south-facing (right) slope in the northern hemisphere.

As mentioned prior, the results illustrated that, on this northeast facing slope, both shortwave and longwave radiation share correlations with weak layer thickness (h_{wl})

(Table 49). For this dataset, the spatial patterns in longwave and shortwave radiation largely coincided with eachother and resulted in co-linear variables (e.g. compare spatial patterns for $L\downarrow$ (Figure 60), $\sum I$ (Figure 62), and $\sum I_t$ (Figure 63) at Plot 1). This can be expected on forest openings on north-facing slopes, since the greatest shading from trees occurs on the upper part of the opening, including the area where sky visibility is greatest. The trees up-slope of the site shade the upper slope and keep it cool during the day, while trees down-slope of the site hinder surface cooling at night. This tells us that on north-facing slopes, buried surface hoar layers may be thickest toward the top of forest openings and thinnest toward the base of forest openings.

An additional reason for this pattern on north-facing aspects is that trees down-slope of the opening receive intense solar radiation on their up-slope sides during the day. This increases the re-radiation from these trees on the lower portion of the site, further enhancing the existing pattern. Such factors could be well modeled using a radiation model (Adams et al., 2004).

Other Weak Layer Properties

Because strength properties of surface hoar are related, in part, to the size, density and shape of surface hoar crystals (Davis et al., 1998; Jamieson and Johnson, 1999; Jamieson and Schweizer, 2000), I expected that shear strength (τ_∞) and microstructural properties (such as f_m and σ_{micro}) of the weak layer to be indirectly related to radiation estimates which influence surface hoar growth and persistence. While these are not direct relationships, they may allow proxies to be correlated to spatial patterns in weak layer strength and microstructure. Given that slab stresses are not constant across any

given plot, variations in shear strength (τ_∞) and microstructural properties may not be caused by surface conditions but rather by strengthening processes driven by slab stresses over time.

Shear strength (τ_∞) was positively correlated with model predictions of cumulative shortwave radiation ($\sum I$) at Plot 1 (Table 50, Figures 165 and 166). This association was likely a direct result of shear strength (τ_∞) being inversely associated with the weak layer thickness which, for surface hoar layers, introduces torsion affects. While both weak layer thickness (h_{wl}) and shear strength (τ_∞) possessed similar associations with shortwave radiation estimates, direct associations between weak layer thickness (h_{wl}) and shear strength (τ_∞) were statistically significant only on the upper slope, at Plots 3 and 4 (Table 57, Figure 173).

Because slab-related loads varied over each plot (Figures 76, 78, and 80), associations between radiation and microstructural variables were not possible to statistically identify. The cumulative exposure time to global shortwave radiation ($\sum t_I$) appeared to negatively influence the mean rupture force (f_m) across Plots 4 and 5 independently (Table 53, Figure 171). Since larger surface hoar crystals can produce larger rupture forces (evident at Plot 5 as a positive correlation between f_m and h_{wl}), it is likely that this association was a result of larger surface hoar crystals being present where exposure to global shortwave radiation was limited. Future studies should utilize a dataset that includes a larger number of slab load, and short- and longwave radiation conditions, so that co-linearity or multiple variables does not obscure the interpretation.

Implications of Spatial Associations on Stability Observations

The spatial correlation between weak layer thickness (h_{wl}) and shear strength (τ_{∞}) at Plot 1 (compare Figures 66.1 and 82.1) and the statistically significant correlations between these variables at Plots 3 and 4 (Figure 173, Table 57) support the general observation that surface hoar is often strongest where it is thinnest. This relationship should be considered and applied during site selection of stability observations on open-forested terrain. If the dominant weakness is known to be a buried surface hoar layer, the observer can try to estimate the direction of spatial trends of weak layer thickness (h_{wl}), based on terrain and vegetation characteristics.

Surface hoar will likely increase with increasing distance from trees. On inclined slopes, areas at the base of the slope will be more affected by trees than areas at the top of the slope, due to the difference in sky obstruction inversely affecting surface cooling. Lastly, patterns in solar radiation can vary a great deal even on a relatively uniform slope, depending on the topography and the presence and distribution of trees around a site. In forest openings on north-facing slopes, the base of the slopes will experience greater exposure to solar radiation because the top of the slope is shaded by up-slope trees. Hence, from these factors we can expect surface hoar growth to be greatest in the middle of the forest opening and toward the top of the opening on north aspects.

These spatial patterns have significant ramifications on safety protocols for snow stability evaluation. Assessing stability at the edge of a forest opening, where the surface hoar is less developed than in the middle of the opening, will result in an overestimation of stability, which may result in a false stable assessment. Only once the observer

reaches a more exposed portion of the slope would the measurements actually be accurate, at which point it may be too hazardous. If on the other hand, the observer finds unstable conditions at the edge of an opening, it is very likely that the buried surface hoar layer will be thicker, weaker and potentially less stable at the middle of the opening. In summation, this study gives evidence that in forest openings on northerly aspects, stability observations on the edges of the openings are suspect to overestimating slope-scale stability and should be treated as the most stable condition. Further, researchers and forecasters conducting time series observations in forest openings need to be mindful of the wide variation in surface hoar crystal sizes that can exist over short distances in these openings.

While this study did not examine other slope aspects, a similar approach can be applied, whereby the observer considers areas that are likely exposed to more or less long and shortwave radiation. Unlike north aspects, forest openings on south aspects experience direct shortwave radiation in areas that cool the most at night-time, resulting in potentially more complex or more uniform patterns in surface hoar development.

Spatial Variability Quantified using Pit-to-Plot Differences

Plot 1 exhibited pit-to-plot differences in weak layer thickness (h_{wl}) (Figure 182), shear strength (τ_{∞}) (Figure 179), residual shear strength (τ_{resid}) (Figure 180) and stablity (S) (Figure 181) that were clearly associated with spatial trends that identified in these phenomena using geostatistical methods (Figures 66.1, 82.1, 84.1, 86.1 respectively). For both shear strength (τ_{∞}) and residual shear strength (τ_{resid}), two of the three

unrepresentative pits were located towards opposite ends of the up-slope transect; significantly greater strength values were observed near the base of the slope and significantly smaller values at the top of the slope (Figures 179and 180). If I exclude unrepresentative pits associated with the spatial trend, the ratio of unrepresentative pits drops from 3/9 (33%) to 1/7 (14 %). This finding illustrates the value of the geostatistical analysis, which allowed me to clearly identify and quantify spatial trends. The geostatistical analysis showed, independent of individual pit distributions, that spatial trends existed. Without a spatial sampling layout conceived for geostatistical analysis, such confirmation would not be possible.

One of the eleven plots sampled by Landry et al. (2004) exhibited very similar effects of a spatial pattern. Observations from his Round Hill trial possessed a pronounced cross-slope spatial trend, whereby the two pits on the far right (Pits 2 and 4) were more stable than the other pits. Evidence that the left side was less stable was provided when the final pit was being sampled (Pit 5) and the entire slope collapsed. Further evidence of a cross-slope trend is that the pit located at the plot center was the only pit that was representative of the slope. Although Landry et al. (2004) identified this pattern in stability rather than shear strength (as was the case in this study), the affect of the spatial trend is the same: spatial trends systematically increase the number of unrepresentative pits.

My pit-to-plot results indicated for stability (*S*), a large number of pits were not representative of their respective plots (Figure 181, Table 75). Landry et al. (2004) observed more uniform conditions in shear strength and stability associated with a

surface hoar layer in 2002, collected at the same Lionhead study site. The surface hoar layer I observed was exposed to the atmosphere for many days, while Landry et al. (2004) sampled a surface hoar layer that was buried by snow fall within a couple days of its formation. The greater variability in my observations supports the possibility that length of exposure time may increase spatial patterns in surface haor layers.

In addition to the possibility that the two surface hoar layers possessed real differences in their spatial properties, three differences in sampling strategies could have influenced the results and caused this discrepancy: 1. Landry et al. (2004) utilized the Quantified Loaded Column test, which includes the existing slab load in the stability test, while my study utilized the shear frame test which measures the shear strength directly with no slab load present, 2. Landry et al. (2004) used large plots (one plot spanned my entire study site extent), while my study utilized smaller plots, 3. Landry et al. (2004) sampled fewer pits per plot, but conducted more samples in each pit than I did.

In summary, the pit-to-plot tests that I conducted indicate that the up-slope trends in weak layer thickness (h_{wl}), shear strength (τ_{∞}), residual shear strength (τ_{resid}) and stablity (S) were pronounced enough to systematically reveal unrepresentative pits on the lower slope at Plot 2 and 5, both of which extend over 14 m x 14 m areas. For example, of the two unrepresentative pits that existed at Plot 5, the pit with above average shear strength (τ_{∞}) was at the base of the plot and a pit with below-average shear strength (τ_{∞}) values was located at the top of the plot. Three unrepresentative pits containing proportionally more shear strength (τ_{∞}) observations with small values than their respective plot distribution (as established with Kolmogorov-Smirnov Test) where

located at the middle or top of Plots 2 and 5. Hence, on the lower slope, there were fewer representative pits or a lesser degree of uniformity. As observed for Plot 1, these unrepresentative pits on the lower slope coincide with up-slope trends in shear strength (τ_∞). These findings illustrate how results from pit-to-plot analysis can be significantly influenced by spatial trends in the observed phenomenon.

Evidence of Spatial Uniformity

The upper site was characterized by uniformity in most snow properties. For example, for shear strength (τ_∞) at Plots 3 and 4, eight out of nine pits were representative of their respective plots, in both their median values and distributions (Figure 179). The upper site was also characterized by subdued patterns in the sky visibility ($v_{\%}$) (Figure 58) and incoming longwave radiation estimates ($L\downarrow$) (Figures 59and 60). This is an indication that the uniformity of snow properties on the upper site may have been related to uniformity of longwave radiation properties.

Other studies have observed uniformity in strength properties of weak layers. Landry et al. (2004) and Logan et al. (2007) observed fairly uniform conditions at a study site in Middle Basin, near Big Sky, Montana. Landry et al. (2004) sampled one large site (approximately 30 m x 30 m) and found one of the five pits to be unrepresentative. Logan et al. (2007) sampled the same spatial extent, except as four small plots (14 m x 14 m), each containing 5 pits, over several weeks. They found only one of the twenty pits to be unrepresentative. Their observations indicate that, despite different sampling densities, the two studies found pit observations to be very representative at their site. A

plausible reason for this is that the site has very uniform substrate and is removed from ridge-top winds. The site was also situated further from trees than was my Lionhead site, which may have fostered a more uniform weak layer formation.

Temporal Processes

If viewed as a single dataset, several snowpack properties appeared erratic over time. When treated as separate upper and lower site datasets, several temporal changes in pattern emerged. Many were associated with strengthening in the weak layer on the upper slope (Figure 128.1) and destabilization on the lower slope (Figure 130.2), associated with a large loading event (Figure 124.2). Three main processes were identified in this study:

1. Weak layer strengthening occurred on the upper slope, as observed through increased shear strength (τ_∞) (Figure 128.1). A decrease of microstructural element length (L) (Figure 137.1) is evidence that this strengthening was related to an increase in bond frequency or contact point.
2. Weak layer areas with smaller loads strengthened more slowly than areas with larger loads.
3. On the lower slope, the weak layer strengthened (Figure 128.2) but a loading event resulted in unchanged residual shear strength (τ_{resid}) (Figure 129.2) and a decrease of stability (S) (Figure 130.2). The most significant change in weak layer microstructure was an increase of the structural element length (L) (Figure

137.2) and a decrease in micro-strength (σ_{micro}) (Figure 139.2), related to a decrease of bonds or contact points.

Strengthening over Time (Observed on Upper Slope)

Significant shear strengthening occurred on the upper slope (Figure 128.1). Stabilization did not increase significantly at either time-step on the upper site (Figure 130.1), although when treated as a single time-step (compare T-1 to T-3, in Figure 130.1), the difference in statbiltiy (S) appears to be larger; this differences was not statistically tested. This was accompanied by a significant decrease of the structural element length (L) (Figure 137.1). This change was likely caused by deformation that resulted in an increased rupture frequency (N_f). The mean rupture force (f_m) decreased significantly, possibility related to the slightly larger surface hoar layer (and presumably larger crystals) present at Plot 4 than at Plot 3 (Figure 131.1). In addition, microstructural changes in the super-stratum (increases of f_m, f_{max}, σ_{micro} (Figures 140.1, 141.1, 145.1) and a decrease of L (Figure 143.1)) indicated that more pronounced strengthening occurred directly above the weak layer than in the weak layer itself.

Instability due to Lack of Load (Lower Slope)

On the lower slope, a more complex situation developed. Shear strength (τ_∞), residual shear strength (τ_{resid}) and stability (S) appeared to be positively related to slab load (Figures 128.2, 129.2, 130.2, respectively). Given that these plots were observed on subsequent days with no loading events, this data indicates that at this early stage in the development of this instability the weak layer was weakest where the load was limited.

Since Plot 2 had smaller slab water equivalencies (HSW_{slab}) and slab stress values than Plot 1, the weak layer may have remained weaker at Plot 2 because the load was insufficient to cause the deformation necessary for strengthening to occur. This would result in the relatively low shear strength (τ_{∞}) (Figure 128.2) and residual shear strength (τ_{resid}) (Figure 129.2) values at Plot 2.

This positive association between load and stability was also evident in the spatial results of micro-strength (σ_{micro}), whereby micro-strength (σ_{micro}) was largest where the load at Plot 2 was greatest (Table 71). Additional evidence that, across space, load positively influenced strengthening at the scale of shear frame observations was visible at Plots 3 and 5, where statistically significant positive relationships exist between the slope-normal slab stress (N_{slab}) and shear strength (τ_{∞}) (Figure 174, Table 58). These observations support previous studies that have identified load as positively influencing strengthening (Jamieson and Johnston, 1999).

Due to the lack of stress that would otherwise foster deformation that eventually causes strengthening, the weak layer would remain relatively weak where the slab was lightest. These weaker zones would strengthen more slowly over time than areas with a greater load. While we are accustomed to recognizing areas with large loads as potential hazards, these observations indicate that weak layers buried below thin or light slabs have the potential to remain unstable longer and hence be more susceptible to fracturing when a new loading event occurs.

Load-Related Instability (Lower Slope)

After the large loading event on March 20, despite continued shear strengthening (Figure 128.2), stability (S) decreased significantly (Figure 130.2). At the microstructural scale this was associated with several changes, including decreases in maximum rupture force (f_{max}) (Figure 135.2), coefficient of variation of rupture force (f_{cv}) (Figure 136.2) and micro-strength (σ_{micro}) (Figure 139.2), and increases in structural element length (L) (Figure 137.2) and the maximum structural element length (L_{max}) (Figure 138.2).

The significant increase of the microstructural element length (L) and the maximum structural element length (L_{max}) within the weak layer between Plots 2 and 5 (Table 35 and Figures 137.2 and 138.2) was likely a direct result of the loading event that preceded the sampling of Plot 5 (Figure 124.2). Due to the increased load, some microstructures may have failed or come so close to failing that they were not differentiable from the SMP signal noise. With fewer intact bonds or microstructures differentiated in a given volume of snow, there was an increase in structural element length (L). The micro-strength (σ_{micro}) decreased significantly as a result of the significant increase of the structural element length (L).

The significant decrease of the maximum rupture force (f_{max}) (Figure 135.2) coincided with the loading event. This may indicate that the increased load caused the residual strength of the strongest microstructures to decrease. The otherwise lack of change of maximum rupture force (f_{max}) at other time-steps indicates that maximum rupture force (f_{max}) was not sensitive to strengthening associated with aging.

The micro-variance of rupture force, quantified as the coefficient of variation of the rupture force (f_{cv}), significantly decreased with the loading event. This means that within the weak layer segments of SMP profiles, variations in the rupture forces became smaller under increased slab load. This is the first study to identify that rupture force micro-variance, quantified as the coefficient of variation of rupture force (f_{cv}), is inversely associated with load and that this micro-estimate may be useful for identifying and quantifying instabilities. Although an in-depth comparison of the coefficient of variation of the rupture force (f_{cv}) and the coefficient of variation of resistance (F_{cv}) was not performed, it should be noted that the coefficient of variation of resistance (F_{cv}) did not change signficantly with the large loading event.

Much like the residual shear strength (τ_{resid}) (Figure 129.2), the mean rupture force (f_m) (Figure 134.2) of the weak layer remained unchanged after the loading event. A logical explanation is that the microstructural strengthening probably occurred over the 20 days between sampling but was offset by the increased load, which resulted in an unchanged residual strength at the sampling scales of both the SMP sensor tip and the shear frame test. In other words, the lack of change may be the result of the loading event countering age-dependent residual shear- and microstructural strengthening. This could only be definitively determined had a plot been sampled directly before and after the last loading event. To more definitively determine the effects of such loading events, I designed a simple field test as described by Lutz et al. (2008a).

Associated with this loading event, the rupture force (f_m) of the super-stratum increased significantly (Figure 140.2). This would suggest that residual strength of

microstructures within the super-stratum increased despite the larger slab load extered on it. This increase of residual strength in the super-stratum may indicate that over the 20 days between plot sampling on the lower site, the increase in residual strength of the super-stratum may have been large enough that a decrease in residual strength, caused by the loading event, could not fully offset the strengthening process.

As a direct result of these findings, I conducted a simple field test to verify that these microstructural estimates directly indicated stability changes associated with loading events. The results from that verification work confirmed these findings, and are summarized in Lutz et al. (2008a).

Step-changes in mean rupture force (Δf_m) and micro-strength ($\Delta \sigma_{micro)}$ decreased (Figures 147and 156), associated with an increase of the super-stratum's mean rupture force (f_m) (Figure 140). My observation that instability was associated with a decrease of microstructural step-change values supports previous observations by Pielmeier et al. (2006), Pielmeier and Schweizer (2007), and Lutz et al. (2008a).

A logical cause of adjacent strata becoming more similar in their microstructural properties, unrelated to loading events, is metamorphism. Regardless of whether kinetic or equilibrium metamorphism governs, if both strata are subjected to similar metamorphic facies, then differences between the layers will be subdued due to vapor transport and deposition. Schneebeli et al. (1999) quantified metamorphic changes related to kinetic growth using the SMP. Whether there is a physical rationale behind the findings that step-changes become subdued with increasing instability should be examined in future studies.

Stratigraphic Delineation Technique

Comparison of Texture-Based Stratigraphic Delineators

The micro-variance estimates texture index (*TI)*, coefficient of variation of resistance (F_{cv}) and coefficient of variation of the rupture force (f_{cv}) were compared in their ability to differentiate the surface hoar layer from adjacent soft, small-grained facets. The initial comparisons showed that f_{cv} is more effective than *TI* and F_{cv} at identifying transitions associated with these layers (Figure 29). The results illustrate that the transition between the surface hoar layer and the soft, small-grained facets was typically characterized by an abrupt transition of f_{cv}, evident in the stratigraphic visualizations (Figure 150).

The ineffectiveness of *TI* and F_{cv} at differentiating these transitions is caused by their sensitivity to low mean resistance values, which, in this dataset, occur in the weak layer itself and in the adjacent layers. While this occurrence may not be typical in denser snowpacks, such as encountered in maritime climates, in continental and inter-mountain climates snowpack instabilities can often involve low density slabs fracturing on soft layers composed of surface hoar or near-surface facets. Hence, texture-based algorithms utilizing *TI* and F_{cv} will not be as sensitive as f_{cv} for detecting such transitions.

Insensitivity of Structural Element Length (*L*) Estimates to Layer Changes

The structural element length (*L*) did not change significantly between the super-stratum and the weak layer, evident in the stratigraphic visualtizations (Figure 152) and the boxplots of step-change values (Figure 153). I believe the cause of the observed

similarity in L in the super-stratum and weak layer is due to the combination of two factors:

1. The softness of the small grained facets results in very small rupture forces.
2. The finite force resolution of the SMP.

Because the super-stratum is soft, relative to the estimated signal noise, very few ruptures are recognized within this stratum, resulting in very large the structural element length (L) values. This means that, regardless of instrumental limitations or presumed differences in adjacent grain types, both the weak layer and the super-stratum possessed few apparent ruptures within a given sample – which is important in determining snow strength. There are two clear implications, relating to stratigraphic delineation:

1. L may not be able to differentiate stratigraphic features if one stratum is very soft and composed of small grains and the other is relatively soft but composed of large structures.
2. If observed ruptures are indicative of micro-strength (σ_{micro}), the lack of differentiation between adjacent strata may be superfluous or it may actually be indicative of a more accurate representation of the weak layer – super-stratum complex, whereby the entire complex is perceived as a stratigraphic weakness.

Spatial Variability over Time

The temporal-spatial analysis (temporal analysis of spatial variability) indicated that spatial properties of snow properties evolved over time. The findings, as discussed in the following sections, support the concepts of spatial divergence and convergence

present in earth surface systems, as presented by Phillips (1999) and hypothesized by Birkeland and Landry (2002) to apply to snowpack stability.

Increased Spatial Variability (Divergence) over Time

Comparison of the semi-variance of snow properties at Plots 2 through 4 revealed that as the slope stabilized, pit- and plot-scale variance of shear strength (τ_{∞}), residual shear strength (τ_{resid}), stability (S), and weak layer micro-strength (σ_{micro}) increased over time (Figures 83, 85 87, and 99 respectively). This means that, in the absence of large snowfall events, it became harder to predict these attributes as the snowpack strengthened and stabilized.

Decreased Spatial Variability (Convergence) over Time

There is evidence that the large loading event prior to Plot 5 sampling caused changes in the spatial structure of weak layer properties. Plot-scale variance (sill values) of stability (S) decreased and the distance to which observations were correlated across the slope (range values) increased (Figure 87). This means that after the loading observations became less variable and the distance between dissimilar observations became larger.

A less pronounced but similar pattern was evident for shear strength (τ_{∞}) and residual shear strength (τ_{resid}) (Figures 83 and 85). Plot 4 possessed the highest sill or plot-scale variance, while Plot 5 possessed a similar autocorrelation range value but a much smaller sill value. This indicates that, not considering plot-scale spatial trends, the predictive strength of individual shear frame measurements increased after the loading

event. These findings support the concept that in an earth surface system divergence occurs until an external forcing event causes divergence, as proposed by Landry and Birkeland (2002).

At Plots 1 through 4, very little local spatial structure existed in the weak layer's mean rupture force (f_m) (high nugget values and small or non-existent partial sill values) (Figure 89). Yet at Plot 5, pronounced local patterns with similarities between neighboring observations (substantially smaller nugget and larger partial sill values) existed (Figure 89). The semi-variance for microstructural estimates of the super-stratum indicated that Plot 5 possessed high plot-scale variability after the loading event (sill value, Figure 111). However, locally, values became more similar (nugget value, Figure 111).

Comparison of the spatial properties of these microstructure estimates of the weak layer and super-stratum indicate that the SMP more effectively captured spatial patterns in the super-stratum than the weak layer. This may be due to the size-ratio of the sensor tip to microstructures. Because grains were smaller in the super-stratum than in the weak layer, the 5 mm segment sampled from the super-stratum contained more rupture information than that of the weak layer, resulting in a more robust average of rupture characteristics in the super-stratum. This could in turn reduce variance between neighboring profiles, which for this study would result in better spatial correlations within the super-stratum than within the weak layer.

Spatial patterns of the step-change values of micro-strength ($\Delta\sigma_{micro}$) indicate that plot-scale variability of micro-strength (σ_{micro}) increased until the loading event, when the

step-change of micro-strength ($\Delta\sigma_{micro}$) between the weak layer and super-stratum became more similar at the plot-scale (Figure 123).

CONCLUSIONS

Summary of Main Research Findings

This section offers a brief overview of the main research findings, most of which stem from the research hypotheses (pages 23 - 25). Detailed descriptions and discussion of these findings are provided in the Results, Discussion, and following Conclusions.

Methodological Developments

1. The coefficient of variation of the rupture force (f_{cv}) effectively differentiated the boundary between the surface hoar and overlying soft small-grained facets. It was useful for automating the stratigraphic sampling of microstructural properties of the weak layer and super-stratum.
2. The coefficient of variation of the rupture force (f_{cv}) is more suited for differentiating changes in texture in soft snow than either the texture index (TI) or the coefficient of variation of resistance (F_{cv})
3. Sky visbility ($v_{\%}$) can be similarly estimated using inexpensive optical field measurements (i.e., Solar Pathfinder) or, through intensive field survey, modeling techniques that involve high-resolution elevation and vegetation information (i.e., G.I.S.).

Environmental Determinants of Weak Layer Formation and Persistence

1. The surface hoar weak layer thickness (h_{wl}) was positively correlated with sky visibility ($v_{\%}$).

2. The surface hoar weak layer thickness (h_{wl}) was negatively correlated with the estimated incoming longwave radiation ($L\downarrow$), modeled for early morning conditions during the formation period.
3. The surface hoar weak layer thickness (h_{wl}) was negatively correlated with the estimated daily cumulative shortwave radiation ($\sum I$), the duration of direct shortwave radiation ($\sum t_I$), and the maximum shortwave radiation (I_{max}), modeled for clear sky conditions during the persistence period.

Temporal Changes in Strength and Stability

1. The surface hoar weak layer strengthened gradually over the sampling period.
2. The stability (S) and micro-strength (σ_{micro}) did not increase significantly at any time-step that did not experience loading.
3. The stability (S) and micro-strength (σ_{micro}) decreased significantly at the second time-step on the lower site which coincided with a large increase in load.

Internal Spatial Associations

1. The surface hoar weak layer shear strength was spatially associated with weak layer thickness (h_{wl})
2. At Plot 5, the surface hoar weak layer shear strength (τ_∞) was positively associated with load.

Temporal Changes in Spatial Variability

1. Spatial variability of shear strength (τ_∞), stability (S), and micro-strength (σ_{micro}) increased (diverged) over time.

2. Spatial variability of shear strength (τ_∞), stability (S), and micro-strength (σ_{micro}) decreased (converged) after a large laoding event.

Radiation Influences on Weak Layer Strength Properties

Longwave and shortwave radiation estimates for the surface hoar formation period possessed pronounced spatial patterns that helped explain spatial patterns of several snow properties, including the weak layer's thickness (h_{wl}), structural element length (L), and shear strength properties. The models estimated that during the day the lower slope received cumulatively more shortwave radiation (quantified by cumulative shortwave radiation $\sum I$) and also received more intense shortwave radiation (quantified by maximum shortwave radiation I_{max}), than the upper slope. At night-time, the lower slope also received more incoming longwave radiation ($L\downarrow$) than the upper slope.

As a result of these patterns in radiation, on the upper slope, where incoming longwave and shortwave radiation were lowest, the weak layer was thickest, possessed the largest structural elements, and sheared easily. Conversely, the weak layer was thinnest, strongest, and possessed the smallest structural element where incoming longwave and shortwave radiation were greatest, which was near the trees at the base of the slope. These spatial patterrns and relationships can be identified across distances as short as 14 m, but only when the spatial patterns of radiation estimates were distinct, as was the case at Plot 2 and Plot 5. Co-linearity between shortwave and longwave variables made it difficult to determine which radiation variable was most critical.

Strength and Stability Properties of Weak Layer

Based on observations made at Plot 1 and 2, three weeks after the surface hoar layer was buried, shear strength (τ_∞), stability, and micro-strength (σ_{micro}) of the weak layer were inversely related to slab load. This indicates that, several weeks after burial the weak layer had strengthened more slowly over time where the slab stresses were smallest. I hypothesize that because of a lack of stress-induced deformation by the slab load, areas with lighter slab loads may remain weaker longer after a loading event and thereby remain more susceptible to fracturing once a new loading event occurs. Future field studies should test this hypothesis.

In the absence of a loading event, significant shear strengthening of the weak layer and stabilization of the snowpack on the upper slope was accompanied by a significant increase of the weak layer's micro-strength (σ_{micro}) (which increased as a result of a significant decrease in the microstructural element length). This change of microstructural element length (L) indicates that the microstructures became shorter, which was the result of increased sintering or slab-induced deformation that resulted in an increased bond frequency.

After the large loading event on March 20, despite continued shear strengthening, stability (S) decreased significantly. Likewise, the maximum rupture force (f_{max}), coefficient of variation of the rupture force (f_{cv}) and micro-strength (σ_{micro}) decreased. Both the microstructural element length (L) and maximum microstructural element length (L_{max}) increased. Micro-strength (σ_{micro}) decreased as a direct result of the increase of the microstructural element length (L). A simple field test conceived and implemented by

Lutz et al. (2008a) verified that changes of these microstructural estimates directly indicate stability changes associated with loading events.

The spatial analysis indicated that shear strength (τ_∞) and its derived stability index (S) demonstrated evolution of spatial properties. This supports the concept of spatial divergence and convergence present in earth surface systems, as presented by Phillips (1999), and confirms Birkeland and Landry's (2002) assertion that these processes may apply to the evolution of snowpack stability. The semi-variance analysis showed that as the slope stabilized, pit- and plot-scale variance of stability increased over time and the distance to which observations were correlated decreased. This means that it becomes harder to predict stability as the snowpack becomes more stable.

Spatial structure changed dramatically after a loading event. Local and plot-scale variance of stability decreased and the distance to which observations were correlated across the slope, in some instances, increased. This means that after the loading, which forced plot-scale instability, observations became less variable and the distance between dissimilar observations became larger. This finding augments the second assertion by Birkeland and Landry (2002) that an external forcing event, such as a large snowfall event, can cause spatial convergence which results in it being easier to predict stability when the snowpack becomes less stable.

There was no evident reason for the changes in spatial properties of microstructural estimates. With the loading event, the pit- and plot-scale variance decreased, as occurred with the shear strength (τ_∞) and stability observations. However,

local spatial structure increased as well, which means that beyond approximately 3 m, estimates become less reliable.

Microstructural estimates of the weak layer on the upper slope were largely devoid of spatial structure. The apparent lack of spatial structure on the upper slope indicated that the microstructural estimates were largely random. On the lower slope spatial structure was observed using the same sampling scheme. The apparent randomness on the upper slope may be an artifact of either natural- or instrumental-related phenomena. To the former, fairly uniform radiation properties on the upper site may have resulted in uniform snow properties. To the latter, where the surface hoar is thicker, the SMP sensor tip interacted with larger structures and pore spaces, which may have resulted in less consistent (more stochastic) microstructural samples than experienced in smaller grained snow types. Supporting this concept, the super-stratum possessed more pronounced spatial structure, in the form of spatial autocorrelation, than observed within the weak layer. Because the super-stratum was composed of small-grained facets that generally possessed structural element length (L) values approximately 10% smaller than observed in the surface hoar layer, the SMP was in contact with more structures within the super-stratum and could therefore produce more robust (and reproducible) estimates in the super-stratum than in the weak layer.

The pit-to-plot uniformity test can be greatly influenced by spatial trends. The number of unrepresentative pits will vary considerably, depending on the configuration and number of pits per plot. The up-slope trend identified in several weak layer properties, quantified using geostatistical analysis, often resulted in unrepresentative plots

positioned at opposite ends of a plot. While pit-to-plot tests are a practical research tool for assessing slope stability, researchers and practitioners must be aware that spatial trends will influence test results and interpretations.

Correlations between Shear Strength (τ_∞) and Microstructural Estimates

Only two plot-scale and three site-scale significant associations could be identified between shear strength (τ_∞) and weak layer microstructural estimates. This may be a direct result of the two types of observations quantifying only peripherally-related phenomena. SnowMicroPen measurements quantify microstructural strength by rupturing individual microstructures while the material is under an applied load. Conversely, a shear frame test quantifies the shear strength of an aggregate of many bonds relieved of overburden. Furthermore, I hypothesize that torsion effects related to the truss-like structure of surface hoar being loaded in shear may affect shear strength measurements.

Recent studies by Lutz et al. (2008a) and Pielmeier and Marshall (2008) have identified significant correlations between column-oriented stability tests, such as compression and rutschblock tests, and SMP measurements. Although in these instances the difference in observation scale is even larger than with a shear frame, the strong associations are possibly due to the weak layer being tested *in-situ* under a pre-existing load.

Implications for Slope Scale Spatial Variability

Microstructural estimates derived from the SMP showed temporal correlations with changes in stability and spatial relationships with slab stresses, indicating that the SMP was recording information that was pertinent to stability. Unexplainable results are the lack of spatial structure and the lack of expected associations with shear frame observations on some plots. This is possibly due to the sampling scheme being applied to small plots (i.e., 14 m x 14 m) on fairly uniform terrain. While spatial structure could, in some instances, be identified because of the well-designed geostatistical sampling layout, by focusing on a topographically uniform slope with no wind loading, I eliminated pronounced spatial structures at the chosen scale of observation. Hence, many variables possess uniform distributions that are best described through their typical (e.g., mean or median) values and their local variation (e.g., standard deviation or inter-quartile range). This type of plot-scale uniformity is helpful for obtaining time series datasets but makes identifying relationships between spatial properties difficult.

This study focused on examining a surface hoar related instability in a forest opening. This work illuminated the challenges and predicaments that avalanche forecasters, ski patrollers, and back country enthusiasts are faced with when trying to choose and sample representative or targeted slopes. It clearly shows that on relatively uniform terrain, significant trends can exist in weak layer strength and thickness due to subtle changes in topography and surrounding tree characteristics. Sampling only one corner of the slope would result in a skewed picture of slope stability. Yet, sampling the middle of the slope, if steep enough, could be hazardous. As Birkeland and Chabot

(2006) recommended, digging more pits in multiple locations (at the range-, basin- or slope-scale) can decrease the chances of false interpretation of slope stability. In addition, with a better understanding of important environmental variables affecting weak layer formation, forecasters could more reliably estimate how the strength of the weak layer changes across a slope, away from their pit. For example, as this study has shown, on north-facing slopes in the northern hemisphere, observers will more likely find thicker and weaker surface hoar layers near the top of forest openings than at the bottom of forest openings.

For researchers, these findings have ramifications for field-based snow studies. During the planning stage of field studies, scientists need to consider the potential for slope-scale trends to be present, even on uniform terrain. This is especially critical for temporal studies attempting to monitor changes in snowpack characteristics over time. If slope-scale trends exist at initial conditions, sampling across the slope over time will mix spatial and temporal variations in a single dataset, making a meaningful spatial or temporal analysis difficult, if not impossible, to conduct.

Hence, temporal studies need to quantify spatial patterns at initial conditions and utilize a sampling scheme that allows for the spatial trend to be accounted for. Two possible options include: 1) re-sampling the same general extent of the slope at each time interval, thereby incorporating the spatial variability into the temporal dataset, or 2) utilizing an initial layout that captures slope-scale patterns and allows for subsequent samples to be de-trended for initial conditions.

Recommendations for Future Studies

There are several areas of study that need to be addressed in future research, as summarized in the following sections.

Observe and Quantify (Temporal Changes of) Spatial Variability

- Develop sampling techniques - sampling schemes and technologies alike - that allow for spatial variability to be assessed over time, despite the presence of pronounced trends. Remote sensing technologies that allow for a large number of observations to be recorded non-destructively in short time periods, such as FMCW radar (Marshall and Koe, 2008), may make this feasible.
- Combining field observations with expansive high-resolution terrain, vegetation, and snowpack surface models, such as those produce using Lidar (Deems and Painter, 2006), will allow for spatial models to be better quantified over larger areas.

Deterministic Models and Predictors of Spatial Patterns of Weak Layer Properties

- Develop sampling strategies that eliminate potential co-linearity of incoming long- and shortwave radiation. This can be done *a priori* by modeling spatial patterns of radiation before conducting snow observations.
- Incorporating process-driving thermo-dynamics models (e.g., RadTherm), snowpack metamorphism model (e.g. SNOWPACK), and mechanical models with large temporal-spatial dataset may enable us to better understand how spatial

variability is influenced by external and internal processes. Initial work by Adams et al. (2004) shows the potential of such comprehensive modeling efforts.

- Our understanding of spatial divergence and convergence of stability-related field observations could be greatly improved if the questions are addressed from mechanics modeling and field observation perspectives simultaneously.
- Further incorporate random field simulations in field-based research and in modeling, since it quantifies how spatial patterns in local mean values can be obscured by observational noise.
- In the absence of high-resolution elevation and vegetation models and complex radiation models, field studies can be efficiently and effectively conducted using a modified Solar Pathfinder to measure sky visibility, and estimate patterns in long- and shortwave radiation at targeted sampling locations. Measurements can be made during winter field campaigns and can target locations where surface hoar (or near surface facets) are most and least well developed, in order to identify effective proxies.

Temporal and Spatial Relationship between Load, Strength, and Stability

- Relationships between slab load and weak layer strength and stability can become better defined through targeted field observations, statistical analysis of past occurrences, and through mechanical modeling. While we are accustomed to recognizing areas with large loads as potential hazards during unstable conditions, observations in this study indicate that weak layers buried below thin or light slabs have the potential to remain unstable longer and hence be more susceptible

to fracturing when a new loading event occurs. Basic statistical analysis of avalanche occurrences may reveal inverse correlations between avalanche activity and slab thickness before the most recent loading event. This may prove particularly useful for snow safety and regional forecasting operations.

SMP-Based Microstructural and Stratigraphic Analysis

- Future studies and forecasting operations need to actively managed SMP signal quality in the field and during pre-processing procedures, to ensure that the measurements produce accurate findings.
- Future snow studies involving SMP profile analysis may find it useful to incorporate the stratigraphic sampling approach outlined in this study, whereby the coefficient of variation of the rupture force was used to identify transitions in texture.
- Incorporating layer-picking algorithms, such as the wavelet application developed by Floyer (2008), into SMP analysis may further stream-line analysis.

REFERENCES CITED

Abe, O., 1999. A new generation ramsonde having multiple sensors. Report of the National Research Institute for Earth Science and Disaster Prevention, National Research Institute of Earth Science And Disaster Prevention, Yamagata, Japan, 59: 11-18.

Adams, E.E., Gauer, P., McKittrick, L.R., Curran, A.R., and Levenan, D.S., 2004. Modeling snow temperature in complex topography. Proceedings of the International Symposium on Snow Monitoring and Avalanches, Manali, India, pp. 87-96.

Anderson, M.C. 1964. Studies of the woodland light climate. 1. The photographic computation of light conditions. Journal of Ecology 52: 27–41.

Bader, H.P., Haefeli, R., Bucher, E., Neher, J., Eckel, O., and Thams, C., 1939. Der Schnee und seine Metamorphose. Beitraege zur Geologie der Schweiz, Geotechnische Serie, Hydrologie Lieferung 3. Kümmerly and Frey, Zürich, pp. 340.

Bader, H., Hansen, B. L., Joseph, J. A., and Sandgren, M. A., 1951. Preliminary investigations of some properties of snow. SIPRE Repost 7. Snow, Ice and permafrost research establishment, Corps of Engineers, U. S. Army. Engineering Experiment Station, Institute of Technology, University of Minnesota, pp. 49.

Bader, H., 1962. The physics and mechanics of snow as a material. U.S.A. Cold Regions Research and Engineering Laboratory, Monograph II-B, pp. 79.

Bader, H. P., and Weilenmann, P., 1992. Modeling temperature distribution, energy and mass flow in a (phase-changing) snowpack. I. Model and case studies. Cold Regions Science and Technology, 20 (2): 157-181.

Bentley, W.A., and Humphreys, W.J., 1962. Snow Crystals. The original book was published by McGraw-Hill in 1931. Dover Publications. New York. pp. 227.

Bird, R.E., and Hulstrom, R.L., 1981. Simplified Clear Sky Model for Direct and Diffuse Insolation on Horizontal Surfaces, Technical Report No. SERI/TR-642-761, Solar Energy Research Institute, Golden, CO., pp.46.

Birkeland, K.W., 1990. The spatial variability of snow resistance on potential avalanche slopes. M.S. thesis, Montana State University, Bozeman, MT., U.S.A., pp. 99.

Birkeland, K.W., 1995 Spatial and temporal variations in snow stability and snowpack conditions throughout the Bridger Mountains, Montana. Ph.D. thesis, Department of Geography, Arizona State University, AZ., U.S.A., pp. 205.

Birkeland, K.W., Hansen, K., and Brown, R., 1995. The spatial variability of snow resistance on potential avalanche slopes. Journal of Glaciology, 44 (137): 183-190.

Birkeland, K.W., and Johnson, R., 1999. The stuffblock snow stability test: comparability with the Rutschblock, usefulness in different snow climates, and repeatability between observers. Cold Regions Science and Technology, 30 (1-3): 115-123.

Birkeland, K.W., 2001. Spatial patterns of snow stability throughout a small mountain range. Journal of Glaciology, 47 (157), 176-186.

Birkeland, K.W., and Landry, C., 2002. Changes in spatial patterns of snow stability through time. Proceedings of the 2002 International Snow Science Workshop, Penticton, BC., Canada, pp. 482-490.

Birkeland, K.W., Kronholm, K., Schneebeli, M., and Pielmeier, C., 2004. Changes in the shear strength and micro-penetration hardness of a buried surface-hoar layer. Annals of Glaciology, 38: 223-228.

Birkeland, K.W., and Chabot, D., 2006. Minimizing "false-stable" stability test results: Why digging more (rather than less) snowpits is a good idea. Proceedings of the 2006 International Snow Science Workshop, Telluride, CO., U.S.A., pp. 498-504.

Blöschl, G., 1999. Scaling issues in snow hydrology. Hydrological Processes, 13: 2149-2175.

Bradley, C.D., 1966. The Snow Resistograph and Slab Avalanche Investigations. International Symposium on Scientific Aspects of Snow and Ice Avalanches. April 5th – 10th, 1965: Davos, Switzerland. International Union of Geodesy and Geophysics (IUGG) and International Association of Scientific Hydrology (IASH); Commission of Snow and Ice. Pub. No. 69.

Bradley, C.C., 1968. The resistogram and the compressive strength of snow. Journal of Glaciology, 7 (51): 499-506.

Brang, P., 1998. Early seedling establishment of Picea abies in small forest gaps in the Swiss Alps. Canadian Journal of Forestry Research, 28: 626-639.

Brown, R., and Birkeland, K., 1990. A comparison of the digital Resistograph with the ram penetrometer. Proceedings of the 1990 International Snow Science Workshop, Bigfork, MT., U.S.A., pp. 19-30.

Campbell, C., and Jamieson, B., 2006. Spatial clusters of slab stability and snowpack properties within avalanche start zones. Proceedings of the 2006 International Snow Science Workshop, Telluride, CO., U.S.A., pp. 44-53.

Campbell, C., and Jamieson, B., 2007. Spatial variability of slab stability and fracture characteristics within avalanche start zones. Cold Regions Science and Technology, 47 (1-2): 134-147.

Campbell Scientific, 1997. LI200X Pyronometer Instruction Manual. Campbell Scientific. Logan, UT., pp. 8.

Campbell Scientific, 2003. SR50 Sonic Ranging Sensor Operator's Manual. Campbell Scientific. Logan, UT., pp. 30.

Campbell Scientific, 2004a. Model 107 Temperature Probe Instruction Manual. Campbell Scientific. Logan, UT., pp. 9.

Campbell Scientific, 2004b. Met One 034B-L Windset Instruction Manual. Campbell Scientific. Logan, UT., pp. 16.

Chabot, D., Kahrl, M., Birkeland, K. W., and Anker, C., 2004. SnowPilot: A "new school" tool for collecting, graphing, and databasing snowpit and avalanche occurrence data with a PDA. Proceedings of the 2004 International Snow Science Workshop, Jackson Hole, WY., U.S.A., pp. 19-24.

Chambers, J. M., Cleveland, W. S., Kleiner, B. and Tukey, P. A., 1983. Graphical Methods for Data Analysis. Wadsworth and Brooks, pp. 395.

Colbeck, S.C., Akitaya, E., Armstrong, R., Gubler, H., Lafeuille, J., Lied, K., McClung, D., and Morris, E., 1990. International Classification for Seasonal Snow on the Ground. International Commission for Snow and Ice (IAHS), World Data Center A for Glaciology, University of Colorado, Boulder, CO., U.S.A., pp. 23.

Conover, W. J., 1971. Practical nonparametric statistics. Wiley, New York, pp. 462.

Conway, H., and Abrahamson, J., 1984. Snow stability index. Journal of Glaciology, 30 (106): 321-327.

Conway, H., and Abrahamson, J., 1988. Snow-slope stability – a probabilistic approach. Journal of Glaciology, 34 (117): 170-177.

Conway, H., and Wilbour, C., 1999. Evolution of snow slope stability during storms. Cold Regions Science and Technology, 30 (1-3): 67-77.

Cooperstein , M., Birkeland, K.W., and Hansen, K., 2004. The effects of slope aspect on the formation of surface hoar and diurnally recrystalized near-surface faceted crystals: implications for avalanche forecasting. Proceedings of the 2004 International Snow Science Workshop, Jackson Hole, WY., U.S.A., pp. 83-93.

Cooperstein , M., 2008. The effects of slope aspect on the formation of surface hoar and diurnally recrystalized near-surface faceted crystals. M.S. thesis, Montana State University, Bozeman, MT., U.S.A., pp. 169.

Cressie, N.A.C., 1993. Statistics for Spatial Data. Revised edition. John Wiley and Sons, New York, pp. 900.

Davis, R., Jamieson, B., Hughes, J., and Johnston, C., 1996. Observations on buried surface hoar – Persistent failure planes for slab avalanches in British Columbia, Canada. Proceedings of the 1996 International Snow Science Workshop, Banff, AB., Canada, pp. 81-85.

Davis, R., Jamieson, B., and Johnston, C., 1998. Observations on buried surface hoar in British Columbia, Canada: Section analyses of layer evolution. Proceedings of the 1998 International Snow Science Workshop, Sunriver, OR., U.S.A., pp. 86-92.

Deems, J.S., and Painter, T. H., 1998. Lidar measurement of snow depth: Accuracy and error sources. Proceedings of the 2006 International Snow Science Workshop, Telluride, CO., U.S.A., pp. 384-391.

DeQuervain, M., 1951. Strength properties of a snow cover and its measurement [Die Festigekeitseigenschaften der Schneedecke und ihre Messung (1950)] SIPRE Transl. 9.

DeQuervain, M., and Meister, R., 1987. 50 years of snow profiles on the Weissfluhjoch and relations to the surrounding avalanche activity (1936/37-1985/86). In: Salm, B. and H. Gubler (eds), Avalanche Formation, Movement and Effects, International Association of Hydrological Sciences, Pub. No. 162, pp. 161-181.

Dowd, T., 1984. A new instrument for determining strength and temperature profiles in snowpack. M.S. thesis, Montana State University, Bozeman, MT., U.S.A., pp. 42.

Dowd, T., and Brown, R.L., 1986. A new instrument for determining strength profiles in snowcover. Journal of Glaciology, 32 (111): 299-301.

Dozier, J., and Frew, J., 1990. Rapid Calculation of Terrain Parameters For Radiation Modeling from Digital Elevation Data. IEEE Transactions on Geoscience and Remote Sensing, 28 (5): 963-969.

Englund, S.R., O'Brien, J.J., and Clark, D.B.. 2000. Evaluation of digital and film hemispherical photography and spherical densiometry for measuring forest light environments. Canadian Journal of Forest Research, 30: 1999-2005.

Eugster, E., 1938. Schneestudien im Oberwallis und ihre Anwendung auf den Lawinenverbau. 2nd. Kümmerly and Frey, Zürich, pp. 84.

Feick, S., Kronholm, K., and Schweizer, J., 2007. Field observations on spatial variability of surface hoar at the basin scale. Journal of Geophysical Research – Earth Surface, 112, F02002, doi:10.1029/2006JF000587.

Floyer, J., 2006. Empirical analysis of snow deformation below penetrometer tips. Proceedings of the 2006 International Snow Science Workshop, Telluride, CO., U.S.A.. pp. 555-561.

Floyer, J., 2008a. Layer detection and snowpack stratigraphy characterisation from digital penetrometer signals, Ph.D. thesis, University of Calgary, Calgary, Canada, pp. 253.

Floyer, J., and Jamieson, B., 2008b. Predicting the fracture character of potential weak layers in penetrometer signals. Proceedings of the 2008 International Snow Science Workshop, Whistler, British Columbia, Canada. pp. 195-203.

Föhn, P. M. B., 1987. The rutschblock as a practical tool for slope stability evaluation, In: Salm, B. and H. Gubler (eds), Avalanche Formation, Movement and Effects, International Association of Hydrological Sciences, Publication No. 162, pp. 223-228.

Föhn, P. M. B., 1989. Snow cover stability tests and the areal variability of snow strength. Proceedings of the 1988 International Snow Science Workshop, Whistler, British Columbia, Canada, pp. 262-273.

Föhn, P. M. B., Camponovo, Ch., and Krüsi, G., 1998. Mechanical and structural properties of weak snow layers measured in-situ. Annals of Glaciology, 25: 1-5.

Föhn, P. M. B., 2001. Simulation of surface-hoar layers for snow-cover models. Annals of Glaciology, 32: 19-26.

Fotheringham, A.S., Brunsdon, Ch. and Charlton, M., 2002. Quantitative Geography: Perspectives on Spatial Data Analysis. Sage Publications Ltd. London. pp. 270.

Frazer, G.W., Canham, C.D., and Lertzman, K.P., 1999. Gap Light Analyzer (GLA), Version 2.0: Imaging software to extract canopy structure and gap light transmission indices from true-color fisheye photographs. Copyright 1999: Simon Fraser University, Burnaby, B.C., and the Institute of Ecosystem Studies, Millbrook, New York.

Frazer, G.W., Fournier, R.A., Trofymow, J.A., and Hall, R.J., 2001. A comparison of digital and film fisheye photography for analysis of forest canopy structure and gap light transmission. Agricultural and Forest Meteorology 2984: 1-16.

Fritton, D. D., 1990. A standard for interpreting soil penetrometer measurements. Soil Science, 150(2): 542-551.

Greene, E., Birkeland, K.W., Elder, K., Johnson, G., Landry, C., McCammon, I., Moore, M., Sharaf, D., Sterbenz, C., Tremper, B., and Williams, K., 2004. Snow, Weather, and Avalanches: Observational Guidelines for Avalanche Programs in the United States. The American Avalanche Association. Pagosa Springs, CO., pp. 136.

Gringarten, E., and Deutsch, C. V., 2001. Teacher's Aide Variogram Interpretation and Modeling. Mathematical Geology. 33 (4): 507-534.

Gubler, H., 1978. Determination of the mean number of bonds per snow grain and of the dependence of the tensile strength of snow on stereological parameters. Journal of Glaciology. 20 (83): 329-341.

Gubler, H., and Rychetnik, J., 1991. Effects of forests near the timberline on avalanche formation. In: H. Bergmann, H. Lang, W. Frey, D. Issler and B. Salm (Editors), Symposium at Vienna 1991 - Snow, Hydrology and Forests in High Alpine Areas, IAHS Publ., 205, pp. 19-37.

Gubler, H. 1998. A model to determine snow surface properties from remote measurements. Proceedings of the 1998 International Snow Science Workshop, Sunriver, OR., U.S.A., pp. 35-48.

Gubler, H., 1999. Physik von Schnee. Instructor notes for the university lecture Physik von Schnee, Eidgenössische Technische Hochschule, Zürich, Switzerland, pp. 204.

Hachikubo, A., and Akitaya, E., 1997. Effect of wind on surface hoar growth on snow. Journal of Geophysical Research - Atmospheres, 102:D4, 4367-4373.

Hachikubo, A., 2001. Numerical modeling of sublimation on snow and comparison with field measurements. Annals of Glaciology, 32: 27-32.

Huang, A.-B., Max., Y. M., John, S. L., 1993. A micromechanical study of penetration tests in granular material. Mechanics of Materials, 16: 133-139.

Hendrikx, J., and Birkeland, K., 2008. Slope scale spatial variability across time and space: comparison of results from two different snow climates. Proceedings of the 2008 International Snow Science Workshop, Whistler, B.C., Canada, pp. 155-162.

Höller, P., 2001. The influence of the forest on night-time snow surface temperature. Annals of Glaciology, 32: 217-222.

Höller, P., 2004. Near-surface faceted crystals on a slope covered with stone pine trees. Proceedings of the 2004 International Snow Science Workshop, Jackson Hole, WY., U.S.A., pp. 83-93.

Iqbal, M., 1983. An introduction to solar radiation. Academic Press, New York, pp. 390.

Jamieson, J.B. 1995. Avalanche prediction for persistent snow slabs, Ph.D. thesis, University of Calgary, AB., Canada, pp. 258.

Jamieson, J.B., and Johnston, C.D., 1999. Snowpack factors associated with strength changes of buried surface hoar layers. Cold Regions Science and Technology, 30 (1-3): 19-34.

Jamieson, J. B., and Schweizer, J., 2000. Texture and strength changes of buried surface-hoar layers with implications for dry snow-slab avalanche release. Journal of Glaciology, 46 (152): 151-160.

Jamieson, J.B., and Johnston, C.D., 2001. Evaluation of the shear frame test for weak snowpack layers. Annals of Glaciology, 32: 59-69.

Joerg, P., Fromm, R., Sailer, R., and Schaffhauser, A., 2006. Measuring snow depth with a terrestrial laser ranging system. Proceedings of the 2006 International Snow Science Workshop, Telluride, Colorado, U.S.A., pp. 452-460.

Johnson, J., and Schneebeli, M., 1997. Snow strength penetrometer. U.S. Patent 5831161. Filed May 2, 1997, and issued November 3, 1998.

Johnson, J., and Schneebeli, M., 1999. Characterizing the microstructural and micromechanical properties of snow. Cold Regions Science and Technology, 30 (1-3): 91-100.

Kobayashi, T., 1961. The growth of snow crystals at low supersaturations. Philos.Mag., 6 (71), 1363-1370.

Kronholm, K., and Schweizer, J., 2003. Snow stability variation on small slopes. Cold Regions Science and Technology, 37: 453-465.

Kronholm, K. 2004. Spatial variability of snow mechanical properties with regard to avalanche formation. Ph.D. thesis, Mathematics and Natural Sciences Faculty, University of Zurich, Switzerland, pp. 187.

Kronholm, K., Schneebeli, M. and Schweizer, J., 2004. Spatial variability of micro-penetration resistance in snow layers on a small slope. Annals of Glaciology, 38: 202-208.

Kronholm, K., and Birkeland, K., 2007. Reliability of sampling designs for spatial snow surveys. Computer and Geosciences, 33: 1097-1110.

Landry, C., Borkowski, J., and Brown, R., 2001. Quantified loaded column stability test: mechanics, procedure, sample-size selection, and trials. Cold Regions Science and Technology, 33 (2-3), 103-121.

Landry, C., 2002. Spatial variations in snow stability on uniform slopes: Implications for extrapolation to surrounding terrain, M.S. thesis, Montana State Univeristy, Bozeman, MT., U.S.A., pp. 194.

Landry, C., Birkeland, K., Hansen, K., Borkowski, J., Brown, R., and Aspinall, R., 2004. Variations in snow strength and stability on uniform slopes. Cold Regions Science and Technology, 39 (2-3), 205-218.

Lehning, M., and Fierz, C., 2008. Assessment of snow transport in avalanche terrain. Cold Regions Science and Technology, 51(2-3), 240-252.

LI-COR, 2005. LI-COR Terrestrial Radiation Sensors Instruction Manual. Lincoln, NB. pp. 41.

Logan, S., 2005. Temporal changes in the spatial patterns of weak layer shear strength and stability on uniform slopes. M.S. thesis, Montana State University, Bozeman, MT., U.S.A., pp. 157.

Logan, S., Birkeland, K.W., Kronholm, K., and Hansen, K.J., 2007. Temporal changes in the slope-scale spatial variability of the shear strength of buried surface hoar layers. Cold Regions Science and Technology, 47 (1–2): 148-158.

Louchet, F., 2001. Creep instability of the weak layer and natural slab avalanche triggerings. Cold Regions Science and Technology, 33 (2-3): 141-146.

Lutz, E., 2003. Investigations of airborne laser scanning signal intensity on glacial surfaces – utilizing comprehensive laser geometry modeling and surface type modeling: a case study: Svartisheibreen, Norway. M.S. thesis, Leopold-Franzen-University Innsbruck, Austria. pp. 113.

Lutz, E., Kronholm, K., Birkeland, K. W., and Hansen, K. J., 2005. Automated delineation of snowpack stratigraphy using a high-resolution snow penetrometer. Geophysical Research Abstracts, 7, 06020

Lutz, E.R., Birkeland, K.W., Kronholm, K., Hansen, K.J., and Aspinall, R., 2007. Surface hoar characteristics derived from a snow micropenetrometer using moving window statistical operations. Cold Regions Science and Technology, 4 (1-2): 118-133.

Lutz, E., Birkeland, K.W., Marshall, H.-P., and Hansen, K., 2008a. Quantifying changes in weak layer microstructure associated with loading events. Proceedings of the

2008 International Snow Science Workshop, Whistler, B.C., Canada. pp. 131-138.

Lutz, E., Birkeland, K.W., and Marshall, H.-P., 2008b. Important factors influencing microstructural estimates derived from the SnowMicroPen. Monitoring, Measuring, and Modeling Snow Processes II, AGU Fall Meeting, Abstract C21C-0579.

Lutz, E., Birkeland, K.W., Marshall, H.-P., in review. Quantifying changes in weak layer microstructure associated with artificial load changes. Cold Regions Science and Technology.

Mackenzie, R., and Payten, W., 2002. A portable, variable-speed, penetrometer for snow pit evaluation. Proceedings of the 2002 International Snow Science Workshop, Penticton, B.C., Canada, pp. 294-300.

Mann, H. B., and Whitney, D. R., 1947. On a test of whether one of two random variables is stochastically larger than the other. Annals of Mathematical Statistics, 18: 50-60.

Marshall, H.P., and Koh, G., 2008. FMCW radars for snow research. Cold Regions Science and Technology, 52 (2): 118-131.

Marshall, H.P., and Johnson, J., under review. Accurate inversion of snow micropenetrometer signals for microstructural and micromechanical properties. Journal of Geophysical Research - Earth Surface.

McClung, D. M., 1981. Fracture mechanical models of dry slab avalanche release. J. Geophys. Res. 86 B11 , 10783-10790.

McClung, D. M., and Schaerer, P., 1993. The Avalanche Handbook. The Mountaineers. Seattle, WA., U.S.A., pp. 271.

McGill, R., Tukey, J. W. and Larsen, W. A., 1978. Variations of box plots. The American Statistician, 32: 12-16.

Mellor, M., 1975. A review of basic snow mechanics, Snow Mechanics Symposium, International Association of Hydrological Sciences Publication No. 114, pp. 251-291.

MFWP, 2009. Montana Field Guide. Web-based field guide partnership between the Heritage Program and Montana Fish, Wildlife and Parks. http://FieldGuide.mt.gov

Mock, J. J., and Birkeland, K. W., 2000. Snow avalanche climatology of the western United States mountain ranges. Bulletin of the American Meteorological Society, 81 (10): 2367-2390.

Myers, D. R., 2004. Microsoft Excel@ Spreadsheet implementation of Bird Clear Sky Model (Bird and Hulstrom, 1981). National Renewable Energy Laboratory, Golden CO.

Nakaya, U., 1938: Artificial snow. Quarterly Journal of the Royal Meteorological Society, 64: 619-624.

NRCS, 2006. National Soil Information System (NASIS), a service of the Natural Resources Conservation Service, USDA. Soil Database for Gallatin National Forest Area, Montana (mt623nasis.mdb). Distribution Generation date: 6/5/2006.

NREL-TP, National Solar Radiation Database, 2007. 1991-2005 Update: User Manual. Technical Report. NREL/TP-581-41364. April 2007. pp. 472.

Nyberg, A., 1939. 'Temperature measurements in an air layer very close to a snow surface.' Statens Meteorologik-Hydrografiska Anstalt, Meddelanden Serien Uppsatser 24: 234-275.

Oke, T. R., 1987. Boundary kayer climates. Routledge, London, U.K. pp. 435.

O'Sullivan, D., and Unwin, D.J., 2002. Geographic Information Analysis. John Wiley and Sons, Inc. Hoboken, New Jersey. pp. 436.

Paterson, W. S. B., 1994. The physicas of glaciers. 3rd Ed. Butterworth Heinemann, Oxford. pp. 480.

Paulcke, W., 1938. Praktische Schnee- und Lawinenekunde. Verlag Julius Springer, Berlin, pp. 218.

Perla, R., Beck, T.M.H., and Cheng, T.T., 1982. The shear strength index of alpine snow. Cold Regions Science and Technology, 6 (1): 11-20.

Perla, R., and Beck, T.M.H., 1983. Instruments and methods: experiences with shear frames. Journal of Glaciology, 29 (103): 485-491.

Phillips, J. D., 1999. Earth surface systems – complexity, order and scale. Blackwell, Malden and Oxford, pp 180.

Pielmeier, C., 2003. Textural and mechanical variability of mountain snowpacks. Ph.D. thesis, Natural Sciences Faculty, University of Bern, Switzerland. pp. 126.

Pielmeier, C., and Schneebeli, M., 2003. Snow stratigraphy measured by snow hardness and compared to surface section images. Cold Regions Science and Technology, 37 (3): 393-405.

Pielmeier, C., Marshall, H.P, and Schweizer, J., 2006. Improvements in the application of the SnowMicroPen to derive stability information for avalanche forecasting. Proceedings of the 2006 International Snow Science Workshop, Telluride CO., U.S.A., pp. 187-192.

Pielmeier, C., and Schweizer, J., 2007. Snowpack stability information derived from the SnowMicroPen signal. Cold Regions Science and Technology, 47 (1), 102-107.

Pielmeier, C., and Marshall, H.P., under review. Snowpack stability derived from multiple quality-controlled SnowMicroPen measurements at the Rutschblock scale. Cold Regions Science and Technology.

Platts, W.S., Armour, C., Booth, G.D., Bryant, M., Bufford, J.L., Cuplin, P., Jensen, S., Lienkaemper, G.W., Minshall, G.W., Monsen, S.B., Nelson, R.L., Sedell, J.R., and Tuhy, J.S., 1987. Methods for evaluating riparian habitats with applications to management. U.S. Department of Agriculture Forest Service, General Technical Report INT-221.

Pyrcz, M.J., and Deutsch, C.V., 2001. The Whole Story of the Hole Effect, Internal manuscript. Centre for Computational Geostatistics 3rd Annual Report, University of Alberta, pp.16.

Pyrcz, M.J., and Deutsch, C.V., 2003. The Whole Story on the Hole Effect. Précis summarizing Pyrez and Deutsch, 2001. Searston, S. (ed). Geostatistical Association of Australasia. Newsletter 18, May 2003.

R Development Core Team, 2008. R: A language and environment for statistical computing. R Foundation for Statistical Computing, Vienna, Austria. ISBN 3-900051-07-0, URL http://www.R-project.org.

Rich, P.M., 1990. Characterizing plant canopies with hemispherical photographs. Remote Sensing Review, 5: 13-29.

Ringold, P. L., Van Sickle, J., Rasar, K., and Schacher, J., 2003. Use of hemispheric imagery for estimating stream solar exposure. Journal of the American Water Resources Association, 39 (6): 1373-1384.

Salm, B., 1977. Snow forces. Journal of Glaciology, 19 (81): 67-100.

Schleiss, V.G., and Schleiss, W. E., 1970. Avalanche hazard evaluation and forecast, Rogers Pass, Glacier National Park. In Gold, L.W. and G.P. Williams, eds. Ice

engineering and avalanche forecasting. Ottawa, Ont., National Research Council of Canada. Associate Committee on Geotechnical Research, pp. 115-122.

Schneebeli, M., and Johnson, J., 1998. A constant-speed penetrometer for high-resolution snow stratigraphy. Annals of Glaciology, 26: 107-111.

Schneebeli, M., Pielmeier, C., and Johnson, J., 1999. Measuring snow microstructure and hardness using a high resolution penetrometer. Cold Regions Science and Technology, 30 (1-3): 101-114.

Schweizer, J., 1999. Review of dry snow slab avalanche release. Cold Regions Science and Technology, 30 (1-3): 43-57.

Schweizer, J., and Wiesenger, T., 2001. Snow profile interpretation for stability evaluation. Cold Regions Science and Technology, 33 (2-3): 179-188.

Schweizer, J., Kronholm, K., Jamieson, J. B., and Birkeland, K.W., 2008. Review of spatial variability of snowpack properties and its importance for avalanche formation. Cold Regions Science and Technology, 51 (2): 253–272.

Shapiro, L.H., Johnson, J.B., Sturm, M., and Blaisdell, G.L., 1997. Snow Mechanics: Review of the state of knowledge and applications. CRELL Report 97-3, pp. 43.

Sommerfeld, R., and Gubler, H., 1983. Snow avalanches and acoustic emissions, Annals of Glaciology, 4: 271-276.

Sommerfeld, R., 1984. Instructions for using the 250 cm^2 shear frame to evaluate the strength of a buried snow surface. Research Note RM-446. Rocky Mountain Forest and Range Experiment Station, pp. 6.

Sturm, M., Johnson, J., and Holmgren, J., 2004. Variations in the mechanical properties of arctic and subarctic snow at local (1-m) to regional (100-km) scales. Proceedings of the International Symposium on Snow Monitoring and Avalanches, Manali, India, pp. 233-238.

Stewart, W.K., 2002. Spatial variability of slab stability within avalanche starting zones. M.S. thesis, University of Calgary, Calgary, Alberta, Canada, pp. 100.

Teti, P.A. and Pike, R.G., 2005. Selecting and testing an instrument for surveying stream shade. B.C. Journal of Ecosystems and Management, 6 (2): 1-16.

Tonne, F, 1999. Horizontoscope: sunshine duration, etc. pp. 18-19. In: Survey Simple Design Tools; A Report of International Energy Agency, Solar Heating and Cooling Programme Task 21; Energy Conservation in Buildings and Community Systems Programme Annex 29: Daylight in buildings. Editors: Jan de Boer, Hans Erhorn. Fraunhofer Institut für Bauphysik, Stuttgart, Germany, pp. 55.

Trautman, S., Lutz, E., Birkeland, K.W., and Custer, S.G., 2006. Relating wet loose snow avalanching to surficial shear strength. Proceedings of the 2006 International Snow Science Workshop, Telluride, CO., U.S.A., pp.71-78.

USGS, 1998. Geology of Montana. United States Geological Survey digital data produced from 1955 survey. Provided by Natural Resource Information System (NRIS).

Wakahama, G., 1985. Kuroiwa, Daisuke. 1916-1983 – Obituary. Journal of Glaciology, 31 (107): 63-64.

Welzenbach, W., 1930. Untersuchungen ueber die Stratigraphie der Schneeablagerungen und die Mechanik der Schneebewegungen nebst Schlussfolgerungen auf die Methoden der Verbauung. Wissenschaftliche Veröffentlichung des Deutschen und Österreichischen Alpenvereins, 9: 114.

Wilcoxon, F., 1945. Individual comparisons by ranking methods. Biometrics Bulletin, 1, pp. 80-83.

Wilson, J. P., and Gallant, J. C. (Eds.), 2000. Terrain analysis: principles and applications. John Wiley and Sons, pp. 438.

APPENDICES

APPENDIX A:

TABLE OF STRATIGRAPHIC SAMPLING METHODS OF SMP PROFILES

Table 80. Overview of five tested methods of microstructural profiles aggregation, the first of which was applied in the final results presented in this documentation

Aggregation Type	Method	Pros	Cons
Weak Layer Top	Align profiles at top of weak layer	1.Reduces group variance at top of weak layer, where shear occurred; 2.Top of weak layer is more reliable than bottom of weak layer (due to inconsistent thin crust at roots of surface hoar)	1.Variation in weak layer thickness results in greater variance toward weak layer base. 2.Relies on delineation of top of weak layer
Weak Layer Center	Align profiles at weak layer center	1.Reduces potential error caused by an inaccurate (individual) weak layer boundary in half.	1.Relies on delineation of weak layer
Ice Crust within sub-strata	Align profiles at ice crust (approx. 2 cm below weak layer)	1.Does not rely on delineation of weak layer but rather that of the consistent distinct ice crust boundary.	1.Possibly introduces variance due to variability in thickness of thin faceted layer between ice crust and surface hoar layer 2.Relies on delineation of crust
Normalized I	Align profiles at all depths within the weak layer by scaling depth values to the group's median weak layer dimensions	1.Assuming weak layer boundaries to be accurate, eliminates group variance caused by varying stratigraphic dimensions. 2. By eliminating such variability, allows for microstructural values of weak layer to be accurately estimated.	1.Stratigraphic dimensions of weak layer are limited to a group's median weak layer dimensions. 2.Relies on delineation of weak layer
Normalized II	Align profiles at all depths from top of weak layer to crust below by scaling depth values to group's median weak layer dimensions	1.Assuming upper boundary of weak layer and ice crust are accurate, eliminates group variance caused by varying stratigraphic dimensions. 2. By eliminating such variability, allows for micro-structural values of weak layer to be accurately estimated	1.Stratigraphic dimensions of weak layer are limited to a group's median weak layer dimensions. 2.Relies on upper boundary of weak layer and of crust

APPENDIX B:

LIMITATIONS OF THE GIS- AND FIELD OBSERVATION- BASED SKY VISIBILITY ESTIMATION TECHNIQUES

The limitation of the presented GIS model and field observations is that in both cases the hemispheric viewshed is based on a horizontal plane. Since longwave radiation fluxes act perpendicular to surfaces, it would be more accurate to use a hemispheric viewshed that is oriented with the slope plane. Although a GIS-model was developed in the course of this study using a slope-oriented hemisphere, it was not applied because no affordable field measurement technique could verify the results. The Solar Pathfinder and the modified camera mount are designed for a horizontally oriented viewshed.

The implication of utilizing a horizontally oriented hemisphere is that the estimated incoming longwave radiation flux does not directly account for the longwave flux associated with the portion of the slope-oriented viewshed located below the horizon (Figure 188). Since the majority of surfaces visible below the horizon are occupied by forest land, it was assumed that the percentage of the horizontal hemispheric viewshed

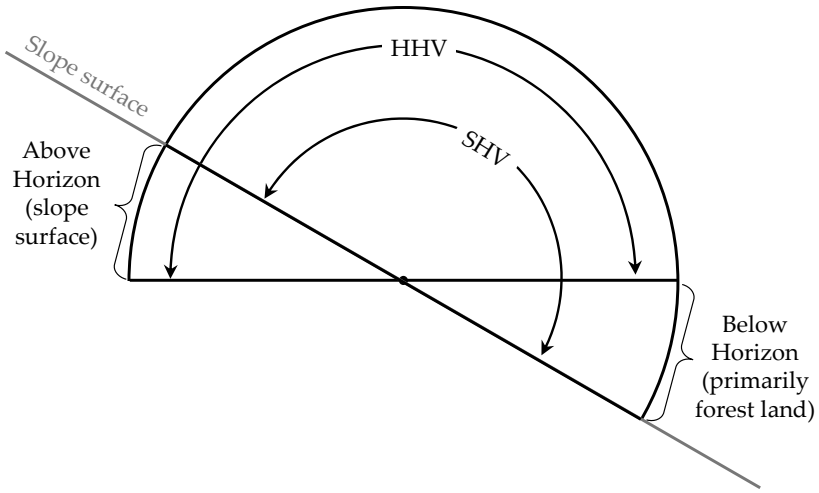

Figure 188. The field observations and GIS model of $v_{\%}$ were estimated using a horizontal hemispheric viewshed (HHV). Although a slope-oriented hemispheric viewshed (SHV) would more accurately model longwave radiation fluxes, because the majority of surfaces visible below the horizon are occupied by forest it was assumed that no major difference in emissivity would be measured.

obstructed by the slope itself (Figure 188) is approximately equal to the percentage of the slope-orientated hemispheric viewshed obstructed by vegetation.

This portion of the slope-oriented viewshed is assumed to have an emissivity equal to the trees, 0.97 and an air temperature equal to T_{air}. In reality, this portion of the viewshed was occupied by forest, snow covered rangeland, and low lying fog a few hundred meters below the study site. These surfaces have previously been estimated as possessing emissivities of 0.97, 1, and 0.875 (Bader and Weilenmann, 1992). The temperature of these surfaces was unknown; although they are at lower elevations than the study site, adiabatic temperatures do not apply as a temperature inversion was often present during the surface hoar formation period.

APPENDIX C:

ATMOSPHERIC DATA FOR RADIATION MODELING

Important estimates of atmospheric conditions, including precipitable water, ozone, and aerosol contents, were obtained from the four nearest stations described in Table 7 (page 123) and illustrated below (Figure 189). The input values for the Bird solar model were derived for January 21 by taking the momentary mean value of Gallatin Field, Dillon, and Idaho Falls station values. Livingston values were excluded for two reasons: 1. including the observations was spatially redundant, given the proximity to, and similarity with, values from Gallatin Field, 2. Livingston was furthest east which, for this time period, was leeward of Gallatin Field.

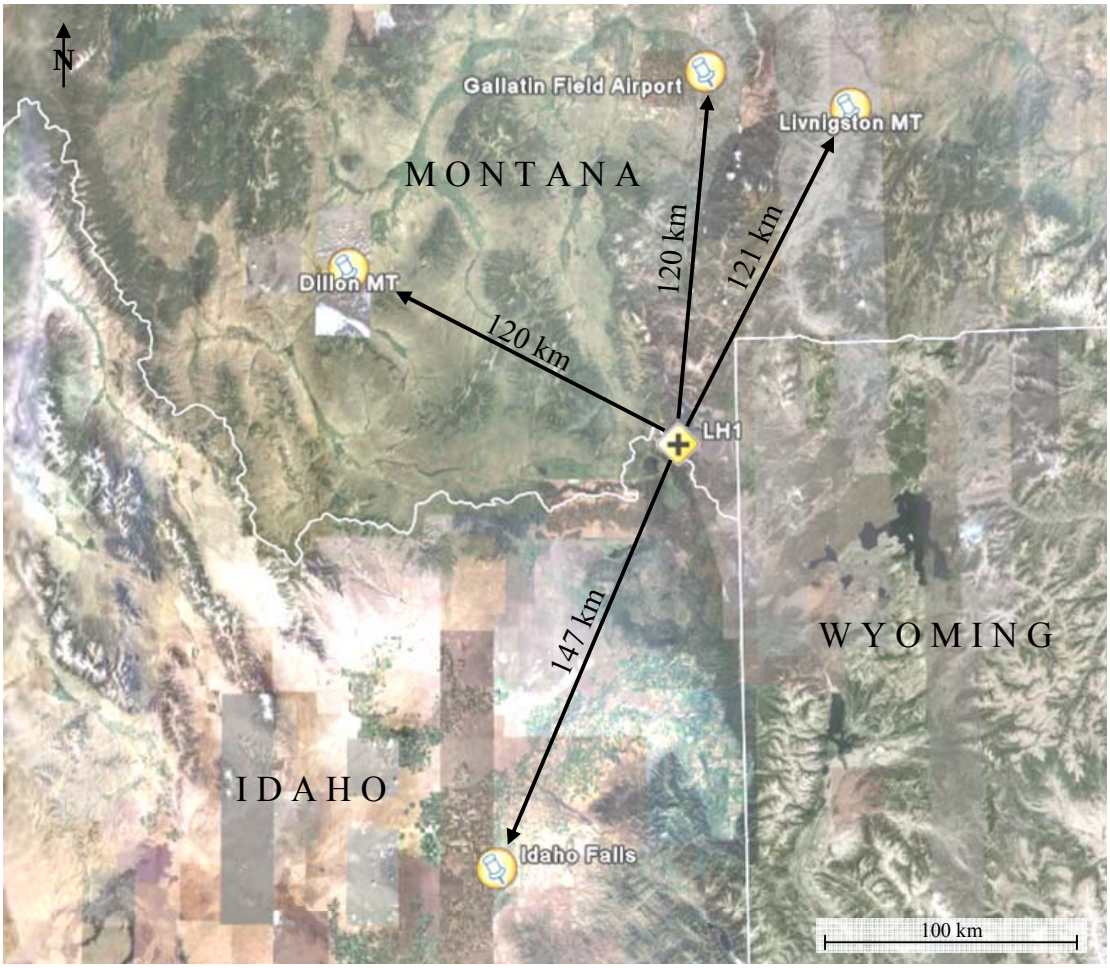

Figure 189. Pseudo-map of Euclidean proximity of the four atmospheric estimates for aerosol content and ozone nearest the Lionhead field site. 'LH1' signifies the location of the field site. White lines represent state boundaries. Google Earth composite image, copyright Google, 2007.

Graphical depictions of the precipitable water content (Figure 190), ozone content (Figure 191), and aerosol content (Figure 192) illustrate the similarities of the values recorded at the different stations during the period of interest.

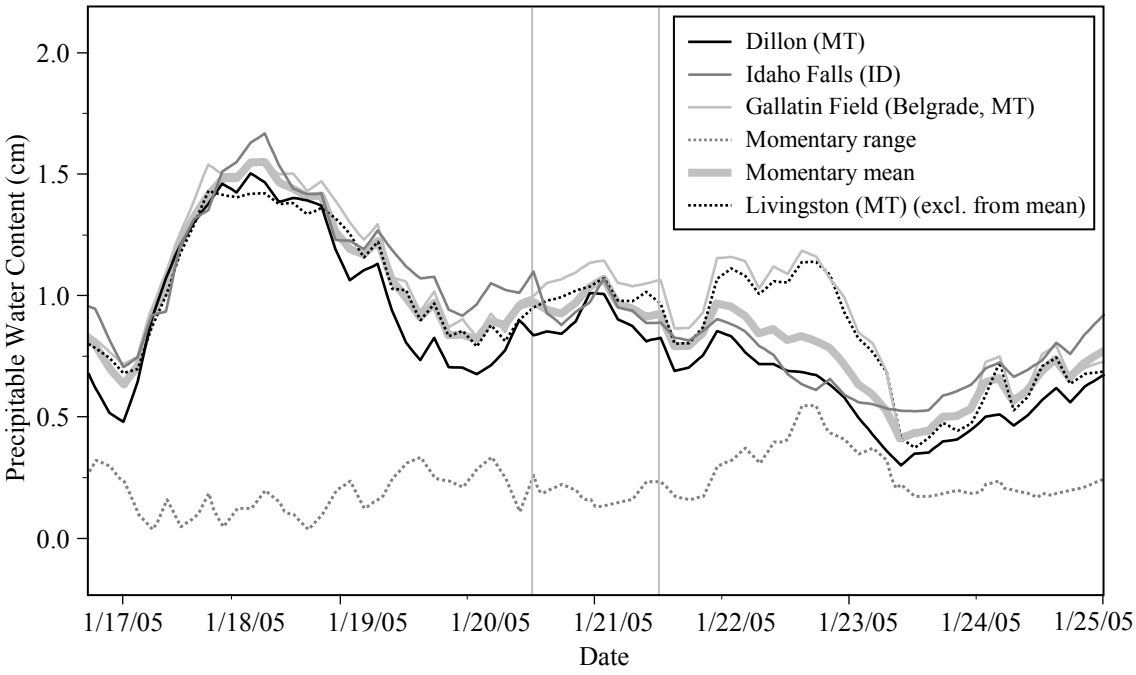

Figure 190. Precipitable water content (cm) values recorded at the four nearest stations. The mean value excludes Livingston values. Vertical gray lines demark observations of January 21, 2005.

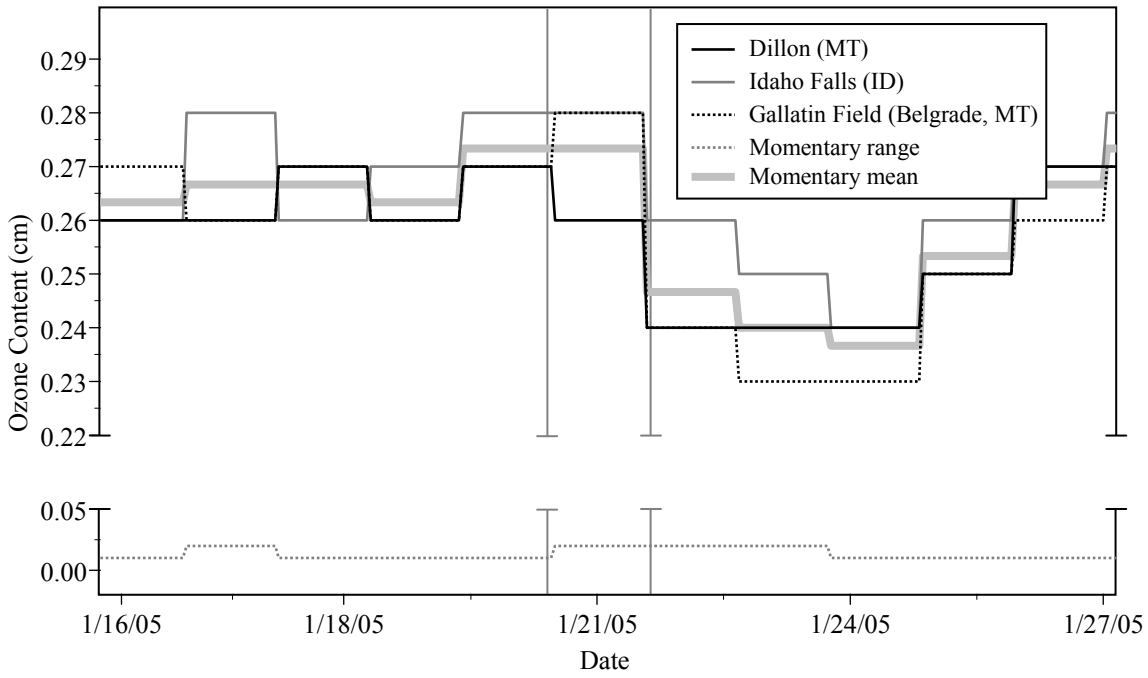

Figure 191. Ozone content (cm) values recorded at the three chosen stations. Vertical gray lines demark observations of January 21, 2005.

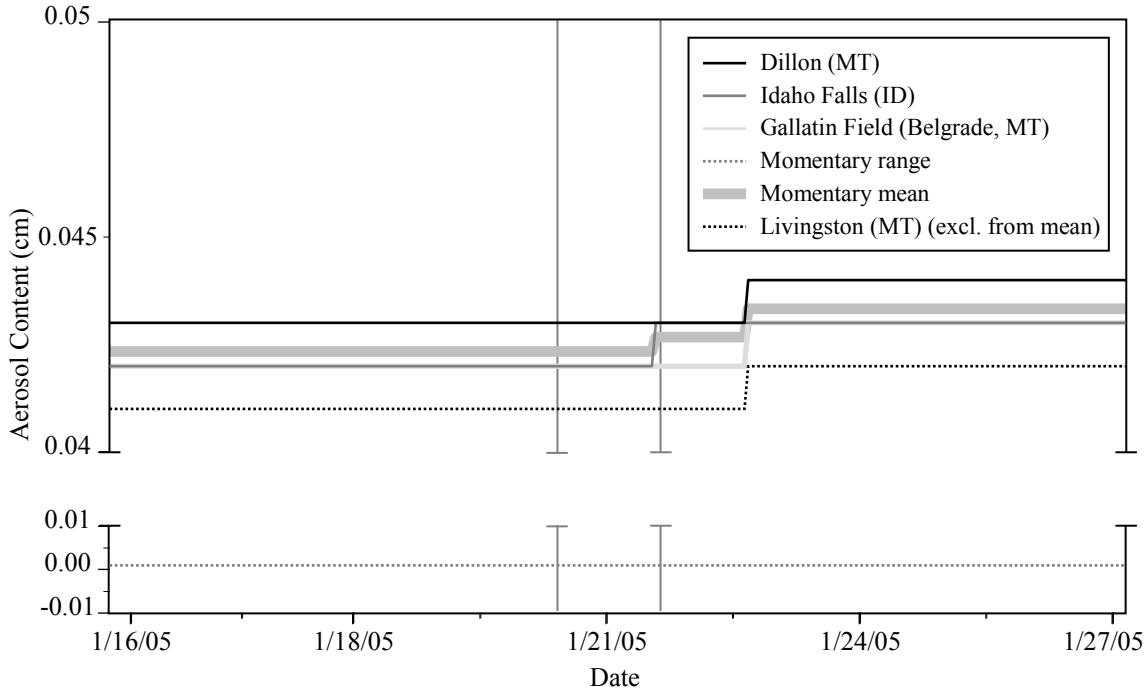

Figure 192. Aerosol content (cm) values recorded at the four nearest stations. The mean value excludes Livingston values. Vertical gray lines demark observations of January 21, 2005.

APPENDIX D:

AVAILABLE SNOW PROFILES

Snow Profile for 1 March, 2005 (Plot 2)

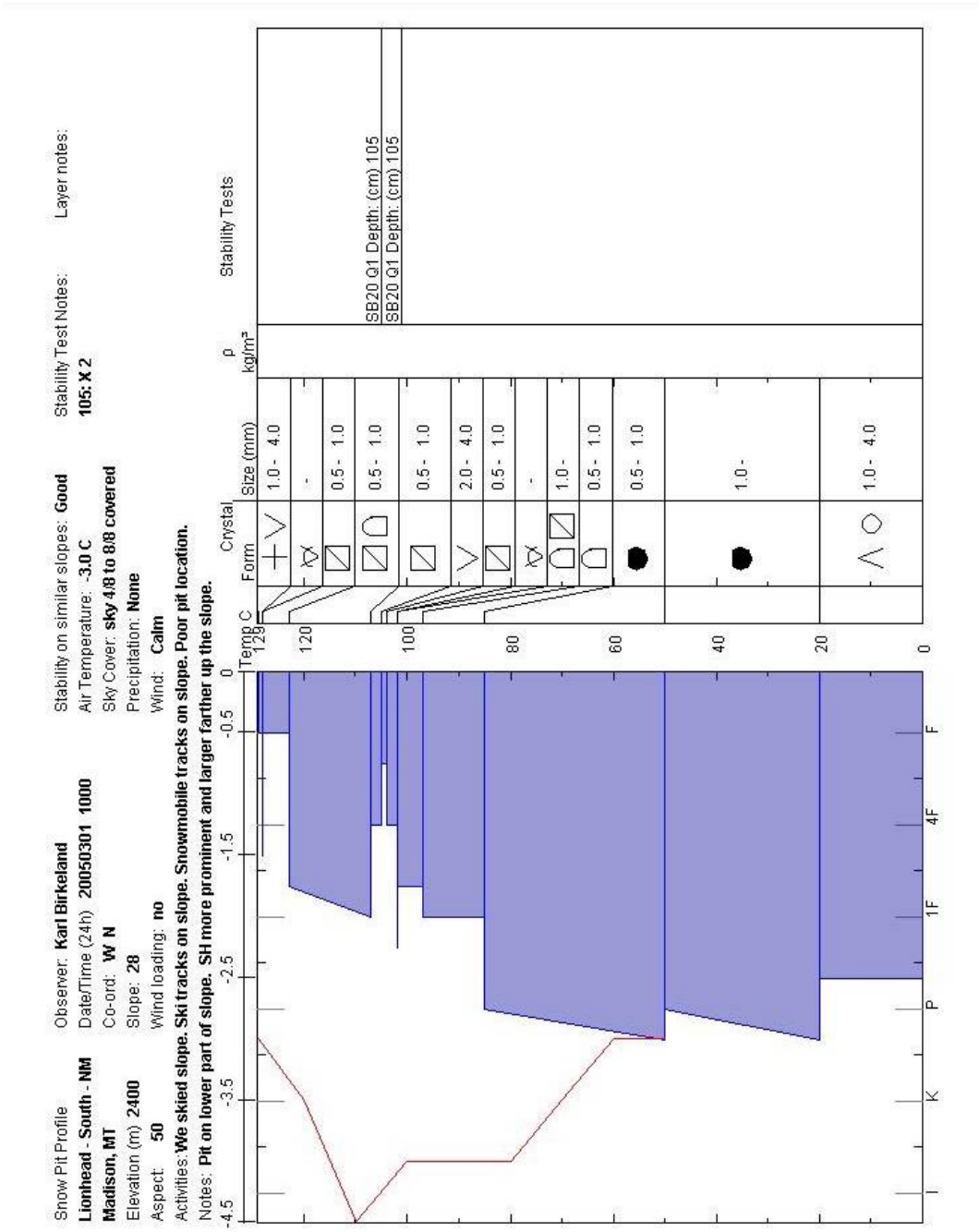

Snow Profile for 8 March, 2005 (Plot 3)

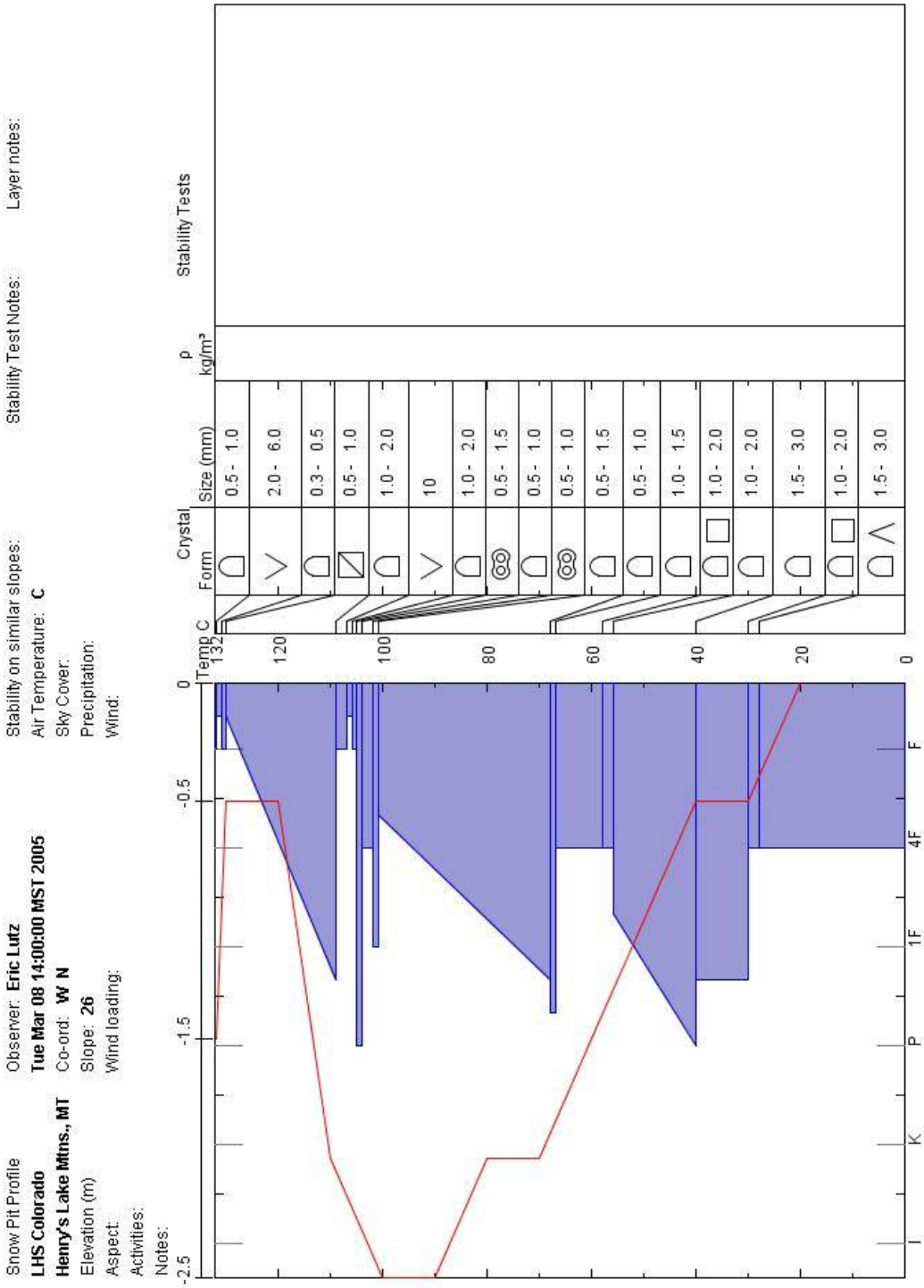

Snow Profile for 14 March, 2005 (Plot 4)

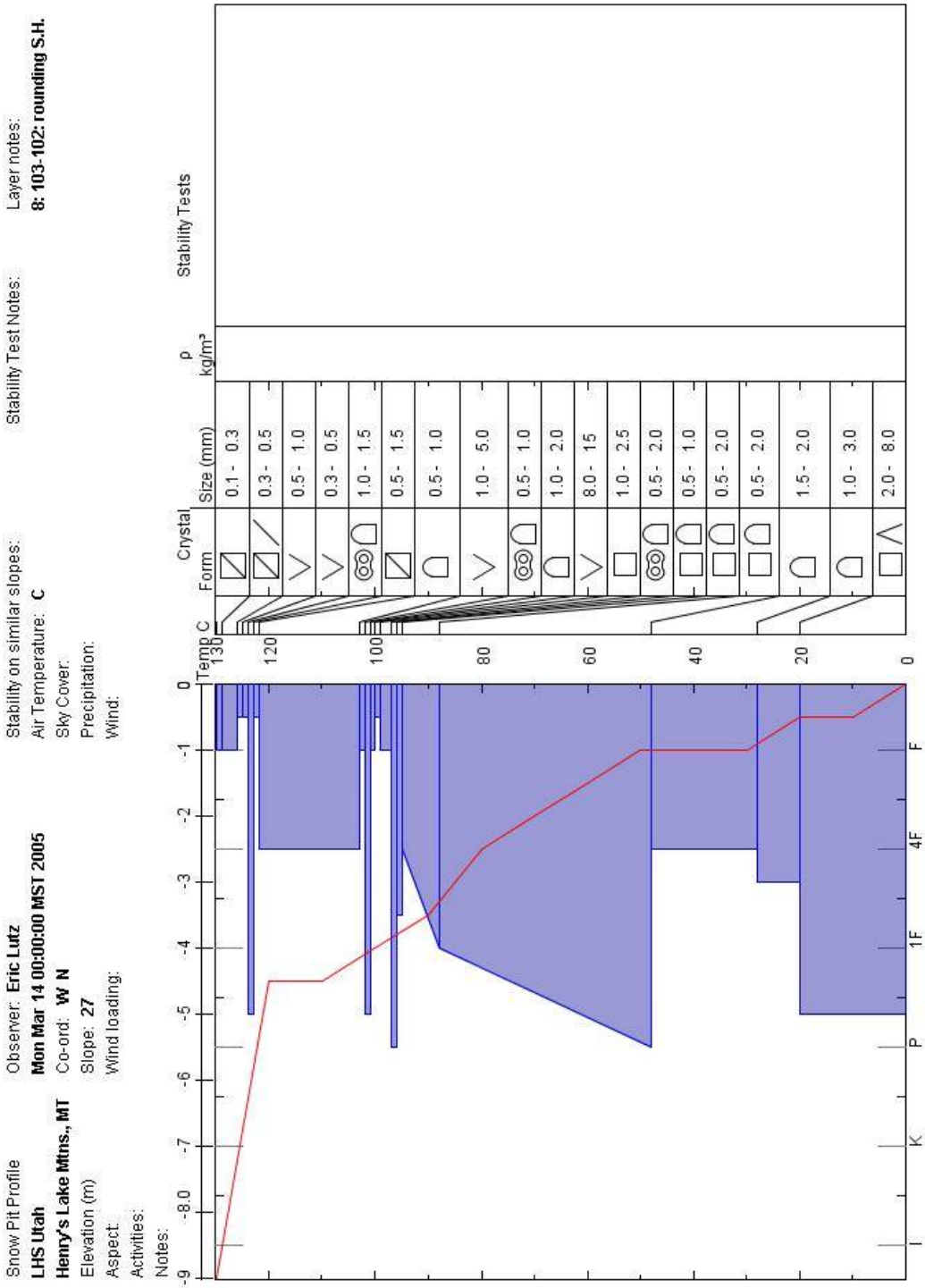

Snow Profile for 21 March, 2005 (Plot 5)

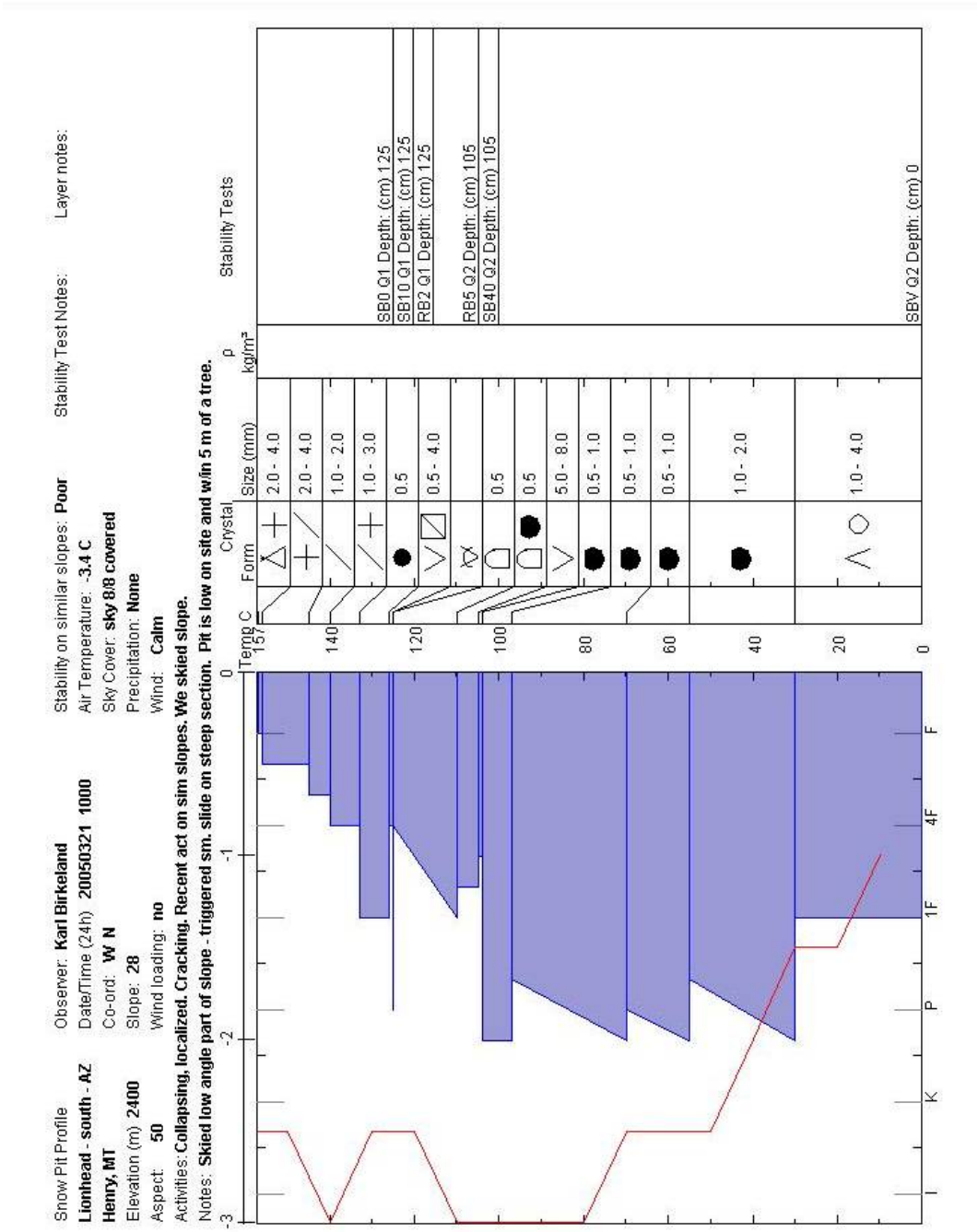

APPENDIX E:

ADDITIONAL POTENTIAL SOURCES OF FIELD AND ANALYSIS ERRORS

SnowMicroPen Measurements

Possible SMP Load Effects

The temporal findings indicated that the snowfall event preceding Plot 5 added 38 mm water equivalent to the slab, and thereby increased V_{slab} by 375 Pa. This added stress appeared to increase L by 0.12 mm to 0.16 mm and decrease σ_{micro} by 0.016 $N \cdot mm^{-2}$ to 0.013 $N \cdot mm^{-2}$ (for plot and sub-plot extents respectively). Under this pretense, it must be considered whether the load of the instrument itself influences measurements.

The SMP weighs approximately 8.5 kg and possesses bipod ski baskets that would apply approximately 5000 Pa vertical stress if the contacted surface supported the baskets. However, as the baskets are settled into the snow, snow compresses below and next to each basket resulting in larger effective 'baskets' or 'footprints'. These packets of compressed snow reduce the applied stress significantly by distributing the load over a larger area of the lower slab. Depending on the stiffness of the lower portion of the slab, the applied stress may influence the weak layer where it is sampled by the SMP (Figure 193).

If slab thickness and hardness were constant across space and time, and if the SMP was always held with the same amount of force on the snowpack, load effects from the SMP would be constant and hence could be corrected for. However, since slab properties vary over space and time, it is safe to assume that the force bulbs from the SMP's bipod baskets vary in their breadth and depth (Figure 193). This may result in the weak layer being affected inconsistently by the SMP's load, which would obviously affect the residual strength or rupture force of microstructures.

Very thin soft slabs may result in the smallest effect, since the force and deformation (compaction) would be directed downward directly under the baskets, resulting in stress and deformation of the weak layer at areas laterally beyond the probe (Scenario 1 of Figure 193). This scenario might also result in a large effect, if the compacted footprint of the baskets compresses enough slab laterally that weak layer below the probe is also influenced.

However, a very thin hard slab would support the force over a larger area. While this would reduce the applied stress of the SMP (by distributing its weight over a larger area), it would also increase the force applied to the zone of the weak layer directly where the probe measures (Scenario 2 of Figure 193). Thick slab may distribute the load most consistently and thereby decrease the influence of the SMP's load on the weak layer (Figure 193).

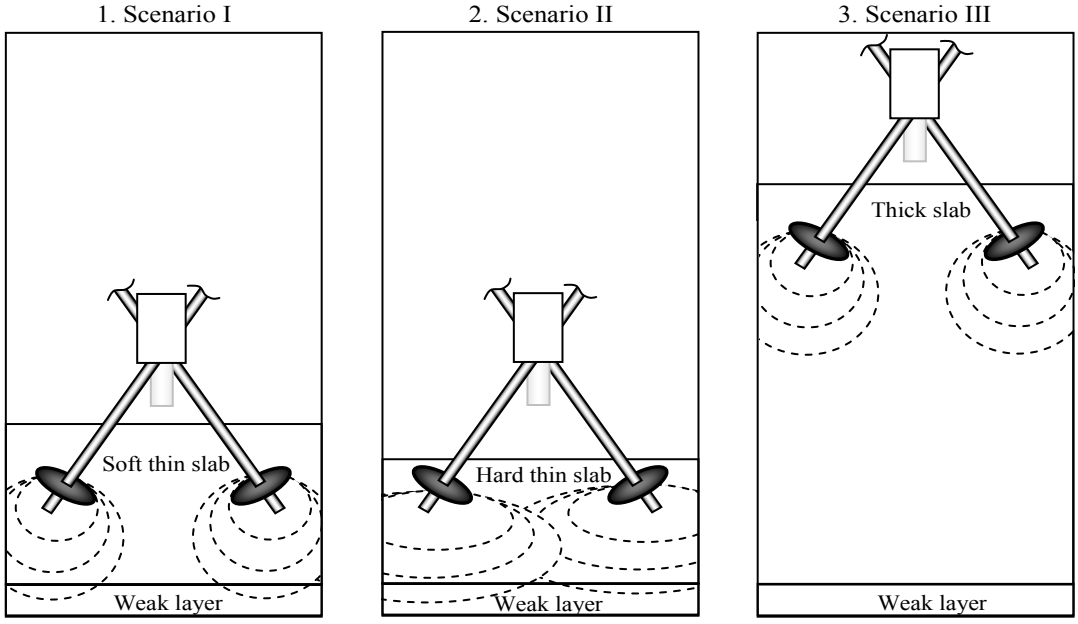

Figure 193. A comparison of three scenarios where a soft slab of three different thicknesses would result in different force concentrations being applied to the weak layer. Dotted lines represent simplified force bulbs near bipod baskets.

Tip-related Snow Deformation

A concern of interpreting microstructural properties from penetrometer profiles involves the interaction between the penetrometer tip and the snow affected by the tip's force bulb (Floyer, 2006). Floyer (2006) interpreted his experimental results as indicating snow deformation was not limited to immediate structures contacting the penetrometer tip, and that a zone of compaction around the tip, rather than the tip itself, was interacting with adjacent structures. This discrepancy may influence microstructural estimates.

Current micro-mechanical models define sample volume as a function of the tip diameter and sampled depth. Floyer's (2006) research indicated that the diameter of a sample volume is likely larger than the tip diameter (since the compaction zone creates a larger cross-sectional area of contact). Because the volumetric extent of the compaction zone is affected by the texture and porosity of the sampled snow, the volume of snow sampled by the SMP probably changes as it passes through different stratigraphic features. The effect of this process on my analysis of transition zones and step-changes between adjacent strata is considered qualitatively.

When we consider the sensor tip passed from poorly bonded, small grain facets into large, vertically and diagonally oriented surface hoar crystals, the complexity of this problem becomes clear. Well preserved buried surface hoar layers possess large pore spaces that cannot transfer stress. However, the large crystal structures themselves may individually apply stress to adjacent structures, before or after their rupture. This results in mechanical interactions beyond the estimated sample volume being recorded. Hence,

estimates derived from the weak layer using current micro-mechanical models may be derived from a greater volumetric extent than is modeled. This may result in an over-estimation of N_f and under-estimation of L.

The small grain facets probably produce a more reproducible compression zone and related force bulb, because more grains are in contact with the tip and their three-dimensional orientation is more isotropic than surface hoar. This means that in the super-stratum, most likely N_f was over-estimated and L was under-estimated more consistently than as experienced in the weak layer. The combined affect is that the apparent step-changes of L may be smaller than it would be if the micro-mechanical models accounted for a compression zone about the sensor tip.

Weather Station Set Up

Weather Station Location

Future studies should carefully consider where to locate weather stations in relation to study sites. Although this weather station was located only 16 m up-slope from the study site, because of an adjacent group of trees, the global shortwave radiation measurements were not representative of the study site during the middle of the day. This hindered a complete verification of the spatially modeled solar radiation values using recorded values.

A pyranometer would be best placed where it most effectively represents the study sites conditions. If possible, ensuring that measurements during the peak solar hours are shadow free would aid in estimating the daily maximum values (large shadows

during the middle of the day make it difficult to estimate what the maximum incoming solar radiation was at noon). In the preparatory stages of a study it would be very useful to conduct a site analysis, utilizing the Solar Pathfinder, to select the best location of the potential weather station sites.

Pyranometer Orientation

Another important consideration in setting up the pyranometer is its three-dimensional orientation. This instrument was oriented parallel to the slope to simulate incoming global shortwave radiation as received on this slope (Kronholm, pers. comm., 2004). Given the slope's orientation, this resulted in cosine (or Lambertian) response or effect for most measurements. The small advantage of a slope-parallel orientation not needing to be transformed is far out-weighed by the gains of a horizontally oriented pyranometer which collects higher quality data that can than be transformed to variable topography.

APPENDIX F:

SEMI-VARIANCE ANALYSIS OF SMP SIGNALS

Micro-fluctuations were also quantified using semi-variance analysis (which determines the variance between force values as a function of lag or measurement distance). This helped verify whether or not the micro-variance in the air signals and snow signals were related to noise For each profile segment, six important semi-variance parameters, including the nugget value (variance between adjacent values), the range and variance values of the first maximum and first minimum, and the population variance were tabulated from the semi-variogram (Figure 194).

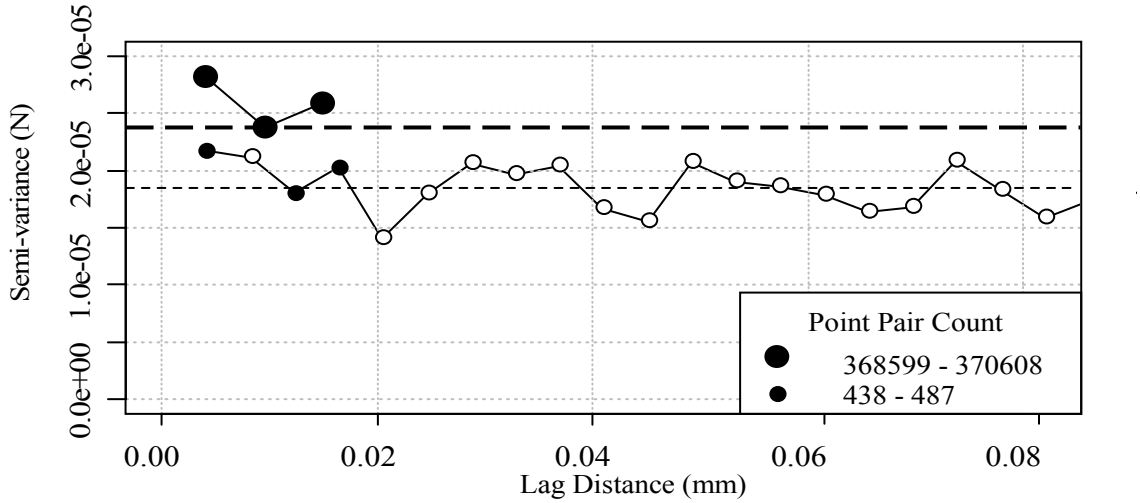

Figure 194. Example of a sample variogram (small points) and the weighted-mean variogram (large points) derived from 55 open air segments. The small black points within the sample variogram were mined and combined with those of another 54 sample variograms to form population averages of the nugget and first and second extreme values (large points). Dotted lines represent corresponding population variances. The negative autocorrelation is indicative of signal noise.

The results from all 55 sample variograms were then pooled using weighted averages that account for the number of SMP profiles and their corresponding point pair counts. This produced a weighted-mean variogram that typifies the auto-correlation of each signal type (open air, air pockets, or snow) (Figure 195). The semi-variance of open air segments possesses a high degree of negative autocorrelation that is typically limited

to immediate neighbors (Figure 195, white circles). This variogram model indicates that immediate neighbors are not correlated, which is typical of noise.

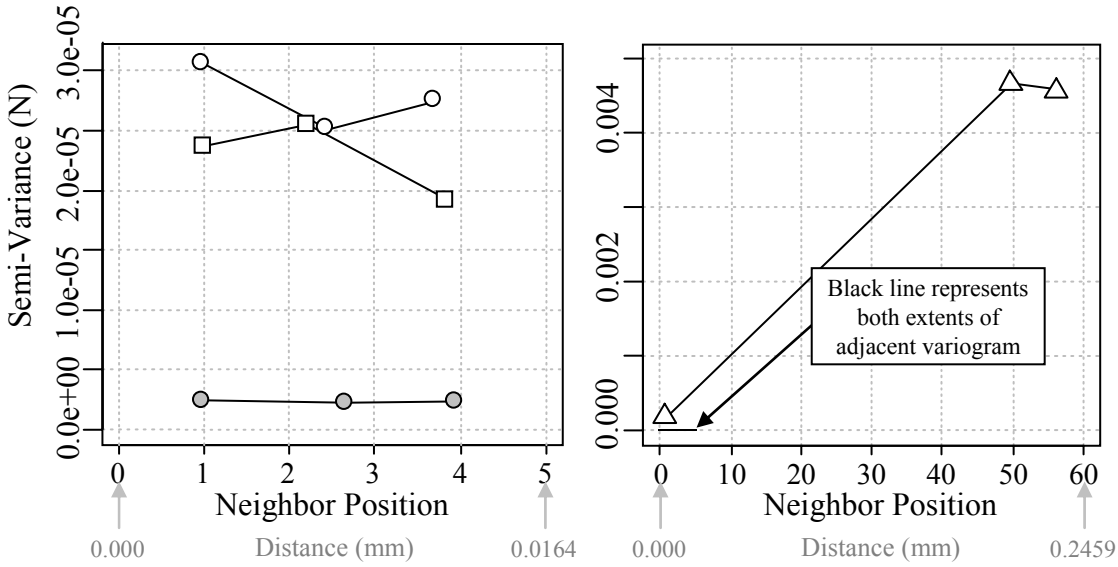

Figure 195. Variograms representing autocorrelation characteristics of the raw resistance signal obtained in open air (white circles), air pockets in weak layer (boxes), entire weak layer (triangles), and a quality 3 air signal (grey circles).

The semi-variance values derived from air pocket segments (Figure 195, white squares) were slightly smaller, indicating that micro-variance is less when the probe is penetrating the snowpack than when the probe is moving through open air. Another discrepancy is that the greatest variance in the air pockets is not limited to adjacent neighbors but rather extends to the first-removed neighbors (distributed over two lag distance instead of only one). This means that typically four force measurements are required to complete force fluctuations instead of only three. A probable explanation for these differences is that, through continuous contact with the penetrometer probe, the snowpack dampens mechanical vibrations generated by the motor or cogs that may otherwise cause the tip to oscillate, which in turn cause the small amplitude - short

wavelength variations in the force signal. Considering that the available contact area of the probe is several magnitudes greater than that of the sensor tip itself, the probe likely absorbs vibrations while the penetrometer moves through snow, reducing the vibrations affecting the sensor and thereby reducing instrument noise.[7, 8]

The 'hole effect' evident in both described variograms indicates the force fluctuations in these signals exhibit periodicity (Pyrcz and Deutsch, 2001 and 2003). Treated as wavelengths, whereby the lag distance of the first minimum equals the return period of a wavelength and the variance at the first maximum equals the wavelength amplitude. If the mechanically induced noise is dampened by probe-snowpack interaction, a decrease in the amplitude and increase of the wavelength may be due to harmonic vibration which possesses a longer wavelength of decreased amplitude.

Quantifying the semi-variance of the force signal obtained in snow samples helps illustrate that the SMP records more than just noise. If noise dominated the signal, the variogram would portray no autocorrelation, or initially negative autocorrelation with periodicity, or a hole effect at greater lag distances, as illustrated by air signals. However, the snow sample variogram depicts a well-defined positive autocorrelation (Figure 195).

The sill (first semi-variance maximum) and population variances for these snow samples are two orders of magnitude (over 100 times) greater than that of the air signal variances. The nugget value equals 1.79×10^{-4} N, indicating that the variance between adjacent resistances values is only one magnitude greater in snow than in air. While it is believed that a large portion of this variance is related to tip-microstructure interactions

(such as instantaneous drops in resistance resulting from ruptured bonds), it is not possible to differentiate between microstructural interactions and instrumental noise using this technique. However, a conservative signal-to-noise ratio for sampling in snow $SNR_{SMP\ in\ Snow}$ can be estimated. If I conservatively assume that the nugget is solely comprised of noise and the partial sill is microstructure-derived, I can calculate a partial sill-to-nugget ratio that represents $SNR_{SMP\ in\ Snow}$

$$SNR_{SMP\ in\ Snow} = (\gamma_{Total\ Sill} - \gamma_{Nugget}) : \gamma_{Nugget}$$

While the signal to noise ratio of air signals is non-existent (e.g., -0.2:1), $SNR_{SMP\ in\ Snow}$ equals 26:1. The discrepancy increases slightly if I relax the assumption that the nugget is comprised solely of noise. This indicates that only a small portion of the variation in resistance values is caused by variance between adjacent measurements, of which only a portion can be assumed to be instrumental noise and not instantaneous microstructural variations.

In the case of open air and air pocket signals, negative auto-correlation corresponded with instrumental noise in the absence of tip-grain interaction. Noise was slightly less when the probe was penetrating the snowpack than when it moved through open air. While in open air the greatest variance is limited to adjacent neighbors, in air pockets the greatest variance extends to the first removed neighbor, presumably due to dampening of mechanical noise.